Transactions of the ASME

Journal of Heat Transfer

Published Quarterly by The American Society of Mechanical Engineers
VOLUME 103 • NUMBER 1 • FEBRUARY 1981

EDITORIAL STAFF
Editor, **J. J. JAKLITSCH, JR.**
Production Editor, **STELLA ROBINSON**
Editorial Prod. Asst., **BETH DARCHI**

HEAT TRANSFER DIVISION
Chairman, **C. L. TIEN**
Secretary, **C. J. CREMERS**
Senior Technical Editor, **K. T. YANG**
Technical Editor, **B. T. CHAO**
Technical Editor, **D. K. EDWARDS**
Technical Editor, **M. EPSTEIN**
Technical Editor, **J. S. LEE**
Technical Editor, **V. E. SCHROCK**
Technical Editor, **R. SIEGEL**

POLICY BOARD, COMMUNICATIONS
Chairman and Vice-President **I. BERMAN**

Members-at-Large
J. W. LOCKE
J. E. ORTLOFF
M. J. RABINS
W. J. WARREN

Policy Board Representatives
Basic Engineering, **F. LANDIS**
General Engineering, **C. F. PHILLIPS**
Industry, **J. E. ORTLOFF**
Power, **R. E. REDER**
Research, **G. P. COOPER**
Codes and Stds., **L. L. ELDER**
Nom. Com. Rep., **J. W. LOCKE**

Business Staff
345 E. 47th St.
New York, N. Y. 10017
(212) 644-7789
Mng. Dir., Publ., **J. J. Frey**

OFFICERS OF THE ASME
President, **CHARLES E. JONES**
Exec. Dir. & Sec'y, **ROGERS B. FINCH**
Treasurer, **ROBERT A. BENNETT**

Journal of Heat Transfer (ISSN 0022-1481) is edited and published quarterly at the offices of The American Society of Mechanical Engineers, United Engineering Center, 345 E. 47th St., New York, N. Y. 10017. ASME-TWX No. 710-581-5267, New York. Second-class postage paid at New York, N. Y., and at additional mailing offices.

CHANGES OF ADDRESS must be received at Society headquarters seven weeks before they are to be effective. Please send old label and new address.

PRICES: To members, $30.00, annually; to nonmembers, $60.00. Single copies, $20.00 each. Add $5.00 for postage to countries outside the United States and Canada.

STATEMENT from By-Laws. The Society shall not be responsible for statements or opinions advanced in papers or . . . printed in its publications (B7.1, para. 3).

COPYRIGHT © 1980 by the American Society of Mechanical Engineers. Reprints from this publication may be made on condition that full credit be given the TRANSACTIONS OF THE ASME, JOURNAL OF HEAT TRANSFER, and the author, and date of publication be stated.

INDEXED by the Engineering Index, Inc.

ANNOUNCEMENTS

TECHNICAL PAPERS

(*Contents continued on page 17*)

Downloaded 04 Feb 2011 to 194.85.80.107. Redistribution subject to ASME license or copyright; see http://www.asme.org/terms/Terms_Use.cfm

TECHNICAL NOTES

Downloaded 04 Feb 2011 to 194.85.80.107. Redistribution subject to ASME license or copyright; see http://www.asme.org/terms/Terms_Use.cfm

J. E. White
Associate Principal Engineer,
Harris Corp.,
Electronic Systems Division,
Melbourne, Fla.

C. J. Cremers
Professor,
Department of Mechanical Engineering,
University of Kentucky,
Lexington, Ky.
Fellow ASME

Prediction of Growth Parameters of Frost Deposits in Forced Convection

Experimental investigations of frost deposition under forced convection conditions have shown that in most cases heat and mass transfer rates become constant after an initial transient period. It is shown that, in such cases, approximately half of the mass transfer from a humid air stream to a frost layer diffuses inward, condenses and increases the density of the frost. The other half is deposited at the surface and increases the thickness of the layer. Approximate expressions for density and thickness of the frost layer are derived and compared with data from the literature and also with experimental work reported in this paper. The correlations are shown to work well for a broad range of experimental conditions.

Introduction

Frost formation in free or forced convection over a cooled surface has been investigated for numerous flow and deposition configurations including cylinders in axisymmetric and crossflow, axial tube flow, refrigerating coils, spheres, flat plates, cryogenic storage tanks, and rectangular ducts. Fifty-four early investigations of such phenomena are discussed in [1] and [2]. These and later studies were primarily concerned with heat and mass transfer in frost formation, and most of them made either direct or indirect inferences about the effective thermal conductivity of frost. Temperatures involved in these investigations ran the gamut from the boiling point of liquid hydrogen to the triple point of water. In all cases, the effective thermal conductivity of frost was recognized as being strongly dependent upon the density and thickness of the frost layer. This makes knowledge of mass transfer behavior in frosting systems essential to analysis of the corresponding heat transfer problem.

The task of tying the heat and mass transfer in frost together is an important step in approaching the point where the former can be calculated from only knowledge of the ambient conditions. For the case of "mature" frost, when the layer has been forming for approximately an hour or more, the problem is somewhat simplified because heat transfer and condensation rates tend to become essentially constant after an initial transient period (e.g. [1, 2]) while the thickness and density of the frost both increase with time. The same effects occur in free convection [3] and it appears that for a wide range of humidities and ambient temperatures the increase in thermal resistance caused by the thickening frost layer is nearly balanced by the decrease in thermal resistance caused by increasing density.

Here we present a model of this problem in which the growth and densification of a frost layer is related to the overall heat and mass transfer to it. For the conditions of steady overall heat and mass transport to a constant density frost layer we show that the density and thickness both increase with the square root of time and that each accounts for about half of the total moisture condensation. Data taken on a cooled flat plate in forced convection exhibit reasonable agreement with the prediction of the model.

Growth and Densification of an Existing Frost Layer

Consider a one-dimensional frost layer that has attained a steady condensation and heat transfer rates at time t_0. The frost surface temperature is found to reach a steady value at the freezing point but the density and thickness continue to increase. We refer to this type of frost behavior as quasi-steady to distinguish it from a true steady state problem [2]. The density and thickness at time t_0 are given by ρ_0 and δ_0, respectively. Assuming there are no density gradients in the frost, conservation of mass for the frost layer may be written as

$$\delta \frac{d\rho}{dt} + \rho \frac{d\delta}{dt} = g_\delta \tag{1}$$

where g_δ is the vapor flux through the plane of the frost surface and, as described above, is a constant for given external conditions. The first term in equation (1) is the densification rate of the frost, and the second term is the condensation rate at the surface. Let the latter be designated as g_c. Equation (1) may then be written

$$\delta \frac{d\rho}{dt} = g_\delta - g_c. \tag{2}$$

Let ϕ be defined by

$$\phi = \frac{g_\delta - g_c}{g_c} \tag{3}$$

Then dividing equation (2) by the surface condensation rate g_c yields

$$\frac{\delta}{\rho}\frac{d\rho}{d\delta} = \phi. \tag{4}$$

This can be integrated to yield

$$\frac{\rho}{\rho_0} = \left[\frac{\delta}{\delta_0}\right]^\phi. \tag{5}$$

A dimensionless time τ may now be defined by

$$\tau = \frac{g_\delta(t - t_0)}{\rho_0 \delta_0} \tag{6}$$

and then equation (5) can be used with equation (1) to yield

$$\frac{\delta}{\delta_0} = (1 + \tau)^{1/\phi + 1} \tag{7}$$

and

$$\frac{\rho}{\rho_0} = (1 + \tau)^{\phi/\phi + 1}. \tag{8}$$

Now it has been demonstrated [4] that an effective thermal conductance can be defined for that portion of the total heat flux that excludes mass transfer effects. The experimental data indicate that, for a given driving temperature difference, this will be proportional to the density or, what is equivalent, to the specific gravity γ of the frost. Then

$$q - i_{sg} g_\delta = \frac{\Lambda \gamma (T_\delta - T_w)}{\delta} = \frac{\Lambda \rho_0}{\rho_f \delta_0}(T_\delta - T_w)(1 + \tau)^{\phi - 1/\phi + 1}. \tag{9}$$

Here Λ is a proportionality constant with the dimensions of thermal conductivity; q is the total heat flux; i_{sg} is the latent heat of sublimation; and ρ_f is the density of water.

Therefore, for the heat flux to be constant as observed for these conditions it is necessary that ϕ approach a value of unity, because T_δ is constant for a constant mass transfer rate to the frost layer. The interpretation of this is that condensation at the surface equals diffusion of water vapor inward from the surface of a quasi-steady frost layer. Thus, for this particular case,

Contributed by the Heat Transfer Division for publication in the JOURNAL OF HEAT TRANSFER. Manuscript received by the Heat Transfer Division, May 27, 1980.

Copyright © 1981 by ASME

Downloaded 20 Dec 2010 to 194.27.225.72. Redistribution subject to ASME license or copyright; see http://www.asme.org/terms/Terms_Use.cfm

$$\frac{\rho}{\rho_0} = \frac{\delta}{\delta_0} = \sqrt{1+\tau}\,. \tag{10}$$

It should be noted that the above analysis carries with it the implication that in this quasi-steady state, half the mass of water vapor adds to the densification of the frost while the other half adds to the thickness of the frost.

Prediction of Densities and Thicknessess Starting at Zero Time

The disadvantage of the analysis presented thus far is that knowledge of quantites not generally known a priori from basic engineering information is required. Further approximations enable us to make predictions of thickness and density growth without reference values of density and thickness.

It was noted by the authors that when mass per unit area of frost is plotted as a function of time, a reasonable fit for the data is a straight line passing through the origin. A typical result is shown in Fig. 1 with the severe scatter to be expected because of the difficulty of measurement. Similar results were noted in previous work [1]. The inplication is that, as a first order approximation, the quasi-steady mass flux can be extrapolated to zero time for the purpose of determining how much mass has been deposited at any given time.

This, in conjunction with the hypothesis that densification of frost accounts for half the mass added to the frost layer, suggests that an approximate solution for density of the frost might be given by

$$\rho = c(g_\delta t)^{1/2} \tag{11}$$

$$\delta = \frac{1}{c}(g_\delta t)^{1/2} \tag{12}$$

where c is a constant.

Evaluation of the constant in equations (11) and (12) cannot be done in the usual manner since there is no reference value available for either the density or thickness. However, it is possible to proceed further by consideration of the thermal aspects of the problem. First divide equation (11) by equation (12). Then $c = (\rho/\delta)^{1/2}$ which can be evaluated from equation (9) so that

$$\rho = \left[\frac{\rho_f(q - i_{sg}g_\delta)}{\Lambda(T_\delta - T_w)}\right]^{1/2}(g_\delta t)^{1/2}. \tag{13}$$

In cases where concentration profiles have a minimal effect on the usual heat transfer coefficient, we may write

$$q - i_{sg}g_\delta = h(T_\infty - T_\delta) \tag{14}$$

where T_∞ is a free-stream or bulk temperature. Making this substitution and dividing both sides of the resulting equation by $\sqrt{\rho_s X}$ where ρ_s is the density of the ice and X is a characteristic length gives

$$\frac{\rho}{\rho_s}\left[\frac{\Lambda\gamma_s(T_\delta - T_w)}{hX(T_\infty - T_\delta)}\right]^{1/2} = \left[\frac{g_\delta t}{\rho_s X}\right]^{1/2}. \tag{15}$$

Also, it follows that

$$\frac{\delta}{X}\left[\frac{hX(T_\infty - T_\delta)}{\gamma_s\Lambda(T_\delta - T_w)}\right]^{1/2} = \left[\frac{g_\delta t}{\rho_s X}\right]^{1/2}. \tag{16}$$

The quantity $hX/\gamma_s\Lambda$ is essentially the ratio of the thermal conductance of the boundary layer to the thermal conductance of the ice making up the frost and so is of the form of a Biot number. This suggests that the characteristic length X might be the same for a fluid dynamics analysis, an energy transfer analysis, or for a problem involving frost deposition.

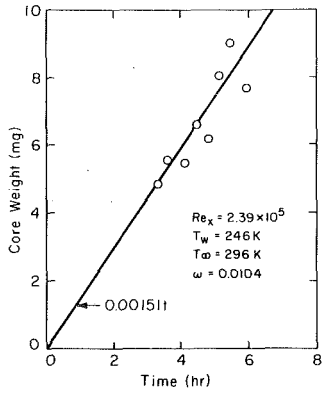

Fig. 1 Frost deposition as a function of time

Therefore, define a Biot number for frost deposition by

$$\mathrm{Bi}_F = \frac{hX}{\Lambda\gamma_s} \tag{17}$$

and a dimensionless temperature by

$$\theta_i = \frac{T_\delta - T_w}{T_\infty - T_\delta}. \tag{18}$$

Here θ_i is clearly related to the insulating value of the frost, since it would be zero if the frost were a perfect conductor and unbounded if the frost were a perfect insulator.

Define a new dimensionless time Υ by

$$\Upsilon = \frac{g_\delta t}{\rho_s X}. \tag{19}$$

Then equations (15) and (16) become

$$\frac{\rho}{\rho_s}\left[\frac{\theta_i}{\mathrm{Bi}_F}\right]^{1/2} = \Upsilon^{1/2} \tag{20}$$

and

$$\frac{\delta}{X}\left[\frac{\mathrm{Bi}_F}{\theta_i}\right]^{1/2} = \Upsilon^{1/2}. \tag{21}$$

Only [1] and [2] present sufficient data, particularly the information required to calculate Λ, for comparison with the above theory. Λ was evaluated from these data as

$$\Lambda = A_2\left[B_1 + \frac{B_2}{2}(T_\delta + T_w)\right] \tag{22}$$

with the constants given by $A_2 = 35.4$, $B_1 = -0.0134$ W/m-K, and $B_2 = 0.000157$ W/m-K^2. This expression is developed fully by White [2]. The constants were empirically determined using data from the literature [1] and data observed by the authors [4].

Experimental Apparatus

Numerous frost deposition observations were made on a cooled flat plate in a rectangular duct and detailed descriptions of these and the equipment are given in [2]. A schematic of the test section is shown

Nomenclature

h = convective heat transfer coefficient
g = mass flux density
q = heat flux density
i_{sg} = heat of sublimation
t = time
T = temperature
X = characteristic distance
γ = specific gravity
δ = frost thickness
θ_i = dimensionless temperature (equation (18))
Λ = effective thermal conductance (equation (22))
ρ = density
τ = dimensionless time after reference state is reached (equation (6))
Υ = dimensionless time after onset of frosting (equation (19))
ϕ = dimensionless ratio of densification rate to thickening rate (equation (3))

Subscripts

c = thickening of frost layer
f = water
F = frost
0 = reference state, when quasi-steady condition is reached
s = ice
w = wall
δ = surface
∞ = ambient

Downloaded 20 Dec 2010 to 194.27.225.72. Redistribution subject to ASME license or copyright; see http://www.asme.org/terms/Terms_Use.cfm

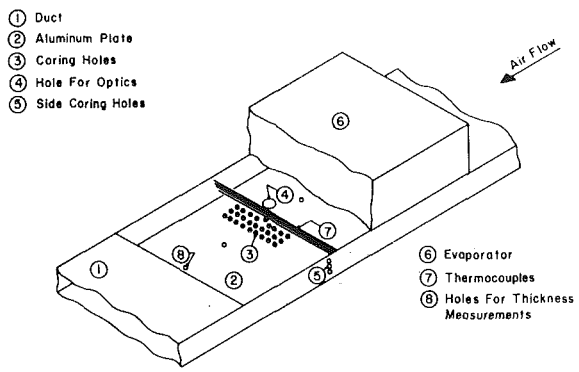

Fig. 2 Schematic view of apparatus

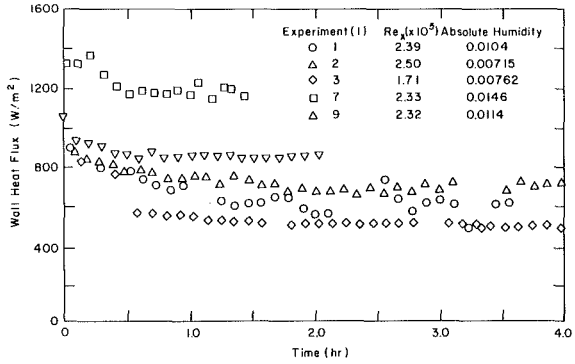

Fig. 3 Heat flux to wall

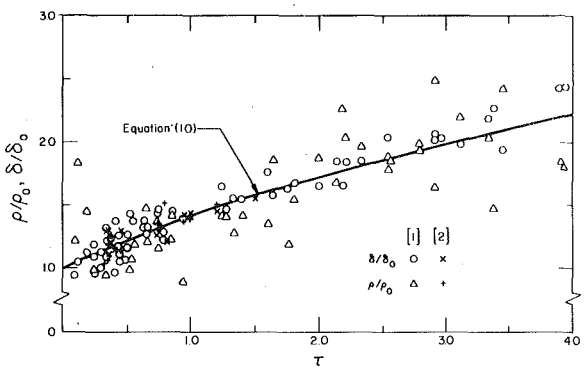

Fig. 4 Frost growth and densification—time measured from reference state

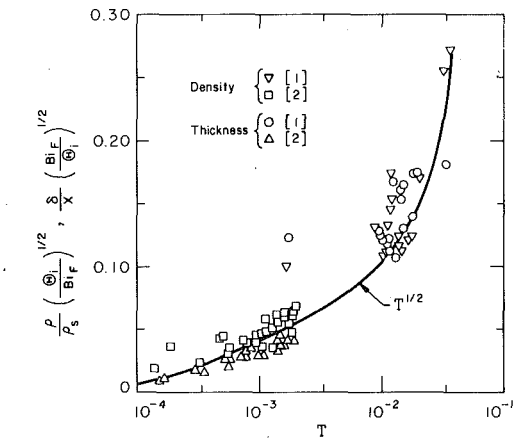

Fig. 5 Frost growth and densification—time measured from onset of frosting

in Fig. 2. A flooded aluminum evaporator was placed on top of the duct as shown. This placement obviated the need for internal fins in the evaporator. Pressure was controlled in the evaporator by use of an evaporator pressure regulator. The refrigerant used was Freon 12.

Moist air was forced through the duct and past the test section by a draw-through centrifugal blower. Velocity profile measurements indicated the flow to be of entry length type with very little acceleration caused by boundary layer development. Reynolds numbers varied from laminar to transitional.

Density was determined by coring with a sharp-edged tube of about 1.5 mm i.d. This collects a sample of frost for which the density is obtained from volume and mass measurements. This was done first from the side to see if density gradients could be detected; however, none were, which agrees with the findings of previous investigations (e.g. [1, 5, 6]). Trammel, et al. [7, 8] reported the existence of density gradients in frost formed on a flat plate in forced convection. However, they measured only the total mass per unit area for a known thickness of frost. Then assuming that there was a decreasing density in the direction away from the surface, they intuitively constructed a density distribution which agreed with the total mass measurements. Shah [1] has shown, theoretically, that the density should increase in the outward direction but could not detect this with his measurements. We recognize that there probably is a variation in density in the direction of heat flow but it is sufficiently small that, as far as our measurements are concerned, density is constant. The densities reported herein, then, come from cores taken normal to the plate with the assumption that the ice mass is uniformly distributed.

Heat transfer rates at the wall were measured with a heat-flux meter having a calibration uncertainty of ±10 percent. Temperature distributions within the frost layers were measured by thermocouples stretched across the duct as shown. These were not needed for this study but were used along with the heat-flux measurements to infer effective thermal conductances reported elsewhere [4]. Surface temperatures were measured by monitoring the thermocouples as they became covered with frost so that temperatures of the surface at other thicknesses could be obtained by interpolation. The actual temperature measurements were made with an uncertainty of ±0.1K. Thicknesses were measured by advancing a depth micrometer to the frost surface and subtracting the reading from the duct height. Deposition rates measured by taking core samples and densities were calculated from mass/volume measurements. The uncertainty in these measurements was caused by the irregularity of the frost surface. It is estimated that the results reported for both thickness and density are reproducible to within ±15 percent at experimental times greater than 30 min.

Results and Discussion

Some typical heat-flux distributions are shown in Fig. 3. These results and those for the frost deposition rate in Fig. 1 substantiated the observations of many others (e. g. [1, 9, 10]) that heat and mass transfer rates tend to become constant after an initial transient period. Periodic fluctuations were observed in heat fluxes when conditions were such that melting occurred at the surface. In such cases, the fluctuations were about a mean steady value. The same sort of cyclic behavior was reported in references [3, 7, 8, 11] and [12] for both free and forced convection. Apparently, condensation is first from the vapor to the solid phase until the thermal resistance of the frost layer is sufficiently high that the surface temperature reaches the triple point temperature. Condensation then occurs to the liquid phase which then somewhat fills the voids causing a denser matrix with increased thermal conductance and a concomitant reduction in surface temperature. Frost then forms directly from the vapor and the process repeats itself.

The prediction of density and thickness, starting with given initial values of these at some reference time, is given by equation (10). This is compared with data from [1] and [2] in Fig. 4. The predictions for the case of starting at zero time, given by equation (20) and (21), are shown in Fig. 5 along with the data from [1] and [2]. In the second case, the characteristic length chosen for correlations of the authors' data was the distance from the leading edge as their surface was in a duct with slowly developing flow. For Shah's data [1], taken in a duct with

Downloaded 20 Dec 2010 to 194.27.225.72. Redistribution subject to ASME license or copyright; see http://www.asme.org/terms/Terms_Use.cfm

an apparently fully developed flow, the duct height was used.

It is difficult to compare the theory developed here with data and other predictions from the literature. However, equations (11) and (12), which postulate a square root of time behavior, can be fitted quite well to frost thickness or density data such as those reported in [5, 11, 13, 14].

The several theories which have been developed for frosting under diverse conditions all predict roughly the same kind of behavior for growth and densification. Basing his work on crystal growth models, Mehra [3] found a square-root of time dependence for the thickness of frost on a vertical cylinder in free-convection as did Schneider [6] for the case of horizontal cylinders in cross-flow. Jones and Parker [17], using a diffusional model found thickness distributions that have a time dependence not explicitly of a square-root form but which can be well matched with such a curve. Finally, Dietenberger, et al. [16] presented theoretical results based on a heat and mass transfer model which involves the Lewis analogy. However, the description of the theory is sufficiently limited that one cannot tell how the thickness and density explicitly vary with time. However, again, their curves can be well matched with ones having a square-root of time dependence.

To confirm the hypothesis advanced concerning equal contributions of the densification and thickening, square-root of time curves were fitted to the experimental densities and thickness. Typical examples are given in [2]. These curves were then differentiated and used with equation (2) to test the hypothesis that densification accounts for half the mass deposition to a frost layer. This procedure was carried out for 14 experiments. The mean value of densification divided by the total mass transfer rate was 0.495, with a high value of 0.631 and a low value of 0.401. The data for the most part agreed with the hypothesis within two percent. As mentioned previously, the mass-transfer rates were found by fitting a least-squares straight line through the data and passing it through the origin. Differentiation yielded the mass transfer rate.

Conclusion

The hypothesis that half the mass transfer to a frost layer results in internal densification is a useful one which leads to reasonable expressions for density and thickness of frost layers as functions of time. Correlation of the expressions for thickness and density starting from zero time are good, considering the number of variables and the wide range of experimental conditions. The results, as they stand, can be used as conceptual models for the development of models for overall thermal conductance. However, if one wishes to directly calculate density or thickness, the mass transfer rate must first be calculated for the quasi-steady condition. This may be done with thickness models such as those in [2, 6, 15, 16] used along with the internal densification hypothesis above.

Acknowledgment

The authors are grateful to the National Science Foundation for partial support of this work under grants GK-12989 and ENG 75-18401.

References

1 Shah, Y. T., "Theory of Frost Formation," Sc.D. thesis, M.I.T., 1968.

2 White, J. E. "Heat and Mass Transfer in Thick Frost Layers," Ph.D. dissertation, University of Kentucky, 1973.

3 Mehra, V. K., "Frost Formation on a Vertical Cylinder with Natural Convection," M. S. Thesis, University of Kentucky, 1980.

4 Cremers, C. J., and White, J. E., "Effective Thermal Conductivity of Frost," submitted to *Proceedings of the XVI International Thermal Conductivity Conf.*, D. C. Larson, ed., Plenum, 1980.

5 Yamakawa, N., Takahashi, N., and Ohtani, S., "Forced Convection Heat and Mass Transfer under Frost Conditions," *Heat Transfer-Japanese Research*, Vol. 1, 1972, pp. 1–10.

6 Schneider, H. W., "Equation of the Growth Rate of Frost Forming on Cooled Surfaces," *International Journal of Heat and Mass Transfer*, Vol. 21, 1978, pp. 1019–1024.

7 Trammel, G. J., Canterbury, J. and Killgore, E. M., "Heat Transfer from Humid Air to a Horizontal Flat Plate Held at Sub-Freezing Temperatures," *ASHRAE Transactions*, Vol. 73, 1967, pp. IV.3.1–IV.3.6.

8 Trammel, G. J., Little, D. C., and Killgore, E. M., "A Study of Frost Formed on a Flat Plate Held at Sub-Freezing Temperature," *ASHRAE Journal*, July, 1968, pp. 42–47.

9 Brian, P. L. T., Reid, R. C., and Brazinsky, I., "Cryogenic Frost Properties," *Cryogenic Technology*, Vol. 5, 1969, pp. 205–212.

10 Brian, P. L. T., Reid, R. C., and Shah, Y. T., "Frost Deposition on Cold Surfaces," *Industrial and Engineering Chemistry Fundamentals*, Vol. 9, 1970, pp. 375–380.

11 Tajima, O., Yamada, H., Kobayashi, Y., and Mizutani, C., "Frost Formation on Air Coolers Part 1: Natural Convection for a Cooled Plate Facing Upward," *Heat Transfer-Japanese Research*, Vol. 1, 1972, pp. 39–48.

12 Kennedy, L. A., and Goodman, J., "Free Convection Heat and Mass Transfer under Conditions of Frost Deposition," *International Journal of Heat and Mass Transfer*, Vol. 17, 1974, pp. 477–484.

13 Yonko, J. D., and Sepsy, C. F., "An Investigation of the Thermal Conductivity of Frost while Forming on a Flat Horizontal Plate," *ASHRAE Transactions*, Vol. 73, 1967, pp. I.1.1–I.1.10.

14 Nakamura, H., "Free Convective Heat Transfer from Humid Air to a Vertical Plate under Frosting Conditions," *Bulletin of the Japanese Society of Mechanical Engineers*, Vol. 17, 1974, pp. 75–82.

15 Jones, B. W., and Parker, J. D., "Frost Formation with Varying Environmental Parameters," ASME JOURNAL OF HEAT TRANSFER, Vol. 97, 1975, pp. 255–259.

16 Dietenberger, M., Kumar, P., and Luers, J., "Frost Formation on an Airfoil: a Mathematical Model I," NASA CR 3129, 1979.

Downloaded 20 Dec 2010 to 194.27.225.72. Redistribution subject to ASME license or copyright; see http://www.asme.org/terms/Terms_Use.cfm

The Transition from Natural-Convection-Controlled Freezing to Conduction-Controlled Freezing

E. M. Sparrow
Fellow ASME.

J. W. Ramsey

J. S. Harris

Department of Mechanical Engineering,
University of Minnesota,
Minneapolis, Minn. 55455

Experiments were performed to study the transition between freezing controlled by natural convection in the liquid adjacent to a freezing interface and freezing controlled by heat conduction in the solidified material. The freezing took place on a cooled vertical tube immersed in an initially superheated liquid contained in an adiabatic-walled vessel. At early and intermediate times, temperature differences throughout the liquid induce a vigorous natural convection motion which retards freezing, but the temperature differences diminish with time and natural convection ebbs. At large times, the freezing rate is fully controlled by heat conduction in the solidified material. The frozen specimens for short and intermediate freezing times are smooth-surfaced and tapered, while those for large times are straight-sided and have surfaces that are overlaid with a thicket of large discrete crystals. These characteristics correspond respectively to those of natural-convection-controlled freezing and conduction-controlled freezing. At early times, the measured mass of the frozen material is identical to that for natural-convection-controlled freezing. At later times, the frozen mass tends to approach that for conduction-controlled freezing, but a residual deficit remains.

Introduction

The recent years have witnessed an upsurge of published papers dealing with freezing, melting, and related problems characterized by a moving interface. For the most part, both in textbooks and in the archival literature (e.g., [1–4]), conduction is assumed to be the sole mode of heat transport. However, in recent experimental work for both freezing and melting, it was demonstrated that natural convection may be at least as important a transport mode as is conduction.

The present research was undertaken to provide fundamental information about the roles of solid-phase conduction and liquid-phase natural convection in freezing. The objective of the paper is to document aspects of the freezing process which have not heretofore been identified or explored in the heat transfer literature. Although the reported freezing experiments are carried out using a specific substance, the phenomena disclosed by the experiments should be operative for freezing in general, except, perhaps, for substances for which there is a density extremum in the liquid phase.

Freezing of a liquid on a cooled surface may be classified according to the participating heat transfer processes. If the liquid is isothermal at its fusion temperature, natural convection does not occur, and the rate of freezing is controlled by conduction heat transfer in the solidified material. This mode of freezing may be termed conduction-controlled freezing. When the temperature of the liquid is above the fusion value, there will be temperature nonuniformities through the liquid, and natural convection will generally occur [5, 6]. This gives rise to a convective heat transfer from the liquid to the freezing interface. It has been demonstrated both analytically [7] and experimentally [6] that the presence of natural convection can significantly retard the rate of freezing and ultimately terminate the freezing altogether.

In both [6] and [7], the temperature difference across the liquid was maintained constant during the freezing period, with the result that the natural convection was also maintained at full strength. Thus, for example, in [6], where the liquid was contained in a vertical cylindrical vessel and the freezing took place on a vertical, co-axial water-cooled tube, the outer surface of the containment vessel was maintained at a constant temperature by a thermostatically controlled water bath.

The maintenance of the natural convection at full strength is the key feature in the aforementioned ultimate suppression of freezing. To demonstrate this, it may be noted that the heat conducted across the solidified layer from the freezing interface to the cooled surface is mainly the sum of two contributions:[1] (1) the latent heat associated with the phase change and (2) the heat transfer by natural convection from the bulk liquid to the interface. As the solidified layer grows thicker, its thermal resistance increases, with a resulting decrease of the heat conduction. When the natural convection is maintained at full strength, the energy balance requires that the rate of freezing must decrease and ultimately go to zero. Thus, the case of maintained natural convection represents an extreme manifestation of the effect of natural convection on freezing.

Although solid-phase conduction continues to play an important role when natural convection acts, it is natural convection which plays a special role. Freezing under these conditions may, therefore, be termed natural-convection-controlled freezing.

In the present research, a pattern of freezing is investigated which evolves progressively from natural-convection-controlled freezing to conduction-controlled-freezing. This evolution will be characterized here as a transition.

For the transition studies, the phase-change liquid is contained in a vessel which is adiabatic, and the freezing process on an immersed cooled surface starts with the temperature of the liquid above the fusion value. As soon as freezing begins, natural convection is initiated and heat is thereby transferred from the bulk liquid to the freezing interface. This convection heat transfer tends to diminish the temperature of the liquid since the outer (adiabatic) bounding surface of the liquid does not permit a compensating heat addition. As a consequence, the natural convection diminishes in strength, but as long as it exists, it continues to transfer heat from the bulk liquid to the interface. Finally, the liquid temperature approaches that of the interface and natural convection ceases. Freezing continues, its rate being controlled by conduction in the solidified material.

The experiments were performed for freezing on a water-cooled vertical tube positioned along the axis of a cylindrical containment vessel situated in an adiabatic environment. The phase-change medium was a paraffin, 99 percent pure n-eicosane, which has a melting temperature of 36.4°C. To provide comparisons for the transition freezing results, supplementary experiments were performed for natural-convection-controlled and conduction-controlled freezing.

Three types of data were collected. First, since the frozen mass is

Contributed by the Heat Transfer Division for publication in the JOURNAL OF HEAT TRANSFER. Manuscript received by the Heat Transfer Division June 12, 1980.

[1] There may be a small contribution from the subcooling of the solid, the neglect of which does not affect the essential point of the discussion.

Copyright © 1981 by ASME

Downloaded 20 Dec 2010 to 194.27.225.72. Redistribution subject to ASME license or copyright; see http://www.asme.org/terms/Terms_Use.cfm

directly related to the energy liberated by the freezing process, the frozen mass was measured as a function of time for each of the thermal operating conditions. Second, photographs were taken to document the change in the shape of the frozen specimens which occurs during the transition from natural-convection- to conduction-controlled freezing. In addition, quantitative data on the shapes of the liquid-solid interfaces were obtained by traverses along the height of the frozen specimens.

It is interesting to note that the freezing configuration studied here may be employed as a model of freezing about an array of vertical tubes situated in a phase-change medium. Such a multi-tube array has been considered in conceptual designs of phase-change storage systems. Consider the plan view of such an array as pictured in Fig. 1. The tubes are on equilateral triangular centers. If the thermal conditions are identical for all tubes, then each tube is surrounded by a hexagonal symmetry envelope that is illustrated by the dashed line in the figure. The symmetry envelope is an adiabatic boundary across which there is no thermal communication. Thus, each tube and its surrounding phase-change material can be treated independently of the other tubes.

A hexagon does not differ appreciably from a circle, so that the hexagonal adiabatic boundary of Fig. 1 may be replaced by a circular adiabatic boundary with little loss of accuracy. Thus, it would appear that a large array of vertical tubes can be modeled by a single vertical tube surrounded by a phase-change medium contained within an adiabatic-walled circular vessel. However, the modeling is imperfect owing to the difference between the velocity boundary condition on a symmetry boundary and that at the wall of a containment vessel. It is, however, known that the velocity distribution in a natural convection flow adjacent to a vertical wall rises steeply and attains its maximum close to the wall. Thus, if the spacing between the freezing interface and the wall of the containment vessel is large compared with the distance between the wall and the point of maximum velocity, the modeling should yield useful results.

Experimental Apparatus

The main components of the experimental apparatus included: (1) a containment vessel for the phase-change medium, (2) the thermal isolation enclosure which served as the adiabatic environment for the containment vessel during a data run, (3) the water-cooled tube on which the freezing took place, (4) a temperature-regulated pumped supply system for feeding water to the cooled tube and (5) a constant-temperature water bath for establishing the initial temperature of the liquid paraffin prior to a data run. Among these, the isolation enclosure contributed most of the uniqueness of the present experiments and was also the component which required the greatest effort in its development.

Thermal Isolation Enclosure. There were three main criteria which were considered during the design of the thermal isolation enclosure. The first is that it be a good insulator so as to minimize heat transfer at the outer boundary of the containment vessel. The second is related to the transient that is brought about by the timewise decrease of the liquid phase-change medium. In particular, the specific heat of the insulating material should be small enough so that the portion of the enclosure adjacent to the containment vessel can follow the transient without liberating significant amounts of stored energy. The last criterion is that the enclosure be of such type and configuration as to enable the containment vessel and the cooled tube to be inserted and positioned within the enclosure with minimum time lapse at the beginning of the data run, and similarly for the removal of the cooled tube bearing the frozen specimen at the end of the data run. A number of enclosure concepts were explored [8], but only the final design will be described here.

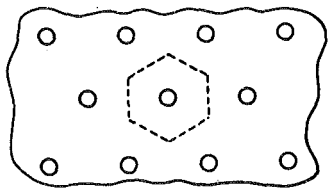

Fig. 1 Typical module in an array of cooled vertical tubes situated in a liquid phase-change medium

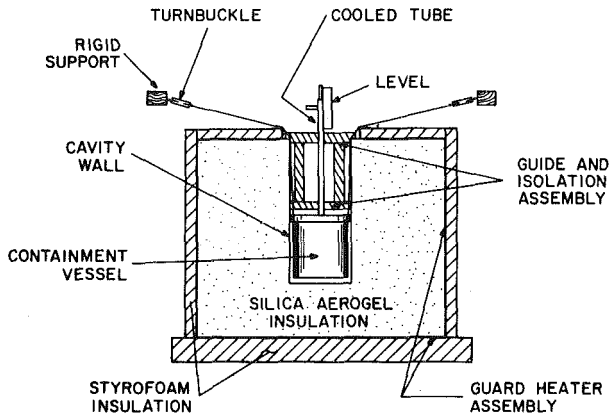

Fig. 2 The thermal isolation enclosure with the containment vessel and cooled tube in place

Figure 2 shows the isolation enclosure with the containment vessel and the cooled tube in place. The main structural element of the enclosure was a corrugated cardboard container, 53 cm high and 40 × 48 cm in horizontal cross section. An 18-cm dia cylindrical cavity made of poster board, centrally positioned in the top surface of the enclosure, extended downward by 38 cm into the enclosure. The enclosure (but not the cavity) was filled with silica aerogel powder insulation. Both the thermal conductivity and specific heat of the aerogel are about 15 percent less than those of air.

The outer surfaces of the cardboard container were sheathed with 0.081-cm thick aluminum panels, with heating tape wound around the enclosure on the outside of the sheathing. The purpose of the sheathing was to distribute the heat provided by the tapes, and the tape-sheathing assembly functioned as a guard heater. The sides, the top, and the bottom of the enclosure were encased by slabs of styrofoam. A centrally positioned circular aperture, 23 cm in diameter, was machined in the top styrofoam slab for access to the cylindrical cavity. A specially designed and fabricated heating unit was used to preheat the cavity prior to the initiation of a data run.

Containment Vessel. As shown in Fig. 2, the containment vessel is positioned just above the bottom of the cavity in the thermal isolation enclosure during a data run. The containment vessel is an open-topped stainless steel cylinder, 15 cm in diameter and 18.4 cm high. A lip at the top of the vessel was pierced at three places around its circumference, 120 deg apart, and a monofilament nylon line was threaded through each pierced hole. As can be seen in Fig. 2, these lines were brought upward through the cavity and out to a turnbuckle-support assembly which enabled the orientation of the containment vessel to be adjusted so that its axis was vertical.

The bottom of the containment vessel was fitted with an insulating disk whose function was to eliminate direct contact between the cooled tube and the lower wall of the containment vessel. Thermal isolation at the otherwise open top of the vessel was achieved with the aid of a styrofoam cap which rested on the lip of the vessel. The cap had a central aperture, 3.2 cm in diameter, to allow insertion of the cooled

Nomenclature

M = frozen mass
ΔT_i = inner temperature difference, $T^* - T_w$
$T_L(0)$ = initial temperature of liquid phase-change medium
T_o = temperature of outer surface of containment vessel
ΔT_o = outer temperature difference for natural-convection runs, $T_o - T^*$
$\Delta T_o(0)$ = outer temperature difference for transitional runs, $T_L(0) - T^*$
T_w = surface temperature of cooled tube
T^* = fusion temperature
t = time

Downloaded 20 Dec 2010 to 194.27.225.72. Redistribution subject to ASME license or copyright; see http://www.asme.org/terms/Terms_Use.cfm

tube into the containment vessel with ample clearance. A fill line was scribed on the inner wall of the containment vessel at a position which resulted in frozen specimens of 11.5 cm height.

To establish the initial temperature of the liquid phase-change medium, the containment vessel was positioned in a large, well-insulated constant-temperature water bath for a period of time prior to a data run. Control of the bath temperature was accomplished by an immersed sensing-heating-circulating unit which could maintain a preset temperature to better than 0.05°C.

Cooled Tube. The freezing took place on a vertical, water-cooled brass tube positioned along the axis of the containment vessel. The tube had an outside diameter of 2.49 cm, a wall thickness of 0.33 cm, and was capped at its lower end. Within the tube was a second tube of smaller diameter which terminated just above the capped end of the outer tube. Chilled water from a closed-loop, pumped refrigeration system entered the top of the inner tube, flowed to the bottom, reversed direction, and passed upward through the annulus between the tubes.

Temperature measurements on the outer surface of the cooled tube were made with three thermocouples respectively positioned at locations 1.3, 6.4, and 11.4 cm from the bottom of the tube. Each thermocouple was situated in a longitudinal groove machined into the surface of the tube. After the thermocouples has been installed, the grooves were filled with copper oxide cement, and the surface was finished so that no discontinuities could be detected.

As indicated in Fig. 2, the tube was centered and positioned vertically by a guide assembly which also served to close the cavity and thermally insulate it from the surroundings. The guide assembly consisted of three members: two parallel styrofoam disks connected by a hollow styrofoam cylinder. A 2.5-cm dia centrally positioned aperture in each disk guided the cooled tube and supported it laterally.

The actual vertical alignment of the cooled tube was accomplished with the aid of a pair of levels attached to the upper end of the tube (one of these levels is shown schematically in Fig. 1). Departures from the vertical were corrected by inserting specially machined wooden wedges between the periphery of the top disk of the guide assembly and the adjacent styrofoam block.

Instrumentation. All temperature measurements were made with specially calibrated teflon-coated 30-gage chromel and alumel wire. Temperatures were measured on the surface of the cooled tube, in the liquid phase-change medium, on the inner wall of the containment vessel, and on the wall of the cavity in the isolation enclosure. Thermocouple emfs were read to 1 μV with the same meter that had been used for the calibrations.

The mass of the frozen specimens was measured by either of two balances, depending on the size of the specimen. An analytical balance with a smallest scale division of 0.1 mg was used for specimens with mass up to 200 g. Larger specimens were weighed on a double-beam balance which could be read to 0.1 g.

Quantitative information on the shape of the liquid-solid interface was obtained by traversing a dial gage along the length of the specimen. For this purpose, the sample was slipped over a mandrel which was held in the collet of a lathe, while the dial gage was affixed to the tool post.

Photographs of all test specimens were taken with Tri-X film to provide a visual record of the change in specimen shape which accompanied the transition from natural-convection-controlled freezing to conduction-controlled freezing.

Experimental Procedure

Prior to the initiation of a data run, three distinct preparatory tasks were carried out in parallel. One of the tasks was to establish the thermal conditions in the isolation enclosure so that the walls of the containment vessel and of the cavity would satisfactorily track the decaying temperature of the liquid phase-change medium. From exploratory tests, it was found appropriate to set the initial temperature of the cavity wall at a value midway between the fusion temperature and the initial temperature of the liquid phase-change medium, using the cavity heater described earlier. In addition, the guard heaters on the outside of the enclosure were set so that the temperature of the aluminum sheathing was about 5.6°C below the fusion value.

The thermal preparation of the enclosure was performed with the containment vessel and the cooled tube absent from the cavity. During this period, the containment vessel was situated in the constant-temperature bath so that the liquid phase-change medium could attain the desired initial temperature for the data run. In addition, the cooled tube, placed in a support rack, was attaining thermal equilibrium with the chilled water flow.

When all components had achieved their desired initial temperatures, the cavity in the enclosure was opened, the heater removed, and the containment vessel transferred from the constant-temperature bath to the cavity. Immediately upon installation in the cavity, the containment vessel was leveled and the styrofoam guide assembly was inserted to seal the cavity. The cooled tube was then inserted through the guide holes and leveled, and at that point of time freezing was initiated. To compensate for any temperature drops during the transfer and installation process, the phase-change liquid had been preheated to a temperature about 1°C above the desired initial temperature for the data run.

To terminate the run after a preselected freezing period, the guide assembly, the cap of the containment vessel, and the cooled tube bearing the frozen specimen were lifted as a unit out of the isolation enclosure. The subsequent separation of the frozen specimen from the tube was accomplished by melting, with water from the building supply being passed through the tube. The water temperature was raised slowly until the melting point was reached, at which moment the specimen was removed from the tube.

As already noted, the mass and surface contour of each frozen specimen were measured. Prior to the contour measurements, the succession of specimens corresponding to different freezing periods for a given set of thermal boundary conditions were brought together and photographed as a group.

Results and Discussion

The freezing process is governed by two characteristic temperature differences. One of these is the temperature difference across the solidified layer, i.e., the difference between the fusion temperature and the temperature of the water-cooled tube. This quantity, which is constant during a data run, will be termed the inner temperature difference ΔT_i. The other temperature difference, to be called the outer temperature difference $\Delta T_o(0)$, is equal to the temperature of the liquid phase-change medium at the start of the data run minus the fusion temperature. If T^* and T_w respectively denote the fusion and wall temperatures and $T_L(0)$ denotes the initial temperature of the liquid, then

$$\Delta T_i = T^* - T_w, \quad \Delta T_o(0) = T_L(0) - T^* \tag{1}$$

The magnitude of ΔT_i controls the conduction heat transfer across the solidified layer, whereas $\Delta T_o(0)$ is an index of the strength of the natural convection during the early stages of freezing, i.e., during the period when natural convection exerts a strong influence on the freezing process.

Three series of data runs were performed, with each series being characterized by fixed values of ΔT_i and $\Delta T_o(0)$. One of these series may be regarded as a baseline case, and the other two series may be considered as systematic variants of the baseline case. The three series are defined by

Table 1 Temperature conditions for the experiments

Series	ΔT_i	$\Delta T_o(0)$
I	27.8°C	17.8°C
II	27.8°C	9.4°C
III	13.9°C	17.8°C

Relative to the baseline series I, the second series is characterized by a smaller value of $\Delta T_o(0)$, which is expected to yield a lesser influence of natural convection. For the third series, relative to the first, there is a smaller value of ΔT_i which gives rise to an expectation of

Downloaded 20 Dec 2010 to 194.27.225.72. Redistribution subject to ASME license or copyright; see http://www.asme.org/terms/Terms_Use.cfm

generally lower freezing rates and relatively greater effects of natural convection. Each series encompassed from eight to ten data runs spanning freezing periods of 5 to 300 min.

The presentation of results will be subdivided into three sections. In the first, photographic information will be presented to demonstrate the changes in the shape of the frozen specimens which accompany the transition from natural-convection-controlled freezing to conduction-controlled freezing. The second part of the presentation conveys quantitative data on the variation of the frozen mass with time. In the final section, quantitative measurements of the interface contours are presented.

Photographic Record of the Transition. The frozen specimens for each series were arranged according to increasing duration of the period of freezing and were photographed in this arrangement. The photographs for the series I, II, and III data runs are presented in Figs. 3, 4, and 5, respectively. The freezing periods for the succession of specimens in each figure are indicated in the figure caption.

All of the figures display a common trend. Starting at short freezing times, the specimens are slim but already display a slight taper, with the thickness of the frozen layer increasing from top to bottom. With increasing freezing time, the specimens grow thicker and the taper becomes more pronounced. All specimens corresponding to small and intermediate freezing times are characterized by smooth surfaces, as is indicated by the photographs.

As the freezing period is further prolonged, the characteristics of the frozen specimens begin to change. First, discrete crystals begin to populate the surface, and as time proceeds the crystals grow and form a thicket-like structure that overlays the solid surface beneath. In the photographs, the initial presence of the crystals is suggestive of a small surface roughness, but at later times the discrete crystals are evident. Accompanying the advent of the crystalline thicket, the taper diminishes so that finally the specimens are nearly straight-sided.

To give perspective to these results, reference may be made [6] to the characteristic specimen shape and surface condition that respectively characterize natural-convection-controlled and conduction-controlled freezing. Specimens produced under natural-convection-controlled freezing are tapered from a narrower top to a wider bottom and are smooth-surfaced. The tapering results from the top-to-bottom decrease of the natural convection heat transfer coefficient, the decrease being due to a thickening of the boundary layer as the liquid flows downward along the specimen. The natural convection motion also prevents the formation of large discrete crystals. In contrast, specimens produced by conduction-controlled freezing are straight-sided but have an overlayment of discrete crystals.

With this background, Figs. 3–5 offer conclusive evidence of a transition from natural-convection-controlled freezing to conduction-controlled freezing. The transition is brought about by the decreasing strength of the natural convection as the liquid transfers heat by convection to the liquid-solid interface, so that its temperature ultimately approaches the fusion value. Other evidences and manifestations of the transition will be presented shortly.

There are some interesting differences in detail among Figs. 3–5. Both Figs. 3 and 4 display clear attainment of the conduction regime (i.e., crystal thicket, straight sides), but in Fig. 4 the crystals appear somewhat more massive. This is consistent with the smaller value of $\Delta T_o(0)$ for Fig. 4, which implies a less-strong initial natural convection and an earlier approach to pure conduction conditions. It can also be seen that the conduction regime is barely achieved in Fig. 5, even though the right-most specimen in that figure corresponds to a longer freezing period than do the right-most specimens in Figs. 3 and 4. This behavior is consistent with the relatively stronger natural convection that is implied by the thermal conditions for Fig. 5.

Further inspection of the figures shows that the longer-time specimens have a somewhat downsloping top. This is due both to an increase in the liquid density as it cools and also to the density increase which accompanies phase change.

Another feature of the larger-time specimens is an outward flare of the cylindrical surface adjacent to the top. This flare is caused by extraneous freezing brought about by slightly lower temperatures at the free surface of the paraffin—a consequence of imperfect insulation.

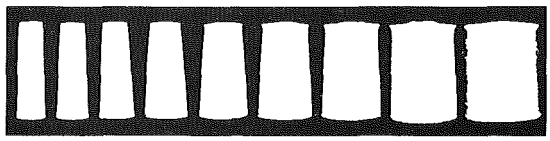

Fig. 3 Timewise evolution of the frozen layer for transitional freezing. Series I data runs: $\Delta T_i = 27.8°C$, $\Delta T_o(0) = 17.8°C$. Freezing times (left-to-right): 10, 20, 30, 60, 90, 120, 150, 195, and 240 min

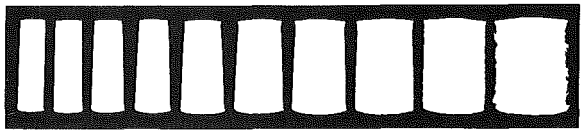

Fig. 4 Timewise evolution of the frozen layer for transitional freezing. Series II data runs: $\Delta T_i = 27.8°C$, $\Delta T_o(0) = 9.4°C$. Freezing times (left-to-right): 5, 10, 20, 30, 60, 90, 120, 150, 180 and 240 min

Fig. 5 Timewise evolution of the frozen layer for transitional freezing. Series III data runs: $\Delta T_i = 13.9°C$, $\Delta T_o = 17.8°C$. Freezing times (left-to-right): 30, 60, 90, 120, 150, 180, 240, and 300 min

Timewise Variation of the Frozen Mass. The amount of energy liberated by the freezing process is intimately related to the mass of the frozen material and, because of this, the mass versus time results are of practical interest. This information is conveyed in Figs. 6, 7, and 8, respectively for series I, II, and III. Each figure contains three sets of data. One set is the data (circular data symbols) for the transition from natural-convection-controlled to conduction-controlled freezing, which is the main focus of the research.

The second set of data (square symbols) is for natural-convection-controlled freezing. These experiments were performed with the containment vessel situated in a constant-temperature water bath during the entire duration of each data run, such that the natural convection in the liquid phase-change medium was maintained at full strength. The quantity ΔT_o which parameterizes the natural-convection data is

$$\Delta T_o = T_o - T^* \tag{2}$$

where T_o is the temperature on the outer surface of the containment vessel. It may be noted that in each figure ΔT_o was set equal to the initial temperature difference $\Delta T_o(0)$ of the transitional runs. The experimental arrangement for the natural convection runs was similar to that of [6], but the data appearing in Figs. 6–8 were collected as an auxiliary to the present study.

The third set of data in Figs. 6–8 is for conduction-controlled freezing, which is achieved by maintaining the liquid phase-change material at the fusion temperature, so that $\Delta T_o(0) = \Delta T_o = 0$. This condition was attained with the containment vessel situated in a constant-temperature water bath during the entire data run. The freezing data for conduction control yielded a remarkably simple and general correlation

$$M = 30.1(\Delta T_i t)^{0.634} \tag{3}$$

where M is the frozen mass in grams, ΔT_i is the inner temperature difference in °C (equation (1)), and t is the freezing time in hours. This correlation was based on experiments covering the range of ΔT_i from 5.6 to 27.8°C. The solid lines (without data symbols) that appear in Figs. 6–8 are representations of equation (3). The relationship between equation (3) and theoretical predictions for conduction-controlled freezing is shown in Fig. 4 of [9] (note the adjustment in the multiplicative constant to accommodate the different specimen heights of the present investigation and [9]). From that figure, it may be observed that the slope of the correlation equation (3) and that of the predictions of theory are in excellent agreement, but the predictions

Downloaded 20 Dec 2010 to 194.27.225.72. Redistribution subject to ASME license or copyright; see http://www.asme.org/terms/Terms_Use.cfm

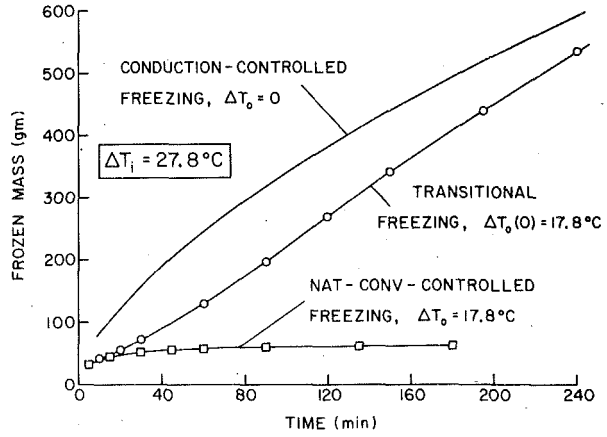

Fig. 6 Timewise variation of the frozen mass for Series I transitional freezing and for natural-convection-controlled and conduction-controlled freezing

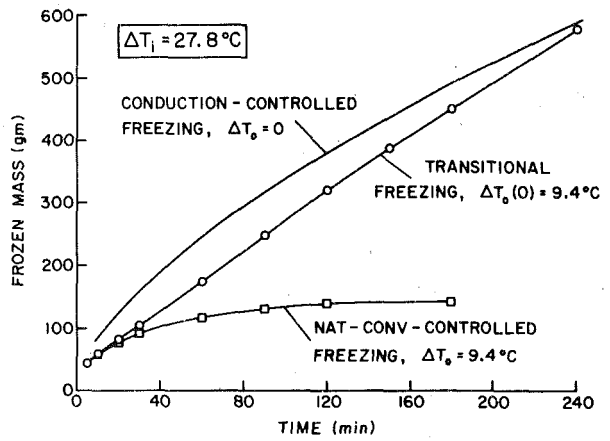

Fig. 7 Timewise variations of the frozen mass for Series II transitional freezing and for natural-convection-controlled and conduction-controlled freezing

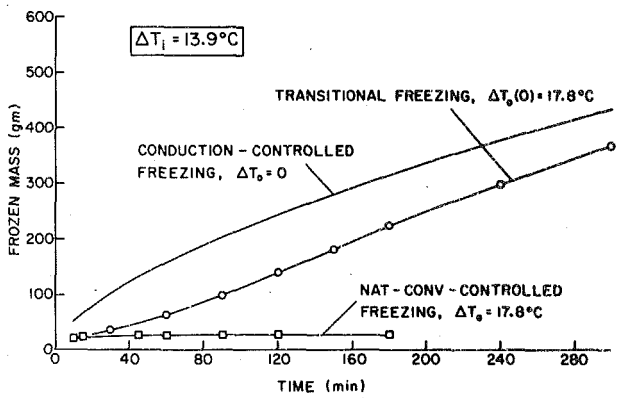

Fig. 8 Timewise variations of the frozen mass for Series III transitional freezing and for natural-convection-controlled and conduction-controlled freezing

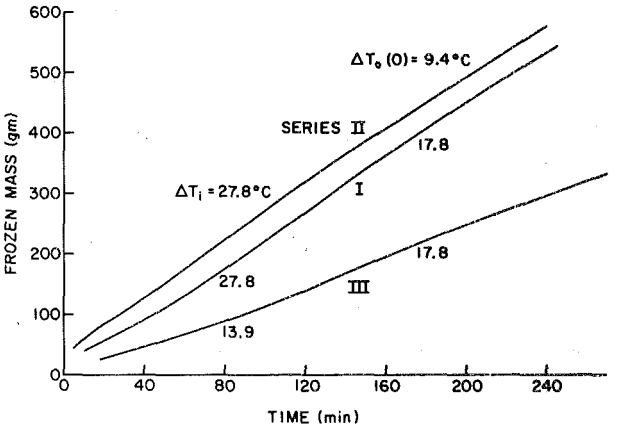

Fig. 9 Comparison of the frozen masses for Series I, II, and III transitional freezing

lie about 20 percent below the data. The probable causes of these deviations are identified in [9].

The results presented in Figs. 6–8 display common trends, but with important differences in detail. In all cases, pure conduction-controlled freezing yields the largest mass of frozen material. The conduction freezing curve rises steeply at first and continues to rise with the passing of time, but at a slower rate due to the increasing thermal resistance of the frozen layer. In contrast, the curve for natural-convection-controlled freezing becomes horizontal after an initial rise, indicating the complete termination of freezing.

At small freezing times, the data for transitional freezing are coincident with those for natural-convection-controlled freezing. Then, the transitional data tend to break away, soaring upward as freezing accelerates due to the diminishing strength of the natural convection that results from the temperature decrease of the liquid. Later, as the natural convection becomes a negligible factor and the additional conductive resistance of new solidified layers asserts itself, the rate of freezing tends to decrease. The earlier acceleration of freezing due to the ebbing of the natural convection and the later deceleration due to increased conduction resistance yields an inflected mass versus time curve for transitional freezing.

The gap between the transitional-freezing and conduction-freezing curves tends to close with increasing time. As can be seen from Figs. 6–8, the extent of the remaining gap at any time is dependent on the size of the mass deficit which must be made up.

Figures 6–8 show that the highly negative impact of maintained natural convection on freezing is substantially moderated when the freezing is carried out in an adiabatic containment vessel such that the natural convection ebbs with time. However, even for the adiabatic-walled vessel, there is a residual deficit in the amount of frozen mass relative to that for pure conduction. Thus, the pure conduction case provides an upper limit for the frozen mass.

The results of Figs. 6–8 verify the expectations that were expressed earlier about the relative importance of natural convection in the three series of experiments. Relative to the baseline series I, the lower value of $\Delta T_o(0)$ for series II implies a lesser influence of natural convection, as is evidenced by the relatively small gap between the conduction and transitional curves. For series III, the lower value of ΔT_i and the common value of $\Delta T_o(0)$ suggests a greater natural convection effect, and this asserts itself in greater percentage differences between the conduction and transitional curves.

The merging of the transitional and natural-convection data at small times lends confidence to the experimental technique. The two sets of data were obtained in different apparatus and with a different experimental technique (and also involved different personnel in the execution of the experiments). In this light, the agreement of the data is a highly affirmative outcome.

A comparison of the transitional freezing results for the three sets of thermal conditions is made in Fig. 9, where mass versus time curves are presented without the corresponding data points. Series I and II have the same inner temperature difference ΔT_i, but the $\Delta T_o(0)$ value is larger for the former. As a result of the larger $\Delta T_o(0)$, there is more natural-convection-related retardation at early times. Thus, a mass deficit between series I and II is established, and this difference persists throughout the range of freezing times that were investigated, even though the percentage difference diminishes.

For series III, the main factor which contributes to the reduction of the frozen mass, relative to series I, is the halving of ΔT_i, but there is also an important influence of natural convection. At small and intermediate times, the ratio of masses for series III and I is about a half, and at larger times the ratio is only slightly greater than a half. Since the corresponding ratio is 0.707 for pure conduction-controlled freezing (equation (3)), the lower ratio for transitional freezing represents an important effect of early and intermediate-time natural convection which persists to larger times.

Downloaded 20 Dec 2010 to 194.27.225.72. Redistribution subject to ASME license or copyright; see http://www.asme.org/terms/Terms_Use.cfm

Evolution of the Liquid-Solid Interface. The shape of the liquid-solid interface was measured for each of the frozen specimens.[2] For each series, the progression of interface contours corresponding to successively longer freezing periods have been plotted on a single graph to display the evolution of the interface. To illustrate the results, one of the three available graphs will be presented here (a complete presentation is available in [8]). The series III results were collected at more regular time intervals than were the other series and have, therefore, been selected for presentation in this paper.

Figure 10 displays the succession of interface contours for the series III runs, where the thickness of the frozen layer is plotted against the axial coordinate for each run. The first six runs were taken at 30 min intervals, while the last two runs are at a 1 hr interval.

The first of the contours (30 min) already displays the tapered bottom-heavy shape that is characteristic of strong natural convection effects. The top-to-bottom flare becomes somewhat greater for the next two contours, as can be verified by comparing the spacing between successive contours at positions near the top and the bottom of the specimens. This trend signals the continued viability of the natural convection.

Then, thereafter, the layer growth is such that the taper is diminished, i.e., the successive contours are more closely spaced at the bottom than at the top. This signals the ebbing of the natural convection and the increasing dominance of conduction. When conduction controls, the thinner portions of the specimen add new frozen material more rapidly than do the thicker portions. The final contour, at 300 min, has only a slight taper.

The dashed line at the top of the graph is an approximate representation of the upper surface of the specimen. The overall configuration of a frozen specimen at a given instant of time may be obtained by extrapolating the interface contour upward until it intersects the dashed line. An outward flare is seen to develop near the top of the interface contour. As noted earlier, this flare is the result of extraneous freezing at the free surface of the paraffin.

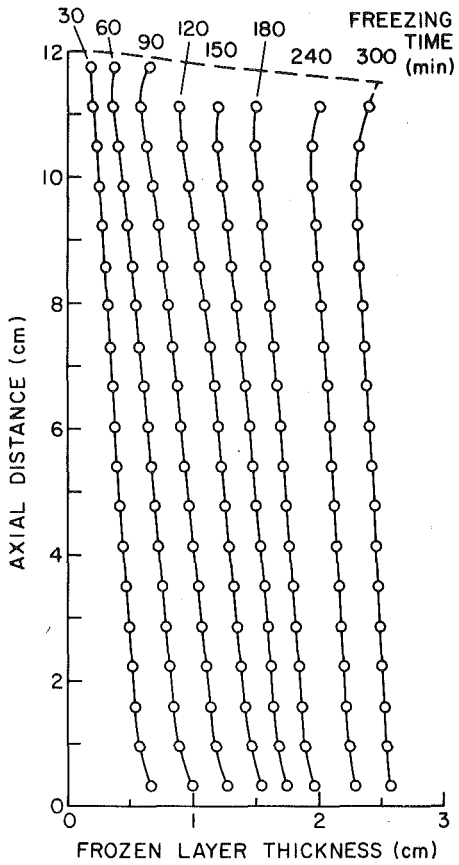

Fig. 10 Evolution of the contour of the liquid-solid interface for Series III transitional freezing

Concluding Remarks

The experiments performed here have demonstrated the nature of the transition between natural-convection-controlled freezing to conduction-controlled freezing. The freezing took place on a vertical, water-cooled tube immersed in a liquid phase-change medium contained in an externally adiabatic vessel. In the early stages of freezing, the liquid superheat (relative to the fusion temperature) induces a vigorous natural convection recirculation, with a corresponding retardation of freezing. The superheat diminishes with time as a result of convective heat transfer from the liquid to the freezing interface (the adiabatic containment vessel precludes heat addition to compensate for the heat loss to the interface). As natural convection ebbs due to the diminished temperature differences in the liquid, the rate of freezing tends to accelerate. At still later times, the rate of freezing decelerates owing to the added conductive resistance of the new layers of frozen material.

At short and intermediate freezing times, the frozen specimens are smooth-surfaced and are tapered, increasing in thickness from top to bottom. At large times, the specimens are straight-sided, with surfaces that are overlaid with a thicket of large discrete crystals. These characteristics are respectively those of natural-convection-controlled freezing and conduction-controlled freezing.

The timewise variation of the mass of frozen material reflects the transition process. At early times, the mass for transitional freezing is identical to that for natural-convection-controlled freezing. At later times, the frozen mass tends to approach toward that for pure conduction-controlled freezing, but a residual deficit remains. In general, conduction-controlled freezing produces a greater mass of frozen material than do the other modes of freezing.

The phenomena identified here, although determined via experiments involving a specific phase-change substance, should be operative for freezing in general, except, perhaps, for substances which exhibit a density extremum in the liquid phase.

[2] For the specimens corresponding to the longer data runs, the crystalline thicket on the outer surface of the specimen was removed prior to the contour measurements.

Acknowledgment

The research reported here was performed under the auspices of the U.S. Department of Energy, contract DE-AS02-79ER10343.

References

1 Eckert, E. R. G., and Drake, R. M., *Analysis of Heat and Mass Transfer*, Chapter 5, McGraw-Hill, New York, 1972.

2 Ozisik, M. N., *Heat Conduction*, Chapter 10, Wiley-Interscience, New York, 1980.

3 Ockendon, J. R., and Hodgkins, W. R., editors, *Moving Boundary Problems in Heat Flow and Diffusion*, Clarendon Press, Oxford, 1975.

4 Wilson, D. G., Solomon, A. D., and Boggs, P. T., *Moving Boundary Problems*, Academic Press, New York, 1978.

5 Bathelt, A. G., Van Buren, P. D., and Viskanta, R., "Heat Transfer During Solidification Around a Cooled Horizontal Cylinder," in Heat Transfer-San Diego-1979, AIChE Symposium Series, Vol. 75, No. 189, 1979, pp. 103–111.

6 Sparrow, E. M., Ramsey, J. W., and Kemink, R. G., "Freezing Controlled by Natural Convection," ASME JOURNAL OF HEAT TRANSFER, Vol. 101, 1979, pp. 578–584.

7 Lapudula, C. A., and Mueller, W. K., "The Effects of Buoyancy on the Formation of a Solid Deposit Freezing on a Vertical Surface," *International Journal of Heat and Mass Transfer*, Vol. 13, 1970, pp. 13–25.

8 Harris, J. S., "The Transition from Natural-Convection-Controlled Freezing to Conduction-Controlled Freezing," Thesis, Department of Mechanical Engineering, University of Minnesota, Minneapolis, Minn, 1980.

9 Sparrow, E. M., Larson, E. D., and Ramsey, J. W., "Freezing on a Finned Tube for Either Conduction-Controlled or Natural-Convection-Controlled Heat Transfer," *International Journal of Heat and Mass Transfer*, in press.

Downloaded 20 Dec 2010 to 194.27.225.72. Redistribution subject to ASME license or copyright; see http://www.asme.org/terms/Terms_Use.cfm

N. W. Wilson[1]
Associate Professor,
Mem. ASME

J. J. Lee
Graduate Student.

Faculty of Engineering and Applied Science,
Memorial University of Newfoundland,
St. John's, Newfoundland, Canada

Melting of a Vertical Ice Wall by Free Convection into Fresh Water

A steady-state two-dimensional finite difference analysis is presented for the heat and momentum transfer resulting when the leading portion of a semi-infinite vertical ice sheet at 0°C melts into fresh water by natural convection. Fluid properties are assumed to be constant and are evaluated beyond the edges of the boundary layers with the exception of fluid density which varies with the local temperature. Results of the analysis are presented for free stream temperatures from 0 to 24.0°C. They include streamlines, velocity profiles, melt velocities, and average Nusselt numbers for the leading 0.7632 m portion of a semi-infinite ice sheet. Overall, the results show three distinct flow regimes: steady upward flow for $T_\infty \leq 4.50°C$, steady downward flow for $T_\infty \geq 6.0°C$ and steady dual or bi-directional flow for $5.70 \leq T_\infty \leq 6.0°C$. In the range $4.50°C < T_\infty < 5.70°C$ the solution failed to converge and since the method is capable of accounting for local recirculations, it is suggested that this flow regime may be transitory in nature.

Introduction

If a vertical isothermal solid boundary is in contact with a surrounding real fluid which is at a temperature different from that of the wall, a steady-state fluid motion will occur near the wall. If the fluid density either increases or decreases monotonically with increasing temperature, such free convection flows are amenable to boundary layer analyses such as can be found in many introductory heat transfer texts. In many engineering applications, free convective heat transfer phenomena occur with fluids which may exhibit density extrema. For example, environmentally exposed vertical surfaces may be in contact with fresh water which exhibits a density extremum at approximately 4.0°C at atmospheric pressure. If the wall and fluid temperatures lie on alternate sides of the temperature at which the density extremum occurs, a simple boundary layer analysis is not directly applicable. Through one portion of the thermal boundary layer the buoyancy forces will be upwards, but through the other portion such forces will be downwards, and a complicated flow structure may result. If a vertical ice surface is in contact with water, analysis is further complicated by the melting or fusion process which occurs at the ice-water interface. While the melting or fusion process can be approximated by applying a blowing or suction boundary condition at the interface, the density extremum distribution necessitates a further extension of such analyses.

As far as is known, the first analytical solution concerned with the effect of the density maximum on natural convection was achieved by Merk [1], who considered heat transfer between a melting sphere of ice and adjacent pure water by using the integral momentum method. He predicted that in the neighborhood of $T_\infty = 5°C$, the Nusselt number has a minimum and the direction of the flow changes from upward at lower temperatures to downward at higher temperatures. Further, he found that the effect of melting is only appreciable for T_∞ greater than the inversion temperature and may be neglected for T_∞ less than the inversion temperature. Ede [2] compared his experimental results for heat transfer from a heated vertical isothermal wall to cold pure water with the predictions made by Merk and found them to be in reasonable agreement except in the region of low Nusselt number.

Dumore, et al. [3] demonstrated experimentally for melting ice spheres that a convective inversion occurs at 4.8°C. Their results indicate that the flow is upward when $T_\infty < 4.8°C$ and downward when $T_\infty > 4.8°C$. A minimum Nusselt number at 5.5°C was obtained by Tkachev [4] in his experimental work with vertical melting ice cylinders. Both experiments and analysis on natural convection heat transfer in regions of maximum fluid density have been carried out by Schechter and Isbin [5]. They substantiated the findings of Dumore, Merk, and Prins that there is a bidirectional flow in the boundary later when heat is transferred from a vertical isothermal flat plate to cold water.

Vanier and Tien [6] studied the influence of density inversion and melting on natural convection heat transfer from vertical surfaces for various wall and bulk temperature combinations. Their numerical boundary layer analysis indicated that for the case of $T_w = 0°C$ a dual flow exists near the wall and for $4.75°C < T_\infty < 6°C$ no solution was found. The effect of melting on the heat transfer rate was found to be small.

Schenk and Schenkels [7] measured natural convection heat transfer for an ice sphere in water for T_∞ from 0 to 10°C and found that a dual flow exists in the range $4°C < T_\infty < 6°C$. In this complicated region, they observed upward flow near the wall and downward flow at some distance away from the wall. Vanier and Tien [8] also performed experiments with ice spheres melting in water from 0 to 20°C and obtained a convective inversion at 5.35°C. The problem of natural convection heat transfer to a horizontal ice cylinder immersed in water was studied both theoretically and experimentally by Takeo Saitoh [9]. A minimum Nusselt number at above $T_\infty = 6°C$ was obtained.

Bendell and Gebhart [10] carried out experiments with vertical melting ice sheets in pure water at various values of T_∞. The experimentally determined heat-transfer results were found to be in good agreement with that from the boundary layer calculations of Gebhart and Mollendorf [11]. For the experimental investigation, a minimum Nusselt number in the range, $2.2°C \leq T_\infty \leq 25.2°C$, was found to occur at $T_\infty = 5.6°C$. Meanwhile a net upflow and a net downflow were deduced from fluid temperature measurements when $T_\infty \leq 5.6°C$ and $T_\infty \geq 5.6°C$ respectively. In reference [11] numerical solutions were not obtainable in the range $4.0°C < T_\infty < 6.8°C$ because of the first order boundary layer approximations. Similar analyses based on [10] were made by Qureshi and Gebhart [12] for a vertical ice plate with a uniform flux condition in water. Carey, et al. [13] reported numerical results for laminar thermal natural convection to or from a vertical isothermal surface in cold water when a density extremum arises. In pure water at atmospheric pressure, they found the flow is bidirectional for T_∞ between 4.75°C and 5.98°C and that convective inversion occurs at some T_∞ between 4.75°C and 5.81°C. Solutions could not be obtained within this range of temperatures.

Wilson and Vyas [14] conducted experiments on the velocity profiles near a vertical ice surface melting into fresh water for $2°C \leq T_\infty \leq 7°C$. Their results indicated steady-state motion upward when the water temperature is below 4.7°C and downward when the water temperature is above 7°C. For intermediate temperatures oscillatory bidirectional flow was observed.

The experimental work of Josberger [15] provides considerable information about the complex flow behavior near a vertical ice surface melting in saline water.

[1] Present address: Department of Mechanical Engineerng, University of Windsor, Windsor, Ontario, Canada.

Contributed by the Heat Transfer Division for publication in the JOURNAL OF HEAT TRANSFER. Manuscript received by the Heat Transfer Division April 18, 1980.

Copyright © 1981 by ASME

Downloaded 20 Dec 2010 to 194.27.225.72. Redistribution subject to ASME license or copyright; see http://www.asme.org/terms/Terms_Use.cfm

In view of the above summary, the scope of the present work can be defined. The analysis should be capable of yielding results for unidirectional upflow, unidirectional downflow, or bidirectional flow. Since steady bidirectional flow would imply that steady recirculation exists within the fluid adjacent to the ice sheet, the analytical model should be capable of readily accounting for such recirculations in steady-state flows.

Analysis

If all fluid properties remain constant with the exception of density in the body force terms, the following equations describe the steady state laminar two dimensional transfer of momentum and energy

$$\frac{\partial}{\partial x}\left(\omega\frac{\partial\psi}{\partial y}\right)-\frac{\partial}{\partial y}\left(\omega\frac{\partial\psi}{\partial x}\right)-\mu\left(\frac{\partial^2\omega}{\partial x^2}+\frac{\partial^2\omega}{\partial y^2}\right)-\frac{\partial}{\partial x}\left(\frac{u^2+v^2}{2}\right)\frac{\partial\rho}{\partial y}+\frac{\partial}{\partial y}\left(\frac{u^2+v^2}{2}\right)\frac{\partial\rho}{\partial x}\pm g\frac{\partial\rho}{\partial y}=0 \quad (1)$$

$$\frac{1}{\rho}\left(\frac{\partial^2\psi}{\partial x^2}+\frac{\partial^2\psi}{\partial y^2}\right)+\omega=0 \quad (2)$$

$$\frac{\partial}{\partial x}\left(T\frac{\partial\psi}{\partial y}\right)-\frac{\partial}{\partial y}\left(T\frac{\partial\psi}{\partial x}\right)-\frac{k}{C_p}\left(\frac{\partial^2T}{\partial x^2}+\frac{\partial^2T}{\partial y^2}\right)=0 \quad (3)$$

where

$$\omega=\frac{\partial v}{\partial x}-\frac{\partial u}{\partial y} \quad (4)$$

$$\rho u=\frac{\partial\psi}{\partial y}\text{ and }\rho v=-\frac{\partial\psi}{\partial x} \quad (5)$$

In writing the above equations, Cartesian co-ordinate systems as shown in Figs. 1(a) and 1(b) have been attached to the melt interface. Thus for dominant upward flow, the gravitational force on a fluid element would be in the negative x direction and the $-\rho g$ term expressed in equation (1) would apply. If the dominant flow direction is downward, the co-ordinate system of Fig. 1(b) is employed along with the $+\rho g$ term in equation (1).

The approach of Lafond [16] was used to define an equation of state relating density to temperature.

In order to complete the analysis, the associated boundary conditions should be considered. At the leading edge of the ice sheet, that is at the bottom of the plate for upflow or the top of the plate for downflow, the fluid is assumed to have no velocity in the direction along the plate. However, the fluid could be flowing in a direction normal to and towards the ice surface. If this is the case, the fluid would be flowing with zero shear stress and with a temperature equal to the value far removed from the wall. Thus, at $x = 0$ (except for $y = 0$)

$$\omega = 0, \psi = 0, T = T_\infty$$

Far removed from the wall, the fluid is at T_∞ and possesses a zero u component of velocity. In addition, $\partial u/\partial y$ is assumed to be zero and $\partial y/\partial x$ is assumed to be small enough to be negligible. Thus for large y

$$\omega = 0, \frac{\partial\psi}{\partial y}=\frac{\partial^2\psi}{\partial y^2}=0, T = T_\infty$$

Along the ice surface, the u-component of velocity is zero, but because of melting, the v-component is non-zero. Heat conduction into the ice is neglected for simplicity. (This corresponds to assuming that the ice is at its fusion temperature throughout). Therefore, the heat transferred to the ice by conduction through the fluid immediately adjacent to the ice can be equated, in the steady state, to the heat required to melt the ice. Thus, the local v-component of velocity at the wall can be expressed as

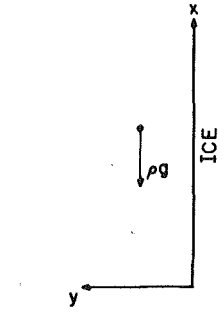

Fig. 1(a) Coordinate system for dominant upflow

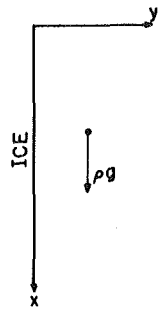

Fig. 1(b) Coordinate system for dominant downflow

$$v_w=-\frac{k}{\rho L}\frac{\partial T}{\partial y}\bigg|_{y=0} \quad (7)$$

Hence, if the temperature profile were known, the stream function could be evaluated along the ice sheet from

$$\psi_w=-\int_0^x \rho v_w dx \quad (8)$$

If the analysis were based upon boundary layer equations, the boundary conditions described so far would be sufficient to describe the flow near the leading portion of the plate. That is, boundary conditions would then need to be specified only at the leading edge, at the ice surface and far removed in the direction normal to the plate. However, if a fully two-dimensional solution is to be found, boundary conditions must be specified at the downstream end. This requires that the flow geometry be carefully identified.

A finite leading portion of a long vertical ice sheet is considered. It is assumed that the ice sheet is immersed in water with all other solid boundaries far removed from the ice surface, and that the ice sheet is much longer than the leading portion over which a solution will be found. This implies that the length of the region of interest of the plate may be arbitrarily chosen provided the x-direction gradients of ω, ψ, T, and ρ are not varying too appreciably at that point. Then the closure boundary values for these variables can be found by linear extrapolation from the interior of the region of interest.

The above equations were cast in finite difference form using the techniques described by Gosman, et al. [17]. That is, central differences were employed for all terms in equations (1–3) except the convection terms which were modelled by upwind differences. The fluid properties with the exception of density were evaluated at T_∞ and a computer program was written in Fortran IV. Typical runs required between 400 and 800 iterations. Complete details of the finite differences formulation and the computer program are given in reference [18].

Results and Discussion

The work of Gosman, et al. is known to yield valid results for an appropriate grid and suitable boundary conditions. A nonlinear 25 by 41 node grid was utilized for $0 \le x \le 0.7632$ m and $0 \le y \le 0.175$ m for all of the results presented here with the nodes most closely spaced near the leading edge in the x direction and near the ice surface in the y direction. Details of the grid are included in reference [18].

Nomenclature

C_p = constant pressure specific heat, J/(kg°C)
g = acceleration of gravity, m/s^2
k = thermal conductivity, W/(m°C)
ℓ = length of plate, m
L = heat of fusion, J/kg
$\overline{\mathrm{Nu}}_\ell$ = average Nusselt number
Pr = Prandtl number
T = local temperature of fluid, °C
T_∞ = bulk temperature of fluid, °C
T_w = temperature of plate, °C
u,v = velocities in x and y directions, m/s
v_w = melt velocity, m/s
x,y = cartesian co-ordinates, m
ρ = local density of fluid, kg/m^3
μ = dynamic viscosity, kg/(m s)
ψ = stream function, kg/(m s)
ω = vorticity, s^{-1}

Downloaded 20 Dec 2010 to 194.27.225.72. Redistribution subject to ASME license or copyright; see http://www.asme.org/terms/Terms_Use.cfm

Various tests were devised to validate the grid. For example, a solution was obtained for the above grid and compared by drawing streamline maps to the solution for the same grid in the x direction but with twice as many nodes at half the original spacings in the y direction. Discernable differences could not be found between the two solutions, and therefore, the 41 node y-direction grid spacing was validated. A similar technique established the sufficiency of the 25 node x-direction grid spacing.

The effect of the extrapolative boundary condition at the downstream end of the plate was numerically investigated by extending the original 25 by 41 node grid to a 51 by 41 node grid for $0 \leq x \leq 1.731$ m and $0 \leq y \leq 0.175$ m. The 51 by 41 node grid was identical to the 25 by 41 node grid for the first 25 nodes in the x-direction. Beyond there, the extra nodes merely extended the region over which a solution was found from $x = 0.7632$ m to $x = 1.731$ m. Over the first 25 x-direction nodes, the two solutions yielded identical streamline contours as is shown in reference [18]. Thus, changing the location of application of the extrapolative closure boundary condition did not noticeably affect the solution upstream from this location. Therefore, it was concluded that this boundary condition may be employed.

Streamline patterns were drawn for representative temperatures for a portion of the flow field from the ice wall to $y = 0.02$ m. Inspection of Fig. 2(a), for example, shows that for $T_\infty = 0.5°C$ fluid is entrained towards the ice surface most strongly near the lower end of the plate and then essentially pumped upward by the buoyancy forces. Although not shown here, at increased free stream temperatures below 2.5°C, the streamlines were more closely crowded together over the whole of the flow field. This corresponds to a more vigorous entrainment and pumping action. For $2.50 < T_\infty \leq 4.50°C$, increasing T_∞ resulted in lessening of the x and y gradients of stream function because of the lowered buoyancy forces in the outer portion of the boundary layer.

For $4.50 < T_\infty < 5.70°C$, converged solutions could not be obtained for either upflow or downflow. The program was run for up to 1500 iterations, and the results either oscillated from iteration to iteration or overflow errors occurred. Various grid configurations and degrees of under-relaxation were employed to obviate this difficulty but all attempts were unsuccessful. In general, two-dimensional finite difference schemes such as the present work can oscillate for steady-state flow conditions if the grid or the boundary conditions are insufficient to describe the phenomena, or if the flow field itself is truly oscillatory. The present analysis is capable of describing steady-state recirculations as is discussed below pertaining to Fig. 2(b). The temperature range through which the present solution was nonconvergent corresponds approximately to that in which the analysis of Bendell and Gebhart fails to obtain solutions. It also corresponds to the range in which the experimental data of Wilson and Vyas showed continual oscillations in the velocity distributions near a melting ice wall. Therefore, it is speculated that if $4.50 < T_\infty \leq 5.70°C$ the flow is oscillatory in nature. Obviously, further work is required to fully investigate this range of temperature.

For $T_\infty = 5.70°C$, a solution could be found with the streamline patterns as shown in Fig. 2(b). Because of the high free stream temperature, the fluid far from the ice wall is significantly lighter than that near the wall. Therefore, the fluid near the wall flows generally downwards. In the region very close to the wall ($y < 0.003$ m) the fluid density increases with increasing y resulting in a localized region of upflow. Hence the $\psi = -0.002$ and -0.001 streamlines show upflow near the wall, and a turning point followed by downflow further from the wall. The sharpness of the turning point in these streamlines is partially attributable to the algorithm used for producing the streamline contours from the stream function data available at the nodes. (Linear interpolations were used over a rectangle enclosed by four adjacent nodes and in order to more adequately describe this turning point with the contouring program an excessively fine grid would be required).

As T_∞ was increased beyond 5.70°C the near wall upflowing region became comparatively weaker because of the increased viscous action in the downflowing region. For $T_\infty > 6.00°C$ upflow was not observed.

Typical velocity profiles at selected positions along the ice surface are shown for selected temperatures in Figs. 3(a) and 3(b). For $T_\infty \leq 4.50°C$ the velocity profiles are wholly upward flowing with both the maximum longitudinal velocity and the boundary layer thickness increasing for increasing distances along the plate. For $T_\infty = 5.70°C$ the dominant flow direction is downwards with a small region near the wall possessing upwards velocities. Both the local velocity maxima and the recirculating boundary layer thickness increase with increasing distance along the plate. As the value of T_∞ is increased beyond 5.70°C the upwards flowing portion of the boundary layer progressively decreases in magnitude and thickness until it almost disappears at $T_\infty = 6.0°C$ as is shown in Fig. 3(b).

In Fig. 4 the calculated velocity profiles at selected locations along the plate for $T_\infty = 2.0°C$ are compared with the experimental data of Wilson and Vyas at $x = 0.05$ m. The analysis appears to predict velocities which are too large at $x = 0.05$ m when compared with the data, but the calculated values for $x = 0.0212$ m compare favorably. This anomaly could be attributed to the use of constant fluid viscosity in the present work or to the fact that the work of Wilson and Vyas was conducted within the confines of a small tank.

The melt velocity distributions (v at $y = 0$) along the ice surfaces are summarized in Fig. 5. Generally, for each of the ranges $0 < T_\infty \leq 4.50$ and $T_\infty \geq 5.73°C$ the melt velocity is highest towards the leading edge of the plate and decreases with increasing x. Also for each range, the melt velocity increases with increasing T_∞. At $T_\infty \approx 5.70°C$ when recirculation is present, the melt velocity is lower than at $T_\infty = 4.5°C$ over the full length of the plate with this reduction being most enhanced near the leading edge.

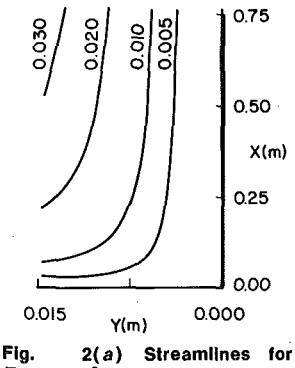

Fig. 2(a) Streamlines for $T_\infty = 0.50°C$

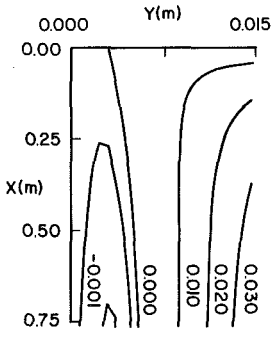

Fig. 2(b) Streamlines for $T_\infty = 5.70°C$

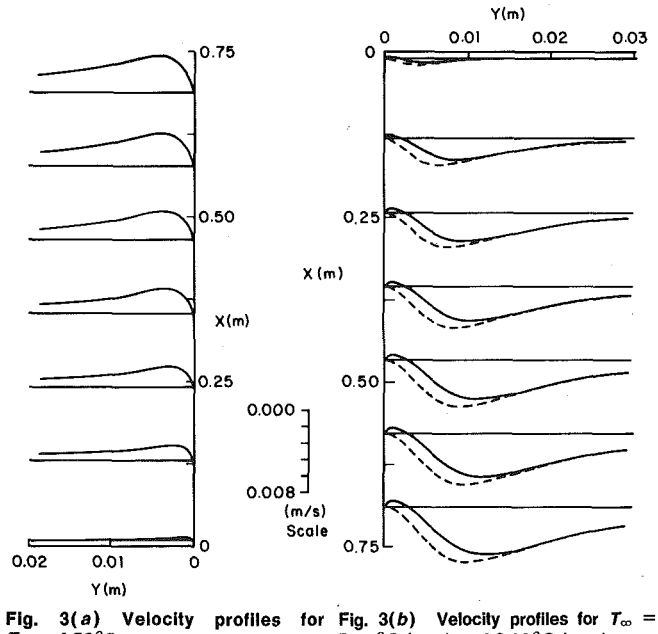

Fig. 3(a) Velocity profiles for $T_\infty = 4.50°C$

Fig. 3(b) Velocity profiles for $T_\infty = 5.70°C$ (——) and 6.00°C (- - -)

Downloaded 20 Dec 2010 to 194.27.225.72. Redistribution subject to ASME license or copyright; see http://www.asme.org/terms/Terms_Use.cfm

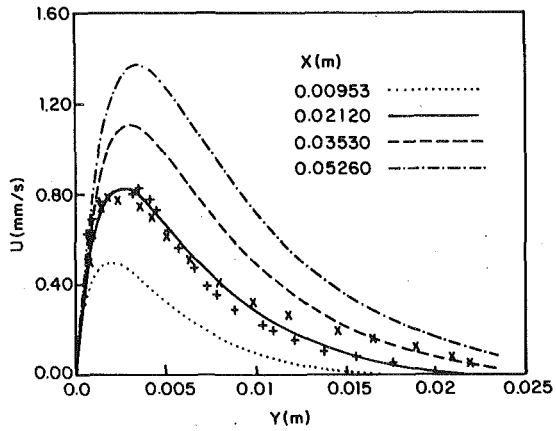

Fig. 4 Comparison of velocity profiles to data of Wilson and Vyas for T_∞ = 2.0°C

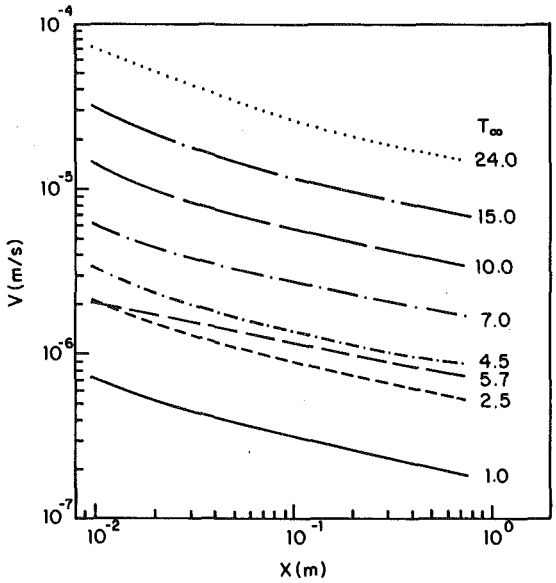

Fig. 5 Melt velocities for selected values of T_∞

Local heat transfer coefficients may be determined by equating the heat required to melt the ice, $\rho v_w L$, to the heat transferred by convection, $-h\ (T_w - T_\infty)$. Thus

$$h = \frac{\rho v_w L}{T_\infty - T_w}$$

In many applications the mean heat transfer coefficient, $\bar{h}$, over a length, ℓ, of a plate is of interest. It is determined from

$$\bar{h} = \frac{1}{\ell}\int_0^\ell h\, dx$$

If the above integration is performed numerically the average Nusselt number, $\overline{\mathrm{Nu}}_\ell$, can then be calculated from

$$\overline{\mathrm{Nu}}_\ell = \frac{\bar{h}\ell}{k}$$

Figure 6 shows the average Nusselt number as a function of T_∞ for the present analysis in comparison with experimental data and previous analyses corrected to a plate length of 0.7632 m as suggested by Bendall and Gebhart. In general the present analysis predicts somewhat higher average heat transfer than the work of either Vanier and Tien or Gebhart and Mollendorf. Because of its ability to account for recirculation near the melt interface, the present work provides information for downflow for $T_\infty \geq 5.70$°C in comparison to $T_\infty \geq 6.8$°C as found by reference [11].

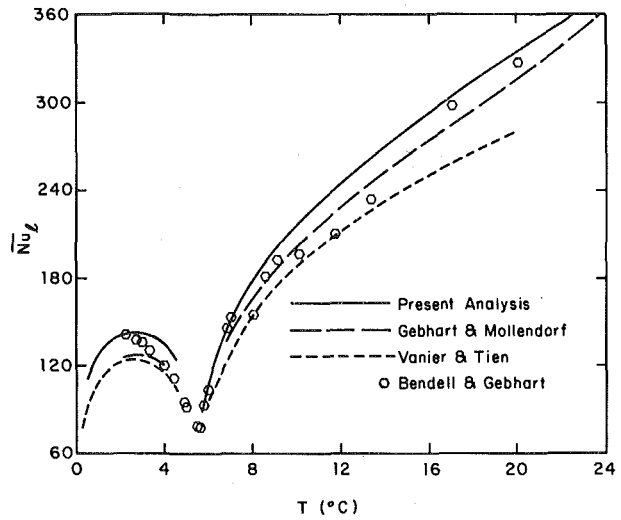

Fig. 6 Average Nusselt numbers for a 0.7632 m vertical plate

Conclusions

The two-dimensional finite difference analysis has predicted the laminar flow and heat transfer characteristics for a vertical ice sheet at 0°C melting into fresh water by free convection under steady state conditions. The results show three distinct flow regimes: dominant upward flow, dominant downward flow and a dual flow regime. The analysis does not yield stable results for $4.50°C < T_\infty < 5.70°C$ and it is suggested that further work, possibly in the form of a transient analysis is necessary in this range. For $5.70°C \leq T_\infty < 6.00°C$ a noticeable upflow occurs near the ice surface, and substantially decreases the average heat transfer rates.

At T_∞ = 2.0°C the analysis predicts velocities somewhat higher than the experimental data of Wilson and Vyas at x = 0.05 m. The predicted profiles for x = 0.0212 m agree well with the data. The calculated overall heat transfer results are about 10 percent higher than the data of Bendell and Gebhart.

Acknowledgments

The authors wish to acknowledge support by the Natural Sciences and Engineering Research Council Canada under grant number A-9204. Memorial University Fellowship support and the PDP 11/60 computer facilities of the Faculty of Engineering and Applied Science, Memorial University made the work possible.

References

1 Merk, H. J., "The Influence of Melting and Anomalous Expansion on the Thermal Convection in Laminar Boundary Layers," *Applied Science Research,* Vol. 4, 1953, pp. 435–452.

2 Ede, A. J., "The Influence of Anomalous Expansion on Natural Convection in Water," *Applied Science Research,* Vol. 5, 1955, pp. 548–560.

3 Dumore, J. M., Merk, H. J., and Prins, J. A., "Heat Transfer from Water to Ice by Thermal Convection," *Nature,* Vol. 172, 1953, pp. 460–461.

4 Tkachev, A. G., "Heat Exchange in Melting and Freezing of Ice," *Problems of Heat Transfer during a Change of State, A Collection of Articles,* AEC-TR-3405, Translated from a publication of the State Power Press, Moscow-Leningrad, 1953, pp. 169–178.

5 Schechter, R. S., and Isbin, H. S., "Natural-Convection Heat Transfer in Regions of Maximum Fluid Density," *AIChE Journal,* Vol 14, 1958, pp. 81–89.

6 Vanier, C. R., and Tien, C., "Effect of Maximum Density and Melting on Natural Convection Heat Transfer from a Vertical Plate," *Chemical Engineering Progress Symposium Series,* Vol. 64, 1968, pp. 240–254.

7 Schenk, J., and Schenkels, F. A. M., "Thermal Free Convection from Ice Sphere in Water," *Applied Sciences Research,* Vol. 19, 1968, pp. 465–476.

8 Vanier, C. R., and Tien, C., "Free Convection Melting of Ice Spheres," *American Institute of Chemical Engineers Journal,* Vol. 16, 1970, pp. 76–82.

9 Takeo Saitoh, "Natural Convection Heat Transfer from a Horizontal Ice Cylinder," *Applied Sciences Research,* Vol. 32, 1976, pp. 429–451.

10 Bendell, M. S., and Gebhart, B., "Heat Transfer and Ice-Melting in Ambient Water near its Density Extremum," *International Journal of Heat and Mass Transfer,* Vol. 19, 1976, pp. 1081–1087.

Downloaded 20 Dec 2010 to 194.27.225.72. Redistribution subject to ASME license or copyright; see http://www.asme.org/terms/Terms_Use.cfm

11 Gebhart, B., and Mollendorf, J. C., "Buoyancy-Induced Flows in Water under Conditions in which Density Extremum may Arise," *Journal of Fluid Mechanics,* Vol. 87, 1978, pp. 673–708.

12 Qureshi, Z. H., and Gebhart, B., "Vertical Natural Convection with a Uniform Flux Condition in Pure and Saline Water at the Density Extremum," Sixth International Heat Transfer Conference, Toronto, Canada, Vol. 2, Aug. 7–11, 1978.

13 Carey, V. P., Gebhart, B., and Mollendorf, J. C., "Buoyancy Force Reversals in Vertical Natural Convection Flows in Cold Water," *Journal of Fluid Mechanics,* Vol. 97, 1980, pp. 279–297.

14 Wilson, N. W., and Vyas, B. D., "Velocity Profiles near a Vertical Ice Surface Melting into Fresh Water," ASME JOURNAL OF HEAT TRANSFER, Vol. 101, No. 2, 1979, pp. 313–317.

15 Josberger, E. G., "Laminar and Turbulent Boundary Layers Adjacent to Melting Vertical Ice Walls in Salt Water," University of Washington, Department of Atmospheric Sciences Report No. 16, ONR Contract N000 14-76-C-0234, May 1979.

16 Lafond, E. C., "Processing Oceanographic Data," U.S. Navy Electronics Laboratory, H.O. Pub. No. 614, U.S. Navy Hydrographic Office, Washington, D.C., 1951, p. 91.

17 Gosman, W. M., Pun, A. K., Runchal, D. B., Spalding, and Wolfstein, M., *Heat and Mass Transfer in Recirculating Flows,* Academic Press, London and New York, 1969.

18 Lee, J. J., "Melting of a Vertical Ice Wall by Natural Convection in Pure or Saline Water," M. Eng. Thesis, Faculty of Engineering and Applied Science, Memorial University, St. John's, Newfoundland, Canada, 1979.

Downloaded 20 Dec 2010 to 194.27.225.72. Redistribution subject to ASME license or copyright; see http://www.asme.org/terms/Terms_Use.cfm

Analytically Determined Fin-Tip Heat Transfer Coefficients

E. M. Sparrow
Fellow ASME

C. F. Hsu
Department of Mechanical Engineering,
University of Minnesota,
Minneapolis, Minn 55455

An analysis was performed to determine the fin-tip heat transfer coefficients for an array of straight longitudinal fins attached to a plane wall. The array is shrouded by an adiabatic surface positioned adjacent to the tips, with a clearance gap between the shroud and the tips. The analysis was carried out for hydrodynamically and thermally developed conditions and for laminar flow. Results were obtained from numerical solutions of the momentum and energy conservation equations for the fluid and the energy equation for the fin, with two-dimensional conduction being permitted in the fin. From the solution, the average fin-tip heat transfer coefficient was evaluated and compared with the average coefficient for a segment of the principal face of the fin that is adjacent to the tip, the segment length being half the tip width. These coefficients were found not to differ too greatly, with the largest deviations being on the order of twenty-five percent. When convective heat transfer at the fin tip was suppressed, the heat transfer coefficients on the tip-adjacent portion of the principal face increased markedly. Because of this compensating effect, the overall performance of the fin is about the same when the tip is either convectively active or adiabatic. In general, large variations of the fin heat transfer coefficient were encountered between the base and the tip, with the smallest values at the base and the largest values at the tip.

Introduction

In the analysis of fins, the treatment of the heat transfer at the fin tip is a matter of uncertainty and, perhaps, of misconception. This is especially true when the tip is of finite thickness. There are at least four models which are variously employed in the representation of the tip heat transfer. These will now be briefly reviewed with a view to motivating the present work.

One of the models, the simplest one, assumes that the tip is insulated. Real fins rarely, if ever, have insulated tips, but a fin which bridges between two walls may experience a thermal symmetry condition which can be construed as equivalent to an insulated tip. In the second model, the tip is assumed to have the same convective heat transfer coefficient as that on the principal faces of the fin. A third model shifts the fin-tip area to the principal faces where it is assumed to have the same convection coefficient as the remainder of the principal faces. The fourth model, sometimes described as being the most exact, acknowledges that the tip heat transfer coefficient is different from that of the principal faces. In all models, the heat transfer coefficients are assumed to be spatially uniform on the respective surfaces.

Whereas the use of a distinct heat transfer coefficient for the tip (i.e., distinct from that of the principal faces) appears to provide the most accurate representation of the heat transfer process, the realities of the present state of knowledge suggest that such an approach is little more than window dressing. A literature survey did not succeed in identifying any available information on the tip heat transfer coefficient. Furthermore, the prospects of accurately measuring the tip coefficient are even less promising than those of measuring the coefficients on the principal surfaces; the latter measurement has rarely been performed [1] and then with somewhat uncertain results. Computation appears to hold greater promise than does experiment as a vehicle for providing fin-tip heat transfer coefficients but, up to the present, computationally determined tip coefficients have not yet been reported.

The present paper appears to be the initial study aimed at determining fin-tip heat transfer coefficients by computation. The system selected for study is an array of longitudinal fins attached to a plane wall. To prevent the heat transfer fluid from bypassing the fins, a shroud consisting of a plane adiabatic surface is positioned adjacent to the tips of the fins. The physical situation is shown in schematic cross sectional view in Fig. 1 along with dimensional notation and coordinates.

The case to be considered here is that where the flow is laminar and hydrodynamically fully developed. For this condition, lateral velocities are absent, but the axial velocity w depends upon the cross sectional coordinates in a complex manner because of the geometrical complexities of the flow cross section.

A number of thermal boundary conditions can be considered. The one selected here is that of a uniform heat input to the fluid per unit axial length (but the local heat flux per unit area is not uniform). This yields a thermally developed regime where all temperatures, both that of the primary heat transfer surface and of the fin, increase linearly in the axial direction (i.e., in the z direction). The primary surface is regarded as being highly conducting and/or sufficiently thick so that its temperature in any cross section is uniform. On the other hand, the fins have finite thermal conductivity. In any cross section, the temperature distribution in any typical fin can vary both with x and y, the extent of the variation depending on the interplay between conduction within the fin and convection on its surface.

The essential feature of the present analysis is that heat transfer coefficients are not specified in advance. Rather, the governing con-

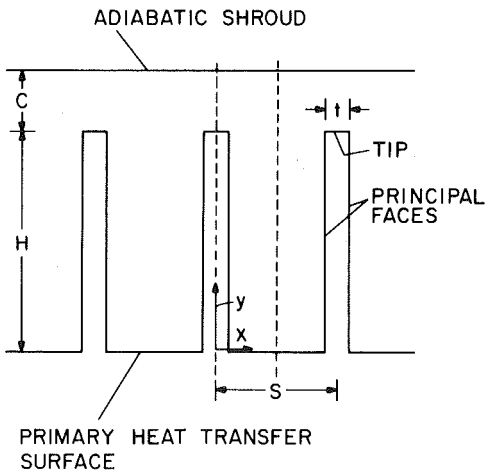

Fig. 1 Schematic cross-sectional view of longitudinal fin array

Contributed by the Heat Transfer Division for publication in the JOURNAL OF HEAT TRANSFER. Manuscript received by the Heat Transfer Division July 3, 1980.

Copyright © 1981 by ASME

Downloaded 20 Dec 2010 to 194.27.225.72. Redistribution subject to ASME license or copyright; see http://www.asme.org/terms/Terms_Use.cfm

servation equations for both the velocity and the temperature fields are solved without reference to the heat transfer coefficients. Local and average heat transfer rates and temperature distributions are determined from these solutions and, with this information, heat transfer coefficients are evaluated.

From an examination of Fig. 1, it can be seen that the geometrical configuration of the problem is specified by the values of four dimensions: the fin height H and thickness t, the interfin center-to-center spacing S, and the clearance C between the fin tips and the shroud. These quantities can be combined into three dimensionless ratios

$$S/H, \qquad t/H, \qquad C/H \tag{1}$$

An additional parameter is the ratio of the thermal conductivities of the fin and the fluid, respectively k_f and k. In selecting values of the k_f/k ratio, the thermal conductivity of the fluid was taken to be approximately that of air (because of the high probability of its use as a heat transfer fluid in a finned system). The k_f values that were considered encompassed the range of the metals commonly used in the fabrication of fins. These estimates led to the selection of the range $1000 \leq k_f/k \leq 10{,}000$ as being physically realistic.

In addition to the solutions corresponding to convective heat transfer on all faces of the fin, an auxiliary set of solutions was obtained for the case where the fin tip is adiabatic. The results from the two sets of solutions (i.e., convective tip versus insulated tip) were compared in order to provide perspectives about certain approximate practices that are employed in the classical approach to the analysis of fins.

What with four independent parameters and two sets of fin-tip heat transfer conditions, a complete exploration of the ranges of all the parameters is prohibitive both from the computational and reportorial standpoints. In view of this, the computations were performed for a carefully selected set of typical cases in order to display the effects of the parameters.

The results are presented both in tabular and in graphical form. The tables convey a variety of heat transfer results. These include average fin-tip heat transfer coefficients and average coefficients for the adjacent portion of a principal face of the fin. Average heat transfer rates for the tip and for the principal faces are also tabulated, as is the dimensionless temperature difference between the primary heat transfer surface (i.e., the base surface) and the fluid bulk. Also listed are the overall fin base-to-tip temperature differences. Certain fluid-flow-related results are also presented in tabular form. The graphs convey distributions of the local heat transfer coefficient, with special emphasis on the tip and on the adjacent portion of a principal face.

The present work bears a superficial relationship to the analysis of [2], which dealt with a shrouded longitudinal array of zero-thickness fins. The zero-thickness model used in [2] precluded consideration of fin-tip heat transfer, which is the main focus of the present work. Furthermore, since the present analysis deals with fins of finite thickness, the computer program and solution methodology developed in [2] is not applicable here.

Analysis and Solution

To begin the analysis, dimensionless variables will be introduced as

$$X = x/H, \qquad Y = y/H, \qquad W = w/(H^2/\mu)(-dp/dz) \tag{2}$$

$$\theta = (T - T_w)/(Q'/k) \tag{3}$$

In the θ definition, the quantity Q' is the rate at which heat is supplied to the flowing fluid per unit axial length in the typical module bounded by the symmetry lines in Fig. 1. In addition, T_w denotes the uniform wall temperature of the primary heat transfer surface (i.e., the base surface) at a typical cross section in the thermally developed regime.

With these definitions, the momentum conservation equation for hydrodynamically developed flow takes the form

$$\partial^2 W/\partial X^2 + \partial^2 W/\partial Y^2 + 1 = 0 \tag{4}$$

With regard to energy conservation, there are two forms, one for the fluid and one for the fin. For the fluid, the condition of thermally developed flow yields

$$\partial T_b/\partial z = \partial T/\partial z = Q'/\rho \bar{w} A c_p \tag{5}$$

in which A denotes the free flow area in a typical module. As can be seen in Fig. 1, the free flow area is an irregular domain which takes an abrupt jog and broadens out to a width $S/2$ just above the fin. Also, it may be noted that

$$A/H^2 = \tfrac{1}{2}(1 + C/H)(S/H) - \tfrac{1}{2}(T/H) \tag{6}$$

With $\partial T/\partial z$ replaced via (5), the dimensionless fully developed energy equation for the fluid becomes

$$\partial^2\theta/\partial X^2 + \partial^2\theta/\partial Y^2 = (W/\overline{W})/(A/H^2) \tag{7}$$

In this equation, the dimensionless mean velocity $\overline{W}$ is defined as

$$\overline{W} = \int_A W dA \Big/ \int_A dA \tag{8}$$

In the fin, the heat transfer is governed by Laplace's equation,

Nomenclature

A = free flow area per module
C = clearance gap, Fig. 1
c_p = specific heat
D_h = hydraulic diameter
f = friction factor, equation (29)
H = fin height, Fig. 1
$\overline{h}_t$ = average fin-tip heat transfer coefficient, equation (18)
$\overline{h}_{ta}$ = average heat transfer coefficient for tip-adjacent portion of principal face, equation (23)
h_f = local principal-face heat transfer coefficient, equation (25)
h_t = local fin-tip heat transfer coefficient, equation (25)
$\hat{h}$ = fictive spatially uniform heat transfer coefficient
k = fluid thermal conductivity
k_f = fin thermal conductivity
L_1, L_2 = lengths between surface-adjacent grid points and fin surface
m = dimensional group, $(2\hat{h}/k_f t)^{1/2}$
$\dot{m}$ = mass flow rate per module
$\dot{m}_{if}$ = mass flow rate in interfin space per module
$\overline{\mathrm{Nu}}_t$ = average fin-tip Nusselt number, equation (24)
$\overline{\mathrm{Nu}}_{ta}$ = average tip-adjacent Nusselt number, equation (24)
Nu_f = local principal-face Nusselt number, equation (26)
Nu_t = local fin-tip Nusselt number, equation (26)
p = pressure
Q' = heat transfer rate per unit axial length, per module
Re = Reynolds number, $\overline{w} D_h/\nu$
S = spacing between fin centers, Fig. 1
T = temperature
T_b = fluid bulk temperature
T_f = local temperature at fin surface
T_t = local tip temperature
T_w = temperature of primary heat transfer surface
t = fin thickness, Fig. 1
W = dimensionless axial velocity, equation (2)
w = axial velocity
$\overline{w}$ = mean axial velocity
X, Y = dimensionless coordinates, x/H, y/H
x, y = cross-sectional coordinates
y' = coordinate, $y - (H - t/2)$
z = axial coordinate
Γ_k = dimensionless thermal conductivity
Γ_μ = dimensionless viscosity
η = fin efficiency
θ = dimensionless temperature, $(T - T_w)/(Q'/k)$
θ_b = dimensionless bulk temperature, $(T_b - T_w)/(Q'/k)$
θ_t = dimensionless tip temperature, $(T_t - T_w)/(Q'/k)$
μ = viscosity
ν = kinematic viscosity
ρ = density

Downloaded 20 Dec 2010 to 194.27.225.72. Redistribution subject to ASME license or copyright; see http://www.asme.org/terms/Terms_Use.cfm

which becomes, in dimensionless terms,

$$(k_f/k)(\partial^2\theta/\partial X^2 + \partial^2\theta/\partial Y^2) = 0 \tag{9}$$

The factor k_f/k may, of course, be discarded without in any way affecting equation (9). It has, however, been retained because its presence facilitates the numerical solution scheme to be described shortly.

Although the boundary conditions may be stated in formal mathematical terms, such a statement is not of direct utility here because of the special techniques that were used to numerically implement the boundary conditions. Therefore, for the present, an informal statement of the boundary conditions will suffice. For the velocity problem, W is zero on all solid surfaces, while $\partial W/\partial X = 0$ on the symmetry lines. For the temperature, $\theta = 0$ all along the primary heat transfer surface (i.e., the base surface), while $\partial\theta/\partial X = 0$ on the symmetry lines and $\partial\theta/\partial Y = 0$ on the shroud. In addition, the temperature and the heat flux are continuous at each point on the fin-fluid interface (i.e., at the exposed surfaces of the fin).

Attention may now be turned to the methodology used to obtain the numerical solutions. The idea underlying the approach is to treat both the free flow area and the fin as a single unified solution domain, rather than as two separate solution domains. This obviates the need to overtly impose matching conditions for the temperature and heat flux at the interface between the domains because the matching occurs automatically.

The unified domain is defined by the closed boundary *abcdefa* in Fig. 2. It is characterized by nonuniform thermophysical properties, as will now be described.

For the velocity problem, imagine that the terms $(\partial^2W/\partial X^2 + \partial^2W/Y^2)$ in equation (4) are multiplied by a dimensionless viscosity Γ_μ. Then,

$$\text{In } bcdDb: \quad \Gamma_\mu = \infty \tag{10a}$$

$$\text{In } abDdefa: \quad \Gamma_\mu = 1 \tag{10b}$$

It may be noted that equation (10*a*) characterizes the fin as a substance having an infinite viscosity, while (10*b*) restores equation (4) to its original form.

The finite-difference grid is laid out so that the interface *dDb* between the two sub-domains defined by equations (10*a*) and (10*b*) is the locus of interfaces between the control volumes situated on either side of the interface. Consider a pair of such interfacing control volumes, each with a grid point centered in it. Let L_1 be the perpendicular distance from one grid point to the interface and L_2 be the perpendicular distance from the other grid point to the interface, and let the viscosities at these points be μ_1 and μ_2. Then, the viscosity μ^* at the interface may be evaluated as [3]

$$\frac{1}{\mu^*} = \frac{L_1/(L_1 + L_2)}{\mu_1} + \frac{L_2/(L_1 + L_2)}{\mu_2} \tag{11}$$

In terms of the Γ_μ values of equations (10)

$$\Gamma_\mu{}^* = (L_1 + L_2)/L_2 \tag{12}$$

where L_1 corresponds to an interface-adjacent control volume in *bcdDb* and L_2 to the mating interface-adjacent control volume in *abDdefa*.

The description of the velocity problem for the unified domain is completed by the statement of the boundary conditions

$$\text{On } abc \text{ and } ef: \quad W = 0 \tag{13a}$$

$$\text{On } cde \text{ and } af: \quad \partial W/\partial X = 0 \tag{13b}$$

Note that no conditions are stated (nor need be stated) on the interface *dDb*. What with equation (10*a*) and the boundary conditions (13), the numerical solution yields $W = 0$ in *bcdDb*. Other numerical aspects of the solutions will be discussed shortly.

The solution methodology for the heat transfer problem will now be described. Consider first a generalized energy equation which is to be applied throughout the entire solution domain *abcdefa*

$$\Gamma_k(\partial^2\theta/\partial X^2 + \partial^2\theta/\partial Y^2) = (W/\overline{W})(A/H^2) \tag{14}$$

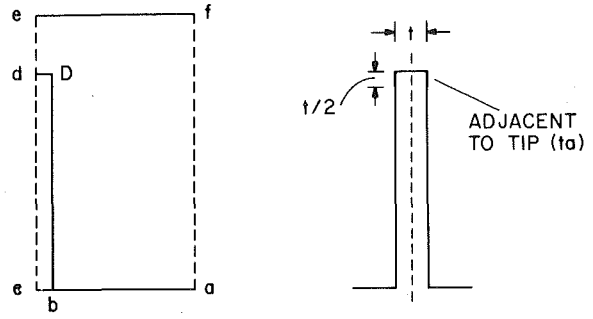

Fig. 2 Diagrams related to the solution methodology (left) and to the definition of the tip-adjacent segment (right)

where $\Gamma_k = 1$ in *abDdefa* and $\Gamma_k = k_f/k$ in *bcdDb*. As already noted, the numerical solution yields $W = 0$ in *bcdDb*. Consequently, equation (14) respectively reduces to equations (7) and (9) in the two subdomains.

Along the interface *dDb*, a dimensionless thermal conductivity $\Gamma_k{}^*$ can be defined in a manner analogous to the definition of μ^* in equation (11)

$$\frac{1}{\Gamma_k{}^*} = \frac{L_1/(L_1 + L_2)}{\Gamma_{k1}} + \frac{L_2/(L_1 + L_2)}{\Gamma_{k2}} \tag{15}$$

If Γ_{k1} is associated with k_f/k and Γ_{k2} is set equal to one, the dimensionless interface conductivity follows as

$$\Gamma_k{}^* = (L_1 + L_2)/(L_1(k/k_f) + L_2) \tag{16}$$

The quantities L_1 and L_2 are the respective distances from the interface-adjacent points in the subdomains *bcdDb* and *abDdefa* to the interface.

The thermal boundary conditions to be used with equation (14) are

$$\text{On } abc: \quad \theta = 0 \tag{17a}$$

$$\text{On } cde \text{ and } fa: \quad \partial\theta/\partial X = 0 \tag{17b}$$

$$\text{On } ef: \quad \partial\theta/\partial Y = 0 \tag{17c}$$

In view of the single-domain formulation, matching conditions along *dDb* are not required.

As noted earlier, a supplemental set of solutions was obtained for the case in which the fin tip *dD* is insulated. For this boundary condition, the interface thermal conductivity $\Gamma_k{}^*$ was set equal to zero at the tip.

The finite-difference scheme used to obtain solutions of the governing equations was a simplified version of that set forth in [3], the simplifications being possible because both of the participating differential equations are Poisson-type equations. Approximately 1700 points were used in the finite-difference grid. High concentrations of points were deployed along the interface *bDd*, especially in the neighborhood of the tip *dD*. Within the fin itself, either five or seven grid points were used across the span of the half thickness, respectively for $t/H = 0.01$ and $t/H = 0.1$. In this connection, it is relevant to note that the temperature was found to be remarkably uniform across the thickness of the fin. The quantitative extent of the slight nonuniformities will be presented later.

The solutions of the governing equations were obtained iteratively, the velocity being solved first and then the temperature. For convergence, it was required that at all grid points, the changes between consecutive iterations be less than 10^{-6} relative to the current value.

Results and Discussion

The heat transfer results will be reported in terms of an assortment of average and local quantities, with the average results being presented first and the local results thereafter. An average heat transfer coefficient $\overline{h}_t$ for the fin tip was defined as

Downloaded 20 Dec 2010 to 194.27.225.72. Redistribution subject to ASME license or copyright; see http://www.asme.org/terms/Terms_Use.cfm

$$\bar{h}_t = (Q_t/A_t)/(\bar{T}_t - T_b) \tag{18}$$

If note is taken of the symmetry around the y-axis (Fig. 1), then

$$Q_t/A_t = (2/t)\int_0^{t/2} q_t dx \tag{19a}$$

$$\bar{T}_t = (2/t)\int_0^{t/2} T_t dx \tag{19b}$$

where q_t and T_t are local quantities (i.e., functions of x) at the tip. Furthermore, the bulk temperature was evaluated from

$$T_b = \int_A TwdA \Big/ \int_A wdA \tag{20}$$

where, as before, A denotes the free flow area. Equations (19) and (20) were rephrased in terms of the variables of the analysis prior to their numerical evaluation.

To provide perspective about the magnitude of $\bar{h}_t$, an average heat transfer coefficient was also evaluated for a segment of the principal face situated immediately adjacent to the tip. This segment (one on each principal face of the fin) is pictured in the right-hand diagram of Fig. 2, where it is designated as the tip-adjacent (ta) segment. As shown there, the segment length is $t/2$, which corresponds to half of the tip surface.[1]

For the tip-adjacent segment

$$Q_{ta}/A_{ta} = (2/t)\int_0^{t/2} q_{ta} dy' \tag{21a}$$

$$\bar{T}_{ta} = (2/t)\int_0^{t/2} T_{ta} dy' \tag{21b}$$

where

$$y' = y - (H - t/2) \tag{22}$$

and, with these,

$$\bar{h}_{ta} = (Q_{ta}/A_{ta})/(\bar{T}_{ta} - T_b) \tag{23}$$

To convey the values of $\bar{h}_t$ and $\bar{h}_{ta}$ in a dimensionless format, Nusselt numbers $\overline{\mathrm{Nu}}_t$ and $\overline{\mathrm{Nu}}_{ta}$ may be introduced. In order that comparisons between $\overline{\mathrm{Nu}}_t$ and $\overline{\mathrm{Nu}}_{ta}$ truly reflect a comparison of $\bar{h}_t$ and $\bar{h}_{ta}$, the same characteristic dimensions should be used in both these Nusselt numbers. Furthermore, to enable direct comparisons of $\bar{h}$ values for fins of different thickness, the characteristic dimension should not involve the thickness. For these reasons, the fin height H was employed in defining $\overline{\mathrm{Nu}}$. Thus,

$$\overline{\mathrm{Nu}}_t = \bar{h}_t H/k, \qquad \overline{\mathrm{Nu}}_{ta} = \bar{h}_{ta} H/k \tag{24}$$

Other average heat transfer information will be conveyed via the ratios Q'_t/Q', Q'_f/Q', and Q'_w/Q', where the prime indicates heat transfer per unit axial length. Among these, Q'_t, Q'_f, and Q'_w represent the heat transfer rates per module at the tip, at a principal face, and at the primary surface. All of these quantities were obtained by integration over the respective surfaces.

Local coefficients for the tip and for a principal face were determined from

$$h_t = q_t/(T_t - T_b), \qquad h_f = q_f/(T_f - T_b) \tag{25}$$

with corresponding Nusselt numbers

$$\mathrm{Nu}_t = h_t H/k, \qquad \mathrm{Nu}_f = h_f H/k \tag{26}$$

where q_t and T_t are local x-dependent tip quantities, and q_f and T_f are local y-dependent quantities on a principal face.

Information about the temperature field will be reported in terms of two dimensionless quantities. One of these, $\theta_b = (T_b - T_w)/(Q'/k)$, pertains to the temperature difference between the primary heat transfer surface and the fluid bulk. The other, $\theta_t/\theta_b = (T_t - T_w)/(T_b - T_w)$, compares the temperature drop from the fin base to the fin tip with the drop from the base to the fluid bulk.

Quantities related to the velocity field will be defined when those results are presented.

Average Heat Transfer Results. The average heat transfer results are presented in Table 1. The table is subdivided into two parts, with results for long and/or thin fins appearing in part (a) and results for shorter and/or thicker fins in part (b). Values of t/H equal to 0.01 and 0.1 have been respectively selected to represent these two classes of fins. In addition to t/H, the table lists the values of four other quantities which parameterize the results. These include the dimensionless spacing ratio S/H, which was assigned values of 0.1 and 0.5 to represent close and intermediate fin spacing; the dimensionless gap clearance C/H, with assigned values of 0.1 and 0.25; and the conductivity ratio k_f/k, equal to 10^3 and 10^4. Note that the cases $t/H = 0.1$ and $S/H = 0.1$ are not compatible, and this accounts for the fact that part (b) of the table is shorter than part (a).

The fourth column of the table, headed *tip*, describes the thermal

[1] Each half of the tip surface can be thought of as being compared with a tip-adjacent segment on each principal face.

Table 1 Average heat transfer characteristics

S/H	C/H	k_f/k	Tip	$\overline{\mathrm{Nu}}_t$	$\overline{\mathrm{Nu}}_{ta}$	Q'_t/Q'	Q'_f/Q'	Q'_{t+f}/Q'	$-\theta_b$	θ_t/θ_b	mH	η
(a) $t/H = 0.01$												
0.1	0.1	10^3	C	770	612	0.0577	0.922	0.980	0.135	0.890	1.58	0.580
			I	—	898	—	0.980	0.980	0.139	0.865	1.54	0.591
		10^4	C	247	197	0.0579	0.929	0.987	0.059	0.205	0.611	0.891
			I	—	333	—	0.987	0.987	0.063	0.193	0.591	0.898
0.1	0.25	10^3	C	41.0	30.6	0.207	0.781	0.988	1.18	0.144	0.420	0.945
			I	—	54.3	—	0.987	0.987	1.22	0.138	0.413	0.947
		10^4	C	40.4	30.2	0.207	0.788	0.995	1.04	0.016	0.138	0.994
			I	—	53.6	—	0.995	0.995	1.09	0.016	0.136	0.994
0.5	0.1	10^3	C	42.9	36.5	0.0163	0.848	0.864	0.177	0.571	1.18	0.700
			I	—	60.8	—	0.865	0.865	0.178	0.570	1.18	0.702
		10^4	C	32.2	27.4	0.0170	0.883	0.900	0.116	0.091	0.403	0.949
			I	—	45.7	—	0.900	0.900	0.116	0.091	0.404	0.949
0.5	0.25	10^3	C	77.8	66.9	0.0350	0.849	0.884	0.206	0.564	1.08	0.733
			I	—	108	—	0.884	0.884	0.207	0.559	1.08	0.735
		10^4	C	60.1	51.8	0.0360	0.885	0.921	0.132	0.092	0.382	0.954
			I	—	83.6	—	0.921	0.921	0.134	0.090	0.379	0.955
(b) $t/H = 0.1$												
0.5	0.1	10^3	C	9.19	12.8	0.0395	0.883	0.923	0.097	0.111	0.440	0.934
			I	—	19.4	—	0.923	0.923	0.098	0.109	0.448	0.938
		10^4	C	8.90	12.4	0.0397	0.887	0.927	0.090	0.012	0.141	0.993
			I	—	18.8	—	0.926	0.926	0.092	0.012	0.142	0.993
0.5	0.25	10^3	C	23.9	21.6	0.117	0.824	0.941	0.110	0.115	0.416	0.941
			I	—	34.5	—	0.941	0.941	0.124	0.102	0.400	0.950
		10^4	C	23.2	21.0	0.117	0.827	0.944	0.102	0.013	0.133	0.994
			I	—	33.7	—	0.944	0.944	0.115	0.011	0.128	0.995

Downloaded 20 Dec 2010 to 194.27.225.72. Redistribution subject to ASME license or copyright; see http://www.asme.org/terms/Terms_Use.cfm

boundary condition at the tip. An entry C in this column indicates convective heat transfer, while an entry I indicates a perfectly insulated tip. All told, Table 1 contains 24 cases.

The fifth and sixth columns of the table convey the average coefficients for the tip and the tip-adjacent portion of the principal face, while the next three columns give heat transfer rates per unit axial length and per module (see Figs. 1 and 2) at the tip (t), at the principal face (f), and at the sum of the two ($t + f$). The next two columns convey temperature information, whereas the last two columns relate to a fin model based on a spatially uniform heat transfer coefficient.

Attention will first be focused on the comparison between the average heat transfer coefficients for the tip and for the tip-adjacent portion of a principal face. From an overall examination of the $\overline{\mathrm{Nu}}_t$ and $\overline{\mathrm{Nu}}_{ta}$ columns of Table 1, it can be seen that for any given case, the tip and tip-adjacent coefficients are not very different—surely less different than what might have been pessimistically conjectured in the past, when no information was available. For the thin fins, the tip coefficients are consistently higher than those for the tip-adjacent region, the differences being in the 15 to 25 percent range. In the case of the thicker fins, the relationship between the coefficients is less regular, with a slightly larger range of deviations. These findings apply for both of the investigated k_f/k ratios; indeed, for a given geometry, $\overline{\mathrm{Nu}}_{ta}/\overline{\mathrm{Nu}}_t$ has identical values for $k_f/k = 10^3$ and 10^4, even though $\overline{\mathrm{Nu}}_{ta}$ and $\overline{\mathrm{Nu}}_t$ are individually affected by k_f/k.

The foregoing observations suggest that in the absence of specific information about a particular case of interest (i.e., defined by the geometric parameters and k_f/k), it would not be unreasonable to use equal values of the heat transfer coefficients for the tip and the tip-adjacent regions.

Attention may now be directed to the response of the tip-adjacent region and of the fin as a whole to the imposition of an adiabatic boundary condition at the fin tip. Examination of the $\overline{\mathrm{Nu}}_{ta}$ column of Table 1 shows that the heat transfer coefficient in the tip-adjacent region increases when the tip is insulated and that the increase is approximately sixty percent for all of the cases investigated (both for the thin fins and the thicker fins). Thus, it appears that nature acts to compensate for the loss of heat transfer surface at the fin tip by bringing about an increase in the heat transfer coefficient along the tip-adjacent region.

The degree of perfection of this compensation can be judged by comparing the respective values of Q'_{t+f} for the cases of the convective and insulated tips, for otherwise identical operating conditions. Such a comparison yields virtually identical values, with the largest deviations (confined to a few isolated cases) being one in the third significant figure. Furthermore, in assessing the comparison, it should be noted that there are certain cases where the fin tip, when it is convectively active, carries a substantial heat load (up to 20 percent of Q'). Even in these cases, where there is substantial redirection of the heat flow when the tip is deactivated, the compensation is perfect.

Another indicator of the degree of compensation is the value of $-\theta_b = (T_w - T_b)/(Q'/k)$. This quantity can be regarded as a measure of the thermal resistance of the system. In general, $-\theta_b$ is very little different for fins with either active or inactive tips.

Thus, left to her own devices, nature yields more or less identical performances for fins with either active or inactive tips. A rather different result would, however, be forthcoming from fin analyses of the type that are currently standard. The difficulty with those analytical models is that they employ identical input values of the heat transfer coefficient for both active- and inactive-tipped fins. This assumption is, however, not valid, and corresponding comparisons of active- and inactive-tipped fins such as are often made in textbooks are of uncertain validity. The root cause of the difficulty goes beyond the models themselves. Fundamentally, the problem lies in the absence of reliable information for the fin heat transfer coefficient. This theme will be revisited in another context shortly.

The foregoing discussion (relating to the comparisons of $\overline{\mathrm{Nu}}_t$ and $\overline{\mathrm{Nu}}_{ta}$ and to the effects of insulating the tip) conveys the main message of Table 1. There are a variety of lesser issues that may be addressed, and a few of these will now be briefly considered. First, it may be noted that the tabulated Nusselt numbers are generally lower at larger values of k_f/k, although the effect is of little significance for the thicker fins. This trend may be rationalized by thinking of increases in k_f/k as being due to an increase in the fin conductivity k_f at a fixed value of the fluid conductivity k. For a fin of fixed dimensions, an increase in thermal conductivity gives rise to increases of both the heat transfer rate and the surface-to-bulk temperature difference in the tip region. The latter increase outweighs the former, with the result that the local heat transfer coefficient is decreased.

With regard to the magnitudes of $\overline{\mathrm{Nu}}_t$ and $\overline{\mathrm{Nu}}_{ta}$, it can be seen that higher values prevail for thin fins than for thicker fins. This relationship can be explained by the same reasoning as was employed for the k_f/k effect. For the thin fins, there are startlingly high Nusselt number values in evidence for certain cases. These values are primarily due to the relatively small temperature differences that prevail (see, for example, the θ columns of the Table).

Also of interest is the trend of the overall thermal resistance (i.e., of $-\theta_b$) with the clearance parameter C/H. At a fixed interfin spacing S/H, the thermal resistance increases as the clearance gap increases. This trend is especially marked when the spacing is small. It is caused by the tendency of the fluid to seek the path of least resistance. For a small interfin spacing, more fluid tends to prefer the clearance gap as a passageway as the gap increases. As a consequence, there is very little convective heat transfer in the interfin space, and this results in a large overall thermal resistance. The last two columns of Table 1 will be discussed later.

Local Heat Transfer Results. Distributions of the local heat transfer coefficient along the principal face of the fin and along the tip are presented in Figs. 3–8. Each figure consists of a main part and an inset. The main part contains the distribution curves for the local coefficients on the tip and on the portion of the principal face adjacent to the tip. The tip coefficients Nu_t span the range $0 \le x \le t/2$, while the face coefficients Nu_f are extended over $0 \le y' \le t/2$ (recall that $y' = y - (H - t/2)$). For Nu_f, curves are given for both the cases of the convectively active tip and the adiabatic tip.

As plotted, the curves in the main part of the figure are for $k_f/k = 10^4$. These curves also represent the results for $k_f/k = 10^3$ in accordance with the relation

$$\mathrm{Nu}_f(10^4) = [\overline{\mathrm{Nu}}_{ta}(10^4)/\overline{\mathrm{Nu}}_{ta}(10^3)]\mathrm{Nu}_f(10^3) \qquad (27)$$

That is, the local coefficients in the tip-adjacent region scale precisely with the ratio of the average values. As a demonstration of this relationship, "data points" are plotted in Fig. 8 which represent Nu_f results for $k_f/k = 10^3$ that have been so scaled. It can be seen that the points fall precisely on the curves for $k_f/k = 10^4$. The same type of relationship applies for Nu_t.

At the right-hand margin of the main part of the figure there is an array of three horizontal lines. These lines respectively correspond to the $\overline{\mathrm{Nu}}_t$ and $\overline{\mathrm{Nu}}_{ta}$ values that are listed in Table 1. Each line is of a type which indicates its correspondence with the distribution curves shown in the figure.

The inset that appears at the upper left of each figure contains Nu_f distributions along the entire height of the fin from $y = 0$ to $y = H$. These results are presented in a graph of lesser size because it is felt that with regard to the main objectives of the work, they are of lesser novelty than the fin tip results. In each inset, it was intended to plot four curves, respectively for $k_f/k = 10^3$ and 10^4 and for the cases of the convectively active tip and the adiabatic tip. The curve designations for these various cases are indicated in the inset of Fig. 3. In some of the insets, fewer than four curves are plotted because overlapping among the curves prevented their resolution within the scale of the graph.

Attention may first be turned to the main parts of Figs. 3–8, i.e., to Nu_t and to Nu_f in the tip-adjacent region of the principal face. In all cases, it is seen that the maximum value of the transfer coefficient occurs at the corner where the tip meets the principal face. Indeed, both Nu_t and Nu_f experience sharp rises in the neighborhood of the corner. Although it is very difficult to resolve events at the corner point with complete certainty, it appears that Nu_f may increase faster

Downloaded 20 Dec 2010 to 194.27.225.72. Redistribution subject to ASME license or copyright; see http://www.asme.org/terms/Terms_Use.cfm

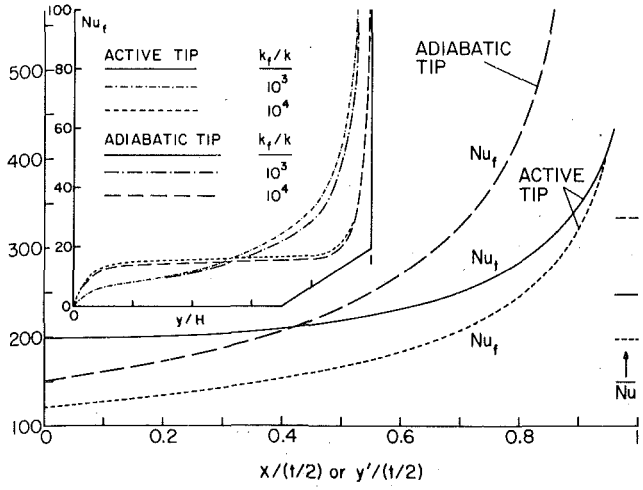

Fig. 3 Local Nusselt number distributions on the fin tip and on the principal face; $t/H = 0.01$, $S/H = 0.1$, $C/H = 0.1$

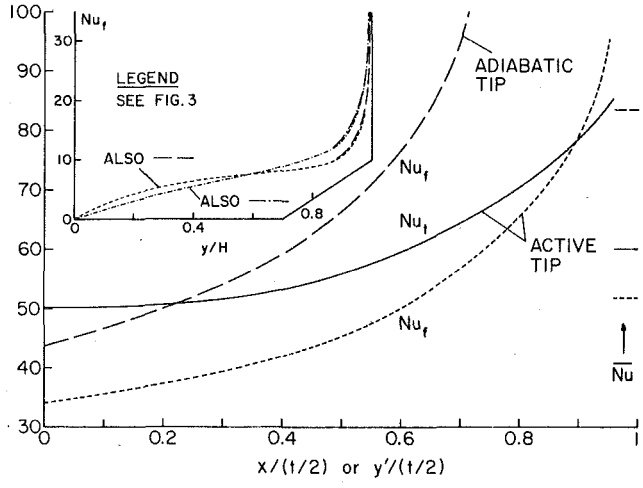

Fig. 6 Local Nusselt number distributions on the fin tip and on the principal face; $t/H = 0.01$, $S/H = 0.5$, $C/H = 0.25$

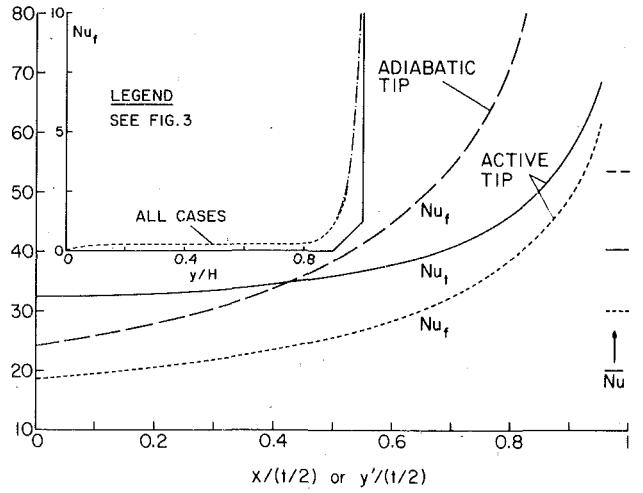

Fig. 4 Local Nusselt number distributions on the fin tip and on the principal face; $t/H = 0.01$, $S/H = 0.1$, $C/H = 0.25$

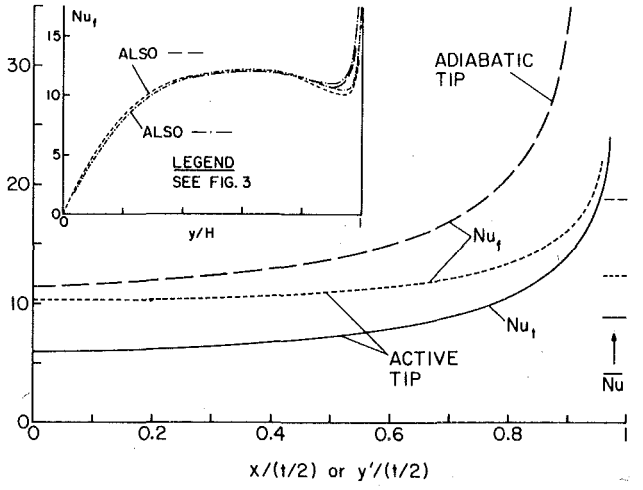

Fig. 7 Local Nusselt number distributions on the fin tip and on the principal face; $t/H = 0.1$, $S/H = 0.5$, $C/H = 0.1$

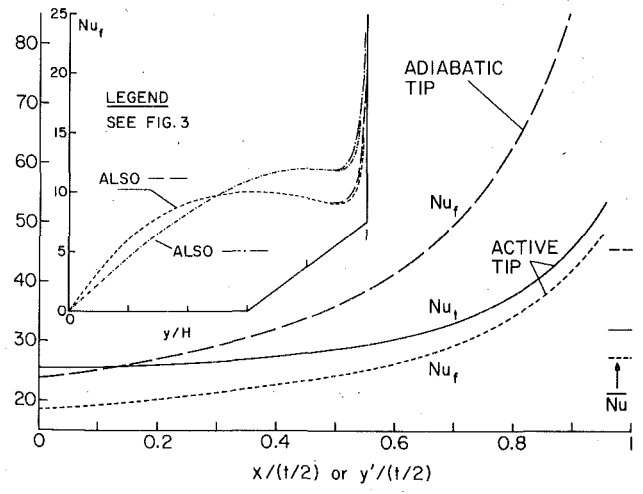

Fig. 5 Local Nusselt number distributions on the fin tip and on the principal face; $t/H = 0.01$, $S/H = 0.5$, $C/H = 0.1$

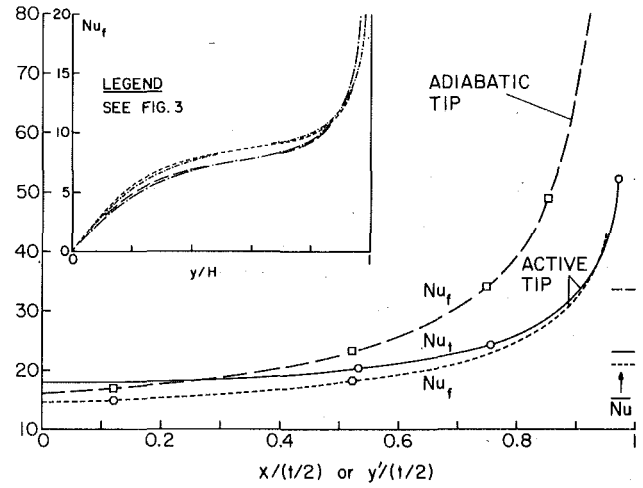

Fig. 8 Local Nusselt number distributions on the fin tip and on the principal face; $t/H = 0.1$, $S/H = 0.5$, $C/H = 0.25$

Downloaded 20 Dec 2010 to 194.27.225.72. Redistribution subject to ASME license or copyright; see http://www.asme.org/terms/Terms_Use.cfm

than Nu_t and, therefore, attain higher values. Away from the corner (but still near the corner), it can be seen that for the most part $Nu_t > Nu_f$.

The response of Nu_f to the deactivation of heat transfer at the fin tip is quite striking. As the corner is approached, Nu_f soars and takes on values that are much, much higher than those for the case of the convectively active tip. It is these elevated values of Nu_t that compensate for the loss of heat transfer surface area when the tip is deactivated. Away from the immediate neighborhood of the corner, the differences between the Nu_t values for the active and inactive tip cases subside.

Attention may be turned to the insets of Figs. 3–8, where base-to-tip distributions of the fin face heat transfer coefficient are presented. The main message of these distributions is the fact of the enormous variation of the heat transfer coefficient along the fin. The general pattern of the variation includes a rapid rise near the fin base, the attainment of a plateau (either flat or gently rising) which extends over most of the fin height, and an extremely sharp increase near the fin tip. That the coefficient varies along the fin is not an altogether new finding since other investigators have demonstrated the existence of such variations. Rather, the special significance of the present results is that they stem from a more complete model of fin heat transfer (finite fin thickness and conductivity, active tip) than that of previously published work.

On the other hand, it is worth calling attention to the profound disparity between the variations of the heat transfer coefficient evidenced in Figs. 3–8 and the constant value of the coefficient that is used in conventional analyses. In addition to quantitative errors, the assumption of a constant coefficient can also lead to erroneous qualitative conclusions such as, for instance, that the rate of fin heat loss is a maximum near the base and a minimum near the tip.

There are certain trends in the insets that are worthy of note. In general, higher heat transfer coefficients are stimulated in the base-adjacent portion of the fin by larger k_f/k ratios, while an opposite trend prevails nearer the tip. Furthermore, although deactivating the tip gives rise to larger h_f values near the tip, lower h_f values are in evidence away from the tip in certain cases.

Before concluding the discussion of the local results, mention may be made of the variation of the temperature across the thickness of the fin. For reporting these results, let Δ_{cs} denote the temperature difference between the centerline of the fin and its surface, both at the same value of y; in addition, let Δ_{sb} denote the surface-to-fluid bulk temperature difference. For $k_f/k = 10^3$, it was found that $\Delta_{cs}/\Delta_{sb} \sim 10^{-3}$, while for $k_f/k = 10^4$, the values of $\Delta_{cs}/\Delta_{sb} \sim 10^{-4}$. These ratios are impressively small. They indicate that the temperature variations across the fin were negligible for the cases that were investigated.

Relation to the Conventional Fin Model. As was noted in the Introduction, conventional fin models are based on the assumption that the heat transfer coefficient is uniform on all the thermally active surfaces of the fin. Although the foregoing presentation has demonstrated that this assumption is not valid, it is still of interest to seek some way to relate the present results to those of the conventional model. The approach used here to relate the two sets of results will now be described.

In the conventional model, a naturally occurring dimensionless group for a rectangular fin of thickness t and height H is

$$mH, \qquad m = (2\hat{h}/k_f t)^{1/2} \tag{28}$$

where $\hat{h}$ denotes the *fictive* spatially uniform heat transfer coefficient. Since, in reality, $\hat{h}$ does not exist (i.e., the heat transfer coefficient is not spatially uniform), it cannot be calculated directly. Here, $\hat{h}$ (or, rather, its dimensionless counterpart mH) will be calculated indirectly by the following procedure:

1 For a fin that is thermally active at the tip as well as at its principal faces, the formula for the fin heat transfer rate as given by the conventional model is equated on a case-by-case basis to the heat transfer rates listed in Table 1 (i.e., for the C cases). When this operation is carried out in dimensionless form, the only unknown is the quantity mH defined by equation (28), and it can, therefore, be determined.

2 A similar procedure is followed for the case where the tip is perfectly insulated. For this case, the literature formula for the heat transfer rate for an insulated-tip fin is equated to the heat transfer rates for the I cases of Table 1.

The aforementioned formulas for the conventional model are found in numerous textbooks and need not be repeated here. Once the mH values were determined, they were employed to evaluate the fin efficiency η from the standard formulas of the conventional model. The resulting values of mH and η are listed in the last two columns of Table 1.

In appraising the trends in the values of mH, it should be noted that k_f and t are involved in the definition of m in addition to $\hat{h}$, and their presence influences the numerical values of mH. Thus, the mH for $k_f/k = 10^3$ are larger than those for $k_f/k = 10^4$ by a factor approximating the square root of ten. Similarly, the values of mH for $t/H = 0.1$ are lower than those for $t/H = 0.01$ by approximately the same factor. If these factors are taken into account, it appears that $\hat{h}$ does not vary appreciably from case to case among those listed in Table 1, with the exception of the case $S/H = 0.1$ and $C/H = 0.25$. The low $\hat{h}$ values for that case reflect the fact that most of the fluid flows through the clearance gap rather than in the interfin space.

The η values display a logical pattern. It is well established that increasing departures of η from unity are indicative of larger temperature variations along the fin. Thus, larger η should be correlated with smaller values of θ_t/θ_b, and smaller η should correspond to larger θ_t/θ_b. Table 1 shows that these expectations are fulfilled.

As a final note, it can be seen that both mH and η are little affected by whether the tip is thermally active or inactive.

Fluid Flow Characteristics. Results will now be presented for two quantities which relate to the velocity field. One of these is the friction factor f, which was evaluated according to the standard definition

$$f = (-dp/dz)D_h/\tfrac{1}{2}\rho\overline{w}^2 \tag{29}$$

where D_h is the conventional hydraulic diameter. Friction factors are listed in Table 2 in terms of the group fRe, in which

$$\mathrm{Re} = \overline{w}D_h/\nu \tag{30}$$

The numerical values of fRe in Table 2 are not very regular with regard to trend. This is because the value of fRe not only reflects the pressure gradient but also the magnitude of the hydraulic diameter. Thus, for a given spacing, the pressure gradient decreases (for a fixed $\overline{w}$) as the clearance increases while the hydraulic diameter increases. The conflict between these opposing tendencies leads to the aforementioned irregular behavior.

The other tabulated velocity-related quantity is the mass flow ratio $\dot{m}_{if}/\dot{m}$. In this ratio, $\dot{m}_{if}$ is the rate of mass flow through the interfin space (i.e., $0 \le y \le H$) while $\dot{m}$ is the total mass flow through a module. The table shows that for a given spacing S/H, the mass flow through the interfin space decreases as the clearance increases. This trend reflects the tendency of the flow to seek the path of least resistance. The shift of the flow from the interfin space to the clearance is most evident at small spacings.

Concluding Remarks

In the present study, the heat transfer characteristics at the tip and at the principal faces of a fin have been determined without a priori specification of the heat transfer coefficient—as is conventional. Rather, the momentum conservation equation for the fluid and the

Table 2 Fluid flow characteristics

t/H	S/H	C/H	fRe	$\dot{m}_{if}/\dot{m}$
0.01	0.1	0.1	89.21	0.815
		0.25	45.09	0.287
	0.5	0.1	71.37	0.964
		0.25	81.37	0.814
0.1	0.5	0.1	70.80	0.957
		0.25	84.21	0.772

Downloaded 20 Dec 2010 to 194.27.225.72. Redistribution subject to ASME license or copyright; see http://www.asme.org/terms/Terms_Use.cfm

energy equations for the fluid and the solid have been solved numerically by finite differences.

The average fin-tip heat transfer coefficient was evaluated and compared with the average coefficient for a segment of the principal face adjacent to the tip, the segment length being equal to half the tip width. These coefficients were found not to differ too greatly in magnitude, with largest deviations on the order of 25 percent. For the most part, the tip coefficients are higher than those on the tip-adjacent principal face. These deviations are smaller than what might have been conjectured in the past, when there was no quantitative information available. On the basis of the present findings, it seems reasonable to use equal values of the tip and tip-adjacent coefficients for those cases where there is no quantitative information about their differences.

When convective heat transfer at the tip was suppressed, the heat transfer coefficients on the tip-adjacent portion of the principal face increased markedly, thereby compensating for the loss of the tip surface area. The overall performance of the fin was found to be about the same when the tip was either convectively active or adiabatic. On the other hand, assessment of different tip conditions by conventional models yields findings at variance with that found here because those models use the same input values of the heat transfer coefficient for the different tip conditions.

The highest local heat transfer coefficient in the system occurs at the corner where the tip and principal face intersect, while the lowest coefficient is at the fin base. The variation between base and tip includes a rapid rise near the base, the attainment of a plateau which extends over most of the fin height, and an extremely sharp rise near the tip. This is to be contrasted with the uniform heat transfer coefficient that is assumed to prevail in the conventional model.

Higher values of k_f/k provide higher heat transfer coefficients in the base-adjacent portion of the fin but lower coefficients nearer the tip.

Acknowledgment

The research reported here was performed under the auspices of NSF Grant 7518141.

References

1 Stachiewicz, J. W., "Effect of Variation of Local Film Coefficients on Fin Performance," ASME JOURNAL OF HEAT TRANSFER, Vol. 91, 1969, pp. 21–26.

2 Sparrow, E. M., Baliga, B. R., and Patankar, S. V., "Forced Convection Heat Transfer from a Shrouded Fin Array With and Without Tip Clearance," ASME JOURNAL OF HEAT TRANSFER, Vol. 100, 1978, pp. 572–579.

3 Patankar, S. V., Numerical Heat Transfer and Fluid Flow, Hemisphere, Washington, 1980.

Downloaded 20 Dec 2010 to 194.27.225.72. Redistribution subject to ASME license or copyright; see http://www.asme.org/terms/Terms_Use.cfm

M. S. Khader[1]
Associate Professor of Mechanical Engineering, Cairo University, Giza, Egypt
Mem. ASME

M. C. Hanna
Graduate Student, Electrical & Computer Engineering, University of South Carolina, Columbia, S. C. 29208

An Iterative Boundary Integral Numerical Solution for General Steady Heat Conduction Problems

An iterative boundary integral numerical method for solving the steady conduction of heat is developed. The method is general for two- and three-dimensional regions with arbitrary boundary shapes. The development is generalized to include the first, second, and third kind of boundary conditions and also radiative boundary and temperature-space dependent convective coefficient cases. With Kirchhoff's transformation, cases of temperature-dependent thermal conductivity with general boundary conditions are also accounted for by the present method. A variety of problems are analyzed with this method and their solutions are compared to those obtained analytically. A comparison between the present method and the finite difference predictions is also investigated for a case of mixed temperature and convective boundary conditions. Moreover, two-dimensional regions with three kinds of boundary conditions and irregular-shaped boundaries are used to illustrate the versatility of the technique as a computational procedure.

Introduction

Integral methods for formulating field governing equations have been a subject of interest to many investigators for several years. Some exact and approximate solutions for these integral equations, depending on the specifics of each problem, were obtained [1, 2]. A fundamental method employed in the classical potential theory is the use of Green's functions for solving the integral equation associated with the Laplace equation [2]. In spite of the generality of this method, it is limited to those problems of simple geometries and boundary conditions. These limitations are due to the mathematical complexity of constructing the required Green's functions for obtaining the solution to the integral equation. A modified version of the method, based on the use of Green's functions together with Green's second formula, has been found to be more practical and less complex [3–5]. The basic idea of this modified version is to cast the field differential equation into a boundary integral equation. The method, which has become popular in recent years, is called the boundary integral equation method (BIE) in the solid mechanics literature [5–7]. This popularity is the result of the use of numerical schemes for solving the integral equations.

In many aspects, the BIE technique for solving boundary value problems proves to be advantageous over the conventional numerical methods of finite difference and finite elements. Since the technique uses only the boundary data in the solution, this in turn reduces the size of the numerical calculations. In addition, the solution at any interior point is easily obtained with a high resolution and without further involvement of the other points. Furthermore, the method does not require any modifications or special handling of points near the domain boundaries, unlike the case of the finite differences. This particular feature makes the BIE method well suited to those problems with irregular-shaped boundaries.

Applications of the boundary integral numerical method to heat conduction problems have received less attention as compared to those problems in solid mechanics. This is due to the limitation of the BIE method to those cases of linear conditions such as constant flux or constant temperature. Many papers have appeared in the literature which show the application of the method to the solution of conduction problems where conductivity and both the temperature and flux at the boundaries are constants [7–10].

Rizzo and Shippy [10] applied the Laplace transform and the boundary integral method to obtain transient solutions for an infinite cylinder with convection from its surface. Chang, et al. [11], and recently Wrobel and Brebbia [12], presented a formulation for the case of transient heat conduction where they directly integrated the equations over the real times.

Khader [13], by employing Kirchhoff's transformation, was able to use the BIE method to solve the steady cases of heat conduction in regions with thermal conductivity dependent on temperature. The technique was limited to those problems with prescribed flux and temperature boundary conditions. The progress achieved so far in applying the BIE method to the solution of heat conduction problems is far from being a general technique. The limitation is imposed by the linearity requirements of both the governing equation and its boundary conditions.

In relation to the problem of heat conduction in regions with temperature dependent thermal conductivity, Sparrow and Koopman [14] devised a solution method for those cases with convective boundary conditions. The method is based on using the Kirchhoff transformation and a numerical iteration procedure. A primary solution for the transformed differential equation, with the linear boundary conditions of the primary problem retained and the convective condition replaced by an assigned temperature condition, is obtained and used as the starting point for the iteration procedure.

In the present investigation, the BIE numerical method is modified to become an iterative technique. This modification enables the method to numerically solve steady-state heat conduction problems with no restrictions imposed on either the conduction equation or its boundary conditions. The present technique is applicable to two- and three-dimensional problems with thermal conductivity or temperature dependent constant and boundary conditions of the first, second and third kinds or their combinations. The method also allows for those nonlinear boundary conditions such as convection, with convective coefficients dependent on both temperature and space, and radiation.

To illustrate the technique and to investigate its accuracy, examples with known exact solutions are used. Moreover, a comparison between the present method and the finite difference predictions is made for illustrating the simplicity of the present technique. Finally, several two-dimensional problems are utilized to demonstrate the generality of the present BIE method for solving those problems of curved and irregular-shaped boundaries with mixed boundary conditions.

Formulation of Approach

The general heat conduction equation for a region occupying a volume V is given as

$$\nabla \cdot (K(T)\nabla T) + q''' = 0 \qquad \text{in V} \tag{1}$$

[1] Currently at the College of Engineering, University of South Carolina, Columbia, S. C. 29208.

Contributed by the Heat Transfer Division for publication in the JOURNAL OF HEAT TRANSFER. Manuscript received by the Heat Transfer Division May 16, 1980.

Copyright © 1981 by ASME

Downloaded 20 Dec 2010 to 194.27.225.72. Redistribution subject to ASME license or copyright; see http://www.asme.org/terms/Terms_Use.cfm

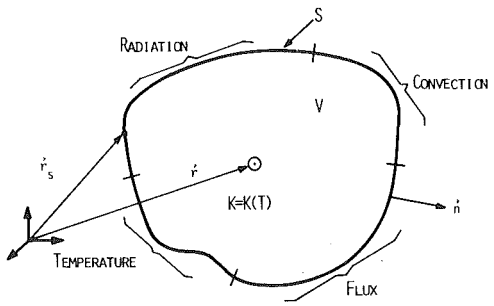

Fig. 1 Heat conduction in a general region with prescribed boundary conditions

where $K(T)$ is the thermal conductivity of the material given as a general function of the temperature. The surface of the region S is subjected to the following types of boundary conditions (see Fig. 1).

i Boundary condition of the first kind

$$T = f_0(\mathbf{r}_s) \tag{2}$$

ii Boundary condition of the second kind

$$\frac{\partial T}{\partial n} = K^{-1} f_0(\mathbf{r}_s) \tag{3}$$

iii Boundary conditions of the third kind

$$K\frac{\partial T}{\partial n} + H(\mathbf{r}_s, T_s)T_s = f_0(\mathbf{r}_s) \quad \text{(convective)} \tag{4}$$

$$K\frac{\partial T}{\partial n} + CT_s{}^4 = f_0(\mathbf{r}_s) \quad \text{(radiative)} \tag{5}$$

where $\mathbf{r}_s$ represents points on the boundary, S, $\partial/\partial n$ defines differentiation with respect to the outward normal to the surface, and $H(\mathbf{r}_s, T_s)$ is the convective heat transfer coefficient as a function of both position and temperature. The general form of equation (4) may represent the cases of free or forced convections, boiling and condensation at boundaries. $f_0(\mathbf{r}_s)$ is a prescribed continuous function on the surface.

Equation (1) and the boundary conditions present a nonlinear problem which has no general theory yet available for its solution. However, if the thermal conductivity and H are constants, the equation becomes linear provided that the radiation condition at the boundary is absent. Moreover, equation (1) with temperature-dependent conductivity can be linearized by Kirchhoff's transformation [13] but the boundary conditions (4) and (5) remain nonlinear. Consequently, no analytical solutions for the equation are generally available. However, the advantage of this transformation will be used in the present investigation as follows. Application of Kirchhoff's transformation to equations (1–5) gives

$$\nabla^2\theta + q'''/K_0 = 0 \tag{6}$$

$$\theta = f(\mathbf{r}_s) \tag{7}$$

$$\frac{\partial\theta}{\partial n} = K_0{}^{-1} f_0(\mathbf{r}_s) \tag{8}$$

and equations (4) and (5) are combined into

$$\frac{\partial\theta}{\partial n} + K_0{}^{-1}H'(\mathbf{r}_s, T_s)\theta_s + K_0{}^{-1}C'\theta_s{}^4 = f_0(\mathbf{r}_s)K_0{}^{-1} \tag{9}$$

where

$$\theta = \int_{T_0}^{T} \frac{K(T)dT}{K_0(T_0)} = L(T)$$

with the inverse transformation $L^{-1}(\theta) = T$,

$$H' = H(\mathbf{r}_s, T_s)T_s/\theta_s$$

and

$$C' = CT_s{}^4/\theta_s{}^4$$

For the case of constant thermal conductivity the transformation is $\theta = T$, $K_0 = K$, $H' = H$ and $C = C'$.

Equations (6) and (9) are now in suitable forms for formulation of the boundary integrals. Consider a function, U, which satisfies $\nabla^2 U = \alpha\delta(|\mathbf{r} - \mathbf{r}_0|)$;[2] Green's theorem [8] gives for both θ of equation (6) and U the following integral equation.

$$\int_V (\theta\nabla^2 U - U\nabla^2\theta)dV = \int_S \left(\theta\frac{\partial U}{\partial n} - U\frac{\partial\theta}{\partial n}\right)dS \tag{10}$$

It has been established by [8] that the form of U is $U_{(3)} = 1/4\pi|\mathbf{r}|$ for three-dimensional cases and $U_{(2)} = -1/2\pi\, LN(|\mathbf{r}|)$ for two-dimensional cases. When the functional form of U is substituted into (10) it leads to

$$\alpha\theta(\mathbf{r}) = \int_S \left(\theta\frac{\partial U}{\partial n} - U\frac{\partial\theta}{\partial n}\right)dS - \int_V (q'''/K_0)U\,dV \tag{11}$$

with

$$\alpha = 4\pi \quad \text{and} \quad U = U_{(3)} \quad \text{(3-D)}$$

$$\alpha = 2\pi \quad \text{and} \quad U = U_{(2)} \quad \text{(2-D)}$$

If all the values of θ and $\partial\theta/\partial n$ are known at each boundary point, equation (11) permits the evaluation of the value of θ at any interior point of the region. This, of course, will contradict the requirements of a well-posed problem, i.e. both temperature and temperature gradient are not known at the same boundary point prior to the solution. However, in the limit as an interior point is allowed to approach a point on the boundary, equation (11) gives [7]

[2] Where $\alpha\delta(|\mathbf{r} - \mathbf{r}_0|)$ is a concentrated heat source at $\mathbf{r}_0$. Extensive review of the BIE method can be found elsewhere [8].

Nomenclature

A = defined by equations (15) and (16)
C = product of Stefan-Boltzmann constant and surface shape factor
C' = as defined in the text
$f_0(\mathbf{r}_s)$, $f(\mathbf{r}_s)$ = space function at the boundary
$\bar{f}(\mathbf{r}_s)$ = defined by equations (15) and (16)
$H(\mathbf{r}_s, T_s)$ = convective heat transfer coefficient as a function of both position and surface temperature, W/m^2 °C
H' = as defined in the text
i = iteration number or index for summation
j = element number
$K(T) \equiv K$ = material thermal conductivity as a function of temperature
$K_0 \equiv K(T_0)$ = material thermal conductivity at a reference temperature
$L(\ )$ = designates transformation operator
M = number of boundary segments (elements)
MM = number of volume cells
$\mathbf{n}$ = outward drawn normal to surface
q = heat flux, W/m^2
q''' = volumetric heat generation, W/m^3
$\mathbf{r}$ = general position coordinate
$\mathbf{r}_s$ = designates surface position
S, s = region surface
SF = surface shape factor
T = temperature, °C or K
T_s = surface temperature, °C or K
$T_\infty(\mathbf{r}_s)$ = surrounding temperature, °C or K
$U_{(2)}$, $U_{(3)}$ = two- and three-dimensional singular solutions of Laplace's equation, respectively
V = region volume
x, y, z = general Cartesian coordinates
(2-D), (3-D) = indicates two- and three-dimensional, respectively
α = numerical coefficient in equation (11)
β = numerical coefficient in equation (12)
θ = transformed temperature
θ_s = transformed surface temperature
∇^2 = Laplacian operator
δ = Dirac's delta function
All dimensions are in SI units.

Downloaded 20 Dec 2010 to 194.27.225.72. Redistribution subject to ASME license or copyright; see http://www.asme.org/terms/Terms_Use.cfm

$$\beta\theta(\mathbf{r}_s) = \int_S \left(\theta \frac{\partial U}{\partial n} - U\frac{\partial \theta}{\partial n}\right) dS - \int_V (q'''/K_0) U\, dV \qquad (12)$$

with

$$\beta = 2\pi \quad \text{and} \quad U = U_{(3)} \quad \text{(3-D)}$$

$$\beta = \pi \quad \text{and} \quad U = U_{(2)} \quad \text{(2-D)}$$

For corners and nonsmooth boundary points, β is equal to the interior angle formed by the tangents at the point [7].

Equation (12) involves only boundary data and is a supplementary equation to equation (11). The solution of (12) provides θ and $\partial\theta/\partial n$, which is the required information needed by equation (11) to compute the temperature θ, at any interior point.

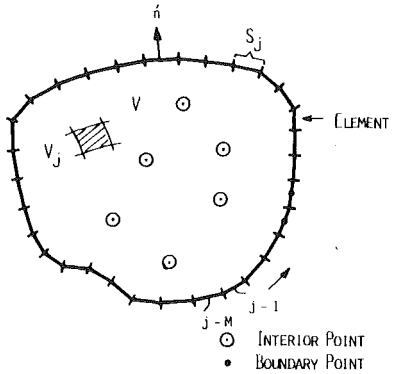

Fig. 2 Boundary descretization

Iteration and Numerical Procedures

In general, no analytical methods are available for the solution of equations (11) and (12). However, for very special geometries, an analytical solution may be obtained using Green's function constructed for the given geometrical region. In this section, a general numerical scheme for the solution of equation (12) is discussed.

The starting point in the present numerical scheme is to divide the boundary of the region, S, under investigation into M piecewise, flat segments as shown in Fig. 2. Equation (12) is then discretized for each of these segments in the form

$$\beta\theta_i(\mathbf{r}_s) + \sum_{j=1}^{MM} \int_{V_j} (q'''/K_0) U\, dV - \sum_{j=1}^{M} \left[\int_{S_j} \theta_j \frac{\partial U}{\partial n} dS - \int_{S_j} U \left(\frac{\partial \theta}{\partial n}\right)_j dS\right] = 0 \qquad (13)$$

where each segment is defined by two nodal points as shown in Fig. 2. For the volume integrals of the heat generation term, MM internal cells are defined and used for their numerical evaluation. These integrals do not introduce any further unknowns, since all the quantities involved are known and hence equation (13) is still a boundary equation. The integrals of equation (13) are all evaluated numerically using a simple quadrature. If equation (13) is written for each boundary segment, a set of M algebraic equations is obtained relating the $2M$ quantities θ and $\partial\theta/\partial n$. Depending on what boundary quantity is known, a total of M values of θ and $\partial\theta/\partial n$ have to be specified and

Table 1 Comparison between exact and BIE predictions

CASE #	BOUNDARY CONDITIONS		PARAMETERS				SOLUTION		TIME SECONDS *
	BOUNDARY (1)	BOUNDARY (2)	a	b	K	H	EXACT	NUMERICAL	
1	CONST. T T_1 = 200C	CONVECT. $T_{\infty 2}$ = 50C	2	3	1.5	10.	T_2 = 57.14 $\left.\frac{\partial T}{\partial n}\right]_2$ = -47.62	T_2 = 57.11 $\left.\frac{\partial T}{\partial n}\right]_2$ = -47.39	2.11
2	CONST. q q = 1000W	RADIATION $T_{\infty 2}$ = 350K	1	.5	2.0	--	T_1=675.07K T_2=425.07K $\left.\frac{\partial T}{\partial n}\right]_2$ = -500	T_1=674.87K T_2=425 K $\left.\frac{\partial T}{\partial n}\right]_2$ = -499.55	3.77
3	CONVECTION $T_{\infty 1}$= 600K	RADIATION $T_{\infty 2}$= 300K	10	10	5.0	20.	T_1=593.18K T_2=320.17K $\left.\frac{\partial T}{\partial n}\right]_2$ = -27.3	T_1=593.17K T_2=320.62K $\left.\frac{\partial T}{\partial n}\right]_2$ = -27.2	4.48
4	CONST. T T_1 = 300K	CONV. + RAD. $T_{\infty 2}$= 500K	1	.25	0.2	1	T_2=494.61K $\left.\frac{\partial T}{\partial n}\right]_2$ = 788.44	T_2=494.65K $\left.\frac{\partial T}{\partial n}\right]_2$ = 773.25	2.83
5	CONST. T T_1= 100C	CONVECTION $T_{\infty 2}$= 20C	1	2	0.5(1+.01T)	3	T_2 = 29.66C $\left.\frac{\partial T}{\partial n}\right]_2$ = -44.71	T_2 = 29.61C $\left.\frac{\partial T}{\partial n}\right]_2$ = -44.52	3.14
6	CONST. q q = 50W	FREE CONV. $T_{\infty 2}$= 25C	1	4	0.5	$2.5(T_2-T_{\infty 2})^{\frac{1}{4}}$	T_1=435.99C T_2 = 35.97C $\left.\frac{\partial T}{\partial n}\right]_2$ = -100	T_1=434.91C T_2 = 35.96C $\left.\frac{\partial T}{\partial n}\right]_2$ = -99.42	3.72
7	CONST. T T_1=2(10^4)C	RADIATION $T_{\infty 2}$= 0C	2	2	1	--	T_2=642.88C $\left.\frac{\partial T}{\partial n}\right]_2$ =-9678.6	T_2=641.88C $\left.\frac{\partial T}{\partial n}\right]_2$ =-9623.5	30.48

* Computational time on an AMDAHL 470 Computer

Downloaded 20 Dec 2010 to 194.27.225.72. Redistribution subject to ASME license or copyright; see http://www.asme.org/terms/Terms_Use.cfm

the equations can then be solved for the remaining unknowns. At this point, the solution of the set of the algebraic equations is a straightforward matter provided that all quantities of $\partial\theta/\partial n$ are either a linear function of temperature or of space. This includes only those types of boundary conditions of equations (2–4) with H and K independent of temperature. On the other hand, if K depends on the temperature or a part of the boundary is subjected to either nonlinear convection or radiation, the resulting set of the equations becomes nonlinear. Solution of these equations, in general, requires a sophisticated and time-consuming iterative numerical procedure, for example the Newton-Raphson method. In addition, convergence to the right solution is not always assured in some cases.

In the present investigation, a simple iterative scheme is developed to solve those problems which possess nonlinear boundary conditions. The scheme starts by rewriting equation (9) in a pseudo-linear form as

$$\frac{\partial\theta}{\partial n} = K_0^{-1}[\bar{f}(\mathbf{r}_s) - A\theta_s] \tag{14}$$

with the coefficient A and $\bar{f}(\mathbf{r}_s)$ in the following form

i convection case

$$A = H(\mathbf{r}_s, T_s)T_s/\theta_s$$
$$\bar{f}(\mathbf{r}_s) = H(\mathbf{r}_s, T_s)T_\infty(\mathbf{r}_s) \tag{15}$$

ii radiation case

$$A = 4CT_{(1)}{}^3T_s/\theta_s$$
$$\bar{f}(\mathbf{r}_s) = 4CT_{(1)}{}^3T_\infty(\mathbf{r}_s) \tag{16}$$

where $T_{(1)}$ is a fictitious temperature obtained by using Rolle's theorem [15] to expand $T_s{}^4$ (or $\theta_s{}^4$) in terms of T_∞. The iteration procedure starts by taking $T_{(1)} = T_s$ (i.e., θ_s) $= T_\infty$ for those elements having boundary conditions in the form of (14). Accordingly, A and $\bar{f}(\mathbf{r}_s)$ are determined from equations (15) and (16). The value of $\partial\theta/\partial n$ is next evaluated and substituted into the set of equations resulting from the use of equation (13) for all elements. Solutions for all the

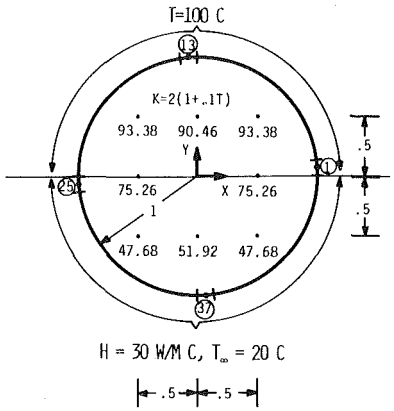

Fig. 3 Heat conduction in a symmetrical region with temperature dependent thermal conductivity

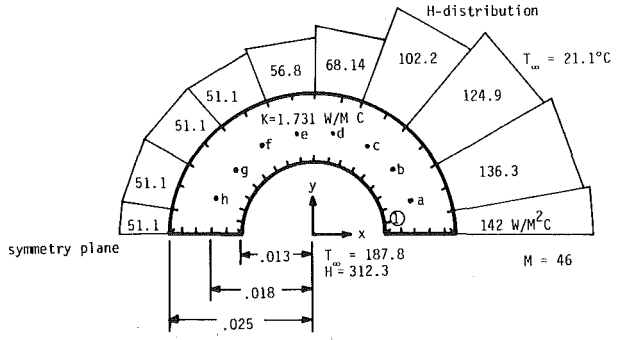

Fig. 4 Heat transfer in a heat exchanger tube with variable surface convective heat transfer coefficients

Table 2 Selected results from BIE solutions

Results for Figure 3 Example			Results for Heat Exchanger Tube Example			Results for Figure 6 Example		
element #	T	$\frac{\partial T}{\partial n}$	element #	T	$\frac{\partial T}{\partial n}$	element #	T	$\frac{\partial T}{\partial n}$
1	100	102.5	1	135.1	0	1	300	-108.96
4	100	15.0	4	90.6	0	5	304.8	50.89
7	100	9.2	7	74.4	-4197	9	402.3	27.44
10	100	7.4	10	79.8	-4235	13	447.9	16.83
13	100	7.1	13	93.8	-2862	17	489.4	10.54
16	100	7.8	16	104.2	-2724	21	500.5	-.20
19	100	10.4	19	108.8	-2591	25	504.6	16.67
22	100	20.0	22	110.2	-2630	29	492.6	0.0
25	63.5	-88.8	25	121.0	0	33	448.9	0.0
28	34.8	-49.6	28	150.8	0	37	476.8	15.94
31	29.0	-34.6	31	157.4	5488	41	496.1	2.93
34	27.1	-28.7	34	156.1	5724	45	502.7	-.20
37	26.7	-27.5	37	153.5	6186	49	552.8	30.80
40	27.5	-30.1	40	149.7	6867	53	600.0	60.33
43	30.2	-38.1	43	146.3	7484	57	500.0	71.95
46	39.3	-58.7	46	144.0	7899	61	530.9	0.0
						65	514.9	0.0
			a	110.5		69	515.0	1.67
			d	122.9		73	477.0	6.67
			g	132.6		77	431.4	-54.29
			f	130.8		81	401.8	-34.52
						85	368.5	-12.33
$\oint qdA = \sum_{j=1}^{48} A_j K_j \left.\frac{\partial T}{\partial n}\right\|_j = 1.385$			$\oint q/KdA = \sum_{j=1}^{46} A_j \left.\frac{\partial T}{\partial n}\right\|_j = .3$			$\oint q/KdA = \sum_{j=1}^{88} A_j \left.\frac{\partial T}{\partial n}\right\|_j = .912$		

Downloaded 20 Dec 2010 to 194.27.225.72. Redistribution subject to ASME license or copyright; see http://www.asme.org/terms/Terms_Use.cfm

unknown values of θ and $\partial\theta/\partial n$ are then obtained by a matrix inversion numerical subroutine. For only those elements where $T_{(1)}$ and T_s (i.e., θ_s) are previously assumed, the new value of θ_s (i.e., T_s) and a new weighted value of $T_{(1)}$ are substituted into equations (15) and (16) where new values of A and $\bar{f}$ are obtained. The procedure is repeated as before until a convergence criterion in the form $|\theta_{s(i+1)} - \theta_{s(i)}|$ reaches a certain tolerance. It has been found that the procedure is stable and converges to the right solution after a few iterations. Accurate solutions for some cases of extreme values of boundary conditions are also obtained using the present numerical scheme (see case 7 in Table 1). These results indicate that the iterative numerical scheme presented is a general and accurate technique for solving this class of heat transfer problems.

Results

As a rigorous test of the present numerical method, a one-dimensional heat conduction problem of a simple rectangular plate is selected. The plate is of a length a, width b, and unit depth. The two lateral surfaces are kept insulated in order that exact solutions can be obtained. The other two boundaries designated ① and ② are then subjected to a variety of practical boundary conditions. A total of seven cases are presented in Table 1 with the associated parameters and boundary conditions. Exact solutions are compared with the numerical predictions obtained. Case number seven is an unrealistic case, but it provides a check on the convergence of the iterative scheme. Examination and comparison of the results indicate that the BIE iterative numerical method is stable and accurate. It should be noted here that for the case of radiative boundary, case 7, an error of about 0.5 percent in the temperature gradient is encountered. This was due to the small error in the temperature predictions of about 0.15 percent and the nonlinearity of the radiation boundary condition.

The second example of Fig. 3 represents a case of heat conduction in a symmetrical region with thermal conductivity dependent on temperature. The circular cross-section has thermal conductivity in the form $K = 2(1 + 0.1T)$; the upper and the lower halves are subjected to a constant temperature and convection, respectively. The numerical results as shown in Table 2 indicate that the solution preserves the symmetry expected with a small error as indicated by the net heat transferred from the boundary.

As an example of a variable surface convection coefficient case, a cross-flow heat exchanger tube is presented. The tube transports a high temperature gas with the cooling fluid flow normal to the tube on the outer surface (see Fig. 4). The coefficient of heat transfer on the outer surface is variable while it assumes a constant value at the inner tube surface. The numerical solution of the problem is shown in Table 2 for both temperatures and heat fluxes. The numerical calculation using the standard Fortran language took about 3 s on an AMDAHL 470 computer.

To demonstrate the accuracy of the solutions obtained by the present method as compared to other numerical techniques, the problem of Fig. 5 is used. The conduction equation for the rectangular region shown is solved by both the BIE and the finite difference techniques. In the finite difference technique a total of 66 grid points are used compared to only 28 elements for the BIE method for the same solution accuracy as shown in Fig. 5. An important fact that should be mentioned with regard to this comparison is that in the finite difference method a total of 66 equations are solved while in the BIE only 28 equations need to be solved. This is translated immediately to a 1:5.6 savings in computer storage requirements. In addition, if the 36 interior temperature values of the finite difference scheme are solved for by using the BIE method, the computer storage requirements stay the same. This important fact makes the BIE method superior to the finite difference and suitable for minicomputer use.

Finally, a very general case of heat conduction in a two-dimensional region with mixed type boundary conditions is investigated. The irregular-shaped boundary of the region consists of flat and curved parts as shown in Fig. 6. Most of the types of boundary conditions encountered in practice are specified in Table 3. The region boundary is divided into 88 segments of different length; numerical results are then obtained for the unknown values of either θ, or $\partial\theta/\partial n$ for each of these segments. The boundary results are then used to calculate the temperature values at 36 interior points. The total numerical calculations took 30.4 s including reading the data and printing the final results. Figure 7 shows the temperature distribution in the x-direction for $y = 0.5$ while the temperatures and the gradients at the region boundary are given in Table 2. As a means of an assessment of the solution accuracy, the net heat transferred from all boundaries is calculated as shown at the end of Table 2.

These solutions for the previous heat transfer examples indicate that the present iterative boundary integral method is accurate and

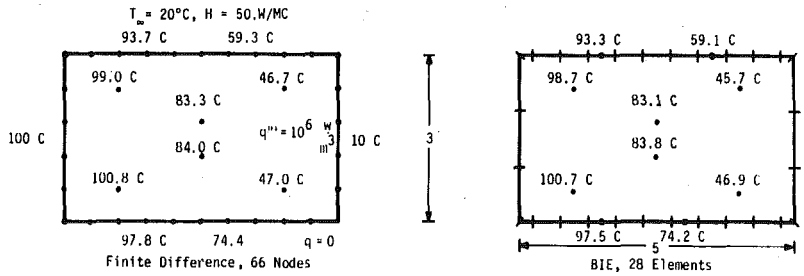

Fig. 5 Finite difference and BIE comparison for a case with heat generation

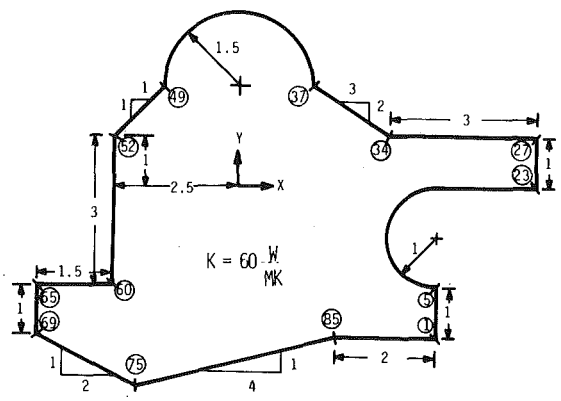

Fig. 6 Two-dimensional plate and boundary conditions

Table 3 Boundary conditions for Fig. 6

Elements	Boundary Condition
1–4	T = 300 K
5–22	Radiation, T_∞ = 500 K, SF = 0.8
23–26	q = 1000 W
27–33	q = 0
34–36	Convection, H = 30, T_∞ = 300 K
37–48	Convection + radiation, H = 20, T_∞ = 500 K, SF = 0.9
49–51	Radiation T_∞ = 600 K, SF = 0.75
52–59	T = 600 K
60–68	q = 0
69–70	q = 100 W
71	q = 200 W
72	q = 300 W
73–75	q = 400 W
76–88	Convection, H = 40, T_∞ = 350 K

Downloaded 20 Dec 2010 to 194.27.225.72. Redistribution subject to ASME license or copyright; see http://www.asme.org/terms/Terms_Use.cfm

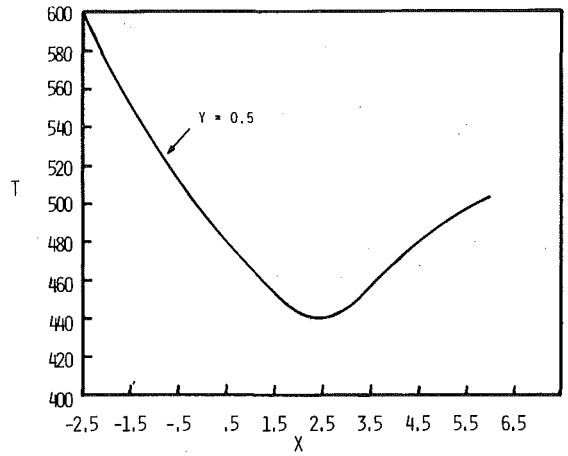

Fig. 7 Temperature distribution for the plate problem

general for solving most of the conduction problems of practical importance. Although the examples cited in the present paper are all of a two-dimensional nature, the method is also suitable for three-dimensional cases. For problems with internal heat generation, the only added effort is the evaluation of the volume integral in equations (11) and (12) which involves known functions. However, for those cases with a constant heat generation term, the problem may be reduced to a case with no heat generation through a particular transformation. In addition, if the heat generation term, q''', is a harmonic function of the space variables, the volume integrals of equations (1) and (3) are transformed directly to surface integrals using Green's theorem. These two cases are discussed in detail in the Appendix.

As a final remark, it should be mentioned here that temperatures calculated at interior points very near the boundary are generally not very accurate. This inaccuracy is a result of the approximation of the actual boundary contour by finite segments. Yet, it has been found that an interior point at a distance comparable to the length of the nearest segment maintains an accuracy comparable to that of other points far from the boundary. This, of course, does not represent a drawback for the method, since temperatures and fluxes at the boundary are obtainable directly without reference to the interior point.

Conclusions

The iterative boundary integral method has been shown to be appropriate for use in numerically solving a variety of steady-heat conduction problems. The method in its present form has no inherent limitations as to the geometric complexity, kind of boundary condition, or the material thermal conductivity.

The method is most suitable for calculating temperature and heat flux at the system boundaries and at a few individual interior points. This feature makes the method superior to available numerical methods, where the solution involves all interior points. As in most of the practical calculations of heat transfer, boundary fluxes and temperatures are the only needed information.[3] However, complete temperature distributions are directly obtainable with minimum efforts. This advantage has been proven to induce a savings in computer storage and time. Another primary advantage of using the boundary integral equation for the numerical solutions rather than the original differential equation is the space reduction of the problem. If the problem is three-dimensional in space, the boundary integral equation is a two-dimensional one which requires less effort and time for its solution.

An important potential for the use of the present method is the steady inverse problem in heat conduction. The known values of the temperature at the interior points may be used to generate a set of equations from equation (11) together with another set of equations as equation (12) for solving the unknown boundary data.

Finally, the present method can be simply extended to include the transient heat conduction problems and to some specific problems of convective heat transfer. This will in turn make the BIE method a more competitive numerical technique to the already existing methods.

[3] For example, fins and heat exchanger tubes.

References

1 Kellogg, O. D., *Foundations of Potential Theory,* Dover, New York, 1953.

2 Morse, P. M., and Feshbach, H., *Methods of Theoretical Physics,* Part II, McGraw-Hill, New York, 1961.

3 Jawson, M. A., "Integral Equation Methods in Potential Theory," *Proceedings Royal Society,* Vol. 275A, 1963, p. 23.

4 MacMillan, W. D., *The Theory of Potential,* Dover, New York, 1958.

5 Symm, G. T., "Integral Equation Methods in Potential Theory," *Proceedings Royal Society,* Vol. 275A, 1963, p. 33.

6 Rizzo, F. J., "An Integral Equation Approach to Boundary Value Problems of Classical Elastostatics," *Quarterly Review of Applied Mathematics,* Vol. 25, 1967, p. 83.

7 Cruse, T. A., and Rizzo, F. J., (ed.), "Boundary Integral Equation Method," *Computational Applications in Applied Mechanics,* ASME Proceedings AMD-Vol. 11, 1975.

8 Jawson, M. A., and Symm, G. T., *Integral Equation Methods of Potential Theory and Elastostatics,* Academic Press, New York, 1970.

9 Alarcon, E., Martin, A., and Paris, "Boundary Elements in Potential and Elasticity Theory," *Computers and Structures,* Vol. 10, 1979, p. 351.

10 Rizzo, F. J., and Shippy, D. J., "A Method of Solution for Certain Problems of Transient Heat Conduction," *AIAA Journal,* Vol. 8, 1971, p. 2004.

11 Chang, Y. P., Kang, C. S., and Chen, D. J., "The Use of Fundamental Green's Functions for the Solution of Problems of Heat Conduction in Anisotropic Media," *International Journal of Heat Mass Transfer,* Vol. 16, 1973, p. 1905.

12 Wrobel, L. C., and Brebbia, C. A., "The Boundary Element Method for Steady State and Transient Heat Conduction," *Proceedings First International Conference in Numerical Methods in Thermal Problems,* University College, Swansea, England, 1979, p. 58.

13 Khader, M. S., "Heat Conduction with Temperature Dependent Thermal Conductivity," 19th National Heat Transfer Conference, ASME Paper No. 80-HT-4, 1980.

14 Sparrow, E. M., and Koopman, R. N., "Heat Transfer in Reactor Components Having Temperature-Dependent Thermal Conductivity," *Nuclear Science and Engineering,* Vol. 42, 1970, p. 406.

15 Carnahan, B., Luther, H. A., and Wilkes, J. O., *Applied Numerical Methods,* John Wiley and Sons, New York, 1969, p. 13.

APPENDIX

Conduction with a Constant Heat Generation Term. For those cases of heat conduction with volumetric heat generation independent of both temperature and space, the following transformation is derived:

$$\theta = \int_{T_0}^{T} \frac{K(T)\,dT}{K(T_0)} + \frac{q'''}{K_0(T_0)N}\,[x^2 + y^2 + z^2]$$

with $N = 4$ (two-dimensional cases) and N = 6 (three-dimensional cases).

This transformation when applied to equation (1) gives

$$\nabla^2\theta = 0$$

where the heat generation term has disappeared. Also, minor modifications of the boundary conditions, equations (7, 8), and (9), are required. This procedure reduces the numerical efforts substantially, since no numerical integration for volume integrals are needed. Accordingly, the same numerical steps for the case with no heat generation will be applied.

Conduction with a Harmonic Function Heat Generation Term. If the heat generation term of equation (1) is a harmonic function of the space variables, the volume integrals of equation (11) and (12) may be expressed as surface integrals. This can be achieved by the use of Green's identity. Accordingly,

$$\int_V (q'''/K_0)U\,dV = \int_S \left[q'''/K_0 \frac{\partial\phi}{\partial n} - \frac{\partial}{\partial n}(q'''/K_0)\phi\right] dS \quad \text{with}$$

$$\phi = |\mathbf{r}| \quad \text{(3-D)}$$

$$\phi = \frac{1}{4}|\mathbf{r}\cdot\mathbf{r}|[LN(|\mathbf{r}|) - 1] \quad \text{(2-D)}$$

Thus, equations (11) and (12) and the rest of the analysis will involve only surface integrals on the boundary.

Downloaded 20 Dec 2010 to 194.27.225.72. Redistribution subject to ASME license or copyright; see http://www.asme.org/terms/Terms_Use.cfm

Unsteady Heat Flow between Solids with Partially Contacting Interface

S. S. Sadhal
Assistant Professor,
Department of Mechanical Engineering,
University of Pennsylvania,
Philadelphia, PA 19104
Assoc. Mem. ASME

The problem of the transient thermal response of two semi-infinite solids not making perfect contact, is treated analytically by modeling the interface to be a series of equally spaced strips making perfect contact. The remaining area is assumed to perfectly insulated, and a criterion is established for the validity of this assumption, taking radiation into consideration. The mixed interface conditions present a considerable difficulty and a long-time perturbation scheme is therefore used to obtain approximate expressions for the transient temperature distributions, average heat flux and the thermal contact resistance. The method is applicable to a large class of problems with mixed boundary conditions for which the existing techniques give exact solutions only for the steady state.

1 Introduction

The heat transfer between two solids not having perfect contact at the interface is of fundamental importance in dealing with contact resistance. In the present study, the contact between two flat surfaces is modeled in two dimensions by a series of equally spaced strips having perfect contact. In the remainder of the region we would have conduction, convection and radiation through the air spaces. Because of the low thermal conductivity of air and the small size of the air gaps, conduction and convection may be ignored. Radiation may be important at large temperatures of the interface, particularly if the region of perfect contact covers only a small fraction of the interface. In the latter part of this analysis, calculations are carried out to establish a criterion for which radiation may be neglected. These calculations show that for metallic solids contacting over only 1 percent of the area with contacts 1 cm apart and interfacial temperatures up to 1000 K, the contribution from radiation is less than 2 percent of that from conduction. Clearly, for such conditions radiation may be neglected.

The above description of the contact is particularly realistic for machined surfaces, or surfaces which are otherwise wavy. The physical situation for the geometry also exists in the case of sheets partially welded at the edges. The heat flow at the interface is described by mixed boundary conditions which cannot be treated by the usual Fourier series. Such boundary conditions lead to sets of dual series equations for which the exact methods developed [1] are restricted to steady-state heat flow. The steady state problem with the interface conditions as described above has been treated exactly by Dundurs and Panek [2].

The difficulty with the unsteady case becomes apparent as the appropriate dual series equations are developed. In view of this difficulty, an approximate solution is found through the use of a long time perturbation scheme. The method used is applicable to a large class of problems for which the exact solutions are available only for the steady state cases. It is perhaps appropriate to note here that if we are dealing with a problem involving "non-mixed" boundary conditions for a semi-infinite medium, an exact unsteady solution for all time may be found analytically.

In the present analysis, we obtain a long-time approximate solution for two solids, initially at different temperatures, brought into contact over a series of equally spaced strips. The problem of the transient response of two solids in contact over a finite circular disk has been treated numerically by Schneider, et al. [3] and analytically for long time by Sadhal [4].

2 Statement of Problem

Two semi-infinite solids initially at uniform but different temperatures are brought together and perfect thermal contact is established over a series of identical, equally spaced strips. The regions between these strips are assumed to be insulated. By recognizing the periodic nature of the problem, we can find planes of symmetry and we can require that the temperature distribution be an even function about these planes. These planes are taken to be a distance ℓ apart. As shown by broken lines in Fig. 1, the planes bisect the insulated regions and the region of perfect contact. The insulated regions are shown by double lines and are taken to be a width $2c^*$.

The initially hotter solid is referred to as region 1 ($y^* > 0$) and the other solid as region 2 ($y^* < 0$), as shown in Fig. 1. The initial temperatures are denoted by T_{10} and T_{20} for regions 1 and 2, respectively. In the rest of the analysis the subscripts 1 and 2 are used in reference to the properties of the corresponding regions.

The conduction process is described by the heat equation which, under the conditions stated for the model, may be written as

$$\left.\begin{aligned} &\frac{\partial^2 T_1}{\partial x^{*2}} + \frac{\partial^2 T_1}{\partial y^{*2}} = \frac{1}{\kappa_1}\frac{\partial T_1}{\partial t}, \quad t > 0; \quad 0 \le x^* \le \ell; \quad y^* > 0, \\ &\text{and} \\ &\frac{\partial^2 T_2}{\partial x^{*2}} + \frac{\partial^2 T_2}{\partial y^{*2}} = \frac{1}{\kappa_2}\frac{\partial T_2}{\partial t}, \quad t > 0; \quad 0 \le x^* \le \ell; \quad y^* < 0, \end{aligned}\right\} \tag{1}$$

subject to

$$\left.\begin{aligned} T_1 &= T_{10}, \quad t = 0; \quad 0 \le x^* \le \ell; \quad y^* \ge 0, \\ T_2 &= T_{20}, \quad t = 0; \quad 0 \le x^* \le \ell; \quad y^* \le 0, \end{aligned}\right\} \tag{2}$$

$$\left.\begin{aligned} \frac{\partial T_1}{\partial x^*} &= 0, \quad x^* = 0, x^* = \ell; \quad t > 0; \quad y^* \ge 0, \\ \frac{\partial T_2}{\partial x^*} &= 0, \quad x^* = 0, x^* = \ell; \quad t > 0; \quad y^* \le 0, \end{aligned}\right\} \tag{3}$$

and

$$\left.\begin{aligned} &T_1 = T_2 \\ &k_1\frac{\partial T_1}{\partial y^*} = k_2\frac{\partial T_2}{\partial y^*}\Big], \quad y^* = 0; \quad t > 0; \quad c^* < x^* \le \ell, \\ &\frac{\partial T_1}{\partial y^*} = \frac{\partial T_2}{\partial y^*} = 0, \quad y^* = 0; \quad t > 0; \quad 0 \le x^* \le c^*, \end{aligned}\right\} \tag{4}$$

where T_1 and T_2 denote the temperature distributions, k_1 and k_2 represent the thermal conductivities, κ_1 and κ_2 refer to the thermal diffusivities, x^* and y^* are the space coordinates, and t is the time.

3 Analysis

By introducing dimensionless variables, $x = \pi x^*/\ell$, $y = \pi y^*/\ell$, $c = \pi c^*/\ell$, $\theta_1 = (T_1 - T_{20})/(T_{10} - T_{20})$, $\theta_2 = (T_2 - T_{20})/(T_{10} - T_{20})$, and then taking the Laplace transform of θ_1 and θ_2 in time we obtain

$$\left.\begin{aligned} -\frac{\ell^2}{\pi^2\kappa_1} + \frac{p\ell^2}{\pi^2\kappa_1}\Theta_1 &= \frac{\partial^2\Theta_1}{\partial x^2} + \frac{\partial^2\Theta_1}{\partial y^2}, \quad 0 \le x \le \pi; \quad y > 0, \\ \frac{p\ell^2}{\pi^2\kappa_2}\Theta_2 &= \frac{\partial^2\Theta_2}{\partial x^2} + \frac{\partial^2\Theta_2}{\partial y^2}, \quad 0 \le x \le \Theta; \quad y < 0, \end{aligned}\right\} \tag{5}$$

Contributed by the Heat Transfer Division for publication in the JOURNAL OF HEAT TRANSFER. Manuscript received by the Heat Transfer Division, April 2, 1980.

Copyright © 1981 by ASME
Downloaded 20 Dec 2010 to 194.27.225.72. Redistribution subject to ASME license or copyright; see http://www.asme.org/terms/Terms_Use.cfm

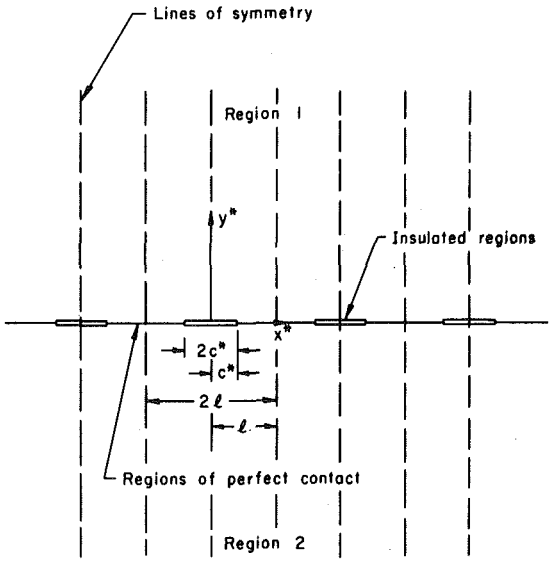

Fig. 1 Two solids in contact over a series of identical, equally spaced strips

subject to

$$\left.\begin{aligned} \frac{\partial \Theta_1}{\partial x} &= 0, \quad x = 0, \quad x = \pi; \quad y \geq 0, \\ \frac{\partial \Theta_2}{\partial x} &= 0, \quad x = 0, \quad x = \pi; \quad y \leq 0, \end{aligned}\right\} \tag{6}$$

and

$$\left.\begin{aligned} \Theta_1 = \Theta_2 \\ k_1 \frac{\partial \Theta_1}{\partial y} = k_2 \frac{\partial \Theta_2}{\partial y} \end{aligned}\right\}, \quad y = 0; \quad c < x \leq \pi,$$
$$\left.\begin{aligned} \frac{\partial \Theta_1}{\partial y} = \frac{\partial \Theta_2}{\partial y} = 0, \quad y = 0; \quad 0 \leq x < c, \end{aligned}\right\} \tag{7}$$

where

$$\Theta_i(x, y, p) = \int_0^\infty e^{-pt}\, \theta_i(x, y, t)dt, \quad i = 1, 2, \tag{8}$$

is the Laplace transform of $\theta_i(x, y, t)$.

In view of (6) the solution may be written as

$$\left.\begin{aligned} \Theta_1 &= \frac{1}{p} + \sum_{n=0}^{\infty} a_{n1} \exp[-(n^2 + p\ell^2/\pi^2 \kappa_1)^{1/2} y] \cos nx, \\ & \qquad y \geq 0, \\ \text{and} \\ \Theta_2 &= \sum_{n=0}^{\infty} a_{n2} \exp[(n^2 + p\ell^2/\pi^2 \kappa_2)^{1/2} y] \cos nx, \\ & \qquad y \leq 0. \end{aligned}\right\} \tag{9}$$

Here a_{n1} and a_{n2} must satisfy

$$a_{n1} = -\frac{k_2\left[n^2 + \frac{p\ell^2}{\pi^2 \kappa_2}\right]^{1/2}}{k_1\left[n^2 + \frac{p\ell^2}{\pi^2 \kappa_1}\right]^{1/2}} a_{n2}, \tag{10}$$

$$\sum_{n=0}^{\infty} (a_{n2} - a_{n1}) \cos nx = \frac{1}{p}, \quad c < x \leq \pi, \tag{11}$$

and

$$\sum_{n=0}^{\infty} a_{n2} \left(n^2 + \frac{p\ell^2}{\pi^2 \kappa_2}\right)^{1/2} \cos nx = 0, \quad 0 \leq x < c. \tag{12}$$

This set of dual series equations (10–12) is not possible to invert with the known analytical techniques, except for $p = 0$ which corresponds to the steady state. Therefore, approximate methods are employed and a perturbation scheme for small p is used to obtain a solution valid for large t.

4 Solution by Perturbation

If we let

$$a_{ni} = \frac{1}{p}\left[a_{ni}^{(0)} + p^{1/2} a_{ni}^{(1)} + p a_{ni}^{(2)} + p^{3/2} a_{ni}^{(3)} + \ldots\right], \quad i = 1, 2 \tag{13}$$

substitute into (10–12), and expand in powers of $p^{1/2}$, we obtain the following after a lot of tedious algebra involving dual cosine series.

$$\left.\begin{aligned} a_{02}^{(0)} &= \frac{k_1 {\kappa_2}^{1/2}}{k_1 {\kappa_2}^{1/2} + k_2 {\kappa_1}^{1/2}}, \quad n = 0, \\ a_{n2}^{(0)} &= 0, \quad n = 1, 2, 3, \ldots. \end{aligned}\right\} \tag{14}$$

$$a_{02}^{(1)} = \frac{2k_1 {\kappa_2}^{1/2} \ell (k_1 + k_2)}{(k_1 {\kappa_2}^{1/2} + k_2 {\kappa_1}^{1/2})^2} \ell n\,(\cos \tfrac{1}{2}c), \tag{15}$$

$$a_{n2}^{(1)} = \frac{k_1 \ell}{\pi (k_1 {\kappa_2}^{1/2} + k_2 {\kappa_1}^{1/2})} \frac{1}{n}\left[P_n(\cos c) - P_{n-1}(\cos c)\right], \quad n = 1, 2, 3, \ldots. \tag{16}$$

$$a_{02}^{(2)} = \frac{4k_1 {\kappa_2}^{1/2} \ell^2 (k_1 + k_2)^2}{\pi^2 (k_1 {\kappa_2}^{1/2} + k_2 {\kappa_1}^{1/2})^3} [\ell n(\cos \tfrac{1}{2}c)]^2, \tag{17}$$

$$a_{n2}^{(2)} = \frac{2k_1 \ell^2 (k_1 + k_2)}{\pi^2 (k_1 {\kappa_2}^{1/2} + k_2 {\kappa_1}^{1/2})^2} \ell n\,(\cos \tfrac{1}{2}c) \frac{1}{n}\left[P_n(\cos c) - P_{n-1}(\cos c)\right], \quad n = 1, 2, 3, \ldots. \tag{18}$$

$$a_{02}^{(3)} = \frac{8k_1 {\kappa_2}^{1/2} \ell^3 (k_1 + k_2)^3}{\pi^3 (k_1 {\kappa_2}^{1/2} + k_2 {\kappa_1}^{1/2})^4} [\ell n(\cos \tfrac{1}{2}c)]^3 - \frac{k_1 {\kappa_2}^{1/2} \ell^3}{32\pi^2 (k_1 {\kappa_2}^{1/2} + k_2 {\kappa_1}^{1/2})^2}\left(\frac{k_1}{\kappa_2} + \frac{k_2}{\kappa_1}\right) \times \sum_{m=1}^{\infty} \frac{1}{m^3}\left[P_m(\cos c) - P_{m-1}(\cos c)\right] \tag{19}$$

$$a_{n2}^{(3)} = \left\{\frac{4k_1 \ell^3 (k_1 + k_2)^2}{\pi^3 (k_1 {\kappa_2}^{1/2} + k_2 {\kappa_1}^{1/2})^3} [\ell n\,(\cos \tfrac{1}{2}c)]^3 + \frac{k_1 k_2 \ell^3}{2\pi^3 (k_1 {\kappa_2}^{1/2} + k_2 {\kappa_1}^{1/2})(k_1 + k_2)}\left(\frac{1}{\kappa_1} - \frac{1}{\kappa_2}\right)\frac{1}{n^3}\right\}\left[P_n(\cos c) - P_{n-1}(\cos c)\right] + \frac{\ell^3 k_1}{32\pi^2 (k_1 {\kappa_2}^{1/2} + k_2 {\kappa_1}^{1/2})(k_1 + k_2)} \times \left(\frac{k_1}{\kappa_2} + \frac{k_2}{\kappa_1}\right) \sum_{m=1}^{\infty} \frac{1}{m^3}\left[P_m(\cos c) - P_{m-1}(\cos c)\right] B_{mn}, \quad n = 1,2,3, \ldots \tag{20}$$

where P_m is the Legendre polynomial of order m, and

Nomenclature

c^* = half-width of regions of no contact
$c = c^*\pi/\ell$, dimensionless half-width
$\mathrm{Fo}_i = \kappa_i t/\ell^2$ = Fourier number
k_1, k_2 = thermal conductivity of solids 1,2
ℓ = width of lines of symmetry
q_{av} = average heat flux
R = thermal resistance
R_{fc} = full-contact thermal resistance
t = time
T_1, T_2 = temperatures in solids 1, 2
T_{10}, T_{20} = initial temperature of solids 1,2
x^*, y^* = cartesian coordinates
$x, y = x^*\pi/\ell, y^*\pi/\ell$, dimensionless cartesian coordinates
$\theta_1 = (T_1 - T_{20})/(T_{10} - T_{20})$ = dimensionless T_1
$\theta_2 = (T_2 - T_{20})/(T_{10} - T_{20})$ = dimensionless T_2
Θ_1, Θ_2 = Laplace transforms of θ_1, θ_2
κ_1, κ_2 = thermal diffusivities of solids 1,2
σ = Stefan-Boltzman constant

Downloaded 20 Dec 2010 to 194.27.225.72. Redistribution subject to ASME license or copyright; see http://www.asme.org/terms/Terms_Use.cfm

$$B_{mn} = \sum_{k=1}^{m} (-1)^{m-k} \int_{\cos^{-1}c}^{1} P_{m-1}(x)[P_n(x) + P_{n-1}(x)]dx. \quad (21)$$

The relation between $a_{n1}^{(i)}$ and $a_{n2}^{(1)}$ is found from (10) to be

$$a_{01}^{(i)} = -\frac{k_2 {\kappa_1}^{1/2}}{k_1 {\kappa_2}^{1/2}} a_{02}^{(i)}, \quad i = 0, 1, 2, 3; \quad (22)$$

$$a_{n1}^{(i)} = -\frac{k_2}{k_1} a_{n2}^{(i)}, \quad i = 0, 1, 2, 3; n \geq 1 \quad (23)$$

and

$$a_{n1}^{(3)} = -\frac{k_2}{k_1}\left[a_{n2}(3) - \frac{1}{2n^2\pi^2}\left(\frac{1}{\kappa_1} - \frac{1}{\kappa_2}\right) a_{n2}^{(1)}\right], \quad (24)$$

The algebra for the derivation of these equations (14–24) is left out for brevity. The details may be obtained from the author upon request.

5 Inversion of the Solutions

Upon the inversion of Θ_1 and Θ_2, into the time domain, we obtain for $|y| > 0$

$$\theta_i(x, y, t) = \delta_{1,i} + a_{0i}^{(0)} \operatorname{erfc}\left[\frac{\ell|y|}{2\pi(\kappa_i t)^{1/2}}\right] + \left\{a_{0i}^{(1)} \frac{\ell}{(\pi t)^{1/2}} + \left[a_{0i}^{(2)} \frac{\ell|y|}{\pi {\kappa_i}^{1/2}} - a_{0i}^{(3)}\right] \frac{1}{2(\pi t^3)^{1/2}}\right\} \exp\left[-\frac{\ell^2 y^2}{2\kappa_i t}\right], \quad i = 1, 2 \quad (25)$$

The temperature distributions at the interface ($y = 0$) are found to be given by series expressions, which upon summation [2] to order $t^{-1/2}$ are given by

$$\theta_1(x, 0, t) = \frac{k_1 {\kappa_2}^{1/2}}{(k_1 {\kappa_2}^{1/2} + k_2 {\kappa_1}^{1/2})} - \frac{\ell}{\pi(\pi t)^{1/2}}\left\{\frac{2k_1k_2({\kappa_2}^{1/2} - {\kappa_1}^{1/2})}{(k_1 {\kappa_2}^{1/2} + k_2 {\kappa_1}^{1/2})^2} \times \ell n(\cos \tfrac{1}{2}c) + \frac{k_2}{(k_1 {\kappa_2}^{1/2} + k_2 {\kappa_1}^{1/2})} H(c - x) \times \ell n\left[\frac{\cos \frac{1}{2}x}{\cos \frac{1}{2}c}\left(\frac{\cos^2 \frac{1}{2}x}{\cos^2 \frac{1}{2}c} - 1\right)^{1/2}\right]\right\} + \ldots, \quad (26)$$

and

$$\theta_2(x, 0, t) = \frac{k_1 {\kappa_2}^{1/2}}{(k_1 {\kappa_2}^{1/2} + k_2 {\kappa_1}^{1/2})} + \frac{\ell}{\pi(\pi t)^{1/2}}\left\{\frac{2k_1k_2({\kappa_1}^{1/2} - {\kappa_2}^{1/2})}{(k_1 {\kappa_2}^{1/2} + k_2 {\kappa_1}^{1/2})^2} \times \ell n(\cos \tfrac{1}{2}c) + \frac{k_1}{(k_1 {\kappa_2}^{1/2} + k_2 {\kappa_1}^{1/2})} H(c - x) \times \ell n\left[\frac{\cos \frac{1}{2}x}{\cos \frac{1}{2}c}\left(\frac{\cos^2 \frac{1}{2}x}{\cos^2 \frac{1}{2}c} - 1\right)^{1/2}\right]\right\} + \ldots, \quad (27)$$

where H denotes the Heaviside step function.

The average heat flux per unit area, q_{av}, across the interface is given by

$$q_{av} = (T_{10} - T_{20}) \frac{k_1k_2}{(k_1 + k_2)} \frac{\pi}{\ell} \frac{k_1 + k_2}{\pi(k_1 {\kappa_2}^{1/2} + k_2 {\kappa_1}^{1/2})} \frac{\ell}{(\pi t)^{1/2}} - \frac{(k_1 + k_2)^3}{\pi^3(k_1 {\kappa_2}^{1/2} + k_2 {\kappa_1}^{1/2})^3} [\ell n(\cos \tfrac{1}{2}c)]^2 \frac{\ell^3}{(\pi t^3)^{1/2}} + \ldots\Big]. \quad (28)$$

By taking the reciprocal of this result we obtain the average resistance, R, for a unit area as

$$R = \frac{(k_1 {\kappa_2}^{1/2} + k_2 {\kappa_1}^{1/2})}{k_1k_2} (\pi t)^{1/2}\left[1 + \frac{(k_1 + k_2)^2}{(k_1 {\kappa_2}^{1/2} + k_2 {\kappa_1}^{1/2})^2} \times [\ell n(\cos \tfrac{1}{2}c)]^2 \frac{\ell^2}{\pi t} + \ldots\right], \quad (29)$$

which may also be written as

$$R = R_{fc}\left[1 + \frac{\left(1 + \frac{k_2}{k_1}\right)^2}{\left[1 + \frac{k_2}{k_1}\left(\frac{\kappa_1}{\kappa_2}\right)^{1/2}\right]^2} [\ell n(\cos \tfrac{1}{2}c)]^2 (\pi \mathrm{Fo}_2)^{-1} + \ldots\right], \quad (30)$$

where $R_{fc} = (k_1 {\kappa_2}^{1/2} + k_2 {\kappa_1}^{1/2})(\pi t)^{1/2}/(k_1k_2)$ is the full contact resistance, and $\mathrm{Fo}_2 = \kappa_2 t/\ell^2$ is the Fourier number based on the lower thermal diffusivity. This result is presented in Fig. 2, where R/R_{fc} is plotted as a function of $\mathrm{Fo}_2/[\ell n(\cos \frac{1}{2}c)]^2$ for contacts between copper and steel, steel and glass, and copper and glass.

6 Effect of Radiation

In order to determine the contribution from radiation, we first obtain the temperature difference across the gap. This difference is obtained from (26–27) to be

$$\Delta T = (T_{10} - T_{20}) \frac{k_1 + k_2}{(k_1 {\kappa_2}^{1/2} + k_2 {\kappa_1}^{1/2})} H(c - x) \ell n\left[\frac{\cos \frac{1}{2}x}{\cos \frac{1}{2}c} + \left(\frac{\cos^2 \frac{1}{2}x}{\cos^2 \frac{1}{2}c} - 1\right)^{1/2}\right] \frac{\ell}{\pi(\pi t)^{1/2}}. \quad (31)$$

The heat flux due to blackbody radiation must therefore be

$$q_{rad} \sim \sigma \Delta T(T_1 + T_2)(T_1^2 + T_2^2) \quad (32)$$

where σ is the Stefan-Boltzman constant and $T_1(x)$ and $T_2(x)$ are the temperatures at the interface. Upon taking the maximum value of the right side of (32) we find that

$$q_{rad} \lesssim 4\sigma(T_{10} - T_{20}) \frac{k_1 + k_2}{(k_1 {\kappa_2}^{1/2} + k_2 {\kappa_1}^{1/2})} \times \ell n\left(\frac{1 + \sin \frac{1}{2}c}{\cos \frac{1}{2}c}\right) \frac{\ell}{\pi(\pi t)^{1/2}} {T_{max}}^3 \quad (33)$$

In order for q_{rad} to be insignificant, we must have $q_{rad} \ll q_{av}$ where q_{av} is given by (28). By requiring this up to an order $t^{-1/2}$ we have

$$T_{max} \ll \left[\frac{k_1k_2}{(k_1 + k_2)} \frac{\pi^2}{4\sigma\ell \ell n\left(\frac{1 + \sin \frac{1}{2}c}{\cos \frac{1}{2}c}\right)}\right]^{1/3}. \quad (34)$$

For metallic solids ($k_1, k_2 \sim 100$ W/(m − K)), with contacts spaced about 1 cm apart ($\ell = 0.01$ m) over 1 percent of the interfacial area ($c = 0.99\pi$), we have

$$T_{max} \ll 4000 \text{ K}. \quad (35)$$

For $T_{max} = 1000$ K with the above specifications, we have

$$q_{rad} \lesssim 230\ \Delta T \frac{\text{W}}{\text{m}^2 - \text{K}}, \quad (36)$$

while

$$q_{av} \sim 14000 \Delta T \frac{\text{W}}{\text{m}^2 - \text{K}} \quad (37)$$

Clearly, for interfacial temperatures below 1000 K we may ignore radiation for metallic conductors.

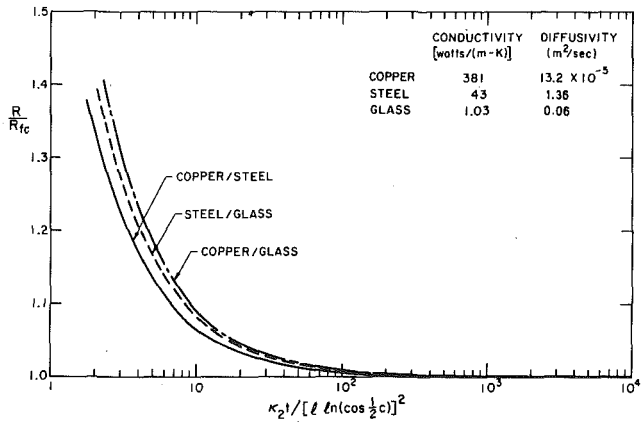

Fig. 2 Unsteady thermal resistances of different pairs of solids as a function of $\kappa_2 t/[\ell\ \ell n(\cos \frac{1}{2}c)]^2$

Downloaded 20 Dec 2010 to 194.27.225.72. Redistribution subject to ASME license or copyright; see http://www.asme.org/terms/Terms_Use.cfm

It is important to note here that the comparisons made in (34–37) are quite conservative because the expression (28) for q_{av} here is for an average heat flux over the entire interface. The conduction heat flux averaged over the contact region only is given by

$$q_{av}^* \sim 1.4 \times 10^6 \, \Delta T \frac{\mathrm{W}}{\mathrm{m}^2 - \mathrm{K}} \tag{38}$$

instead of (37).

7 Discussion

The present analysis provides useful results for situations in which we have a large fraction of the interface in contact. This corresponds to the case in which $c/\pi \ll 1$. In fact, when $c = 0$, we have full contact and the only terms in the solution that count are those of leading order. These terms then satisfy the boundary conditions exactly. For cases when $c/\pi \lesssim 1$, however, the higher order corrections become unrealistically large, except for correspondingly large values of the Fourier number, $\mathrm{Fo}_i = \kappa_i t/\ell^2$. As a suitable criterion for validity, we can require that the dominant term in the highest order be much smaller than the next lower order term. For equations (25–30) such a criterion would lead to the condition that

$$\frac{(k_1 + k_2)^2}{(k_2 \kappa_1^{1/2} + k_1 \kappa_2^{1/2})^2} [\ell \mathrm{n}(\cos \tfrac{1}{2} c)]^2 \frac{\ell^2}{\pi t} \ll 1. \tag{39}$$

The validity of the results is further restricted by equation (34) which is the condition for radiation to be unimportant. For metallic solids with interfacial temperatures up to 1000 K, we may neglect radiation unless the contact spacing is very large (say, greater than 1 m). Radiation turns out to be of increasing importance as the contact regions are spread wider, even if the fraction of contact is kept constant. This turns out to be the case because the temperature difference across the gap increases with ℓ for a given average heat flux. Since for a constant q_{av}, ΔT increases with ℓ, q_{rad} must also increase with ℓ as observed in (33).

For the situations in which radiation is important the adiabatic boundary condition may be modified to include a nonzero conductance. Such a boundary condition, however, would not allow the solution to be expressed in an explicit form even for the steady state. An attempt to do so will lead to a set of dual series equations for which explicit inverses are not available. The numerical calculation of the series coefficients through the use of a truncated Fourier series is indeed possible.

The results obtained are applicable to heat transfer problems in the general area of contact resistance. The model is somewhat idealized for an arbitrary shape of the contact region. For machined surfaces, however, it is very realistic. The resistance as given by equation (30) and plotted in Fig. 2 increases with ℓ even if the fraction of contact remains unchanged. This is because the wider spacing of the contact regions causes heat flow lines to be constricted to a greater depth thus increasing the resistive effect. The resistance is observed to go down with increasing fraction of contact, as expected.

The present work is valid only for large Fourier numbers and therefore it would be particularly valuable to obtain a short-time solution. Such a solution would probably require the use of a singular perturbation scheme. Again, radiation would be difficult to incorporate. The radiation problem for a homogeneous surface of a semi-infinite solid with nonzero transmissivity has been treated by Lick [5].

It is desirable to experimentally verify the results and check for the validity of the model. Temperature measurements at the interface by means of thermocouples, for various Fourier numbers, may be used to verify the results.

References

1 Sneddon, I. N., *Mixed Boundary Value Problems in Potential Theory*, North Holland, 1966.

2 Dundurs, J. and Panek, C., "Heat Conduction Between Bodies with Wavy Surfaces," *International Journal of Heat and Mass Transfer*, Vol. 19, 1976, pp. 731–736.

3 Schneider, G. E., Strong, A. B., and Yovanovich, M. M., "Transient Thermal Response of Two Bodies Communicating Through a Small Circular Contact Area," *International Journal of Heat and Mass Transfer*, Vol. 20, 1977, pp. 301–308.

4 Sadhal, S. S., "Transient Thermal Response of Two Solids in Contact Over a Circular Disk," *International Journal of Heat and Mass Transfer*, Vol. 23, 1980, pp. 731–733.

5 Lick, W., "Transient Energy Transfer by Radiation and Conduction," *International Journal of Heat and Mass Transfer*, Vol. 8, 1966, pp. 119–127.

Downloaded 20 Dec 2010 to 194.27.225.72. Redistribution subject to ASME license or copyright; see http://www.asme.org/terms/Terms_Use.cfm

E. J. Patula
Research Laboratory,
U. S. Steel Corporation,
Monroeville, Pa. 15146
Mem. ASME

Steady-State Temperature Distribution in a Rotating Roll Subject to Surface Heat Fluxes and Convective Cooling[1]

With the higher rolling speeds used in modern cold-rolling mills, proper roll cooling has become a critical factor in avoiding problems of excessive roll spalling and poor thermal crowning. Poor thermal crowning of rolls can severely affect the shape and profile of sheet and strip products. To determine the influence of cooling practices on roll temperature, a mathematical model was developed that determines the two-dimensional (radial and circumferential) steady-state temperature distribution in a rotating roll subject to constant surface heat input over one portion of the circumference and convective cooling over another portion of the circumference. The model is analytical in nature, as opposed to a direct numerical simulation, which enables extensive parametric studies to be performed conveniently. The solution technique can be used to solve numerous problems involving any combination of surface boundary conditions that have, at most, a linear dependence with respect to the surface temperature.

With the use of the principle of superposition, the present solution can be utilized to solve problems where various regions of the surface have constant heat fluxes.

Results of the present analysis indicate that for normal cold-rolling situations during steady operation, the penetration of the effects of the surface heating and cooling that occur during every roll revolution is usually less than 4 percent of the radius. Furthermore, the bulk of the roll is at a uniform temperature that can be calculated quite accurately by neglecting all internal temperature gradients. The location of the cooling regions relative to the heat-input regions has little effect on the bulk roll temperature in this situation. This approximation would be useful for computing bulk roll temperature, which could be utilized in future models for determining thermal crowns, but would not be suited for determining accurate temperatures at the roll surface.

Introduction

With the higher rolling speeds used in modern cold-rolling mills for producing flat metal products, the problems of roll cooling have become more difficult and more critical. Improper or insufficient cooling can lead not only to shortened roll life due to spalling caused by thermal stresses, but it can also significantly affect the shape or crown of the roll, which could result in poor shape and/or profile. To investigate the influence of cooling practice on thermal crowning, it is first necessary to develop a good understanding of the thermal aspects of the roll. Considerable work has been done to develop thermal models of rolls.

Cerni and his co-workers [1, 2] studied the thermal-stress problem of hot rolling. They provided a transient analytical solution for the two-dimensional temperature distribution in a roll subjected to 360 deg convective cooling and to a line heat source. They did not analyze the problem where cooling is present over a portion of the roll only. The work of Stevens, Ivens, and Harper [3] provided some interesting and significant experimental results relating to the transient temperature buildup in rolls. However, their work was conducted for specific roll dimensions and speeds. On the basis of this work, Parke and Baker [4] developed a finite difference model of the transient two-dimensional thermal distribution in a roll. Again, their work was conducted for specific roll dimensions and speeds.

One drawback with computer simulations is that the analysis of many different cases and situations can be costly and time-consuming. However, analytic solutions offer the advantage of enabling extensive parametric studies to be performed conveniently. Furthermore, an analytic solution can serve as a convenient and valuable check point for computer solutions. An analytic model developed by Haubitzer [5] calculates the two-dimensional steady-state temperature distribution in a rotating roll that has a prescribed surface temperature. However, a more realistic approach would be to utilize surface boundary conditions involving convection and prescribed heat fluxes. Therefore, an attempt was made to develop an analytic solution for the temperature distribution in a rotating roll that would be more representative of operating conditions.

The purpose is to increase the understanding of the thermal aspects of the roll and to provide a closed-form solution technique for calculating temperature distributions that is based upon as few simplifying assumptions concerning the roll as possible. This paper presents the results of this investigation.

Theoretical Analysis

Definition of Problem. The problem is to determine the steady-state temperature distribution in a long cylinder that rotates at a constant surface speed and is subject to certain boundary conditions at the surface (Fig. 1). The analysis is based on the following assumptions:

1 The cylinder is long and, therefore, axial heat conduction can be neglected.
2 The rotational speed is constant.
3 The cylinder is heated and cooled at various locations around the periphery, but the heat input and cooling are uniform along the axis.
4 The thermal properties are uniform throughout the cylinder

[1] Note: It is understood that the material in this paper is intended for general information only and should not be used in relation to any specific application without independent examination and verification of its applicability and suitability by professionally qualified personnel. Those making use thereof or relying thereon assume all risk and liability arising from such use or reliance.

Contributed by the Heat Transfer Division of THE AMERICAN SOCIETY OF MECHANICAL ENGINEERS 19th AIChE/ASME National Heat Transfer Conference, San Diego, Calif., August 6–8, 1979. Revised manuscript received by the Heat Transfer Division March 24, 1980.

Copyright © 1981 by ASME
Downloaded 20 Dec 2010 to 194.27.225.72. Redistribution subject to ASME license or copyright; see http://www.asme.org/terms/Terms_Use.cfm

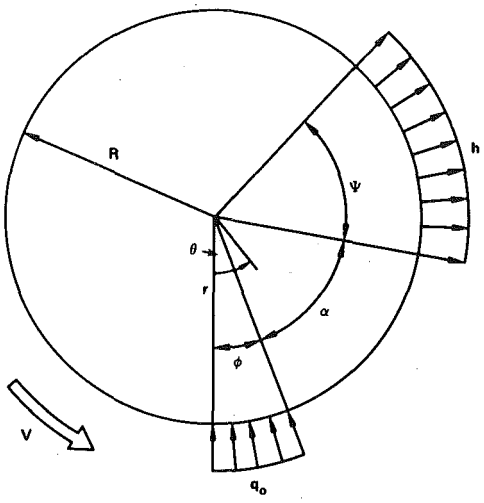

Fig. 1 Schematic of rotating roll showing locations of heat input and heat loss

and are independent of temperature.

5 The heat input is supplied by a constant-heat-flux source, and the cooling is convective.[2]

6 The temperature has reached steady state relative to an Eulerian reference frame [6] that is fixed in space relative to the surface boundry conditions and does not rotate with the cylinder. The Eulerian approach considers a specific control volume in space and analyzes material that enters and leaves the control volume in addition to material occupying the control volume at any give time. Therefore, the temperature for any control volume in the cylinder does not change with time.

As a consequence of assumptions 1–4, the temperature distribution depends only on the two spatial dimensions r and θ. Assumption 5 is made so that the classical differential equation solution technique can be utilized. Assumption 6 implies that only the steady-state situation will be considered.

With respect to a fixed Eulerian reference frame, the differential equation that governs the temperature field is [6]

$$\left.\frac{\partial T}{\partial t}\right|_{\text{Eulerian}} + \bar{v}\cdot\nabla T = a\nabla^2 T \tag{1}$$

where $a = k/\rho c$ is the thermal diffusivity. The material velocity $\bar{v}$ is a function of position but has a component in the θ-direction only. For steady-state conditions and for cylindrical polar coordinates, equation (1) becomes

$$\frac{1}{r}\frac{\partial}{\partial r}\left(r\frac{\partial T}{\partial r}\right) + \frac{1}{r^2}\frac{\partial^2 T}{\partial \theta^2} = \frac{V}{aR}\frac{\partial T}{\partial \theta} \tag{2}$$

where V is the cylinder surface speed. Equation (2) is to be solved subject to the boundary conditions shown in Fig. 1. These are

$T(0,\theta)$ is finite

$$-k\frac{\partial T(R,\theta)}{\partial r} = \begin{cases} -q_0 & ; \quad 0 < \theta < \phi \\ 0 & ; \quad \phi < \theta < \phi + \alpha \\ hT(R,\theta); & \phi + \alpha < \theta < \phi + \alpha + \Psi \\ 0 & ; \quad \phi + \alpha + \Psi < \theta < 2\pi \end{cases} \tag{3}$$

where h is the heat-transfer coefficient, which is assumed constant. The problem, as defined, is to solve for the temperature difference between the roll and the coolant reference temperature (that is, if the coolant temperature were T_0 and the actual roll temperature where T^*, then $T = T^* - T_0$). Therefore, the problem is to determine the temperature, T, which satisfies both the differential equation in equation (2) and the boundary conditions in equation (3).

Problem Solution. The classical approach of separation of variables cannot be used in its usual form but a more general version of the technique will work [7]. Assume that a solution of the differential equation can be represented as

$$T = \mathcal{R}(r)e^{in\theta} \tag{4}$$

where $\mathcal{R}(r)$ is a complex function. Substituting equation (4) into equation (2) and cancelling out common terms yields the differential equation which must be satisfied by $\mathcal{R}$.

$$r^2\mathcal{R}'' + r\mathcal{R}' - \left(i\frac{nV}{Ra}r^2 + n^2\right)\mathcal{R} = 0 \tag{5}$$

where the prime indicates differentiation with respect to r. The problem has been reduced to determine the solution of the ordinary differential equation (5). Using the following change of independent variable,

$$x = \sqrt{\frac{nV}{Ra}}\,r \tag{6}$$

Equation (5) becomes

$$x^2\frac{d^2\mathcal{R}}{dx^2} + x\frac{d\mathcal{R}}{dx} - (ix^2 + n^2)\mathcal{R} = 0 \tag{7}$$

The solutions to equation (7) may be found in reference [8] and are called Kelvin functions.[3] The two general solution forms are

$$\begin{aligned} \mathcal{R}_1 &= ber_n(x) + i\,bei_n(x) \\ \mathcal{R}_2 &= ker_n(x) + i\,kei_n(x) \end{aligned} \tag{8}$$

From the general properties of Kelvin functions and from the boundary condition that the solution must remain bounded as r (and x) approaches zero, the general solution form $\mathcal{R}_2$ cannot be included because its value becomes infinite as r (and x) approaches zero. The

[2] The only restriction is that the heat input and heat loss be linear functions of temperature.

[3] Kelvin functions are related to Bessel functions with a complex argument.

Nomenclature

a = thermal diffusivity, ft²/hr
a_n = complex constant
$b_n = a_n + (-1)^n a_n$, if $n \geq 1$; a_0, if $n = 0$
c = specific heat, Btu/lb-°F
$c_n = i[a_n - (-1)^n a_n]$
e_m = real constant of Fourier series for the surface boundary conditions
f = function representing boundary condition at roll surface
g_m = real constant of Fourier series for the surface boundary conditions
h = heat-transfer coefficient for cooling region, Btu/hr-ft²-°F
$i = \sqrt{-1}$
k = thermal conductivity, Btu/hr-ft-°F
m = index for an infinite series
n = index for an infinite series
P_n = real coefficient of infinite-series solution
Q = heat-input rate defined by equation (13), Btu/hr-ft²
q = heat-input rate per unit area, Btu/hr-ft²
R = outside radius of roll, ft
r = radial coordinate
S_n = real coefficient of infinite-series solution
T = temperature difference defined as $T^* - T_0$, °F
T_0 = coolant temperature, °F
T^* = actual roll temperature, °F
T_{bulk} = bulk-roll temperature difference, °F
t = time, hr
V = roll-surface speed, ft/hr
$\bar{v}$ = roll-velocity vector, ft/hr
x = independent variable defined by equation (6)
α = angle of separation between the heat-input and the cooling regions, radians
θ = angular coordinate
λ_n = parameter defined in equation (12)
ρ = roll density, lb/ft³
ϕ = angle for heat input, radians
Ψ = angle for convective cooling, radians
∇ = gradient operator
∇^2 = laplacian operator

Downloaded 20 Dec 2010 to 194.27.225.72. Redistribution subject to ASME license or copyright; see http://www.asme.org/terms/Terms_Use.cfm

solution to the orginal differential equation (2) may be written as a superposition of functions of the form in equation (4), i.e.

$$T(r,\theta) = \sum_{n=-\infty}^{\infty} a_n \left[ber_n\left(\sqrt{\frac{nV}{Ra}}r\right) + i\, bei_n\left(\sqrt{\frac{nV}{Ra}}r\right)\right] e^{in\theta} \quad (9)$$

where a_n is a complex constant. Expanding equation (9) yields

$$T(r,\theta) = b_0 + \sum_{n=1}^{\infty} b_n \left[ber_n\left(\sqrt{\frac{nV}{Ra}}r\right)\cos(n\theta) - bei_n\left(\sqrt{\frac{nV}{Ra}}r\right)\sin(n\theta)\right] + c_n\left[ber_n\left(\sqrt{\frac{nV}{Ra}}r\right)\sin(n\theta) + bei_n\left(\sqrt{\frac{nV}{Ra}}r\right)\cos(n\theta)\right] \quad (10)$$

where b_n and c_n are real constants given by

$$b_n = \begin{cases} a_n + (-1)^n a_n, \text{ if } n \geq 1; \\ a_0, \text{ if } n = 0 \end{cases}$$

$$c_n = i(a_n - (-1)^n a_n)$$

It should also be noted that the following relations for transforming the Kelvin functions of imaginary arguments and negative orders have been used:

$$ber_{-n}(ix) = i^n\left[\cos\left(\frac{3n\pi}{2}\right) ber_n(x) - \sin\left(\frac{3n\pi}{2}\right) bei_n(x)\right]$$

$$bei_{-n}(ix) = -i^n\left[\cos\left(\frac{3n\pi}{2}\right) bei_n(x) + \sin\left(\frac{3n\pi}{2}\right) ber_n(x)\right]$$

The problem has now been reduced to determining the constant, real coefficients, b_n and c_n, in equation (10) by using the boundary condition at the surface, $r = R$. Equation (10) is general in that it is the solution form for any surface-boundary condition. It should also be noted that the solution is in the form of a Fourier series with respect to θ. Therefore, the surface gradient $\partial T/\partial r|_{r=R}$ represents a Fourier series as a function of θ. The boundary conditions can be satisfied by expanding the right-hand-side of equation (3) in a Fourier series utilizing the expression for T, given by equation (10), and equating the coefficients of similar trigonometric functions.

Representing the right-hand side of the boundary condition in equation (3) with a Fourier series yields

$$f(\theta) = \begin{cases} -q_0 & ; \quad 0 < \theta < \phi \\ 0 & ; \quad \phi < \theta < \phi + \alpha \\ hT(R,\theta); & \phi + \alpha < \theta < \phi + \alpha + \Psi \\ 0 & ; \quad \phi + \alpha + \Psi < \theta < 2\pi \end{cases} \quad (11)$$

and

$$f(\theta) = \frac{e_0}{2} + \sum_{m=1}^{\infty} e_m \cos(m\theta) + g_m \sin(m\theta)$$

where

$$e_m = \frac{1}{\pi}\int_0^{2\pi} f(\theta)\cos(m\theta)\, d\theta$$

$$g_m = \frac{1}{\pi}\int_0^{2\pi} f(\theta)\sin(m\theta)\, d\theta$$

The coefficients e_m and g_m are determined by substituting the expression for $f(\theta)$, given by equation (11), and breaking the limits of integration to coincide with the definition of $f(\theta)$; i.e., 0 to ϕ, ϕ to $\phi + \alpha$, etc.

The left-hand side of equation (3) is obtained by taking the derivative of the temperature representation in equation (10) and evaluating it at the surface.

The relationships for determining b_n, c_n, $n = 0, 1, 2, \ldots$ are obtained by equating the Fourier series for the surface heat flux to the Fourier series generated in equation (11). The coefficients of like trigonometric functions must be equal. This procedure represents an extension of the work of Kantrovich and Krylov who use the technique to solve Laplace's equation on a circular domain where the boundry conditions are mixed [9].

The relationship for determining the b_n, c_n, $n = 0, 1, 2, \ldots$ are

$\underline{m = 0}$

$$1 = P_1\Psi + \sum_{n=1}^{\infty}\left\{\frac{1}{n}\left[P_{n+1} + S_{n+1}\frac{bei_n(\lambda_n)}{ber_n(\lambda_n)}\right] \times [\sin[n(\alpha+\phi+\Psi)] - \sin[n(\alpha+\phi)]] + \frac{1}{n}\left[P_{n+1}\frac{bei_n(\lambda_n)}{ber_n(\lambda_)} - S_{n+1}\right][\cos[n(\alpha+\phi+\Psi)] - cos[n(\alpha+\phi)]]\right\}$$

$\underline{m \geq 1}$

$$\frac{\sin(m\phi)}{m\phi} = \frac{P_1}{m}[\sin[m(\alpha+\phi+\Psi)] - \sin[m(\alpha+\phi)]] + \sum_{n=1}^{\infty}\left\{\left[P_{n+1} + S_{n+1}\frac{bei_n(\lambda_n)}{ber_n(\lambda_n)}\right]\int_{\alpha+\phi}^{\alpha+\phi+\Psi}\cos(n\theta)\cos(m\theta)\, d\theta + \left[S_{n+1} - P_{n+1}\frac{bei(\lambda_n)}{ber(\lambda_n)}\right]\int_{\alpha+\phi}^{\alpha+\phi+\Psi}\sin(n\theta)\cos(m\theta)\, d\theta\right\} + \frac{\pi k\lambda_m}{hR}\left[P_{m+1}\frac{ber_m'(\lambda_m)}{ber_m(\lambda_m)} + S_{m+1}\frac{bei_m'(\lambda_m)}{ber_m(\lambda_m)}\right]; \quad (12)$$

$$\frac{1-\cos(m\phi)}{m\phi} = -\frac{P_1}{m}[\cos[m(\alpha+\phi+\Psi)] - \cos[m(\alpha+\phi)]] + \sum_{n=1}^{\infty}\left\{\left[P_{n+1} + S_{n+1}\frac{bei_n(\lambda_n)}{ber_n(\lambda_n)}\right]\int_{\alpha+\phi}^{\alpha+\phi+\Psi}\cos(n\theta)\sin(m\theta)\, d\theta + \left[S_{n+1} - P_{n+1}\frac{bei_n(\lambda_n)}{ber_n(\lambda_n)}\right]\int_{\alpha+\phi}^{\alpha+\phi+\Psi}\sin(n\theta)\sin(m\theta)\, d\theta\right\} + \frac{\pi k\lambda_m}{hR}\left[S_{m+1}\frac{ber_m'(\lambda_m)}{ber_m(\lambda_n)} - P_{m+1}\frac{bei_m'(\lambda_m)}{ber_m(\lambda_m)}\right]$$

where

$$P_{n+1} = \frac{b_n}{q_0\phi/h}ber_n(\lambda_n),$$

$$S_{n+1} = \frac{c_n}{q_0\phi/h}ber_n(\lambda_n),$$

$$bei_m'(\lambda_m) = \frac{m}{\lambda_m}bei_m(\lambda_m) + \frac{1}{\sqrt{2}}[bei_{m+1}(\lambda_m) - ber_{m+1}(\lambda_m)],$$

$$ber_m'(\lambda_m) = \frac{m}{\lambda_m}ber_m(\lambda_m) + \frac{1}{\sqrt{2}}[ber_{m+1}(\lambda_m) + bei_{m+1}(\lambda_m)]$$

$$\lambda_m = \sqrt{m}\sqrt{\frac{VR}{a}}$$

The relationships in equation (12) determine the coefficients, b_n and c_n, which can then be substituted into equation (10) to determine the temperature distribution. The coefficients are coupled in equation (12) because of the particular boundary condition utilized. Consequently, in theory, equation (12) represents an infinite set of algebraic equations that must be solved simultaneously to determine the infinite number of unknowns. For practical applications, only a finite number of terms are retained in the infinite-series solution. Therefore, if 40 terms are felt to be necessary, only 40 terms of equation (12) are utilized to calculate the 40 coefficients. In the limit, the more terms retained, the better the accuracy of the solution. For boundary conditions involving specified temperatures or heat fluxes, the relationships analogous to equation (12) are uncoupled and the coefficients can be determined explicitly.

Special Case: $\alpha \to 0$, $\phi \to 0$, and $\Psi \to 2\pi$. In the case where the area of the heat input is reduced to a point and the remainder of the cylinder is cooled by convection, equation (12) becomes uncoupled. Taking the limit of equation (12) as $\alpha \to 0$, $\Psi \to 2\pi$, $\phi \to 0$, and $q_0 \to \infty$ such that the product of $q_0\phi$ remains finite, Equation 12 can be solved to provide the following:

$$b_0 = \frac{Q}{2\pi h}$$

Downloaded 20 Dec 2010 to 194.27.225.72. Redistribution subject to ASME license or copyright; see http://www.asme.org/terms/Terms_Use.cfm

$m \geq 1$

$$b_m = \frac{Q}{\pi hD}\left[\frac{k\,\lambda_m}{hR}\,ber_m'(\lambda_m) + ber_m(\lambda_m)\right]$$

$$c_m = \frac{Q}{\pi hD}\left[\frac{k\lambda_m}{hR}\,bei_m'(\lambda_m) + bei_m(\lambda_m)\right], \qquad (13)$$

$$Q = \lim_{\phi \to 0} (q_0\phi),$$

$$D = \left[\frac{k}{hR}\,\lambda_m\,ber_m'(\lambda_m) + ber_m(\lambda_m)\right]^2 + \left[\frac{k}{hR}\,\lambda_m\,bei_m'\,(\lambda_m) + bei_m\,(\lambda_m)\right]^2.$$

and λ_m is defined in equation (12). The expression for this special case agrees with the solution given by Cerni [1] for the steady-state situation. However, Cerni treats this special case only and does not consider the problem where regions of the roll periphery have no heat transfer.

Results and Discussion

To provide numerical samples, a computer program was written to solve the system of algebraic equation (12) for various values of the input parameters. It should be observed that the parameters h, R, k, V, and a enter the problem as two dimensionless groups $\sqrt{VR/a}$ and $k/(hR)$. The heat-input rate can also be eliminated by defining a dimensionless temperature as Th/Q, where Q equals $q_0\phi$. Consequently, information concerning the shape and behavior of the temperature distributions can be obtained without specific knowledge of the heat-transfer coefficient, h, or the heat-input rate, q_0. However, these quantities would have to be determined and specified if actual cylinder temperatures were desired. The best results were obtained whenever 40 terms ($n = 40$) were retained in the expansion. Therefore, 81 coefficients were calculated. Theoretically, the accuracy should increase if more terms are retained; however, numerical problems were encountered in evaluating the Kelvin functions whenever n was greater than 40.

Dimensionless temperature distributions were obtained for various combinations of input parameters. An exhaustive parametric study would be too lengthy to include in the present study; therefore, only representative cases will be presented. Figures 2–5 show the surface temperature as a function of angular position for various values of the spray location. The figures indicate that as the location of the cooling spray is moved farther from the point of heat input, a cusp begins to form at the point where cooling is initiated. Furthermore, for the parameters considered, the surface-temperature variation around the periphery dissipates quickly into the cylinder interior.

This fact is shown more clearly in Figs. 6 and 7, which present temperature distributions as functions of the radius for two locations of the cooling spray. In both situations, the penetration of the surface-temperature variations is approximately 6 percent of the radius. Therefore, 94 percent of the cylinder remains at a constant uniform temperature under steady-state conditions. These examples are for cases involving relatively slow rotational speeds as compared with speeds that typically occur during cold-rolling situations. For rolling situations involving higher speeds, the penetration would be significantly less. Conversely, for lower rotational speeds the penetration would be greater.

In determining thermal crown in a roll, the primary effect would come from the bulk roll interior. The surface variations would have a tremendous influence on the surface thermal-stress pattern and subsequent spalling characteristics but would be insignificant relative to the determination of thermal crown. An estimate of the penetration of the surface-temperature variation can be obtained. Considering the form of the solution indicated in equation (10) and the relationships in equation (12) that determine the coefficients, it is seen that the radial dependence of the temperature can be expressed as a ratio of Kelvin functions evaluated at the desired radial location to the Kelvin function at the surface. Therefore, the radial dependence will be proportional to terms like

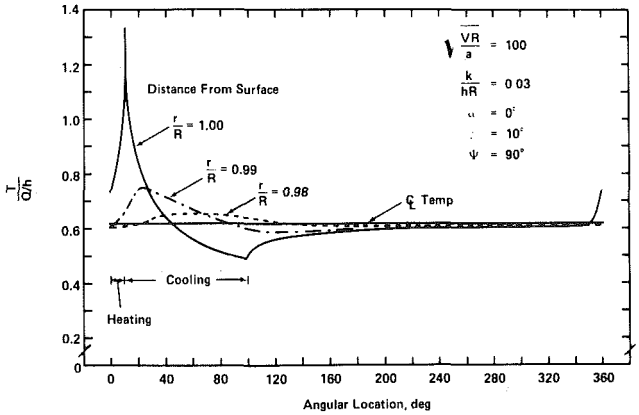

Fig. 2 Roll temperature versus angle for $\alpha = 0$ deg

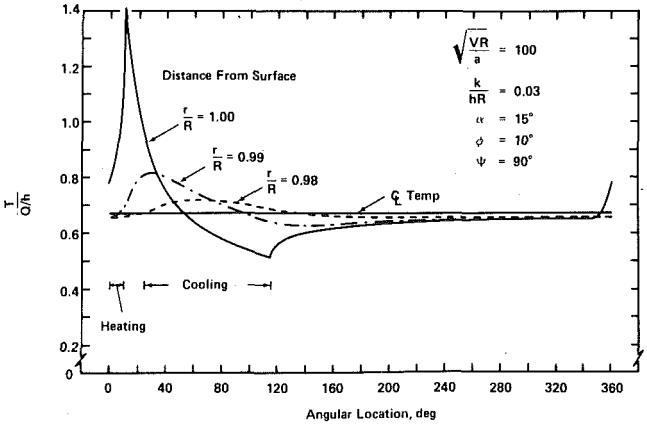

Fig. 3 Roll temperature versus angle for $\alpha = 15$ deg

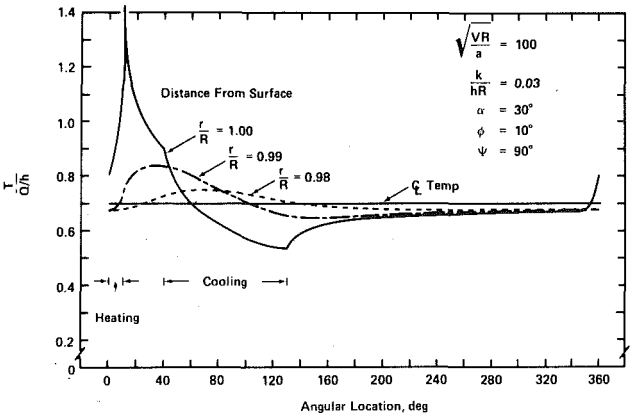

Fig. 4 Roll temperature versus angle for $\alpha = 30$ deg

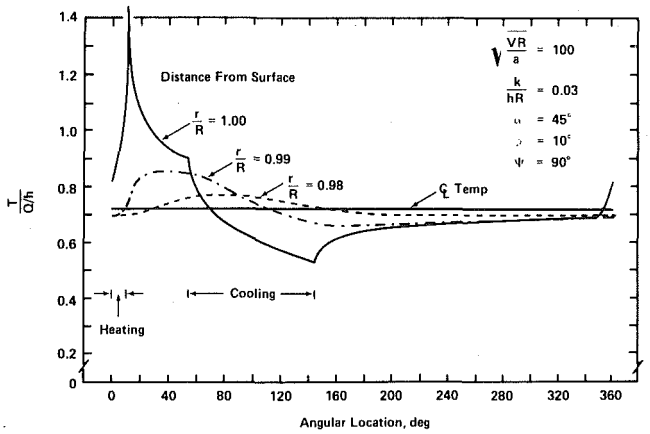

Fig. 5 Roll temperature versus angle for $\alpha = 45$ deg

Downloaded 20 Dec 2010 to 194.27.225.72. Redistribution subject to ASME license or copyright; see http://www.asme.org/terms/Terms_Use.cfm

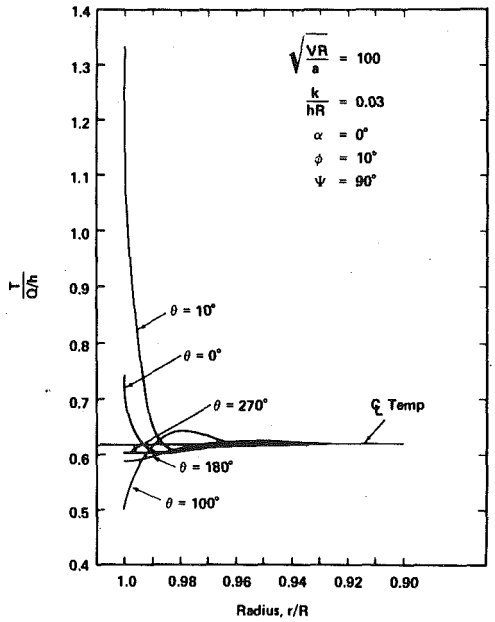

Fig. 6 Roll temperature versus radius for $\alpha = 0$ deg

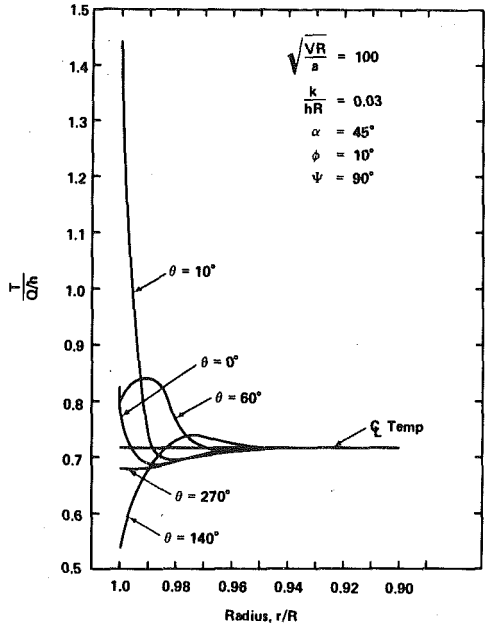

Fig. 7 Roll temperature versus radius for $\alpha = 45$ deg

$$T(r,\theta) \sim \frac{ber_n\left(\lambda_n \frac{r}{R}\right)}{ber_n(\lambda_n)} \tag{14}$$

For values of λ_n that are large and for values of r close to R, the asymptotic expansions for the Kelvin functions with large argument may be used to obtain [10]

$$\frac{ber_n\left(\lambda_n \frac{r}{R}\right)}{ber_n(\lambda_n)} = \frac{e^{\lambda_n/\sqrt{2}\,(r/R1)}}{\sqrt{\frac{r}{R}}} \tag{15}$$

The radial temperature dependence is negligible whenever the value of the exponent is less than minus 3. Therefore, if

$$\frac{\lambda_n}{\sqrt{2}}\left(\frac{r}{R} - 1\right) < -3, \tag{16}$$

or, using the definition of λ_n in equation (12),

$$\frac{r}{R} < 1 - \frac{3\sqrt{2}}{\sqrt{n}\sqrt{\frac{VR}{a}}} \tag{17}$$

then the temperature is essentially the roll centerline temperature. For example, when n equals 1 and $\sqrt{VR/a}$ equals 100 (which is representative of commercial cold-rolling situations), the influence of the surface-temperature variation is negligible at a distance in from the surface of 4 percent of the radius.

Another fact illustrated in Figs. 2–5 is that for the conditions considered, the value of the centerline temperature changes very little whenever the spray location is changed. This is better illustrated in Fig. 8, which presents the roll-centerline temperature as a function of the spray location angle, α, for typical values of operating parameters. The figure indicates that for the parameters selected, the centerline temperature is rather insensitive to cooling-spray location except for the cases where $\sqrt{VR/a}$ and $k/(hR)$ have low values. For typical cold-rolling situations involving a 24 in. dia. (0.6 m) steel roll with a surface speed of 3000 ft/min (1.52 m/s) and a heat-transfer coefficient of 600 Btu-hr-ft^2-°F (3410 W/m^2–K), the dimensionless parameters $\sqrt{VR/a}$ and $k/(hR)$ have values of 600 and 0.043, respectively. Therefore, from Fig. 8, typical cold-rolling situations are characterized by the fact that for steady-state conditions, the roll-centerline temperature, and consequently the bulk of the roll, is relatively insensitive to the cooling-spray location. It would, however, be affected by the area over which cooling is applied.

For most cold-rolling situations, the bulk of the roll cross section is at a uniform temperature, which is the centerline value. The centerline temperature is given in equation (10) by the value of the coefficient, b_0. Using equation (12), the asymptotic expansion for b_0 for large values of the dimensionless quantity $(\sqrt{VR/a})\,[k/(hR)]$ can be written as

$$b_0 = \frac{q_0\phi}{h\Psi} + 0\left(\frac{1}{\sqrt{\frac{VR}{a}}\frac{k}{hR}}\right). \tag{18}$$

Whenever the heat input reduces to a line source, the product $q_0\phi$ should be replaced by Q, as defined in equation (13). It is interesting to note that the first term of the expansion is just the steady-state bulk temperature that would be calculated if all internal temperature gradients were neglected. In this situation for steady-state conditions, the heat input equals the heat output. Therefore,

$$q_0 R\phi = hR\Psi T_{\text{bulk}} \tag{19}$$

where T_{bulk} is the bulk temperature.[4] Solving for the bulk temperature yields

$$T_{\text{bulk}} = \frac{q_0\phi}{h\Psi} \tag{20}$$

To determine the reasonableness of the assumption of neglecting all internal thermal gradients, the difference between the centerline temperature and the bulk temperature was computed for various operating conditions. The percentage difference is presented in Fig. 9 as a function of the parameter $(\sqrt{VR/a})\,[k/(hR)]$. The results indicate that the error associated with using the simplified bulk temperature to represent the roll-centerline temperature is less than 10 percent whenever the parameter $(\sqrt{VR/a})\,[k/(hR)]$ exceeds 10. For the typical cold-rolling situations described previously, the value of this parameter is usually greater than 26. Therefore, from Fig. 9, the error associated with using the bulk temperature in this situation would be less than 5 percent.

Conclusions

The exact solution for the two-dimensional steady-state temperature distribution in a rotating cylinder roll subject to a constant heat input and a convective-cooling boundary condition has been devel-

[4] The fluid temperature has again been subtracted so that T_{bulk} represents a temperature difference.

Downloaded 20 Dec 2010 to 194.27.225.72. Redistribution subject to ASME license or copyright; see http://www.asme.org/terms/Terms_Use.cfm

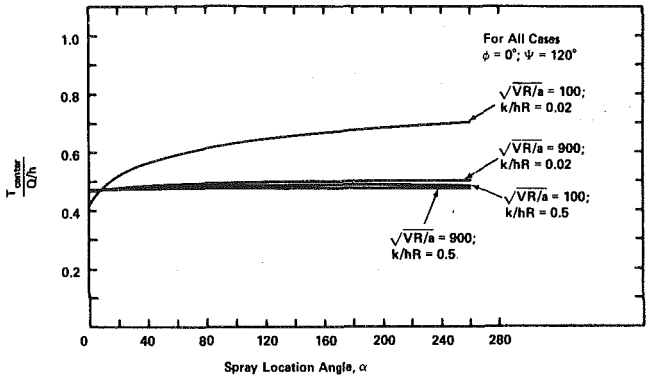

Fig. 8 Centerline temperature versus spray location for various operating conditions

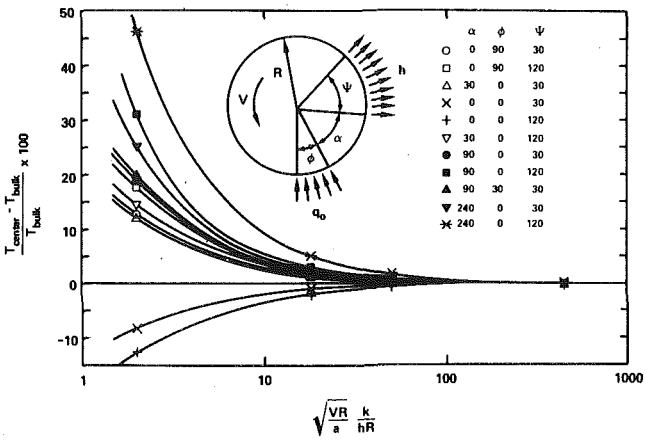

Fig. 9 Difference between centerline temperature and bulk temperature based on negligible internal gradients

oped. The solution technique is an extension of the standard method of separation of variables and results in an infinite-series solution form. The same solution method can be utilized to solve problems involving any combination of surface boundary conditions if the boundary condition is at most a linear function of the surface temperature or temperature gradient. With use of the principle of superposition, the present solution can be utilized to solve problems where various regions of the surface have constant heat fluxes.

Results of the present analysis indicate that for normal cold-rolling situations under steady-state conditions, the penetration of the effects of the surface heating and cooling that occur during every roll revolution is usually less than 4 percent of the radius. In addition, the bulk of the roll is at a uniform temperature, the value of which can be calculated quite accurately by neglecting all internal temperature gradients if $(\sqrt{VR/a})\ [k/(hR)]$ is greater than 10. This approximation is insensitive to the location of the cooling-water sprays relative to the heat-input region. The approximation would be useful for estimating bulk-roll temperatures that would be used to compute thermal roll crowns. The approximation is not accurate for predicting temperatures at the roll surface, which are very dependent on the particulars of the heat input and cooling-spray locations. Therefore, the bulk-roll approximation would not be suited for estimating thermal stress at the roll surface, which could contribute to spalling.

Reference

1 Cerni, S., "The Temperature and Thermal Stresses in the Rolling of Metal Strip," Doctorial Dissertation, Dept. of Mechanical Engineering, Carnegie-Mellon University, 1961.

2 Cerni, S., Weinstein, A. S., and Zorowski, C. F., "Temperatures and Thermal Stresses in the Rolling of Metal Strip," *Iron and Steel Engineer Year Book,* 1963, p. 717.

3 Stevens, P. G., Ivens, K. D., and Harper, P., "Increasing Work-Roll Life by Improved Roll-Cooling Practice," *Journal Iron Steel Institute (London),* Vol. 209, Jan 1971, pp. 1–11.

4 Parke D. M., and Baker, J. L. L., "Temperature Effects of Cooling Work Rolls," *Iron and Steel Engineer,* Dec 1972, Vol. 49, pp. 83–88.

5 Haubitzer, W., "Steady State Temperature Distribution in Rolls," *Archiv fuer das Eisenhuttenwesen,* 1974, 46, (10) pp. 635–638.

6 Arpaci, *Conduction Heat Transfer,* Addison-Wesley, New York, 1966, pp. 325–328.

7 Arpaci, op. cit., p. 325.

8 Abramowitz M., and Stegun, I. A., *Handbook of Mathematical Functions,* National Bureau of Standards, Applied Mathematics Series No. 55, May 1968, p. 379.

9 Kantrovich and Krylov, "Approximate Methods of Higher Analysis," Interscience Publishers, 1958, pp. 54–61.

10 Op. cit., p. 383.

Downloaded 20 Dec 2010 to 194.27.225.72. Redistribution subject to ASME license or copyright; see http://www.asme.org/terms/Terms_Use.cfm

C. K. Hsieh
Mechanical Engineering Department,
University of Florida,
Gainesville, Fla. 32611

K. C. Su
Bell Laboratories,
Whippany, N.J. 07981

A Methodology of Predicting Cavity Geometry Based on the Scanned Surface Temperature Data — Prescribed Heat Flux at the Cavity Side

A methodology is developed to predict a rectangular cavity lying underneath the surface of a plane wall that dissipates heat by convection to the surroundings. This is also the surface whose temperature is scanned. For a prescribed constant heat flux applying on the cavity surface the cavity depth can be predicted by equating the heat in and out of the system. An analytical procedure is developed that permits checking of the assumed cavity wall position based on comparison between the calculated and the measured surface temperatures. The method is also extended to the prediction of holes in a three-dimensional body (parallelepiped). Examples are provided to illustrate applications.

Introduction

Of the three types of inverse heat-conduction problems found in the heat transfer literature [1–9], the least investigated is one that involves a partially unknown system geometry. The purpose of the problem is to determine this geometry based on the additionally measured temperature on the surface. This inverse problem received attention only recently because of its application in nondestructive testing using infrared scanning.

Unlike the other problems, the inverse problem just mentioned can not be solved by conventional methods. While the problem itself was originated from the infrared scanning technique which has often been considered as an alternative to X-ray computerized axial tomography (CAT) [11–16] because the mechanisms involved in these processes are different, the X-ray tomography analysis can not be used in the solution of the inverse problem [10]. On the other hand, methods in applied mathematics (e.g., conformal mapping) are of little help either [9]. Only a numerical scheme was found useful in the literature [9]. The method used was a forward searching scheme to determine the cavity top; this was followed by a trial-and-error procedure to check the cavity wall position. The method is convenient when the cavity has a prescribed wall *temperature*, but is useless if the cavity has a prescribed *heat flux* (to be explained later under Example and Discussion). For this reason, it is felt desirable to develop a new method that is specifically designed to treat the latter problem. It is the purpose of this paper to describe such a method.

Description of Problem

The basic system under investigation is depicted in Fig. 1. A plane wall having a rectangular cavity in the bottom surface is scanned by using an infrared scanner in order to measure the temperature on its top surface as it dissipates heat by convection to the surroundings. The lower boundary is subjected to a constant heat flux. The right boundary is adiabatic, which is physically valid if L is large compared to w. Because of temperature symmetry it is possible to use only one half of the system for analysis. This also permits the use of an adiabatic condition at $x = 0$. It is further assumed that the test body is homogeneous and the system is in steady state. There is no heat source or sink inside the system. Variations of temperature in the z direction (perpendicular to the plane of Fig. 1), as well as the thermophysical properties with temperatures, are ignored. Both the convective coefficient and the ambient temperature are treated as constants. The purpose of the problem is to determine the cavity size based on the scanned temperature on the surface.

Methodology

For a constant and uniform heat flux applied on the lower boundary, an analytical solution is convenient to predict the cavity. The cavity depth must be determined first; this can be done by equating heats in and out of the system. Since the top surface temperature is measured, and the left and right boundaries of the system are adiabatic, it follows that the depth of the cavity d is related to the top surface heat dissipation Q_t by

$$d = (Q_t/f) - L, \quad f \neq 0 \tag{1}$$

where f represents the constant heat flux imposed on the lower boundary.

With the cavity depth found, the cavity wall position can be determined by using an intrinsic matching scheme that utilizes one portion of the observed surface temperature profile to predict and match the remaining surface temperature profile. In more specific terms, because of the irregular geometry, the entire system can be divided into two regions along an assumed cavity wall (see Z_1 and Z_2 in the rightmost figure of Fig. 2). Then, taking Z_1 first in the analysis, it is possible to determine the heat flux across the dotted boundary based on the measured temperature on the top surface of Z_1. This cross heat flux is subsequently used as a portion of the boundary conditions in problem Z_2 to determine its top surface temperature. The assumed wall position is correct if this calculated temperature matches the measured temperature. In practice, since the heat flux

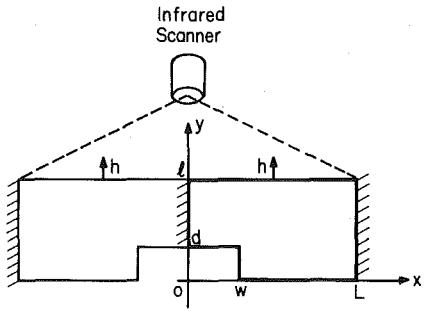

Fig. 1 Schematic of a two-dimensional system under investigation

Contributed by the Heat Transfer Division of THE AMERICAN SOCIETY OF MECHANICAL ENGINEERS and presented at the Winter Annual Meeting, Dec. 2–7, 1979, New York, N.Y. Revised manuscript received by the Heat Transfer Division August 29, 1980. Paper No. 79-WA/HT-45.

Copyright © 1981 by ASME

Downloaded 20 Dec 2010 to 194.27.225.72. Redistribution subject to ASME license or copyright; see http://www.asme.org/terms/Terms_Use.cfm

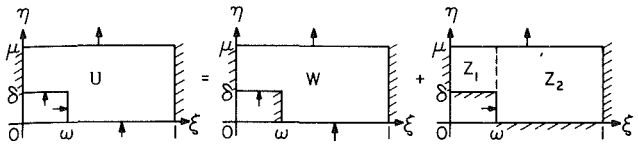

Fig. 2 Illustration of a superposition technique

is evaluated across the dotted boundary, and the cavity wall has a prescribed heat flux, a situation of mixed boundary conditions will not occur in problem Z_2 [17]. Although a small-scale trial-and-error is still needed in the solution to recheck the (cavity) wall position and since this wall position is closely related to where the peak temperature is found on the surface, the initial trials can be made with good approximation. This point will be further examined later in an example.

Analysis

The system under investigation is presented in Fig. 2. The problem can be formulated in terms of dimensionless groups with the governing equation given as,

$$\nabla^2 U = 0 \tag{2}$$

where

$$U = U(\xi,\eta)$$

subjected to boundary conditions:

$$\frac{\partial U(\omega,\eta)}{\partial \xi} = -\frac{fL}{kT_A}, \quad 0 \le \eta \le \delta \tag{3}$$

$$\frac{\partial U(0,\eta)}{\partial \xi} = 0, \quad \delta \le \eta \le \mu \tag{4}$$

$$\frac{\partial U(1,\eta)}{\partial \xi} = 0, \quad 0 \le \eta \le \mu \tag{5}$$

$$\frac{\partial U(\xi,\delta)}{\partial \eta} = -\frac{fL}{kT_A}, \quad 0 < \xi \le \omega \tag{6}$$

$$\frac{\partial U(\xi,0)}{\partial \eta} = -\frac{fL}{kT_A}, \quad \omega \le \xi < 1 \tag{7}$$

$$\frac{\partial U(\xi,\mu)}{\partial \eta} = -\mathrm{Bi}\, U(\xi,\mu), \quad 0 < \xi < 1 \tag{8}$$

In the above equations the dimensionless groups are defined as follows:

$$U = \frac{T(x,y) - T_A}{T_A},\ \xi = \frac{x}{L},\ \eta = \frac{y}{L},\ \omega = \frac{w}{L},\ \delta = \frac{d}{L},\ \mu = \frac{\ell}{L},\ \mathrm{Bi} = \frac{hL}{k}$$

The problem U can be divided into two subproblems using the superposition technique,

$$U(\xi,\eta) = W(\xi,\eta) + Z(\xi,\eta) \tag{9}$$

The subproblem W satisfies the governing equation,

$$\nabla^2 W = 0 \tag{10}$$

and the boundary conditions:

$$\frac{\partial W(\omega,\eta)}{\partial \xi} = 0, \quad 0 \le \eta \le \delta \tag{11}$$

$$\frac{\partial W(0,\eta)}{\partial \xi} = 0, \quad \delta \le \eta \le \mu \tag{12}$$

$$\frac{\partial W(1,\eta)}{\partial \xi} = 0, \quad 0 \le \eta \le \mu \tag{13}$$

$$\frac{\partial W(\xi,\delta)}{\partial \eta} = -\frac{fL}{kT_A}, \quad 0 < \xi \le \omega \tag{14}$$

$$\frac{\partial W(\xi,0)}{\partial \eta} = -\frac{fL}{kT_A}, \quad \omega \le \xi < 1 \tag{15}$$

$$\frac{\partial W(\xi,\mu)}{\partial \eta} = -\mathrm{Bi}\, W(\xi,\mu), \quad 0 < \xi < 1 \tag{16}$$

A pictorial presentation of these conditions is given in the middle diagram of Fig. 2.

The subproblem Z satisfies the governing equation

$$\nabla^2 Z = 0 \tag{17}$$

and the boundary conditions:

$$\frac{\partial Z(\omega,\eta)}{\partial \xi} = -\frac{fL}{kT_A}, \quad 0 \le \eta \le \delta \tag{18}$$

$$\frac{\partial Z(0,\eta)}{\partial \xi} = 0, \quad \delta \le \eta \le \mu \tag{19}$$

$$\frac{\partial Z(1,\eta)}{\partial \xi} = 0, \quad 0 \le \eta \le \mu \tag{20}$$

$$\frac{\partial Z(\xi,\delta)}{\partial \eta} = 0, \quad 0 < \xi \le \omega \tag{21}$$

$$\frac{\partial Z(\xi,0)}{\partial \eta} = 0, \quad \omega \le \xi < 1 \tag{22}$$

$$\frac{\partial Z(\xi,\mu)}{\partial \eta} = -\mathrm{Bi}\, Z(\xi,\mu), \quad 0 < \xi < 1 \tag{23}$$

Fig. 2 again depicts these conditions pictorially.

In the solution of problem W, the insulated cavity wall enables one to drop the ξ dependency in the analysis. The top surface temperature is uniform and can be derived by equating equations (14–16), giving,

$$W(\mu) = f/(hT_A) \tag{24}$$

This uniform temperature distribution is somewhat unexpected, but is necessarily true based on the constant h and T_A assumed in the analysis. This point can be readily verified by using an electric analogy.

As has been discussed previously, problem Z can be split into two problems, Z_1 and Z_2. Let the heat flux across the dotted boundary be denoted as g, $Z_1(\xi,\eta)$ can be derived using the separation of variables technique as:

$$Z_1(\xi,\eta) = \sum_{n=1}^{\infty} \frac{1}{\lambda_n \sinh h\lambda_n \omega} \frac{2(\lambda_n^2 + \mathrm{Bi}^2)}{(\mu - \delta)(\lambda_n^2 + \mathrm{Bi}^2) + \mathrm{Bi}} \times \cosh h\lambda_n \xi \cos\lambda_n(\eta - \delta) \int_0^{\mu-\delta} g(\nu) \cos\lambda_n \nu d\nu \tag{25}$$

Nomenclature

Bi = hL/k
C_n = equation (30)
d = depth of cavity
f = heat flux
G = equation (28)
g = cross heat flux
h = convective coefficient
k = thermal conductivity
L = length of system in x direction
ℓ = thickness of system in y direction
Q = total heat flow per unit depth of system
T = temperature
$U = [T(x,y) - T_A]/T_A$
$W = W(\xi,\eta)$, see equation (24)
w = width of cavity
x,y = independent variables
$Z = Z(\xi,\eta)$
$\delta = d/L$
$\eta = y/L$
λ_m, λ_n = eigenvalues
$\mu = \ell/L$
ν = dummy variable of integration
$\xi = x/L$
$\omega = w/L$

Subscripts

A = ambient
S = surface
t = total
1,2 = regions
I, II, III, IV = quadrants

Downloaded 20 Dec 2010 to 194.27.225.72. Redistribution subject to ASME license or copyright; see http://www.asme.org/terms/Terms_Use.cfm

which is valid for $0 \le \xi \le \omega$, $\delta \le \eta \le \mu$. λ_n are the roots of $\lambda_n \tan\lambda_n(\mu - \delta) = \text{Bi}$.

The temperature at the top surface can be found by substituting μ for η in the above equation and rewriting it as follows:

$$Z_1(\xi,\mu) = \sum_{n=1}^{\infty} \frac{\cos\lambda_n(\mu-\delta)}{\lambda_n \sinh\lambda_n\omega} \frac{2(\lambda_n^2 + \text{Bi}^2)}{(\mu-\delta)(\lambda_n^2+\text{Bi}^2)+\text{Bi}} \times \cosh\lambda_n\xi \int_0^{\mu-\delta} g(\nu)\cos\lambda_n\nu d\nu \quad (26)$$

where $0 \le \xi \le \omega$.

The cross heat flux term $g(\nu)$ in the above equation is now to be determined. This can be done by replacing the integral by a summation using Simpson's rule as:

$$\int_0^{\mu-\delta} g(\nu)\cos\lambda_n\nu d\nu = \frac{\Delta\nu}{3}[G_1 + 4(G_2 + G_4 + \ldots + G_{m-1}) + 2(G_3 + G_5 + \ldots + G_{m-2}) + G_m] \quad (27)$$

where

$$G_i = g[(i-1)(\Delta\nu)]\cos\lambda_n(i-1)(\Delta\nu) \quad (28)$$

and $i = 1, 2, \ldots m$

With this substitution, the terms in equation (26) can be regrouped as follows:

$$Z_1(\xi,\mu) = g(0)\sum_{n=1}^{\infty} C_n \cosh\lambda_n\xi + 4g(\Delta\nu)\sum_{n=1}^{\infty} C_n \cosh\lambda_n\xi\cos\lambda_n(\Delta\nu) + 2g(2\Delta\nu)\sum_{n=1}^{\infty} C_n \cosh\lambda_n\xi\cos\lambda_n 2(\Delta\nu) + \ldots + g[(m-1)(\Delta\nu)]\sum_{n=1}^{\infty} C_n \cosh\lambda_n\xi\cos\lambda_n(m-1)(\Delta\nu) \quad (29)$$

where

$$C_n = \frac{(\Delta\nu)\cos\lambda_n(\mu-\delta)}{3\lambda_n\sinh\lambda_n\omega} \frac{2(\lambda_n^2+\text{Bi}^2)}{(\mu-\delta)(\lambda_n^2+\text{Bi}^2)+\text{Bi}} \quad (30)$$

$g(\nu)$ can then be solved using the method of simultaneous linear equations. It is noted that, to make the matrix multiplication compatible in the solution, the number of unknowns in g must be chosen to be equal to the number of Z_1 used as inputs.

The solution of problem Z_2 can again be made using the separation of variables technique. The top surface temperature distribution is

$$Z_2(\xi,\mu) = \sum_{m=1}^{\infty} \frac{1}{\lambda_m \sinh\lambda_m(1-\omega)} \frac{2(\lambda_m^2+\text{Bi}^2)}{\mu(\lambda_m^2+\text{Bi}^2)+\text{Bi}} \times \cosh\lambda_m(1-\xi)\cos\lambda_m\mu \times \left(\frac{fL}{kT_A}\frac{1}{\lambda_m}\sin\lambda_m\delta - \int_\delta^{\mu} g(\eta)\cos\lambda_m\eta d\eta\right) \quad (31)$$

which is valid in the range $\omega \le \xi \le 1$. The eigenvalues λ_m are roots of

$$\lambda_m \tan\lambda_m\mu = \text{Bi}$$

The crosswise heat flux determined earlier can be used together with $g(\nu) = -(fL/kT_A)$ for $0 \le \eta \le \delta$ to solve the integral in equation (31).

Example and Discussion

A numerical experiment was made to validate the methodology presented in this paper. Gaussian elimination was used to compute the temperatures in plane walls having specified cavity geometries and heat fluxes. The computed surface temperatures were subsequently used as inputs to an inverse problem to predict the cavity geometry. A sample case is presented in Fig. 3 where test conditions are summarized in the legend.

As is shown in the figure, the hot spot on the surface is located near the cavity wall, which is quite unexpected. It was shown in a previous paper [9] that, for a prescribed cavity temperature, the hot spot was located at the cavity center. This displacement of the hot spot in the present case can be ascribed to the constant-temperature W term,

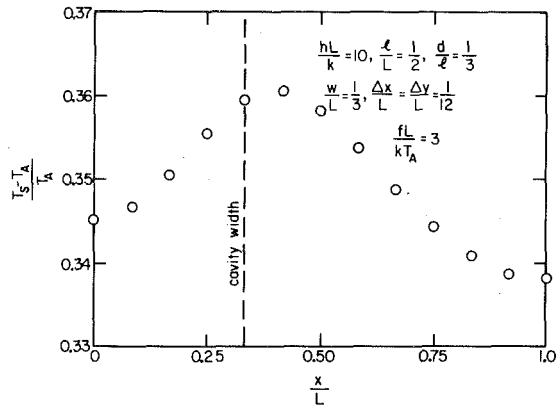

Fig. 3 Surface temperature distribution for a sample test

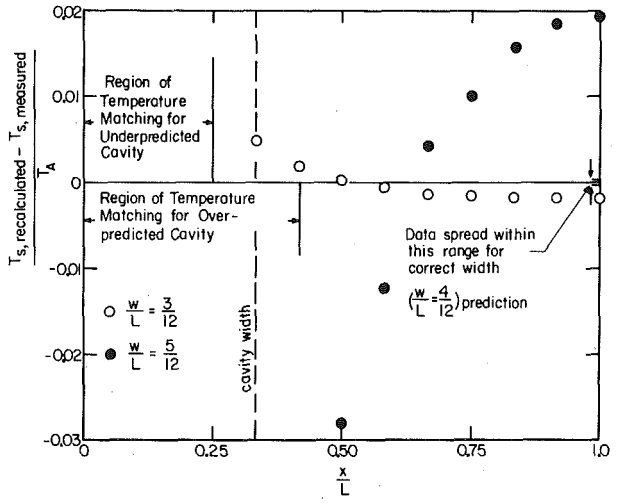

Fig. 4 Recheck of cavity wall position for problem given in Fig. 3

represented by equation (24), and the additional contribution due to Z in equation (9). This latter contribution raises the temperature near the cavity wall because of the additional heat flux crossing the wall.

Following the methodology given, the cavity depth was predicted using equation (1). This was followed by the determination of the cavity width which involved a series of trials of wall positions. To illustrate the trend of data in the searching process, the data in Fig. 3 were used as inputs to evaluate a dimensionless temperature difference between the calculated and the measured temperatures on Z_2 as shown plotted in Fig. 4. If the tested cavity width is exact, the dimensionless temperature difference falls within a narrow band stretching between −0.08 to 0.11 percent. This is identified by tick marks drawn on the right-side scale of the figure. It is noted that this good result was obtained by using only five terms in the Simpson's rule (see equation (27)). Correspondingly, only five heat flux values were generated along the dotted boundary and used in the analysis of Z_2.

An underprediction of cavity width by one mesh size (Δx) yields evaluated surface temperatures in the range of $4/12 \le x/L \le 1$ different from the measured values (see open circles). The trend of data is totally reversed if the cavity width is overpredicted by one mesh size (see closed circles). This drastic change of trend can be explained by referring to the surface temperature plot shown in Fig. 3. The dimensionless temperature slope near the cavity wall, between points $(x/L) = 0.25$ and 0.33 is 0.05225, which is fairly close to that found between points $(x/L) = 0.1667$ and 0.25 (value: 0.0635). However, the slope between points $x/L = 0.33$ and 0.4167 is 0.00106, which is 80 percent lower than needed (0.05225). As a result, the calculated temperatures right to the predicted (cavity) width for the overpred-

Downloaded 20 Dec 2010 to 194.27.225.72. Redistribution subject to ASME license or copyright; see http://www.asme.org/terms/Terms_Use.cfm

icted case shows a drastic change in slope from the underpredicted case. Such a trend reversal is highly desirable as it provides a clue to where the cavity wall is located in the searching process.

A point of interest is the comparison between the methodology developed in this paper and the one reported in [9]. Recalling that the method used in [9] involved a numerical searching process to determine the cavity top, this was followed by a recalculation and matching of the surface temperature based on the assumed cavity wall. The method was shown to be convenient from the application standpoint. Since the cavity temperature was specified in [9], it is natural to use this temperature as a clue in the prediction process. However, in the present case, it is the surface heat flux that is specified at the cavity side; the cavity temperature is *not* known a priori. Experience has shown that the specified heat flux can not be used to predict the cavity using the numerical scheme. The problem lies in the fact that, near the cavity top, the heat flow is close to being unidirectional; q is, therefore, invariant there in the y direction. The resolution of using q to identify the cavity top is thus poor.

On the other hand, it still appears to be possible in the present problem to recalculate and match the surface temperatures using the numerical method in an effort to search for cavity width once the cavity depth is found. Such an approach turns out to be inconvenient. Since none of the boundaries has a specified temperature in the original problem, an ill-conditioned situation arises, which calls for an infinite number of steps to reach a convergence in the iterative solution [18]. Although the Gaussian elimination to solve simultaneous equations is still valid, it can pose a problem to the computer storage if the tested system is large. The proposed methodology is, therefore, more economical and is well-suited for the problem given.

Attention is now directed to the error analysis. Because of the reliance of the present solution on the exact analysis, a detailed error analysis calls for complicated statistical procedures of least squares. In practice, the uncertainty in the measurement of surface temperatures is probably Gaussian, which will lead to a Gaussian error distribution in the cavity prediction. It is felt that this error analysis will be one of the important tasks of the future experimental studies and the present paper is primarily devoted to the presentation of methodology; a simplified analysis is attempted below that is focused on the effect of the Biot number used in the analysis.

An overestimation of h in the Biot number will increase Q_t, thus leading to an overprediction of the cavity depth d (see equation (1)). Unfortunately, for the present problem it is not possible to use the temperatures at the cavity center and the system edge to estimate the h value (such an estimation was, nevertheless, possible in [9]). This can be illustrated by referring to Newton's law,

$$(T_s/T_A) - 1 = f/(hT_A) \tag{32}$$

which is strictly valid where T_s is measured at a point remote from the cavity wall. Under such a condition, the direction of heat flow is everywhere perpendicular to the bounding top and bottom surfaces, and a condition can not be realized everywhere inside our system. To use equation (32) to estimate h is inaccurate as it can be shown using the example illustrated in Fig. 3.

If the surface temperature at the cavity center is used in equation (32), $(f/hT_A) = 0.3453$, which represents a 15.1 percent overprediction (correct value 0.3). By using the temperature at the system edge, this parameter is dropped down to 0.3381, still an unsatisfying 12.7 percent overprediction. Physically, this simple analysis reveals that the heat transfer is not unidirectional along the *total* thickness. Reliance on the simple estimation as that which equation (32) provides is certainly inadequate. It should be further noted that one may argue that a small cavity could probably lead to a better estimation of h based on the surface temperature at the system edge. Such a statement is logically unsound because the cavity size is unknown a priori.

Extension to Three-Dimensional Systems

An attempt is made to extend the foregoing analysis to the prediction of a cavity in a three-dimensional body (parallelepiped) as shown in Fig. 5. It is noted that, because there are four surfaces now

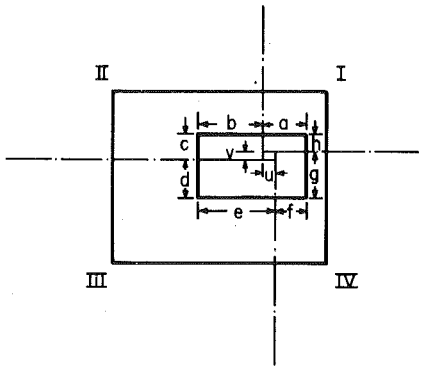

Fig. 5 Partition of system into four quadrants in a three-dimensional analysis

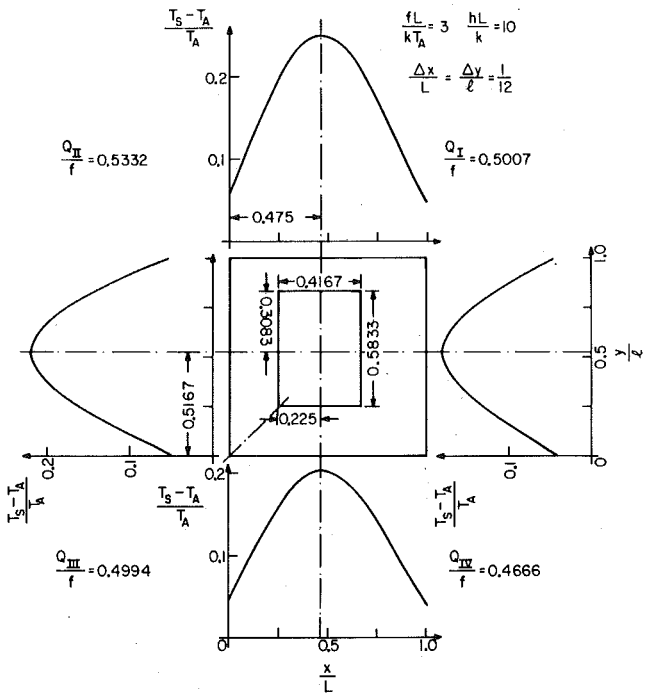

Fig. 6 Prediction of hole in a three-dimensional sample test

dissipating heat by convection, the boundary conditions for this new problem have been changed to the extent that the previously developed, two-dimensional analysis can no longer be used here without modifications (this point will be further elaborated on later). Nevertheless, equation (1) is still valid and this equation will be shown to be useful to the solution of a special class of problem that does not rely on a complicated analytical procedure.

For the system shown in Fig. 5, heat can be freely dissipated from four exposed surfaces. The observed surface temperatures exhibit four peak points, one on each surface (see the temperature plots surrounding the test body in Fig. 6). Unlike the two-dimensional problems studied before, these peak points are located somewhere near the cavity center. Based on this characteristic, sectioned planes can be erected that pass through these peak points and are perpendicular to the cavity boundary as shown by the dash-dotted lines marked in Fig. 5. With the help of these lines the entire system can be divided into four quadrants as labeled by Roman numerals in the figure. It is now possible to consider these lines as adiabatic planes and use equation (1) to write

$$a + h = (Q_I/f) \tag{33}$$

$$b + c = (Q_{II}/f) \tag{34}$$

Downloaded 20 Dec 2010 to 194.27.225.72. Redistribution subject to ASME license or copyright; see http://www.asme.org/terms/Terms_Use.cfm

$$d + e = (Q_{III}/f) \tag{35}$$

$$f + g = (Q_{IV}/f) \tag{36}$$

where Q's represent the total heat dissipation from the surfaces inside each quadrant. In addition, four equations can be written based on geometry as follows:

$$a + b = e + f \tag{37}$$

$$c + d = g + h \tag{38}$$

$$|a - f| = u \tag{39}$$

$$|g - d| = v \tag{40}$$

where u and v can be found experimentally by comparing peak-temperature locations on opposite surfaces.

It is clear from equations (33–40) that eight equations are available to solve for eight unknowns a through h. In practice, one of the equations among (33–36) is dependent, which can be proved by considering a special case when $u = v = 0$. With the shortage of one condition, it is necessary to revert to the exact analysis we had before to generate another relation. While it is still possible to do so analytically, the analysis will become quite lengthy. This can be visualized by referring to Fig. 5 where in the first quadrant the vertical (outside) surface now becomes a convective boundary. Hence, additional superposition is needed in dealing with sectioned regions inside this quadrant. Recognizing that such an analytical procedure involves no new methodology other than the one already presented, it will be shown below that a simple technique can be developed that represents an extension of equation (1) and is yet powerful enough to deal with a special class of three-dimensional problems.

In the event that two adjoining walls of the hole are located equidistant from the outside surfaces, a situation that is readily detectable from the surface temperature symmetry near the corner, an additional adiabatic plane can be placed inside this corner. In this way a simple heat transfer analysis permits the determination of one hole dimension among the eight unknowns. This can be illustrated by referring to the example given in Fig. 6, in which a numerical experiment is provided to generate the surface temperature profiles as shown by the plots surrounding the test body. These temperatures are, in turn, used as inputs in equations (33–40) to predict the cavity. For the sample test shown, the additional adiabatic plane is located at the lower left corner. This permits the evaluation of $(e/L) = 0.2275$ based on the analysis of heat dissipation from the left portion of the bottom boundary. This e value represents an overprediction by 1.1 percent. Using this predicted e, values of $a(=f)$, $c(=h)$ and $d(=g)$ can be computed respectively as 0.1941, 0.3058 and 0.2725. These values are accurate to within 1.3 percent; errors are primarily numerical.

Concluding Remarks

For a convective boundary appearing on the cavity side the problem becomes more complicated because none of the heat flux or temperatures are available at this side of the surface. A pattern recognition scheme is useful for this problem as reported in [19].

It is well known in nondestructive testing using infrared scanning that the uncertainty in flaw detection is larger for small cavities located deep below the surface. With the methodology presented in this paper, this observation takes a new perspective. A small cavity reduces the width of Z_1 thereby making the evaluation of cross heat flux less accurate. In actual testing, a small cavity will also smear out the surface temperature causing the matching of surface temperatures on Z_2 to be less conclusive.

Acknowledgment

The research reported here was performed under the auspices of the National Science Foundation grant ENG-7710630.

References

1 Stolz, G., Jr., "Numerical Solutions to an Inverse Problem of Heat Conduction for Simple Shapes," ASME JOURNAL OF HEAT TRANSFER, Vol. 82, 1960, pp. 20–26.

2 Frank, I., "An Application of Least Squares Method to the Solution of the Inverse Problem of Heat Conduction," ASME JOURNAL OF HEAT TRANSFER, Vol. 85, 1963, pp. 378–379.

3 Burggraf, O. R., "An Exact Solution of the Inverse Problem in Heat Conduction Theory and Applications," ASME JOURNAL OF HEAT TRANSFER, Vol. 86, 1964, pp. 373–382.

4 Sparrow, E. M., Haji-Sheikh, A., and Lundgren, T. S., "The Inverse Problem in Transient Heat Conduction," ASME *Journal of Applied Mechanics*, Vol. 86, 1964, pp. 369–375.

5 Beck, J. V., Discussion to "The Inverse Problem in Transient Heat Conduction," ASME *Journal of Applied Mechanics*, Vol. 87, 1965, pp. 472–473.

6 Beck, J. V., and Wolf, H., "The Nonlinear Inverse Heat Conduction Problem," ASME Paper No. 65-HT-40, 1965.

7 Beck, J. V., "Nonlinear Estimation Applied to the Nonlinear Inverse Heat Conduction Problem," *International Journal of Heat and Mass Transfer*, Vol. 13, 1970, pp. 703–716.

8 Chen, M. M., Pedersen, C. O. and Chato, J. C., "On the Feasibility of Obtaining Three Dimensional Information from Thermographic Measurements," ASME *Journal of Biomedical Engineering*, Vol. 99, No. 2, 1977, pp. 58–64.

9 Hsieh, C. K., and Su, K. C., "Methodologies of Predicting Cavity Geometry Based on the Scanned Surface Temperature Data—Prescribed Surface Temperature at the Cavity Side," ASME JOURNAL OF HEAT TRANSFER, Vol. 102, No. 2, 1980, pp. 324–329.

10 Gambarelli, J., Guerinel, G., Chevrot, L., and Mattei, M., *Computerized Axial Tomography*, Springer-Verlag, Berlin Heidelbert, 1978.

11 Hsieh, C. K., and Ellingson, W. A., "The Feasibility of Using Infrared Scanning to Test Flaws in Ceramic Materials," *Proceedings of the Fifteenth International Thermal Conductivity Conference*, Plenum, New York, 1978, pp. 11–22.

12 Hsieh, C. K., Ellingson, W. A., and Su, K. C., "A Model Study for Quantitative Flaw Detection Using Infrared Scanning," *British Journal of Non-destructive Testing*, July 1979, pp. 185–192.

13 Hsieh, C. K., Ellingson, W. A., and Su, K. C., "Computer Modeling of Heat Transfer Through Refractory Lined Transfer Lines in Coal Gasification System," Argonne National Laboratory Technical Report, in press.

14 Kutzscher, E. W., and Zimmermann, K. H., "Scanning Infrared Inspection System Applied to Nondestructive Testing of Bonded Aersopace Structures," *Applied Optics*, Vol. 7, No. 9, 1968, pp. 1715–1720.

15 Dixon, R. D., Lassahn, G. D. and DiGiallonardo, A., "Infrared Thermography of Subsurface Defects," *Materials Evaluation*, Vol. 30, No. 4, 1972, pp. 73–86.

16 McCullough, L. D., and Green, D. R., "Electrothermal Nondestructive Testing of Metal Structures," *Materials Evaluation*, Vol. 30, No. 4, 1972, pp. 87–95.

17 Sneddon, I. N., *Mixed Boundary Value Problems in Potential Theory*, John Wiley, 1966, pp. 7–10.

18 Clausing, A. M., "Numerical Methods in Heat Transfer," *Advanced Heat Transfer* (Editor: B. T. Chao), University of Illinois Press, Urbana, 1969, pp. 188.

19 Su, K. C., "Methodologies for Cavity Prediction Based on Analysis of Surface Temperature Distributions," Ph.D. Dissertation, University of Fla, 1979.

Downloaded 20 Dec 2010 to 194.27.225.72. Redistribution subject to ASME license or copyright; see http://www.asme.org/terms/Terms_Use.cfm

Microconvective Thermal Conductivity in Disperse Two-Phase Mixtures as Observed in a Low Velocity Couette Flow Experiment

C. W. Sohn
M. M. Chen

Department of Mechanical and Industrial Engineering,
University of Illinois at Urbana-Champaign,
Urbana, IL 61801

Eddy transport associated with microscopic flow fields in shearing two-phase flows was investigated. Although such microconvective effects are expected to be present in all disperse two-phase flows, usually they are masked by other collateral mechanisms and could not be studied critically. In the present study, effective thermal conductivities of neutrally buoyant solid-fluid mixtures were measured in a rotating Couette flow apparatus. Low Reynolds numbers were used to avoid the effects of turbulence. Significant enhancement in effective thermal conductivity was observed when the Pe_d were high. Here $Pe_d = ed^2/\alpha_f$ where e is the local mean shear rate, d is the particle diameter, and α_f is the thermal diffusivity of the fluid. Volume fractions employed were $\phi = 0.15$ and 0.30 for polyethylene beads (2.9 mm in diameter) in a mixture of silicone oil and kerosene, and $\phi = 0.15$ for polystyrene particles (0.3 mm in diameter) in a mixture of silicone oil and Freon-113. Single-phase liquid mixtures were also measured in various shear rates to show that the thermal conductivity was independent of shear rate and hence the observed phenomenon was not an instrumental artifact. The dependence of conductivity on particle Peclet number appeared to approach a power law relationship $k_e \propto Pe_d^{1/2}$ for high Peclet numbers ($300 < Pe_d < 2000$).

Introduction

It has been known that heat transfer rates in two-phase systems are frequently higher than in single-phase fluids at comparable flow conditions. A number of mechanisms can be responsible for the enhanced transport processes. Examples are the effects of latent heat, effects associated with particle-scale or bubble-scale microconvection, effects of increased velocity gradient at the wall, the contribution of turbulent eddies, etc. Usually these mechanisms could not be separated and examined experimentally. The present investigation is focused on the microconvective effects in a disperse two-phase mixture generated by the relative motion between the two phases in shear flow. Such a microconvection manifests itself in a form of eddy conductivity. The origin of such a microconvective thermal conductivity has been described [1].

Since shear fields are present in most two-phase flows, the shear-induced microconvection is expected to be a common feature in most disperse two-phase flows such as bubbly flows, mist flows, and solid-fluid slurries. In a typical two-phase heat transfer, however, the microconvective effect is masked by other simultaneous processes and could not be studied in detail individually. In the present study, this effect is separated from other effects and measured quantitatively in low Reynolds number, rotating Couette flow using a neutrally buoyant solid-fluid suspension.

The rationales for this approach are as follows.

1 The basic physics of microconvective transport in fluid-solid two-phase systems should be similar to that in fluid-fluid two-phase systems. This would be particularly true if the discontinuous phase in the fluid-fluid system consists of very small bubbles since it is known that small bubbles tend to behave like solid spheres with apparently nonslip, rigid boundaries. The use of solid-fluid mixtures, on the other hand, permits better control in the mean diameter and size distribution of the discontinuous phase.

2 In a rotating Couette flow with radial heating, the mean velocity vector is always perpendicular to the mean temperature gradient vector, thus bulk convection due to primary fluid motion is eliminated.

3 The use of neutrally buoyant mixtures eliminates the mean velocity difference between the two phases. Such mean velocity difference may also contribute to the microconvective effect. As a consequence, only shear-induced microconvection is observed.

4 The use of a high viscosity fluid phase prevents turbulence and reduces the effects of secondary flows due to free convection. Another advantage of the rotating Couette flow geometry is that the shear rate is relatively uniform in the gap.

Description of the Apparatus

The conductivity of the two-phase mixture was observed in the annulus of a rotating Couette flow apparatus with a stationary inner cylinder and a rotating outer cylinder. The detailed design of the apparatus is shown in Fig. 1.

The inner cylinder was made of brass with 85.7 mm (3⅜ in.) o.d., 305 mm (12 in.) length, and 1.59 mm (1/16 in.) thickness. The outer cylinder was also made of brass with 133.4 mm (5¼ in.) i.d., 305 mm (12 in.) length, and 3.18 mm (⅛ in.) thickness. Thus the gap width between the two cylinders was 23.8 mm (15/16 in.).

The heater was made of No. 24 B&S size chromel wire (Hoskins Mfg. Co., Detroit, Mich.), wound on a Bakelite tube with 85.6 mm o.d., 305 mm length, and 3.18 mm thickness. V-grooves of 1.59 mm deep were cut spirally along the surface of the Bakelite tube, and the heater wire was embedded inside the grooves. The spacing of heater wire was five turns per each 25.4 mm (1 in.) interval.

The hollow interior of the heater tube was filled with small hollow glass beads (pearlite, Silbrico Corp., Hodgkins, Ill.) to eliminate the possibility of free convection within the empty space. The heater was composed of five separately heated segments. The heating rate into each segment was adjusted to achieve uniform surface temperature along the cylinder surfaces. Heat flows radially outward through the test medium in the annulus toward the outer cylinder which was kept at a constant temperature by thermostat-controlled cooling water running through the water jacket.

Temperatures were measured at the inner and outer brass cylinders with ten copper-constantan thermocouples and five thermistors, respectively. The thermocouples were embedded in the inner cylinder wall by hard silver blazing and the thermistors were embedded in the

Contributed by the Heat Transfer Division for publication in the JOURNAL OF HEAT TANSFER. Manuscript received by the Heat Transfer Division July 2, 1980.

Copyright © 1981 by ASME

Downloaded 20 Dec 2010 to 194.27.225.72. Redistribution subject to ASME license or copyright; see http://www.asme.org/terms/Terms_Use.cfm

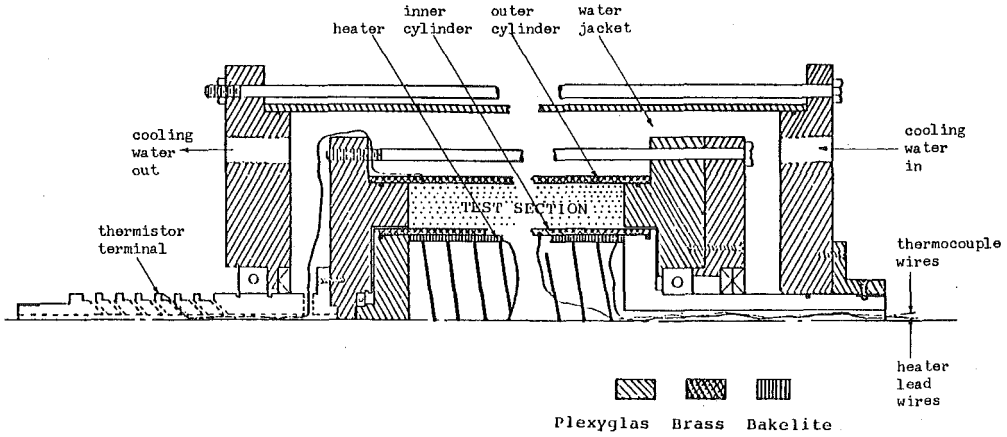

Fig. 1 Construction details of test section

outer cylinder wall and sealed with epoxy resins. In order to eliminate possible end effects, only the middle 44 mm segment of the test section was used for conductivity measurements. This segment had its own independent power input and temperature instrumentation. The uniformity of axial temperature distribution insured negligible axial conduction in the middle 44 mm test section. A schematic illustration of the experimental setup is shown in Fig. 2.

Two different suspensions were tested in these experiments. The first consisted of high density polyethylene pellets (Allied Chemical Co., Baton Rouge, La.) in a liquid mixture of 9.73 parts by volume of 12,500 cs silicone oil (Dow Corning 200 silicone fluid) and 1 part of industrial grade kerosene. The specific gravity of the solid and liquid were 0.960, the liquid specific gravity being measured by a hydrometer. Properties of each constituent for test suspensions are given in Table 1.

In order to test the matching of density between particle and liquid phases, a small amount (10 cc) of the test suspension was placed in a test tube and rotated in a centrifuge (IEC Clinical Centrifuge, Damon/IEC Div., Needham Heights, Mass.) at a rotational speed of 3470 rpm. The arm of the centrifuge was about 150 mm which could produce about 2000 g centrifugal acceleration. No discernible separation between the particle and liquid phases was observed after 1 minute of centrifugation. After about 3 min, separation between the two phases appeared and the bottom 10 mm portion of the 120 mm test tube contained only pure liquid phase. Thus if the sample was laid in the gravitational field only (1 g acceleration), it would take about 6000 minutes (100 hr) for a particle to settle 10 mm due to the density difference. Generally speaking, the particle and oil mixture was observed to remain in uniform suspension for more than two days at room temperature.

The second test suspension was made of polystyrene particles in 12,500 cs silicone oil and Freon 113 mixture. The average diameter of the particles was 0.3 mm which was about one order of magnitude

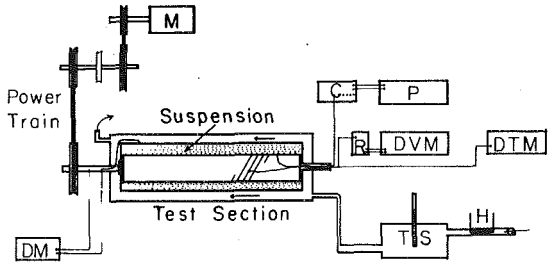

Fig. 2 Schematic diagram of experimental system (M = driving motor, DM = digital multi-meter, C = heater control box, P = power supply, R = thermo-couple electronic junction, DVM = digital volt-meter, DTM = digital thermometer, TS = thermostat, H = heater)

less than that of the polyethylene particles. The purpose of the experiments with the second suspension was to examine the particle Peclet number dependence at low Peclet numbers.

Observations by Karnis, et al. [7] showed that the concentration of particles in a dense suspension within a Couette channel was uniform except for a thin particle-depleted layer near the wall. The presence of the particle-depleted layer has been known through the "sigma" phenomenon whereby the apparent viscosities of suspension clays, soils, and mineral paste when measured in capillary viscometers were found to decrease with decreasing tube radius [8]. The depth of the layer is estimated to be about one particle diameter in Couette flow [9]. In order to avoid serious wall effects, small particle to gap ratio is desirable. The gap ratios employed were about 1/9 for the polyethylene particles and 1/80 for the polystyrene particles.

The working formula for the experimental determination of the effective thermal conductivity is discussed as follows: The absence of radial mean convection in the cylindrical Couette flow geometry

Nomenclature

C_1, C_2, C_3 = general constants
c_p = specific heat at constant pressure
d = particle diameter
e = shear rate (= $|du/dy|$)
f = function
g = gravitational acceleration constant
k = thermal conductivity (refer to subscript section)
n = exponent for a power-law relationship
Pe = Peclet number (refer to subscript section)
q = heat flux
R = radius of cylinder
T = temperature (refer to subscript section)
ΔT = temperature difference ($T_i - T_o$)
u, v = velocity components
r, θ = spatial coordinates
α = thermal diffusivity
β = temperature coefficient of volume expansion
ρ = density
μ = dynamic viscosity
ν = kinematic viscosity
ϕ = particle volume fraction
ω = rotational speed of outer cylinder

Subscripts

d = related to particle diameter
e = effective
elec = related to electrical heating
f = related to liquid phase
i = related to inner cylinder
o = related to outer cylinder or unenhanced state
obs = observed
r, θ = related to r and θ coordinates
s = related to solid phase
w = related to wall
visc = related to viscous dissipation

Downloaded 20 Dec 2010 to 194.27.225.72. Redistribution subject to ASME license or copyright; see http://www.asme.org/terms/Terms_Use.cfm

enables one to adopt the following energy equation:

$$[1/r(d/dr)[rk(r)][dT/dr] + \mu[r(d/dr)(v_\theta/r)]^2 = 0 \quad (1)$$

where v_θ is the tangential velocity given by

$$v_\theta = \omega f(r) \quad (2)$$

where ω is the angular velocity of the outer cylinder.

After two integrations, equation (1) leads to

$$T_i - T_o = [(R_i q_w)/k]\, \ell n\, (R_i/R_o) + (\mu\omega^2/k) I(R_i, R_o) \quad (3)$$

where

$$I(R_i, R_o) = \int_{R_i}^{R_o} \left[(1/r) \int_{R_i}^{r} r^3[(d/dr)(f(r)/r)]^2 dr\right] dr \quad (4)$$

The first term on the right-hand side of equation (3) represents the contribution due to electrical heating; the second term is due to viscous dissipation. The measured quantities in the experiments were outer surface temperature, T_o, inner surface temperature, T_i, and power input, q_w.

The relative importance of viscous heating versus wall heating is proportional to $\mu\omega^2/q_w$. By using low viscosity fluids and high wall heating rates, the viscous heating effects could be minimized or eliminated. However, these measures would lead to higher Rayleigh numbers thus increasing the potential of possible errors due to free convection. Furthermore, the high temperature differences accompanying high values of q_w also aggravates temperature-dependent variable property effects. For the present experiments, q_w was chosen to give a temperature difference in the range of 10 to 20 K. The fluid viscosity was chosen so that the maximum correction for viscous heating, using the method described below, is about 10 percent. After applying the dissipation correction, the maximum uncertainty due to dissipation effect was less than 0.3 percent for high shear data ($Pe_d \simeq 2{,}000$ and 20 for polyethylene and polystyrene, respectively) and less than 0.1 percent for low shear data ($Pe_d \simeq 200$ and 2 for polyethylene and polystyrene suspension, respectively). Thus, the degrading of accuracy by viscous heating was insignificant. This was especially true at the lower rotation rates because of the dependence of the viscous dissipation term on the angular velocity.

Published studies of free convection in vertical slots [10, 11] have shown that for Rayleigh numbers less than 1000, the velocity vector of the free convection current is always perpendicular to the temperature gradient vector and hence plays no role in heat transfer. In the present experiments, the Rayleigh number rarely exceeds 900. As an experimental check, the apparatus was operated both horizontally and vertically and identical results were obtained. Thus the effects of free convection was judged to be insignificant. The particle Reynolds number, ed^2/ν, associated with shear induced rotation was in the range of $Re < 0.03$ for the polyethylene suspensions and in the range of $Re < 0.0006$ for the polystyrene suspensions.

The correction of viscous dissipation was made by *in situ* experimental methods rather than resorting to equation (3). One of the difficulties in the employment of equation (3) was that if the medium is non-Newtonian, the viscosity is not only a material property but may also depend on the angular velocity [12–14]. To avoid these problems, for runs at high angular velocities, i.e. at high Peclet numbers, an identical run was performed with no electrical heating. Thus, the contribution of viscous dissipation was identified separately and the true ΔT due to electrical heating could be determined. The underlying mechanism for this correction scheme originates from the linearity of the energy equation. Specifically, equation (3) can be written as follows.

$$T_{obs} = T_i - T_o = (C_1 q_w/k) + (C_2/k) = \Delta T_{elec} + \Delta T_{visc} \quad (5)$$

ΔT_{obs} is the observed temperature difference which includes the contribution of viscous dissipation as well as electrical heating. The contribution due to dissipation, ΔT_{visc}, was measured separately by running the apparatus without external power input and subtracted from $(T_i - T_o)$ yielding the net contribution (ΔT_{elec}) due to electrical heating. Based upon that temperature difference and supplied power, the effective thermal conductivity is determined from the first part of the right-hand side of equation (3).

Experimental Results

The observed results are presented in terms of conductivity enhancement ratios as a function of particle Peclet number.

$$k_e/k_o = Cf(Pe_d) \quad (6)$$

$$Pe_d = ed^2/\alpha_f \quad (7)$$

where k_e is the effective thermal conductivity in shear flow, k_o the static conductivity, e, the mean shear rate, d, the characteristic linear dimension of a particle, and α_f, the thermal diffusivity. Theoretical and dimensional arguments for the appropriateness of Peclet number for the representation of the enhancement of conductivity was given by Chen and Sohn [1] and will be discussed further below.

Figure 3 shows the observed conductivity for the silicone oil-kerosene liquid mixture which has been used as the liquid phase of polyethylene suspensions. Figure 4 shows the experimental results for test suspensions of polyethylene particles at $\phi = 0.15$ and 0.30 and polystyrene suspension at $\phi = 0.15$. Figure 3 shows that the observed conductivity for single-phase fluid mixture was independent of the angular velocity. Thus the shear-dependent conductivities for multiphase mixture, to be discussed below, were not due to a methodological artifact. The results in Fig. 3 were compared with predictions based on Li's formula [15] for miscible mixtures. The agreement was within 5 percent.

In contrast to the conductivity of the liquid ($\phi = 0$), the conductivity of the tested suspensions showed a strong dependence on applied shear rates as could be seen in Fig. 4 which showed k_e/k_o as a function of particle Peclet numbers. It should be noted that the ranges of shear rates for the polyethylene suspension tests and the polystyrene suspension tests were the same but the difference in diameters between the two particles resulted in orders of magnitude differences of the Peclet numbers.

Particles or bubbles in shear flow rotate at a rate proportional to the shear rate e, thus creating an eddy in the fluid phase. Such eddies induce microconvection effects associated with the surface velocity, ed, and eddy length scale, d. Thus the Peclet number, ed^2/α_f, represents a measure of the eddy scale convection effects as compared to conduction. At sufficiently high Peclet numbers, the microconvective effects represent an additional transport mechanism over and

Table 1 Properties of each constituent for test suspensions

	Suspension I: (90.7 percent Silicone Oil + 9.3 percent Kerosene) + High Density Polyethylene (HDPE) Particles			
	Silicone Oil [2]	Kerosene [3]	Mixture	HDPE [4]
ρ(kg/m^3)	975	823	960	960
k(W/m K)	0.155	0.145	0.154	0.46–0.52
ν (m^2/s)	125×10^{-4}	0.020×10^{-4}	76.6×10^{-4}	—
c_p (J/Kg K)	1.59×10^{-3}	2.09×10^{-3}	1.64×10^{-3}	2.41×10^{-3}
	Suspension II: (80.6 percent Silicone Oil + 19.4 percent Freon 113) + Polystyrene Beads			
	Silicone Oil [2]	Freon 113 [5]	Mixture	Polystyrene [6]
ρ (Kg/m^3)	975	1,565	1,111	1,111
k (W/m K)	0.155	0.075	0.141	0.105
ν (m^2/s)	125×10^{-4}	0.010×10^{-4}	46×10^{-4}	—
c_p (J/Kg K)	1.59×10^{-3}	0.916×10^{-3}	1.46×10^{-3}	1.19×10^{-3}

Downloaded 20 Dec 2010 to 194.27.225.72. Redistribution subject to ASME license or copyright; see http://www.asme.org/terms/Terms_Use.cfm

above molecular transport thus leading to an enhancement of the apparent conductivity. This phenomenon clearly exists in all disperse two-phase flows, not only in solid slurry flows. It may well be an important contributor to the higher observed heat transfer rates in two-phase systems especially those not involving phase change [16].

Examination of Fig. 4 showed that the data appear to fall into two regimes. In the low Peclet number regime ($Pe_d > 50$), the enhancement of thermal conductivity was modest. Here the microconvection probably can be viewed as a perturbation of the basically molecular transport. In the high Peclet number regime ($Pe_d < 300$) the effective conductivity was several times higher than molecular conductivity indicating that microconvective effects dominate the transport. In this regime, the data appear to approach the power-law relationship

$$k_e/k_o = f(\phi, \ldots)\, Pe_d{}^n;\ n = 1/2 \text{ for } Pe_d > 300 \qquad (8)$$

The actual exponents for all data with $Pe_d > 300$ were 0.49 and 0.45 for $\phi = 0.30$ and 0.15, respectively, as determined from least square procedures. It is interesting to note that 1/2 power law is reminiscent of other thermal boundary layer type of convection processes at high Peclet numbers.

Shear-dependent thermal conductivities were also reported by Ahuja [17]. His experiments were based on gross heat transfer measurements in a shell and tube heat exchanger arrangement, employing the Graetz entrance flow solutions to evaluate the thermal conductivities for a saline/polystyrene latex suspension in the circular tube. When his shear rates were converted into estimated ranges of Peclet numbers, his data appear to be in semi-quantitative agreement with the present results. However, since the shear rate is not uniform in Poiseuille flow and since the Graetz solutions are for a uniform conductivity fluid with rather specific boundary conditions difficult to duplicate in a heat exchanger, the value of his data was probably largely qualitative. Quantitative comparison between Ahuja's data and the present results would not be meaningful. In addition, because of the quality of data and small range of shear rates covered, it was not possible to determine a reliable value of the exponent n in equation (8) from Ahuja's data.

For dilute suspensions in which particle-particle interaction can be neglected, theoretical results for conductivity enhancement have been presented by Leal [18] for low Pe_d, and Nir and Acrivos [19] for high Pe_d. The seeming agreement between the weak Pe_d dependence of the present low Pe_d data and the prediction of $n = 1/11$ by Nir and Acrivos for high Pe_d is fortuitous since the regimes and physical mechanisms are different. In addition, our data at low Pe_d lack the precision to check Leal's prediction that microconvective contribution (the perturbation) is proportional to $Pe_d{}^{3/2}$. In any case, the volume fractions employed in the present experiments, $\phi = 0.15$ and 0.3, are much too high for particle-particle interactions to be neglected. Agreement with either theory is thus not expected.

A somewhat disturbing feature of the present data is the lack of quantitative agreement between the two $\phi = 0.15$ curves employing different suspensions. The cause of this disagreement is not understood. Perhaps it is associated with the property difference between the constituent materials or other factors not considered in the present investigation, including the effect of particle size and electrostatic forces. In other words, although the present results show that the microconvective enhancement is closely associated with the particle Peclet number, Pe_d, there are clearly many other parameters which also affect the enhancement ratio. It is hoped that this communication will stimulate other investigations in this important and interesting phenomenon.

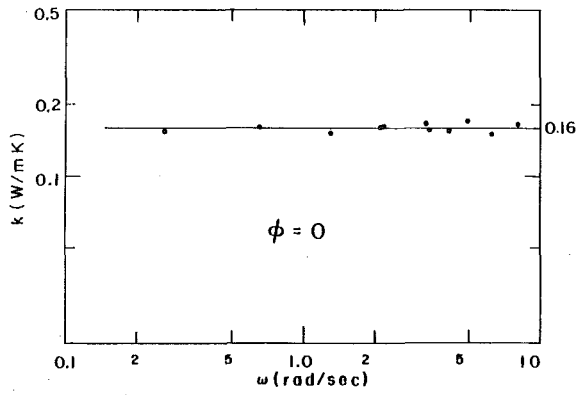

Fig. 3 Thermal conductivity of liquid mixture of silicone oil and kerosene

Conclusions

The following conclusions can be drawn from the present results:

1 In shear flow, disperse two-phase mixtures exhibit a higher effective thermal conductivity as a consequence of microconvection. The phenomenon is similar to the eddy conductivity in turbulence. As a result, the effective conductivity of such a mixture is not only a material property but it also depends on flow parameters as well.

2 The particle Peclet number defined in equation (7) appears to be an appropriate parameter for the intensity of the microconvection effect. However, two suspensions with different k_f/k_s ratios did not yield identical microconvective effects at the same Pe_d. Presumably parameters other than Pe_d also play important roles and should be investigated.

3 At high Pe_d ranges (greater than 300), effective conductivity appears to approach the power law $Pe_d{}^{1/2}$. Further experimental verifications of this trend at even higher Pe_d would be desirable.

4 The same physical phenomenon is expected to exist in disperse liquid-liquid and liquid-vapor system. Because of the deformability of the particles and the possibility of bubble coalescence and breakup, the phenomenology would be much more complex. The importance of microconvection in these systems should be assessed.

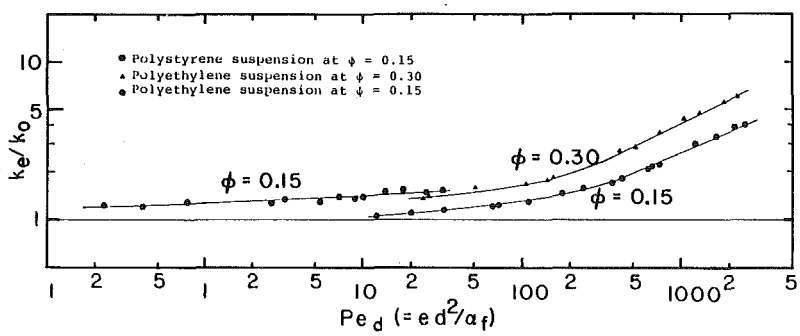

Fig. 4 The enhancement ratio of conductivity (k_e/k_o) as a function of particle Peclet number (Pe_d)

Downloaded 20 Dec 2010 to 194.27.225.72. Redistribution subject to ASME license or copyright; see http://www.asme.org/terms/Terms_Use.cfm

Acknowledgment

The authors wish to express their indebtedness to the Heat Transfer Program, National Science Foundation, for supporting this research and to June Kempka for typing the manuscript.

References

1 Chen, M., and Sohn, C. W., "Enhancement of Thermal Conductivity of Disperse Two-Phase Mixtures in Shear Flow," 2nd Multi-Phase Flow and Heat Transfer Symp.-Workshop, Apr 16–18, 1979, University of Miami.

2 "Information about Silicone Fluids: Dow Corning 200 Fluid," Dow Corning, Midland, Mich.

3 *CRC Handbook of Tables for Applied Engineering Science,* 2nd ed., 1976, CRC Press, pp. 90–2, 533.

4 "PAXON: High Density Polyethylene, Grade AD 60-007," Allied Chemical Corp., Baton Rouge, La.

5 "Transport Properties of "FREON" Fluorocarbons, Freon Product Information," 1973, E. I. du Pont de Nemours & Co.

6 *Chemical Engineers' Handbook,* R. H. Perry and C. H. Chilton, eds., McGraw-Hill, New York, pp. 23–63.

7 Karnis, A., Goldsmith, H. L., and Mason, S. G., "The Kinetics of Flowing Dispersions, I. Concentrated Suspensions of Rigid Particles," *Journal of Colloid Science,* Vol. 22, 1966, pp. 531–53.

8 Goldsmith, H. L., and Mason, S. G., "The Microrheology Dispersions," *Rheology Theory and Applications,* Vol. 4 (F. R. Eirich, ed.), Academic Press, New York, 1967, pp. 85–250.

9 Vand, V., "Viscosity of Solutions and Suspensions," *Journal Physics of Colloid Chemistry,* Vol. 52, 1948, pp. 277–321.

10 Eckert, E. R. G., and Carlson, W. O., "Natural Convection in an Air Layer Enclosed between Two Vertical Plates with Different Temperatures," *International Journal of Heat and Mass Transfer,* Vol. 2, 1961, pp. 106–120.

11 Elder, E., "Laminar Free Convection in Vertical Slots," *Journal of Fluid Mechanics,* Vol. 23, 1965, pp. 77–98.

12 Frisch, H. L., and Simha, R., "The Viscosity of Colloidal Suspensions and Macro-Molecular Solutions," Chap. 14 in *Rheology,* F. R. Eirich, ed., Vol. 1, 1956, Academic Press, New York.

13 Rutgers, R., "Relative Viscosity and Concentration," *Rheology Acta,* Band 2, 1962, pp. 305–348.

14 Jeffrey, D. J., and Acrivos, A., "The Rheological Properties of Rigid Particles," *AIChE Journal,* Vol. 22, No. 3, 1976, pp. 417–432.

15 Li, C. C., "Thermal Conductivity of Liquid Mixtures," *AIChE Journal,* Vol. 22, 1976, pp. 927–930.

16 Corlett, T. L., and Knudsen, J. G., "Heat Transfer Characteristics of Liquid-Liquid Dispersions flowing in an Annulus," *AIChE Symposium Series,* Vol. 73, No. 164, 1977, pp. 261–267.

17 Ahuja, A. S., "Augmentation of Heat Transport in Laminar Flow of Polystyrene Suspensions, I. Experiments and Results," *Journal of Applied Physics,* Vol. 46, 1975, pp. 3408–3416.

18 Leal, L. G., "On the Effective Conductivity of a Dilute Suspension of Spherical Drops in the Limit of Low Particle Peclet Number," *Chemical Engineering Communications,* Vol. 1, 1972, pp. 21–31.

19 Nir, N., and Acrivos, A., "The Effective Thermal Conductivity of Sheared Suspensions," *Journal of Fluid Mechanics,* Vol. 78, 1976, pp. 33–48.

Downloaded 20 Dec 2010 to 194.27.225.72. Redistribution subject to ASME license or copyright; see http://www.asme.org/terms/Terms_Use.cfm

Md. Alamgir[1]
LOCA Systems Technology,
General Electric Co.,
175 Curtner Ave.,
San Jose, Calif. 95125
Assoc. Mem. ASME

J. H. Lienhard[1]
Professor,
Mechanical Engineering Department,
University of Houston,
Houston, Tex 77004
Fellow ASME

Correlation of Pressure Undershoot During Hot-Water Depressurization[2]

A method is devised for correlating the extent that the pressure of a system undershoots the saturation pressure during a rapid depressurization in water. The dependent variables in the correlation are the initial water temperature and the depressurization rate. The correlation is motivated by classical nucleation theory, and based on data from a variety of sources. The probable error of pressure undershoots predicted by the correlation is ±10.4 percent.

Introduction

When high-temperature, high-pressure, water is suddenly depressurized it passes from a subcooled to a superheated state. It finally reaches a pressure, p_n, far enough below its normal boiling pressure, p_{sat}, that it flashes explosively into vapor. We call $(p_{sat} - p_n)$, the *pressure undershoot*. Such a depressurization can occur routinely as the result of turbulent fluctuations of hot water in a nozzle. And there is concern that it could result in the unhappy event of a hot water line fracture in a steam power plant.

Figure 1 shows the path such a depressurization might take. Starting at an initial point, i, it follows an isentropic path which we have shown [1] to remain within a degree or so of isothermal. When the liquid pressure falls below the saturation pressure at the initial temperature, nucleation starts to occur. The faster depressurization occurs, the greater the pressure undershoot will be, and the greater will be the violence with which flashing occurs.

There is increasing interest in the pressure undershoot, among people concerned with predicting the two-phase flow following a rapid depressurization. One reason is that the undershoot helps to determine the initial conditions on the subsequent blowdown process; another is that the influence of the resulting pressure rarefaction wave on structures must be fully understood. Within the past decade relevant observations of the pressure undershoot have been made by Edwards and O'Brien [2], Kenning and Thirunavukkarasu [3], Rassokhin, et al. [4], workers in this laboratory [1, 5], Hooper, et al. [6], Friz, et al. [7], and Sozzi and Fedrick [8], among others.

The aim of the present paper is to propose a rational strategy for correlating the pressure undershoot in terms of the relevant system variables, and to construct such a correlation using both prior measurements and original data.

Formulation of Correlation

Homogenous Nucleation. The classical theories of Volmer, Döring, Kagan, etc. (see discussion by Skripov [9], sections 11 and 12) hold that nucleation occurs when the "potential barrier" to nucleation, $4\pi r_c^2\sigma/3$, is within an order of magnitude of kT. The critical nucleus radius, r_c, (see a useful recent discussion by Ward, et al. [10]) can be simplified with negligible error to (see [9], section 8) to

$$r_c = 2\sigma/(1 - v_f/v_g)(p_{sat} - p_n) \tag{1}$$

Then

$$j \frac{\text{nucleation events}}{\text{molec. collision}} \equiv \frac{J \dfrac{\text{nuc. events}}{m^3 - s}}{N_A B/v_f} = e^{-\text{Gb}} \tag{2}$$

where the Gibbs number, Gb, is the potential barrier divided by kT. B is the frequency with which a liquid molecule interacts with its neighbors—approximately (kT/Planck's constant) or about 10^{13}/s. The rapid heating experiments of Skripov, et al. [11] give typical limiting values of

$$J \simeq 10^{34}\, m^{-3}\, s^{-1}; j \simeq 10^{-5}; \text{Gb} \simeq 11$$

Normally, nucleation occurs at much larger values of Gb than 11.

Heterogeneous Nucleation at High Superheat in Practical Systems. Nucleation of superheated water in real systems usually occurs at the walls where there are sizable surface imperfections. In such cases nucleation eventually becomes a deterministic phenomenon to be predicted by direct analysis of permanent gas pockets, contact angles, and surface geometry.

But as long as the process is initiated stochastically by molecular disturbances, the Gibbs number can be multiplied by a heterogeneity factor ϕ, where $\phi < 1$, to reduce it to a conventional homogeneous nucleation value. When nõ true heterogeneous elements are present, the true value of ϕ remains well within an order of magnitude of unity. It can be considerably smaller if such elements as gas pockets are present.

We presume that, if physical heterogeneities are small enough, they can be dealt with using the homogeneous theory and will respond randomly to molecular fluctuations. When they become at all sizable they must be treated deterministically. At that point the present correlation will reveal the limitation by breaking down.

We further note that, since nucleation should occur in the plane of the wall,[3] N_A/v_f should be replaced by $(N_A/v_f)^{2/3}$, as has been suggested by Blander and Katz [12], in equation (4). Combining these ideas, we modify equation (2) as follows for use in the present problem.

[3] This was observed to be the case in [3], and one would expect it to be generally true.

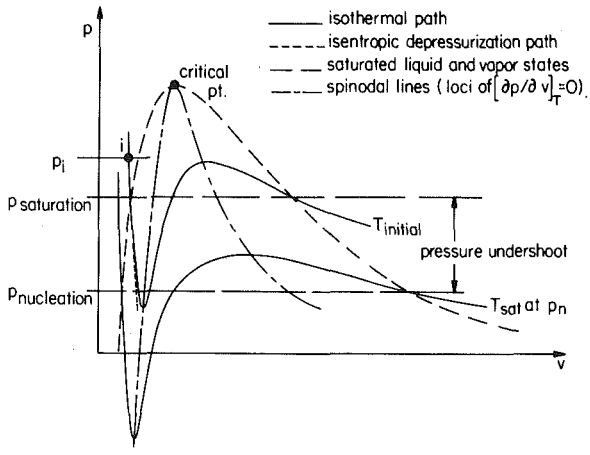

Fig. 1 The depressurization process

[1] Most of this work was done while both authors were associated with the Boiling and Phase-Change Laboratory, Mechanical Engineering Department, University of Kentucky, Lexington, Ky.

[2] This work was supported by the Electric Power Research Institute under research contract, RP-687-1 with Balraj Sehgal serving as contract manager.

Contributed by the Heat Transfer Division for publication in the JOURNAL OF HEAT TRANSFER. Manuscript received by the Heat Transfer Division October 24, 1979.

Copyright © 1981 by ASME

Downloaded 20 Dec 2010 to 194.27.225.72. Redistribution subject to ASME license or copyright; see http://www.asme.org/terms/Terms_Use.cfm

$$J \frac{\text{nucl. events}}{\text{m}^2 - \text{s}}$$

$$= \left(\frac{N_A}{v_f}\right)^{2/3} B \exp\left[-\frac{16\pi\sigma^3}{3kT\left(1-\frac{v_f}{v_g}\right)^2 (p_{sat}-p)^2}\phi\right] \quad (3)$$

Notice that J takes on an altered meaning here. It is now based on area instead of volume.

Our problem is that of determining how to specify a criterion for nucleation in terms of J. Figure 2 shows a typical depressurization process leading up to nucleation, on pressure-time coordinates. This is one of our own traces but it is typical of other people's measurements as well. Between p_{sat} and the minimum pressure, which we identify as p_n, we can write

$$p_{sat} - p = \Sigma' t \quad (4)$$

where Σ' is the constant rate of depressurization in atm/s and p is any local pressure $< p_{sat}$. We identify p_n as the pressure at which the almost linear rate of depressurization is abruptly halted. This presumably occurs when superheating cannot proceed any further.

The total density of nuclei, Z, that are triggered up to the time, t_n, at which depressurization is halted is

$$Z \frac{\text{nuclei}}{\text{m}^2} = \int_0^{t_n} J dt \quad (5)$$

Combining equations (4) and (3) and putting the result in equation (5) we obtain, after integration,

$$Z = \left(\frac{N_A}{v_f}\right)^{2/3} B \frac{(p_{sat}-p_n)}{\Sigma'} [e^{-\eta\phi} - \sqrt{\pi\eta\phi}\ \text{erfc}\ \sqrt{\eta\phi}] \quad (6)$$

where

$$\eta \equiv \frac{16\pi\sigma^3}{3kT\left(1-\frac{v_f}{v_g}\right)^2 (p_{sat}-p_n)^2} = \frac{\text{Gb}}{\phi} \quad (7)$$

Equation (6) provides a basis for predicting the point beyond which a given depressurization must be halted. This will occur before an entire surface is covered by nuclei as shown in Fig. 3. We say "before" because a new nucleus multiplies its size many times within microseconds of inception. We therefore set Z equal to its upper limit

$$Z = 1/2\sqrt{3}\, r_c^2 \quad (8)$$

in equation (6) and use equation (1) to get

$$e^{-\eta\phi} - \sqrt{\pi\eta\phi}\ \text{erfc}\ \sqrt{\eta\phi} = \frac{\Sigma'\left(1-\frac{v_f}{v_g}\right)}{\left(\frac{N_A}{v_f}\right)^{2/3} B \sqrt{\frac{36kT\sigma}{\pi}}\, \eta^{1/2}} \quad (9)$$

That Z is in fact much smaller than the value given in equation (8) is not important as long as equation (8) expresses the correct functional dependence for Z. The reason is that we must next establish

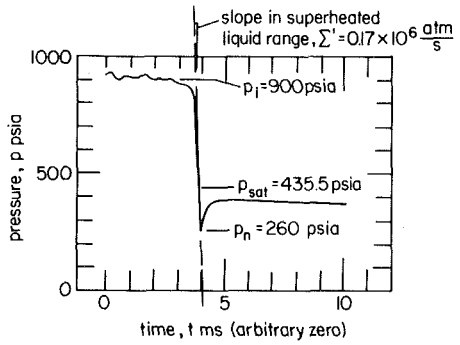

Fig. 2 A typical pressure-time history in the present 5.08 cm pipe experiments. Local temperature is 233.9°C. (pressure transducer #PT-1, run No. HW-20)

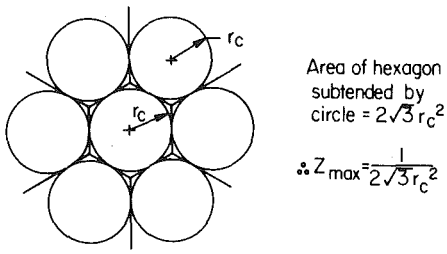

Fig. 3 Maximum conceivable density of nuclei on pipe wall. Actual p_n will be reached when some growth has occurred and $r \gg r_c$

ϕ by correlation using equation (9). The use of equation (8) leads to a lower numerical value of ϕ, which correctly reflects the fact that early bubble growth contributes an additional kind of heterogeneity to the system as nucleation progresses.

A Correlation for the Heterogeneity Factor, ϕ

The right-hand side of equation (9) contains information which is known in any experimental determination of p_n. The left-hand side includes the unknown heterogeneity factor, ϕ. We therefore seek to evaluate ϕ using the existing data[4] of [1–8], and new data obtained in a 2 in. (5.08 cm) i.d. tube which was similar to the ½ in. (1.27 cm) i.d. tube used in [1]. These new data are described [15].

In reducing data for cases in which Σ' was less than about 0.004 Matm/s we encountered a difficulty that did not occur when depressurization was more rapid. Instead of falling almost linearly prior to p_n, as indicated in Fig. 2, the pressure fell in a ragged and/or sawtooth fashion. The point, p_n, could no longer be identified with any confidence. This was true of all the data in [6] and [7] and two of our 5.08 cm i.d. pipe data.

These data are included in our subsequent graphs, but they are not used in any of the correlations nor in the assessments of their accuracy. The correlations should likewise be restricted to use at depressuri-

[4] Data from the first pressure transducer in the experiments of [5] proved to be based on temperatures that were slightly high. A rational correction was devised in [15] and applied to the results.

Nomenclature

B = frequency of interaction of a molecule with its neighbors ($\simeq kT$/Planck's constant)
Gb = the Gibbs number, W_{cr}/kT or $\eta\phi$
J = frequency of nucleation events per unit volume or per unit area (distinguished in context)
j = nucleation events per molecular collision
k = Boltzmann's constant
N_A = Avogadro's number
p, p_i, p_n, p_{sat} = pressure. Initial pressure, minimum pressure in depressurization process, saturation pressure at initial temperature, T_i
r_c = critical radius of an unstable nucleus (see equation (1))
t, t_n = time: time at which nucleation is too dense to permit further depressurization
T, T_c, T_i, T_r = temperature: critical temperature; initial temperature in a depressurization process; reduced temperature, T_i/T_c
v, v_f, v_g = molar specific volume: molar specific volume of saturated liquid and of saturated vapor at T_i
Z = total number of nuclei per m^2 that occur during depressurization between p_{sat} and p_n
η = Gb/ϕ
σ = surface tension between liquid and vapor
Σ' = the rate of depressurization (expressed in Matm/s in the present study)
ϕ = the heterogeneity factor, or ratio of the potential barrier for heterogeneous nucleation to that for homogeneous nucleation

Downloaded 20 Dec 2010 to 194.27.225.72. Redistribution subject to ASME license or copyright; see http://www.asme.org/terms/Terms_Use.cfm

zation rates in excess of 0.004 Matm/s. Notice that the failure of depressurization to yield a sharp p_n, in these cases, is the result of large deterministic nucleation sites being activated. We anticipated that this would occur when depressurization is too slow to reach the large numbers of sites that will be activated by molecular fluctuations.

The procedure for correlating ϕ with the two independent variables, $T_r \equiv T_i/T_c$ and Σ', was as follows: The available depressurization data (p_n, T_i, Σ') were encoded[5] on cards and the relevant properties of water (v_f, v_g, σ, and p_{sat}) were written as functions of T, based on data from [13] and [14]. This information gives the right-hand side of equation (9) for each measurement. This made it possible to establish a set of values of ϕ for corresponding values of T_i and Σ' using Newton's iteration.

Next, we assumed:

$$\phi(T_r, \Sigma') = f_1(T_r) \cdot f_2(\Sigma') \tag{10}$$

Initially $f_2(\Sigma')$ was set equal to unity and $f_1(T_r)$ was obtained in the form of a simple power law function in T_r. Next, the ϕ values were divided by this f_1 and the quotient, $f_2(\Sigma')$ was correlated as a linear function in $\Sigma'^{0.8}$. This procedure was repeated and convergence was achieved after several iterations each, for f_1 and f_2. The result was

$$\phi = 0.1058\, T_r^{28.46}\,(1 + 14\,\Sigma'^{0.8}) \tag{11}$$

for Σ' expressed in Matm/s. The ranges in which the correlation has been found to represent the data are

$$0.62 \leqslant T_r \leqslant 0.935$$

$$0.004 \text{ Matm/s} \leqslant \Sigma' \leqslant 1.803 \text{ Matm/s}$$

For lower values of Σ' and T_r we believe that the present model is inapplicable.

That the choice of the functions, f_1 and f_2 was realistic is shown in Figs. 4(a) and 4(b) where ϕ/f_2 and ϕ/f_1 are plotted against T_r and Σ', respectively. The accuracy of these representations is clearly very high with correlation coefficients of 0.99 and 0.95, respectively. Notice the scattered data to the left of $\Sigma' = 0.004$ Matm/s in Fig. 4(b). These points are excluded from the correlation.

We should alert the reader to the fact that equation (11) gives values of the inhomogeneity factor, ϕ, that vary from 0.055 down to 2×10^{-7}. The smaller of these values of ϕ suggest substantial inhomogeneities that should possibly be treated *deterministically*, as conventional nucleation sites. There are two important reasons why such small values of ϕ can still be treated stochastically without contradicting the kinetic theory.

In the first place, an inhomogeneity (or nucleation site) can still be triggered by molecular fluctuations if it is small enough, and only a very small inhomogeneity is needed to reduce ϕ greatly. Thus we expect the stochastic kinetic theory to be valid even when ϕ is considerably less than unity.

In the second place, the values of ϕ that we report are *apparent* values subject to increasing distortion as T_r and Σ' are reduced. We have already noted that the apparent value of ϕ is made far smaller than the actual ϕ at p_n by the fact that bubble growth occurs during the few microseconds needed to make p_n visible on the oscilloscope trace. Furthermore, the presence of a very small inhomogeneity greatly increases p_n and, with it, the value of r_c. We calculate our apparent values of ϕ at the observed p_n—not at the associated pure-homogeneous point, where the actual value of ϕ would be a great deal larger.

We are able to tell where the present stochastic treatment ultimately fails by observing where the correlation based on it ceases to unify diverse data. The data for $\Sigma' < 0.004$ Matm/s undoubtedly reflect such a failure and would have to be predicted using a deterministic model.

[5] Computer output showing the data, and/or the results derived from them, can be obtained from the authors on request.

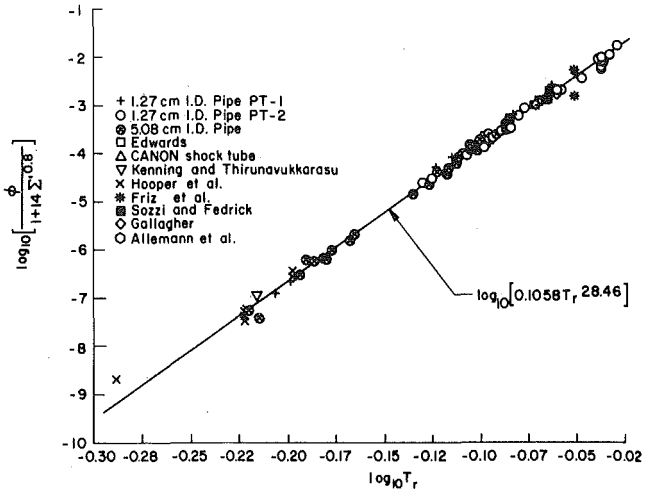

Fig. 4(a) The function $f_1(T_r) = \phi/f_2(\Sigma')$

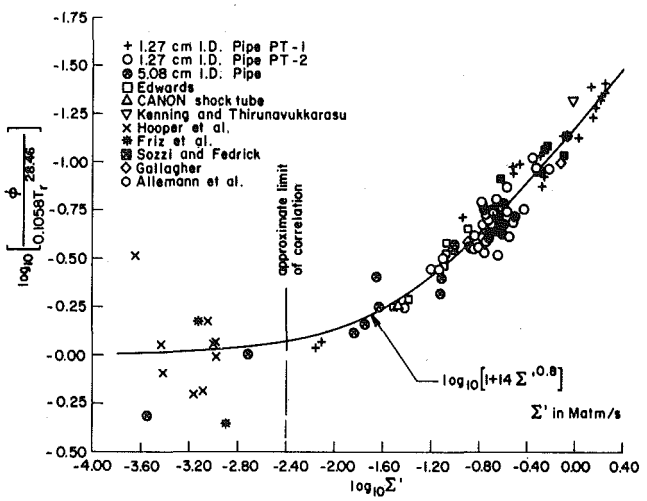

Fig. 4(b) The function $f_2(\Sigma') = \phi/f_1(T_r)$

Fig. 4 Correlations of $f_1(T_r)$ and $f_2(\Sigma')$, where $\phi = f_1(T_r) \cdot f_2(\Sigma')$

The Pressure Undershoot Correlation

Once an apparent value of ϕ is established, we need only note that the dimensionless pressure undershoot correlation can be written (recall equation (7)) in the form

$$\frac{1}{\sqrt{\eta\phi}} = \frac{1}{\sqrt{\text{Gb}}} = \frac{(p_{sat} - p_n)}{1.33\,\dfrac{\sigma^{3/2}\,T_r^{13.73}\,(1 + 14\,\Sigma'^{0.8})^{0.5}}{\sqrt{kT_c}\left(1 - \dfrac{v_f}{v_g}\right)}} \tag{12}$$

The data yield an average value of $1/\sqrt{\text{Gb}}$ equal to 0.188. This corresponds with Gb = 28.2 ± 5.8, where we have reported the probable error. Thus the final correlation takes the form:

$$p_{sat} - p_n = 0.252\,\frac{\sigma^{3/2}\,T_r^{13.73}\,(1 + 14\,\Sigma'^{0.8})^{0.5}}{\sqrt{kT_c}\left(1 - \dfrac{v_f}{v_g}\right)} \tag{13}$$

where the dimensions of Σ' are Matm/s and the remaining dimensions are self-consistent.

The Gibbs function of 28.2 is based on the assumption that $Z = 1/2\sqrt{3}\,r_c^2$. Actually, as we noted previously, Z should be based on the average radius to which bubbles have grown when further nucleation becomes impossible. Accordingly, Z should be smaller and the actual value of ϕ should be larger. Thus some bubble growth following nu-

Downloaded 20 Dec 2010 to 194.27.225.72. Redistribution subject to ASME license or copyright; see http://www.asme.org/terms/Terms_Use.cfm

cleation is reflected in Gb, making it appear smaller, as it also made the effective inhomogeneity seem smaller than it is.

The deviation of the actual nucleation pressure, p_n, from the value given by the correlation, is plotted against T_r in the form $(p_{n_{correl.}} - p_{n_{expt.}})/(p_{sat} - p_{n_{expt}})$, in Fig. 5. It shows that the correlation represents the data within a standard error of ±10.4 percent.

It is important to note that the only system variables that influence $(p_{sat} - p_n)$ are T_r and Σ'. The differences in water preparation, surface finish of the metallic containers, etc., in the different systems, are not evident. Since the water was generally subjected to high pressure prior to depressurization, the pipe walls were generally well-wetted. It is possible that commercially finished steel, which was used in all the experiments, provided a common level of surface inhomogeneity, as well.

For the convenience of the engineer who wants to read the magnitude of p_n directly in terms of Σ' and T_i, we plot equation (13) in these dimensional terms in Fig. 6.

Conclusions

1 A correlation has been developed on the basis of classical nucleation theory. It suggests that the Gibbs number for nucleation in water during depressurization from high pressure is about 28.2 ± 5.8. This result may or may not be restricted to commercially finished pressure vessels and tubing. It corresponds to

$$j \simeq 10^{-12} \frac{\text{nucl. events}}{\text{molec. collisions}}$$

or with

$$J \simeq 10^{18} \frac{\text{nucl. events}}{\text{m}^2 - \text{s}}.$$

And it includes some post-nucleation bubble growth in the inhomogeneity factor. (J or j would be much smaller without the distortions reflected in ϕ.)

2 The pressure undershoot that can be anticipated in a linear depressurization process (equation (4)) is given within ±10.4 percent by equation (13). This result has been established in the ranges: $0.62 \leqslant T_r \leqslant 0.935$ and $0.004 \text{ Matm/s} \leqslant \Sigma' \leqslant 1.803 \text{ Matm/s}$.

Acknowledgment

We are grateful to Dr. H. K. Züst for contributing useful ideas to the formulation of the present correlation.

References

1 Borkar, G. S., Trela, M., and Lienhard, J. H., "A Rapid Hot-Water Depressurization Experiment," EPRI Report NP-527, Dec. 1977.

2 Edwards, A. R., and O'Brien, T. P., *Journal British Nuclear Energy Society*, Vol. 9, 1970, p. 125.

3 Kenning, D. B. R., and Thirunavukkarasu, K., "Bubble Nucleation Following a Sudden Pressure Reduction in Water," *Heat Transfer 1970, Proceedings of Fourth International Heat Transfer Conference*, Paris-Versailles, Vol. 5, 1970, p. B. 29.

4 Rassokhin, N. G., Kuzevanov, V. S., Tsiklauri, G. V.; Marinchek, A., and Sella, J., "Critical Conditions with Unsteady Outflow of a Two-Phase Medium with a Pipeline Break," *Teplofizika Vysokikh Temperatur*, Vol. 15, No. 3, 1977, p. 539.

5 Lienhard, J. H., Alamgir, Md., and Trela, M., "Early Response of Hot Water to Sudden Release from High Pressure," ASME JOURNAL OF HEAT TRANSFER, Vol. 100, No. 3, 1978, pp. 473–479.

6 Hooper, F. C., Faucher, G., and Eidlitz, A., "Pressure Effects on Bubble Growth in the Flashing of Superheated Water," *Heat Transfer 1970, Proceedings of Fourth International Heat Transfer Conference*, Paris-Versaille, Vol. 5, 1970, pp. B2.3, 1–11.

7 Friz, G., Riebold, W., and Schulze, W., "Studies on Thermodynamic Non-Equilibrium in Flashing Water," *Transient Two-Phase Flow, Proceedings of the CSNI Specialists Meeting*, Aug. 3, 4, 1976, Toronto, AEC of Canada Ltd., May 1978, pp. 511–523.

8 Sozzi, G. L., and Fedrick, N. A., "Decompression Waves in a Pipe and Vessel Containing Subcooled Water at 1000 psi," NEDE-13333, General Electric Company, Mar. 1973.

9 Skripov, V. P., *Metastable Liquids*, (English Translation) John Wiley and Sons, New York, 1974.

10 Ward, C. A.; Balakrishnan, A.; and Hooper, F. C., "On the Thermodynamics of Nucleation in Weak Gas-Liquid Solutions," ASME *Journal of Basic Engineering*, Vol. 92, No. 4, 1970, pp. 695–703.

11 Skripov, V. P., Ermankov, G., Sinitsin, E., Baidakov, V., Bulanov, N., Danilov, N., and Nikitin, E., "Superheated Liquids: Thermophysical Properties, Homogeneous Nucleation and Explosive Boiling-Up," ASME Paper No. 77-HT-87, ASME AIChE Heat Transfer Conference, Salt Lake City, Aug 15–17, 1977.

12 Blander, M., and Katz, J. L., "Bubble Nucleation in Liquids," *AIChE Journal*, Vol. 21, No. 5, 1975, pp. 833–838.

13. Meyer, A., McClintock, R. B., Silvestri, G. J., and Spencer, R. C., Jr., *Thermodynamic and Transport Properties of Steam*, The 1967 ASME Steam Tables, ASME, New York, 1967.

14 "Release of Surface Tension of Water Substances," The Int'l. Assn. for the Properties of Steam, Dec. 1976, available from the Exec. Sec. of the IAPS, Off. of Std. Ref. Data, Nat'l Bur. of Stds. USA.

15 Alamgir, Md., Kan, C. Y., and Lienhard, J. H., "An Experimental Study of the Rapid Depressurization of Hot Water," ASME JOURNAL OF HEAT TRANSFER, Vol. 102, No. 3, 1980.

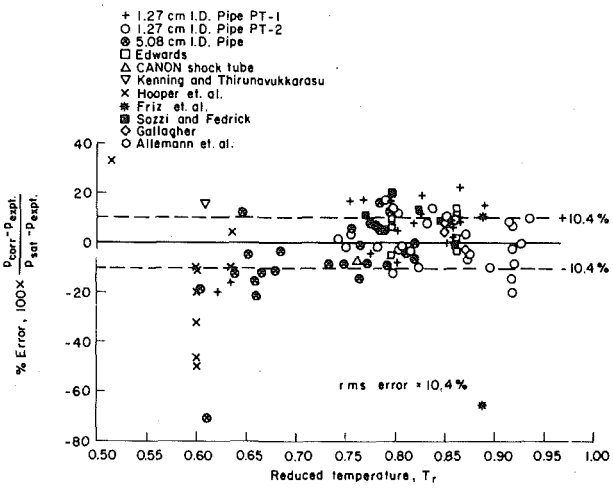

Fig. 5 The comparison of available p_n measurements with the present correlation

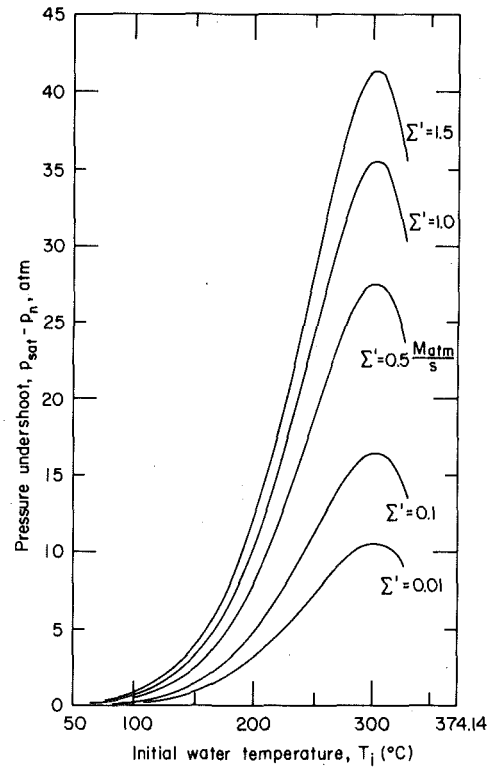

Fig. 6 The pressure undershoot given by equation (13)

Downloaded 20 Dec 2010 to 194.27.225.72. Redistribution subject to ASME license or copyright; see http://www.asme.org/terms/Terms_Use.cfm

Bubble Growth During Decompression of a Liquid

Y. S. Cha
Mechanical Engineer,
Components Technology Division,
Mem. ASME

R. E. Henry[1]
Associate Director,
Reactor Analysis and Safety Division

Argonne National Laboratory,
Argonne Ill. 60439

The solution of the diffusion equation in spherical coordinates subject to time-dependent boundary conditions is derived. The solution can be employed to describe the growth of either a diffusion-controlled gas bubble or a heat transfer-controlled vapor bubble provided that convection effect is negligible. It is shown that the Epstein-Plesset solution for a gas bubble in a constant pressure field and the Jones-Zuber solution in a Cartesian coordinate system for a vapor bubble in a variable pressure field are special cases of the present solution. Numerical results obtained from the present analysis compare favorably with available experimental data for the growth of both gas and vapor bubbles during decompression processes.

Introduction

Bubble growth dynamics play an important role in both cavitation and boiling. There are three different mechanisms that can control the rate of growth or collapse of a bubble. These mechanisms are referred to as inertia-controlled, heat transfer-controlled, and diffusion-controlled growth or collapse in the literature. A general review of all aspects of bubble dynamics can be found in reference [1]. In this paper, discussions will be limited to the heat transfer-controlled and diffusion-controlled bubble growth. Only relevant and more recent work will be mentioned.

Theoretical studies of the heat transfer-controlled growth of a vapor bubble in a uniformly superheated liquid and in a constant pressure field have been reported by Plesset and Zwick [2], and by Forster and Zuber [3]. Recently, Jones and Zuber [4] reported the results of vapor bubble growth in variable pressure fields and found that the variable pressure effects can be quite important. Theofanous, et al. [5] reported the numerical solution of bubble growth in time-dependent pressure fields. Their results also include the effects of nonequilibrium at the liquid-vapor interface, inertia of the liquid, and surface tension.

Theoretical studies of the diffusion-controlled growth of a gas bubble in a constant pressure field have been reported by Epstein and Plesset [6] and by Birkhoff, et al. [7]. The latter included the convection term in the governing equation. Recently, Minkowycz, et al. [8] reported the numerical results of simultaneously solving the extended Rayleigh equation and the diffusion equation. Scriven [9] reported the results of simultaneously solving the heat conduction and the diffusion equations.

The purpose of this paper is to provide a simple description of either heat transfer or diffusion-controlled growth of a bubble in time-dependent pressure fields, including the effect of variable density in the bubble with the liquid-vapor or gas interface assumed to be in thermodynamic equilibrium. Comparison of the results of the present analysis with experimental data are presented.

Growth of a Gas Bubble

Formulation. Consider a spherical gas bubble in a dilute liquid-gas solution. If mass transfer by convection is neglected, the diffusion equation becomes

$$\frac{\partial C}{\partial t} = \delta\left(\frac{\partial^2 C}{\partial r^2} + \frac{2}{r}\frac{\partial C}{\partial r}\right) \tag{1}$$

The initial and boundary conditions are

$$C(r, 0) = C_i; \quad \lim_{r\to\infty} C(r, t) = C_i; \quad C(R, t) = C_s(t) \tag{2}$$

It can be shown [8] that if the following new variables are introduced,

$$\eta = r/R - 1; \quad \tau = \delta t/R^2; \quad \phi = r(C - C_i)/R \tag{3}$$

Equations (1) and (2) become

$$\frac{\partial \phi}{\partial \tau} = \frac{\partial^2 \phi}{\partial \eta^2} \tag{4}$$

$$\phi(\eta, 0) = 0; \quad \lim_{\eta\to\infty} \phi(\eta, \tau) = 0; \quad \phi(0, \tau) = C_s - C_i \tag{5}$$

The solution to equations (4) and (5) is readily available [10].

$$\phi(\eta, \tau) = \frac{\eta}{2(\pi)^{1/2}} \int_0^\tau \frac{[C_s(\tau - \lambda) - C_i]e^{-\eta^2/(4\lambda)}}{\lambda^{3/2}} d\lambda \tag{6}$$

The quantity relevant to the present problem is the concentration gradient at the bubble boundary which, after being transformed back to physical variables, turns out to be

$$\left(\frac{\partial C}{\partial r}\right)_{r=R} = \frac{C_i - C_s(0)}{(\pi\delta t)^{1/2}} - J + \frac{C_i - C_s}{R} \tag{7}$$

where

$$J = \frac{1}{R(\pi)^{1/2}} \int_0^{\delta t/R^2} \frac{C_s'(\lambda)d\lambda}{(\delta t/R^2 - \lambda)^{1/2}} \tag{8}$$

and $C_s'(\lambda)$ represents the derivative of C_s with respect to λ.

Applying a mass balance at the bubble boundary gives

$$4\pi R^2 \delta \left(\frac{\partial C}{\partial r}\right)_{r=R} = \frac{d}{dt}\left(\frac{4}{3}\pi R^3 \rho_g\right) \tag{9}$$

From equations (7) and (9), the following equation is obtained.

$$\rho_g \frac{dR}{dt} + \frac{R}{3}\frac{d\rho_g}{dt} = \delta\left[\frac{C_i - C_s(0)}{(\pi\delta t)^{1/2}} - J + \frac{C_i - C_s}{R}\right] \tag{10}$$

For the special case of constant density and constant saturation concentration, equation (10) reduces to that reported by Epstein and Plesset [6]. The integral J represents additional mass transfer due to pressure variation.

As a first approximation, the effects of viscosity, surface tension, and liquid inertia are neglected. As demonstrated by Birkhoff, et al. [7], this assumption is justified as long as the bubble size is not extremely small. The saturation concentration can then be related to the system pressure by employing Henry's law:

$$C_s = HP \tag{11}$$

The initial concentration can be expressed as

$$C_i = bHP_i \tag{12}$$

Thus, the solution is supersaturated initially if $b > 1$ and undersaturated if $b < 1$. The density variation in the bubble is assumed to follow the polytropic relation

$$P\rho_g^{-n} = \text{constant} \tag{13}$$

[1] Present address: Fauske and Associates, Inc., 627 Executive Drive, Willowbrook, IL 60521.

Contributed by the Heat Transfer Division and presented at the 18th AIChE/ASME National Heat Transfer Conference, San Diego, Calif., Aug. 6–8, 1979. Revised manuscript received by the Heat Transfer Division March 13, 1980. Paper No. 79-HT-73.

Copyright © 1981 by ASME

Downloaded 20 Dec 2010 to 194.27.225.72. Redistribution subject to ASME license or copyright; see http://www.asme.org/terms/Terms_Use.cfm

Equations (10–13) together with the initial condition, $R = R_i$ at $t = 0$, completely determine the growth of the bubble provided that the variation of the system pressure is specified.

Numerical Results. As an example, the growth of a gas bubble in a CO_2-water system is studied for an exponential pressure decay

$$P - P_f = (P_i - P_f) \exp(-at) \tag{14}$$

Equations (10–14) are solved numerically with a numerical integration for the integral J and a fourth-order Runge-Kutta numerical scheme for the ordinary differential equation (10).

Figure 1 shows the calculated results of the growth of a bubble under various decompression processes. The instantaneous decompression case shown in Fig. 1 is calculated by assuming constant values of ρ_g and C_s and thus corresponds to the Epstein-Plesset solution. It is obvious that the Epstein-Plesset solution is the limiting case ($a \to \infty$) of the present solution. Figure 2 shows the typical dimensionless concentration profile at various instants. As t becomes larger, the dimensionless concentration profile approaches that of the instantaneous decompression case. This behavior can also be expected by examining equation (10). As $t \to \infty$, the pressure ceases to vary and C_s becomes constant. Thus, both the integral J and $d\rho_g/dt$ vanish and equation (10) becomes identical to that of Epstein and Plesset.

An interesting result can be observed by examining the limit of the integral J as $t \to \infty$. Substituting equations (11) and (14) into equation (8):

$$J = -\frac{aHR(P_i - P_f)}{\delta(\pi)^{1/2}} \int_0^{\delta t/R^2} \frac{\exp(-aR^2\lambda/\delta)d\lambda}{(\delta t/R^2 - \lambda)^{1/2}} \tag{15}$$

As demonstrated by Jones and Zuber [4], this integral J can be transformed into a better-known form by introducing the following new variables:

$$z = \left[\frac{aR^2}{\delta}\left(\frac{\delta t}{R^2} - \lambda\right)\right]^{1/2}; \quad w = (at)^{1/2} \tag{16}$$

Equation (15) becomes,

$$J = C_1 D(w) \tag{17}$$

where

$$C_1 = -2H(P_i - P_f)(a/\pi\delta)^{1/2} = \text{constant}$$

and

$$D(w) = \exp(-w^2) \int_0^w \exp(z^2)dz \tag{18}$$

$D(w)$ is the so-called Dawson Integral and has the following property:

$$D(w) \to \frac{1}{2w} \quad \text{as} \quad w \to \infty$$

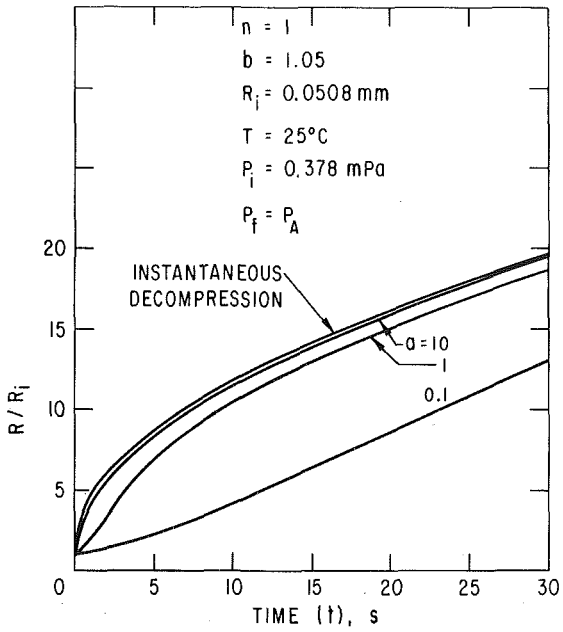

Fig. 1 Calculated results of the growth of a gas bubble in a CO_2-water system under various decompression processes

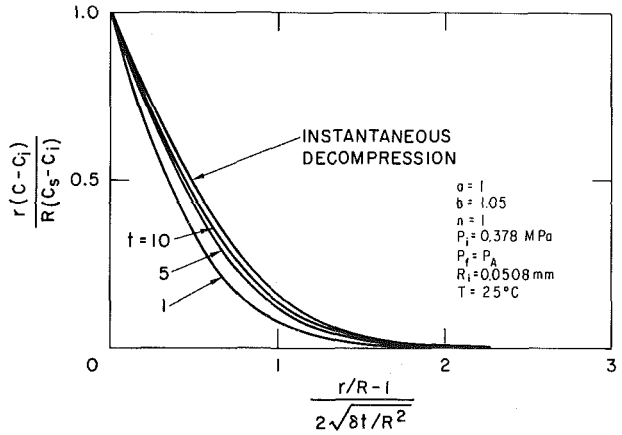

Fig. 2 Calculated results of nondimensional concentration profiles at various instants for a gas bubble in a CO_2-water system during a decompression process

Therefore,

$$J \to \frac{C_1}{2(at)^{1/2}} \quad \text{as} \quad (at)^{1/2} \to \infty$$

Nomenclature

a = constant defined in equation (14)
B = gas constant
b = constant defined in equation (12)
C = concentration
$C_s(0)$ = saturation concentration correspond to the initial pressure P_i
c = specific heat of liquid
$D(w)$ = Dawson integral defined by equation (18)
H = Henry's law constant
i_{fg} = latent heat of vaporization
I = integral defined by equation (22)
J = integral defined by equation (8)
Ja_T = Jakob number defined by equation (30)
Ja_P = Jakob number defined by equation (31)
k = thermal conductivity of liquid
n = polytropic exponent
P = pressure
$P(R)$ = liquid pressure at bubble boundary
P_g = gas or vapor pressure inside the bubble
R = bubble radius
$\dot{R}$ = velocity of bubble boundary, dR/dt
$\ddot{R}$ = acceleration of bubble boundary, d^2R/dt^2
r = radial coordinate
t = time
T = temperature of liquid
$T_s(0)$ = saturation temperature corresponding to the initial pressure P_i
$T_s(\infty)$ = saturation temperature corresponding to the final pressure P_f
V = volume
w = variable defined in equation (16)
z = variable defined in equation (16)
ρ = density
α = thermal diffusivity of liquid
δ = diffusion coefficient
η = variable defined in equation (3)
ϕ = variable defined in equation (3)
τ = variable defined in equation (3)
λ = dummy variable in τ
θ = variable defined in equation (32)
μ = liquid viscosity
σ = surface tension

Subscripts

A = atmospheric
c = cavity
f = final
g = gas or vapor
i = initial
ℓ = liquid
s = saturation

Downloaded 20 Dec 2010 to 194.27.225.72. Redistribution subject to ASME license or copyright; see http://www.asme.org/terms/Terms_Use.cfm

Thus, the integral J approaches zero at a rate inversely proportional to the square root of time which is much slower than the exponential decay of the pressure.

Comparison with Experimental Results. Experimental data for the growth of a gas bubble in a liquid-gas solution during a decompression process were reported by Buehl in his dissertation [11], which was later published by Buehl and Westwater [12]. Before making a direct comparison between the present analysis and the experimental results reported by Buehl, certain precautions must be taken. First of all, Buehl measured the growth of a bubble in a CO_2-water system from an artificial nucleation site which was a reentrant cavity with a large volume beneath the cavity opening. As pointed out by Westwater [13], this kind of cavity provides a good gas trap and therefore is an excellent site. Secondly, the experimental set-up employed by Buehl provided a very fast decompression process (the system pressure dropped to its final value in a matter of 1 s). Most of the experimental results reported by Buehl showed that immediately after the decompression of the system, the bubble at the artificial site had already reached a size with a radius much larger than the dimension of the cavity opening. For example, during a fast decompression test from 0.378 MPa to 0.101 MPa (atmospheric pressure), the mean radius of the bubble upon its first appearance shortly after the decompression was 0.588 mm. This radius was much larger than the dimension of the small opening (0.102 mm) at the surface of the artifical site [12]. Since diffusion was unlikely to contribute much during the growth of a bubble in such a short period of time, the large bubble was likely the result of a rapid expansion of the trapped gas in the large cavity. The volume of the bubble during its first appearance was 0.852 mm^3, and by postulating that the volume of trapped gas equals that of the cavity, the bubble volume for an isentropic expansion is 0.615 mm^3 and 0.946 mm^3 for an isothermal expansion. Thus, the initial large radius observed by Buehl and Westwater [12] was likely an expansion (closer to an isothermal than an isentropic process) of the trapped gas in the cavity.

To make a comparison between the present analysis and the experimental results reported by Buehl, we must modify the analysis described previously to include the effect of trapped gas in the cavity. Equation (9) can be altered as follows:

$$4\pi R^2\delta\left(\frac{\partial C}{\partial r}\right)_{r=R} = \frac{d}{dt}\left[\left(\frac{4}{3}\pi R^3 + V_c\right)\rho_g\right] \tag{19}$$

where V_c is the volume of the cavity. Equation (10) then becomes

$$\left(\frac{R}{3} + \frac{V_c}{4\pi R^2}\right)\frac{d\rho_g}{dt} + \rho_g\frac{dR}{dt} = \delta\left[\frac{C_i - C_s(0)}{(\pi\delta t)^{1/2}} - J + \frac{C_i - C_s}{R}\right] \tag{20}$$

Equation (20) and equations (11–14), together with the initial condition $R = R_i$ at $t = 0$, are solved numerically. Figure 3 shows the comparison between the calculated and the measured growth of a bubble for two different initial pressures. In the calculations, R_i is taken to be half the length of the small opening of the artificial site (0.051 mm) and the constant a is set equal to five which corresponds to the case that the system pressure dropped to its final value in about 1 s. This selection is compatible with the experiments. The agreements between the experimental and the calculated results are good. There were a series of data reported in Buehl's dissertation [11]. All the experimental results showed the same general tendency, i.e., there is a fast growth initially which results from the expansion of gas trapped in the cavity, followed by slow growth later on when diffusion is the dominating mechanism. However, some inconsistency existed among these data. For example, Run 28 and Run 29 showed a much faster initial growth rate than that of Run 17 even though the initial pressures were the same for these tests. Furthermore, bubbles growing in a liquid with an initial pressure of 0.202 MPa showed a much faster growth rate than those that had initial pressure of 0.340 MPa. This abnormal behavior and inconsistency was not explained in Buehl's dissertation. However, it was recognized that an accurate specification of the cavity site was probably not achieved in these tests. The results of the present analysis indicate that the initial growth rate of the bubble depends strongly on the size of the nucleation site. Therefore, the inconsistency of experimental data could be the result of different sizes of the artificial nucleation sites used in the experiments. In view of the uncertainty of the cavity size used in the experiments, the results shown in Fig. 3 should be judged only in a qualitative sense; i.e., equation (20) is capable of predicting the trend of the experimental results reports by Buehl.

Growth of a Vapor Bubble

Formulation. It will be assumed that the liquid properties are constant and the liquid temperature at the interface is equal to the saturation temperature according to the system pressure. Equations (1) through (8) then also apply to heat conduction problem when C and δ are replaced by T and α, respectively. Thus, an equation similar to equation (7) can be written as

$$\left(\frac{\partial T}{\partial r}\right)_{r=R} = \frac{T_i - T_s(0)}{(\pi\alpha t)^{1/2}} - I + \frac{T_i - T_s}{R} \tag{21}$$

where

$$I = \frac{1}{R(\pi)^{1/2}}\int_0^{\alpha t/R^2}\frac{T_s'(\lambda)d\lambda}{(\alpha t/R^2 - \lambda)^{1/2}} \tag{22}$$

If R approaches infinity, the third term on the right hand side of equation (21) vanishes and equation (21) reduces to a solution reported by Jones and Zuber [4]. They employed the solution for a plane interface plus a spherical correction factor in their analysis.

Applying energy and mass balance at the bubble boundary yields

$$4\pi R^2 k\left(\frac{\partial T}{\partial r}\right)_{r=R} = i_{fg}\frac{d}{dt}\left(\frac{4}{3}\pi R^3\rho_g\right) \tag{23}$$

Combining equations (21) and (23);

$$\frac{dR}{dt} = \frac{k}{i_{fg}\rho_g}\left[\frac{T_i - T_s(0)}{(\pi\alpha t)^{1/2}} - I + \frac{T_i - T_s}{R}\right] - \frac{R}{3\rho_g}\frac{d\rho_g}{dt} \tag{24}$$

The saturation temperature can be related to the system pressure by employing the Clausius-Clapeyron equation

$$\frac{dT}{dP} = \frac{T}{\rho_g i_{fg}} \tag{25}$$

and the ideal gas equation

$$P = \rho_g BT \tag{26}$$

Equations (25) and (26) can be combined to give

$$\frac{\rho_{gi}}{\rho_g} = \frac{T_s}{T_s(0)}\exp\left\{\frac{i_{fg}}{B}\left[\frac{1}{T_s} - \frac{1}{T_s(0)}\right]\right\} \tag{27}$$

and

$$\frac{1}{T_s} = \frac{1}{T_s(0)} - \frac{B}{i_{fg}}\ln\left(\frac{P}{P_i}\right) \tag{28}$$

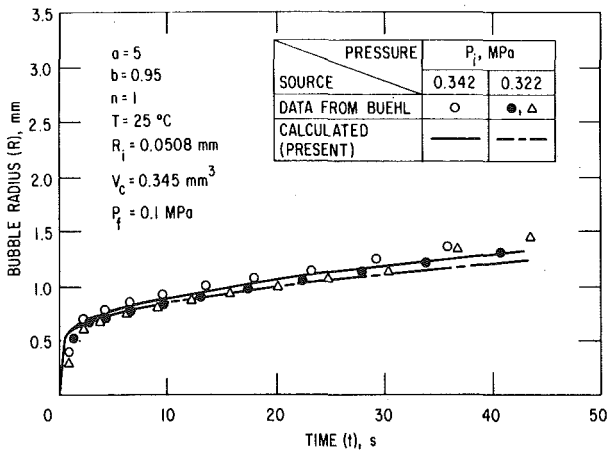

Fig. 3 Comparison of the calculated results with experimental data for the growth of a gas bubble from an artificial site during decompression of a CO_2-water system

Downloaded 20 Dec 2010 to 194.27.225.72. Redistribution subject to ASME license or copyright; see http://www.asme.org/terms/Terms_Use.cfm

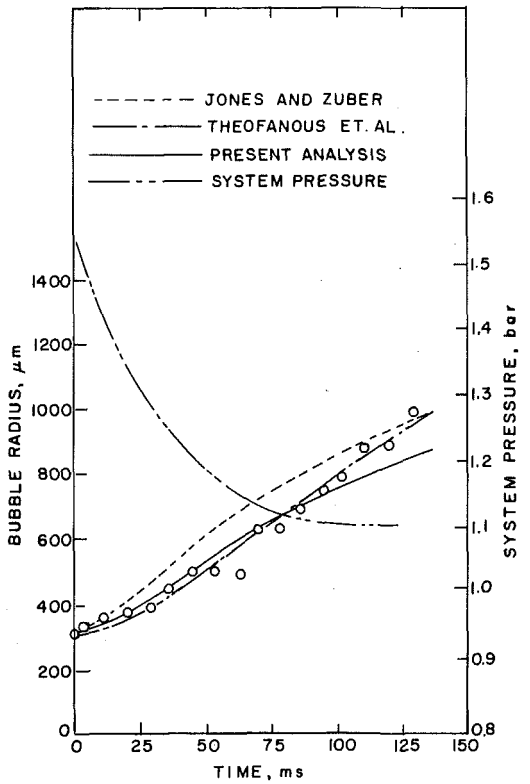

Fig. 4 Comparison of the calculated results with data of Hewitt and Parker for the growth of a vapor bubble in liquid nitrogen with $Ja_T = 0$, $Ja_P = 3.71$, and $a = 0.0299\ ms^{-1}$ (Fig. 6 of reference [4])

Equations (24, 27), and (28) then determine the growth of a vapor bubble provided that the variation of the system pressure is specified.

Comparison with Experimental Results. The data for nitrogen bubbles in a pool of nitrogen reported by Hewitt and Parker [14] will be compared with the present analysis. The experimental pressure variation is approximately exponential, so equation (14) can be employed. Using equations (14) and (25), we obtain from equation (24)

$$\frac{dR}{dt} = \left(\frac{\rho_{gi}}{\rho_g}\right)\left\{Ja_T\left(\frac{\alpha}{\pi t}\right)^{1/2} + Ja_P\left(\frac{4a^2\alpha t}{\pi}\right)^{1/2} \chi \int_0^{\pi/2} \sin\theta \exp\left(-\alpha t \sin^2\theta\right) d\theta + Ja_P\left(\frac{\alpha}{R}\right)\left[\frac{T_i - T_s}{T_s(0) - T_s(\infty)}\right] + \left[\frac{RBT_s(0)}{3Pi_{fg}}\right]\frac{dP}{dt}\left(1 - \frac{i_{fg}}{BT_s}\right)\exp\left[\frac{i_{fg}}{B}\left(\frac{1}{T_s(0)} - \frac{1}{T_s}\right)\right]\right\} \quad (29)$$

where

$$Ja_T = \frac{\rho_\ell c[T_i - T_s(0)]}{\rho_{gi} i_{fg}} \quad (30)$$

$$Ja_P = \frac{\rho_\ell c[T_s(0) - T_s(\infty)]}{\rho_{gi} i_{fg}} \quad (31)$$

and

$$\sin^2\theta = \frac{\lambda R^2}{\alpha t} \quad (32)$$

Generally, $T_i \neq T_s(0)$, and

$$T_i = T_s(0) \text{ only if } Ja_T = 0$$

For given values of Ja_T, Ja_P, i_{fg}, α, a, and B, equations (14) and (27–29) can then be employed to calculate the growth of a vapor bubble when the system pressure decays exponentially. Comparisons of the calculated and the experimental results are shown in Figs. 4–6,

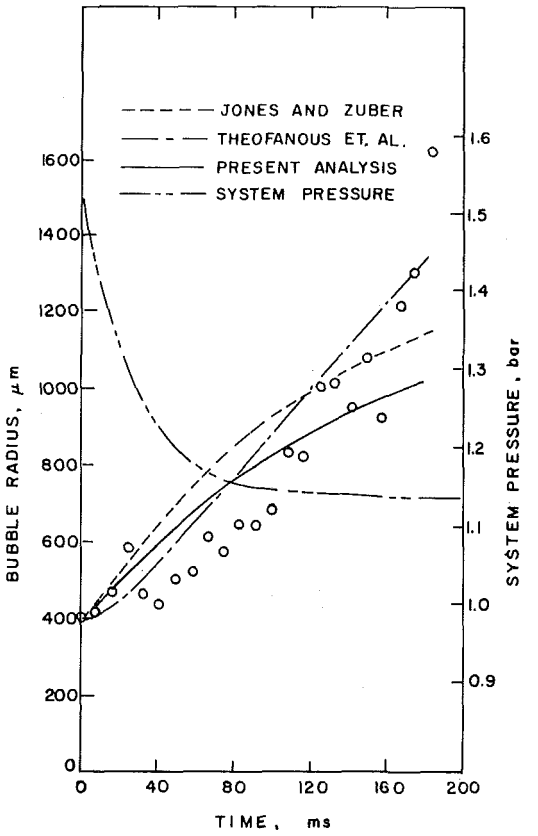

Fig. 5 Comparison of the calculated results with data of Hewitt and Parker for the growth of a vapor bubble in liquid nitrogen with $Ja_T = 0$, $Ja_P = 3.32$, and $a = 0.0414\ ms^{-1}$ (Fig. 7 of reference [4])

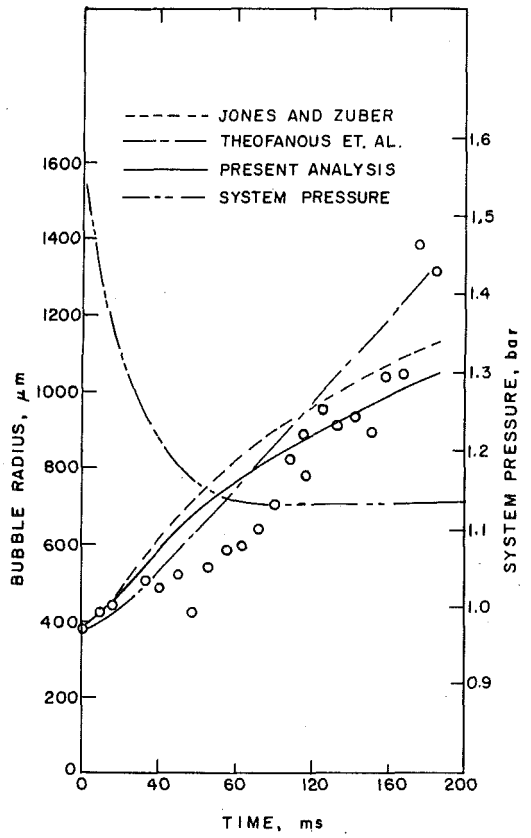

Fig. 6 Comparison of the calculated results with data of Hewitt and Parker for the growth of a vapor bubble in liquid nitrogen with $Ja_T = 0$, $Ja_P = 3.383$, and $a = 0.0371\ ms^{-1}$ (Fig. 8 of reference [4])

Downloaded 20 Dec 2010 to 194.27.225.72. Redistribution subject to ASME license or copyright; see http://www.asme.org/terms/Terms_Use.cfm

and they are seen to be in good agreement. Also shown in Figs. 4–6 are the calculated results of Jones and Zuber [4] and of Theofanous, et al. [5]. The Jones-Zuber approximate solution, using a spherical correction factor, overpredicts slightly the growth of a vapor bubble as compared to the present analysis. For small time intervals, the present results deviate only slightly from the more exact analysis of Theofanous et al. which includes the effects of nonequilibrium at the bubble interface, surface tension, liquid inertia, and convective contribution. This deviation becomes larger as time increases and is likely the result of neglecting convective contribution in the present analysis.

Discussions

The result of the present analysis appears to compare favorably with experimental result of the growth of either a vaporous or a gaseous bubble during a decompression process in spite of the many assumptions made in order to obtain such a simplified analysis. However, it is important to understand the limitations of the present analysis. This can be achieved by examining the various assumptions made in this paper.

The most serious assumption is the neglect of convective contribution during the growth processes. This assumption is valid only if

$$\delta/(R\dot{R}) \gg 1 \quad \text{for a gas bubble}$$

and

$$\alpha/(R\dot{R}) \gg 1 \quad \text{for a vapor bubble}$$

Using the result shown in Fig. 3, we found that during the slow growth period of a gas bubble,

$$\frac{\delta}{R\dot{R}} \cong \frac{2 \times 10^{-5}}{(0.1) \times (2 \times 10^{-3})} = 0.1$$

For a vapor bubble, we found from Fig. 4 that

$$\frac{\alpha}{R\dot{R}} \cong \frac{8 \times 10^{-4}}{(0.08) \times (0.6)} = 0.017$$

Thus, convective contribution cannot be neglected in either case. Neglecting convection effect should result in underpredicting significantly the growth rate. The fairly good agreement between present predictions and experiments shown in Fig. 3 (for the slow growth period) and in Figs. 4 to 6 suggests that we may have neglected other effects which are also important.

The equation of motion of the bubble boundary is

$$\rho\left(R\ddot{R} + \frac{3}{2}\dot{R}^2\right) = P(R) - P \tag{33}$$

Where $P(R)$ is the pressure in the liquid at the bubble boundary, and P is the pressure in the liquid at infinity (system pressure). The pressure inside the bubble is given by

$$P_g = P(R) + 2\sigma/R + 4\mu\dot{R}/R \tag{34}$$

The present analysis neglected the inertia terms in equation (33) and assumed that $P(R) = P$. Neglecting inertia effect results in underestimating $P(R)$ which in turn results in underestimating C_s and T_s. This would result in overpredicting the growth rate according to equations (10) and (24). However, inertia effect is small in view of the small growth velocity shown in Figs. 3 to 6. For example, using Fig. 4, it can be shown that $\rho\dot{R}^2$ is of the order of 10^{-2} N/m^2 which is small compared to the variation of the system pressure (10^3 N/m^2).

The present analysis also neglected the effects of surface tension and viscosity in equation (34) and assumed that $P_g = P(R)$. Neglecting these effects results in underestimating P_g. This also results in overpredicting the growth rate since the gas or vapor in the bubble overexpands. Using the results shown in Fig. 4, it can be shown that the viscous term in equation (34) is small compared to the liquid pressure $P(R)$. However, during early stage of the growth, the surface tension term in equation (34) is of the order of 10 or 10^2 N/m^2 which is not negligible compared to $P(R)$.

Thus, the effect of neglecting the convective contribution is compensated partially by the effect of neglecting surface tension contribution during early stage of the growth. This is supported by comparing the present results with the results of Theofanous, et al. [5], which included the effects of convection, surface tension, liquid inertia, and nonequilibrium at the interface. As shown in Figs. 4–6, the results of the present analysis deviates only slightly from the results of Theofanous, et al., during the early stage of growth. This deviation becomes larger as time increases. This is likely to be the result of decreasing influence of surface tension as the bubble increases in size and an indication that convective contribution is not negligible since the nonequilibrium effect was shown to be insiginficant in this case by Theofanous, et al. (The results were insensitive to the accommodation coefficient.)

Conclusions

We have shown that the solution of the diffusion equation in spherical coordinates with time-dependent boundary conditions can be employed to accurately describe either a diffusion-controlled or a heat transfer-controlled growth of a bubble in variable pressure fields. Good agreement is observed with the available experimental data for both a vapor bubble in liquid nitrogen and a gas bubble in CO_2-water solution during decompression processes. It is pointed out that the knowledge of the precise volume of the cavity is extremely important in determining the growth of a gas bubble during a decompression process if the growth of the bubble begins from an artificial site that contains a significant volume of trapped gas. Neglecting convective contribution in the present analysis results in underpredicting significantly the growth of a bubble during a decompression process. This effect, however, is probably compensated by the effect of neglecting surface tension during early stage of the growth while the size of the bubble is still relatively small.

References

1 Plesset, M. S., and Prosperetti, A., "Bubble Dynamics and Cavitation," *Annual Review Fluid Mechanics*, Vol. 9, 1977, pp. 145–185.

2 Plesset, M. S., and Zwick, S. A., "The Growth of Bubbles in Superheated Liquids," *Journal Applied Physics*, Vol. 25, 1954, pp. 493–500.

3 Forster, H. K., and Zuber, N., "Growth of a Vapor Bubble in a Superheated Liquid," *Journal Applied Physics*, Vol. 25, 1954, pp. 474–478.

4 Jones, O. C., Jr., and Zuber, N., "Bubble Growth in Variable Pressure Fields," ASME JOURNAL OF HEAT TRANSFER, Vol. 100, 1978, pp. 453–459.

5 Theofanous, T., Biasi, L., Isbin, H. S., and Fauske, H., "A Theoretical Study on Bubble Growth in Constant and Time-Dependent Pressure Fields," *Chemical Engineering Science*, Vol. 24, 1969, pp. 885–897.

6 Epstein, P. S., and Plesset, M. S., "On the Stability of Gas Bubbles in Liquid-Gas Solutions," *Journal Chemical Physics*, Vol. 18, No. 11, 1950, pp. 1505–1509.

7 Birkhoff, G., Margulies, R. S., and Horning, W. A., "Spherical Bubble Growth," *Physics Fluids*, Vol. 1, No. 3, 1958, pp. 201–204.

8 Minkowycz, W. J., France, D. M., and Singer, R. M., "Behavior of Inert Gas Bubbles in Forced Convective Liquid Metal Circuits," ASME JOURNAL OF HEAT TRANSFER, 1976, pp. 5–11.

9 Scriven, L. E., "On the Dynamics of Phase Growth," *Chemical Engineering Science*, Vol. 10, 1959, pp. 1–13.

10 Churchill, R. V., *Operational Mathematics*, McGraw-Hill, New York, 1958, pp. 132–134.

11 Buehl, W. M., "Effect of Contact Angle on Growth of Bubbles," Ph.D. Dissertation, Dept. of Chem. Eng., University of Illinois, 1964.

12 Buehl, W. M., and Westwater, J. W., "Bubble Growth by Dissolution: Influence of Contact Angle," *AIChE Journal*, Vol. 12, No. 3, 1966, pp. 571–576.

13 Westwater, J. W., "Measurements of Bubble Growth During Mass Transfer," in *Cavitation in Real Liquids*, Davis, R., ed., Elsevier Publishing, 1964, pp. 34–54.

14 Hewitt, H. C., and Parker, J. D., "Bubble Growth and Collapse in Liquid Nitrogen," ASME JOURNAL OF HEAT TRANSFER, Vol. 90, 1968, pp. 22–26.

Downloaded 20 Dec 2010 to 194.27.225.72. Redistribution subject to ASME license or copyright; see http://www.asme.org/terms/Terms_Use.cfm

J. H. Lienhard[1]
Professor,
Mechanical Engineering Department,
University of Houston,
Houston, Tex 77004
Fellow ASME

Amir Karimi
Research Assistant,
Boiling and Phase Change Laboratory,
Mechanical Engineering Department,
University of Kentucky,
Lexington, KY 40506
Student Mem. ASME

Homogeneous Nucleation and the Spinodal Line[2]

The limit of homogeneous nucleation in a liquid is shown to lie very close to its liquid spinodal line. It is also argued that the homogeneous nucleation prediction should be based on a comparison of the critical work of nucleation with the "potential well" energy instead of the kinetic molecular energy. The result is a new prediction of the liquid spinodal line for water that is valid to large negative pressures. This prediction compares well with spinodal points obtained by extrapolating liquid and vapor water data with the Himpan equation.

Introduction

Objective. There have been some problems in the literature as to the relation between the homogeneous nucleation limit and the spinodal line. Indeed, when we [1] argued that the two were nearly the same in a superheated liquid, but quite different in a subcooled vapor, we were questioned sharply by referees. Some of them objected that the spinodal line was a fictional limit that could not ever be demonstrated experimentally.

At the time, our evidence that the two liquid limits were nearly the same was strong, but only circumstantial. A direct argument must still be offered to show that the two limits lie close to one another. Such a demonstration would have considerable value because the spinodal line—not the homogeneous limit—defines the local minimum in a correct equation of state. But only the latter can be established experimentally. If the two are close, then the spinodal line will be known as well. We would then have another constraint to add in the formulation of an equation of state that will have validity in the metastable liquid regime.

The Spinodal Limit. Conventional equations of state are written to describe the gas and liquid states as though they were continua—not made of molecules. Since such equations must satisfy the Maxwell-Gibbs requirement that

$$\int_{g_f}^{g_g} dg = \int_{\text{sat liquid}}^{\text{sat vapor}} v dp = 0 \tag{1}$$

we expect their isotherms to pass through ridges or "spines" of local maxima and minima defined by

$$\left.\frac{\partial p}{\partial v}\right|_T = 0 \tag{2}$$

Since the regions between these spines (or "spinodal lines" as they are called) is unstable, the state of real fluids cannot be brought all the way to either spinodal line. Molecular fluctuations will inevitably destabilize the fluid before the spine of instability is reached.

We subscribe to the view that the spinodal limit is nevertheless a physically useful concept in that the equation of state of a real fluid must satisfy both equations (1) and (2). Furthermore, we have previously shown [1, 2] that observations of homogeneous nucleation in liquids probably reach values quite close to the spinodal line. By providing an analytical demonstration that this is true, we will make it possible to specify the liquid spinodal in an equation of state for water. This is a key step in a program that we have undertaken (see [3]) to develop a fundamental equation that can be used in the metastable regimes.

How Close to the Spinodal Line Can a Fluid Be Brought?

The minimum work required to bring a fluid from a homogeneous nucleation temperature, T_n, to the spinodal temperature, T_s, at the same pressure, p_n, is given by the change of the thermodynamic availability between the two points, Δa.

$$\Delta a = (h_s - h_n) - T_n (s_s - s_n) \tag{3}$$

where the reference, or dead state, is specified as the pressure, p_n, and the initial temperature, T_n. Figure 1 shows this hypothetical process. Notice that we arbitrarily consider an isobaric process. If there exists a path requiring less energy, then the calculation based on the isobaric model will be conservative.

Since the process from point (n) to point (s) is isobaric, equation (3) becomes

$$\Delta a = \int_{T_n}^{T_s} \left(c_p - \frac{T_n}{T} c_p\right) dT, \tag{4}$$

and the problem of evaluating the minimum work reduces to that of specifying $c_p(T)$ in the neighborhood of the spinodal line. We know from elementary thermodynamic considerations that

$$\underset{T \to T_s}{\text{Limit}}\, c_p(T) = \infty; \quad \underset{T \to T_s}{\text{Limit}} \left[\int_T^{T_s} c_p dT \text{ and } \int_T^{T_s} \frac{c_p dT}{T}\right] = \text{finite} \tag{5}$$

Among the functions that satisfy these conditions are: $c_p \sim (T_s - T)^{-b}$ where $1 > b > 0$, and $c_p \sim \ln(T_s - T)$. So too is any c_p that approaches infinity at T_s as a power weaker than a linear function of $(T - T_s)$.

We can clearly form an upper bound on Δa by factoring out the largest value of $(T - T_n)/T$. Thus

$$\Delta a_{\text{upper bound}} \equiv \Delta a_u = \frac{T_s - T_n}{T_s} \int_{T_n}^{T_s} c_p dT \tag{6}$$

Substituting any one of the acceptable c_p functions in equation (6) we obtain

$$\Delta a_u = D\, c_p(T_n) \frac{(T_s - T_n)^2}{T_s} \tag{7}$$

where D is a number larger than unity. The value of Δa_u per molecule is then $\Delta a_u / N_A$.

The conventional homogeneous nucleation theory says that nucleation is virtually sure to occur when the critical work required to trigger nucleation is on the order of magnitude of $10kT_n$ per nucleus.[3] It follows that

$$\frac{10kT_n}{N_n} < \frac{D\, c_p(T_n)}{N_A} \frac{(T_s - T_n)^2}{T_s} \tag{8}$$

where N_n is the number of liquid molecules in the region displaced by a nucleus bubble. Then

$$\frac{(T_s - T_n)^2}{T_n T_s} > \frac{10}{D} \frac{R}{c_p(T_n)} \frac{1}{N_n} \tag{9}$$

---

[1] This work was done while the first author was at the University of Kentucky.

[2] This work was done under the support of the Electric Power Research Inst. (EPRI Contract RP 678-1) with Balraj Sehgal as project manager.

Contributed by the Heat Transfer Division for publication in the JOURNAL OF HEAT TRANSFER. Manuscript received by the Heat Transfer Division July 15, 1980.

[3] The background for this assertion is developed in the next section.

Copyright © 1981 by ASME

Downloaded 20 Dec 2010 to 194.27.225.72. Redistribution subject to ASME license or copyright; see http://www.asme.org/terms/Terms_Use.cfm

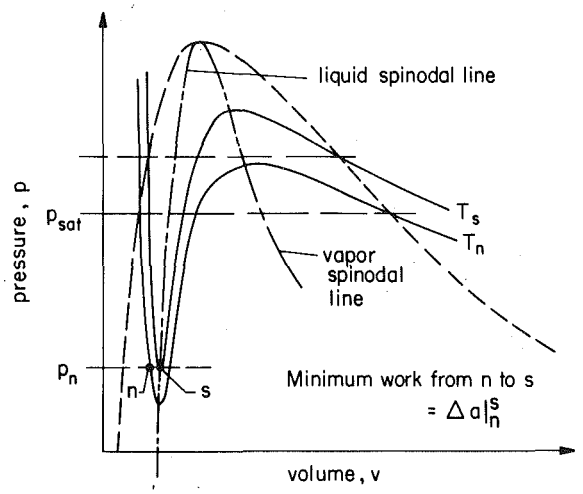

Fig. 1 Process of triggering nucleation from the point of homogeneous nucleation, *n*, to the point, *s*, on the spinodal line at the same pressure

where the molar ideal gas constant, $R \equiv kN_A$.

Consider next the order of magnitude of the three factors on the left side of equation (9): The term $(10/D) < 10$. R/c_p clearly approaches zero at the spinodal line, but we do not yet know how close T_n is to T_s. However, for water at 1 atm, R is 0.46 kJ/kg − K while c_p is 4.2 kJ/kg − K at saturation and at least 2.5 times this value at T_n (see, e.g., [3]). Thus for water, $R/c_p < 0.04$ and for other liquids it will be much less. Finally, Skripov [4] has calculated N_n for a variety of organic fluids at high pressure. He obtained numbers between 270 and 1010 at his observed nucleation temperatures. For water at 1 atm, N_n increases to 4000.

It follows that for water at 1 atm, $(T_s - T_n)/T_n$ is *substantially* less than 0.01 and for organic substances the result should be still less owing to far smaller values of R/c_p. Then in general

$$T_s - T_n \ll \sqrt{T_n T_s} \simeq T_n \tag{10}$$

If a comparable argument were developed for the vapor phase spinodal line, an equation similar to equation (9) would result. But in this case, N_n can be very small because there are very few vapor molecules within a volume equal to that occupied by a nucleus drop.

Equation (10) will therefore no longer be true. Nucleation thus occurs very close to the liquid spinodal, but we cannot expect it to occur anywhere near the vapor spinodal. This is exactly what we showed previously with experimental data in [1].

On Locating the Spinodal

The conventional nucleation theory tells us that (see, e.g., [4]):

$$j \frac{\text{nucleation events}}{\text{molecule-collision}} = \frac{J \dfrac{\text{Nucleation events}}{\text{m}^3\text{s}}}{N \dfrac{\text{molecules}}{\text{m}^3} B \dfrac{\text{collisions}}{\text{s}}} = e^{-\text{Gb}} \tag{11}$$

where the Gibbs number, Gb, is

$$\text{Gb} = \frac{\text{critical work to trigger nucleation}}{kT} \tag{12}$$

The value of j at which nucleation absolutely must occur is the largest possible one. It corresponds with the minimum possible value of the critical work.

One way of specifying the maximum possible value of j is to imagine that just one nucleation event occurs every relaxation-time within the population of liquid displaced by the nucleus bubble of radius, r_c. Thus,

$$j = \left[\frac{\text{collisions}}{\text{relaxation time}}\right]\left[\frac{s}{B \text{ collisions}}\right]\left[\frac{1}{\frac{4}{3}\pi r_c{}^3 m^3}\right] \times \left[\frac{M}{N_A}\frac{gm}{\text{molecules}}\frac{m^3}{\rho_f\, gm}\right] \tag{13}$$

This calculation and the experimental data of Skripov, et al. (see, e.g., [5].) can be interpreted to give somewhat varying results, but a good upper bound appears to be in the neighborhood of:

$$j \simeq (10)^{-5} \text{ or Gb} \simeq 11.5 \tag{14}$$

This corresponds with $J \simeq 10^{34}\ \text{m}^{-3}\ \text{s}^{-1}$.

The prediction of the spinodal line is then completed by substituting this value of j in equation (11), using Frenkel's expression [6]

$$\text{critical work} = 4\pi r_c{}^2\sigma/3 \tag{15}$$

and a critical nucleus given by [4]

$$r_c = 2\sigma/[(1 - v_f/v_g)(p_{\text{sat}} - p_n)] \tag{16}$$

Such predictions have frequently been offered in the past to predict homogeneous nucleation and they have worked fairly well at the spinodal temperatures that occur at positive pressures. These temperatures are usually in the range: $0.9 \lesssim T_s/T_c < 1.0$ (see, e.g., [4]).

A Modification of the Conventional Theory

Equations (11) and (12) are based on the concept that nucleation will occur as the critical work approaches the order of magnitude of the kinetic energy of molecules, characterized by kT. We believe that the comparison should be made, not with the disturbance energy

Nomenclature

a = isobaric, thermodynamic availability function, $h - (T_{\text{dead state}})s$
B = rate of molecular interactions or "collisions"
b = exponent of $(T_s - T)$ in a specific heat formula
c_p = molar specific heat at constant pressure
D = a number on the order of unity
Gb = the Gibbs number, critical work/characteristic energy of the fluid
g = the Gibbs free energy, $h - Ts$
h = molar enthalpy
J = volumetric rate of nucleation events
j = rate of nucleation events per molecular interaction
k = Boltzmann's constant
M = molecular weight
N = molecules per unit volume at nucleation
N_A = Avogadro's number
p = pressure
R = ideal gas constant
r_c = critical radius of an unstable nucleus
s = molar entropy
T = temperature
v = molar specific volume
$\alpha, \beta, \delta, \gamma$ = constants in the Himpan equation of state (19)
$\Delta a, \Delta a_u$ = change in availability from (n) to (s). Upper bound on Δa
ρ = density, 1/v

Subscripts

c = a property at the thermodynamic critical point (except as it appears in r_c)
f, g = the saturation liquid and vapor states
n = a property at the point of homogeneous nucleation
s = a property on a spinodal line
sat = a property that is saturated at $T = T_n$

Downloaded 20 Dec 2010 to 194.27.225.72. Redistribution subject to ASME license or copyright; see http://www.asme.org/terms/Terms_Use.cfm

which can, in fact, vary enormously about the value of kT, but rather it should be compared with the fixed value of the energy required to separate one molecule from another.

This energy can best be characterized as the potential well energy, ϵ (see, e.g., [7]). This energy can be expressed in terms of the critical temperature as

$$\epsilon \simeq 0.77\, kT_c \tag{17}$$

Thus we propose to alter equations (12) and (11) to read

$$\mathrm{Gb} = \frac{\text{critical work}}{kT_c} = 11.5 \tag{18}$$

Figure 2 shows the resulting homogeneous-nucleation/spinodal line calculated from equations (11, 15) and (16), based on both equations (12) and (18). They are presented on pressure-temperature coordinates and the saturated liquid-vapor line is included for comparison. The two curves are nearly identical in the range of positive pressure because T_s remains close to T_c, but the curves diverge strongly at lower temperatures. We must next provide experimental evidence to show that the curve based on ϵ or kT_c is superior to that based on kT.

The Approximate Location of the Spinodal Line by Extrapolation

The isotherms of a correct equation of state must match the known isotherms of water and steam in the stable regimes, it must satisfy equation (1), and it must define the two spinodal lines correctly. We seek an equation of state that is cubic in volume like the van der Waals equation, and which can be fitted to these facts, all of which are known except perhaps the location of the spinodal line. We cannot use the van der Waals equation for this purpose because it has no free constants and it is only exactly true for a fluid with a critical compressibility equal to $^3/_8$.

We therefore used the Himpan cubic equation of state [8]

$$p = \frac{RT}{v-\beta} - \frac{\gamma}{(v-\alpha)(v-\delta)} \tag{19}$$

to fit the known facts. These facts consist of equation (1), the 1970 U.K. steam table vapor density and $(\partial p/\partial v)_{T_{sat}}$ data [9], and very precise liquid density data from Skripov's group [10–12] which extend into the superheated liquid regime. The Himpan equation has been proven to display the essential features of a correct equation of state and to give a good representation of real fluid data in the stable regimes. With four free constants it can provide a very close fit to any given isotherm.

We have used it to fit 38 different isotherms in the range $130°\mathrm{C} \leqslant T \leqslant 300°\mathrm{C}$ and $0.63 \leqslant p \lesssim 111$ bar. A modified Marquart subroutine for a nonlinear least squares [13] was used to evaluate α, β, δ, and γ in each of the 38 cases. Each isotherm was then differentiated to locate the spinodal pressure in accordance with equation (2).

The resulting spinodal points are compared with the two homogeneous nucleation/spinodal line predictions. The points compare quite well with the prediction based on $j = 10^{-5}$ or Gb = 11.5 and the use of kT_c in place of kT. There is increasing scatter in the extrapolation points as the temperature is reduced. This occurs because, as the temperature becomes less, minor discrepancies in the measured density at positive pressures are increasingly influential in the extrapolation.

Figure 3 shows a typical Himpan isotherm and the equation that defines it. The liquid data of Evstefeev [11] to which it is fitted in the liquid regime are included and the very high accuracy of the fit is given in the inset.

We therefore propose that, within a few degrees Celsius, the new homogeneous nucleation prediction can be used to specify T_s at a given pressure. Our future program of research will be to use this equation to re-establish α, β, δ, and γ for each isothermal equation. We can then use these resulting newly created data within the metastable regimes to rebuild the Keenan et al. fundamental equation [14] for water in such a way as to correctly account for the metastable regimes.

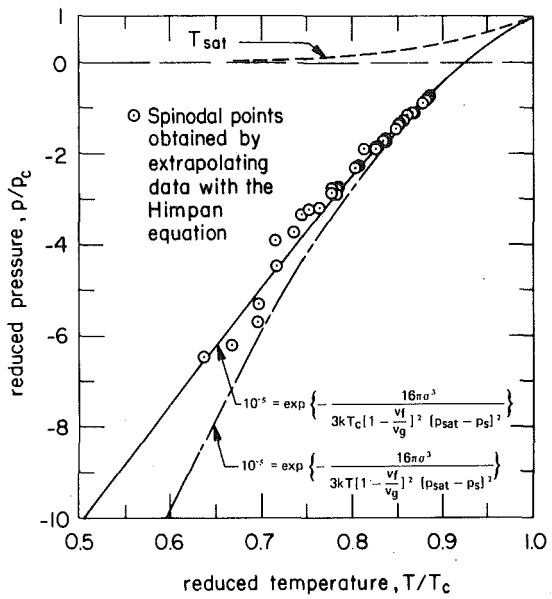

Fig. 2 Comparison of the present prediction with the conventional prediction and with data extrapolations

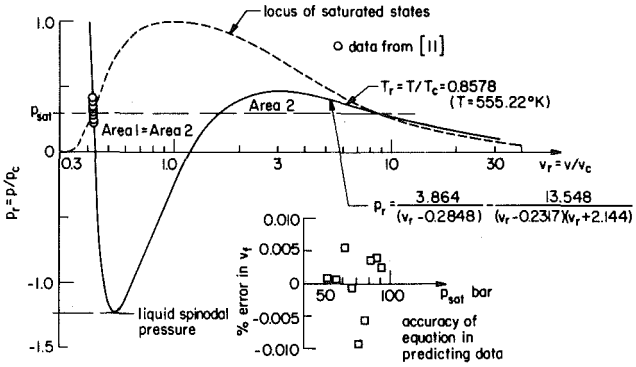

Fig. 3 A typical Himpan equation isotherm

Conclusions

1 The difference between the highest possible liquid homogeneous nucleation temperature and the liquid spinodal temperature at the same pressure is negligible in comparison with the spinodal temperature. Therefore we can use the homogeneous nucleation temperature as a close approximation to the spinodal temperature.

2 The first conclusion does not apply in the metastable vapor regime.

3 The appropriate energy to use in the denominator of Gb appears to be kT_c instead of kT.

4 The spinodal line for liquid water is given to good accuracy by

$$10^{-5} = \exp\left[-\frac{16\pi\sigma^3}{3kT_c\left[1-\frac{v_f}{v_g}\right]^2 (p_{\mathrm{sat}}-p_s)^2}\right] \tag{20}$$

References

1 Lienhard, J. H., and Karimi, A., "Corresponding States Correlations of the Extreme Liquid Superheat and Vapor Subcooling," ASME JOURNAL OF HEAT TRANSFER, Vol. 100, No. 3, 1978, pp. 492–495.

2 Lienhard, J. H., "Correlation for the Limiting Liquid Superheat," *Chemical Engineering Science*, Vol. 31, 1976, pp. 847–849.

3 Karimi, A. H., and Lienhard, J. H., "Toward a Fundamental Equation

Downloaded 20 Dec 2010 to 194.27.225.72. Redistribution subject to ASME license or copyright; see http://www.asme.org/terms/Terms_Use.cfm

for Water in the Metastable States," VIth European Thermophysical Properties Conference, Dubrovnik, Jugoslavia, June 26–30, 1978. *High Temperatures—High Pressures*, Vol. 11, 1979, pp. 511–517.

4 Skripov, V. P., *Metastable Liquids*, (English Transl.) John Wiley and Sons, New York, 1974.

5 Skripov, V. P., Ermankov, G., Sinitsin, E., Baidakov, V., Bulanov, N., Danilov, N., and Nikitin, E., "Superheated Liquids: Thermophysical Properties, Homogeneous Nucleation and Explosive Boiling-up," ASME paper No. 77-HT-87, ASME-AIChE Heat Transfer Conf., Salt Lake City, Aug. 15–17, 1977.

6 Frenkel, J., *Kinetic Theory of Liquids*, Dover, New York, 1955.

7 Tien, C. L., and Lienhard, J. H., *Statistical Thermodynamics*, Hemisphere, McGraw-Hill, Washington, D.C., 1979, Chapter 9.

8 Himpan, J., "Die definitive Form der neuen thermischen Zustandsgleichung nest ihren stoffkonstanten von über 100 verschiedenen Stoffen," *Monatschefte für Chemie*, Vol. 86, 1955, pp. 259–268.

9 United Kingdom Committee on the Properties of Steam, *UK Steam Tables in SI Units*, Edward Arnold, 1970.

10 Chukanov, V. N., and Skripov, V. P., "Specific Volumes of Severely Superheated Water," *Teplofizika*, Vol. 9, No. 4, 1971, pp. 739–745.

11 Evstefeev, V. N., and Chukanov V. N., "Specific Volumes of Metastable (Superheated) Water," *Thermophysics of Metastable Liquids*, 1977, pp. 43–47.

12 Estefeev, V. N., Chukanov, V. N., and Skripov, V. P. "Specific Volumes of Superheated Water," *High Temperature*, Vol. 15, No. 3, 1977, pp. 550–552.

13 Fletcher, R., "A Modified Marquart Subroutine for Non-Linear Squares," *Harwell Report*, AERE R.6799, 1971.

14 Keenan, J. H., Keyes, F. G., Hill, P. J., and Moore, J. G., *1969 Steam Tables*, John Wiley & Sons, New York, 1969.

Downloaded 20 Dec 2010 to 194.27.225.72. Redistribution subject to ASME license or copyright; see http://www.asme.org/terms/Terms_Use.cfm

E. Oker
Senior Engineer,
Ford Motor Company,
Dearborn, Mich.

H. Merte, Jr.
Professor,
Department of Mechanical Engineering and
Applied Mechanics,
University of Michigan,
Ann Arbor, Mich.
Mem. ASME

Semi-Transparent Gold Film as Simultaneous Surface Heater and Resistance Thermometer for Nucleate Boiling Studies

A large (22 × 25 mm) semi-transparent thin film of gold, approximately 400 Å in thickness, is deposited on a glass substrate for simultaneous use as a heat source and resistance thermometer. Construction techniques and calibration procedures are described, and a sample application to a transient boiling process is included with simultaneous high speed photographs taken through the thin film from beneath.

Introduction

In a study of transient and steady nucleate boiling of liquid nitrogen (LN_2) and Refrigerant 113 (R113) under reduced gravity [1], it was desired to observe, by high-speed photography, the formation, growth and departure of vapor bubbles from beneath the heating surface and to measure simultaneously the instantaneous spatial average surface temperature without substantial interference with the phenomena. The imposed disturbances, for which the responses were sought, were step increases in the heat flux and a sudden removal of body forces in a drop tower.

A semi-transparent gold film on glass was selected as a means of meeting these objectives. The thin film acts as an electrical resistance heat source and as a resistance thermometer with negligible heat capacity. This paper presents the techniques used to achieve a desired degree of stability and precision in temperature measurement for nucleate boiling applications. For the transient processes, where the instrumentation introduced the largest uncertainties, accuracies in surface temperature measurement of $\pm(0.5 - 0.9)$ K were obtained over the range of 77 K to 370 K.

Previous Work

The use of semitransparent thin films of SnO_2 on glass as a heat source for boiling has been reported [2, 3], where viewing of the boiling process from beneath was desired. This type of surface has been commercially available from several manufacturers and is very durable. Unfortunately, the temperature coefficient of resistance of SnO_2 is too small to permit its use as a resistance thermometer. Thin films of chromium and nickel (200 to 1500 Å thick) on glass have been successfully used as resistance thermometers for measurements of average surface temperature in order to calculate the heat transfer coefficients with condensing organic vapors [4], in the range between room temperature and 125°C. Accuracies approaching 0.01°C have been reported over short periods of time [5].

For the accurate measurement of temperature it is important that the temperature coefficient of resistance, defined as α in equations (1) and (2), be reasonably large.

$$\alpha = \frac{1}{R_0}\frac{dR}{dT} \tag{1}$$

If α is constant this may be integrated to

$$R(T) = R_0[1 + \alpha(T - T_0)] \tag{2}$$

For thin films the resistance R may be expressed in terms of ohms-per-square[1] in cases where the thickness of the film is an uncertain parameter, and will be termed specific resistance. The resistance characteristics of thin films may differ from those of their bulk metals [6]. For gold thin films of thickness between 1900 Å and 2500 Å the resistivity was found to lie between 1.2 and 1.4 times that for the bulk (i.e. $\rho/\rho_b = 1.2$–1.4) [7]. On the other hand, the temperature coefficient of resistance for gold thin films was found to lie in the range $\alpha/\alpha_b = 0.47$–0.82 at room temperature [8].

The resistance of thin films as deposited is generally unstable in that it changes with time, a process designated as aging. The instability has been attributed to the state of strain that occurs within thin films as they crystallize during deposition, and to the relieving of this strain, along with the agglomeration that occurs within the structure of the film as it becomes exposed to higher temperatures [7, 8]. Heating of the thin films for some period of time tends to accelerate the aging (or annealing) process by promoting the removal of strains. For gold this begins at about 150°C, and is accompanied by a decrease in resistance. Very thin films, on the order of 200 Å in thickness, agglomerate when heated above the recrystallization temperature. For gold this takes place at 450°C and is accompanied by an increase in resistance [8]. A near-equilibrium condition between these two effects may be attained by appropriate annealing, so that subsequent heatings below this annealing temperature will cause little or no change in the film structure. The annealing process could be eliminated if the substrate was heated during deposition (500°C for gold).

The influence, on film resistance, of parameters such as annealing time and temperature, film thickness and substrate temperature during deposition were investigated for 24 different metals [7]. Reductions in resistance of 25–30 percent were observed due to annealing, with a preferred annealing temperature found specific to each metal, and influenced somewhat by film thickness. The influence of film thickness and annealing temperature on the temperature coefficient of resistance was studied over the range of thickness 75–2000 Å and temperature 25–600°C, for various pure and alloy metals deposited both by sputtering and vaporization [8]. No definite correlation was found between α and the film thickness, but the type of substrate and the method of deposition were found to have a significant effect on α.

Gold grids 0.1–0.25 mm wide and 4–6 μm thick were used to measure surface temperatures of glass, vycor and fused silica specimens up to 1160 K [9]. The temperature coefficient of resistance was found to be dependent on the grid thickness and annealing temperature level, and repeatability of calibration was reported to be within 2 percent.

Apparatus

A number of metals were considered for the thin film application reported here. These included nickel, stannous oxide, platinum, aluminum and gold. Gold was selected for use as the semi-transparent resistance heater and resistance thermometer, having the rapid response required for the transient nucleate boiling studies, providing a suitable balance between transparency, specific resistance and

[1] The resistance of any unit square of a thin film.

Contributed by the Heat Transfer Division for publication in the JOURNAL OF HEAT TRANSFER. Manuscript received by the Heat Transfer Division July 7, 1980.

Copyright © 1981 by ASME

Downloaded 20 Dec 2010 to 194.27.225.72. Redistribution subject to ASME license or copyright; see http://www.asme.org/terms/Terms_Use.cfm

temperature coefficient of resistance, and being reasonably stable after annealing.

Pyrex glass surfaces 25 × 38 × 5 mm were first completely covered on one surface with gold, approximately 300–400 Å in thickness, by vacuum deposition. The techniques are well described in the literature (e.g., [6]). The two opposite ends were then coated with a relatively thick layer of silver 7 mm wide to serve as the contact area for the current and voltage taps, leaving a 25 × 25 mm effective test surface area. The appropriate coating thickness was determined on a trial-and-error basis as a compromise between sufficient transparency and a reasonably low specific resistance. Relative thickness of the film during deposition was monitored with a mass sensitive crystal oscillator mounted adjacent to the test surface and receiving the same rate of deposition as the glass substrate. The surfaces were then oven annealed at 275°C for 15 min. In several instances the surfaces were annealed in reducing atmospheres of N_2 with 3 percent H_2 to determine the influence, if any, of oxidation. No effect was detected, so this procedure was abandoned. The effect of annealing on the measured film properties will be presented in the next section.

Of particular importance was the technique by which the current and potential connections were made to the thick silver contacts on the ends of the test surface. Figure 1 shows the final arrangement that was evolved and found satisfactory over the range of temperature 80 K to 350 K. The glass substrate was supported in a recessed Teflon base having an opening under the central part in order to view the surface from beneath. The glass was clamped only over the silver contacts, beginning with a brass clamp which exerted pressure onto a Teflon bar and hence onto a gold foil strip 0.025 mm thick, which itself pressed onto the silver and acted as the current-carrying conductor. The soft Teflon ensured a large surface contact area between the gold foil and silver strip with minimal electrical contact resistance. For the potential contact, a small piece of the current-carrying gold foil was cut out and an independently supported and electrically insulated gold foil potential contact was formed. Since this contact carried negligible current any contact resistance present here had negligible effect.

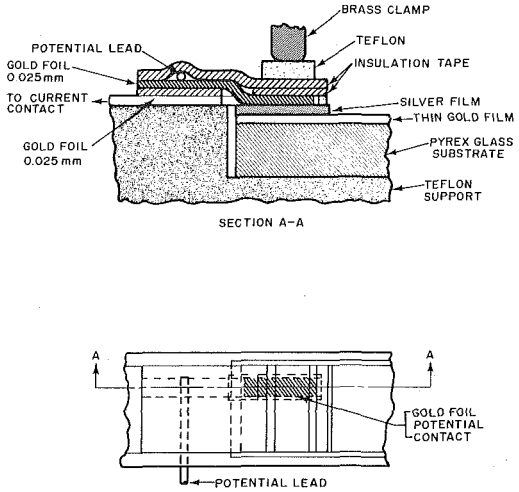

Fig. 1 Current and potential connections used on thin film

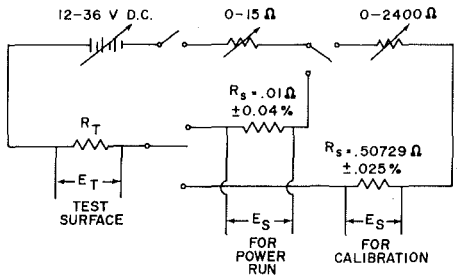

Fig. 2 Calibration and power circuit

Calibration

Because the thickness of the thin films could not be reproduced with sufficient accuracy it was necessary to calibrate each surface individually. Figure 2 shows the electrical circuit, used for both calibration and test runs, which provides for the measurement of current and voltage across the test section. During calibration it is important that the heat generated within the thin film be negligibly small so that the surface is at the same temperature as the medium in which it is immersed. A relatively large standard resistance for current measurement, R_s, is therefore necessary to achieve the desired degree of precision in the corresponding voltage measurement, and is shown in Fig. 2. Calibration currents up to 95 ma, which corresponds to a heat flux level of 5 W/m^2 for the system used, produced negligible self-heating effects. To achieve the stability of the current necessary at the higher levels of current used for the boiling tests, up to 10 amperes, all external resistances were immersed in oil for heat dissipation, and all resistance changes in the circuit were made with heavy duty copper knife switches.

Boiling heat transfer studies were conducted using both R113 and liquid nitrogen; therefore, it was necessary to calibrate the test surfaces in two different corresponding ranges. Calibrations over the range of 295-370 K were performed for R113 using a thermostated silicon oil bath in which the temperature was held constant with ±0.005 K. Liquid temperature was measured with a platinum resistance thermometer and Mueller Bridge Assembly, with an uncertainty of ±0.01 K. For LN_2, temperature variations over the range 76–90 K were obtained by regulating the pressure of saturated LN_2 in a pressure vessel. The temperature of the LN_2 was measured with a previously calibrated thermocouple in conjunction with a precision potentiometer, with a total uncertainty of ±0.03K.

The resistance was calculated from Ohm's Law, using the notation of Fig. 2.

$$R_T = \frac{E_T}{E_s} x R_s \tag{3}$$

For calibration and steady-state boiling test runs the precision potentiometer was used, with uncertainties of ±0.015 percent in the measurements of E_s and E_T. For the transient tests a 7700 series eight-channel Sanborn recorder with Model 8803 high gain d-c amplifiers was used for recording the transient values of E_s and E_T. By calibration of the recorder with the potentiometer prior to and following each test, it was possible to measure E_s and E_T with uncertainties estimated to be no greater than ±0.06 and ±0.02 percent of the measured values, respectively.

The uncertainties in E_T, E_s and R_s were next combined, using the procedure described by Kline and McClintock [10], to provide the net uncertainty in the computed resistance R_T. For the calibration of the surface the resulting uncertainty in R_T is ±0.033 percent, while for the steady-state and transient test runs it increases to ±0.045 and ±0.073 percent, respectively. The increases in uncertainty arise because of the larger uncertainties in the current-measuring resistance R_s and in the voltage-measuring instruments. From these uncertainties and the uncertainties in calibration temperatures mentioned previously, the maximum uncertainty in the slope dR/dT of the cal-

Nomenclature

Å = angstroms
E = voltage
R = resistance
T = temperature
α = temperature coefficient at resistance
ϵ_n = uncertainty of measurement n
ρ = resistivity

Subscripts

b = bulk
c = calibration point
m = measured
0 = reference
R = resistance
s = slope

Downloaded 20 Dec 2010 to 194.27.225.72. Redistribution subject to ASME license or copyright; see http://www.asme.org/terms/Terms_Use.cfm

ibration curves is calculated as ±0.6 percent of the nominal slope at the R113 temperature levels and ±1.6 percent of the nominal slope at liquid nitrogen temperature levels.

Calibration curves for one test surface in the liquid nitrogen temperature range are given in Fig. 3, and demonstrate the effects of annealing. The two upper curves were obtained prior to annealing, and the typical decrease in resistance with aging should be noted. A decrease of 17 percent in the specific resistance occurs as a result of annealing for 15 min at 275°C, and is accompanied by a 49 percent increase in the slope dR/dT, and a 78 percent increase in the temperature coefficient of resistance α.

After the annealing process, shifting of the calibration curve continues to take place, but with the resistance now increasing with time and at a slower rate, as may be seen in Figs. 4 and 5. This has also been observed with thicker films of gold [8], and is postulated as being due to agglomeration.

Three complete calibrations of one test surface at liquid nitrogen temperature levels are given in Fig. 4. The first two sets are separated by one day, and the data virtually overlay each other. The third complete calibration took place 203 days later, with an increase of 6 percent in the resistance level, and an apparent increase of 0.5 percent in the slope. This, however, lies within the ±1.6 percent uncertainty in the slope measurement during calibration. Two single-point calibrations were made before and after the third complete calibrations, as indicated. Each of these two points itself consists of two single point calibrations, separated by a series of boiling tests lasting about four hours. No detectable shift in the single point calibrations occurred during each of the four-hour periods, and hence two more points overlap the two points plotted.

Two complete calibrations of one test surface at near room temperature conditions are shown in Fig. 5, separated by one day. An upward shift of 1 percent occurs, with a 1.3 percent decrease in slope. This change in slope is just slightly greater than the maximum uncertainty of ±0.6 percent in each of the slopes at room temperature levels. The resistance level at room temperature here is in substantial agreement with the measurement of Belser [7] using gold films 400 Å in thickness, also at room temperature.

Based on the experimental observations above and elsewhere [5] that, after annealing, the calibration curves are linear and that successive calibration curves are simply displaced parallel to each other, a new calibration curve may be determined by a single new calibration point once a complete calibration has been made.

It is now possible to convert the uncertainties in resistance R and slope dT/dR into a temperature uncertainty. Considering the maximum possible uncertainty in each case and neglecting the products of the small uncertainties, the following expression results:

$$\epsilon_T = \frac{\Delta(T_m - T_c)}{T_m - T_c} = \epsilon_R \frac{R_m + R_c}{R_m - R_c} + \epsilon_s \tag{4}$$

where T_m = temperature to be measured, R_m = measured resistance at temperature T_m, T_c = temperature at single calibration point, R_c = measured resistance at temperature T_c, ϵ_R = fractional uncertainty of resistance measurement, ϵ_s = fractional uncertainty of slope dT/dR. Calibration took place at 300 K and using the values of $\epsilon_R = 0.00045$ and $\epsilon_s = 0.006$ presented earlier for steady-state boiling tests, a measurement of a nominal 20 K above this single point calibration temperature would have an uncertainty in $(T_m - T_c)$ of $\pm\epsilon_T = \pm 3.0$ percent. For $(T_m - T_c) = 20$ K, the uncertainty in T_m would be ±0.6 K plus the uncertainty of T_c. Equation (4) gives the maximum uncertainty in that the directions of the uncertainties are taken so as to produce the largest possible value of ϵ_T. If the procedure of reference [10] is followed, which introduces a probability into the directions of the uncertainties when combining them, the uncertainty in the example above becomes ±0.4 K (instead of ±0.6 K) in T_m for $(T_m - T_c) = 20$ K.

Complete calibrations at LN_2 temperature levels were made with five different test surfaces. The resistance-temperature slope dR/dT (= αR_0 from equation (2)) for each of these is plotted versus R in Fig. 6. The differences in resistances for the various surfaces are primarily consequences of differences in film thickness. The slope dR/dT increases approximately linearly as R increases, which means that the temperature coefficient of resistance is approximately constant, calculated as $\alpha = 4.1 \times 10^{-3}\text{K}^{-1}$. This is almost the same as the value for bulk gold at LN_2 temperature levels $\alpha_b = 4.0 \times 10^{-3}\text{K}^{-1}$, as calculated from the data in reference [11]. At 77.8 K, we thus have the ratio $\alpha/\alpha_b = 1.03$.

The data tabulated in reference [11] also give $\alpha_b = 4.0 \times 10^{-3}\text{K}^{-1}$ at room temperature, which is somewhat different from the value $\alpha_b = 3.4 \times 10^{-3}\text{K}^{-1}$ listed in reference [8].

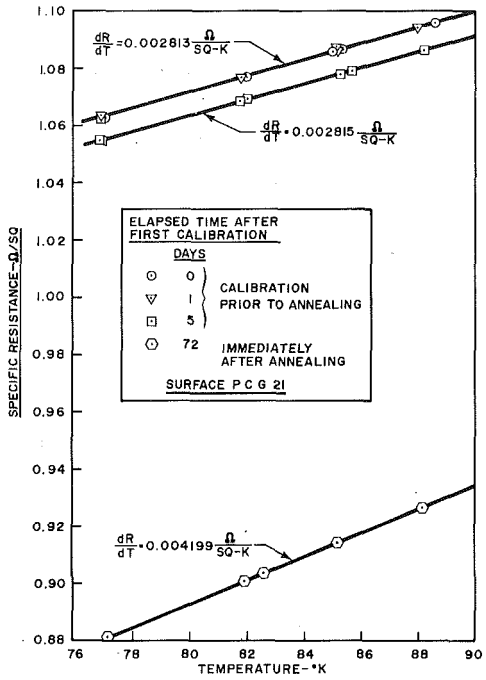

Fig. 3 Calibration in liquid nitrogen, showing typical effect of annealing

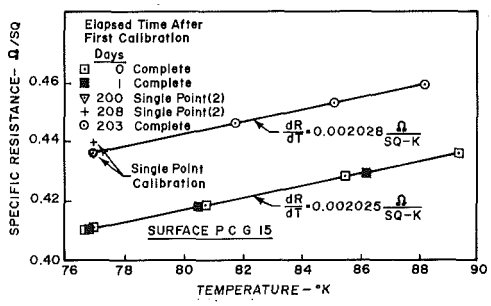

Fig. 4 Calibration at LN_2 temperature levels, showing stability of temperature coefficient of resistance

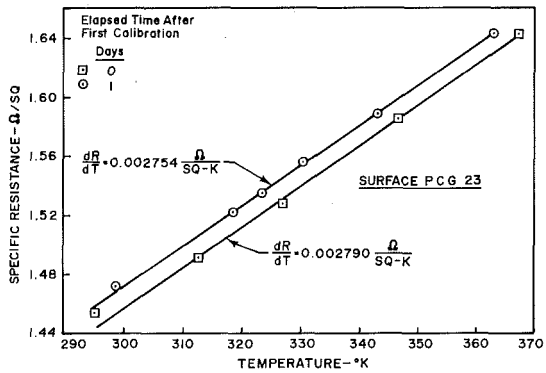

Fig. 5 Calibration at ambient temperature levels

Downloaded 20 Dec 2010 to 194.27.225.72. Redistribution subject to ASME license or copyright; see http://www.asme.org/terms/Terms_Use.cfm

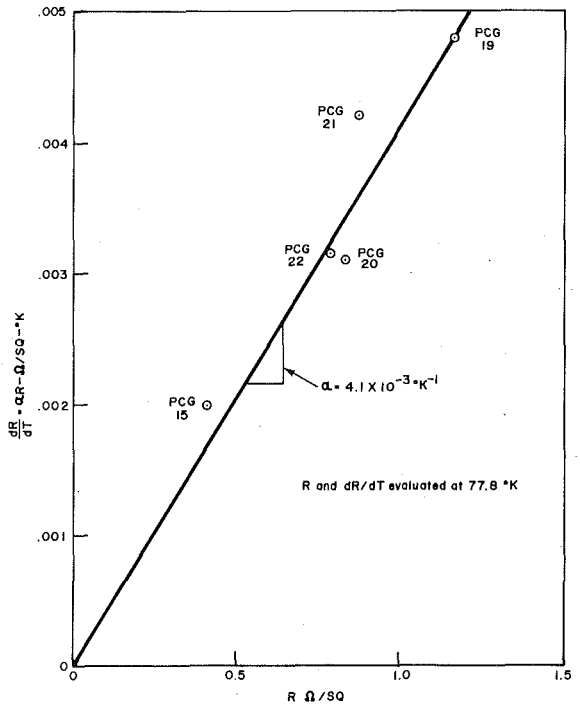

Fig. 6 Resistivity slopes for five different gold thin-film surfaces

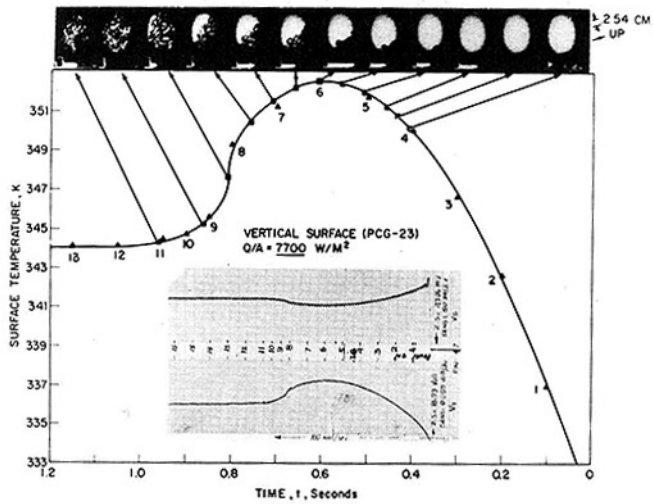

Fig. 7 Typical transient surface temperatures with boiling heat transfer of R113 at atmospheric pressure

Sample Application

An example of results, using the gold thin film surface as a resistance heater and for surface temperature measurement with nucleate boiling, are shown in Fig. 7. The liquid, R113, is saturated at atmospheric pressure (approximately 321 K), and no heat transfer is taking place initially. At zero time, proceeding from right to left, a d-c current of 4.85 amperes is suddenly passed through the thin film. The recording of the transient current and voltage drop across the surface is shown in the center of Fig. 7, and the corresponding average surface temperatures computed from these are plotted. High speed motion pictures were taken simultaneously through the semi-transparent gold surface, and are shown along the top. It may be noted that nucleate boiling does not appear until about 0.5 seconds after the onset of heating, corresponding to a heater surface superheat of approximately 31 K. During this interval transient heat transfer by conduction takes place both in the glass substrate and in the liquid, followed by transient natural convection in the liquid. Then as nucleate boiling spreads across the surface, the average surface temperature decreases until a steady-state condition is reached after about one second. This time period depends on factors such as heat flux input and surface orientation. Corresponding transient results were also obtained using liquid nitrogen, both at standard gravity and zero gravity.

Further details of experimental results are presented in reference [1]. During the course of the research it was learned, on an admittedly unplanned basis, that it was not possible to operate at heat flux levels greater than about 75 percent of the critical heat flux level without damaging the thin film, most likely because of the low heat capacity and thermal conductivity of the film and/or the substrate [12].

Conclusions

1 Semi-transparent thin films of gold, approximately 400 Å in thickness deposited on an insulating substrate, can be used simultaneously as a resistance thermometer and as a heating element for relatively high power densities, sufficient to boil LN_2 and R113 vigorously. The temperature range successfully covered to date is 77 to 370 K.

2 The transparency permits viewing from beneath the boiling surface with simultaneous measurement of the temperature at the liquid-solid interface, not at some point removed. The low heat capacity of the thin film also ensures rapid response, not possible with thermocouples.

3 These gold films appear to have the same temperature coefficient of resistance as the bulk material, and remained quite stable once the surface was annealed.

4 Temperature measurements were attainable under these conditions with a maximum uncertainty between ±0.3 and ±0.9 K, depending on the temperature level and upon the precision of the voltage-measuring instrument used.

Acknowledgments

This work was performed in part under NASA contract NAS-8-20228. The interest and support of Mr. Leon Hastings of the George D. Marshall Space Flight Center is gratefully acknowledged.

References

1 Oker, E., and Merte, H., Jr., "Transient Boiling Heat Transfer in Saturated Liquid Nitrogen and F113 at Standard and Zero Gravity," Technical Report 074610-52-F, Oct. 1973, Department of Mechanical Engineering, Heat Transfer Laboratory, The University of Michigan, Ann Arbor, Mich.

2 Westwater, J. W., and Kirby, D. B., "Bubble and Vapor Behavior on a Heated Horizontal Plate During Pool Boiling Near Burnout," *Chemical Engineering Progress Symposium Series*, Vol. 61, No. 57, 1965.

3 Judd, R. L., and Merte, H., Jr., "Evaluation of Nucleate Boiling Heat Flux Predictions at Varying Levels of Subcooling and Acceleration," *International Journal of Heat and Mass Transfer*, Vol. 15, No. 5, 1972.

4 Winding, C. C., Topper, L., and Baus, B. V., "Metal-Film Resistance Thermometers for Measuring Surface Temperatures," *Industrial Engineering Chemistry*, Vol. 47, 1955, p. 386.

5 Simpson, T. B., and Winding, C. C., "Properties of Evaporated Metal Films Related to Their Use for Surface Temperature Measurements," *AIChE Journal*, Vol. 2, 1956, p. 113.

6 Holland, L., *Vacuum Deposition of Thin Films*, John Wiley and Sons, New York.

7 Belser, R. B., "Electrical Resistance of Thin Metal Films Before and After Artificial Aging by Heating," *Journal of Applied Physics*, Vol. 28, 1957, p. 109.

8 Belser, R. B., and Hicklin, W. H., "Temperature Coefficient of Resistance of Metallic Films in the Temperature Range of 25° to 600°C," *Journal of Applied Physics*, Vol. 3, 1959, p. 313.

9 Moeller, C. E., "Gold Film Resistance Thermometers for Surface Temperature Measurements," *Fifth Symposium on Temperature*, Paper R7-29, Sheraton Park Hotel, Washington, D.C., June 21–24, 1971.

10 Kline, S. J., and McClintock, F. A., "Describing Uncertainties in Single Sample Experiments," *Mechanical Engineering*, Vol. 75, 1953.

11 Roth, W. A., and Scheel, K. *Physikalisch-Chemische Tabellen*, 5th ed., Vol. 2, verlag von Julius Springer, Berlin, 1923, p. 1051.

12 Carne, M., and Charlesworth, D. H., "Thermal Conduction Effects on the Critical Heat Flux in Pool Boiling," AIChE Preprint No. 11, *8th National Heat Transfer Conference*, Los Angeles, Calif., Aug. 8–11, 1965.

Downloaded 20 Dec 2010 to 194.27.225.72. Redistribution subject to ASME license or copyright; see http://www.asme.org/terms/Terms_Use.cfm

L. Nghiem
Technical University, Munich, Federal Republic of Germany

H. Merte
University of Michigan, Ann Arbor, Mich. Mem. ASME

E. R. F. Winter
Technical University, Munich, Federal Republic of Germany

H. Beer
Technical Hochschule, Darmstadt, Federal Republic of Germany

Prediction of Transient Inception of Boiling in Terms of a Heterogeneous Nucleation Theory

Transient boiling in water and Freon 113 with various heater surfaces was investigated experimentally with step power inputs. It was observed that the inception or onset of boiling depends not only on the temperature, but is time dependent as well. This dependence can be explained in terms of a heterogeneous nucleation theory based on the homogeneous nucleation theory. The influence of the heater surface was accounted for by a nucleation factor which is liquid-specific. With this factor and one experimental value of inception for a given system, the time dependence of inception temperature can be computed.

Introduction

An understanding of factors which lead to the inception of boiling is of importance in the design of cooling systems associated with phase transition. Transient boiling can be found for example in cryogenic storage tanks with a loss of vacuum insulation. It is observed [1] that the transient superheat can be far in excess of that required to initiate boiling with steady-state heating. This results in high pressure transients upon phase change. In those cases, it is necessary to predict the superheat required to initiate boiling. In contrast with most works on transient boiling, which deal with the microgeometrical properties of the wall used in the tests, the purpose of this investigation is to obtain generalized data for transient inception of boiling and to determine the characteristic parameters which would be applicable to other boiling systems. A step power input is used, being not only the severest transient possible, but the simplest to prescribe.

Experimental

Six combinations of fluid/surfaces were investigated, in order to obtain results common to different systems.

Test liquids. Water and Freon 113 at saturation temperature and atmospheric pressure were chosen because of their significantly different properties, particularly surface tension.

Test walls: Three types of heater/resistance thermometers were used:

- Thin gold-film, measuring 20 × 2 mm and 400 Å in thickness, vacuum deposited on a glass substrate 50 × 40 × 5mm. The fabrication of this type of heater is described in reference [2]. Electrical contacts are made on the widened ends of the heater (Fig. 1). Aging and calibration procedures are given in references [2] and [3].
- Platinum wire 0.15 mm dia and 24 mm long.
- Copper wire, 0.2 mm dia and 24 mm long.

The roughness of the heater surfaces varied from 0.5 to 8 μm rms.

Test Section. The heaters were positioned horizontally approximately 5 cm below the surface of the liquid in the boiling vessel. The experimental apparatus consisted of: (1) a mechanical facility (Fig. 2), which includes a test vessel equipped with glass windows. The vessel is mounted in a vacuum chamber for thermal insulation, and is connected to a system of valves, which allow: (i) degassing of system prior to filling, (ii) filling the vessel, (iii) distilling the liquid, (iv) calibrating the heater resistance-surface temperature and (v) oper-

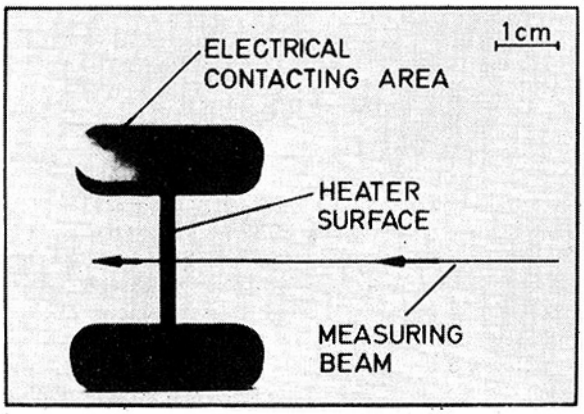

Fig. 1 Thin-film heater, vacuum deposited on glass substrate

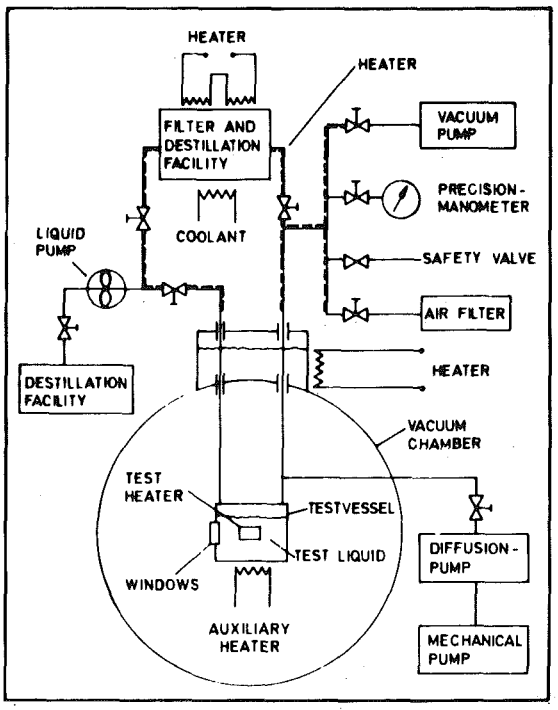

Fig. 2 Mechanical facility

Contributed by the Heat Transfer Division and presented at The 19th ASME/AIChE Joint Heat Transfer Conference, Orlando, Fla., July 27–30, 1980. Revised manuscript received by the Heat Transfer Division July 7, 1980. Paper No. 80-HT-113.

Copyright © 1981 by ASME

Downloaded 20 Dec 2010 to 194.27.225.72. Redistribution subject to ASME license or copyright; see http://www.asme.org/terms/Terms_Use.cfm

ation of the experiments at subatmospheric pressure, (2) an optical facility, comprising a vibration-dampened support on which the vacuum chamber and the test vessel are mounted, a holographic interferometer and a high-speed camera. This configuration allows the optical determination of the onset of convection and the inception time, which is defined as the time required for the onset of nucleation from the initiation of heating, (3) the transient heating circuitry (Fig. 3). The current through the heater is controlled by resistance R_v. The input power is maintained constant during the run. Measuring the voltages across the heater and a standard resistance allows the determination of the instantaneous surface heat-flux and spacial average wall-temperature, (4) the instrumentation (Fig. 4), which consists of two different circuits, one for calibration of the heaters (current source, DVM's, potentiometer), and one for the transient runs themselves (main power supply, UV-recorder, oscilloscope). The synchronization device in Fig. 4 performs the following run sequence: (i) upon start, to accelerate the UV-recorder (0.2–4 m/s) and (ii) simultaneously switch on the power supply and trigger markers on the film and on the UV-paper to locate the beginning of the heating period.

The following results were obtained with each of the six surface-fluid combinations:

- steady-state boiling curve $\dot{Q}''_{SS}$ versus ΔT_{SS}
- wall-superheat $\Delta T(\tau)$ with $\dot{Q}''_{SS}$ as parameter
- heat flux to fluid Q'' versus time τ with $\dot{Q}''_{SS}$ as parameter
- transient boiling curve $\dot{Q}$ versus ΔT with $\dot{Q}''_{SS}$ as parameter

Results

Figure 5 shows the transient wall superheat versus time curves with different heat fluxes applied to the thin-film in Freon 113. Since the heat flux is slightly time dependent (5 percent variation), it was necessary to characterize this parameter by its stationary state $\dot{Q}''_{SS}$. The peaks of these curves, marked with *IB* (incipient boiling) in Fig. 5 are the points of inception of boiling. The minimum incipient superheat for this system is $\Delta T_{SSI} = 50$ K, below which a phase change does not occur. As the heat flux is increased, it is important to note that the inception time decreases and higher superheats are required for the inception of boiling (up to 90 K at 0.9 s). Inception superheat is thus *not* constant for a given system but is time dependent (dotted line, Fig. 5). The high superheats are typical for smooth walls and test liquids of low surface tension [4]. This results in an explosive inception causing the superheat to decrease abruptly, in this case, to approximately 15 K for steady-state boiling.

With water, on the other hand, the formation of vapor occurs "smoothly", as shown in Fig. 6 for the system platinum wire/water (points marked with *IB*). The inception superheat is lower than the associated steady-state boiling temperature, resulting in a further rise of the wall superheat even after the onset of boiling. As with the system thin film/Freon 113, it was found that the inception superheat is increased as the inception time is decreased (dotted line in Fig. 6). This fact was also observed in liquid nitrogen [5], but no explanation for this could be found in the common literature. The same result was obtained with all remaining combinations of test liquid/heater wall, regardless of the wall's microgeometrical characteristics, orientation, gravity fields [5]. A full report of experimental results is given in references [3, 5].

Analysis

To explain the time dependence of the inception superheat, it

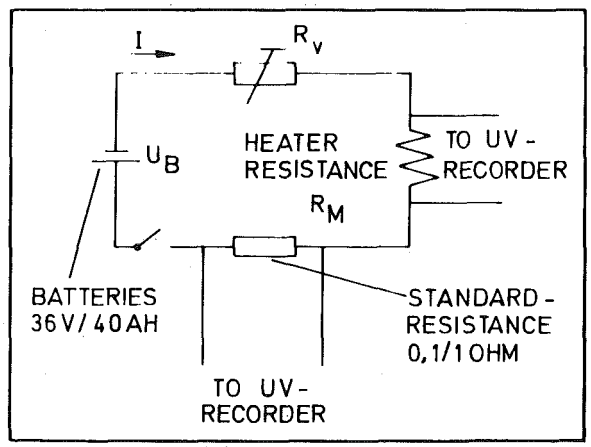

Fig. 3 Transient heating circuit

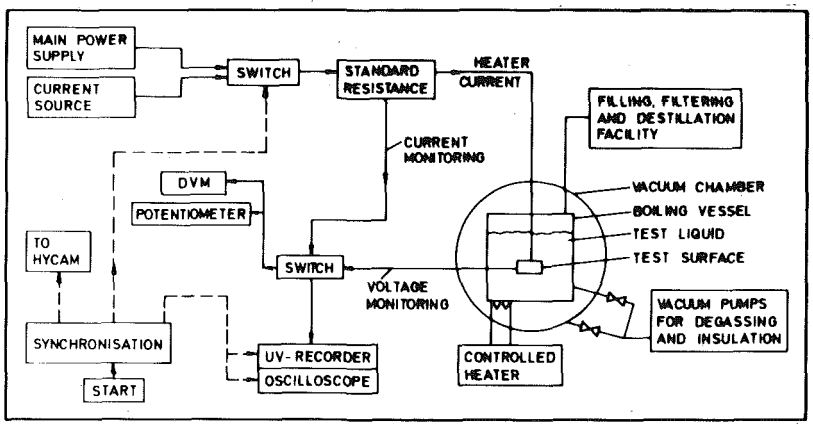

Fig. 4 Electrical facility

Nomenclature

A = nucleation work, $\dot{J}$
a, b = constants
F = nucleation factor, defined by equation (1)
h = Planck's constant, $h = 6.6 \times 10^{-34}$Js
J = nucleation rate, $cm^{-3}s^{-1}$
k = Boltzmann's constant, $k = 1.38 \times 10^{-23}$ J/K
n = molecules/volume cm^{-3}
p = pressure, Pa
$\dot{Q}''$ = heat flux, W/m^2
r = bubble radius, m
R = electrical resistance, ohm
T = temperature, K
ΔT = superheat, K
v = specific volume, m^3/kg
λ = heat of vaporization, J/kg
σ = surface tension, N/m
τ = time, s

Subscripts

c = critical
het = heterogeneous nucleation
hom = homogeneous nucleation
IB = incipient boiling
ℓ = liquid
S = saturation
SS = steady-state boiling
SSI = steady-state inception
v = vapor

Downloaded 20 Dec 2010 to 194.27.225.72. Redistribution subject to ASME license or copyright; see http://www.asme.org/terms/Terms_Use.cfm

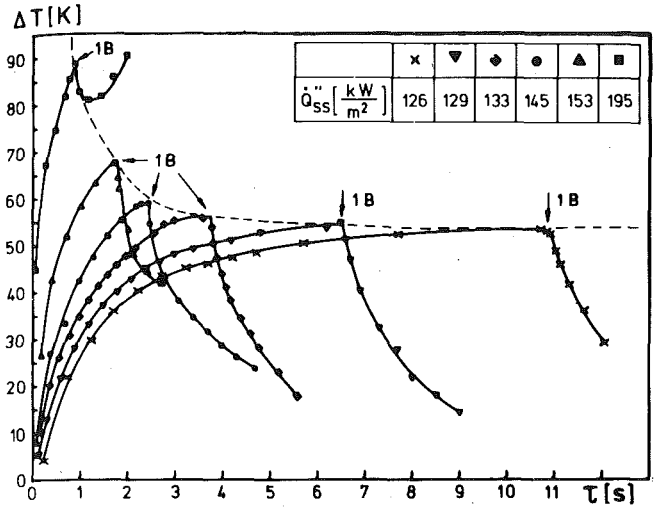

Fig. 5 Transient superheat ΔT versus time τ with different heat-fluxes $\dot{Q}''_{ss}$ (system thin-film/Freon 113, T_S = 320 K, p = 1 bar). Inception points are marked with (*IB*)

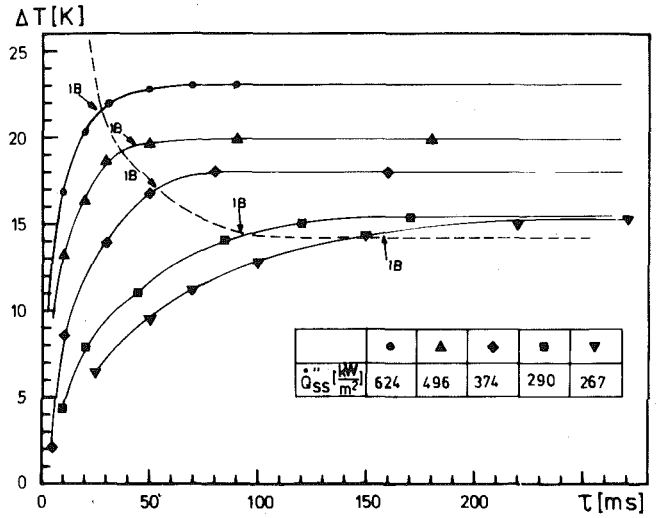

Fig. 6 Transient superheat ΔT versus time τ with different heat-fluxes $\dot{Q}''_{ss}$ (system platinum-wire/water, T_S = 373 K, p = 1 bar). Inception points are marked with (*IB*)

seemed appropriate to consider the phase transition as a physical process in the liquid. The analysis of the microgeometry of nucleation sites at a heating surface is commonly found in the boiling literature [6, 7], generally in conjunction with some model for a transient thermal boundary layer as in reference [8]. Such an approach was considered impractical in the present work for the following reasons: With the several test surfaces used and with the different transient inception superheats observed for any one test surface, any measured cavity dimensions would have no significance; free convection was present in all tests [3, 9] and contributes to a large error in applying the conduction equations to compute the temperature distribution in the liquid boundary layer; finally it is believed that the consideration of microgeometrical characteristics of the wall surface would be restricted to a particular surface only. A generalized approach was therefore undertaken with the aim of obtaining a characteristic number which would be applicable to all systems tested.

The energy level required for the phase transition in a liquid is given by a homogeneous nucleation theory [10] in terms of A_{hom} (homogeneous nucleation work). With this theory, the homogeneous nucleation temperature for water and Freon 113 are computed to be approximately 540 and 434 K, respectively. Referring to Fig. 5, the incipient superheat with the thin film in Freon 113 can be in excess of 90 K, a value close to the 110 K required for homogeneous nucleation, and decreases to 50 K for long inception times. The dotted lines in Figs. 5 and 6 thus show that by increasing the heat flux, and implicitly decreasing the inception time, it is possible to initiate boiling at all superheat values from the homogeneous nucleation temperature (even with a wall) down to the minimal required inception temperature T_{SSI}, which is a system variable.

In an attempt to incorporate the influence, on nucleation time, of system variables such as properties and microgeometry of the heated surface and convection effects, a "nucleation factor" is introduced in the equations of the homogeneous nucleation theory, defined by

$$F = (A_{\text{het}}/A_{\text{hom}}) \tag{1}$$

A_{het} is the work required to activate a nucleation site in a heterogeneous circumstance. The variation in F then corresponds to a boiling inception temperature T_{IB} ranging from T_{SSI} to T_{hom}.

For a liquid at a pressure P_ℓ and a superheat temperature T, which produces a "normal" saturation pressure P_s (for a vapor bubble $r = \infty$), for thermodynamic equilibrium the critical spherical bubble size r_c is given by

$$\frac{P_s}{P_\ell} = 1 + \frac{2\sigma}{r_c P_\ell} \tag{2}$$

The only assumption in equation (2) is that the system state is far enough from the thermodynamic critical state so that $v_v \gg v_\ell$. A further product of this assumption is that $P_s = P_v$, the vapor pressure within the bubble. For nucleation to occur the bubble formed must exceed the critical bubble size given by equation (2) by at least one molecule. The expression of Fisher [11] for the homogeneous nucleation rate of bubbles of critical size, neglecting the term for the free energy of activation for the motion of an individual molecule of liquid past its neighbors into or away from the bubble surface, is given by

$$J = \frac{nkT}{h} e^{-(A_{\text{hom}}/kT)} \tag{3}$$

where

$$A_{\text{hom}} = \frac{4}{3}\pi\sigma {r_c}^2 \tag{4}$$

Nucleation will occur when a bubble of critical size forms per unit volume in a reasonable time, say τ s. This τ will be termed the nucleation time, and neglects the time required to achieve a steady state of embryo distribution in any transient process. In equation (3) then, $J \propto 1/\tau$, and for our present purposes the proportionality will be taken as an equality. For the heterogeneous nucleation case, replacing A_{hom} in equation (3) by A_{het} of equation (1), with equations (2, 4) and the Clausius-Clapyron equation, and $v_v \gg v_\ell$ the resulting expression relates the nucleation time τ, the nucleation factor F, and the superheated liquid temperature T

$$\frac{T - T_s}{T_s} = \left\{ 1 - \left(\frac{P_\ell v_v}{\lambda}\right)_{T=T_s} \ln\left[\left(\frac{16\pi\sigma^3 F}{P_\ell^2 3kT \ln\dfrac{nkT\tau}{h}}\right)^{1/2} + 1\right]\right\}^{-1} - 1 \tag{5}$$

The application of a homogeneous nucleation theory to the heterogeneous case may be viewed in the following way: Homogeneous nucleation occurs as a result of random fluctuations which produce local "vapor clusters". The probability that a cluster of an appropriate critical size will form is a function not only of the temperature level of the fluid but of the size of the system of superheated liquid under consideration as well. The system consisting of the superheated thermal boundary layer is considered to be sufficiently large so that a nucleation density $J = 1/\tau$ implied in equations (5) and (3) triggers the onset of boiling. Since the heterogeneous nucleation takes place in the fluid adjacent to the solid surface, the fluid temperature is taken to be the wall temperature.

For a given fluid-surface combination, then, setting $T = T_{IB}$ and $\tau = \tau_{IB}$ from measurement, F in equation (5) becomes a function only of the fluid properties. This is a continuously varying characteristic

Downloaded 20 Dec 2010 to 194.27.225.72. Redistribution subject to ASME license or copyright; see http://www.asme.org/terms/Terms_Use.cfm

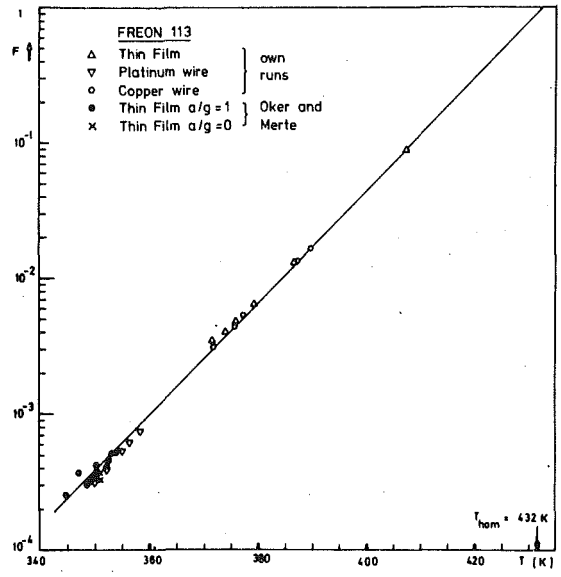

Fig. 7 Nucleation factor F versus inception temperature T for Freon 113 (p = 1 bar, T_S = 320 K)

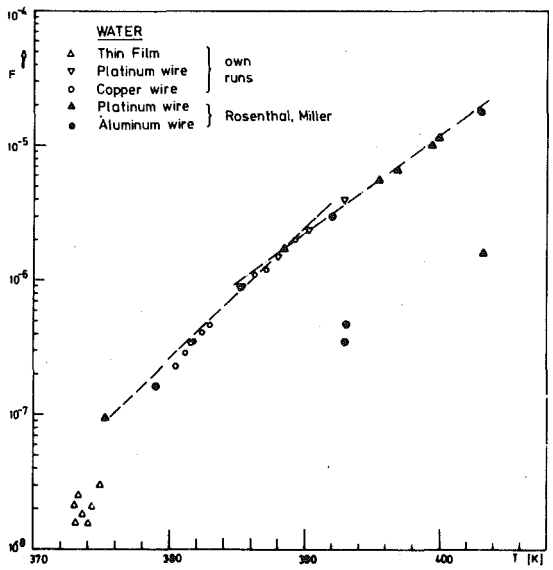

Fig. 8 Nucleation factor F versus inception temperature T for water (p = 1 bar, T_S = 373 K)

number, which can serve to correlate, for various heater surfaces, the relationship between the inception temperature and inception time for transient boiling processes. Different surfaces are located at different F-ranges. F has the following extremum values:

$$F = 1;\ T_{IB} = T_{\text{hom}} \text{ (homogeneous nucleation)} \quad (6)$$

$$F = 0;\ T_{IB} = T_s \text{ (no nucleation possible)} \quad (7)$$

F was computed using the experimental results such as Figs. 5 and 6 for T_{IB} and τ_{IB}, using the "macroscopic" surface tension [10].

Discussion

The F-curves for water and Freon 113 thus obtained are shown in Figs. 7 and 8, with additional data from [5] for Freon 113 and from [12] for water. The latter data were obtained with exponentially increasing power inputs, which perhaps accounts for some of the scatter. The straight lines are approximations to the data with $F = a \exp(bT)$ for the different combinations used. Setting those approximations in equation (5) one obtains $T_{IB} = f(\tau_{IB})$, which gives the relationship between inception temperature and inception time for a particular system.

Of particular interest is the direct comparison of the F-curves for the two different liquids used. Since F is already a dimensionless parameter, it remains only to define a dimensionless inception boiling temperature which will satisfy equations (6) and (7), as $(T_{IB} - T_s)/(T_{\text{hom}} - T_s)$. The experimental results are shown as the solid curves in Fig. 9. Also, shown are the corresponding uncertainty limits of the experimental measurements.

Since the measurements cover rather different parts of the dimensionless temperature, an extrapolation was performed for each fluid, using similarity considerations which would also satisfy equations (6) and (7), by taking the ratios of the F's for the two fluids with equation (5). The results are shown as dashed lines in Fig. 9. The typical shape of F for $(T_{IB} - T_S)/(T_{\text{hom}} - T_S) < 0.2$ shows the asymptotic decrease on the log scale to $F = 0$, with corresponding larger uncertainties at low incipient superheats (as in the runs with water or steady-state boiling). In transient boiling with Freon 113, the errors in the determination of F are lower, since the superheats are generally higher. Thus, it is possible to explain the time dependence of the inception superheat in that a shorter inception time requires a higher temperature (kinetic energy) level.

Data are reported [13] on the nucleation resulting from the pulse heating of a platinum wire 0.02 mm dia in water at atmospheric pressure. Nucleation occurred at very near the homogeneous nucleation temperature in τ_{IB} = 0.03 ms, placing this data point in the upper right hand corner of Fig. 9. The pulse heating of platinum wires with a variety of organic liquids also showed agreement with the homogeneous nucleation theory [14], expressing this factor in terms of contact angles on the surface. Such an approach was not successful in correlating the various data presented here.

The prediction of the heat flux at the inception of boiling is not carried out here since it is system dependent. However, since $T_{IB} = f(\tau_{IB})$ is known, one can apply the usual equations of transient conduction and free convection to determine the inception heat flux.

In the experimental work conducted here, the liquids were degassed as extensively as appeared practical, although no quantitative measurements of dissolved gases were made. It is conjectured that the effect of dissolved gases would be to move the nucleation factor F to lower values in Fig. 9.

Conclusions

Transient inception of boiling was explained in terms of a hetero-

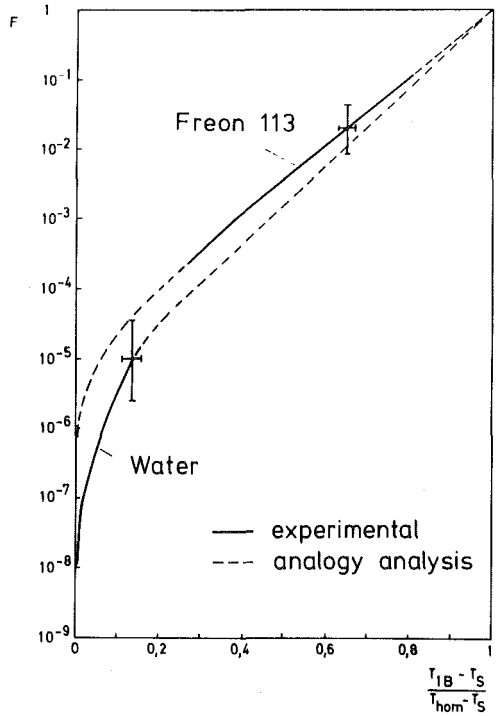

Fig. 9 Nucleation factor F versus dimensionless inception temperature for Freon 113 and water ($T = T_S$, p = 1 bar)

Downloaded 20 Dec 2010 to 194.27.225.72. Redistribution subject to ASME license or copyright; see http://www.asme.org/terms/Terms_Use.cfm

geneous nucleation theory based on the homogeneous nucleation theory. A liquid-dependent nucleation factor is introduced as a function of dimensionless inception temperature and determined experimentally for water and Freon 113. With this factor, it is possible to consider the inception as a transient nucleation process, and to compare the performance of different systems by a single F-number. In addition, in spite of the variability of F, homogeneous and heterogeneous nucleation, and transient and steady-state boiling can be considered as essentially the same process.

Acknowledgments

The authors wish to express their appreciation for the support of this work by the German Research Society (DFG) in Bonn, FRG.

References

1 Kawamura, et al., "Heat Transfer and DNB Heat Flux in Transient Boiling," 4th Int. Heat Transfer Conf., Versailles, 1970.

2 Oker, E., and Merte, H., "Semi-Transparent Gold Film as Simultaneous Surface Heater and Resistance Thermometer for Nucleate Boiling Studies," ASME JOURNAL OF HEAT TRANSFER, This issue, pp. 65–68.

3 Nghiem, X. L., "Holographic Investigation of Transient Boiling," Diss., TU Munich, 1980.

4 Joudi, K. A., and James, D. D., "Incipient Boiling Characteristics at Atmospheric and Subatmospheric Pressures," ASME JOURNAL OF HEAT TRANSFER, Vol. 99, 1977, p. 398.

5 Oker, E., and Merte, H., "Transient Boiling Heat Transfer in Saturated Liquid Nitrogen and F113 at Standard and Zero Gravity," NASA Rept., 074610 52F, 1973.

6 Cole, R., "Boiling Nucleation," *Advances in Heat Transfer*, Vol. 10, Academic Press, New York, 1974.

7 Schultz, R. R., and Cole, R., "Bubble Nucleation and Growth Instabilities in Transient Boiling," *Proceedings 6th International Heat Transfer Conference*, Toronto, Vol. 1, 1978, p. 133.

8 Hsu, Y. Y., and Graham, R. W., "An Analytical and Experimental Study of the Thermal Boundary Layer and Ebulition Cycle in Nucleate Boiling," NASA TND-594, 1961.

9 Oker, E., and Merte, H., "A Study of Transient Effects Leading up to Inception of Nucleate Boiling," *Proceedings 6th International Heat Transfer Conference*, Toronto, Vol. 1, 1978, pp. 139–144.

10 Volmer, M., *Kinetik der Phasenbildung*, Verlag Theodor Stein-kopff, Dresden, 1939.

11 Fisher, J. C., "The Fracture of Liquids," *Journal of Applied Physics*, Vol. 19, 1948, p. 1062.

12 Rosenthal, M. W., and Miller, R. L., "Experimental Study of Transient Boiling," ORNL-2294, Oak Ridge Nat. Lab., 1957.

13 Skripov, V. P., *Metastable Liquids*, Wiley, New York, 1974, pp. 103–104.

14 Simpson, H. C., and Walls, A. S., "A Study of Nucleation Phenomena in Transient Pool Boiling," *Proceedings Institute Mechanical Engineers*, 1965–66, Vol. 180, Pt3C.

Downloaded 20 Dec 2010 to 194.27.225.72. Redistribution subject to ASME license or copyright; see http://www.asme.org/terms/Terms_Use.cfm

Critical Heat Flux Experiments and Correlation in a Long, Sodium-Heated Tube

D. M. France
R. D. Carlson
T. Chiang

Argonne National Laboratory,
Argonne, Ill.

W. J. Minkowycz

Department of Energy Engineering,
University of Illinois,
Chicago, Ill. 60680

Critical heat flux (CHF) experiments were performed in the Steam Generator Test Facility (SGTF) at Argonne National Laboratory for application to liquid metal fast breeder reactor steam generators. The test section consisted of a single, straight, vertical, full-scale LMFBR steam generator tube with force-circulated water boiling upwards inside the tube heated by sodium flowing countercurrent in a surrounding annulus. The test section tube parameters were as follows: 10.1 mm i.d., 15.9 mm o.d., material = 2¼ Cr − 1 Mo steel, and 13.1 m heated length. Experiments were performed in the water pressure range of 7.0 to 15.3 MPa and the water mass flux range of 720 to 3200 kg/m²-s. The data exhibited two trends: heat flux independent and heat flux dependent. Empirical correlation equations were developed from over 400 CHF tests performed in the SGTF. The data and correlation equations were compared to the results of other CHF investigations.

Introduction

The phenomenon of critical heat flux (CHF) in boiling systems continues to receive substantial attention in the engineering literature. Heat transfer usually changes drastically and abruptly at CHF from excellent heat transfer to very poor heat transfer, producing consequences that are extremely important for a multitude of applications. Two recent review articles [1, 2] include bibliographies of over 100 references each of *recent* publications in this important area. The amount of experimental data collected, empirical correlation equations developed, and predictive mathematical models formulated has still not led to satisfactory *general* methods for predicting the occurrence of CHF in any given system. As is usual in two-phase flow, the scope of the CHF phenomenon has been subdivided into classes of more specific and restrictive circumstances, each of which has been treated independently in the engineering literature. Considerably better success has generally been achieved in the analysis of the separate subdivisions than can presently be obtained for the more general conditions. However, considerable disagreement and conflicting data still exist concerning CHF even within these subdivisions. Thus, developmental work in the area of CHF continues at a fast pace as a consequence of the importance of the phenomenon.

One class of CHF analysis that has received less experimental attention than many of the others is flow-boiling CHF inside of tubes where the heat is supplied by a flowing fluid on the outside of the tubes. An important application of this class is in the analysis, design, and development of steam generators for liquid metal fast breeder reactor (LMFBR) electric power plants. Experimental investigations have been performed in small, laboratory-type systems as well as in large systems prototypical of full-scale steam generators in an attempt to provide the CHF information necessary to support the design of LMFBR steam generators. Experiments of the prototypic type require liquid metal heating of boiling water in relatively large systems (10 to 20 m long tubes are common) and, as a result, data obtained in such systems have been quite limited. Because of the problems and uncertainties associated with the application of experimental data from smaller, nonprototypic systems to full-scale steam generator designs, the liquid metal heated prototypical experiments are generally preferred. These latter experiments are intended to provide measurements directly applicable to full-scale designs. However, among the limited experimental data of the prototypic type that have been reported in the engineering literature, discrepancies exist in the prediction of CHF.

The prediction of CHF in liquid metal heated, flow-boiling water has generally been made by empirical correlation equations that were "fit" to experimental data. However, various fundamental questions arise concerning this procedure and the way in which the data are represented. The more prominent of these are discussed in subsequent sections, but as a consequence of them, and of the sparsity of available prototypic data, the objective of this investigation was to obtain and correlate experimental data over a wide range of parameters typical for LMFBR steam generator application, employing a full-scale prototypical experimental test section. Experimental results and an empirical correlation equation are presented.

Experimental Facility

The Steam Generator Test Facility (SGTF) at Argonne National Laboratory (ANL) is a sodium and water facility designed to accommodate full-scale LMFBR steam generator tubes with vertical lengths in excess of 20 m. The maximum nominal operating parameters are as follows: power = 1 MW, sodium volumetric flowrate = 0.0044 m^3/s at 650°C, water pressure = 16.5 MPa, water volumetric flowrate = 0.0082 m^3/s. The water and sodium piping circuits are both closed loops delivering flow to and from the test section. The facility is described in some detail in [3] and [4].

The SGTF test section is shown schematically in Fig. 1. It consists of a straight, vertical, round water tube with inside diameter = 10.1 mm, outside diameter = 15.9 mm, material 2¼ Cr − 1 Mo steel, and heated length = 13.1 m. Water was force-circulated upwards in the tube, and sodium flowed countercurrent in the surrounding concentric annulus; the inside shell diameter was 31.5 mm. Spacers, which were designed to have minimal fin effect and low flow disturbance, were placed at 0.6 m and 0.9 m axial increments along the test section to maintain concentricity between the tube and shell. The mixed mean temperatures of the sodium and water at the test section inlet and outlet were measured with stainless steel sheathed thermocouples (T.C.) placed in the flow as shown in Fig. 1. Two thermocouples were provided at each location, and mixers were placed upstream of the sodium stream thermocouples at the inlet and outlet to the test section. The principal instruments used for determining the critical heat flux were the 102 select wire, chromel-alumel thermocouples spot welded to the outside of the shell, as shown in Fig. 1. These shell thermocouples were spaced at 0.3 m axial increments in a straight line with three additional thermocouples placed at 90 deg increments around the shell at several axial locations. Additional thermocouples were placed on the shell at several axial locations to decrease the axial spacing to 76.2 mm. At these locations, a stainless steel sheathed thermocouple, 0.81 mm o.d., was brazed into the water tube wall from the sodium side. These internal, or tube, thermocouples are indicated in Fig. 1. Sodium flow was measured with an electromagnetic flowmeter and water flow with a turbine flowmeter. High accuracy pressure gauges and pressure transducers were used to measure water

Contributed by the Heat Transfer Division for publication in the JOURNAL OF HEAT TRANSFER. Manuscript received by the Heat Transfer Division, May 29, 1980.

Copyright © 1981 by ASME

Downloaded 20 Dec 2010 to 194.27.225.72. Redistribution subject to ASME license or copyright; see http://www.asme.org/terms/Terms_Use.cfm

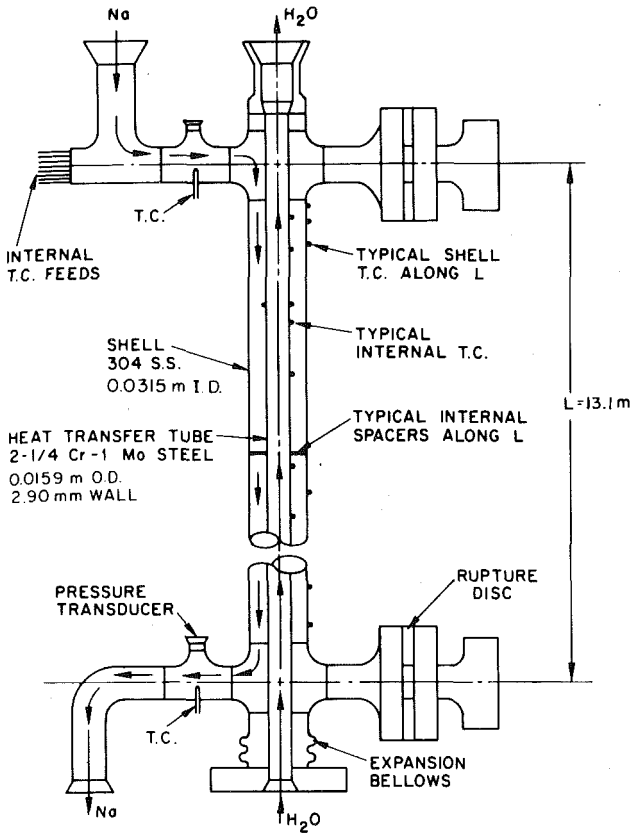

Fig. 1 SGTF test section schematic

pressure with an accuracy of ±0.02 MPa.

The stream thermocouples, internal thermocouples, sodium and water flowmeters, and water pressure transducers were all calibrated externally to the test facility, and all calibration equipment was traceable to U. S. National Bureau of Standards specifications. The shell thermocouples were calibrated in place by a series of isothermal tests over the full range of SGTF operating temperatures. These tests also determined test section heat loss (which was minimal).

Heat balance tests served as a final check on the accuracy of the stream thermocouples and the sodium and water flowmeters. These tests were conducted with subcooled liquid inside the entire test section tube. The results were generally within ±2 percent. Heat balance tests were conducted at regular intervals throughout the entire test series to insure the continued accuracy of the instruments. At the same time, other important data sensors were checked for accuracy.

The outputs from all of the 150 SGTF sensors were recorded by a high-speed, computerized data acquisition system. The controllers of any experimental system, whether manual or automatic, induce low frequency oscillations in pressures, temperatures, and flows. The automatic feedback controllers in the SGTF were normally adjusted so that the period of these system induced oscillations was of the order of 1 min, and the amplitudes were minimized. However, small axial movement of the CHF position in the test section tube caused shell temperatures in the CHF region to vary significantly as the boiling alternated between nucleate and film types. Consequently, it was necessary to record all of the sensor signals in a time period significantly less than the system oscillation period. All of the sensor outputs on the SGTF were recorded by the data acquisition system in a time period of 0.03 s, representing one data scan. Multiple data scans were recorded during each test run at time intervals of 10 s to 1 min. The accuracy of the entire data acquisition system was checked at regular intervals by comparison with instruments with calibrations traceable to the U. S. National Bureau of Standards.

Several continuous output instruments were used to monitor the chemical quality of the water in the SGTF. During testing, the following parameter ranges were maintained:

(1) Dissolved oxygen	10 ppb maximum
(2) pH	9 to 10
(3) Hydrazine residual	10 to 50 ppb
(4) Cation conductivity at 25°C	3 micro-mho/cm maximum

The oxide content of the sodium was kept low by cold trapping and dump tank storage.

Experimental Procedure

Five parameters were used to specify a test in the SGTF: water mass flux, water pressure, water inlet subcooling, sodium flowrate, and temperature of the sodium at the inlet to the test section. Tests were performed at all 16 combinations of the following water parameters (some intermediate values were also employed):

$$\text{pressure} = 7.0, 10.1, 13.0, 15.3 \quad \text{MPa}$$

$$\text{mass flux} = 720, 1440, 2400, 3200 \quad \text{kg/m}^2\text{·s}$$

For each combination of water pressure and mass flux, the other three parameters were varied to obtain the largest possible range of critical heat flux. (Water always entered the test section with a minimum of 20°C subcooling.) Additionally, each test was conducted so that CHF occurred in an area of the test section where the shell thermocouple spacing was 76.2 mm, and a tube thermocouple was located within the transition boiling zone. Generally, a test proceeded by establishing all parameters except the sodium inlet temperature, which was increased until CHF first occurred at the top of the test section, the water exit. The sodium inlet temperature was then increased further until CHF was positioned as described above, and the appropriate tube thermocouple was showing the relatively large amplitude fluctuations indicative of transition boiling. When all system parameters were steady, multiple data scans were recorded by the computer data acquisition system and stored for subsequent analysis.

Typical shell and tube thermocouple measurements are shown in Fig. 2 by square and circular symbols, respectively. In this test, all of the tube thermocouples gave steady readings, with the exception of the tube thermocouple located 12.2 m downstream of the water inlet to the test section. The fluctuation of this thermocouple output indicated that it was within the transition boiling zone, and its amplitude is shown in Fig. 2. At this same location, the plot of shell tem-

Nomenclature

A_i, B_i, δ = constants in correlation equations (5) and (6)
C_p = specific heat, J/kg·K
d = inside diameter of water tube ($2r_a$), m
$f_1(r)$ = initial sodium temperature distribution at $z = 0$, °C
G = mass flux, Mg/m²·s
k = thermal conductivity of sodium, W/m·K
k_e = effective turbulent thermal conductivity of sodium, W/m·K
L = heated tube length, 13.1 m
P = pressure, MPa
P_r = reduced pressure, P/P_{critical}
$\dot{q}'_{\text{LOSS}}$ = measured test section heat loss, W/m
$\dot{q}''$ = heat flux, MW/m²
ρ = sodium density, kg/m³
r = radial coordinate measured from the centerline of the water tube, m
T = sodium temperature, °C
V = sodium axial velocity, m/s
X_c = critical water quality
Y = measured shell temperature, °C
z = axial coordinate in direction of sodium flow, m

Subscripts

a = inside surface of water tube
b = outside surface of water tube
c = inside surface of sodium shell (outer annulus tube)
EXIT = outlet from test section
IN = inlet to test section
OUT = outlet from test section
s = outside surface of sodium shell

Downloaded 20 Dec 2010 to 194.27.225.72. Redistribution subject to ASME license or copyright; see http://www.asme.org/terms/Terms_Use.cfm

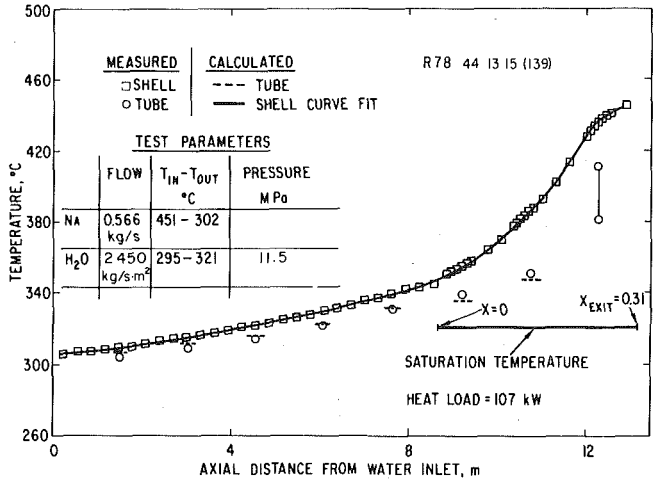

Fig. 2 Typical experimental measurements

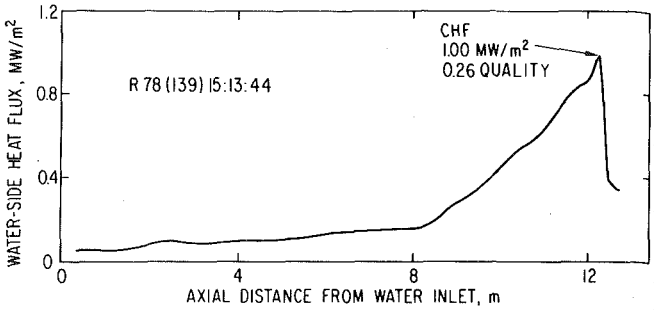

Fig. 3 Axial heat flux distribution

perature as a function of axial test section distance (as determined from the shell thermocouple measurements and shown in Fig. 2) exhibited a sharp change in slope, indicating the existence of CHF in agreement with the tube thermocouple indication.

Data Analysis

In order to determine the critical heat flux and critical quality for each test, it was necessary to determine the axial heat flux distribution from the measured shell temperatures. In contrast to experiments employing resistance heating of the tube wall, the heat flux in a temperature-controlled system must be calculated rather than measured. This situation generally leads to increased data scatter. Since considerable discrepancies and scatter exist among data obtained from resistance-heated experiments, a special attempt was made to minimize data scatter in the present experiments by adopting a more comprehensive data analysis than has been generally applied in previous temperature-controlled CHF experiments. The analysis included some effects previously neglected and assumed to be of second order. The data analyses of [5] and [6], for example, assumed fully developed sodium temperature profiles by using the heat flux calculated from the slope of the shell temperatures as the water heat flux. Although this assumption was shown to introduce a maximum error of approximately 8 percent in [6], it was removed in the present analysis where the sodium temperature profile was calculated as a function of axial and radial distance.

The sodium temperature in the annulus is governed by the energy equation

$$\rho C_p V \frac{\partial T}{\partial z} = k_e \left(\frac{\partial^2 T}{\partial r^2} + \frac{1}{r} \frac{\partial T}{\partial r} \right) + \frac{\partial k_e}{\partial r} \frac{\partial T}{\partial r} \tag{1}$$

where the axial conduction term was neglected on the basis of an order of magnitude calculation. (Axial conduction is generally not negligible at CHF in heat-flux-controlled systems [7].) In the current application, the flow is turbulent, and the quantities $T(r,z)$ and $V(r)$ are the time-averaged temperature and velocity distributions, respectively. It is assumed that the sodium flow is fully developed hydrodynamically, but developing thermally. (Although the velocity is not an explicit function of the axial coordinate z, it does vary in this direction as the fluid properties change with temperature.) The velocity distribution, $V(r)$, and the effective thermal conductivity, $k_e(r)$, used in equation (1) were determined from the Quarmby model [8].

The energy equation is of the parabolic type, and the solution progresses from the sodium inlet to the test section at $z = 0$. The initial condition is

$$T(r,0) = f_1(r) \tag{2}$$

The boundary conditions for equation (1) were determined from two measurements: (1) the axial temperature of the sodium shell at $r = r_s$, and (2) the radial heat loss determined from isothermal tests discussed previously. The heat loss was small as a consequence of the test section insulation, and the surface at $r = r_s$ was nearly adiabatic. As a result, two boundary conditions were imposed at the inside radius of the sodium shell, $r = r_c$:

$$T(r_c,z) = Y(z) \tag{3}$$

and

$$2\pi r_c k \left. \frac{\partial T}{\partial r} \right|_{r_c} = -\dot{q}'_{\mathrm{LOSS}}(z) \tag{4}$$

where $Y(z)$ and $\dot{q}'_{\mathrm{LOSS}}(z)$ are the axial temperature measurement at r_s and the radial heat loss, respectively.

Solution of equation (1) with initial and boundary conditions (2–4) is a problem of the inverse heat conduction type since both boundary conditions are imposed at $r = r_c$. Some problems of the inverse type may be solved with standard implicit finite difference methods with varying degrees of accuracy. However, solutions of this type are not *generally* possible, and were found to be completely inadequate in the present case where small inaccuracies in $Y(z)$ were reflected violently at $r = r_b$. Thus, a nonlinear estimation method first suggested by Beck [9] was employed to solve the current problem.

Analysis of a data scan proceeded by first fitting cubic spline functions to the measured shell temperatures as a function of axial distance. The data were smoothed by the spline fits by minimizing the second derivatives in the least squares sense. This technique was employed successfully in [6, 10], and [11] because it is conducive to determination of first derivatives used in the calculation of heat flux. The spline function was used for the function $Y(z)$ in equation (3). Next, a convenient form of the sodium radial temperature distribution at the test section inlet, $f_1(r)$ was chosen, and the method of [9] was employed to solve equation (1) to yield the axial and radial temperature distributions in the sodium annulus from which the heat flux to the water and the water quality were calculated. It was found that the choice of $f_1(r)$ did not affect CHF results unless CHF was positioned rather close to the top of the test section, in which case $f_1(r)$ had to be chosen such that its effect damped out in a distance shorter than normal.

The axial heat flux distribution calculated from the test data of Fig. 2 is shown in Fig. 3. The axial distribution is far from uniform, a point that is considered in the Discussion section. The CHF location was taken as the point of maximum heat flux. It marks the point of change from good heat transfer to poor heat transfer termed nucleate and film boiling, respectively, by analogy to pool boiling. The terms departure from nucleate boiling (DNB), dryout, and burnout are also used in the engineering literature to describe the same phenomenon, although the usage of these terms is often more restrictive than the general name, critical heat flux (CHF).

The accuracy of the data analysis was checked in three ways. First, having calculated the heat flux and temperature at the outside of the water-steam tube, $r = r_b$, the radial temperature distribution was calculated in the tube wall at axial locations where tube thermocouples were embedded in the wall at known depths. The calculated temperatures at these thermocouple junctions are compared with the

Downloaded 20 Dec 2010 to 194.27.225.72. Redistribution subject to ASME license or copyright; see http://www.asme.org/terms/Terms_Use.cfm

measured temperatures in Fig. 2. The dashed lines are the calculated values and show good agreement with the measurements (circular symbols). The second method of checking the data analysis was to analyze SGTF data scans by a completely independent method. This analysis was performed by the General Electric Company (GE) using the method of [10] and [11]. The GE analysis accounted for differences between the shell temperature and sodium bulk temperature in the calculation of water heat flux. Two data scans from different tests in the SGTF were analyzed, and excellent agreement was obtained with results from the present analysis. Finally, good agreement was found among data from GE experiments and the present experiments employing the same diameter water tube, water pressure, and water mass flux [10] at low values of heat flux, as discussed in a subsequent section.

The reproducibility of SGTF data was confirmed in two ways. First, results of analyses of different data scans obtained from a single test intercompared well. Second, tests performed on different days using the same parameters yielded consistent results.

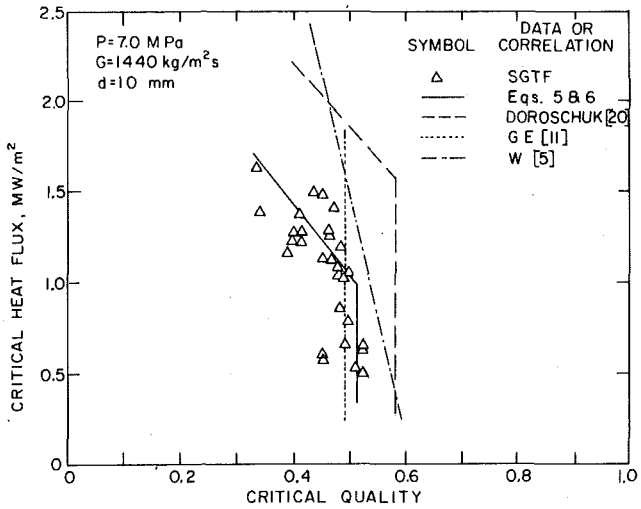

Fig. 4 Critical heat flux trends

Results

Over 400 tests were performed in the SGTF similar to the test depicted in Figs. 2 and 3, and each yielded a single CHF data point, i.e., the heat flux and quality at CHF for a given water flowrate and pressure. A typical set of CHF data are shown in Fig. 4 for a fixed water pressure and mass flux, using coordinates of local heat flux versus quality. Of primary importance before proceeding to a mathematical representation of the data is the establishment of the correct trends, and this is a point of current disagreement among various investigators. Older correlation equations which are based on considerable data generally represent the data as a straight line with a negative slope on the heat flux versus quality plot. Examples of some of these correlations which are currently used in various applications as given in [12] are Bowring [13], Kon'Kov [14], Thompson and Macbeth [15], Biasi [16], Westinghouse-Bettis [17], Westinghouse-III [18], and Kirby [19]. More recently, Doroschuk [20] found that his extensive data were best represented by dividing the plot into two regions, one with trends similar to the older correlations, and the other as a vertical line, i.e., with no heat flux dependence. Evaluating all of the SGTF data clearly showed the two-region trend found by Doroschuk.

The two-region trend of the SGTF data is seen in the data shown in Fig. 4. It consists of a heat flux dependent region and a heat flux independent region, termed CHF of the first and second kinds, respectively, by authors from the USSR. These data are the first reported in the open literature (other than USSR data) that show these two distinct trends. Additional plots of SGTF data given in Fig. 5 cover a range of water pressure and water mass flux values. The coordinates have been normalized to facilitate comparison, and the two-region trend is evident in all cases. (It is possible to represent the data of Figs. 4 and 5 by single lines showing a heat flux dependence over the entire range. However, such a procedure would introduce undesirable preferential error between the data and the correlating lines (equations) and is clearly not as appropriate a representation as the two trends used.)

As a result of the form of the CHF data obtained in the experiments performed in the SGTF, it was evident that the data would be represented best by a two-region relation of the type presented by Doroschuk [20]. However, the SGTF data agreed with Doroschuk's

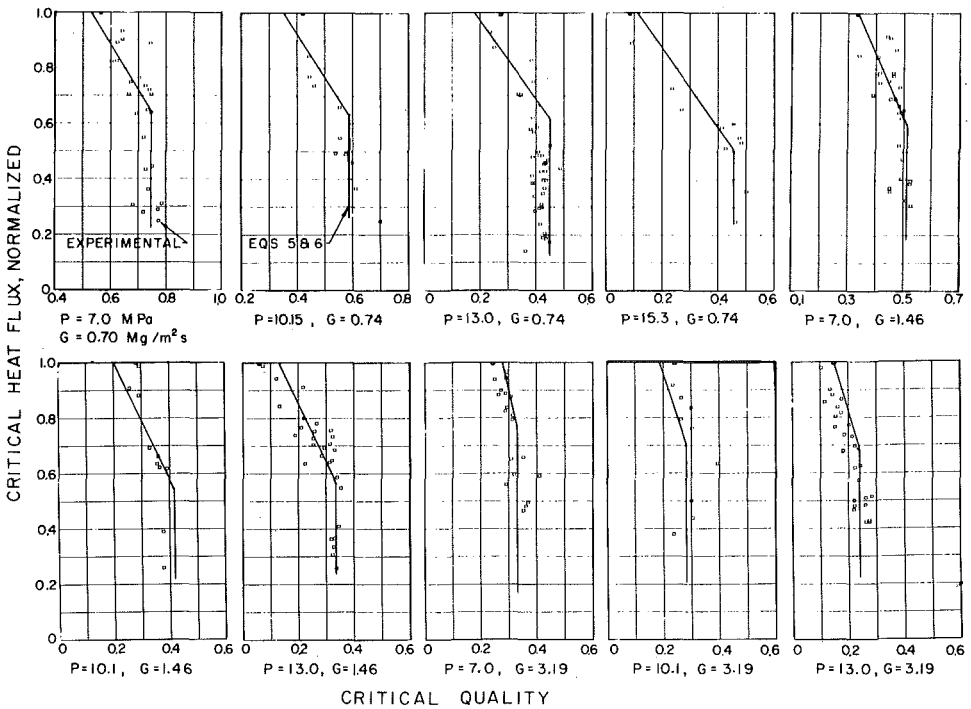

Fig. 5 Two trend results in SGTF data

Downloaded 20 Dec 2010 to 194.27.225.72. Redistribution subject to ASME license or copyright; see http://www.asme.org/terms/Terms_Use.cfm

correlation equation of [20] in a qualitative but not in a quantitative manner, as shown in Fig. 4. Thus, a new pair of correlation equations was developed which represented all of the 400 SGTF data well. Those equations are given below.

$$X_c = \left[\sum_{i=1}^{4} B_i P_r^{(i-1)}\right]\left[\frac{G}{1.356}\right]^{(B_5+B_6P_r^{B7})}\left[\frac{1}{100d}\right]^{0.15} \quad (5)$$

and

$$X_c = \left\{\sum_{i=1}^{3} A_i G^{(i-1)} + P_r \sum_{i=4}^{6} A_i G^{(i-4)} + P_r^{3.06} \sum_{i=7}^{9} A_i G^{(i-7)}\right\} \dot{q}''(100d)^{\delta} + \sum_{i=10}^{12} A_i G^{(i-10)} + P_r \sum_{i=13}^{15} A_i G^{(i-13)} + P_r^{2.3} \sum_{i=16}^{18} A_i G^{(i-16)} \quad (6)$$

Equations (5) and (6) represent the heat flux independent and dependent trends of the data, respectively. The units of the input parameters and ranges of applicability of the correlation follow:

$0.72 \le G \le 3.2$ Mg/m^2·s
$0.317 \le P_r \le 0.693$
0.3 MW/m^2 $\le \dot{q}''$
$0.008 \le d \le 0.020$ m
minimum X_c given in Fig. 6.

The limits on heat flux, diameter, and minimum critical quality given in Fig. 6 are discussed subsequently, and coefficients A_i and B_i, and δ are given in Tables 1 and 2. The correlation is easily applied by calculating values of X_c from both equations (5) and (6) for given pressure, flow, tube diameter, and heat flux; the smaller value is the appropriate one to use.

Predictions of correlation equations (5) and (6) are shown in Fig. 4 at conditions corresponding to the data. The agreement is good, and the two trends of the data are clearly reproduced by the correlation. Comparison between correlation equations (5) and (6) and all of the data obtained in the SGTF is shown in Fig. 7. The root mean square error is 14.7 percent.

The application range of correlation equations (5) and (6) is restricted to the limits of the data base, the 400 SGTF tests. However, as discussed in [1], it is insufficient to define the applicable parameter range by the maximum and minimum parameters employed in the test series. For example, the maximum heat flux obtained in the test series occurring at a given pressure and mass flux may be significantly higher than the maximum heat flux obtained at other combinations of pressure and mass flux. It is inappropriate to use the former heat flux as the maximum limit of the correlation over all pressures and mass fluxes. Thus, the limits of applicability of correlation equations (5) and (6) are given in Fig. 6. The correlation applies to heat fluxes above 0.3 MW/m^2 and to qualities above minimum values as a function of pressure and mass flux, as shown in Fig. 6.

The mathematical form of correlation equations (5) and (6) is somewhat more complex than many existing CHF correlations. This situation presents no problem for current computer design codes and was necessary for two reasons. First, the two data trends discussed previously required individual representation. The second reason is related to non-monotonic trends observed in the data. The effect of mass flux on the critical quality, X_c, in the heat flux independent

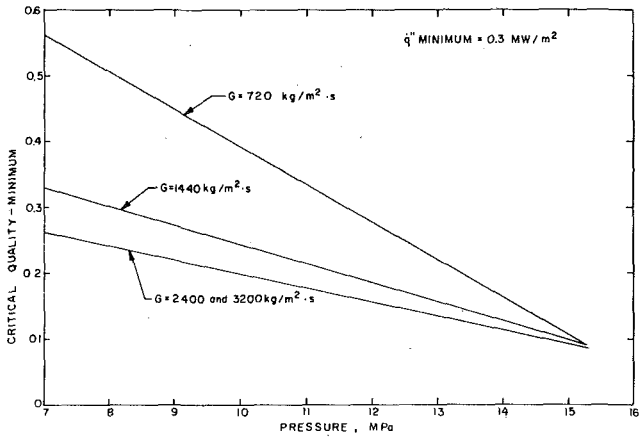

Fig. 6 Parameter limits on CHF correlation equations

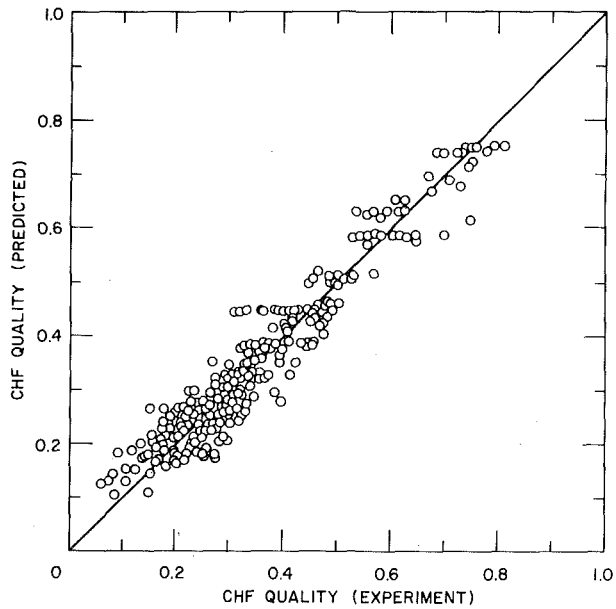

Fig. 7 Predictions of equations (5) and (6) compared with SGTF data

Table 1 Coefficients A_i and B_i for correlation equations (5) and (6)

i	A_i	B_i
1	−0.5342	−0.1141
2	0.3165	5.4591
3	1.399×10^{-4}	−14.156
4	0.0563	10.53
5	−0.1766	−0.5945
6	−0.1562	0.6149
7	−3.0142	2.3341
8	1.9119	
9	−0.0347	
10	2.0629	
11	−0.7871	
12	0.0409	
13	−1.6528	
14	−0.0440	
15	0.4001	
16	0.4202	
17	0.8756	
18	−0.6053	

Table 2 Coefficient δ for correlation equations (5) and (6)

	δ	
G \ P	7.0 to 10	10 to 15.3
0.72 to 2.4	0.5	$0.5 + 0.2\left(\frac{0.452 - \mathrm{Pr}}{0.234}\right)\left(\frac{2.4\text{-}G}{1.683}\right)$
2.4 to 3.2	0.5	0.5

G = (Mg/m^2·s)
P = (MPa)

Downloaded 20 Dec 2010 to 194.27.225.72. Redistribution subject to ASME license or copyright; see http://www.asme.org/terms/Terms_Use.cfm

region was found to change within the pressure range of the data, 7.00 MPa to 15.3 MPa. Also, the effect of heat flux on the critical quality in the heat flux dependent region was found to change with pressure and mass flux. Both of these data trends are also found in the data of [20].

All of the SGTF data upon which correlation equations (5) and (6) are based were obtained from a single diameter test section tube, $d = 10$ mm. A diameter effect was included in the correlation, but it is not based on SGTF data. It was adapted from the diameter effect of the correlation of [20] and is in good agreement with the diameter effect of the correlation of [5]. The diameter effects of [5] and [20] are relatively weak in a limited diameter range around the SGTF tube diameter of 10 mm. The maximum effect is at high pressure and low mass flux. It is recommended that the correlation not be applied outside the tube diameter range of 8 mm $\leq d \leq$ 20 mm.

Discussion

Several interesting questions arise related to the data and correlation equations presented in the preceeding sections. One of the more important of these deals with the two CHF data trends observed. One might ask why these two trends have only been observed in the SGTF and USSR data. The answer appears to be that most other experimentors observed one or the other of the trends and not both, either because of test section limitations or because of a lack of data. In this regard, it is helpful to divide CHF experimentation into two categories: short tubes and long tubes. Confining the discussion to straight, vertical tubes with the boiling fluid subcooled at the inlet, there is extensive data in the engineering literature obtained in short tubes. The correlation equations of [13–19] are based mostly on this type of data. As a consequence of the short test section lengths, the critical heat fluxes obtained were relatively high, and the trend was similar to the heat flux dependent portion of the SGTF data obtained at higher heat fluxes. The short tube lengths precluded the experiments from being carried to low heat fluxes (at the water mass fluxes of the SGTF data) where the second trend (heat flux independent) was observed in the SGTF data.

Having noted some consistency in trends between the SGTF CHF data and short tube data, long tube data were considered. (It is important to be cognizant of the fact that trends of data and not magnitudes are being compared. Quantitative data comparisons will be made subsequently.) Two recent CHF investigations performed in long, sodium-heated tubes were reported in [5] and [11]. Both of these experiments produced data at relatively low heat fluxes. The data of [11] exhibited the heat flux independent trend found in the SGTF data. The data of [5] were correlated with an equation that exhibited a weak heat flux dependence which is not a lot different from the heat flux independent trend of SGTF data. The number of experiments performed in both of these investigations was limited as compared with the SGTF data. Perhaps more data would have revealed the two-trend situation found in the SGTF data by improving trend interpretation and by increasing the parameter ranges. However, the trends observed are consistent with the heat flux independent trend found in the SGTF data at low heat fluxes. The CHF correlation equations of [5] and [11] are shown in Fig. 4 evaluated at the water mass flux and pressure of the SGTF data.

A third set of long tube data was reported in [20], and the CHF correlation equation is plotted in Fig. 4. The two trends are seen to be similar to the SGTF data trends; however, there are large quantitative differences.

In the preceding paragraphs, consistencies were shown between the two trends observed in the SGTF data and other CHF data, even though single trends were observed in them. The next important question to consider concerns the quantitative differences among SGTF data and these other data. This point introduces the subject of axial heat flux distribution along the length of the test section. As discussed in [1], it is well established that CHF will occur at different conditions in short tubes as a function of the axial heat flux distribution. The correlation equations of [13–19] are based mostly on uniform heat flux tests in short tubes. This fact, coupled with the relatively high heat fluxes of the data bases and the resulting single

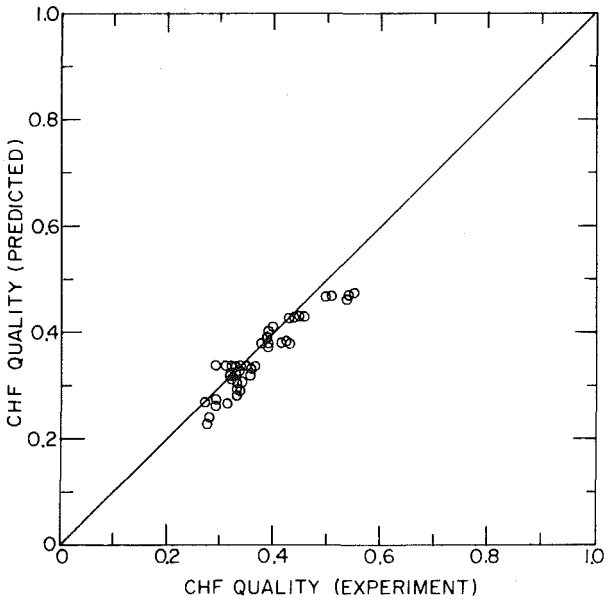

Fig. 8 Predictions of equations (5) and (6) compared with data of reference [5]

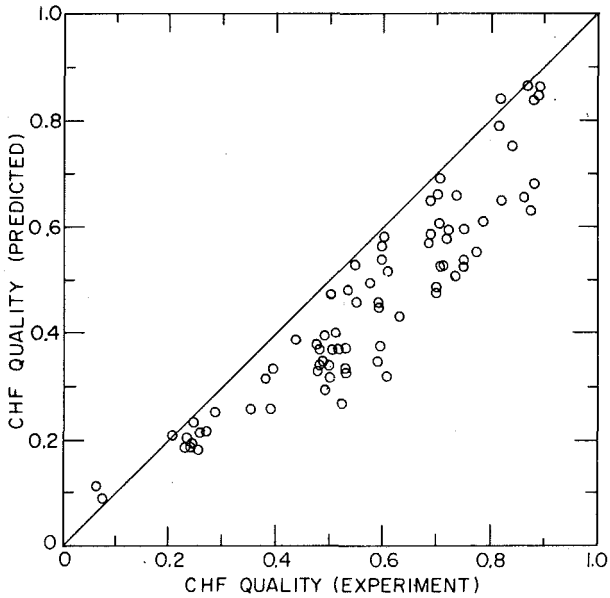

Fig. 9 Predictions of equations (5) and (6) compared with data of reference [11]

trends observed, produced the not so surprising result that none of these correlation equations predicted the SGTF data well. Similarly, the correlation equations of [5] and [11] did not predict the SGTF data well as a consequence of the single trends of their data bases. However, correlation equations (5) and (6) predict the data of [5] and [11] reasonably well, as seen in Figs. 8 and 9. The correlation is somewhat conservative with respect to the data of [11]. The SGTF data, equations (5) and (6), and the data of [11] are in good agreement at lower values of critical heat flux, as discussed in [10]. The larger discrepancies shown in Fig. 9 occur systematically at higher heat fluxes.

A final comparison was made between equations (5) and (6), representing SGTF data, and the data of [20]. The result, shown in Fig. 10, is preferential in nature. Good agreement was obtained at the higher water mass fluxes. The large discrepancies between equations (5) and (6) and the data of [20] occur at low mass fluxes and high heat fluxes. The question arises as to whether these discrepancies are attributable to the fact that the long tube of [20] was uniformly heated

Downloaded 20 Dec 2010 to 194.27.225.72. Redistribution subject to ASME license or copyright; see http://www.asme.org/terms/Terms_Use.cfm

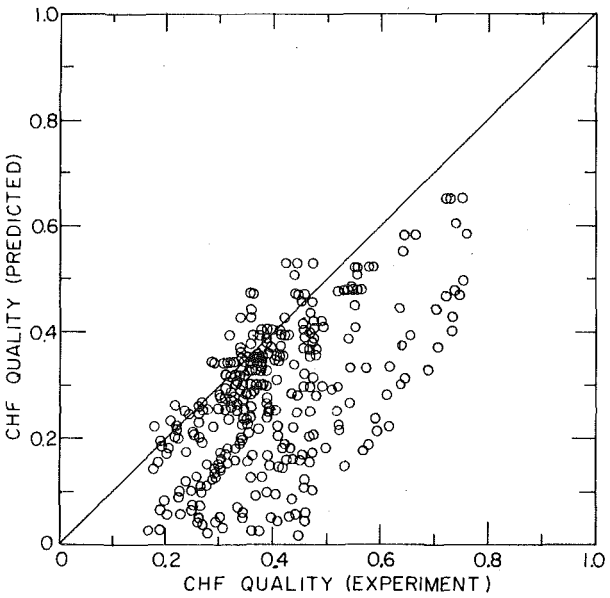

Fig. 10 Predictions of equations (5) and (6) compared with data of reference [20]

in a heat flux controlled system. This effect is important in short tubes as mentioned previously, but there is evidence [21] that it is not very important in long tubes. It is interesting, however, that when non-uniform heating was employed by the authors of [20], the data moved in the direction of the SGTF data [22]. This effect was also observed previously in Freon boiling experiments [6].

A final interesting question related to the data and correlation equations presented is related to the local conditions treatment of the data. Hewitt [1] gave reasonable and convincing arguments that the local heat flux should not be an important correlating parameter in annular flow CHF. Indeed, the portion of the SGTF data that is clearly in the annular flow regime shows no local heat flux dependence. It is not clear whether the heat flux dependent data are also entirely in annular flow. The argument of USSR investigators as to the cause of the two data trends points to a different CHF mechanism in each trend region, which could be attributed to different flow regimes. However, the local heat flux versus quality plot still serves as a good correlating basis for all of the data. This situation was also true for the SGTF data.

Conclusions

Critical heat flux data were obtained in a long, sodium-heated test section tube over a large parameter range. An elaborate data reduction technique was applied. The data trends were similar to the trends observed by Doroschuk [20] and represent the first available sodium-heated CHF data obtained outside the USSR that support those trends.

The data from over 400 tests in the ANL Steam Generator Test Facility were empirically correlated by equations (5) and (6) over the parameter range

$$7.0 \leq P \leq 15.3 \text{ MPa}$$
$$720 \leq G \leq 3200 \text{ kg/m}^2\text{-s}$$

The correlation agreed well with the sodium-heated CHF data from the experiments of [5], and some agreement was found with the sodium-heated data of [11] and the long tube data of [20]. The correlation equations (5) and (6) are believed to be the most accurate and most extensive developed to date for direct application to sodium-heated steam generator tubes.

Acknowledgments

The authors appreciate the independent analysis of SGTF data performed at the General Electric Company under the direction of Dr. S. Wolf.

This work was performed under the auspices of the United States Department of Energy.

References

1 Hewitt, G. F., "Critical Heat Flux in Flow Boiling," *Proceedings of Sixth International Heat Transfer Conference,* Toronto, Canada, Vol. 6, Aug. 1978, pp. 143–171.

2 Bergles, A. E., "Burnout in Boiling Heat Transfer Part III: High-Quality Forced-Convection Systems," *Nuclear Safety,* Vol. 20, No. 6, Nov.–Dec. 1979, pp. 671–689.

3 Stevens, H. C., and France, D. M., "Development of a Thermal/Hydraulic Test Facility for Full-Scale LMFBR Steam Generator Tubes," *Transactions of the American Nuclear Society,* Vol. 22, 1975, pp. 538–540.

4 France, D. M., Carlson, R. D., Chiang, T., and Priemer, R., "Characteristics of Transition Boiling in Sodium-Heated Steam Generator Tubes," ASME JOURNAL OF HEAT TRANSFER, Vol. 101, No. 2, May 1979, pp. 270–275.

5 Hwang, J. Y., Efferding, L. E., and Waszink, R. P., "Sodium-Heated Evaporator Critical Heat Flux Experiments at Subcritical Pressure Conditions for Commercial LMFBR Plant Application," ASME Paper No. 76-JPGC-NE-10, Sept. 1976.

6 France, D. M., "DNB in Liquid Metal Heated Forced Convection Boiling," *International Journal of Heat Mass Transfer,* Vol. 16, 1973, pp. 2343–2354.

7 Groeneveld, D. C., "The Thermal Behavior of a Heated Surface at and beyond Dryout," AECL-4309, Nov. 1972.

8 Quarmby, A., "An Analysis of Turbulent Flow in Concentric Annuli," *Applied Scientific Research,* Vol. 19, July 1968, pp. 250–273.

9 Beck, James V., "Nonlinear Estimation Applied to the Nonlinear Inverse Heat Conduction Problems," *International Journal of Heat Mass Transfer,* Vol. 13, 1970, pp. 703–716.

10 Wolf, S., France, D. M. and Holmes, D. H., "Recent Advances in Evaluating Critical Heat Flux Conditions in LMFBR Steam Generators," ASME Paper No. 77-WA/NE-11, Nov. 1977.

11 Wolf, S., and Holmes, D. H., "Critical Heat Flux in a Sodium-Heated Steam Generator Tube," 17th National Heat Transfer Conference, AIChE preprint, Aug. 1977, pp. 275–282.

12 Tong, L. S., *Boiling Crisis Critical Heat Flux,* U. S. Atomic Energy Commission Office of Information Services, 1972.

13 Bowring, R. W., "A Simple but Accurate Round Tube, Uniform Heat Flux, Dryout Correlation over the Pressure Range 0.7–17 MN/m^2 (100–2500 PSIA)," AEEW-R-789, Mar. 1972.

14 Kon'Kov, A. S., "Experimental Study of the Conditions under which Heat Exchange Deteriorates when a Steam-Water Mixture Flows in Heated Tubes," *Teploenergetika,* Vol. 13, No. 12, 1966, pp. 53–57.

15 Thompson, B., and Macbeth, R. V., "Boiling Water Heat Transfer, Burnout in Uniformly Heated Round Tubes: A Compilation of World Data with Accurate Correlations," AEEW-R356, July 1964.

16 Biasi, L., et al., "Studies of Burnout: Part III, A New Correlation for Round Ducts and Uniform Flux and Its Comparison with World Data," *Energia Nucleare,* Vol. 14, No. 9, 1967, pp. 530–536.

17 Goldman, K. M., and Thomas, D. E., USAEC Report WARD-MRP-92, Westinghouse Atomic Power Division, 1961.

18 Tong, L. S., *Journal of Nuclear Energy,* Vol. 21, 1967, p. 241.

19 Kirby, G. J., "A New Correlation of Non-Uniformly Heated Round Tube Burnout Data," AEEW-R500, July 1966.

20 Doroschuk, V. E., Levitan, L. L., and Lantzman, F. P., "Investigation in Burnout in Uniformly Heated Tubes," ASME Paper No. 75-WA/HT-22, Dec. 1975.

21 Cumo, M., Farello, F. E., and Palazi, G., "Temperature Controlled and Heat Flux Controlled Systems," CNEN Report No. CNEN/RT/ING(76) 8, 1975.

22 Doroschuk, V. E., Levitan, L. L., Lantzman, E. P., Nigmatulin, R. I., and Borevsky, L. Ya., "Investigation into Burnout Mechanisms in Steam-Generating Tubes," *Proceedings of Sixth International Heat Transfer Conference,* Toronto, Canada, Aug. 1978, Vol. 1, pp. 393–398.

Downloaded 20 Dec 2010 to 194.27.225.72. Redistribution subject to ASME license or copyright; see http://www.asme.org/terms/Terms_Use.cfm

B. T. Beck
Assistant Professor of Mechanical Engineering,
Kansas State University,
Manhattan, Kan.

G. L. Wedekind
Professor of Engineering,
Oakland University,
Rochester, Mich.
Mem. ASME

A Generalization of the System Mean Void Fraction Model for Transient Two-Phase Evaporating Flows

The system mean void fraction model has been successful in the prediction of a variety of transient evaporating and condensing flow phenomena; however, applications of the model have been restricted to physical situations involving complete vaporization or condensation. The major contribution of this paper is the development of a generalization of the existing system mean void fraction model, applicable to the broader class of transient two-phase flow problems involving incomplete vaporization. Present applications of the generalized system mean void fraction model to transient evaporating flows indicate good agreement with experimental void fraction and mass flux response data available in the literature. These data represent a variety of different flow geometries, types of fluids, and a wide range of operating conditions.

Introduction

The system mean void fraction model [1] is simpler than any of the major types of transient two-phase flow models listed by Collier [2] and Wallis [3]; in fact, simplicity is its principal virtue. It is based on an integral formulation approach, which yields a system of ordinary rather than partial differential equations governing the response of the important physical *boundary* phenomena.

The basic form of the model was originally introduced by Wedekind and Stoecker [4, 5] to predict the response of the mixture-vapor transition point (effective point of complete vaporization) to changes in the inlet mass flowrate. Applications of the model have also included the response of outlet flowrate [1] and system pressure drop [6]. Furthermore, existing applications have included not only transient evaporating flows, but transient condensing flows as well [1, 7].

Thus far, however, specific applications of the system mean void fraction model to transient evaporating flows have been restricted to the class of problems in which complete vaporization[1] takes place. Although the concept of a system mean void fraction for incomplete vaporization had been recognized earlier [1], a viable method of applying it had not yet been devised. The principal objective of this paper is to introduce a generalization which capitalizes on this concept, thereby extending the capability of the model to the broader class of problems involving incomplete vaporization.

In order to visualize the physical basis for the proposed generalization, it is helpful to compare evaporating flow systems undergoing complete and incomplete vaporization. First, it is possible to interpret the motion of the effective point of complete vaporization, as the propagation of the particular value of void fraction equal to unity.[2] Furthermore, the transient response of the outlet vapor flowrate at a fixed observation point can be related to the propagation of this specific representative void [1]. Now consider the general schematic of an evaporating flow system undergoing incomplete vaporization as depicted in Fig. 1.[3] Let Z be a fixed observation point where it is

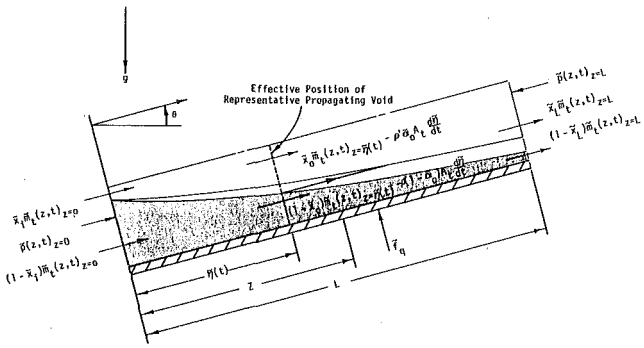

Fig. 1 Simplified schematic of evaporating flow system undergoing incomplete vaporization from saturated inlet conditions

desired to predict the transient response of variables such as flow quality, void fraction, and mass flowrate. Let attention be focused on a specific representative propagating void, $\tilde{\alpha}(z, t)_{z=\bar{\eta}(t)} = \tilde{\alpha}_0$, other than unity, which passes by the observation point during the transient. The goal of the present generalization is to predict this transient response at the fixed observation point by relating the relevant variables to the propagation of this specific representative void.[4] A means for selecting an appropriate representative void will be discussed later.

Development of Proposed Generalization

System Mean Void Fraction. Consider that portion of the two-phase region upstream of the effective position of the specific representative propagating void, $\tilde{\alpha}_0$. Then, by analogy with the complete vaporization case [1], a generalized nonfluctuating system mean void fraction may be defined as

$$\bar{\alpha}(t) \equiv \frac{1}{\tilde{\eta}(t)} \int_{z=0}^{\tilde{\eta}(t)} \tilde{\alpha}(z, t)dz \tag{1}$$

where

$$\tilde{\alpha}(z, t)_{z=\tilde{\eta}(t)} = \tilde{\alpha}_0 \tag{2}$$

implicitly defines $\tilde{\eta}(t)$, the nonfluctuating effective position within the two-phase region associated with the particular value of area mean void fraction, $\tilde{\alpha}_0$.

[1] In applications to transient condensing flows [1], the model was likewise restricted to the class of problems involving complete condensation.

[2] This interpretation is in keeping with the concept of void propagation as referenced in the literature [8–11].

[3] The annular flow configuration depicted here is for schematic purposes only, and is not in any way intended to imply that annular flow conditions necessarily always exist; nor are such conditions a necessary prerequisite to the proposed generalized model.

Contributed by the Heat Transfer Division for publication in the JOURNAL OF HEAT TRANSFER. Manuscript received by the Heat Transfer Division November 1, 1979.

[4] The extension of this concept to transient two-phase condensing flows is presently under investigation.

Copyright © 1981 by ASME

Downloaded 20 Dec 2010 to 194.27.225.72. Redistribution subject to ASME license or copyright; see http://www.asme.org/terms/Terms_Use.cfm

Of major importance to the development of the proposed generalization is the concept that the generalized system mean void fraction is invariant with time during a transient. A sufficient condition for this time invariance is that the area mean void fraction, $\tilde{\alpha}(z, t)$, can be expressed as

$$\tilde{\alpha}(z, t) = \tilde{\alpha}(\xi) \tag{3}$$

where the dimensionless variable, ξ, is given by

$$\xi \equiv z/\tilde{\eta}(t) \tag{4}$$

Although for a uniform heat flux and steady state true similarity exists, it is recognized that during a transient, similarity is only an approximation [20, 21]. Therefore, if used for other than estimating the system mean void fraction, it may introduce significant errors. This will be discussed in a later section.

Response of Representative Propagating Void. The present analysis will be based on the following simplifications:

1 Random fluctuations due to the stochastic nature of the two-phase flow process are assumed to exhibit negligible influence on the deterministic system transients.
2 Viscous dissipation, axial heat conduction and kinetic and gravitational potential energy contributions are neglected.
3 Properties of the liquid and vapor are assumed to be saturation properties, evaluated at the system mean pressure.
4 Spatial and temporal variations in system pressure are assumed to exhibit negligible influence on the conservation of mass and energy principles.
5 The generalized system mean void fraction is invariant with time.
6 Uniform applied heat flux.

As mentioned earlier, a key to the simplicity of the generalized system mean void fraction model is the assumption that even during a transient the system mean void fraction remains constant. Like its counterpart for the special case of complete vaporization, this assumption has the effect of uncoupling[5] the conservation of mass and energy principles from the transient form of the momentum principle, representing an analytical simplification of considerable magnitude. Thus, for the class of transient evaporating flow phenomena for which the time invariance is valid, these transient phenomena are governed by thermal mechanisms which can be represented by the conservation of mass and energy principles. All that is needed from the momentum principle is sufficient information to determine the system mean void fraction.[6]

Conservation of Mass Principle. Application of the conservation of mass principle to the liquid and vapor within the portion of the two-phase region upstream of the propagating void, $\tilde{\alpha}_0$ as indicated in Fig. 1, and incorporating the above assumptions, yields,

$$\frac{d}{dt}\int_{z=0}^{\tilde{\eta}(t)} \{\rho(1-\tilde{\alpha}) + \rho'\tilde{\alpha}\}A_t dz = \tilde{m}_t(z, t)_{z=0} - \tilde{m}_t(z, t)_{z=\tilde{\eta}(t)} + \{\rho(1-\tilde{\alpha}) + \rho'\tilde{\alpha}\}A_t \frac{d\tilde{\eta}(t)}{dt} \tag{5}$$

Conservation of Energy Principle. Application of the conservation of energy principle in a similar fashion to the above region yields

$$\frac{d}{dt}\int_{z=0}^{\tilde{\eta}(t)} \{\rho h(1-\tilde{\alpha}) + \rho' h'\tilde{\alpha}\}A_t dz = \int_{z=0}^{\tilde{\eta}(t)} \tilde{f}_q P dz + \{[h(1-\tilde{x}) + h'\tilde{x}]\tilde{m}_t\}_{z=0} - \{[h(1-\tilde{x}) + h'\tilde{x}]\tilde{m}_t\}_{z=\tilde{\eta}(t)} + \{\rho h(1-\tilde{\alpha}) + \rho' h'\tilde{\alpha}\}A_t \frac{d\tilde{\eta}(t)}{dt} \tag{6}$$

Combined Conservation Equations. Combining equations (5) and (6) so as to eliminate $\tilde{m}_t(z, t)_{z=\tilde{\eta}(t)}$, the mass flowrate leaving the subregion relative to the flow channel, and introducing the definitions given in equations (1) and (2), yields the following equation governing the response of $\tilde{\eta}(t)$, the effective position of the representative propagating void:

$$\{\rho - (\rho - \rho')(1-\tilde{x}_0)\}(\tilde{\alpha}_0 - \bar{\alpha})(h' - h)A_t \frac{d\tilde{\eta}(t)}{dt} + \bar{f}_q P\tilde{\eta}(t) = (h' - h)(\tilde{x}_0 - \tilde{x}_i)\tilde{m}_t(z, t)_{z=0} \tag{7}$$

where

$$\bar{f}_q \equiv \frac{1}{\tilde{\eta}(t)}\int_{z=0}^{\tilde{\eta}(t)} \tilde{f}_q dz \tag{8}$$

represents the spatial-average of the local applied heat flux. In its present form, equation (7) provides for the presence of transverse

[5] A similar uncoupling has been observed and discussed by Inayatullah and Nicoll [15] regarding an extension of Zuber and Staub's drift-flux formulation [9]. In their partial differential equation formulation, the uncoupling results from replacing the substantive derivative of pressure by the partial time derivative of pressure at some point in the flow channel. The implications are that the phenomena involved appear to be largely thermally governed.

[6] Estimation of the system mean void fraction from existing steady-state void fraction relationships is discussed in the Appendix.

Nomenclature

A_t = total cross-sectional area of flow channel, m^2
d = diameter of tube or equivalent diameter of flow channel, m
f_q = peripherally-averaged applied heat flux, W/m^2
G = instantaneous local total mass flux, g/m^2-s
h = enthalpy of saturated liquid, J/g
h_i = enthalpy of subcooled liquid at inlet, J/g
L = length of evaporating flow system, m
L_a = length of adiabatic section, m
m_t = local total mass flowrate of fluid (liquid and vapor), g/s
p = local pressure of fluid, N/m^2
P = inside perimeter of flow channel, m
P_T = total power input, W
t = time, s
t' = dummy time variable, s
$\bar{t}_D$ = estimated average delay time (see reference [20])
T_i = temperature of subcooled liquid at inlet, °C
x = local instantaneous flow quality
x_i = flow quality at inlet
x_0 = flow quality at effective position of representative propagating void
z = axial position in evaporating flow system measured from inlet, m
Z = position of a fixed observation point within evaporating flow system, m
α = instantaneous area mean void fraction
α_i = void fraction at inlet
α_0 = representative propagating void
η = instantaneous effective position of representative propagating void, m
θ = angle of inclination of evaporating flow system measured from the horizontal
λ = dummy time variable, s
ξ = dimensionless similarity variable
ρ = density of saturated liquid, g/m^3
τ = time constant characterizing response of effective position of representative propagating void, s
τ_i = characteristic time defined by equation (11), s
τ_m = time constant of exponential inlet mass flowrate change, s

Subscripts and Superscripts

Unless otherwise indicated above, subscripts i and f generally represent initial and final steady-state values, respectively. Physical quantities which possess a tilde (˜) are generally considered to be nonfluctuating (or time-averaged), where fluctuating is in reference to the inherent stochastic nature of the two-phase flow process. The tilde is omitted, for simplicity, in reference to fluid properties other than pressure. Barred (¯) quantities are generally considered to be nonfluctuating and spatially-averaged, where the averaging is presumed to take place within the appropriate region under consideration. Primed (′) symbols of quantities refer to saturated vapor.

Downloaded 20 Dec 2010 to 194.27.225.72. Redistribution subject to ASME license or copyright; see http://www.asme.org/terms/Terms_Use.cfm

distributions of void and velocity and relative velocity between phases. Also, note that equation (7) reduces to the result previously obtained for the special case of complete vaporization [1] when $\tilde{\alpha}_0 \to 1$.

General Solution; Abritrary Heat Flux and Inlet Mass Flowrate. The general solution to equation (7) for an arbitrary and simultaneous variation in applied heat flux and inlet mass flowrate, subject to the initial conditions

$$\tilde{\eta}(t)_{t=0} = \tilde{\eta}_i, \quad f_q(t)_{t=0} = \bar{f}_{q,i}, \tilde{m}_t(z,t)_{t=0} = \tilde{m}_{t,i} \tag{9}$$

may be expressed as follows:

$$\tilde{\eta}(t) = \tilde{\eta}_i \exp\left\{-\int_{\lambda=0}^{t}\left[\frac{\bar{f}_q(\lambda)}{\bar{f}_{q,i}}\right]\frac{d\lambda}{\tau_i}\right\}\left\{1 + \int_{t'=0}^{t}\left[\frac{\tilde{m}_t(0,t')}{\tilde{m}_{t,i}}\right] \times \exp\left\{\int_{\lambda=0}^{t}\left[\frac{\bar{f}_q(\lambda)}{\bar{f}_{q,i}}\right]\frac{d\lambda}{\tau_i}\right\}\frac{dt'}{\tau_i}\right. \tag{10}$$

where τ_i is a "characteristic time" defined by

$$\tau_i \equiv \frac{\{\rho - (\rho - \rho')(1 - \tilde{x}_0)\}(h' - h)(\tilde{\alpha}_0 - \bar{\alpha})A_t}{\bar{f}_{q,i}P} \tag{11}$$

Constant Heat Flux and Exponential Inlet Mass Flowrate. Now, let the inlet mass flowrate change be represented by the following exponential function of time:

$$\tilde{m}_t(0,t) = \tilde{m}_{t,f} + (\tilde{m}_{t,i} - \tilde{m}_{t,f})e^{-t/\tau_m} \tag{12}$$

Then, substituting equation (12) into (10), assuming a constant heat flux, yields after rearrangement

$$\frac{\tilde{\eta}(t) - \tilde{\eta}_f}{\tilde{\eta}_i - \tilde{\eta}_f} = e^{-t/\tau} + \frac{(\tau_m/\tau)}{[1 - (\tau_m/\tau)]}\{e^{-t/\tau} - e^{-t/\tau_m}\} \tag{13}$$

where the initial and final effective positions of the representative void, $\tilde{\eta}_i$ and $\tilde{\eta}_f$, are given by

$$\tilde{\eta}_i = \frac{\tilde{m}_{t,i}(h' - h)(\tilde{x}_0 - \tilde{x}_i)}{\bar{f}_q P}, \quad \tilde{\eta}_f = \frac{\tilde{m}_{t,f}(h' - h)(\tilde{x}_0 - \tilde{x}_i)}{\bar{f}_q P} \tag{14}$$

and where τ represents the exponential time constant characterizing the response of the effective position of constant void for the case of constant heat flux, and is given by

$$\tau = \frac{\{\rho - (\rho - \rho')(1 - \tilde{x}_0)\}(h' - h)(\tilde{\alpha}_0 - \bar{\alpha})A_t}{\bar{f}_q P} \tag{15}$$

It is of interest to note that equation (13) reduces to the appropriate response for a step change in inlet mass flowrate as $(\tau_m/\tau) \to 0$.

A careful examination of the system time constant, τ, will show that it is a monotonically increasing function of the specific representative void. Note that, during a transient, this suggests a departure from similarity.

Response of Flow Quality, Void Fraction, and Flowrate. Thus far in this analysis, the use of similarity has been limited to evaluating the system mean void fraction. For complete vaporization [1], this was its only use. However, for incomplete vaporization, similarity also represents a means of relating the transient response of the flow quality, void fraction, and mass flowrate at a fixed observation point, Z, to the propagation of a specific representative void, $\tilde{\alpha}_0$.

In terms of flow quality, a similarity relationship about a fixed observation point, Z, can be obtained from the steady state conservation of mass and energy principles, and takes the form

$$\tilde{x}(Z,t) = \tilde{x}_i + (\tilde{x}_0 - \tilde{x}_i)\frac{Z}{\tilde{\eta}(t)} \tag{16}$$

Use of the above relationship for a fixed observation point, Z, requires the selection of a specific representative void, $\tilde{\alpha}_0$, and its corresponding flow quality $\tilde{x}_0$. Once this selection is made, the effective position $\tilde{\eta}(t)$ of the representative void $\tilde{\alpha}_0$ can be determined from equations (10) or (13).

Under circumstances where the system transients involved remain quite small, the variation in void fraction and flow quality at some fixed observation point, Z, will also be small. Thus, virtually any specific void observed to pass by this point may be used as the representative void; all will yield essentially the same transient response.

For larger transients, to minimize potential errors due to a departure from similarity, the representative void is perhaps best selected on the basis of some sort of average. For this purpose, the representative void corresponding to the average of the initial and final steady-state flow quality seems most appropriate. This results in a void propagation symmetrical about the fixed observation point.

The void fraction response at the fixed observation point, Z, may be evaluated in terms of the flow quality response by means of a suitable relationship[7] of the form

$$\tilde{\alpha}(Z,t) = \tilde{\alpha}(\tilde{x}(Z,t)) \tag{17}$$

Applying the conservation of mass and energy principles to the two-phase mixture, the instantaneous mass flowrate response at a fixed observation point, Z, may be expressed as follows [20]:

$$m_t(Z,t) = \frac{\left[1 - \left(\frac{\rho'}{\rho}\right)\right]\frac{\bar{f}_q PZ}{(h' - h)} + \left\{1 - \left[1 - \left(\frac{\rho'}{\rho}\right)\right](1 - \tilde{x}_i)\right\}\tilde{m}_t(0,t)}{\left\{1 - \left[1 - \left(\frac{\rho'}{\rho}\right)\right][1 - \tilde{x}(Z,t)]\right\}} \tag{18}$$

Departures from Similarity. The existence of a generalized similarity relationship was introduced as a sufficient condition for the assumed time-invariance of the generalized system mean void fraction. In the initial conceptual development of the system mean void fraction model, Wedekind [21] was able to establish approximate upper and lower bounds for the possible departure from similarity. A more quantitative estimate of the departure from similarity, and the resulting influence on the system response, has been given by Beck [20]. The predominant effect is to introduce a time-delay. Such time delays are a characteristic of two-phase flow models based on continuity-wave theory [8, 9]. Although the time-dependence of the system mean void fraction may be significant under certain circumstances, such as with oscillatory inlet flow variations [20] of sufficiently high frequency, it becomes insignificant for transients sufficiently slow so as to allow time for redistribution [1] to occur.

Applications to Transient Evaporating Flows

The specific types of transients to be considered include the response of the outlet void fraction and outlet mass flux to decreases in inlet mass flowrate. These particular system responses are of interest because of their importance to the operation of boiling water nuclear reactor systems. As such, they include the added complexity of inlet subcooling. However, these tests represent the best experimental data currently available in the literature that provide a means of directly evaluating the concepts embodied in the proposed generalized system mean void fraction model.

In order for the generalized system mean void fraction model to predict such transients, the analysis presented earlier for the two-phase region must be extended beyond the assumption of saturated inlet conditions to include the influence of the motion of the so-called boiling boundary. This has been accomplished utilizing a consistent integral formulation approach. The details of this extension, and its application to the transients to be considered here, are discussed in reference [20].

Outlet Void Fraction Response. Outlet void fraction response measurements of Shiralkar, et al. [10], initiated by exponential decreases in inlet mass flowrate, are shown in Figs. 2 and 3. These tests simulate conditions possible during a hypothetical reactor accident, involving the loss of a recirculation pump. These tests also represent a considerable range of inlet subcooling. In each case the system was subjected to approximately a 50 percent exponential decrease in inlet mass flowrate.

Superimposed on the experimental data shown in Figs. 2 and 3 is

[7] A number of such relationships have been proposed [16–19] for steady-state conditions.

Downloaded 20 Dec 2010 to 194.27.225.72. Redistribution subject to ASME license or copyright; see http://www.asme.org/terms/Terms_Use.cfm

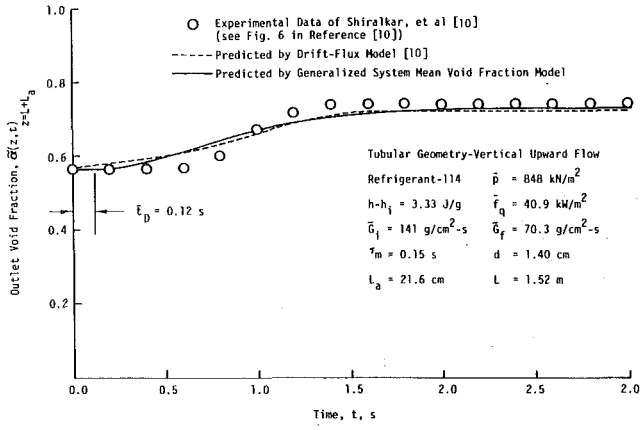

Fig. 2 Response of outlet void fraction to exponential decrease in inlet flowrate

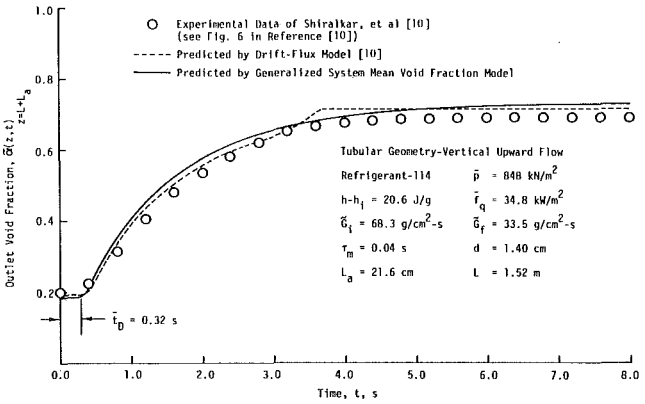

Fig. 3 Response of outlet void fraction to exponential decrease in inlet flowrate

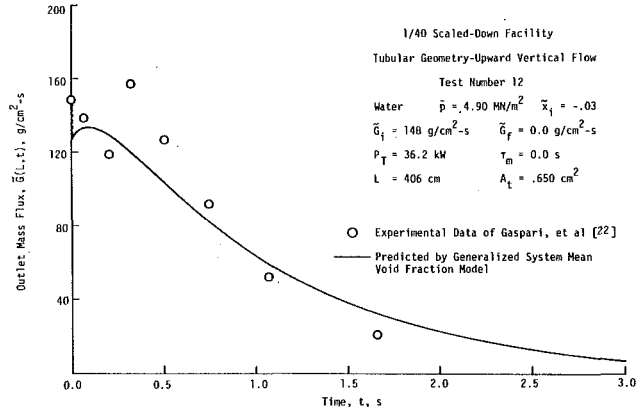

Fig. 4 Response of outlet mass flux to inlet flowrate shutdown

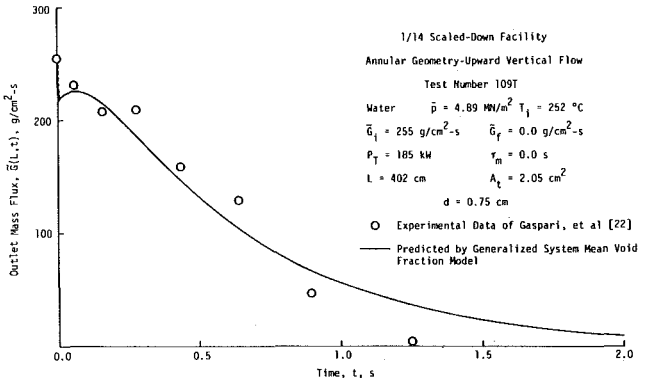

Fig. 5 Response of outlet mass flux to inlet flowrate shutdown

the analytical prediction of outlet void fraction response based on the proposed generalized model, indicated by the smooth solid line. An extension of the drift-flux model, evaluated by Shiralkar, et al. [10], is also shown for comparison purposes as a broken line in the above figures. The proposed model is seen to predict the observed void fraction response quite well. Furthermore, this model also compares favorably, during the transient and the final steady-state conditions, with the more complex analytical solutions obtained from the drift-flux partial differential equation formulation.

Outlet Mass Flux Response. A comparison of predicted outlet mass flux response with experimental measurements of Gaspari, et al. [22] is shown in Fig. 4. This transient was initiated by a complete and rapid shutdown of inlet flowrate, approximating a step decrease. The measured mass flux was obtained indirectly by estimating the instantaneous slope from the corresponding discretely measured mass holdup data. It is of interest to note that even in this extreme situation corresponding to a complete flow shutdown, the generalized system mean void fraction model does quite a reasonable job of predicting the transient, particularly if consideration is given to the possible scatter in the experimental data.

In Fig. 5 the predictions of the proposed generalization are compared with additional experimental mass flux response measurements of Gaspari et al. [22], for a similar type of transient. These measurements represent a considerable increase in power level and initial mass flux over the previous experimental data. Once again, the predictions of the proposed generalized system mean void fraction model compare favorably with the experimental measurements.

Summary and Conclusions

The primary purpose of this paper has been to present a generalization of the system mean void fraction model, applicable to the broader class of transient two-phase flow problems involving incomplete vaporization. This generalization has been developed by focusing attention on a specific representative propagating void within the two-phase region and utilizing an integral formulation approach, conceptually similar to that originally introduced for complete vaporization; in fact, the complete vaporization is now included as a special case. The result is a system of ordinary differential equations governing the transient response of important boundary phenomena such as flow quality, void fraction, and mass flowrate, expressed solely in terms of the important system parameters involved.

A key to the simplicity of the model is the identification of a time-invariant generalized system mean void fraction. This has the effect of completely uncoupling the conservation of mass and energy principles from the transient form of the momentum principle, representing an analytical simplification of considerable magnitude. Although the concept of time invariance for the generalized system mean void fraction represents only an approximation during a transient, it would appear that at least for transients sufficiently slow, the approximation is indeed quite good.

The ability of the proposed generalized model to accurately predict a variety of system transients has been demonstrated by comparison with experimental void fraction and mass flux response data available in the literature, and by comparison with corresponding predictions based on the drift-flux model. The transients considered encompassed a variety of different flow geometries, types of fluids, and a wide range of operating conditions, even under such extreme conditions as a complete shutdown of the inlet mass flowrate.

This proven capability suggests that, at least under certain conditions, the major physical mechanisms involved in transient two-phase flow phenomena are simpler than those portrayed by the more complex partial differential equation models. The degree of analytical simplification achieved and the clearer interpretation of the major physical mechanisms involved represent some of the primary advantages of the generalized system mean void fraction model as a tool in the analysis of transient two-phase evaporating flows.

Acknowledgments

The authors would like to acknowledge the National Science Foundation, Engineering Division, Mechanical Sciences and Engi-

Downloaded 20 Dec 2010 to 194.27.225.72. Redistribution subject to ASME license or copyright; see http://www.asme.org/terms/Terms_Use.cfm

neering Section, Heat Transfer Program for its part in the support of this research under Grant GK-35884.

References

1 Wedekind, G. L., Bhatt, B. L., and Beck, B. T., "A System Mean Void Fraction Model for Predicting Various Transient Phenomena Associated with Two-Phase Evaporating and Condensing Flows," proceedings of the *NATO Advanced Study Institute on Two-Phase Flows and Heat Transfer,* Istanbul, Turkey, Aug. 1976, and published in the *International Journal of Multiphase Flow,* Vol. 4, 1978, pp. 97–114.

2 Collier, J. G., *Convective Boiling and Condensation,* McGraw-Hill, 1972.

3 Wallis, G. B., *One-Dimensional Two-Phase Flow,* McGraw-Hill, New York, 1969.

4 Wedekind, G. L., and Stoecker, W. F., "Transient Response of the Mixture-Vapor Transition Point in Horizontal Evaporating Flow," *ASHRAE Transactions,* Vol. 72, Part II, 1966.

5 Wedekind, G. L., and Stoecker, W. F., "Theoretical Model for Predicting the Transient Response of the Mixture-Vapor Transition Point in Horizontal Evaporating Flow," ASME JOURNAL OF HEAT TRANSFER, Vol. 90, Feb. 1968, pp. 165–174.

6 Beck, B. T., and Wedekind, G. L., "A System Mean Void Fraction Model for Predicting Transient Pressure Drop in Two-Phase Evaporating Flows," presented at the 2nd Multi-Phase Flow and Heat Transfer Symposium-Workshop, Miami Beach, Fla. Apr. 16–18, 1979.

7 Wedekind, G. L., and Bhatt, B. L., "An Experimental and Theoretical Investigation into Thermally Governed Transient Flow Surges in Two-Phase Condensing Flow," *Two-Phase Transport and Reactor Safety,* Vol. II, Hemisphere Publishing Corp., Proceedings of the Two-Phase Flow and Heat Transfer Symposium-Workshop, Fort Lauderdale, Florida, Oct. 1976, pp. 691–211; also ASME JOURNAL OF HEAT TRANSFER, Vol. 99, No. 4, Nov. 1977, pp. 561–567.

8 Zuber, N., and Staub, F. W., "An Analytical Investigation of the Transient Response of the Volumetric Concentration in a Boiling Forced-Flow System," *Nuclear Science and Engineering,* Vol. 30, 1967, pp. 268–278.

9 Zuber, N., and Staub, F. W., "The Propagation and the Waveform of the Vapor Volumetric Concentration in Boiling, Forced Convection System Under Oscillatory Conditions," *International Journal of Heat and Mass Transfer,* Vol. 9, 1966, pp. 871–895.

10 Shiralkar, B. S., Schnebly, L. E., and Lahey, R. T., Jr., "Variation of the Vapor Volumetric Fraction During Flow and Power Transients," *Nuclear Engineering and Design,* Vol. 25, 1973, pp. 350–368.

11 Hancox, W. T., and Nicoll, W. B., "A General Technique for the Prediction of Void Distributions in Non-Steady Two-Phase Forced Convection," *International Journal of Heat and Mass Transfer,* Vol. 14, 1961, pp. 1377–1394.

12 Wedekind, G. L., "An Experimental Investigation into the Oscillatory Motion of the Mixture-Vapor Transition Point in Horizontal Evaporating Flow," ASME JOURNAL OF HEAT TRANSFER, Vol. 93, 1971, pp. 47–54.

13 Wedekind, G. L., and Beck, B. T., "Theoretical Model of the Mixture-Vapor Transition Point Oscillations Associated with Two-Phase Evaporating Flow Instabilities," ASME JOURNAL OF HEAT TRANSFER, Vol. 96, 1974, p. 138.

14 Wedekind, G. L., and Beck, B. T., "Correlation Between Outlet Flowrate and Mixture-Vapor Transition Point Oscillations in Two-Phase Evaporating Flow," proceedings of the *Fifth International Heat Transfer Conference,* Tokyo, Japan, Vol. IV, Sept. 1974, p. 220.

15 Inayatullah, G., and Nicoll, W. B., "Prediction of Flashing Diabatic Steam-Water Flows," Waterloo Research Institute, Sept. 1976, Report No. 16.

16 Zuber, N., and Findlay, J. A., "Average Volumetric Concentration in Two-Phase Flow Systems," ASME JOURNAL OF HEAT TRANSFER, 1965, p. 453.

17 Fujie, H., "A Relation Between Steam Quality and Void Fraction in Two-Phase Flow," *AICHE Journal,* Vol. 10, 1964, p. 227.

18 Levy, S., "Steam-Slip—Theoretical Prediction from Momentum Model," ASME JOURNAL OF HEAT TRANSFER, Vol. 82, 1960, p. 113.

19 Zivi, S. M., "Estimation of Steady-State Steam Void Fraction by Means of the Principle of Minimum Entropy Production," ASME JOURNAL OF HEAT TRANSFER, Vol. 86, 1964, p. 247.

20 Beck, B. T., "A Generalization of the System Mean Void Fraction Model with Applications to Transient Two-Phase Evaporating Flows," Ph.D. Thesis, Oakland University, Rochester, MI, Aug. 1978.

21 Wedekind, G. L., "Transient Response of the Mixture-Vapor Transition Point in Two-Phase Horizontal Evaporating Flow," Ph.D. Thesis, University of Illinois, 1965.

22 Gaspari, G. P., Riccardo, G., Premoli, A., and Sandri, C., "Mass Holdup, Pressure and Time-to-Dryout Predictions under LOCA Conditions. Comparisons with Scaled-Down Experimental Results," ASME Paper No. 74-WA/HT-43, Nov. 1974.

23 Staub, F. W., and Zuber, N., "Void Response to Flow and Power Oscillations in a Forced-Convection Boiling System with Axially Non-uniform Power Input," *Nuclear Science and Engineering,* Vol. 30, 1967, pp. 296–303.

24 Hancox, W. T., and Nicoll, W. B., "A Wall Shear Stress Formula for Adiabatic Two-Phase Flow," CWAPD-210, Westinghouse Canada Limited, Nov. 1976.

APPENDIX

For steady-state evaporating flow with saturated inlet conditions the generalized similarity relationship[8] may be expressed as follows:

$$\tilde{x}(z, t) = \tilde{x}_i + (\tilde{x}_0 - \tilde{x}_i)\xi \tag{19}$$

where the similarity variable, ξ, is given from equation (4) as

$$\xi \equiv z/\tilde{\eta}(t) \tag{20}$$

Introducing equation (19) into the definition of the generalized system mean void fraction given by equation (1) yields

$$\bar{\alpha} = \int_{\xi=0}^{1} \tilde{\alpha}(\xi)d\xi = \frac{1}{(\tilde{x}_0 - \tilde{x}_i)} \int_{\tilde{x}=\tilde{x}_i}^{\tilde{x}_0} \tilde{\alpha}(\tilde{x})d\tilde{x} \tag{21}$$

The steady-state void fraction relationships used in this paper to evaluate the system mean void fraction were selected primarily on the basis of their ability to accurately represent available experimental steady-state void fraction measurements for each particular fluid and flow situation considered. For comparison with the outlet void fraction transient measurements of Shiralkar, et al. [10] presented in Figs. 2 and 3, Zuber and Findlay's void fraction relationship [16] was used to facilitate direct comparison of the predictions of the proposed generalization with those of the drift-flux model, also evaluated by Shiralkar, et al. [10]. A more sophisticated version of the Zuber and Findlay relation suggested by Hancox and Nicoll [24] was utilized for comparisons with the outlet mass flux transients presented in Figs. 4 and 5. This relationship was used because of its relative simplicity and known accuracy in representing void fraction for steam-water systems over the entire range of flow quality. A more detailed description of these void fraction relationships and their use in evaluating the parameters associated with the generalized system mean void fraction model is given in reference [20].

[8] This relationship is strictly valid only for uniform heat flux; however, even if the heat flux is nonuniform, equation (19) will yield an estimate of the flow quality distribution, provided that $\tilde{\eta}$ is based on the spatially-averaged (or system mean) heat flux, $\bar{f}_q$. Staub and Zuber [23] have investigated the influence of nonuniform heat flux in both steady-state and transient conditions, and found the effect on the local void fraction (and hence flow quality) distribution to be small even for significant departures from uniformity.

Downloaded 20 Dec 2010 to 194.27.225.72. Redistribution subject to ASME license or copyright; see http://www.asme.org/terms/Terms_Use.cfm

Droplet Evaporation in High Temperature Environments

G. M. Harpole
TRW Systems,
Redondo Beach, CA 90278,
Mem. ASME

Axisymmetric-stagnation-point convective heat and mass transfer solutions are presented for water evaporating into dry air and into pure steam for free stream temperatures from 373K to 1450K and radiative to convective heat flux ratios from 0 to 2. Effects of (1) blowing (evaporation), (2) variable fluid properties, (3) interdiffusion (binary diffusion with nonequal heat capacities), and (4) radiation are all included. A simple correlation which fits these stagnation point solutions within 3 percent is presented. Whole droplet heat transfer is shown to behave much like stagnation-point heat transfer when the Reynolds number is on the order of 100. Blowing and other high temperature effects on whole droplet heat and mass transfer can be estimated with stagnation point solutions. The ratio of stagnation point solutions with and without high temperature effects should multiply no-blowing constant-fluid-properties whole-droplet heat transfer correlations as a correction factor. Such a corrected whole-droplet correlation compares favorably with experimental data in the literature.

Introduction

Significant portions of the droplets in sprays to quench fires, nuclear reactor emergency core cooling sprays, and high pressure combustor sprays can have Reynolds numbers on the order of 100. Models for such sprays are typically based on the behavior of individual droplets, which are assumed independent of each other. The external flow and heat transfer from a gas to single liquid droplets often behave as quasi-steady laminar flow forced convection heat transfer to a solid sphere. Internal circulation, free stream turbulence, accelerations, and oscillations typically have only small effects on the external flow and heat transfer to droplets when the Reynolds number is on the order of 100 [1–10]. A water droplet surface is typically an isotherm, because liquid side Peclet numbers are usually so large that liquid near the surface circulates from the front of the droplet to the back much faster than heat can diffuse into the droplet. An isothermal droplet surface allows the internal heat transfer to be separated from the external heat transfer. General solutions of the internal heat transfer are presented by Johns and Beckman [11] and Watada, et al. [12]. The present work is concerned with external heat and mass transfer.

Many workers have determined external droplet Nusselt numbers for the case of low temperature differences (constant fluid properties without blowing) as a function of Reynolds number and Prandtl number; much of these data are reviewed by Pruppacher and Klett [13], Clift, et al. [14], Rowe, et al. [15], and Fuchs [16]. In what are perhaps the most accurate sphere Nusselt number experiments, Beard and Pruppacher [17] and Pruppacher and Rasmussen [18] suspended water droplets without a stinger by an air flow at the terminal velocity in a vertical wind tunnel with turbulence levels below 0.3 percent. They found

$$Nu_D = 1.56 + 0.616 Re^{1/2} Pr^{1/3} \quad (1)$$

for $2.5 < Re < 3320$ and $Pr = 0.71$. Numerical computations for sphere Nusselt number by Woo and Hamielec [19], Navier-Stokes equations solutions and fully elliptic energy equation solutions, for $Pr = 0.71$ and $Re = 5, 10, 30, 57, 100, 200$, and 300 all agree with the Beard and Pruppacher experimental correlation (equation (1)) to better than 2 percent.

Equation (1) is based on a single Prandtl number, $Pr = 0.71$, so the Prandtl number exponent of 1/3 is somewhat arbitrary and is based on tradition. Whole sphere heat transfer data has essentially the same Prandtl number dependence that laminar boundary layer heat transfer does. High-Schmidt-number sphere mass transfer into water ($Sc \cong 1250$) has a $Sc^{1/3}$ dependence [15], while the high Schmidt (Prandtl) number limit for laminar boundary layer heat transfer has this same 1/3 power proportion. Rowe, et al. [15] show that for sphere heat transfer data into air ($Pr = 0.7$) to follow the same correlation as for sphere heat transfer data into water ($Pr = 6.8$) that $Pr^{0.39}$ should be used instead of $Pr^{1/3}$. Gases typically have Prandtl and Schmidt numbers of order one, and for this $0.3 < Pr < 3$ range, laminar stagnation point boundary layer heat transfer is proportional to $Pr^{0.38}$, essentially the same as for whole sphere heat transfer. Equation (1) can be rewritten for use in the $0.3 < Pr < 3$ range as

$$Nu_D = 1.56 + 0.626 Re^{1/2} Pr^{0.38} \quad (2)$$

Local heat and mass transfer studies [5, 19] show that overall external heat and mass transfer to spheres is dominated by a boundary-layer-like flow on the front half of the sphere when the Reynolds number is on the order of 100. The axisymmetric stagnation-point-flow boundary-layer solution is an exact solution of the Navier-Stokes equations [20], and so it is valid without the usual thin-boundary-layer restriction. However, the boundary-layer energy equation for heat transfer at an axisymmetric stagnation point is different from the fully elliptic energy equation. The Woo and Hamielec [19] numerical solutions of Nusselt number at the forward stagnation-point of a sphere for Reynolds numbers from 5 to 300 are correlated with a standard deviation of 1.3 percent by

$$Nu = 0.953 + 1.320 Pr^{0.38} Re^{1/2} \quad (3)$$

while the stagnation-point Nusselt number from first order boundary layer theory is $Nu = 1.320 Pr^{0.38} Re^{1/2}$. Sphere stagnation point heat transfer is within 7 percent of first order boundary layer axisymmetric-stagnation-point heat transfer when the Reynolds number is 100 or higher, and this stagnation point heat flux is about twice the overall sphere heat flux.

The effects of blowing and variable fluid properties on axisymmetric stagnation-point heat transfer are nearly the same as these effects on heat transfer through other laminar boundary layers. Virtually all proposed boundary-layer variable-fluid-property corrections—reference state methods, Couette flow models, and correction factors—are independent of the pressure gradient. The effect of blowing on heat transfer at an axisymmetric stagnation-point will be shown to be nearly the same as this effect on a flat plate with zero pressure gradient. Heat transfer correction factors based on stagnation-point solutions should be nearly the same as correction factors based on heat transfer into the boundary-layer on the front half of the droplet, and this boundary-layer dominates the whole droplet heat transfer. However, blowing also causes earlier separation on a sphere [21], which further reduces heat transfer.

Boundary Layer Equations

The boundary-layer equations for flow over an axisymmetric body

Contributed by the Heat Transfer Division of THE AMERICAN SOCIETY OF MECHANICAL ENGINEERS and presented at the Winter Annual Meeting, December 2–7, 1979, New York, NY. Revised manuscript received by the Heat Transfer Division July 30, 1980. Paper No. 79-WA/HT-6.

Copyright © 1981 by ASME

Downloaded 20 Dec 2010 to 194.27.225.72. Redistribution subject to ASME license or copyright; see http://www.asme.org/terms/Terms_Use.cfm

with heat transfer and binary diffusion for conservation of mass, momentum, mass species, and energy are, respectively,

$$\frac{\partial}{\partial x}(r\rho u) + \frac{\partial}{\partial y}(r\rho v) = 0 \tag{4}$$

$$\rho u \frac{\partial u}{\partial x} + \rho v \frac{\partial u}{\partial y} = \rho_e u_e \frac{\partial u_e}{\partial x} + \frac{\partial}{\partial y}\left(\mu \frac{\partial u}{\partial y}\right) \tag{5}$$

$$\rho u \frac{\partial m_1}{\partial x} + \rho v \frac{\partial m_1}{\partial y} = \frac{\partial}{\partial y}\left(\rho \mathcal{D} \frac{\partial m_1}{\partial y}\right) \tag{6}$$

$$\rho c_p u \frac{\partial T}{\partial x} + \rho c_p v \frac{\partial T}{\partial y} = \frac{\partial}{\partial y}\left(k \frac{\partial T}{\partial y}\right) + \rho \mathcal{D}(c_{p_1} - c_{p_2}) \frac{\partial m_1}{\partial y} \frac{\partial T}{\partial y} \tag{7}$$

where x is the coordinate along the surface, y is normal to the surface, r is the perpendicular distance from the symmetric axis to the surface. The boundary conditions in the free steam, $y \to \infty$, are

$$T = T_e, \quad m = m_{1e}, \quad u = u_e \tag{8abc}$$

The boundary conditions at the surface, $y = 0$, are

$$T = T_w, \quad m_1 = m_{1w}, \quad u = 0 \tag{9abc}$$

$$v = \left(k \frac{\partial T}{\partial y} - q_r\right) \Big/ \rho h_{fg} = -\frac{\mathcal{D}}{1 - m_{1w}} \frac{\partial m_1}{\partial y} \tag{9d}$$

Equation (9d) is specifically for evaporation of species 1 from the surface when there is no flux of species 2 across the surface. The radiative heat flux, q_r, in equation (9d) actually represents the local net heat flux at the surface by all sources other than evaporation and convection in the external boundary layer.

Conservation of mass, equation (4), is satisfied by defining a stream function, Ψ, as

$$\rho u r = \frac{\partial \Psi}{\partial y} \qquad \rho v r = -\frac{\partial \Psi}{\partial x}. \tag{10}$$

The boundary-layer equations (4–9) can be cast in similarity variables with the Mangler-Levy-Lees transformation

$$d\xi = \rho_e \mu_e u_e (r/D)^2 dx \tag{11a}$$

$$d\eta = [\rho u_e/(2\xi)^{1/2}](r/D)dy. \tag{11b}$$

The boundary-layer equations can be made dimensionless by defining

$$f = \Psi/(2\xi)^{1/2}D \tag{12a}$$

$$\theta = (T - T_w)/(T_e - T_w) \tag{12b}$$

$$\phi = (m_1 - m_{1e})/(m_{1w} - m_{1e}). \tag{12c}$$

For the special case of the stagnation-point of a sphere, $r = x$ and $u_e = 3u_\infty x/D$. The boundary-layer equations are self-similar for an axisymmetric stagnation-point in that the only independent variable is η, where

$$\eta = (6\mathrm{Re})^{1/2} \int_0^y (\rho/\rho_e)dy/D, \tag{13}$$

and $\mathrm{Re} = \rho_e u_\infty D/\mu_e$. These stagnation-point equations are

$$\left(\frac{\rho\mu}{\rho_e\mu_e} f''\right)' + ff'' + 0.5\left[\frac{\rho_e}{\rho} - (f')^2\right] = 0 \tag{14}$$

$$\frac{1}{\mathrm{Sc}_e}\left(\frac{\rho^2 \mathcal{D}}{\rho_e{}^2 \mathcal{D}_e} \phi'\right)' + f\phi' = 0 \tag{15}$$

$$\frac{1}{\mathrm{Pr}_e}\left(\frac{c_{pe}}{c_p}\right)\left(\frac{\rho k}{\rho_e k_e}\theta'\right)' + f\theta' + \frac{1}{\mathrm{Sc}_e}\left(\frac{\rho^2 \mathcal{D}}{\rho_e{}^2 \mathcal{D}_e}\right)\left(\frac{c_{p1} - c_{p2}}{c_p}\right)(m_{1w} - m_{1e})\phi'\theta' = 0 \tag{16}$$

with boundary conditions

$$f'(0) = \theta(0) = 0 \quad \phi(0) = 1 \tag{17a}$$

$$f'(\infty) \to 1 \quad \theta(\infty) \to 1 \quad \phi(\infty) \to 0 \tag{17b}$$

$$f(0) = \left(\frac{m_{1e} - m_{1w}}{m_{1w} - 1}\right)\left(\frac{\rho_w{}^2 \mathcal{D}_w}{\rho_e{}^2 \mathcal{D}_e}\right)\frac{1}{\mathrm{Sc}_e}\phi'(0) \tag{18a}$$

$$f(0) = -\frac{c_{pe}(T_e - T_w)}{h_{fg}}\left(\frac{\rho_w k_w}{\rho_e k_e}\right)\frac{1}{\mathrm{Pr}_e}\theta'(0) - \frac{q_r D}{h_{fg}\mu_e(6\mathrm{Re})^{1/2}} \tag{18b}$$

$$f(0) = -\frac{c_{pe}(T_e - T_w)}{h_{fg}}\left(\frac{\rho_w k_w}{\rho_e k_e}\right)\frac{1}{\mathrm{Pr}_e}\left(1 + \frac{q_r}{q_c}\right)\theta'(0) \tag{18c}$$

where primes denote $d/d\eta$. In the present work species 1 is water vapor and species 2 is air. The free stream mass fraction of water vapor, m_{1e}, is set to zero for dry air flows and one for water vapor flows. The fluid properties used for pure air, pure water vapor, and air-water vapor mixtures are given in the Appendix. Equations (18abc) represent blowing (evaporation); equation (18b) is equivalent to equation (18c). The blowing parameter for heat transfer,

$$B = \frac{c_{pe}(T_e - T_w)}{h_{fg} - q_r/\dot{m}''} = \frac{c_{pe}(T_e - T_w)}{h_{fg}}\left(1 + \frac{q_r}{q_c}\right) \tag{19a}$$

and the blowing parameter for mass transfer,

$$B_m = \frac{m_{1e} - m_{1w}}{m_{1w} - 1} \tag{19b}$$

are based on equations (18c) and (18a), respectively.

Heat and mass transfer are not necessarily analogous when the wet-bulb temperature approaches the boiling point, because binary diffusion affects heat transfer. The third term in equation (16) represents this effect of binary diffusion on energy transport. This term is insignificant for low ambient temperatures, but is significant for high ambient temperatures; $(m_{1w} - m_{1e})$ is only about 0.03 when the ambient air temperature is 373 K, but it reaches about 0.3 when T_e = 1250 K. Even with equal heat capacities, heat and mass transfer are not necessarily analogous, because the fluid property ratios in the species and energy equations are different. The dependence of these fluid properties on mass fraction is more significant than their temperature dependence.

The convective heat flux at the surface is given by

$$q_c = -k_w \left.\frac{\partial T}{\partial y}\right|_w = k_w(\rho_w/\rho_e)(6\mathrm{Re})^{1/2}\theta'(0)(T_w - T_e)/D \tag{20}$$

Nomenclature

a = weighting factor for blowing parameter
B = blowing parameter
c_p = heat capacity at constant pressure
D = droplet diameter
$\mathcal{D}$ = mass diffusion coefficient
f = dimensionless stream function, $f' = u/u_e$
h_{fg} = latent heat of vaporization
k = thermal conductivity
m = mass fraction
M = molecular weight
Nu = Nusselt number, $q_c D/k_e(T_e - T_w)$
P_{vap} = vapor pressure
Pr = Prandtl number, $\mu c_p/k$
q = heat flux
Re = Reynolds number, $\rho_e u_\infty D/\mu_e$
Sc = Schmidt number, $\mu/\rho\mathcal{D}$
T = temperature
u = velocity in the x direction
u_∞ = droplet speed relative to the ambient gas
x = distance along the surface
y = distance normal to the surface
α = temperature exponent of $(\rho k)^{-1}$
$\eta = (6\mathrm{Re})^{1/2} \int_0^y (\rho/\rho_e)dy/D$
$\theta = (T - T_w)/(T_e - T_w)$
μ = viscosity
ρ = density
$\phi = (m_1 - m_{1e})/(m_{1w} - m_{1e})$

Subscripts

c = convective
D = droplet averaged
e = of the free stream
m = for mass transfer
r = radiative
w = at the droplet surface
1 = species 1, water vapor
2 = species 2, air

Downloaded 20 Dec 2010 to 194.27.225.72. Redistribution subject to ASME license or copyright; see http://www.asme.org/terms/Terms_Use.cfm

so that the Nusselt number is

$$\mathrm{Nu} = q_c D/k_e(T_w - T_e) = \frac{(\rho k)_w}{(\rho k)_e}(6\mathrm{Re})^{1/2}\theta'(0). \quad (21)$$

The mass flux of water vapor at the surface relative to the mass average velocity is

$$j_{1w} = -\rho_w \mathcal{D}_w \left.\frac{\partial m_1}{\partial y}\right|_w$$

$$= -\rho_w \mathcal{D}_w (\rho_w/\rho_e)(6\mathrm{Re})^{1/2}\phi'(0)(m_{1w} - m_{1e})/D \quad (22)$$

so that the Nusselt number for mass transfer is

$$\mathrm{Nu}_m = j_{1w}D/\rho_e \mathcal{D}_e(m_{1w} - m_{1e}) = -\frac{(\rho^2\mathcal{D})_w}{(\rho^2\mathcal{D})_e}(6\mathrm{Re})^{1/2}\phi'(0) \quad (23)$$

The absolute surface mass flux is

$$\dot{m}'' = \frac{j_{1w}}{1 - m_{1w}} = -(q_c + q_r)/h_{fg}. \quad (24)$$

Stagnation Point Solutions

The axisymmetric stagnation-point laminar boundary-layer equations (14–17, 18*a*), and (18*c*) were solved for water droplets evaporating in pure air and in pure water vapor at ambient temperatures from 373 to 1450 K and with radiative to convective heating ratios from 0 to 2. Fluid property correlations given in the Appendix were used. A finite difference method with three point central differences and quasilinearization was used to solve the equations simultaneously [22]. Computed wet-bulb temperatures for evaporation into air are given in Table 1. The computed wet-bulb temperatures agree within 2 K with those measured by Downing [23] (only the 373, 450, and 650 K ambient temperature cases could be compared). Yuen and Chen [24, 25] evaporated water from a porous sphere in air at ambient temperatures up to 1250 K. They measured the temperature of the water as it entered the sphere center, which they claim to be close to the surface temperature, which should be close to the wet-bulb temperature. These measured temperatures agree with the computed wet-bulb temperatures with a standard deviation of 4 K. The surface mass fraction of water, m_{1w}, is very sensitive to wet-bulb temperature; a 15 K difference in wet-bulb temperature can change m_{1w} by a factor of two. The wet-bulb temperatures and the rest of the solution depend on the total pressure and the ambient mass fraction; the total pressure has been taken as 1 atm and $m_{1e} = 0$ for the air flow cases. Computed values of $\theta'(0)$ and $\phi'(0)$ for water stagnation-points evaporating into pure air and $\theta'(0)$ for water stagnation-points evaporating into pure water vapor are given in Tables 2 and 3. Nusselt numbers for heat and mass transfer can be obtained from $\theta'(0)$ and $\phi'(0)$ by using equations (21) and (23).

Correlation of Stagnation Point Solutions

A simple correlation for the effects of blowing and variable fluid properties on stagnation point heat and mass transfer would be convenient for engineering use. The Stewart and Prober [26] heat transfer tables for blowing with constant fluid properties at an axisymmetric stagnation point are correlated within about one percent by

$$\mathrm{Nu} = 1.320\,\mathrm{Pr}^{0.38}(1 + B)^{-0.70}\mathrm{Re}^{1/2} \quad (25)$$

for the range $0.3 < \mathrm{Pr} < 3$ and $B < 3$. For a flat plate boundary layer with zero pressure gradient, the Stewart and Prober tables indicate heat transfer varying as about $(1 + B)^{-0.74}$, nearly the same as for stagnation points. The heat transfer solutions of Bade [27] are for no blowing, $\mathrm{Pr} = 2/3$, $\rho_e/\rho = T/T_e$, and $\mu/\mu_e = k/k_e = (T/T_e)^{1-\alpha}$ at an axisymmetric stagnation point. Bade's tabulated solutions in the range $0.2 \le T_w/T_e \le 1$ and $0 \le \alpha \le 0.35$ are correlated within about one percent by

$$\mathrm{Nu}^+ = 1.320\,\mathrm{Pr}^{0.38}[1 + (0.327\,\alpha - 0.0844)(1 - T_w/T_e)]\,\mathrm{Re}^{1/2}, \quad (26)$$

where the fluid properties for Nu^+ and Re are evaluated at ambient conditions. Assuming that the blowing and variable fluid property effects act independently, the Nusselt number for blowing with variable fluid properties would be

$$\mathrm{Nu}^* = 1.320\,\mathrm{Pr}^{0.38}(1 + B)^{-0.7}[1 + (0.327\,\alpha - 0.0844)(1 - T_w/T_e)]\mathrm{Re}^{1/2}. \quad (27)$$

In fact, computations by Dewey and Gross [28] for blowing with variable fluid properties for $B = 2.5$, $T_w/T_e = 0.4$, and $\alpha = 0.3$ agree with equation (27) to within two percent.

Equation (27) is based on solutions assuming constant heat capacities and fluid properties being functions of temperature only, which is typical of single species systems, such as water evaporating into pure water vapor. However, the further assumption of $\mu/\mu_e = k/k_e = (T/T_e)^{1-\alpha}$ was made, while for water vapor μ/μ_e is much different from k/k_e. The constant, α, should be obtained from the density – thermal conductivity product as

$$\alpha = \frac{ln((\rho k)_e/(\rho k)_w)}{ln(T_w/T_e)}, \quad (28)$$

so that the energy equation will closely match reality, while the momentum equation may deviate somewhat from the truth. Equation (27) correlates the present results for water stagnation points evaporating into pure water vapor to within about 3 percent, as can be seen in the Fig. 1(*a*) plots of the ratio of actual Nusselt number from

Table 1 Wet bulb temperature for air flow [K]

q_r/q_c	Ambient Temperatures 373 K	450 K	650 K	850 K	1050 K	1250 K	1450 K
0.0	303.5	313.9	329.1	337.4	342.8	346.6	349.5
0.1	304.6	315.3	330.7	339.0	344.3	348.0	350.8
0.2	305.6	316.6	332.1	340.4	345.6	349.2	351.9
0.4	307.5	319.0	334.7	342.8	347.8	351.3	353.8
0.7	309.9	321.9	337.8	345.6	350.4	353.7	356.0
1.0	311.9	324.5	340.4	348.0	352.5	355.5	357.7
1.5	314.8	327.9	343.7	350.9	355.1	357.9	359.8
2.0	317.2	330.7	346.3	353.2	357.0	359.6	361.4

Table 2(*a*) $\theta'(0)$ for air flow

q_r/q_c	Ambient Temperatures 373 K	450 K	650 K	850 K	1050 K	1250 K	1450 K
0.0	0.4423	0.4214	0.3805	0.3496	0.3228	0.2986	0.2762
0.1	0.4424	0.4211	0.3792	0.3472	0.3195	0.2946	0.2717
0.2	0.4424	0.4208	0.3778	0.3448	0.3163	0.2907	0.2673
0.4	0.4423	0.4201	0.3749	0.3399	0.3097	0.2830	0.2589
0.7	0.4421	0.4189	0.3704	0.3324	0.3001	0.2720	0.2469
1.0	0.4418	0.4175	0.3657	0.3250	0.2909	0.2615	0.2359
1.5	0.4413	0.4150	0.3578	0.3130	0.2764	0.2457	0.2194
2.0	0.4406	0.4124	0.3499	0.3017	0.2631	0.2316	0.2051

Table 2(*b*) $\theta'(0)$ for water vapor flow

q_r/q_c	Ambient Temperatures 450 K	650 K	850 K	1050 K	1250 K	1450 K
0.0	0.5221	0.4937	0.4719	0.4517	0.4322	0.4131
0.1	0.5199	0.4871	0.4620	0.4394	0.4182	0.3979
0.2	0.5177	0.4807	0.4526	0.4279	0.4052	0.3839
0.4	0.5134	0.4685	0.4351	0.4068	0.3817	0.3589
0.7	0.5071	0.4514	0.4115	0.3792	0.3516	0.3274
1.0	0.5010	0.4357	0.3907	0.3554	0.3263	0.3015
1.5	0.4913	0.4122	0.3607	0.3224	0.2920	0.2669
2.0	0.4819	0.3914	0.3355	0.2955	0.2648	0.2400

Table 3 $-\phi'(0)$ for air flow

q_r/q_c	Ambient Temperatures 373 K	450 K	650 K	850 K	1050 K	1250 K	1450 K
0.0	0.4236	0.4061	0.3767	0.3549	0.3356	0.3175	0.3002
0.1	0.4243	0.4071	0.3776	0.3554	0.3355	0.3168	0.2989
0.2	0.4249	0.4079	0.3784	0.3557	0.3352	0.3160	0.2976
0.4	0.4261	0.4095	0.3797	0.3560	0.3343	0.3139	0.2945
0.7	0.4277	0.4115	0.3811	0.3557	0.3322	0.3102	0.2894
1.0	0.4291	0.4131	0.3819	0.3547	0.3295	0.3060	0.2841
1.5	0.4311	0.4155	0.3823	0.3522	0.3243	0.2986	0.2751
2.0	0.4327	0.4173	0.3819	0.3489	0.3185	0.2911	0.2664

Downloaded 20 Dec 2010 to 194.27.225.72. Redistribution subject to ASME license or copyright; see http://www.asme.org/terms/Terms_Use.cfm

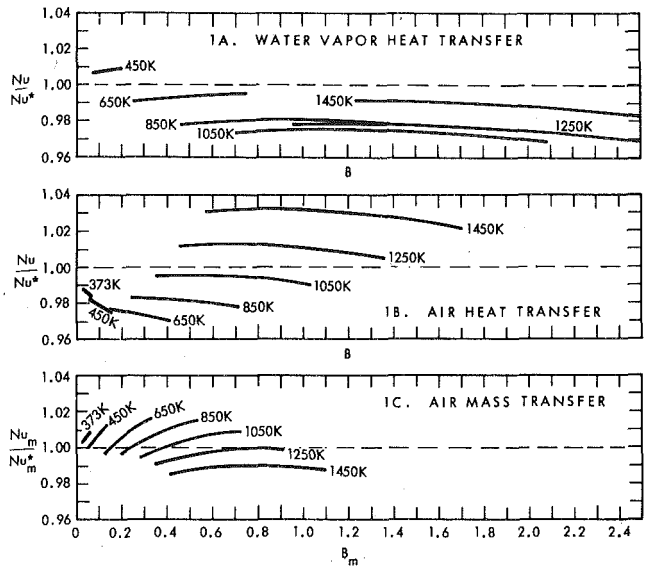

Fig. 1 Ratio of Nusselt number to Nusselt number correlation for stagnation-point flows

equation (21) to estimated Nusselt number from equation (27). Note that the end points of these Nu/Nu* curves at each ambient temperature correspond to $q_r/q_c = 0$ for the lowest value of B and $q_r/q_c = 2$ for the highest value of B. The nearly horizontal Nu/Nu* curves in Fig. 1(b) indicate that $(1 + B)^{-0.7}$ correctly represents the effect of blowing. The variable fluid properties correction, $1 + (0.327\ \alpha - 0.0844)\ (1 - T_w/T_e)$, is about 0.85 for the 1050, 1250, and 1450 K water vapor heat transfer cases. For the $T_e = 1450$ K and $B = 2.5$ case, the combined effect of blowing and variable fluid properties is to reduce the Nusselt number for evaporation into water vapor by a factor of 3, and equation (27) predicts this reduced Nusselt number within 2 percent.

Evaporation of water into air is more complicated than the single species (evaporation into water vapor) case, because the heat capacity, density and other fluid properties depend on mass fraction. Higher blowing rates correspond to higher mass fractions of water vapor at the surface, so that blowing and variable fluid properties are coupled. Gross, et al. [29] and Mills and Wortman [30] correlated such foreign gas injection problems by weighting the blowing parameter with ratios of the molecular weights of the two species raised to a constant power. The present solutions for water evaporating into air can be well correlated using the Mills and Wortman approach. The no-blowing (zero normal velocity at the surface and zero mass fraction of water everywhere) Nusselt number, Nu^+, is given by equation (26). The temperature dependence of air properties is mostly accounted for by evaluating the fluid properties in Nu, Pr, and Re at ambient conditions (ambient conditions are required for equation (26)), since $\alpha \cong 0.26$ for air. The Nusselt number with blowing is

$$Nu^* = Nu^+ (1 + aB)^{-0.7} \tag{29}$$

where a is determined by fitting the numerical solutions. For mass transfer, Nu, Nu*, Pr, α, a, and B, are replaced in equation by Nu_m, Nu_m*, Sc, α_m, a_m, and B_m, respectively, where

$$\alpha_m = \frac{ln((\rho^2\mathcal{D})_e/(\rho^2\mathcal{D})_w)}{ln(T_w/T_e)} \tag{30}$$

Equations (29) fit the present numerical solutions for water evaporating into air to within 3 percent with a = 1.60 and $a_m = 1.63$ (see Figs. 1(b) and 1(c)). Equations (29) fit the Mills and Wortman [30] axisymmetric-stagnation-point solutions for water injected into air to within 2 percent with a = 1.08 and $a_m = 1.50$. The differences between the present solutions and the Mills and Wortman solutions (up to 4 percent for mass transfer and up to 21 percent for heat transfer) are very likely due to different fluid property correlations. Mills and Wortman used the rigid sphere kinetic theory model, while curve fits of experimental fluid property data were used for the present solutions (see Appendix).

Estimated Whole Droplet Heat and Mass Transfer

Reliable and complete theoretical solutions for whole sphere heat and mass transfer with blowing and variable fluid properties are not available. For low Reynolds number flow (Stokes flow) Montlucon [31] shows that the droplet heat transfer correction factor for blowing is $(1/B)\ln(1 + B)$. The Navier-Stokes equations have been solved for flow over a sphere with blowing for Reynolds numbers 40 and 100 with $v_w/u_\infty = 0.1$ [21], but the energy equation was not solved for these flows. Hoffman and Ross [32] used a Galerkin method solution of the Navier-Stokes equations for flow over a droplet with uniform blowing with an integral boundary-layer formulation of the energy equation to estimate the blowing correction factor for heat transfer. They found that $(1 + B)^{-0.6}$ accurately correlated this correction factor for $0 < B < 3.5$ and $20 < Re < 400$. However, in actual droplet evaporation the blowing would be nonuniform and higher where the heat transfer is higher, near the forward stagnation point, so that a blowing correction factor stronger than $(1 + B)^{-0.6}$ would be expected in this actual case. Moreover, the Hoffman and Ross theoretical method predicts local Nusselt numbers in the wake region that decrease with angle and Reynolds number, which should increase with these parameters, and it predicts average Nusselt numbers proportional to $Re^{1/3}$ in the high Reynolds number limit, which should be proportional to $Re^{1/2}$.

Only Sayegh and Gauvin [33] attempted solving the difficult Navier-Stokes and fully elliptic energy equations with variable fluid properties for flow over a sphere. They used $\rho_e/\rho = T/T_e$, $\mu/\mu_e = k/k_e = (T/T_e)^{0.8}$, and Pr = 0.672, for which Bade [27] has computed stagnation-point solutions (the $T_w/T_e = 0.8$ case in Bade's table has a typographical error, the 0.640 should be 0.650). Sayegh and Gauvin correctly reproduced constant fluid properties solutions previously computed by Woo and Hamielec [19], but for Re = 50 they predict the percent decrease in stagnation-point Nusselt numbers due to variable fluid properties to be four times that of Bade's solutions. Sayegh and Gauvin found negative drag coefficients for $T_w/T_e = 0.25$, so their treatment of the variable fluid properties terms is suspect.

In the absence of more exact solutions, the effects of blowing and variable fluid properties on whole droplet heat and mass transfer can be estimated by correcting no-blowing constant-fluid-properties whole-droplet Nusselt numbers with ratios of stagnation-point Nusselt numbers, as

$$Nu_D = (1.56 + 0.626\ Pr^{0.38}Re^{1/2})\ \frac{Nu^*}{Nu_0}, \tag{31}$$

where Nu* is from equation (29) and $Nu_0 = 1.320\ Pr^{0.38}Re^{1/2}$ from equation (29) with $B = 0$ and $T_w = T_e$. Equation (31) can be further corrected with Nu/Nu* from Fig. 1, but this further correction is small. All fluid properties in Nu_D, Nu, Nu_0, Pr, and Re are evaluated at ambient conditions. Equation (31) does not account for a shift in the separation point due to blowing. Hamielec, Hoffman, and Ross [21] show that at a Reynolds number of 100 a uniform blowing value of $v_w/u_\infty = 0.1$ results in shifting the separation point 9 deg forward from where separation occurs for no blowing. This uniform $v_w/u_\infty = 0.1$ blowing corresponds to a blowing parameter, B, of 0.465 at the stagnation point and higher values of the blowing parameter at other points on the sphere. For actual droplet evaporation the blowing parameter is uniform, and the normal velocity at the surface, v_w, is nonuniform.

The blowing parameter, equation (19a), depends on the heat flux ratio q_r/q_c, which may be suspected of being a function of position on the sphere. The radiative heat flux, q_r, actually represents the local net heat flux at the surface by all sources other than evaporation and convection in the external flow. Some droplet evaporation experiments are run with the droplets hung on small thermocouple wires. The heat conducted into the droplet through these wires divided by the droplet surface area acts like a radiative heat flux and should be added on as part of "q_r." Internal circulation redistributes heat deposited in the droplet by radiation and makes the droplet more nearly isothermal. The "q_r" values include this heat redistribution before the heat reaches the surface. Wet-bulb (surface) temperatures are a function of q_r/q_c for evaporation of a droplet into another species (see

Downloaded 20 Dec 2010 to 194.27.225.72. Redistribution subject to ASME license or copyright; see http://www.asme.org/terms/Terms_Use.cfm

Table 1), so that q_r/q_c must be constant if the surface temperature is constant. Thus, for a well mixed or isothermal droplet, the radiative heat input would be spread to all points on the surface such that the local q_r/q_c would be uniform, and then $q_r/q_c = (\overline{q_r/q_c}) = \overline{q_r}/\overline{q_c}$, and the blowing parameter would be uniform.

Water droplets 1 mm in diameter falling at terminal velocity would have surface velocities on the order of 0.1 m/s [2], and this internal circulation would essentially eliminate temperature gradients on the droplet surface. However, for an insulating droplet, such as for experiments using wetted porous ceramic spheres, radiative heating might not be redistributed; q_r would be the local radiative heat flux. This radiative heat flux is often uniform, which results in q_r/q_c being larger on the back of the sphere than on the front of the sphere for an insulating droplet. Overall heat transfer to an insulating droplet can be higher than for the corresponding well mixed case, because the higher blowing parameter on the back of the insulated droplet does little to reduce overall heat transfer, while the blowing parameter on the front half is lower. For an insulating droplet with a uniform radiative heat flux, q_r/q_c in the blowing parameter should be replaced with $\overline{q_r}/S\overline{q_c}$, where S is a value between one and the ratio of stagnation-point to whole-sphere convective heating. The well mixed droplet case is thought to be a good engineering approximation in most instances.

Experimental Comparisons

The few existing high temperature droplet evaporation studies include droplet Nusselt numbers correlated by (1) starting with a Nusselt number relation believed to be correct for low temperature differences, (2) evaluating fluid properties in that correlation at a reference temperature and a reference composition, and (3) multiplying by a blowing correction factor which is a function of the blowing parameter only. These evaporation studies have been conducted in high temperature wind tunnels with either air flow or steam flow. A variety of blowing corrections and reference temperatures have been used.

Yuen and Chen [25] use a $(1 + B)^{-1}$ blowing correction factor for evaporation of either water or methanol into air. The present $(1 + 1.60B)^{-0.7}$ blowing correction for water evaporating into air agrees with the Yuen and Chen $(1 + B)^{-1}$ correlation to 1 percent for the $0 < B < 0.49$ range of their data. The present use of a weighting factor on the blowing parameter in the blowing correction factor, $(1 + aB)^{-0.7}$, is based on the work of Mills and Wortman [30] and Gross, et al. [29], who show that the weighting factor, "a," is the ratio of the free stream molecular weight to the molecular weight of the injectant with this quotient raised to a constant power. For methanol evaporating into air, "a" is nearly unity, because the molecular weight of methanol is nearly the same as that of air, so that the present suggested blowing correction factor for methanol evaporating into air is $(1 + B)^{-0.7}$. The Yuen and Chen methanol data for air temperatures around 870 K falls about 6 percent below their correlation, while their methanol data for air temperatures around 470 K falls about 3 percent above their correlation, with the 670 K air temperature data falling half way between the 470 K data and the 870 K data. Using the present $(1 + B)^{-0.7}$ instead of the Yuen and Chen $(1 + B)^{-1}$ would bring their methanol data nearly to a single line by accounting for 8.4 of the 9 percent discrepancy.

Downing [23, 34] evaporated droplets of acetone, benzene, hexane, and water into a heated air flow. Downing's blowing correction factor is $[(1/B)\ln(1 + B)][1 - 0.40(1 - (1/B)\ln(1 + B))]$, and he used both a reference temperature and a further correction factor based on the surface to ambient temperature ratio. The present estimated droplet Nusselt number, equation (31) further corrected with Nu/Nu* from Fig. 1, Downing's correlation, and Downing's water evaporation data all agree for his low air temperature cases. However, for water evaporating into air at his highest air temperatures, 613 K, the present correlation and Downing's data agree, while his own correlation is about 6 percent below his data, apparently due to an effort to use the same correlation for all of his liquids. Thus, the presently proposed droplet Nusselt number formula, equation (31), correlates Downing's water evaporation data better than his own correlation does.

Ross and Hoffman [35] evaporated water droplets into a water vapor flow with the walls independently heated such that $\overline{q_r}/\overline{q_c}$ ranged from 0 to 4.0 and B ranged from 0.04 to 0.30. They used a $(1 + B)^{-0.6}$ blowing correction in their Nusselt number correlation. The difference between $(1 + B)^{-0.6}$ and $(1 + B)^{-0.7}$ is at most 2.7 percent for the Ross and Hoffman data. The Ross and Hoffman Nusselt number correlation falls from 6 to 8 percent below the presently proposed droplet Nusselt number formula, equation (31), for the range of their data.

Narasimhan and Gauvin [36] evaporated water from porous ceramic spheres into water vapor with blowing parameters as high as 2.5 for their relevant data (aided flow with $Gr/Re^2 < 0.2$). They studied combined forced and free convection, and found that Nusselt numbers for opposed flow were 47 percent higher than those for aided flow even when $Gr/Re^2 < 0.01$. Clift, et al. [14] review combined free and forced convection on spheres, and explain, that although Nusselt numbers for opposed, aided, and cross flow are the same when $Gr/Re^2 < 0.1$ and Gr is on the order of 100, unsteady wake interaction effects at higher Grashof numbers result in higher Nusselt numbers for opposed flow. Narasimhan and Gauvin had Grashof numbers as high as 5500. Narasimhan and Gauvin use $(1 + B)^{-0.6}$ blowing correction in their Nusselt number correlation for aided flow, as Ross and Hoffman did. Narasimhan and Gauvin had an insulated droplet, and their $(1 + B)^{-0.6}$ correction can be interpreted as a $(1 + B)^{-0.7}$ correction with $q_r/q_c = \overline{q_r}/S\overline{q_c}$.

Conclusions

The laminar boundary-layer equations for evaporation of water at an axisymmetric-stagnation-point into pure steam flows and into dry air flows have been solved for free stream temperatures from 373 to 1450 K and radiative to convective heat flux ratios from 0 to 2. These stagnation point solutions are all correlated within about 3 percent by equations (26) and (29). The blowing correction factor is $(1 + aB)^{-0.7}$, where $a = 1$ for water evaporating into steam, $a = 1.60$ for heat transfer with water evaporating into air, and $a_m = 1.63$ for mass transfer with water evaporating into air.

Whole droplet heat transfer behaves much like stagnation point heat transfer; the common $Pr^{0.38}Re^{1/2}$ dependence has been shown previously. Corrections to whole droplet heat transfer for the high temperature effects of blowing with variable fluid properties can be estimated with stagnation-point solutions. The ratio of stagnation-point solutions with and without blowing and variable fluid properties should multiply no-blowing constant-fluid-properties whole-droplet heat transfer correlations as a correction factor, such as equation (31). Equation (31) correlates the high-temperature-environment droplet evaporation data available in the literature fairly well, and in some cases, equation (31) correlates this data better than the original correlations do. Blowing causes separation to occur earlier, and this effect is expected to cause a small further decrease in droplet Nusselt number.

Acknowledgment

This work was supported by National Science Foundation grant ENG 77-04807.

References

1 Berry, E. X., and Pranger, M. R., "Equations for Calculating the Terminal Velocities of Water Droplets," *Journal of Applied Meteorology*, Vol. 13, 1974, pp. 108–113.

2 LeClair, B. P., Hamielec, A. E., Pruppacher, H. R., and Hall, W. D., "A Theoretical and Experimental Study of the Internal Circulation in Water Drops Falling at Terminal Velocity in Air," *Journal of Atmospheric Sciences*, Vol. 29, 1972, pp. 728–740.

3 LeClair, B. P., Hamielec, A. E., and Pruppacher, H. R., "A Numerical Study of the Drag on a Sphere at Low and Intermediate Reynolds Numbers," *Journal of Atmospheric Sciences*, Vol. 27, 1970, pp. 308–315.

4 Raithby, G. D., and Eckert, E. R. G., "The Effect of Tubulence Parameters and Support Position on the Heat Transfer from Spheres," *International Journal of Heat Mass Transfer*, Vol. 11, 1968, pp. 1233–1252.

5 Galloway, T. R., and Sage, B. H., "Thermal and Material Transfer from Spheres: Prediction of Local Transport," *International Journal of Heat Mass Transfer*, Vol. 11, 1968, pp. 539–549.

6 Beard, K. V., "On the Acceleration of Large Water Droplets to Terminal Velocity," *Journal of Applied Meteorology*, Vol. 16, 1977, pp. 1068–1071.

Downloaded 20 Dec 2010 to 194.27.225.72. Redistribution subject to ASME license or copyright; see http://www.asme.org/terms/Terms_Use.cfm

7 Wang, P. K., and Pruppacher, H. R., "Acceleration to Terminal Velocity of Cloud and Rain Drops," *Journal of Applied Meteorology*, Vol. 16, 1977, pp. 275–280.
8 Marchildon, E. K., and Gauvin, W. H., "Effects of Acceleration, Deceleration, and Particle Shape on Single-Particle Drag Coefficients in Still Air," *AIChE Journal*, Vol. 25, 1979, pp. 938–948.
9 Manning, W. P., and Gauvin, W. H., "Heat and Mass Transfer to Decelerating Finely Atomized Sprays," *AIChE Journal*, Vol. 6, 1960, pp. 184–190.
10 Lin, C. L., and Lee, S. C., "Transient State Analysis of Separated Flow Around a Sphere", *Computers and Fluids*, Vol. 1, 1973, pp. 235–250.
11 Johns, L. E., and Beckmann, R. B., "Mechanism of Dispersed-Phase Mass Transfer in Viscous, Single Drop Extraction Systems," *AIChE Journal*, Vol. 12, 1966, pp. 10–16.
12 Watada, H., Hamielec, A. E., and Johnson, A. I., "A Theoretical Study of Mass Transfer with Chemical Reaction in Drops", *Canadian Journal of Chemical Engineering*, Vol. 48, 1970, pp. 255–260.
13 Pruppacher, H. R., and Klett, J. D., *Microphysics of Clouds and Precipitation*, D. Reidel, Boston, 1978.
14 Clift, R., Grace, J. R., and Weber, M. E., *Bubbles, Drops, and Particles*, Academic Press, New York, 1978.
15 Rowe, P. N., Claxton, K. T., and Lewis, J. B., "Heat and Mass Transfer from a Single Sphere in an Extensive Flowing Fluid," *Transactions of the Institute of Chemical Engineers*, Vol. 43, 1965, pp. T14–T31.
16 Fuchs, N. A., *Evaporation and Droplet Growth in Gaseous Media*, Pergamon Press, New York, 1959.
17 Beard, K. V., and Pruppacher, H. R., "A Wind Tunnel Investigation of the Rate of Evaporation of Small Water Drops Falling at Terminal Velocity in Air," *Journal of Atmospheric Sciences*, Vol. 28, 1971, pp. 1455–1464.
18 Pruppacher, H. R., and Rasmussen, R., "A Wind Tunnel Investigation of the Rate of Evaporation of Large Water Drops Falling at Terminal Velocity in Air," *Journal of Atmospheric Sciences*, Vol. 36, 1979, pp. 1255–1260.
19 Woo, S.-W., and Hamielec, A. E., "A Numerical Method of Determining the Rate of Evaporation of Small Water Drops Falling at Terminal Velocity in Air," *Journal of Atmospheric Sciences*, Vol. 28, 1971, pp. 1448–1454.
20 Schlichting, H., *Boundary-Layer Theory*, 6th ed., McGraw Hill, New York 1968, pp. 91–92.
21 Hamielec, A. E., Hoffman, T. W., and Ross, L. L., "Numerical Solution of Navier-Stokes Equation for Flow Past Spheres," *AIChE Journal*, Vol. 13, 1967, pp. 212–224.
22 Harpole, G. M., *Droplet Evaporation in High Temperature Environments*, Ph.D. dissertation, Univ. Calif., Los Angeles, 1980.
23 Downing, C. G., *The Effect of Mass Transfer on Heat Transfer in the Evaporation of Droplets of Pure Liquids*, Ph.D. dissertation, Univ. Wis., Madison, 1960.
24 Yuen, M. C., and Chen, L. W., "Heat Transfer Measurements of Evaporating Liquid Droplets," NU-ME/AS Rep. 76-2, Dept. Mech. Engr., Northwestern Univer., 1976.
25 Yuen, M. C., and Chen, L. W., "Heat Transfer Measurements of Evaporating Droplets," *International Journal of Heat Mass Transfer*, Vol. 21, 1978, pp. 537–542.
26 Stewart, W. E. and Prober, R., "Heat Transfer and Diffusion in Wedge Flows with Rapid Mass Transfer," *International Journal of Heat Mass Transfer*, Vol. 5, 1962, pp. 1149–1163.
27 Bade, W. L., "Stagnation-point Heat Transfer in a High-Temperature Inert Gas," *Physics of Fluids*, Vol. 5, 1962, pp. 150–154.
28 Dewey, C. F. and Gross, J. F., "Exact Similar Solutions of the Laminar Boundary-Layer Equations," *Advances in Heat Transfer*, Vol. 4, 1967, pp. 317–446.
29 Gross, J. F., Hartnett, J. P., Masson, D. J., and Gazley, C., "A Review of Binary Laminar Boundary Layer Characteristics," *International Journal of Heat Mass Transfer*, Vol. 3, 1961, pp. 198–221.
30 Mills, A. F., and Wortman, A., "Two-Dimensional Stagnation Point Flows of Binary Mixtures," *International Journal of Heat Mass Transfer*, Vol. 15, 1972, pp. 969–987.
31 Montlucon, J., "Heat and Mass Transfer in the Vicinity of an Evaporating Droplet," *International Journal of Multiphase Flow*, Vol. 2, 1975, pp. 171–182.
32 Hoffman, T. W., and Ross, L. L., "A Theoretical Investigation of the Effect of Mass Transfer on Heat Transfer to an Evaporating Droplet," *International Journal of Heat Mass Transfer*, Vol. 15, 1972, pp. 599–617.
33 Sayegh, N. N., and Gauvin, W. H., "Numerical Analysis of Variable Property Heat Transfer to a Single Sphere in High Temperature Surroundings," *AIChE Journal*, Vol. 25, 1979, pp. 522–534.
34 Downing, C. G., "The Evaporation of Droplets of Pure Liquids at Elevated Temperatures: Rate of Evaporation and Wet-Bulb Temperatures," *AIChE Journal*, Vol. 12, 1966, pp. 760–766.
35 Ross, L. L., and Hoffman, T. W., "Evaporation of Droplets in a High Temperature Environment," *3rd International Heat Transfer Conf.*, Vol. 5, 1966, pp. 50–59.
36 Narasimhan, C., and Gauvin, W. H., "Heat and Mass Transfer to Spheres in High Temperature Surroundings," *Canadian Journal of Chemical Engineering*, Vol. 45, 1967, pp. 181–188.
37 Hilsenrath, J., Hoge, H. J., Beckett, C. W., Masi, J. F., Benedict, W. S., Nuttal, R. L., Fano, L., Touloukian, Y. S., and Woolley, H. W., *Tables of Thermodynamic and Transport Properties of Air, Argon, Carbon Dioxide, Carbon Monoxide, Hydrogen, Nitrogen, Oxygen and Steam*, Pergamon Press, New York, 1960.
38 Schmidt, E., *Properties of Water and Steam in SI Units*, Springer-Verlag, New York, 1969.
39 Mason, E. A., and Monchick, L., "Transport Properties of Polar Gas Mixtures," *Journal of Chemical Physics*, Vol. 36, 1962, pp. 2746–2757.
40 Marrero, T. R. and Masson, E. A., "Gaseous Diffusion Coefficients," *Journal of Physics and Chemistry Reference Data*, Vol. 1, 1972, pp. 3–118.
41 Edwards, D. K., Denny, V. E., and Mills, A. F., *Transfer Processes*, McGraw-Hill, New York, 1976.
42 Wilke, C. R., "A Viscosity Equation for Gas Mixtures," *Journal of Chemical Physics*, Vol. 18, 1950, pp. 517–519.

APPENDIX

Properties of Air-Water Vapor Mixtures

The following correlations for the properties of air, water vapor, and air-water vapor mixtures were used in solving stagnation-point convection, equations (14–18). Equations and tables from references [37–42] were used. All temperatures are in degrees Kelvin. These correlations were used for temperatures ranging from 303 to 1450 K.

For pure air

$M = 29$

$k\ [\mathrm{W/mK}] = 3.227 \times 10^{-3} + 8.3894 \times 10^{-5}T - 1.958 \times 10^{-8}T^2$

$\mu\ [\mathrm{kg/ms}] = 6.109 \times 10^{-6} + 4.604 \times 10^{-8}T - 1.051 \times 10^{-11}T^2$

$\mathrm{Pr} = 0.647 + 5.5 \times 10^{-5}T$ for $T > 600$ K

$\mathrm{Pr} = 0.815\text{–}4.958 \times 10^{-4}T + 4.514 \times 10^{-7}T^2$ for $T \leq 600$ K

For pure water vapor

$M = 18$

$k\ [\mathrm{W/mK}] = 1.024 \times 10^{-2} - 8.21 \times 10^{-6}T + 1.41 \times 10^{-7}T^2 - 4.51 \times 10^{-11}T^3$

$\mu\ [\mathrm{kg/ms}] = 4.07 \times 10^{-8}T - 3.077 \times 10^{-6}$

$c_p\ [\mathrm{Ws/kg\ K}] = 8137 - 37.340T + 0.07482T^2 - 4.956 \times 10^{-5}T^3$ $T < 535$ K

$c_p\ [\mathrm{Ws/kg\ K}] = 1854 - 0.1194T + 8.304 \times 10^{-4}T^2 - 2.777 \times 10^{-7}T^3$ $T \geq 535$ K

$h_{fg}\ [\mathrm{Ws/kg}] = 2.257 \times 10^6 + 2.595 \times 10^3\ (373.15\text{-}T)$

$P_{\mathrm{vap}}\ [\mathrm{atm}] = (T/373.15)^{13.8} + 2.5 \times 10^{-4}\ (T\text{-}373.15)$

For air-water vapor mixtures

$\mathcal{D}_{12}\ [\mathrm{m^2/s}] = 1.732 \times 10^{-9}T^{1.685}$ $T \leq 400$ K

$\mathcal{D}_{12}\ [\mathrm{m^2/s}] = 5.385 \times 10^{-10}T^{1.88}$ $T > 400$ K

$c_p = m_1 c_{p1} + (1 - m_i)c_{p2}$

$x_1 = 1/[1 + (1/m_1 - 1)(M_1/M_2)]$ $x_2 = 1 - x_1$

$\rho\ [\mathrm{kg/m^3}] = (x_1M_1 + x_2M_2)/(0.08205T)$

$\phi_{ij} = [1 + (M_j/M_i)^{1/4}(\mu_i/\mu_j)^{1/2}]^2(8 + 8M_i/M_j)^{-1/2}$

$\mu = x_1\mu_1/(x_1 + x_2\phi_{12}) + x_2\mu_2/(x_2 + x_1\phi_{21})$

$k = x_1k_1/(x_1 + x_2\phi_{12}) + x_2k_2/(x_2 + x_1\phi_{21})$

Downloaded 20 Dec 2010 to 194.27.225.72. Redistribution subject to ASME license or copyright; see http://www.asme.org/terms/Terms_Use.cfm

F. A. Morrison, Jr.
University of California,
Lawrence Livermore National Laboratory,
Livermore, Calif. 94550
Mem. ASME

S. K. Griffiths
NSF Graduate Fellow,
Department of Mechanical and Industrial Engineering,
University of Illinois at Urbana-Champaign,
Urbana, Ill. 61801
Student Mem. ASME

On the Transient Convective Transport from a Body of Arbitrary Shape[1]

The net rate of transient convective heat transfer from a body at uniform temperature in steady flow is shown to be invariant to pointwise reversal of the flow. Such reversal is physically possible in both creeping and potential flows. Creeping flow and the unseparated potential flow of a low Prandtl number fluid yield physically important transfer problems. Additionally, the theorem is applicable to problems for which flow reversal has no physical significance; numerical reversal of any incompressible streaming flow will leave the net transfer rate unchanged. The proof is not based on symmetry and places no restriction on the shape of the body. It remains valid over the entire range of Reynolds and Peclet numbers even though local transfer rates may differ significantly in the two directions of flow. The theorem applies to the analogous mass transport and is generalized to include a homogeneous first order reaction decreasing the concentration.

Introduction

Under quite general conditions, Brenner [1] demonstrated that the overall rate of steady heat transport from an isothermal body is invariant to pointwise flow reversal. Thus, potential or creeping flow past an arbitrarily shaped body will, when reversed, produce the same net transport rate. This result remains true even with high Peclet numbers where local transport rates differ tremendously under flow reversal. Symmetry is not invoked in the argument; the result holds for asymmetric geometries or flows.

Examples illustrating Brenner's theorem are provided by analyses [2, 3] of transport in an electrically induced flow about a drop. Although the drop is spherical, flow reversal is nontrivial. In one direction, fluid on a contacting stream surface approaches the drop radially on the equatorial plane, then sweeps across a hemispherical surface to exit along the polar axis. In a reversed flow, approach is along the axis and departure on the plane. For both high [2] and low [3] Peclet numbers, flow reversal leaves the steady transfer rate unaltered.

The high Peclet number analysis included the transient response to a step change in the temperature difference between the drop and the surrounding fluid. While equality of steady transfer rates in the two flow directions was anticipated, the transient rates, surprisingly, are also equal at all times. The integral expressions for these rates yield identical results when evaluated numerically.

This remarkable fact leads to the conjecture that invariance to flow reversal may be more generally true for transient transport. In this paper, that conjecture will be affirmed.

Chen and Pfeffer [4] numerically investigated steady mass transport from a translating sphere in the presence of an inert second sphere. Calculations, with and without a homogeneous first order reaction, apparently showed that the overall steady transfer rate is invariant to reversal of the creeping flow. Brenner [5] generalized his theorem to include the effect of such chemical reaction and also noted the simple extension to assemblages of bodies moving in concert. The transient mass transport with this chemical reaction is treated in our Appendix. The theorem remains valid with this generalization.

Analysis

An isolated body of arbitrary shape is immersed in a fluid flowing about it. The fluid is incompressible with constant material properties. Viscous dissipation and radiative transport are presumed negligible. The temperature distribution in this flow field is governed by the energy equation

$$\alpha\nabla^2 T - \mathbf{v}\cdot\nabla T = \frac{\partial T(t)}{\partial t} \tag{1}$$

The temperature distribution is T in this "forward" flow. α is the thermal diffusivity, t is the time and $\mathbf{v}$ is the velocity distribution in the forward flow. A different distribution $\overline{T}$ results in the "reversed" flow and is governed by

$$\alpha\nabla^2\overline{T} + \mathbf{v}\cdot\nabla\overline{T} = \frac{\partial\overline{T}(t)}{\partial t} \tag{2}$$

In this reversed flow, the fluid velocity is everywhere equal and opposite to that of the forward flow.

The surface of the body is at a uniform temperature T_B while the fluid is initially everywhere at temperature zero. We seek to prove that up to any time t, the total heat transferred from the body is the same for the two flow directions. In this event, the instantaneous overall heat transfer rate must, at any time, be identical for the two flow directions. As in the steady transport, we shall be able to prove this under somewhat more general conditions on the body surface.

At any time σ, taken to be less than t, equation (1) is

$$\alpha\nabla^2 T - \mathbf{v}\cdot\nabla T = \frac{\partial T(\sigma)}{\partial\sigma} \tag{3}$$

while at time $t - \sigma$, the equivalent expression for the reversed flow, equation (2), is

$$\alpha\nabla^2\overline{T} + \mathbf{v}\cdot\nabla\overline{T} = -\frac{\partial\overline{T}(t-\sigma)}{\partial\sigma} \tag{4}$$

We shall hold t constant throughout the argument.

Multiplying equation (3) by $\overline{T}(t-\sigma)$ and equation (4) by $T(\sigma)$ and then subtracting produces

---

[1] Work performed under the auspices of the U. S. Department of Energy by the Lawrence Livermore National Laboratory under contract number W-7405-ENG-48.

This report was prepared as an account of work sponsored by the United States Government. Neither the United States nor the United States Department of Energy, nor any of their employees, nor any of their contractors, subcontractors, or their employees, makes any warranty, express or implied, or assumes any legal liability or responsibility for the accuracy, completeness or usefulness of any information, apparatus, product or process disclosed, or represents that its use would not infringe privately-owned rights.

Reference to a company or product name does not imply approval or recommendation of the product by the University of California or the U. S. Department of Energy to the exclusion of others that may be suitable.

Contributed by the Heat Transfer Division for publication in the JOURNAL OF HEAT TRANSFER. Manuscript received by the Heat Transfer Division May 1, 1980.

Copyright © 1981 by ASME

Downloaded 20 Dec 2010 to 194.27.225.72. Redistribution subject to ASME license or copyright; see http://www.asme.org/terms/Terms_Use.cfm

$$\alpha[\overline{T}(t-\sigma)\nabla^2 T(\sigma) - T(\sigma)\nabla^2\overline{T}(t-\sigma)] - \mathbf{v}\cdot[\overline{T}(t-\sigma)\nabla T(\sigma) + T(\sigma)\nabla\overline{T}(t-\sigma)] = \overline{T}(t-\sigma)\frac{\partial T(\sigma)}{\partial\sigma} + T(\sigma)\frac{\partial\overline{T}(t-\sigma)}{\partial\sigma} \quad (5)$$

Following rearrangement and the application of some simple identities, equation (5) becomes

$$\nabla\cdot\{\alpha[\overline{T}(t-\sigma)\nabla T(\sigma) - T(\sigma)\nabla\overline{T}(t-\sigma)]\} - \mathbf{v}\cdot\nabla[\overline{T}(t-\sigma)T(\sigma)] = \frac{\partial}{\partial\sigma}[\overline{T}(t-\sigma)T(\sigma)] \quad (6)$$

Since the fluid is incompressible

$$\nabla\cdot\mathbf{v} = 0 \quad (7)$$

equation (6) can be further simplified. Application of the vector identity

$$\mathbf{v}\cdot\nabla\phi = \nabla\cdot(\mathbf{v}\phi) - \phi\nabla\cdot\mathbf{v} \quad (8)$$

where ϕ is a scalar field, then yields

$$\nabla\cdot\{\alpha[\overline{T}(t-\sigma)\nabla T(\sigma) - T(\sigma)\nabla\overline{T}(t-\sigma)] - \mathbf{v}\overline{T}(t-\sigma)T(\sigma)\} = \frac{\partial}{\partial\sigma}[\overline{T}(t-\sigma)T(\sigma)] \quad (9)$$

Now, we integrate equation (9) over the fluid volume bounded internally by the body surface B and externally by a spherical surface S centered about the body. We also integrate with respect to time from the start of the process to time t later. Application of the divergence theorem allows this to be written

$$\int_0^t\iint_{B+S}\{\alpha[\overline{T}(t-\sigma)\nabla T(\sigma) - T(\sigma)\nabla\overline{T}(t-\sigma)] - \mathbf{v}\overline{T}(t-\sigma)T(\sigma)\}\cdot\hat{n}\,dA\,d\sigma = \int_0^t\iiint_V\frac{\partial}{\partial\sigma}[\overline{T}(t-\sigma)T(\sigma)]\,dV\,d\sigma \quad (10)$$

$\hat{n}$ is an outward drawn unit normal on the fluid surfaces. It extends into the body B and out of the spherical shell. A and V are the surface area and volume of the region.

Since both temperature distributions are everywhere continuous for all time greater than zero and continuous in the limit as time approaches zero, we can interchange the order of integration for the right side of equation (10). Having done this, we integrate immediately with respect to time and find that the integral vanishes by virtue of the uniform initial condition. Separating the surface integrals on the left side of equation (10) and rearranging gives

$$\int_0^t\iint_B\{\alpha[\overline{T}(t-\sigma)\nabla T(\sigma) - T(\sigma)\nabla\overline{T}(t-\sigma)] - \mathbf{v}\overline{T}(t-\sigma)T(\sigma)\}\cdot\hat{n}\,dA\,d\sigma = -\int_0^t\iint_S\{\alpha[\overline{T}(t-\sigma)\nabla T(\sigma) - T(\sigma)\nabla\overline{T}(t-\sigma)] - \mathbf{v}\overline{T}(t-\sigma)T(\sigma)\}\cdot\hat{n}\,dA\,d\sigma \quad (11)$$

Let us examine the integral over the body surface. If the body surface is at a uniform constant temperature T_B for all time and if there is no net fluid source or sink within the body, i.e.,

$$\iint_B \mathbf{v}\cdot\hat{n}\,dA = 0 \quad (12)$$

we simply have

$$\alpha T_B\int_0^t\iint_B[\nabla T(\sigma) - \nabla\overline{T}(t-\sigma)]\cdot\hat{n}\,dA\,d\sigma \quad (13)$$

on the left side of equation (11). The body could, for example, be porous and the flow would still satisfy equation (12).

Additionally, the same simplification can be obtained if regions of the body surface are insulated and impermeable but not necessarily at temperature T_B. Such regions make no contribution to the left side of equation (11). As the normal components of the fluid velocity and temperature gradient are both zero, they make no contribution to the heat transfer. These boundary conditions on the body are identical to those described by Brenner [1] in his analysis of steady transport.

Substituting expression (13) into equation (11) and multiplying by $\rho C_p/T_B$ gives

$$\int_0^t\iint_B k[\nabla T(\sigma) - \nabla\overline{T}(t-\sigma)]\cdot\hat{n}\,dA\,d\sigma = -T_B{}^{-1}\int_0^t\iint_S\{k[\overline{T}(t-\sigma)\nabla T(\sigma) - T(\sigma)\nabla\overline{T}(t-\sigma)] - \rho C_p\mathbf{v}\overline{T}(t-\sigma)T(\sigma)\}\cdot\hat{n}\,dA\,d\sigma \quad (14)$$

ρ is the density, C_P the specific heat at constant pressure and k is the thermal conductivity of the fluid.

Remembering that $\hat{n}$ is an inward normal to the body, we note that the net heat transferred from the body during the time interval from 0 to t is, for the forward flow,

$$Q = \int_0^t\iint_B k\nabla T(\sigma)\cdot\hat{n}\,dA\,d\sigma \quad (15)$$

while, for the reversed flow,

$$\overline{Q} = \int_0^t\iint_B k\nabla\overline{T}(t-\sigma)\cdot\hat{n}\,dA\,d\sigma \quad (16)$$

We thus have an expression for the difference between the heat transferred for the two flow directions in terms of the solutions on surface S, a surface which we shall let recede from the body. From equations (14, 15) and (16),

$$Q - \overline{Q} = T_B{}^{-1}\int_0^t\iint_S\{k[-\overline{T}(t-\sigma)\nabla T(\sigma) + T(\sigma)\nabla\overline{T}(t-\sigma)] + \rho C_p\,\mathbf{v}\overline{T}(t-\sigma)T(\sigma)\}\cdot\hat{n}\,dA\,d\sigma \quad (17)$$

It remains only to show that the integral over surface S vanishes. To do this, the radius of the spherical surface is allowed to increase without bound, thus permitting us to examine only the asymptotic behavior of the transport at large distances from the body.

Sufficiently far from the body, at time t and all prior times, the (positive definite) temperatures and the absolute values of the temperature gradients are less than their values in the subsequent steady state. This constraint will permit us to show that each of the three integrated terms on the right side of equation (17) vanishes as the spherical radius r of the surface increases without bound.

Taking the first of these terms and using the subscript f to denote the ultimate steady-state, we have

Nomenclature

A = area
C_p = specific heat at constant pressure
c = concentration
D = molecular diffusivity
K = reaction rate constant
k = thermal conductivity
$\hat{n}$ = unit normal vector
Q = heat transferred from body
r = radius of spherical surface
T = temperature
t = time
U = fluid speed relative to translating body
V = volume bounded by surfaces B and S
$\mathbf{v}$ = velocity
$\hat{z}$ = unit vector in direction in uniform streaming
α = thermal diffusivity
θ = polar angle
ρ = density
σ = time

Subscripts

B = body surface
f = final steady state
S = spherical surface

Downloaded 20 Dec 2010 to 194.27.225.72. Redistribution subject to ASME license or copyright; see http://www.asme.org/terms/Terms_Use.cfm

$$\overline{T}(t-\sigma) \leq \overline{T}_f \tag{18}$$

and

$$|\nabla T(\sigma)\cdot\hat{n}| \leq |\nabla T_f\cdot\hat{n}| \tag{19}$$

for sufficiently large r. Thus

$$\overline{T}(t-\sigma)|\nabla T(\sigma)\cdot\hat{n}| \leq \overline{T}_f|\nabla T_f\cdot\hat{n}| \tag{20}$$

in this region.

We now examine the asymptotic behavior of this expression at large r. Considering first the case of a translating body, the fluid velocity far from the body approaches uniform streaming. In the frame of the body,

$$\mathbf{v} \sim U\hat{z} \text{ as } r \to \infty \tag{21}$$

where U is the speed of translation and $\hat{z}$ is a unit vector indicating the direction. Remaining terms in the velocity may be as large as o[1]; they are $O[r^{-1}]$ in a creeping flow and $O[r^{-3}]$ in potential flow. Using this outer flow and the steady form of equation (1), we find the well known [6] asymptotic relation.

$$T_f \sim \frac{\dot{Q}_f}{4\pi kr}\exp[-Ur(1-\cos\theta)/2\alpha] \text{ as } r \to \infty \tag{22}$$

A dot denotes differentiation with respect to time. θ is the polar angle measured from the $\hat{z}$ direction. Correspondingly, equation (2) yields

$$\overline{T}_f \sim \frac{\dot{\overline{Q}}_f}{4\pi kr}\exp[-Ur(1+\cos\theta)/2\alpha] \text{ as } r \to \infty \tag{23}$$

Substituting equations (22) and (23) into equation (20) gives us

$$\overline{T}(t-\sigma)|\nabla T(\sigma)\cdot\hat{n}| \leq \frac{\dot{Q}_f\dot{\overline{Q}}_f}{(4\pi kr)^2}\frac{U(1-\cos\theta)}{2\alpha}\exp(-Ur/\alpha) \text{ as } r \to \infty \tag{24}$$

$$= o[r^{-2}] \text{ as } r \to \infty \tag{25}$$

or, in fact, $o[r^{-n}]$ for arbitrary n.

In the absence of translation, $\mathbf{v}$ vanishes far from the body as it does, for example, in the electroconvective flow of [2, 3]. In this case,

$$T_f \sim \frac{\dot{Q}_f}{4\pi kr} \text{ as } r \to \infty \tag{26}$$

and

$$\overline{T}_f \sim \frac{\dot{\overline{Q}}_f}{4\pi kr} \text{ as } r \to \infty \tag{27}$$

Consequently,

$$\overline{T}(t-\sigma)|\nabla T(\sigma)\cdot\hat{n}| \leq \frac{\dot{Q}_f\dot{\overline{Q}}_f}{(4\pi k)^2 r^3} \text{ as } r \to \infty \tag{28}$$

$$= o[r^{-2}] \text{ as } n \to \infty \tag{29}$$

Obviously, the second term on the right side of equation (17) is similarly bounded for either case.

$$T(\sigma)|\nabla\overline{T}(t-\sigma)\cdot\hat{n}| = o[r^{-2}] \text{ as } r \to \infty \tag{30}$$

The final term on the right side of equation (17) is likewise bounded because the fluid velocity approaches uniform streaming in the presence of translation and approaches zero in its absence. In either case

$$|\mathbf{v}\cdot\hat{n}|\overline{T}(t-\sigma)T(\sigma) = o[r^{-2}] \text{ as } r \to \infty \tag{31}$$

Substituting equations (25) or (29, 30) and (31) into equation (17) and noting that the area of surface S is $O[r^2]$, we find that the entire integral vanishes. Accordingly, we have found that

$$Q = \overline{Q} \tag{32}$$

for any arbitrary time t. The total heat transferred up to any time is independent of the flow direction. It follows immediately that the instantaneous heat transfer rate is invariant to flow reversal.

This result need not be limited to the transport following a single step change in temperature difference between the body and the surrounding fluid. The equations governing this transport are linear. Thus, by Duhamel's theorem, the temperature solutions for a series of steps in the temperature difference may be superposed to describe any time dependent uniform body temperature. As the transport rates associated with each step are invariant to flow reversal, their sums must also be invariant. The theorem therefore holds when the body temperature T_B is not constant in time. Consequently, we also conclude that the transient temperature response of a homogeneous closed body must be invariant to flow reversal if the body is at a uniform temperature throughout.

Discussion

As intended, we have shown that the overall rate of transient heat transfer from a body with uniform surface temperature is invariant to pointwise flow reversal. This holds for bodies of arbitrary shape and asymmetric geometries and flows; symmetry is not invoked in the argument. The theorem is valid even for high Peclet number transport in which local transport rates may differ tremendously under flow reversal. It is also not limited to a step change in the temperature difference between the body and the surrounding fluid. Solutions for the response due to a series of steps in the temperature difference may be superposed to establish validity of the theorem for any time dependent body temperature.

Flow reversal is physically possible in both potential and creeping flows. Moreover, physically significant transport problems occur in creeping flow and, for low Prandtl number fluids, in the unseparated potential flow outside the viscous boundary layer. Beyond these limits, the theorem is valid and applicable even when flow reversal is not physically possible or has no physical significance. Numerical calculations of transport rates may therefore be checked against calculations for the numerically reversed flow, thus providing an unusually comprehensive global test. The theorem is valid and useful in this context for any incompressible streaming flow past a closed body at uniform temperature—regardless of the Reynolds or Prandtl numbers.

Acknowledgment

The authors wish to thank Lewis Thigpen for his careful study of the manuscript and helpful suggestions.

References

1 Brenner, H., "On the Invariance of the Heat Transfer Coefficient to Flow Reversal in Stokes and Potential Streaming Flows Past Particles of Arbitrary Shape," *Journal of Mathematical and Physical Sciences*, Vol. 1, 1967, pp. 173–179.

2 Morrison, F. A., "Transient Heat and Mass Transfer to a Drop in an Electric Field," ASME JOURNAL OF HEAT TRANSFER, Vol. 99, 1977, pp. 269–273.

3 Griffiths, S. K., and Morrison, F. A., "Low Peclet Number Heat and Mass Transfer from a Drop in an Electric Field," ASME JOURNAL OF HEAT TRANSFER, Vol. 101, 1979, pp. 484–488.

4 Chen, W. C., and Pfeffer, F., "Mass Transfer Rates with First-Order Homogeneous Chemical Reaction," *Chemical Engineering Progress Symposium Series*, No. 105, Vol. 66, 1970, pp. 109–122.

5 Brenner, H., "Invariance of the Overall Mass Transfer Coefficient to Flow Reversal during Stokes Flow Past One or More Particles of Arbitrary Shape," *Chemical Engineering Process Symposium Series*, No. 105, Vol. 66, 1970, pp. 123–126.

6 Carslaw, H. S., and Jaeger, J. C., *Conduction of Heat in Solids*, Second ed., Oxford University Press, Oxford, 1959.

APPENDIX

Extension of the theorem to mass transfer with a homogeneous first order reaction is accomplished with little change to the argument in the body of the paper. Using c to denote concentration, D to signify molecular diffusivity and with a reaction rate constant K, the concentration in the forward flow obeys

$$D\nabla^2 c - \mathbf{v}\cdot\nabla c - Kc = \frac{\partial c(t)}{\partial t} \tag{A1}$$

This relation replaces equation (1) describing the temperature distribution. For the reversed flow,

Downloaded 20 Dec 2010 to 194.27.225.72. Redistribution subject to ASME license or copyright; see http://www.asme.org/terms/Terms_Use.cfm

$$D\nabla^2\bar{c} + \mathbf{v}\cdot\nabla\bar{c} - K\bar{c} = \frac{\partial\bar{c}(t)}{\partial t} \tag{A2}$$

The boundary and initial conditions are analogous to those imposed on the temperatures.

Following the main argument through equation (5), we find that the reaction rate terms cancel in the concentration equivalent of equation (5). It remains only to note that because the reaction will deplete the concentration, the analogs to the thermal asymptotic relations are sufficient to bound the asymptotic behavior. The extension of the theorem then follows.

Downloaded 20 Dec 2010 to 194.27.225.72. Redistribution subject to ASME license or copyright; see http://www.asme.org/terms/Terms_Use.cfm

Y. Mori
Professor.

K. Hijikata
Assistant professor.

Tokyo Institute of Technology,
Meguro, Tokyo, Japan

S. Hirasawa
Researcher.

W. Nakayama
Chief researcher.

Mechanical Engineering Research Laboratory,
Hitachi Ltd.,
Tsuchiura, Ibaragi, Japan

Optimized Performance of Condensers with Outside Condensing Surfaces

The purpose of this paper is to find an optimum surface geometry of vertical condenser tubes where condensation takes place on the outer surfaces. The guiding principle on optimum condensation performance is to make the thickness of condensate liquid on the surfaces as thin as possible. A vertical tube with longitudinally parallel tiny fins is preferable because condensate is made thinner over the widest possible region. According to an analysis, there are four controlling factors for the optimum fin; sharp leading edge, gradually changing curvature of fin surface from tip to the root, wide groove between fins to collect condensate and horizontal discs attached to the tube to remove condensate. The analytical result is checked by experiments using R-113. The optimum fin shape, fin pitch and spacing of discs are found by numerical calculations for R-113 and water.

Introduction

Condensers with a highly enhanced performance are urgently required in new energy resource developments such as binary cycles in geothermal and ocean thermal plants and waste heat recovery plants. Many methods [1] for enhancing condensation heat transfer have been proposed, but few of them have been studied from the standpoint of optimization by exploiting enhancement mechanisms to the fullest extent. The purpose of this study is to investigate the optimum finned tubular condensers where vapor condenses on the outside surfaces of the tubes. Condensers of this configuration are preferable because of less pressure loss to the vapor flow. When vapor condenses on horizontal tube banks the heat transfer coefficient becomes smaller on the lower rows of the tubes due to thickening layers of condensate. Also in vertical tube condensers, the tubes have a deteriorating heat flow on the lower parts due to thickening liquid layers.

The guiding principle to develop condensers with a highly enhanced performance is to make the liquid film as thin as possible over the possibly widest condensing heat transfer surface. To realize this principle, the authors have taken up vertical tubes of which outside condensing surfaces have an array of vertical small fins and disk attachments to remove condensate from the fin surfaces before the liquid becomes too thick. Figure 1 shows a tube studied in this report. Circular disks are attached in order to remove the condensate flowing down from above and to expose new condensing surfaces below disks. The main advantages of this tube arrangements over other forms are as follows.

(1) It is possible to exploit a wider condensing surface than a horizontal tube whose lower part of the surface is covered with a pendent liquid layer. (2) Forced removal of the condensate by disks not only avoids the deterioration of heat transfer on the lower part but also prompts direct contact heat transfer between liquid drops freely falling from the disks and flowing vapor. It was reported in reference [2] that a vertical finned tube with the disks has high heat transfer coefficients about twice those on a tube without the disks. However, they did not provide a reason why or the optimum distance of the runoff disks. The present paper reports the optimizing process for the selection of the best fin shape and disk spacing, and at the same time provides full information on designing optimum condensers with outside condensing surfaces.

Condensation on Vertical Surfaces with an Array of Fins

There are many studies of condensation along finned surfaces. Among them, references [3–5] report that a heat transfer surface with many small sharp-edged fins has a very high condensation heat transfer coefficient in comparison with a smooth surface. The enhancement is found to be brought by the following mechanisms: On sharp fin tips with a very small radius of curvature, a strong surface tension aids the removal of condensate from the tips, thereby producing a very thin liquid film. In addition to this effect, the liquid layers on side surfaces of the fins are also expected to become locally very thin when the action of surface tension to bring the liquid into grooves between fins is strong enough. Condensed liquid near the tip of the fins is driven nearly horizontally towards the grooves by the surface tension and the liquid flows vertically down the grooves under gravity [5].

The effect of surface tension on condensation on a finned surface was first recognized by Gregorig [6]. However, his work may be justified near the fin tip as his analysis is made under the condition of thin film thickness; therefore it cannot be applicable to the region between the tip and the trough and the trough region where the film is very thick. Pertaining to the fundamental equation, the equation reduced by Gregorig is the differential equation of the second order. The fundamental equation introduced in this paper of the fourth order which is reported for the first time pertains to the film condensation around fins. This big difference of the equations is caused from the assumption of thin film made in the Gregorig analysis, and the authors would like to emphasize that the present analysis uses much less restrictive assumptions than Gregorig's analysis; therefore, the results are applicable to fins having shapes of much wider variety and to more various conditions where the thickness of film is thick in or near the trough than the one considered in the previous litera-

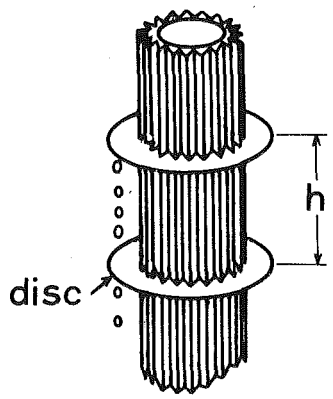

Fig. 1 Vertical tube

Contributed by the Heat Transfer Division for publication in the JOURNAL OF HEAT TRANSFER. Manuscript received by The Heat Transfer Division February 14, 1980.

Copyright © 1981 by ASME

Downloaded 20 Dec 2010 to 194.27.225.72. Redistribution subject to ASME license or copyright; see http://www.asme.org/terms/Terms_Use.cfm

ture. Besides, Gregorig's optimum contour is difficult to manufacture due to the restriction of thin film thickness over the whole surface, so we have chosen three configurations as representative of practical importance and easy manufacturing.

Edwards, et al. [7] proposed a condensation model of a heat transfer surface with triangular fins on the assumption of liquid film attaching to the tip of fins with a contact angle. The effect of a locally thin condensate film on the side of fins was not considered in their calculations. Fujii, et al. [8] analyzed condensation on a vertical surface with sinuous fins, but also did not take the effect of locally thin film on fin surfaces into account. Panchel, et al. [9] also analyzed a sinuous fin, but the surface temperature of the fin was assumed to be constant. Recently, Webb [10] studied the optimization of a fluted surface, but he made the same approximation as Gregorig's. Surface tension of the condensate in the trough induces a strong suction flow near the side surface of the fin. The analysis of Gregorig type [10] does not include this side surface effect, which plays an important role in enhancement performance, and is unable to accurately predict the overall performance of enhanced condensation surface. In reference [10], the temperature of the fluted surface was assumed to be constant. So, the conduction effect of fin materials could not be investigated even though it is very important when the fin has an enhanced performance and high surface heat flux. Variation of the condensate film thickness and variation of the local heat transfer coefficient in the vertical direction are newly analyzed in our paper. This point is very important in contrasting the contributions of the present work and reference [10]. The analysis by reference [10] cannot make analyses of performance of runoff disks and of optimization of a spacing of the disks, because the condensate is pulled up by capillary force in the troughs in the neighborhood above the disks. This is an important phenomenon to be taken into account to find an optimum spacing of the runoff disks. Optimization of the disk spacing was totally out of scope of reference [10].

Figures 2, 3 and 4 are the cross-sectional views of three representative contour of fins which are used in analyses in the present paper. Figure 2 shows the triangular fin with a small leading edge radius. Figure 3 shows the wavy fin with rather larger radii at the leading edge and the groove bottom. Figure 4 shows the fin having a sharp leading edge and a wide flat-bottomed groove which should hold more condensate than the other fins.

Fundamental Equations

In comparison with the small height and pitch of fins, the radius of the tube is large enough to be neglected in analyses, so that we will discuss a vertical heat transfer surface on which fins are provided. The vertical length of the surface is taken as h corresponding to the spacing of disks which remove condensate from the condensing surface. As the analyses on the three fins shown in Figs. 2–4 are similar, only the analysis on the triangular fin in Fig. 2 is shown in detail.

The geometry of the surface is specified by the following three factors: r_0 = fin edge radius of curvature, p = fin pitch and b = fin height. e is the thickness of condensate at the bottom of the groove.

In the analysis on the triangular fin shown in Fig. 2, the coordinates are x in the gravitational direction, y in the horizontal direction and z in the direction normal to the fin surface. The half tip angle θ of fin is given by

$$\theta = \tan^{-1}(p/2b) \tag{1}$$

The side surface of the fin is divided into three regions for the analysis: These are the leading edge region (region I, $y = 0 \sim a$), bottom region (region III, $y > c$) and intermediate region (region II, $y = a \sim c$). Adopting the assumption in our previous report [5], the leading edge of the fin forms a parabola in region I which is smoothly connected with the surface in region II. So it is convenient to employ parabolic coordinates (ξ,η) to analyze region I. The cross-sectional contour of the fin is assumed by the parabola of η = s and the leading edge radius of the fin is given by $r_0 = s^2$. The boundary separating region I and II is given by $\xi = s/\tan\theta$ where the angle of inclination of the parabola $\eta = s$ to the line $\eta = 0$ is θ. The y coordinate at $\xi = s/\tan\theta$ is $a = s^2/(2 \sin\theta \tan\theta)$.

The following assumptions are made in the analysis.

1 Vapor is saturated and interfacial shear between liquid and vapor is negligible.

2 Temperature distribution due to thermal conduction in the fin is approximately one-dimensional, that is, temperature varies from the root toward the tip, but it is constant in the direction normal to the symmetric line (AB in Fig. 2).

3 In momentum and energy equations, inertial and convective terms are small compared with viscous, gravity and conductive terms as made in the Nusselt analysis.

4 Variation of condensate flow rate in the gravitational direction in regions I and II and variation of the curvature of liquid film surface in the gravitational direction in regions I and II are much smaller than those in the horizontal direction along the fin surface.

5 As the liquid film is thin in regions I and II, changes in velocity and temperature along the surface are smaller compared with those in the direction normal to the surface. Hence, the boundary layer approximation is applicable.

6 Even at the top of leading edge, there always exists a film of finite thickness.

7 The contour of liquid-vapor interface in region III is largely determined by surface tension and is approximated by a circular arc.

These assumptions are justified as follows. The analytical result obtained by use of R-113 and a copper triangular fin of h = 50mm, p = 0.7mm and b = 0.61mm for ΔT = 10K is used as a representative case for the assessment.

This analysis includes thermal conduction effect in the fin. In re-

Nomenclature

a = length of region I (m)
b = depth of groove (m)
c = length of regions I and II (m)
d_h = hydraulic radius of liquid film in region III (m)
e = thickness of condensate liquid at groove bottom (m)
G = liquid flow rate in region III (m^3/s)
g = acceleration of gravity (m/s^2)
h = spacing of disks or vertical length of heat transfer surface (m)
L = specific latent heat (J/kg)
p = pitch of fin (m)
r_e = radius of liquid film surface in region III (m)
r_0 = radius of fin leading edge (m)
s = value of η at fin surface ($m^{1/2}$)
T = temperature (K)
T_{w1} = temperature at fin root (K)
t = thickness of the fin at the root (m)
u = velocity in x direction in region III (m/s)
V = liquid volumetric flow rate (m^2/s)
x = coordinate in gravitational direction (m)
y = coordinate in horizontal direction along fin surface (m)
z = coordinate in horizontal direction to fin surface (m)
α = average heat transfer coefficient based on the projected area (W/m^2K)
ΔT = temperature difference between vapor and condensing surface (K)
δ = thickness of condensate film (m)
δ_η = thickness of condensate film in η coordinate ($m^{1/2}$)
ϵ = length of free surface in region III (m)
θ = half tip angle of fin
λ = thermal conductivity (W/mK)
μ = viscosity (kg/ms)
ρ = density (kg/m^3)
ω = distance from fin tip towards the root (m)
σ = surface tension (N/m)
ξ = parabolic coordinate ($m^{1/2}$)
η = parabolic coordinate ($m^{1/2}$)

Subscripts

c = point bounding regions II and III
s = saturated vapor
w = fin surface
1 = condensate

Downloaded 20 Dec 2010 to 194.27.225.72. Redistribution subject to ASME license or copyright; see http://www.asme.org/terms/Terms_Use.cfm

gard to assumption (2), a detailed calculation of two-dimensional thermal conduction in an equilateral triangular fin shows that the maximum temperature variation in the direction normal to the symmetric line is less than 8 percent of that along the symmetric direction. As for assumption (3), the numerical result obtained under the condition cited above shows

$$\left(\frac{\text{inertia term}}{\text{viscous term}}\right)_{\max} = 0.01, \quad \left(\frac{\text{convective term}}{\text{conductive term}}\right)_{\max} = 0.08.$$

As for assumption (5), the result shows $(\partial\delta/\partial y)_{\max} = 0.06$, therefore, the changes in velocity and temperature in the y direction are less than about 6 percent of those in the z direction. Pertaining to assumption (6), the radius of curvature at the leading edge should be finite, and the finite thickness of liquid film is physically acceptable. Assumption (7) will be discussed later.

As explained in our previous report [5], the equation to determine the thickness of liquid film in region II is written as

$$\frac{\sigma}{3\mu}\frac{d}{dy}\left[\delta^3\frac{d}{dy}\left(\frac{d^2\delta}{dy^2}\Big/\left\{1+\left(\frac{d\delta}{dy}\right)^2\right\}^{3/2}\right)\right] = \frac{\lambda_1(T_s - T_w)}{\rho L\delta} \tag{2}$$

The left side is the differentiation of the flow rate drawn to the y direction by surface tension and the right side represents condensing rate.

According to assumption (2), the conduction equation in the fin is

$$\lambda_w \frac{d}{dy}\left[\frac{dT_w}{d(y\cos\theta)}\, y\sin\theta\right] = -\frac{\lambda_1(T_s - T_w)}{\delta} \tag{3}$$

Equation (2) is written in terms of the parabolic coordinate [4].

$$\frac{\sigma}{3\mu}\frac{1}{\sqrt{\xi^2+s^2}}\frac{d}{d\xi}\left[\delta_\eta{}^3\left\{\sqrt{\xi^2+s^2}\frac{d^3\delta_\eta}{d\xi^3} - \frac{3\xi^2}{(\xi^2+s^2)^{3/2}}\frac{d\delta_\eta}{d\xi} + \frac{3\xi(s+\delta_\eta)}{(\xi^2+s^2)^{3/2}}\right\}\right] = \frac{\lambda_1(T_s - T_w)}{\rho L\sqrt{\xi^2+s^2}\delta_\eta} \tag{4}$$

where δ_η is film thickness expressed by η coordinate. Equation (3) is also written as

$$\frac{\lambda_w s}{\sqrt{\xi^2+s^2}}\frac{d^2T_w}{d\xi^2} = -\frac{\lambda_1(T_s - T_w)}{\sqrt{\xi^2+s^2}\delta_\eta} \tag{5}$$

The radius of circular arc in region III is given from the geometry of the groove as

$$r_e = \frac{(e\sin\theta - \delta_c)^2 + (e\sin\theta\tan\theta + \epsilon/\cos\theta)^2}{2\epsilon + 2\delta_c\sin\theta} \tag{6}$$

where δ_c is the thickness of liquid film at $y = c$, and ϵ is the length of

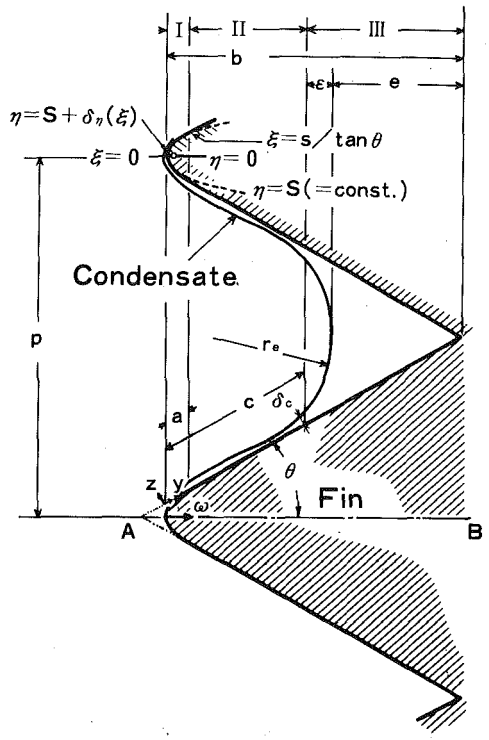

Fig. 2 Triangular fin

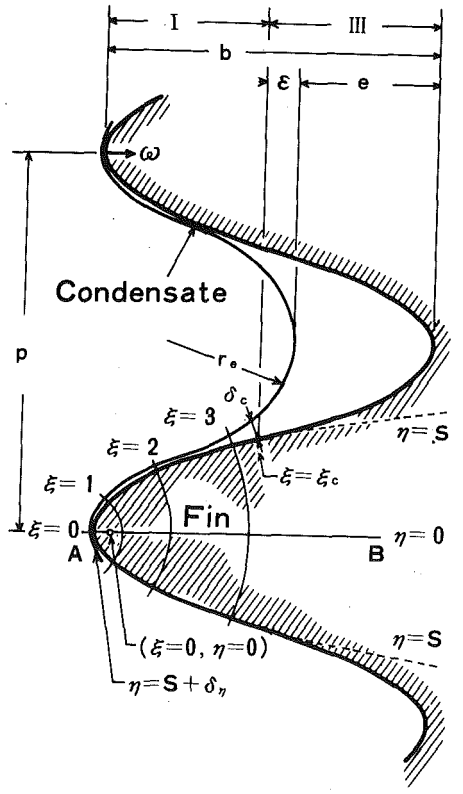

Fig. 3 Wavy fin

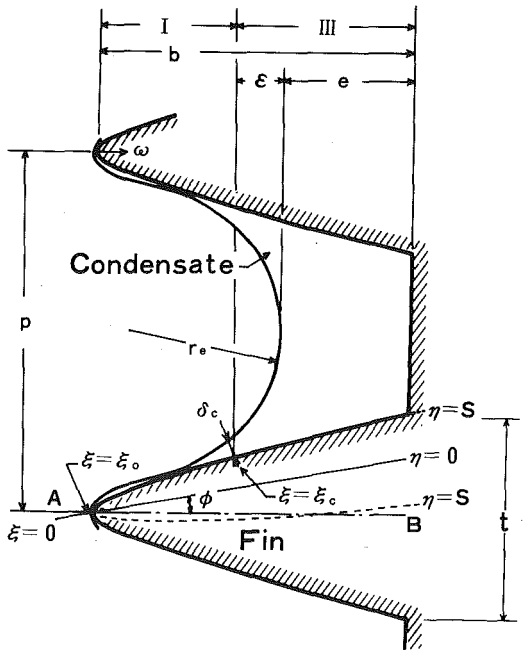

Fig. 4 Flat bottomed groove

Downloaded 20 Dec 2010 to 194.27.225.72. Redistribution subject to ASME license or copyright; see http://www.asme.org/terms/Terms_Use.cfm

free surface in region III.

In reference to Fig. 2, ϵ and e are related to c as

$$\epsilon = \frac{(b - c\cos\theta)\{1 - \sin(30\text{ deg} + \theta)\}}{(1/\sin\theta) - \sin(30\text{ deg} + \theta)} \tag{7}$$

$$e = b - c\cos\theta - \epsilon \tag{8}$$

by matching the slopes of the film surfaces at $y = c$ and taking them as tan 30 deg. The difference of the results between taking them as tan 30 deg and tan 45 deg is about 3 percent. The fact that a slight change in the contour of region III gives little effect on the results proves the propriety of assumption (7).

The liquid film is thick in region III, and the liquid velocity in this region in the horizontal direction is small compared with that in the gravitational direction. Therefore, the force balance is maintained between viscous force and gravity, and we have

$$\mu\left(\frac{\partial^2 u}{\partial y^2} + \frac{\partial^2 u}{\partial z^2}\right) + \rho g = 0 \tag{9}$$

where u is the velocity in the gravitational direction. The volumetric flow rate G in region III is obtained for a given e by integrating the above equation using a finite element method. Then the following relation is obtained for an equilateral triangular fin.

$$G = 0.0212\,\rho\, g e^4/\mu. \tag{10}$$

The boundary conditions are

$$\xi = 0: \quad \frac{d\delta_\eta}{d\xi} = 0, \quad \frac{d^3\delta_\eta}{d\xi^3} = 0, \quad \frac{dT_w}{d\xi} = 0, \tag{11}$$

$$\xi = s/\tan\theta, \quad y = a: \quad \delta = \sqrt{\xi^2 + s^2}\,\delta_\eta,$$

$$\frac{d\delta}{dy} = \tan\left[\tan^{-1}\left\{\frac{\delta_\eta + s + \xi(d\delta_\eta/d\xi)}{\xi - (s + \delta_\eta)(d\delta_\eta/d\xi)}\right\} - \theta\right],$$

$$\frac{d^2\delta}{dy^2} = \left[\{\xi^2 + (\delta_\eta + s)^2\}\frac{d^2\delta_\eta}{d\xi^2} + \left\{\xi - (s + \delta_\eta)\frac{d\delta_\eta}{d\xi}\right.\right.$$
$$\left.\left. + \xi\left(\frac{d\delta_\eta}{d\xi}\right)^2\right\}\frac{d\delta_\eta}{d\xi} - s - \delta_\eta\right] \Big/ \left\{\xi - (s + \delta_\eta)\frac{d\delta_\eta}{d\xi}\right\}^3,$$

$$\frac{d}{dy}\left[\left(\frac{d^2\delta}{dy^2}\right) \Big/ \left\{1 + \left(\frac{d\delta}{dy}\right)^2\right\}^{3/2}\right] = \frac{1}{\xi^2 + s^2}\frac{d^3\delta_\eta}{d\xi^3}$$
$$- \frac{3\xi^2}{(\xi^2 + s^2)^3}\frac{d\delta_\eta}{d\xi} + \frac{3\xi(s + \delta_\eta)}{(\xi^2 + s^2)^3} \tag{12}$$

$$y = c: \quad \delta = \delta_c,$$

$$\frac{d\delta}{dy} = \tan\left[\sin^{-1}\{\cos\theta - \epsilon(2\cos\theta - 1)/[r_e(2 - 2\sin\theta - \cos\theta)]\}\right],$$

$$\left(\frac{d^2\delta}{dy^2}\right) \Big/ \left\{1 + \left(\frac{d\delta}{dy}\right)^2\right\}^{3/2} = \frac{1}{r_e}, \tag{13}$$

$$\frac{\sigma}{3\mu}\left[\delta^3\frac{d}{dy}\left\{\left(\frac{d^2\delta}{dy^2}\right) \Big/ \left[1 + \left(\frac{d\delta}{dy}\right)^2\right]^{3/2}\right\}\right] = V_c, \tag{14}$$

$$G = 2\int_0^x V_c\,dx \tag{15}$$

$$\omega = b;$$

$$T_w = T_{w1} \tag{16}$$

where ω is the distance from fin tip to the root, T_{w1} is the temperature of the fin at the root and r_e is calculated from equation (6) which contains the information such as e and ϵ about the geometry of the trough. The analysis on the other fins (Figs. 3 and 4) can be made similarly. Equation (11) expresses the symmetry condition at the leading edge of the fin. Equation (12) expresses that film surface contours in regions I and II are smoothly connected with the third derivative at the matching location of both regions. Equation (13) expresses that the contours in regions II and III are smoothly connected with the second derivative. Equations (14) and (15) express that the liquid flow rate in the x direction in region III is equal to the total volume of the liquid flowing into region III from region II.

Average heat transfer coefficient α is obtained from condensate flow rate $G_x = h$ leaving the groove as

$$\alpha = \frac{\rho L G_{x=h}}{hp(T_s - T_{w1})} \tag{17}$$

Equations (2–5) are integrated by the Runge-Kutta method with the boundary conditions (11–14) and (16). The calculation is that values of δ_c and V_c at $y = c$ are corrected iteratively so as to satisfy the boundary condition (11) at $\xi = 0$ within following accuracy range.

$$\left|\frac{d\delta_\eta}{d\xi}\right| < 10^{-4}, \quad \left|\frac{\sigma}{3\mu}s\delta_\eta{}^3\frac{d^3\delta_\eta}{d\xi^3}\right| < 10^{-8}$$

As the result the relation between e and V_c is obtained. With that relation and equation (10), equation (15) is integrated numerically and heat transfer coefficient α is obtained by equation (17). Grid spacings in the numerical calculation are taken as

$$\Delta x = 5\text{ mm}$$

$$\Delta y = (c - a)/40, \quad \Delta\xi = s/(10\tan\theta)$$

The error in the resultant average heat transfer coefficient α is estimated to be within 3 percent.

At points a little above the disk which removes the condensate from the condensing surface, the condensate is pulled up by capillary action and fills fin grooves. In this region, force balance is maintained by surface tension and gravity and equation (18) is used.

$$\sigma\frac{d}{dx}\left(\frac{1}{r_e}\right) + \rho g = 0 \tag{18}$$

The contour of wavy fins shown in Fig. 3 is assumed to consist of two parabolas forming the leading edge part and the groove bottom. The whole shape of slender fins shown in Fig. 4 is assumed to be a parabola directly connected with the flat bottom. Therefore, both analyses are made in parabolic coordinates that are similar to the analyses in region I of the triangular fin.

Numerical solutions to the above equations enable parametric surveys to find the optimum geometry of fins for a specified fluid and working condition. Prior to optimizing analysis, the proof of the adequacy of the flow model and analysis described above is made by experiments which will be explained next.

Experiments to Prove the Theory

One of the purposes of this paper is to find the fin configuration that produces the highest heat transfer performance for a given vertical length of the condenser surface. From numerous possible fin configurations and considering thermal conduction effect which is very important to fins of high performance and heat flux, the authors have

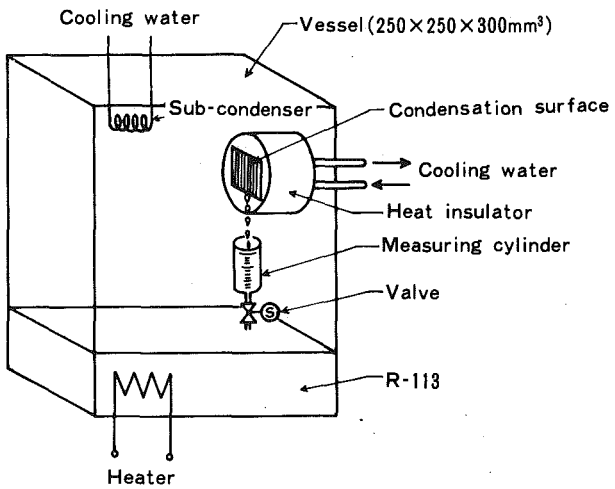

Fig. 5 Experimental apparatus

Downloaded 20 Dec 2010 to 194.27.225.72. Redistribution subject to ASME license or copyright; see http://www.asme.org/terms/Terms_Use.cfm

chosen three configurations as representative ones of practical importance. The choice is thought to be rational in view of the existing manufacturing techniques, and the analysis of heat transfer on these fins focussing on optimizing condensation preformance should be contrasted to the previous ones [10] that considered only fluted (sinsoidally continuous) surfaces under condition of thin film thickness over the whole fin surface.

Equilateral triangular fins manufactured with high precision were used in experiments, to prove the adequency of the flow model and the analysis based on the fundamental differential equation of the fourth order and to make an accurate comparison between theory and experiments. Based on the consideration mentioned above a vertical surface of 50mm height was tested. As the fin size is much smaller than the width and height of the tested surface, the tested surface well simulates the outside surface of a vertical condenser tube with tiny fins.

The sketch of the experimental apparatus is shown in Fig. 5. The test surface, the heater to generate vapor and the sub-condenser were set in a sealed acrylic vessel. The vertical heat transfer surface was attached to a backing copper block. The block was cooled by water from its back and thermally insulated by a surrounding ethylene tetrafluoride (Teflon). The liquid condensed on the test surface was gathered by a special trough (not shown in the figure) and poured into a measuring cylinder. The magnetic valve underneath the cylinder closed the outlet of the cylinder, so that the condensation rate was measured by the rise of liquid level in the cylinder with a stop watch. Average condensation heat flux on the heat transfer surface was then found by dividing the rate of latent heat flow by the projected area of the test surface (50×50 mm^2). Care was taken to purge noncondensable gases before every run of the experiment.

Vapor temperature T_s was measured by five copper-constantan thermocouples of 0.2mm in diameter. Vapor temperature in the vessel was found constant within 0.1K. The temperature difference ΔT and the heat transfer coefficient α are defined as $\Delta T = T_s - T_{w1}$ and $\alpha = q/\Delta T$, respectively. Here T_{w1} is the averaged temperature at the fin root, and q is the heat flux. In order to find T_{w1}, temperatures of the copper block at the points 2mm behind fin tips were measured by thermocouples of 0.2mm in diameter. They were set at several positions such that the one at the center, and others at the upper, lower, left and right locations. Reading of these thermocouples were considered to yield the averaged temperature at the surface 2mm from the fin tip. Meanwhile, from the measurement of condensation rate, the averaged heat flux was obtained as mentioned above. From these averaged temperature and heat flux, the temperature at the fin root was calculated taking thermal conduction in the copper block into account, and this was defined as T_{w1}.

The condensation rate at the sub-condenser was controlled to maintain constant temperature, and the vapor generation rate by the heater was maintained constant. In the analysis the fin root temperature is assumed constant, but the wall temperature of the test surface was found to vary in the vertical direction. The local temperature difference ΔT slightly increased in the gravitational direction and was about 0.8 times as large as the mean value at the upper part of the surface. Average heat transfer coefficient α of such surface is estimated to vary by about 5 percent from the value of the theoretical prediction. It was also attempted to find the accuracy of measurement by thermocouples, and error within 15 percent in α was found. Closer examination revealed that this was caused by tip soldering condition of thermocouples.

The equations in the previous sections are solved using the dimensions of the test surface and the physical properties of R-113 at 325K. The leading edge radius r_0, one or the most crucial factors for enhancement, was determined by microphotographic examination of the cut-out specimen as about 10^{-5} m. Figure 6 compares the predicted and experimental values of the condensation heat transfer coefficient, α, and the temperature difference ΔT. The test surface in this comparison had fins of pitch p = 1.0mm, and height b = 0.87mm. The theoretical prediction is in good agreement with the experimental data. The three additional curves are shown in Fig. 6 to emphasize the enhancement mechanism brought by surface tension. The lowest curve is Nusselt's theoretical solution of filmwise condensation on a smooth surface. The curve just above the Nusselt's solution is obtained by multiplying the Nusselt's solution by the area increase due to the fins (a factor of 2). It is obvious that the enhancement of a factor of 7 on the smooth surface cannot be explained by the increase of heat transfer area. This is caused by surface tension effects at fin tip, on side surface and at groove bottom. In order to confirm the predicted optimum spacing of runoff disks, experiments by use of vertical long finned tube with disks is under way; the results will be reported shortly.

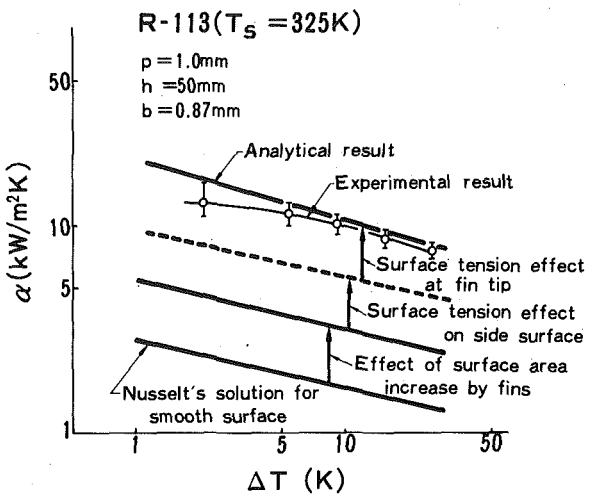

Fig. 6 Relation between ΔT and α

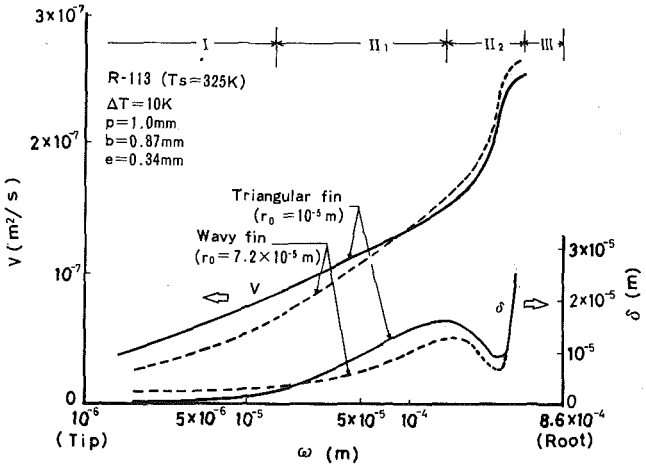

Fig. 7 Flow rate of condensate and film thickness

Optimum Fin Shape and Disk Spacing

A procedure to find the optimum fin shape which fully utilizes surface tension effect is described. Figure 7 is shown for comparison of local heat transfer rates of different fin configurations to explain enhanced heat transfer rate by utilizing the thin film region on a surface of fin, which has not been reported or drawn attention but is very important to condensation heat transfer enhancement of real fins. Figure 7 shows the variations in volumetric flow rate of condensate V and film thickness δ along the surfaces of the triangular fin (Fig. 2) and wavy fin (Fig. 3); where in case of R-113, for copper fin p = 1.0mm, b = 0.87mm, e = 0.34mm and ΔT = 10K. The abscissa ω is the distance from fin tip towards the root. The film thickness is about 0.6μm at the tip. Near the tip ($\omega < 1.5 \times 10^{-5}$ m, region I) the flow rate on the triangular fin is larger than that on the wavy fin. This

Downloaded 20 Dec 2010 to 194.27.225.72. Redistribution subject to ASME license or copyright; see http://www.asme.org/terms/Terms_Use.cfm

result is consistent with our previous report [4] and the fin with a sharp leading edge yields a thinner condensate film. On the other hand in the intermediate region ($\omega = 1.5 \times 10^{-5}$ m $\sim 1.7 \times 10^{-4}$ m, region II_1) the difference between the flow rates decreases and at $\omega = 1.7 \times 10^{-4}$ m the flow rate of wavy fin catches up to that of triangular fin. This is due to the fact that the side surface of the triangular fin is flat, while the surface tension caused by the curvature of the surface of the wavy fin controls the increase of the film thickness along the fin surface and causes enhanced condensation performance. It is concluded from this fact that a fin, the side surface curvature of which varies gradually to zero from tip to the root, is preferable. Figure 7 shows that after a swell the film thickness decreases again to become locally thin at about $\omega = 3 \times 10^{-4}$ m. This phenomenon causes an enhancement of condensation performance of the same order for both fins and the points of minimum thickness occur almost at the same distance from the leading edges because both fin grooves have almost same widths. From this discussion, the contour of the flat-bottomed fin shown in Fig. 4 is preferable. The reasons are that the leading edge radius is smaller, the curvature of side surface gradually decreases and the points of the minimum thickness of film near the boundary between regions II and III are located far away from the leading edge as the width of the groove is too large to hold the domain of thin film very widely.

Figure 8 shows the relation between average heat transfer coefficient α and spacing h of the disks, which remove condensate from the condensing surface, for both wavy and flat-bottomed copper fins using R-113. Figure 8 also shows the existence of optimum spacing for fins. This is explained as follows: For wider spacing, a lot of vapor condenses on the tube surface filling the grooves in the lower part with condensate resulting in deteriorating condensing performance. On the contrary, for narrower spacing, the tube has a smaller average heat transfer coefficient because due to surface tension in the lower part of the tube, condensate on the disk is pulled up along the grooves, and fills them resulting in deteriorating condensing performance. Figure 8 further shows that flat-bottomed fin has a performance of about 8 percent higher than that of wavy fin at the maximum α. It should be noted that the flat-bottomed fins of $t = 0.23$mm have a performance less dependent on spacing than the wavy fins. This is a very important feature from manufacturing and cost standpoints when used in a practical condenser. It should also be noted that the optimum spacing of disks is smaller than 200mm not only for R-113 but for water and therefore the liquid film is laminar and no serious wave motion of liquid surface does occur.

Figure 9 shows the relation between average heat transfer coefficient α and the fin pitch p for flat-bottomed copper fins when steam is condensed on the fins. As small grooves are easily filled up with condensate, the heat transfer coefficient is low for tubes of smaller fin pitches. On the contrary, a tube with fins of too large pitches has a smaller number of fin tips and heat transfer coefficient is low as the heat transfer enhancement effect is not utilized enough. The condenser tube provided with fins of the optimum pitch for a given fluid has the highest performance. The optimum value of fin pitch is $p = 0.5$mm for the case of Fig. 9. In this figure, data for dropwise condensation and several enhanced tubes are also shown [6, 11–14]. As reference [15] reported, a scatter of data over a range of 190 $\sim$ 350 kW/m^{2}K for dropwise condensation, two representative data [11], [12] are shown. It should be stressed that the maximum heat transfer coefficient for an optimum flat-bottomed fin is much higher than those of the enhanced tubes reported so far in [6, 13, 14] and is rather close to that of dropwise condensation with consideration of variation in data for dropwise condensation.

The procedure to find the optimum configuration for given operating conditions is summarized as follows.

1 The optimum value of one parameter is calculated using the present analysis. For example the value of the other parameters must be assumed. In the case of Fig. 8, the optimum value of the spacing of disks is calculated.

2 Using the obtained value of the parameter, for example the spacing of disks, the calculation is repeated until the optimum values for all parameters are found.

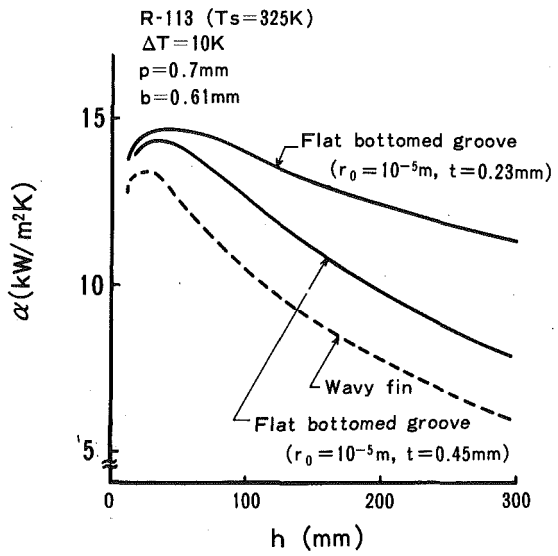

Fig. 8 Relation between h and α

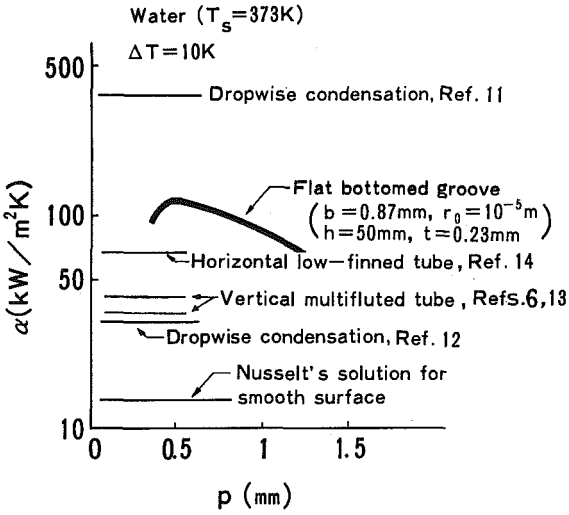

Fig. 9 Relation between p and α

This paper takes thermal conduction of copper fin into consideration. An analysis of optimum geometry for alternative fin materials and internal configuration will be reported elsewhere.

Conclusion

Theoretical analyses and experiments are carried out to investigate the optimum performance and geometry of vertical tubular condensers with small longitudinally parallel fins or the outside condensing surface. The guiding principle of this paper is to keep the film as thin as possible over the possibly widest surface by use of surface tension. Our conclusions are:

1 The experimental results for triangular fins prove the accuracy of the flow model and the analysis.

2 The optimizing study reveals that a vertical tube provided with small fins, the side surface curvature of which gradually varies from fin tip to the root, with a sharp leading edge, a flat groove bottom, and circular disks to remove condensate is most preferable as a condenser tube configuration.

3 The optimum pitch of fins and the optimum spacing of the disks are found. For example, a copper tube of 50mm in spacing of disks and of fins of 0.5mm in pitch and 0.87mm in height has ten times higher

Downloaded 20 Dec 2010 to 194.27.225.72. Redistribution subject to ASME license or copyright; see http://www.asme.org/terms/Terms_Use.cfm

average heat transfer coefficient than a smooth tube.

4 The optimized condensing surface of small flat-bottomed fins has heat transfer coefficient close to that of dropwise condensation.

References

1 Williams, A. G., Nandapurkar, S. S., and Holland, F. A., "A Review of Methods for Enhancing Heat Transfer Rates in Surface Condensers," *The Chemical Engineer,* No. 233, 1968, pp. CE 367–373.

2 Oak Ridge National Laboratory, Energy Division Annual Progress Report for Period Ending Sept. 1977, ORNL-5364, 1978.

3 Nakayama, W., Daikoku, T., Kuwahara, H., and Kakizaki, K., "High-Flux Heat Transfer Surface "THERMOEXCEL"," *Hitachi Review,* Vol. 24, No. 8, 1975, pp. 329–334.

4 Hirasawa, S., Hijikata, K., Mori, Y., and Nakayama, W., "Effect of Surface Tension on Laminar Film Condensation along a Vertical Plate with a Small Leading Radius," *Proceedings of Sixth International Heat Transfer Conference,* Vol. 2, 1978, pp. 413–418.

5 Hirasawa, S., Hijikata, K., Mori, Y., and Nakayama, W., "Effect of Surface Tension on Laminar Film Condensation (Study of Condensate Film in a Small Groove)," *Transactions of ASME,* Vol. 44, 1978, pp. 2041–2048.

6 Gregorig, R., "Hautkondensation an feingewellten Oberflächen bei Berücksichtigung der Oberflächenspannungen," *Zeitschrift für angewandte Mathematik and Physik,* Vol. V, 1954, pp. 36–49.

7 Edwards, D. K., Gier, K. D., Ayyaswamy, P. S., and Catton, I., "Evaporation and Condensation in Circumferential Grooves on Horizontal Tubes," ASME Paper No. 73-HT-251, 1973.

8 Fujii, T., and Honda, H., "Laminar Filmwise Condensation on a Vertical Single Fluted Plate," *Proceedings of Sixth International Heat Transfer Conference,* Vol. 2, 1978, pp. 419–424.

9 Panchal, C. B., and Bell, K. J., "Analysis of Nusselt-Type Condensation on a Vertical Fluted Surface," *Proceedings of the 18th National Heat Transfer Conference, Condensation Heat Transfer,* 1979, pp. 45–54.

10 Webb, R. L., "A Generalized Procedure for the Design and Optimization of Fluted Gregorig Condensing Surfaces," ASME JOURNAL OF HEAT TRANSFER, Vol. 101, 1979, pp. 335–339.

11 Takeyama, T., and Shimizu, S., "On the Transition of Dropwise-Film Condensation," *Proceedings of Fifth International Heat Transfer Conference,* Vol. 3, 1974, pp. 274–278.

12 Peterson, A. C., and Westwater, J. W., "Dropwise Condensation of Ethylene Glycol," *Chemical Engineering Progress Symposium Series,* Vol. 62, 1966, p. 135.

13 Newson, I. H., and Hodgson, T. D., "The Development of Enhanced Heat Transfer Condenser Tubing," *Desalination,* Vol. 14, 1978, p. 291.

14 Beaty, K. O., and Katz, D. L., "Condensation of Vapors on Outside of Finned Tubes," *Chemical Engineering Progress,* Vol. 44, 1948, p. 55.

15 Tanasawa, I., "Dropwise Condensation, The Way to Practical Applications," *Proceedings of Sixth International Heat Transfer Conference,* Vol. 6, 1978, pp. 393–404.

Downloaded 20 Dec 2010 to 194.27.225.72. Redistribution subject to ASME license or copyright; see http://www.asme.org/terms/Terms_Use.cfm

R. O. Warrington, Jr.
Associate Professor.

Gordon Crupper, Jr.
Research Assistant.

Mechanical Engineering Department,
Montana State University,
Bozeman, Mont. 59717

Natural Convection Heat Transfer Between Cylindrical Tube Bundles and a Cubical Enclosure

Natural convection heat transfer from a fixed array of four isothermal, heated cylinders to an isothermal, cooled cubical enclosure was experimentally investigated for both a horizontal and vertical position of the array. Included in this study are heat transfer, flow visualization, and temperature profile results for Prandtl numbers in the range of .7 to 3.1 × 10^4 and Rayleigh numbers, based on gap width, in the range of 6.3 × 10^5 to 6.9 × 10^8. Several geometric effects were observed. The vertical configuration convected less heat than the horizontal while a rotation about the vertical axis for each of these configurations had negligible effect on the overall heat transfer. The heat transfer results were correlated and compared with previous enclosure results. The heat transfer correlations fit the data with an average deviation of less than 10 percent.

Introduction

Investigation in the area of heat transfer by natural convection within enclosures has increased dramatically in the last decade. This increase has been in response to advances in electrical packaging, solar heating technology, nuclear reactor safety, and handling of nuclear waste. Most recently the demands for energy conservation have increased the importance for a better understanding of natural convection within enclosures.

Many studies have been made of natural convection from tube banks to an infinite atmosphere. Eckert and Soehngen [1] used a Zehnder-Mach interferometer to study arrays of horizontal cylinders. Eckert and Soehngen reasoned that the effect of the warmer wake around the upper tubes reduced the heat transferred since the temperature differential had decreased. Conversely, the staggered tube banks were not in the natural convection plume and an induced fluid movement of cooler air resulted in a greater heat transfer.

Lieberman and Gebhart [2] investigated the interactions between the natural convective flows of several closely spaced surfaces by using long, horizontal wires in a parallel array at several spacings and inclinations. Other investigations, which include temperature and velocity measurements about a line source, have been conducted by Brodowicz and Kierkus [3], and Forstrom and Sparrow [4]. All of the aforementioned investigators found that cool air is induced into the plume from the sides and below the source. The influence of tube spacing and array on natural convection heat transfer coefficients for horizontal tube bundles has been determined experimentally by Tillman [5]. Conclusions by Tillman indicate that tube spacing has more effect on the heat transfer than the type of array.

Natural convection from vertical tube bundles to an infinite atmosphere has been studied by Davis and Perona [6]. They utilized 42 tubes arranged in seven staggered rows of six tubes per row. Their experimental results compared favorably with theoretical results with the exception of the values in the region where the end support system had an apparent influence.

Natural convection from tube banks to an enclosure has received only limited attention. Powe, Bishop, and others [7–11] experimentally and analytically studied the heat transfer to an enclosure from a single inner geometry. In addition, Kuehn and Goldstein [12] have developed an analytical model for multiple cylinders with a cylindrical enclosure (two-dimensional problem). Their results have not been verified experimentally. The effects of an incomplete enclosure on natural convection from a vertical array of horizontal cylinders has been investigated by Marsters [13, 14].

The study of vertical tube bundles in enclosures has been mainly within the low Prandtl number range. Dutton and Welty [15] researched the effects of cylinder spacing on the heat transferred from a vertical rod bundle in a vertical cylindrical enclosure utilizing liquid mercury as the fluid medium and uniform heat flux applied to the rod bundle. Results of this study showed that there is a strong dependence on cylinder spacing.

The purposes of this study are to determine the heat transferred between a set of four isothermal, heated cylinders and an isothermal, cooled cubical enclosure, to determine the effect of the position of the tubes within the enclosure, and to compare the results with the findings of previous studies on heat transfer from single bodies to an enclosure. Four fluids and inner body positions are utilized in studying the heat transferred. The body positions include the set of cylinders in both a horizontal and vertical position and include a 45 deg rotation about the vertical axis for each position. The fluids used are air, water, 99 percent glycerin, and a Dow-Corning 20 cs fluid.

Although the heat transfer problem is coupled with a fluid-flow problem, the intent of this study is directed primarily toward the heat transfer problem. Flow visualization and temperature profiles within the enclosure were obtained to aid in evaluating the heat transfer.

Apparatus and Procedure

The apparatus for this investigation consisted of a water jacketed cubical outer body, cooling system, power source, and a four cylinder inner body with supporting elements. One outer body system was used to obtain heat transfer data and temperature profiles while a separate system was utilized to photograph flow patterns. The assembled outer body and peripheral components are shown in Fig. 1 for the heat transfer apparatus. The outer body was constructed from 1.27 cm thick, type 6061 aluminum with an inner 26.67 cm cubical chamber. This was a jacketed design consisting of a separate 3.175 cm wide rectangular channel for each face of the cube. Access to the test chamber was provided through a 25.4 cm removable circular plate on the top inner face and a completely removable outer face. A closed system consisting of a chiller, pump, and storage reservoir provided water to cool the outer body.

The flow rate of cooling water through each channel was controlled by a valve which fed four inlet and outlet ports. This arrangement allowed the temperature of each face to be controlled independently in order to achieve an isothermal outer body (to within 2 K).

The outer body used for flow visualization was nearly identical to the one previously described. The major difference was that the body was constructed from a clear polyvinyl and all portions were painted black except for a light source slot placed vertically on one side and one clear face which allowed photographs to be taken of the plane illuminated by the light source. An identical cooling system was installed and the monitoring and power devices were slaved from the heat transfer system. This system is described more fully in [11].

Contributed by the Heat Transfer Division for publication in The JOURNAL OF HEAT TRANSFER. Manuscript received by The Heat Transfer Division February 4, 1980.

Copyright © 1981 by ASME

Downloaded 20 Dec 2010 to 194.27.225.72. Redistribution subject to ASME license or copyright; see http://www.asme.org/terms/Terms_Use.cfm

The inner body design consisted of four identical copper cylinders and a supporting system which allowed it to be symmetrically centered in the enclosure in either the horizontal or vertical position. Each cylinder was 17.78 cm long, 4.12 cm o.d., and 32 cm thick. This inner body is shown in Fig. 2 in the horizontal position. A direct current power source and several sets of heat tapes on the inside of each of the cylinders provided heating for the inner body. Cylinder temperatures were determined from thermocouples imbedded in each cylinder. The inner body temperature variation never exceeded 12 percent of the temperature difference between the inner and outer bodies and averaged 4 percent for all of the data.

To obtain temperature profiles within the test chamber, the outer body was designed with nine thermocouple probe ports. These consisted of one common and four additional ports on each of two separate axes. One axis was on a vertical plane through the center of the cube while the other was the vertical plane through the edge of the cube. The five ports in each axis were at 0, 34, 80, 120, and 160 deg measured downward from the top center vertical axis of the body. Each thermocouple port had a center tube which moved through a fixed port tube. A vernier caliper attached to the thermocouple probe fixed the location of the probe within the enclosure to within 0.0025 cm. These probes are shown in Figs. 1 and 2.

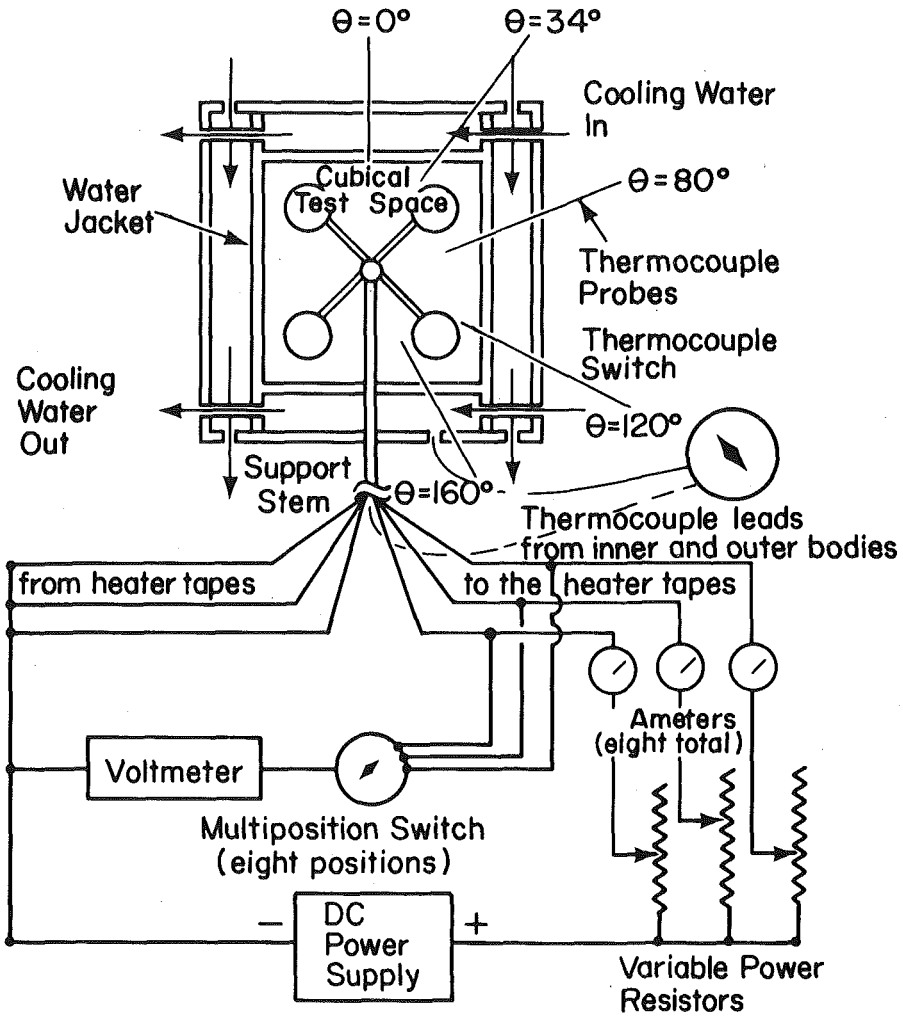

Fig. 1 Heat transfer apparatus

Nomenclature

A_c = total area of the cylinders
B = distance traveled by the boundary layer on the inner body
c_p = specific heat at constant pressure
g = acceleration of gravity, 9.81 m/s^2
Gr_x = Grashof number, $\rho^2 g\beta(T_i - T_o)x^3/\mu^2$
h = average heat transfer coefficient, $Q/A_c\Delta T$
k = thermal conductivity
L = hypothetical gap width, $R_o - R_i$
Nu_x = Nusselt number, hx/k
Pr = Prandtl number, $c_p\mu/k$
Q = heat transfer by convection
R = local position of thermocouple probe (R = 0 at cube center)
Ra_x = Rayleigh number, $\rho^2 g\beta(T_i - T_o) \times x^3 c_p/\mu k$
Ra_x^* = modified Rayleigh number, $\mathrm{Ra}_x(L/R_i)$
R_i = inner body hypothetical radius equal to the radius of a sphere having a volume equal to the volume of the inner cylinders
R_o = outer body hypothetical radius equal to the radius of a sphere having a volume equal to the volume of the outer body
$R(\Theta)$ = length from enclosing cube surface to cube center for angular position Θ
T = local temperature
T_i = temperature of the inner body
T_o = temperature of the outer body
x = any characteristic dimension
β = thermal expansion coefficient
μ = dynamic viscosity
Θ = temperature probe angular location
ρ = density

Downloaded 20 Dec 2010 to 194.27.225.72. Redistribution subject to ASME license or copyright; see http://www.asme.org/terms/Terms_Use.cfm

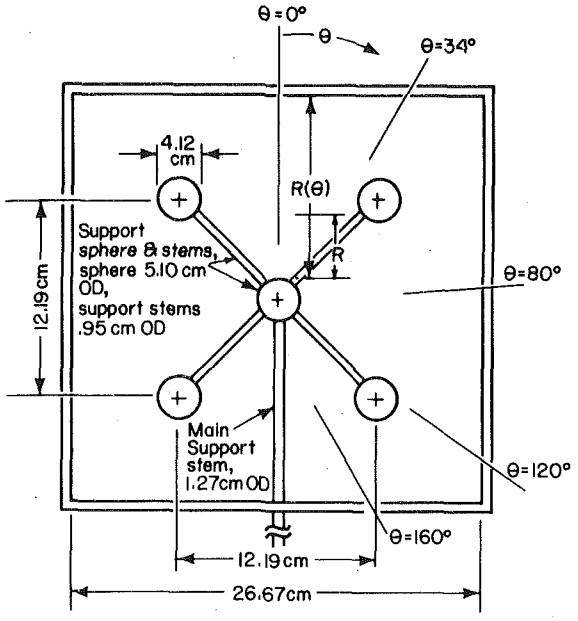

Fig. 2 Inner body geometry

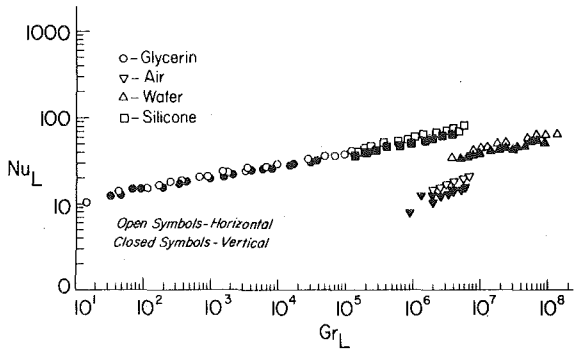

Fig. 3 Nu_L versus Gr_L for all the heat transfer data

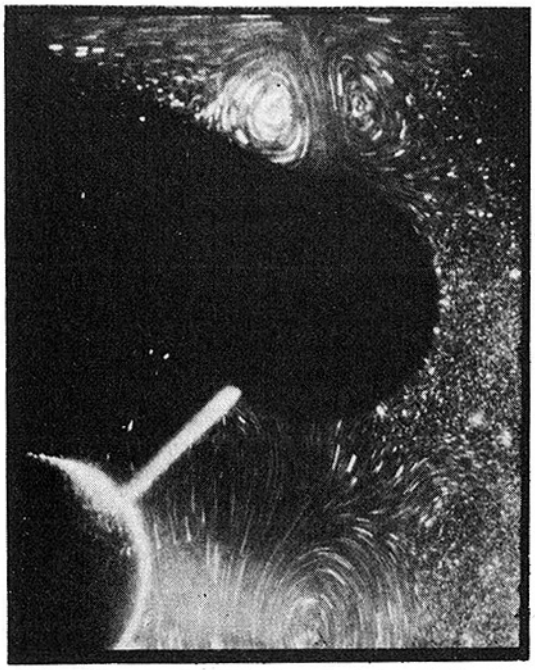

Fig. 4 Flow pattern around upper horizontal cylinder with 20 cs fluid and ΔT = 10.71 K

Sixteen fluid/geometry combinations were used to obtain 166 heat transfer data points. With one of the fluids (air, water, 20 cs silicone oil, or glycerin) in the enclosure the power was applied to the cylinders and, after equilibrium was established (approximately 2 hr), the power input, inner body temperature, and outer body temperatures were recorded. The maximum temperature difference between the inner and outer body was 90°C. Temperature profiles were obtained for selected heat transfer runs. Flow visualization results were also obtained using air and the silicone oil with tracer particles of smoke and fluorescent paint, respectively.

The heat transferred by natural convection was obtained by subtracting the radiation and conduction losses from the total power input. The conduction losses were obtained analytically assuming one-dimensional conduction down the insulated stem. Since the water, silicone oil, and glycerin are opaque to radiation, only the air data needed the radiation correction. The radiation loss was obtained by evacuating the test space (approximately 15 μm) and taking the difference between the total power input and the conduction losses.

Results

All of the fluid properties were evaluated at the arithmetic mean of the inner and outer body temperatures. The hypothetical gap width and boundary layer length which have been used in past investigations [7–11, 16] were also used as the characteristic dimensions in this investigation. The hypothetical gap width ($R_o - R_i$) is defined as the distance from an imaginary outer sphere whose volume is equal to the volume of the cube to an imaginary inner sphere whose volume is equal to the volume of all the cylinders. The boundary layer length is the distance traveled by the boundary layer on the inner body assuming no flow separation. For the cylinders in the vertical position, the boundary layer length was the cylinder height plus the diameter and for the cylinders in the horizontal position, the boundary layer length was one-half the circumference of the cylinder.

Geometric effects were found to be significant and were generally consistent among the different fluids. When the inner body was changed from the horizontal to the vertical configuration there was a significant decrease in the heat transferred. This decrease was exhibited for all fluids; however, the relative magnitude varied for each fluid. The decrease in heat transfer between the two geometries is most pronounced in the low viscosity range (air) and becomes almost negligible in the high viscosity range (glycerin) as seen in Fig. 3. The resulting average decrease was 28, 8, 8, and 2 percent for air, water, silicone, and glycerin, respectively. This suggests that the fluid viscosity tends to damp out geometric effects as has been postulated by other investigators [9, 10].

Another interesting trend of the data in Fig. 3 is that the slope decreases as the Prandtl number increases. The exponent of the Grashof number decreases from about 0.25 for air to 0.20 for water and to 0.17 for the heavy oils (20 cs and 350 cs silicone oil) and glycerin. Examination of natural convection heat transfer data from a single inner body to an enclosure [7, 9] showed that these data also exhibited this same trend. (This was evident only after examining their original Nusselt number versus Grashof number plots.) The increase in slope of the air data in Fig. 3 was not an indication of transition to turbulent flow but rather some scatter in the data at the lower Grashof numbers.

The effects of the heat transferred by the lower cylinder on the upper cylinder in the horizontal position are similar to those observed by Eckert and Soehngen [1]. The lower cylinder preheated the fluid resulting in a reduced capacity of the fluid to transfer heat as moved around the upper cylinder. When the average Nusselt number for the upper cylinder was compared to the lower, the results were 84 percent of the bottom cylinder for air, 70 percent for glycerin, 89 percent for water, and 75 percent for silicone. Only in-line cylinders were considered in this study.

Since each cylinder had two sets of heater tapes, one set on the upper half (upper half refers to the cylinder in its vertical position) and the other set on the lower half, a similar comparison was available for the cylinders in the vertical position. The resulting average Nusselt

Downloaded 20 Dec 2010 to 194.27.225.72. Redistribution subject to ASME license or copyright; see http://www.asme.org/terms/Terms_Use.cfm

number for the top half of each cylinder compared to the bottom was 81 percent for air, 58 percent for glycerin, 64 percent for water, and 65 percent for silicone. The effect of the smaller driving force for heat transfer is more pronounced in the vertical configuration than in the horizontal. This would explain, in part, why the Nusselt number was consistently higher in the horizontal position than in the vertical position.

Another reason for the increased heat transfer from the cylinders in the horizontal position was the large eddies observed in the flow field for this geometry. These eddies can be seen in Fig. 4. In this figure the gravitational acceleration vector is acting vertically downward, the horizontal cylinder is in the center of the figure and the support sphere is visible in the bottom left corner of the figure. The two eddies directly above the cylinder and the large eddy below the cylinder enhanced the natural convection heat transfer in the enclosure. These eddies were not evident for the cylinders in the vertical position.

The inner body, in both the horizontal and vertical configurations, was rotated 45 deg within the enclosure. This rotation had negligible effect on the heat transfer and only a small influence on the temperature profiles. This influence on the temperature profiles is shown in Fig. 5 for the cylinders in the horizontal position and in Fig. 6 for the cylinders in the vertical configuration. (Figure 2 defines R and $R(\Theta)$ for the $\Theta = 0$ deg probe.) The temperature inversions in these figures were also observed by other investigators [7–11] and are due to the high rate of angular heat transport compared to the radial transport of heat. For the cylinders in the horizontal position the $\Theta = 120$ deg probe struck the inner cylinder resulting in the precipitous drop in the temperature shown in Fig. 5 ($R/R(\Theta) = .5$). Another precipitous drop in the temperature occurred at the outer body ($R/R(\Theta) = 1$) for all of the probe locations except at $\Theta = 160$ deg where there was very little convective activity. These large temperature gradients are due to the high velocity boundary layers at the inner and outer bodies. As a final point regarding the temperature distribution, all of the flow visualization and temperature profile data showed fully recirculating flows, the test fluids did not stratify.

The heat transfer coefficient and the resulting Nusselt number in the correlations that are presented below are averages based on the total heat transferred by natural convection from the four cylinders and their total surface area. All of the heat transfer correlations were obtained using a standard least squares curvefitting technique. The deviation referred to below is the absolute difference between the data and the equation value divided by the data value and the average percent deviation is the sum of these individual deviations divided by the total number of data points.

The best correlation for the cylinders in the vertical position is

$$\mathrm{Nu}_L = 0.262\ \mathrm{Ra}_L^{0.268}\ \mathrm{Pr}^{0.028} \tag{1}$$

with an average percent deviation of 4.53 and a maximum percent deviation of 18.48. In terms of a single correlating parameter, the best fit is

$$\mathrm{Nu}_L = 0.264\ \mathrm{Ra}_L^{0.274} \tag{2}$$

with an average percent deviation of 9.34 and a maximum percent deviation of 30.58. For the cylinders in the horizontal position the results are

$$\mathrm{Nu}_L = 0.498\ \mathrm{Ra}_L^{0.245}\ \mathrm{Pr}^{-0.002} \tag{3}$$

and

$$\mathrm{Nu}_L = 0.496\ \mathrm{Ra}_L^{0.245} \tag{4}$$

with average percent deviations of 6.92 and 6.95 and maximum percent deviations of 14.74 and 15.27, respectively.

Evaluation of equations (2) and (4) at a Rayleigh number of 10^7 (approximately midrange in Fig. 7) showed that there was a 15 percent decrease in the Nusselt number for the cylinders in the vertical position as compared to the horizontal position. These results are similar to those obtained for a single cylinder in an infinite atmosphere. Using correlations given by McAdams [17] for a single cylinder in the vertical and horizontal position, there was a 10 percent decrease in the Nusselt number for the cylinder in the vertical position as compared to the horizontal position.

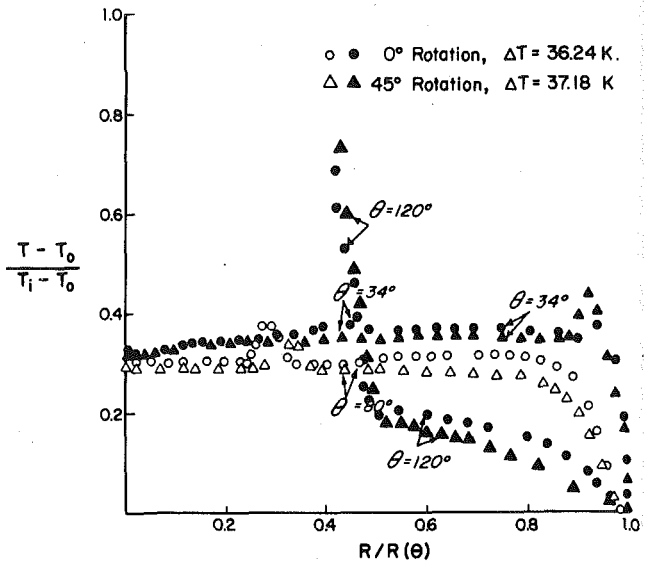

Fig. 5 Temperature profile for rotation about the vertical axis with silicone-horizontal position

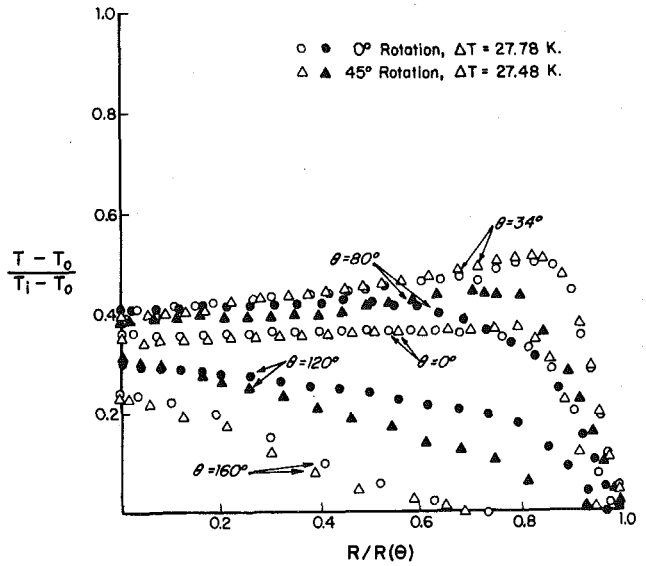

Fig. 6 Temperature profile for rotation about the vertical axis with glycerin-vertical position

For all of the heat transfer data the best correlations are in terms of the boundary layer length. These are

$$\mathrm{Nu}_B = 0.277\ \mathrm{Ra}_B^{0.274}\ \mathrm{Pr}^{0.012} \tag{5}$$

and

$$\mathrm{Nu}_B = 0.286\ \mathrm{Ra}_B^{0.275} \tag{6}$$

with average percent deviations of 8.44 and 9.30 and maximum percent deviations of 24.85 and 28.63, respectively. Figures 7 and 8 show several of these correlations.

Correlations are available [9, 10] for the natural convection heat transfer from a single vertical cylinder to an enclosure. These correlations are in terms of a modified Rayleigh number defined by

$$\mathrm{Ra}^* = \mathrm{Ra}\ (L/R_i). \tag{7}$$

These correlations are

$$\mathrm{Nu}_B = 0.578\ \mathrm{Ra}_B^{*0.239} \tag{8}$$

and

Downloaded 20 Dec 2010 to 194.27.225.72. Redistribution subject to ASME license or copyright; see http://www.asme.org/terms/Terms_Use.cfm

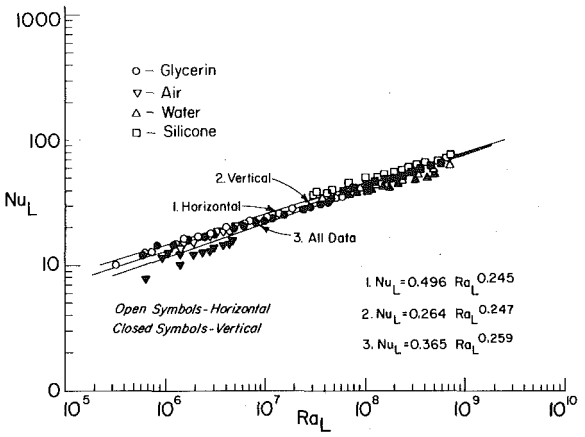

Fig. 7 Nu_L versus Ra_L for all the heat transfer data

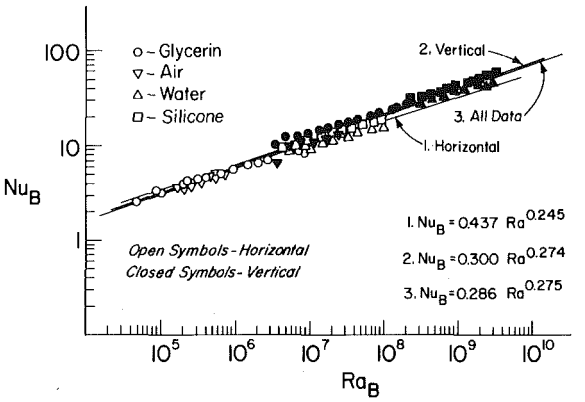

Fig. 8 Nu_B versus Ra_B for all the heat transfer data

$$Nu_L = 0.151\ Ra_L^{*0.295} \tag{9}$$

with average percent deviations of 14.49 and 17.74, respectively. When the present vertical cylinder array data were compared to these correlations the average percent deviations were 24.76 and 9.31, respectively. The boundary layer length used was the total boundary layer length for all four cylinders.

The empirical equations in this study were developed using a hypothetical gap width, L, which was 12.84 cm (R_o = 16.54 cm and R_i = 3.71 cm). The fluid properties were all evaluated at $(T_i + T_o)/2$. The foregoing equations fit all of the data for $3.2 \times 10^5 < Ra_L < 6.9 \times 10^8$, $7.6 \times 10^4 < Ra_B < 5.2 \times 10^9$, and $0.7 < Pr < 31{,}000$.

Conclusion

This study has extended the data available for natural convection heat transfer in enclosures to more complex inner body geometries. Of the configurations studied there was no appreciable effect due to rotation of the inner body about its vertical axis. However, a significant difference was noticed between the vertical and horizontal configuration of the set of cylinders. The vertical position showed a decrease in the heat transferred relative to the horizontal position. This was attributed to a complex interaction between the boundary layer length, the flow patterns which resulted from the geometry, and the cross-sectional area exposed to the upward flow. These geometric effects were noticed to decrease with increasing Prandtl number. A logical extension beyond this study will include increasing the number of cylinders and varying their spacing, diameter, and length.

References

1 Eckert, E. R. G., and Soehngen, E., "Studies on Heat Transfer in Laminar Free Convection With the Zehnder-Mach Interferometer," Technical Report No. 5745, USAF, Air Material Command, Dayton, Ohio, 1948.

2 Lieberman, J., and Gebhart, B., "Interactions in Natural Convection from an Array of Heated Elements, Experimental," *International Journal of Heat and Mass Transfer,* Vol. 12, 1969, pp. 1385–1396.

3 Brodowicz, K., and Kierkus, W., "Experimental Investigation of Laminar Free Convection in Air Above Horizontal Wire With Constant Flux," *International Journal of Heat and Mass Transfer,* Vol. 9, 1966, pp. 81–94.

4 Forstrom, R., and Sparrow, E., "Experiments on the Buoyant Plume Above a Heated Horizontal Wire," *International Journal of Heat and Mass Transfer,* Vol. 10, 1967, pp. 321–330.

5 Tillman, E., "Natural Convection Heat Transfer from Horizontal Tube Bundles," ASME Paper No. 76-HT-35, Aug. 1976.

6 Davis, L., and Perona, J., "Development of Free Convection Axial Flow Through a Tube Bundle," *International Journal of Heat and Mass Transfer,* Vol. 16, 1973, pp. 1425–1438.

7 Scanlan, J., Bishop, E., and Powe, R., "Natural Convection Between Concentric Spheres," *International Journal of Heat and Mass Transfer,* Vol. 13, 1970, pp. 1857–1872.

8 Bishop, E., Mack, L., and Scanlan, J., "Heat Transfer by Natural Convection Between Concentric Spheres," *International Journal of Heat and Mass Transfer,* Vol. 9, 1966, pp. 649–661.

9 McCoy, C., Powe, R., Bishop, E., Weber, N., and Scanlan, J., "Free Convection Between a Vertical Cylinder and a Spherical Enclosure," *Proceedings of the Fifth International Heat Transfer Conference,* Tokyo, 1974.

10 Warrington, R., "Natural Convection Heat Transfer Between Bodies and Their Enclosures," Ph.D. Dissertation, Montana State University, 1975.

11 Powe, R., Eyler, L., and Scanlan, J., "Flow Studies for Natural Convection Between a Sphere and Its Cubical Enclosure," ASME Paper No. 75-HT-61, San Francisco, 1975.

12 Kuehn, T., and Goldstein, R., "Correlating Equations for Natural Convection Heat Transfer Between Horizontal Circular Cylinders," *International Journal of Heat and Mass Transfer,* Vol. 19, 1976, pp. 1127–1134.

13 Marsters, G., and Paulus, G., "Effects of Confining Walls on Heat Transfer From a Vertical Array of Heated Horizontal Cylinders," *Transactions Canadian Society of Mechanical Engineers,* Vol. 1, No. 4, 1972, pp. 219–22.

14 Marsters, G., "Effects of Confining Walls Upon Natural Convection From a Heated Horizontal Cylinder," *Proceedings of the 4th Canadian Conference of Applied Mechanics,* June 1973, pp. 789–790.

15 Dutton, J., and Welty, J., "An Experimental Study of Low Prandtl Number Natural Convection in an Array of Uniformly Heated Vertical Cylinders," ASME Paper No. 75-HT-AAA, Feb. 1975.

16 Leinhard, J., "On the Commonality of Equations for Natural Convection from Immersed Bodies," *International Journal of Heat and Mass Transfer,* Vol. 16, 1973, pp. 2121–2123.

17 McAdams, W. H., *Heat Transmission,* 3rd Ed., McGraw-Hill, New York, 1954, pp. 172–177.

Downloaded 20 Dec 2010 to 194.27.225.72. Redistribution subject to ASME license or copyright; see http://www.asme.org/terms/Terms_Use.cfm

Natural Convection in Horizontal Duct Connecting Two Fluid Reservoirs

A. Bejan
A. N. Rossie

Department of Mechanical Engineering,
University of Colorado,
Boulder, Colo 80309

The paper reports an experimental study of natural convection between two water reservoirs connected through a two-dimensional horizontal duct. The flow field was visualized and the velocities were measured using the thymol blue pH indicator method. The temperature field in the duct region and the heat transfer rate through the duct were also measured. It is shown that the duct flow consists of two streams in counterflow, the warmer stream occupying the upper half of the channel. The two streams are insulated from one another by a mid-depth buffer layer. The measurements demonstrate that the heat transfer mechanism differs fundamentally from the mechanism envisioned in the Bejan and Tien theory [6]. It is also suggested that the basic design of the experimental apparatus can be used in future studies of stability of shear flows in stratified fluids.

Introduction

Contemporary problems related to the energy crisis and the environment have stimulated the present interest in the fluid mechanics and heat transfer characteristics of buoyancy-induced flows in enclosures (cavities). Two comprehensive reviews, one of them very recent, document very well this body of research and its engineering importance [1, 2]. One class of free convection phenomena, not well-documented in the literature, is the interaction between two enclosures (reservoirs) communicating through relatively smaller openings (windows, cracks). These phenomena have important practical applications in a number of fields, such as energy conservation in buildings, fire research, inland and coastal hydrodynamics (two-lake systems), solar energy storage, nuclear reactor core performance, etc. Recent developments in the technology of rotating superconducting electric machines indicate that free convection currents induced in liquid helium have the capability of shuttling heat away from a winding hot spot (normal zone) through small openings present between conductors [3]. Thus, free convection through small openings is thought to play a major role in the safety (thermal stability) of rotating superconducting windings bathed in liquid helium.

The literature on natural convection between two fluid reservoirs communicating via a small opening is limited. In a two-part paper, Brown and Solvason [4, 5] studied the heat exchange through a rectangular opening (window) in a partition. Their study included windows in vertical and horizontal partitions. More recently, Bejan and Tien [6] reported a theory for the heat transfer between two fluid reservoirs connected through a horizontal flat duct. This theory is expected to hold strictly in the limit Ra $H/L \to 0$, however, the authors recommend a range of finite Ra H/L in which the theory is thought to yield acceptable heat transfer results.

The objective of this paper is to report a fundamental experimental study which documents the most basic features of the free convection phenomenon. This study has a clear engineering focus motivated by the practical applications mentioned in the beginning of this section. The only theoretical result available on this phenomenon [6] is asymptotically valid; therefore, to "extrapolate" it to a real situation can lead to significant errors. For this reason, we decided to design an apparatus which simulates a *real* situation, namely, a common fluid (water) and a set of channel dimensions compatible with those of commercial, man-made ducts. Our experiment was not designed to test the theory of reference [6]. As shown below, our experimental results and conclusions are the first of their kind because they are made in a parametric domain where nothing is known, analytically or experimentally. The present study breaks new ground.

Contributed by the Heat Transfer Division for publication in the JOURNAL OF HEAT TRANSFER. Manuscript received by the Heat Transfer Division April 14, 1980.

Experimental Apparatus

The apparatus constructed for this experiment is shown in Fig. 1. The central compartment of the apparatus is the H-shaped cavity filled with water. This cavity consists of a horizontal flat duct positioned symmetrically between two identical parallelipipedic reservoirs. The flat duct is 5.1 cm deep, 30.5 cm long and 25.4 cm wide, while each of the lateral reservoirs is 30.5 cm deep, 25.4 cm long and 25.4 cm wide. The entire structure is built out of plexiglass sheet 0.63 cm thick. The plexiglass structure is surrounded on all sides by a plywood enclosure leaving a 7 cm-wide gap between plexiglass and plywood. This gap was filled with glass wool as thermal insulation.

During experiments, the water cavity was heated in the horizontal

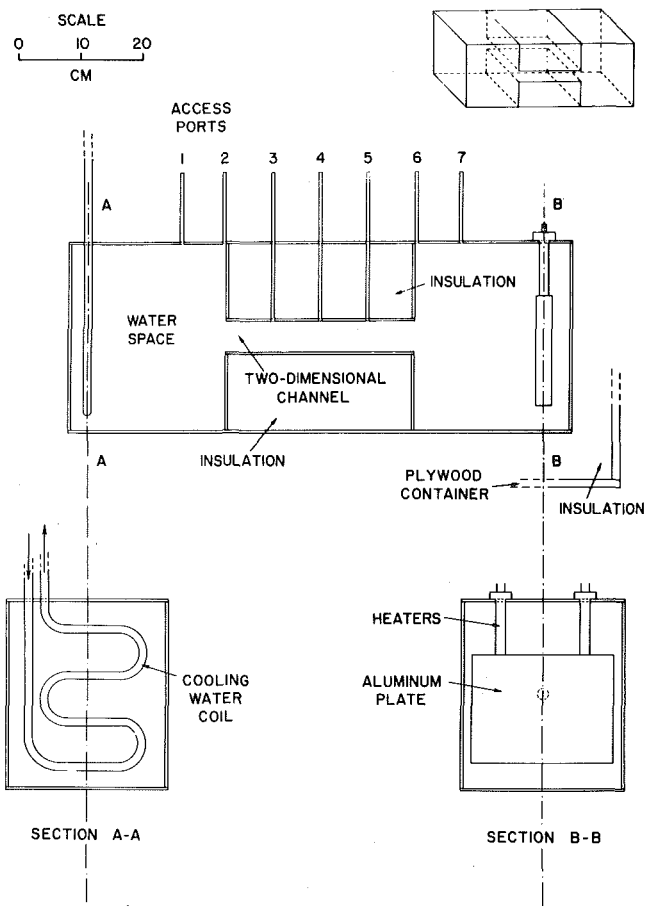

Fig. 1 Schematic drawing of experimental apparatus

Copyright © 1981 by ASME

Downloaded 20 Dec 2010 to 194.27.225.72. Redistribution subject to ASME license or copyright; see http://www.asme.org/terms/Terms_Use.cfm

direction between the heater plate B-B and the cooling water coil A-A shown in Fig. 1. The heater plate consists of two vertical electric heaters embedded in a massive aluminum plate with a thickness of 2.5 cm. The heater and the cooling coil are positioned 21 cm away from the respective openings of the flat duct in order to minimize the effect of vertical end-walls on the fluid mechanics of the two-dimensional channel.

Access to the water chamber was provided through seven ports (numbered 1–7 on Fig. 1) positioned every 7.6 cm along the middle longitudinal line of the lid. Each access port is a stainless-steel tube with an inside diameter of 3.2 mm. Through each port we lowered to predetermined depths temperature and velocity probes discussed in detail in the next sections. The flow was examined visually through two lateral windows cut into the insulation in line with the two-dimensional channel. These windows are not shown in Fig. 1, however, they are visible in the photographs (Figs. 2, 3).

The experimental procedure consisted of achieving a succession of steady states fixing the power input to the heater plate. The cooling coil temperature was fixed by the temperature of the laboratory water supply which oscillated within ±1°C from day to night. Fortunately, these temperature fluctuations did not constitute a problem since the time constant of the apparatus is roughly 5 hr, and the actual recording of data required no more than 2 hr. At the heated end, the temperature fluctuations which could have been caused by changes in the voltage supply were avoided by inserting a constant-voltage transformer between the heaters and the building electric power supply.

Flow Visualization and Velocity Measurements

The flow pattern was made visible using the thymol blue pH indicator method originally described by Baker [7]. The same method was used successfully in a number of thermal convection experiments [8–10]. The negatively charged electrode which marks the fluid was introduced verticaly through each of the seven access ports, across the two-dimensional channel. As anode we used one of the nearest steel access tubes.

In Fig. 2 we show a panoramic view of the natural counterflow induced in the channel by the differential heating of the lateral reservoirs. We made this photograph possible by placing the cathode in the center of the channel and leaving it charged at −6V for 5–10 min. The blue sheet generated by the vertical electrode is swept toward the cold side (to the left) through the upper half of the channel, and toward the warm side (to the right) through the lower half of the channel. In time, the blue gradually disappears as the marked fluid comes in contact with adjacent (unmarked) regions. For the same reason, the line of zero velocity survives longest. This line is visible in Fig. 2. The lighter streaks of irregular shape enclosed by the zero velocity line are the remains of horizontal streaks disturbed by buoyant hydrogen bubbles formed on the cathode before the voltage was turned off and the photograph taken.

The zero velocity line demonstrates that the lateral reservoirs exchange heat via a horizontal counterflow in which each of the two branches becomes narrower as the fluid approaches the exit. Consequently, in each branch the fluid experiences a slight horizontal acceleration as it moves from one end of the channel to the other. This effect is illustrated also by the sequence of photographs assembled in Fig. 3, in which we show blue streak patterns generated under access ports 2–6 after approximately 20 s of cathode activity. Another effect visible in this sequence of photographs is the decrease in viscosity with

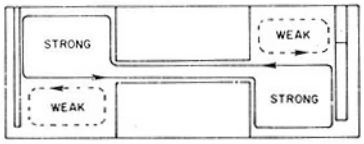

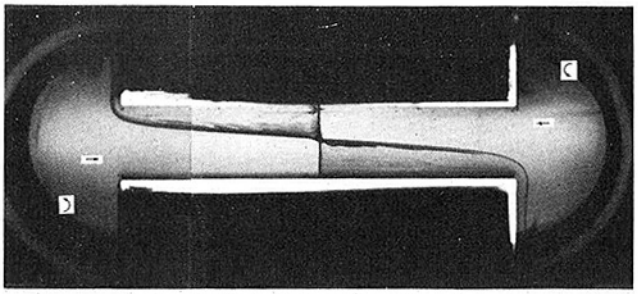

Fig. 2 Line of zero velocity in the two-dimensional channel (Ra = 5.43 × 10^6)

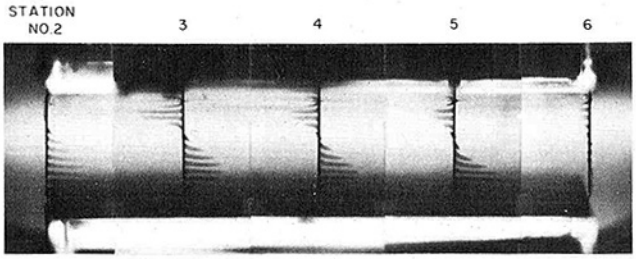

Fig. 3 Thymol blue visualization of velocity distribution across the two-dimensional channel (Ra = 1.26 × 10^7)

increasing temperature: the velocity gradient at the top wall of the channel is greater than at the bottom wall.

We carried out a number of quantitative velocity measurements based on photographic recordings of the type shown in Fig. 3. The velocity results are presented in Figs. 4 and 5, showing not only the variation of velocity profile with longitudinal position (station number) but also the effect of increasing Rayleigh number, Ra. As in reference [6], we defined the Rayleigh number based on the duct depth (H = 5.1 cm) and the maximum temperature difference ΔT encountered in the duct,

$$\mathrm{Ra} = \frac{g\beta H^3 \Delta T}{\alpha \nu}. \tag{1}$$

The maximum temperature difference ΔT was measured between the two "starting corners" where the two branches of the counterflow enter the duct region. In the present experiments, the temperature difference ΔT varied between 2 and 10°C. Comparing Figs. 4 and 5 we see that the peak velocities increase by roughly 40 percent as Ra increases from 5.43×10^6 to 1.93×10^7.

It is worth mentioning that each of the velocity points plotted in Figs. 4 and 5 are based on measuring the physical length Δx of an individual blue streak and the time Δt required to generate the streak. Due to the wake which forms directly behind the 0.8 mm-dia cathode, the local free stream velocity v_∞ is actually greater than $\Delta x/\Delta t$. Applying the method originally described by Imberger [10], we combined the Δx, Δt measurement, with a calibration curve determined experimentally for the ratio $v_\infty/(\Delta x/\Delta t)$ as a function of distance behind the cathode. The result of the ensuing trial-and-error calculation is the free stream velocity v_∞.

The visualization experiments allow us to make the observation

Nomenclature

B = parameter, equation (7)
g = gravitational acceleration
H = vertical dimension of duct
k = thermal conductivity
L = horizontal dimension of duct
Nu = Nusselt number, equation (5)
Pr = Prandtl number
Q = heat transfer rate through the duct
Ra = Rayleigh number, equation (1)
Ri = Richardson number, equations (2, 3)
T = temperature
ΔT = maximum temperature difference in the duct region
u = horizontal velocity
W = duct width
x = horizontal position
y = vertical position
Y = vertical dimension of hot plate swept by cold fluid
z = dimensionless vertical position, $z = y/H$
α = thermal diffusivity
β = coefficient of thermal expansion
δ = thickness of vertical boundary layer
ν = kinematic viscosity
ρ = density

Downloaded 20 Dec 2010 to 194.27.225.72. Redistribution subject to ASME license or copyright; see http://www.asme.org/terms/Terms_Use.cfm

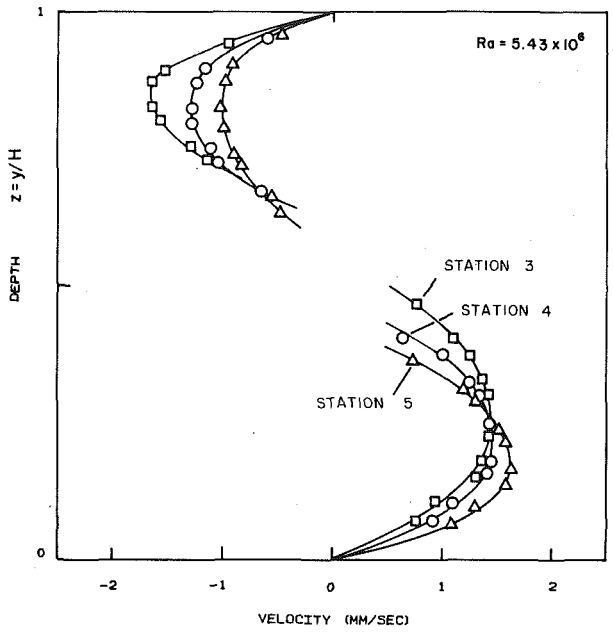

Fig. 4 Velocity distribution across the duct (stations 3–5, Ra = 5.43 × 10^6)

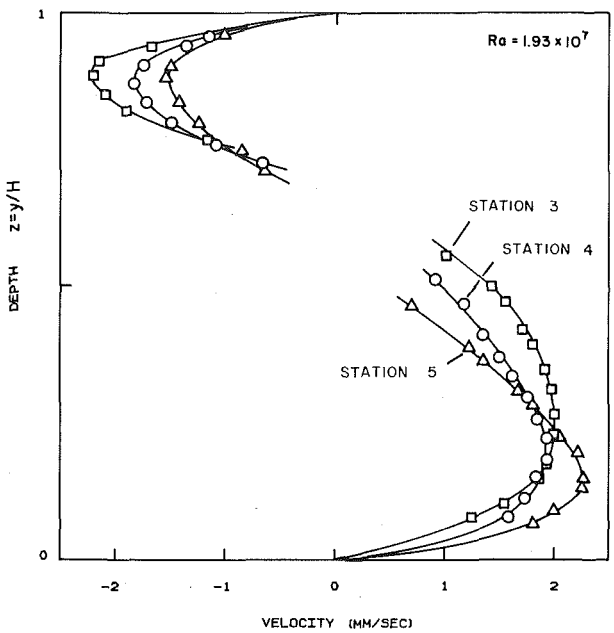

Fig. 5 Velocity distribution across the duct (stations 3–5, Ra = 1.93 × 10^7)

that fluid is drawn horizontally from both reservoirs into the duct. This observation contradicts the intuitive drawing which prefaces the Bejan and Tien theory for the laminar flow in the duct (see Fig. 1 of reference [6]). We summarized our visual observations in the schematic drawing shown in the top half of Fig. 2: the fluid contained in the upper half of the warm reservoir and in the lower half of the cold reservoir does not participate in the exchange which takes place between reservoirs.

Finally, we note that the velocity profile at station 4 (Figs. 4, 5) is not purely antisymmetric as would be expected from the temperature boundary conditions placed around the vertical longitudinal cross-section of the apparatus. This effect is explained by the fact that the actual experiment is not purely symmetric. The two lateral walls, particularly the two windows through which we viewed the flow, allowed some heat transfer from the ambient to the channel (T_{room} = 25–26°C). Consequently, in longitudinal planes near the two lateral walls the warm (upper) branch of the counterflow was augmented. By mass conservation over the duct cross-section, in the central longitudinal plane (station 4) the lower branch appears to be stronger. However, the mass defect between the two branches is considerably smaller than the flow in each branch (this can be seen more clearly in Fig. 2). The viscosity effect also contributes to the departure from a purely antisymmetric profile: from 25 to 30°C the viscosity of water decreases by 11 percent.

Temperature Measurements

We measured the temperature distribution in the H-shaped cavity using a precision thermistor mounted at the lower extremity of a rack-and-pinion mechanism with dial indicator. The thermistor probe was lowered into the cavity through each of the seven access ports. The temperature readings are accurate within 0.1°C, while the vertical position measured on the dial indicator is accurate within 0.5 mm.

Figures 6(*a–e*) show the temperature distribution as a function of longitudinal position and Rayleigh number. In particular, Fig. 6(*c*) summarizes the measurements taken through the three most central access ports in the duct region. The basic feature of the temperature field is the stratification in the vertical direction. This effect is particularly visible in the center portion of the duct (Fig. 6(*c*)) where the upper branch of the counterflow is clearly warmer than the lower branch. Figure 6(*c*) reveals also a weak horizontal temperature gradient; for example, the temperature along the upper wall decreases in the direction of flow. All these features are visible also in Fig. 7 where we plotted the pattern of isotherms corresponding to Ra = 2.76 × 10^7.

The temperature profiles of Fig. 6(*c*) indicate that the experimental apparatus is quite effective in providing adiabatic boundary conditions for the duct fluid. The adiabatic wall condition does not seem to deteriorate as the Rayleigh number increases. Another important feature of the duct temperature profile is that it has three inflexion points, hence, the vertical temperature gradient has three minima, one at mid-depth and the other two on the adiabatic boundaries. For example, the temperature gradient measured at station 4 (case C, Fig. 6(*c*)) reaches the minimum value 0.31°C/cm at mid-depth (z = 0.15) and 2.38°C/cm and z = 0.85. The temperature gradient at mid-depth ("CL" in Fig. 6(*c*)) is comparable with the gradient measured at the same depth in the lateral reservoirs. We conclude that the two branches of the duct counterflow are only in marginal thermal contact, since they interact across a distinct mid-layer serving as buffer. Although the velocity measurements obtained using the thymol blue technique (Figs. 4, 5) did not yield reliable data for the buffer layer, the photographs (Fig. 3) suggest that in the buffer layer the fluid shear is less than in the two branches of the counterflow.

In conclusion, the temperature measurements demonstrate that the duct flow departs from the fully-developed counterflow envisioned by Bejan and Tien [6] for the central region. The fully-developed counterflow suggested in [6] is of the type found analytically by Cormack, et al. [11] and experimentally by Imberger [10] in horizontal rectangular enclosures. We attribute this departure to the fact that the duct is too tall (Ra is too high) for the two branches to feel each other and exchange a substantial amount of heat by vertical diffusion.

The thermal stratification of the two lateral reservoirs is documented in Figs. 6(*a, b, d, e*). Each half-reservoir which serves as sink for the duct fluid is practically isothermal due to strong thermal mixing visible in the upper-left and lower-right corners of Fig. 2. The stratification is much stronger in the remaining spaces, namely, in the upper half of the hot reservoir and in the lower half of the cold reservoir. The hot reservoir measurements show that the apparatus loses heat through the upper wall of the warm reservoir. We determined the order of magnitude of this heat loss by performing a special experiment described in the Heat Transfer section of this article.

The earlier observation that the fluid is drawn horizontally into the duct is now explained by the vertical stratefication of the two reservoirs. Without stratification, the streamlines would enter the duct radially, from all angles (as foreseen in reference [6]). With stratification, the fluid is drawn from a thin layer situated in the reservoir at the same level as the entrance to the duct [12]. This form of "se-

Downloaded 20 Dec 2010 to 194.27.225.72. Redistribution subject to ASME license or copyright; see http://www.asme.org/terms/Terms_Use.cfm

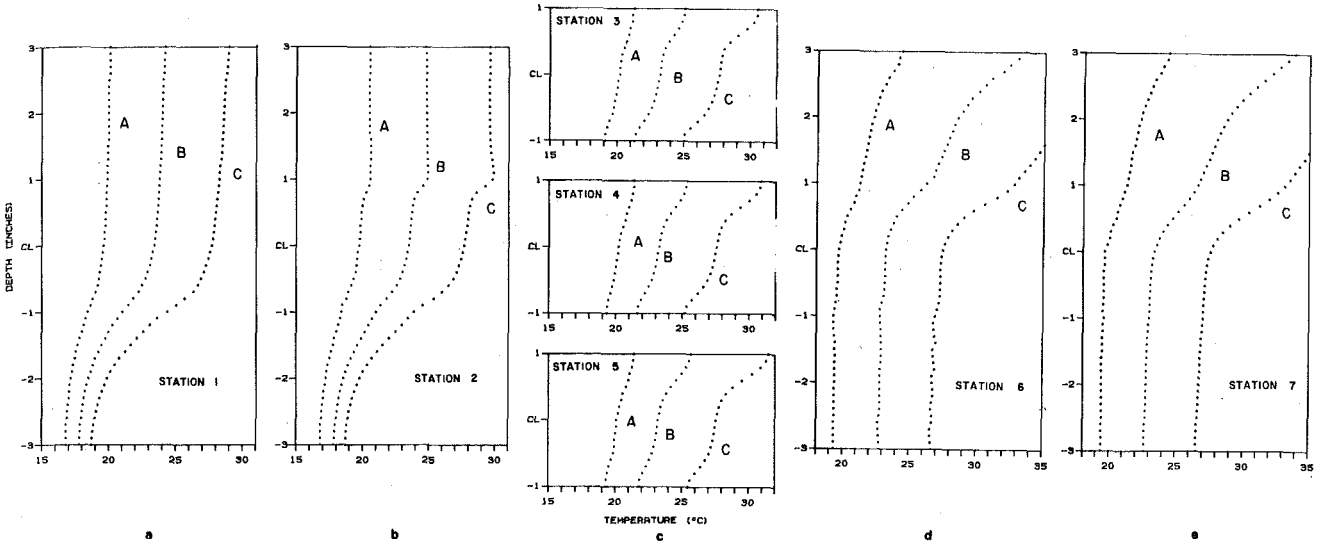

Fig. 6 Temperature variation with vertical position: (*a*) station 1, (*b*) station 2, (*c*) stations 3–5, (*d*) station 6, (*e*) station 7; (A) Ra = 5.43×10^6, (B) Ra = 1.26×10^7, (C) Ra = 2.76×10^7, (CL) = centerline

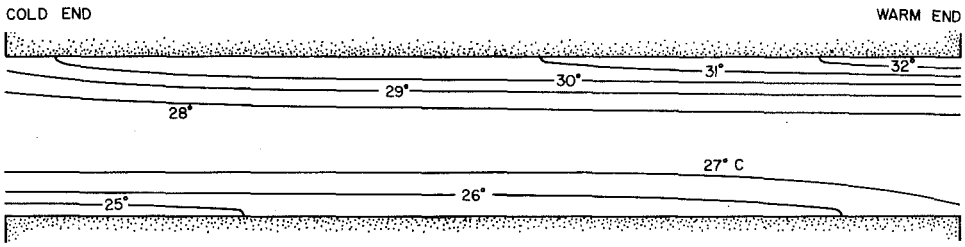

Fig. 7 Pattern of isotherms in the channel region (Ra = 2.76×10^7)

lective" horizontal withdrawal is also accompanied by backflow in adjacent horizontal layers (see reference [13]). The backflow is responsible for the weak cells visible in the upper half of Fig. 2.

Stability

The temperature and velocity measurements reported in the preceding sections can be used further to study the stability of the duct counterflow. When the stratification is thermal, subject to the Boussinesq approximation, the local Richardson number depends on the local temperature and velocity gradients,

$$\mathrm{Ri} = \frac{g\beta \dfrac{\partial T}{\Delta y}}{\left(\dfrac{\partial u}{\partial y}\right)^2} \tag{2}$$

According to Mile's criterion [14], "Ri > 1/4 everywhere in the fluid" is the sufficient condition for a continuously stratified inviscid flow to be stable to small disturbances.

The dashed lines in Fig. 8 show the local Ri under access port No. 4 when Ra = 1.93×10^7. We obtained the Ri(z) curve by fitting seventh-order polynomials to the corresponding velocity and temperature profiles, and substituting the polynomial expressions into definition (2). The Richardson number is zero at the top and bottom adiabatic walls, and infinite at two levels where the shear is zero. In the buffer region Ri reaches a clear minimum, $\mathrm{Ri}_{\min} \cong 6.7$ at $z \cong 0.65$, one order of magnitude above the critical value 1/4. Near the adiabatic walls Ri falls below 1/4; however, in these regions the solid boundaries promote stability [15]. The Richardson number calculations agree with the experimental observation that the duct shear flow is stable even at the highest Rayleigh number achieved in the apparatus (Ra = 2.76×10^7). We were unable to increase the Rayleigh number above this limit because, while trying to increase the Joule heating in the hot plate, the plexiglass-plexiglass epoxy seal failed due to overheating (see the stratification in the upper, "stagnant", half of the warm reservoir, Figs. 6(*d*, *e*).

Figure 8 shows the dynamics of the Ri(z) distribution as Ra increases: the solid lines represent the local Richardson number in the limit Ra → 0, $H \ll L$. In this limit, the local Richardson number becomes

$$\mathrm{Ri}(z) = \frac{\mathrm{Pr}}{6} \frac{z^4 - 2z^3 + z^2}{\left(z^2 - z + \dfrac{1}{6}\right)^2} \tag{3}$$

In Fig. 8, we plotted the theoretical result (3) for water at 25°C (Pr = 6.3), showing that the theoretical Ri(z) curve has the same general features as the experimental curve corresponding to Ra = 2.76×10^7. The differences between the two curves suggest that in the buffer region Ri decreases as the Rayleigh number increases. Due to the temperature-dependent properties of water, the experimental $\mathrm{Ri}_{\min}$ in the buffer region migrates upward from its asymptotic level $z = 0.5$. The double-inflexion in the experimental Ri(z) curve suggests that as Ra increases, a second $\mathrm{Ri}_{\min}$ may develop in the lower half of the duct.

These observations point toward the opportunity of using apparatuses similar to the present design (Fig. 1) to systematically investigate the transition to instability in stratified shear flows. Figure 8 and equation (3) show two ways in which the Richardson number may be adjusted by the experimentalist. One way, discussed already, is by increasing the Rayleigh number. The other approach consists of decreasing the Prandtl number: in water, this can be achieved by steadily increasing the bulk temperature. It is interesting to note that the minimum Ri in the Ra → 0 limit is simply

$$\mathrm{Ri}_{z=1/2} = \frac{3}{2}\mathrm{Pr}, \tag{4}$$

suggesting that in low Prandtl number fluids with Pr < 1/6 the buffer region Ri always falls under the critical 1/4 value.

Regarding the use of our apparatus design in stability studies of stratified shear flows, it is worth pointing out that an apparatus of similar design was employed by Lofquist [16] who achieved density stratification by circulating (pumping) a salt water layer under a fresh water pool. The advantage of our design would be that the circulation and the stratification occur naturally. At the same time, the natural

Downloaded 20 Dec 2010 to 194.27.225.72. Redistribution subject to ASME license or copyright; see http://www.asme.org/terms/Terms_Use.cfm

occurrence of circulation and stratification enhances the flow control problem; however, as pointed out in the preceding paragraph, in our design one could use the Prandtl number to control the approach to instability.

Heat Transfer

The net heat transfer between the two reservoirs via the horizontal duct is reported in Fig. 9. The Nusselt number for overall heat transfer is defined as

$$\mathrm{Nu} = \frac{Q}{k\,HW(\Delta T/L)} \tag{5}$$

where Q(watts) is the net heat transfer rate, W the duct horizontal width (25.4 cm) and ΔT the maximum duct temperature difference used in definition (1). The net heat transfer rate Q is equal to the electric power dissipated in the heater plate B-B (Fig. 1) minus a correction attributed to heat loss across the top wall of the warm fluid reservoir (Figs. 6(*d*, *e*)). We measured the size of this correction by conducting a separate experiment in which we powered the heater plate but did not run water through the cooling coil A-A (Fig. 1). The steady state achieved in this manner is the result of the balance between the heater plate heat input and the heat loss to the ambient across the 7 cm thick glass wool insulation surrounding the water cavity. In the heat loss experiment we were able to simulate top wall-ambient temperature differences comparable with the differences encountered during the experiments documented in Figs. 2–7. Thus, we obtained an estimate of the water-air heat loss present in the duct heat transfer experiments: The heat loss was always under 28 percent of the heater plate power input, the largest share (28 percent) being lost at the highest Rayleigh number studied, Ra = 2.76×10^7.

In Fig. 9 we show a comparison between our heat transfer measurements and the only theoretical prediction available in the literature. The theory of [6] reports the Nusselt number in implicit form;

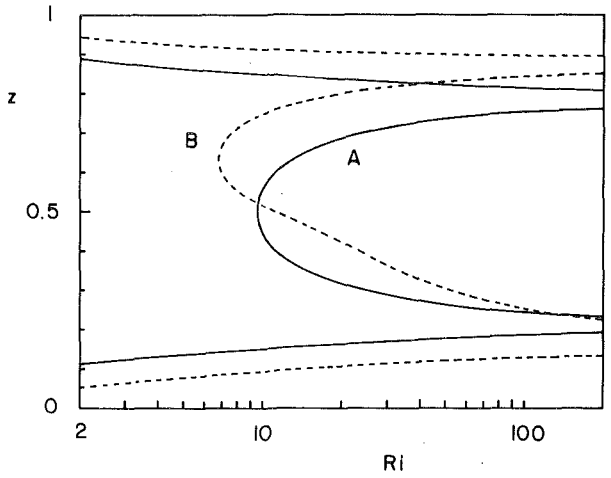

Fig. 8 Local Richardson number versus vertical position in the duct, $z = y/H$ (station 4)

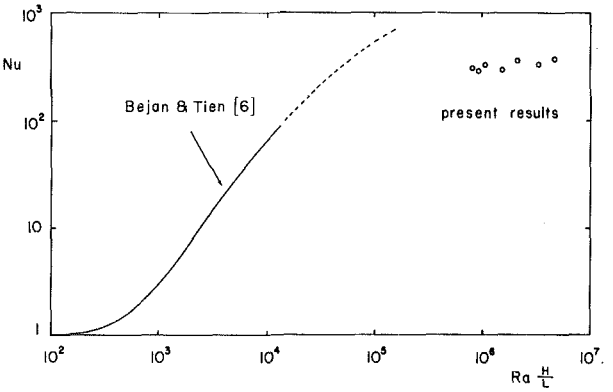

Fig. 9 Heat transfer results versus the theory of reference [6].

a more useful version of this result is the parametric representation

$$\mathrm{Nu} = B\left[1 + (2.76)10^{-6}\,B^2\left(Ra\,\frac{H}{L}\right)^2\right] \tag{6}$$

where parameter B is given by

$$B = \frac{\left[1 + 0.0024\,\mathrm{Ra}\left(\frac{H}{L}\right)^2\right]^{1/2} - 1}{0.0012\,\mathrm{Ra}\left(\frac{H}{L}\right)^2} \tag{7}$$

For the present geometry (H/L = 1/6), the Nusselt number given by equations (6) and (7) is thought to be approximately valid in the range $\mathrm{Ra}H/L < 1.33 \times 10^4$ [6]. This range is highlighted in Fig. 9 by the solid portion of the theoretical curve.

Figure 9 shows that the experimental Nu results depart appreciably from the Bejan and Tien theory [6], suggesting that the reservoir-to-reservoir heat transfer mechanism differs from the mechanism envisioned theoretically for the Ra → 0 limit. In the theory, the thermal resistance between the two reservoirs was due to the thermal contact in the vertical direction between the two branches of the duct counterflow. As demonstrated by Figs. 6(*c*) and 7, in the present experiment the two branches of the counterflow are effectively insulated from one another by the mid-depth buffer region. Since the end-to-end thermal resistance (insulation value) of a counterflow heat exchanger varies inversely with the thermal resistance in the stream-to-stream direction [18], in the present experiment the channel counterflow poses no resistance to heat transfer in the horizontal direction despite a finite ΔT measured between the two "starting" corners. The fact that the experimental data follow more closely a relationship of the type

$$\mathrm{Nu} \sim \left(\mathrm{Ra}\,\frac{H}{L}\right)^{1/4} \tag{8}$$

suggests that the resistance to reservoir-to-reservoir heat transfer is situated not in the duct but between each of the two vertical end planes (A-A, B-B) and their adjacent fluid reservoirs. In the warm reservoir heat is being transferred from the hot plate to an almost isothermal pool of cold fluid occupying the lower half of the reservoir. (See Fig. 6(*e*); the fluid in the upper half does not leave the warm reservoir.) Similarly, in the cold reservoir the cooling coils extract heat from the fluid occupying the upper half of the reservoir.

We can derive a more exact version of relation (8) on the basis of dimensional analysis. The net heat exchange between reservoirs can be written as

$$Q \sim YWk\,\frac{\Delta T}{\delta} \tag{9}$$

where Y is the height over which the hot plate is swept by cold fluid, while δ is the thickness of the boundary layer lining the hot plate. Note that in our experiment the temperature difference between the two starting corners (ΔT) is practically the same as the ΔT between each vertical end-plate (coil) and the well-mixed pool surrounding it (see, for example, the top portion of Fig. 6(*a*), and the bottom of Fig. 6(*e*)). Gill [17] showed that the boundary layer thickness is of order

$$\delta \sim \left(\frac{\alpha\nu Y}{g\beta\Delta T}\right)^{1/4} \tag{10}$$

Combining expressions (9, 10) with definition (5) we find

$$\mathrm{Nu} \sim \left(\frac{L}{H}\right)^{5/4}\left(\frac{Y}{H}\right)^{3/4}\left(\mathrm{Ra}\,\frac{H}{L}\right)^{1/4} \tag{11}$$

Assuming that Y is equal to the half-height of the hot plate, $Y \approx 10.9$ cm, expression (11) becomes

$$\mathrm{Nu} \sim 16.6\left(\mathrm{Ra}\,\frac{H}{L}\right)^{1/4} \tag{12}$$

This order-of-magnitude estimate is in fair agreement with the best line of slope 1/4 drawn through the experimental data of Fig. 9

Downloaded 20 Dec 2010 to 194.27.225.72. Redistribution subject to ASME license or copyright; see http://www.asme.org/terms/Terms_Use.cfm

$$\mathrm{Nu} \cong 9.1 \left(\mathrm{Ra}\frac{H}{L}\right)^{1/4} \quad (13)$$

In conclusion, the Nusselt number defined in equation (5) obeys a proportionality of type (11), in which the missing numerical coefficient is of order one. It is important to remember that the actual heat transfer rate Q depends only on the size and the position of the hot plate relative to the horizontal channel, Y. Unlike in the theory of reference [6], the heat transfer rate does not depend on the channel dimensions, H and L. The path of heat flow between the two endplates can be traced by following the "strong" cell sketched in the upper half of Fig. 2. Cold fluid enters from the left, passes through the channel and reaches the bottom end of the heated plate (ΔT). Traveling upward along the heater, the stream temperature is raised to ΔT. Later, the warm stream (ΔT) travels unaffected through the channel and reaches the top end of the cooling screen. Descending along the cold wall, the stream temperature decreases by ΔT.

Further evidence supporting the above argument is contained in the velocity measurements reported in Figs. 4 and 5. Gill argued that the total mass flux carried by the convective cell generated between two vertical walls, A-A and B-B, is also proportional to $\mathrm{Ra}^{1/4}$. In the present experiment, the convective cell set in motion by differential heating is strangled by the duct. We can then estimate the change in mass flux with increasing Ra, by calculating the change in longitudinal velocity in the duct region. For example, we find that the peak velocity in the lower (cold) branch under station No. 5 increases from 1.62 mm/s in Fig. 4 to 2.24 mm/s in Fig. 5. This amounts to a 38 percent increase in mass flux, which matches the increase exhibited by $\mathrm{Ra}^{1/4}$, $(1.93 \times 10^7/5.43 \times 10^6)^{1/4} = 1.37$.

Criterion for Transition from the Theoretical Counterflow [6] to the Present Regime.

The dimensional argument substantiated in the preceding section enables us to establish the parametric domain in which the present experimental observations can be expected, vis-a-vis the parametric domain in which the theory envisioned in reference [6] is valid. We demonstrated that the fundamental difference between the two regimes (channel counterflows) is that, whereas in the theory the heat imparted to the vertical end boundary layer is lost in the horizontal duct by vertical diffusion from the warm branch to the cold branch of the counterflow, in the present experiment this heat is retained by the warm branch. Therefore, the theoretical counterflow [6] is possible as long as vertical diffusion in the duct is capable of off-setting the convective heat transfer to the end layers (heat transfer in the horizontal direction).

According to the Gill scaling discussed already, the vertical diffusion is of order $Q_y = kLW\Delta T/H$ while the horizontal convective heat transfer is of order $Q_x = \text{"}\dot{m}c_p\ \Delta T\text{"} = \rho W c_p\ \Delta T \alpha Y/\delta$ where δ is given by equation (10). A balance between the two heat flows is achieved when $\mathrm{Ra}^{1/4} = L/H\ (H/Y)^{3/4}$. In conclusion, it is necessary that

$$\mathrm{Ra} < \left(\frac{L}{H}\right)^4\left(\frac{H}{Y}\right)^3, \text{ for the Bejan and Tien theory [6] to be valid} \quad (14)$$

and

$$\mathrm{Ra} > \left(\frac{L}{H}\right)^4\left(\frac{H}{Y}\right)^3, \text{ for the present regime to be observed.} \quad (15)$$

In the present experiment, the geometric right-hand side of these inequalities is of order 50. Thus, we would have to set $\Delta T = 10^{-5}K$ in order to witness transition to the regime of theory [6]. Or, leaving ΔT, L and Y intact, we would have to use a gap height $H = 2.4$ mm.

There are two important conclusions to be drawn here. First, a counterflow of the type visualized in reference [6] does not occur in the engineering applications we are most concerned with. Second, the range in which the Bejan & Tien theory is valid (Ra <50) is *drastically* narrower than $\mathrm{Ra} < 1.33 \times 10^4$ suggested in reference [6] as the range in which "the heat transfer predictions are acceptable."

Criterion (14, 15) explains the disagreement shown in Fig. 9 between the Nu-Ra measurements and the theoretical prediction based on reference [6].

Conclusions

The experiment described in the preceeding sections demonstrated that the flow in the horizontal duct region consists of a two-branch countercurrent in which the upper branch is warmer than the lower branch. In the parametric domain covered by over experiment, $H/L = 1/6$ and $5.43 \times 10^6 < \mathrm{Ra} < 2.76 \times 10^7$ the vertical heat transfer between the two branches is inhibited by a mid-depth buffer region. The temperature distribution in the buffer region is similar to the distribution found in the adjacent reservoirs. The reservoir fluid is thermally stratified; the stratification accounts for reservoir fluid being drawn horizontally into the duct region.

The heat transfer measurements revealed a Nusselt number—Rayleigh number dependence of the type found in cavities heated and cooled between the vertical walls, $\mathrm{Nu} \sim \mathrm{Ra}^{1/4}$. We concluded that in our experiment the resistance to heat transfer posed by the duct is small compared with the two boundary layer resistances lining the heated/cooled walls of the reservoirs. Therefore, the heat transfer mechanism is different than the one described by Bejan and Tien [6] for the Ra $H/L \to 0$ limit. The apparatus design employed in this experiment proved adequate in the stability study of shear flow in stratified fluid.

Acknowledgment

This research was conducted under the auspices of National Science Foundation Research Grant No. ENG 78-20957. We thank Mr. R. Yewell and Prof. J. Imberger for their contributions. We also thank Messrs. C. E. Coet, K. A. Rupp and R. C. Cowgill for constructing the apparatus and its instrumentation. Prof. M. S. Uberoi read the manuscript and made a number of useful comments.

References

1 Ostrach, S., "Natural Convection in Enclosures," *Advances in Heat Transfer*, Vol. 8, 1972, p. 161.

2 Catton, I., "Natural Convection in Enclosures," *Proceedings Sixth International Heat Transfer Conference*, Vol. 6, 1978, p. 13.

3 Schwoerer, J. A., and Smith, J. L., Jr., "Transient Cooling of a Fault-Worthy Superconducting Electric Generator," paper presented at the Cryogenic Engineering Conference, Madison, Wisc Aug. 21–24, 1979.

4 Brown, W. G. and Solvason, K. R., "Natural Convection through Rectangular Openings in Partitions—1. Vertical Partitions," *International Journal Heat and Mass Transfer*, Vol. 5, 1962, p. 859.

5 Brown, W. G., "Natural Convection through Rectangular Openings in Partitions—2. Horizontal Partitions," *International Journal Heat and Mass Transfer*, Vol. 5, 1962, p. 869.

6 Bejan, A. and Tien, C. L., "Laminar Free Convection Heat Transfer through Horizontal Duct Connecting Two Fluid Reservoirs at Different Temperatures," ASME JOURNAL OF HEAT TRANSFER, Vol. 100, 1078, p. 725.

7 Baker, D. J., "A Technique for the Precise Measurement of Small Fluid Velocities," *Journal of Fluid Mechanics*, Vol. 26, 1966, p. 573.

8 Sparrow, E. M., Husar, R. B., and Goldstein, R. J., "Observations and Other Characteristics of Thermals," *Journal Fluid Mechanics*, Vol. 41, 1970, p. 793.

9 Eichhorn, R., Leinhard, J. H., and Chen, C. C., "Natural Convection from Isothermal Spheres and Cylinders immersed in a Stratified Fluid," Paper N.C. 1.3, *Proceedings of the 5th International Heat Transfer Conference*, Tokyo, 1974.

10 Imberger, J., "Natural Convection in a Shallow Cavity with Differentially Heated End Walls. Part 3. Experimental Results," *Journal Fluid Mechanics*, Vol. 65, 1974, p. 247.

11 Cormack, D. E., Leal, L. G., and Imberger, J., "Natural Convection in a Shallow Cavity with Differentially Heated End Walls. Part 1. Asymptotic Theory," *Journal Fluid Mechanics*, Vol. 65, 1974, p. 209.

12 Turner, J. S., *Buoyancy Effects in Fluids*, Cambridge University Press, 1979, p. 89.

13 Imberger, J., and Fandry, C., "Withdrawal of a Stratified Fluid from a Vertical Two-Dimensional Duct," *Journal Fluid Mechanics*, Vol. 70, 1975, p. 321.

14 Miles, J. W., "On the Stability of Heterogeneous Shear Flows," *Journal Fluid Mechanics*, Vol. 10, 1061, p. 496.

15 Hazel, P., "Numerical Studies of the Stability of Inviscid Stratified Shear Flows," *Journal Fluid Mechanics*, Vol. 51, 1972, p. 39.

16 Lofquist, K., "Flow and Stress near the Interface between Stratified Liquids," *Physics of Fluids*, Vol. 3, p. 158, 1960.

17 Gill, A. E., "The Boundary Layer Regime for Convection in a Rectangular Cavity," *Journal Fluid Mechanics*, Vol. 26, 1966, p. 515.

18 Bejan, A., "A General Variational Principle for Thermal Insulation System Design," *International Journal Heat Mass Transfer*, Vol. 22, Febr 1979, p. 219.

Downloaded 20 Dec 2010 to 194.27.225.72. Redistribution subject to ASME license or copyright; see http://www.asme.org/terms/Terms_Use.cfm

M. Epstein
F. B. Cheung
T. C. Chawla
G. M. Hauser

Reactor Analysis and Safety Division,
Argonne National Laboratory,
Argonne, Ill. 60439

Effective Thermal Conductivity for Combined Radiation and Free Convection in an Optically Thick Heated Fluid Layer

The effective thermal conductivity for radiative heat transfer within an optically thick fluid layer undergoing high Rayleigh number convection is derived. This result is combined with available "pure" free-convection heat-transfer correlations to obtain closed-form analytical descriptions of the gross properties of a radiating fluid layer heated internally or from below. These simple solutions compare favorably with recent work in which the governing energy equation incorporating both turbulent heat transport and thermal radiation is solved numerically.

1 Introduction

During a postulated meltdown accident for a fast breeder nuclear reactor, a layer of molten fuel and steel debris could form at the bottom of the reactor vessel. The heat generated by the radioactive decay of fission products is usually sufficient to generate a highly turbulent free-convective flow within the molten layer. Knowledge of the magnitudes of heat fluxes at the upper and lower boundaries of the layer is necessary for predicting the onset of boiling within the melt, as well as for bounding the downward rate of penetration through the melting structure below the fuel layer. Since the melting point of molten ceramic reactor fuel is about 3000 K, heat losses from fuel layers probably cannot be accounted for by free convection alone; internal thermal radiation should contribute to the total heat flow to the boundaries. Accordingly, the problem of combined turbulent free convection and internal radiation in a layer of fluid heated internally or from below has been the subject of some recent research.

Anderson [1] considered internal radiation to be a diffusion process (Rosseland "optically thick" approximation) and used a constant, effective, free-convective diffusivity to model combined radiation and free convection in a layer of molten UO_2. Cho, et al. [2] used the Rosseland diffusion approximation and an eddy convective heat-transport model advanced by Cheung [3] to study the same problem. Anderson's constant-convective-diffusivity model was found to underestimate the contribution of internal radiation at high Rayleigh numbers. Chawla, et al. [4] recently solved the problem of simultaneous free convection and radiation in a gray fluid layer. The governing energy equation incorporated an exact integral formulation for the radiation flux and, again, Cheung's model for the eddy convection. The validity of the optically thick diffusion approximation for molten-ceramic-fuel layers was confirmed by this numerical investigation (see Section 7). Cheung and Novas [5] recently carried out numerical computations for coupled turbulent-free convection and internal radiation in a layer heated from below (Rayleigh-Bénard problem) using the eddy-diffusivity formulation proposed by Cheung.

Our emphasis here is on developing a simple procedure for estimating the combined effects of internal radiation and free convection in a fluid layer heated internally and/or from below. In what follows, we sidestep many of the numerical complications associated with the use of an eddy-diffusivity model for convective heat transport and, instead, exploit the free-convection model proposed by Howard [6] to obtain closed-form analytical descriptions of the gross properties of a heated, optically thick, fluid layer. By suitably combining an effective radiative heat conductivity, suggested by Howard's diffusion-layer instability model, with existing empirical correlations obtained for free convection alone, one can easily describe effects attributable to internal thermal radiation. We will focus our attention on two simple, yet realistic, example problems, but the principle and method elucidated by these examples indeed carry over to more complex situations.

2 Effective Radiative Conductivity

The formulation of combined free convection-radiative heat transport is relatively simple when the fluid layer is optically thick. Nevertheless, even with this most simple radiation model, the rigorous solution for the heat transfer must be obtained by means of numerical integration and usually involves a complex two-point boundary value problem. It is recognized that an important simplification to this class of problems is possible if an appropriate, effective "radiative conductivity", k_r, which represents both the internal radiation and molecular conduction components to the heat transport, can be identified. The existence of such an effective conductivity is based on the fact that, under optically thick conditions, the term representing radiation in the governing energy equation is similar to the heat-conduction term. If k_r is known, then it is not necessary to solve the governing equation, because every experiment or analysis of free convection without thermal radiation may be regarded as supplying a solution of the combined problem with the difference that k_r replaces the molecular conductivity.

It would seem that a major drawback associated with the notion of an effective conductivity is that it cannot be determined until the whole free convection problem of interest is solved.[1] Fortunately, a means of deriving a priori an effective radiative conductivity generally applicable to optically thick, heated fluid layers at high Rayleigh numbers is suggested by Howard's diffusion-layer instability model of turbulent-free convection [6]. This model and its connection with internal thermal radiation are discussed in some detail in the next section.

3 Howard's "Surface Renewal" Model

We consider the situation illustrated in Fig. 1 in which a horizontally infinite layer of fluid is confined between two isothermal surfaces and heated from below at a steady rate. This special case of free convection exhibits the essential features of the well known Ray-

Contributed by the Heat Transfer Division for publication in the JOURNAL OF HEAT TRANSFER. Manuscript received by the Heat Transfer Division March 7, 1980.

[1] The only exceptional case is when the temperature difference across the fluid layer is small compared with the absolute fluid temperature level. The radiation term in the energy equation can then be linearized and the expression for k_r is readily obtained (see below). In several gas-cooled fast-reactor safety applications, however, the estimated temperature difference between the horizontal boundaries of a molten UO_2 layer is too large to justify a linearized radiation term.

Copyright © 1981 by ASME

Downloaded 20 Dec 2010 to 194.27.225.72. Redistribution subject to ASME license or copyright; see http://www.asme.org/terms/Terms_Use.cfm

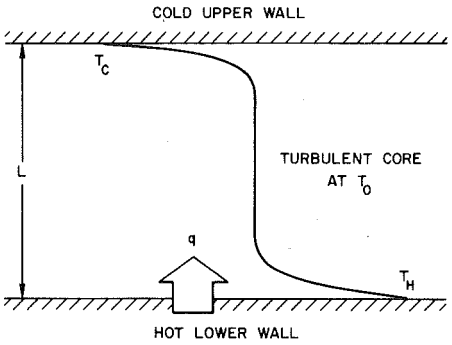

Fig. 1 Schematic of the bottom-heated horizontal fluid layer

leigh-Bénard problem. The layer depth and the temperature difference between the hot and cold surfaces, $T_H - T_C$, are assumed to be much larger than those at which convective instability sets in and we temporarily ignore internal thermal radiation. Laboratory observations [7] of highly turbulent free convection between two horizontal surfaces indicate that the fluid temperature varies only in the boundary layers near each surface, as shown in Fig. 1. Over most of the fluid layer (or turbulent core) the temperature is approximately uniform. Moreover, assuming constant physical properties, the temperature profile is approximately symmetric with respect to the temperature in the turbulent core, T_0.

Howard suggested that the growth and release of thermal plumes from the boundary layers would cause repeated, gross replacement of the fluid within the layers with fluid from the well mixed bulk. He presumed that molecular conduction and "surface renewal" controls heat transfer between the surface and fluid. The boundary (or density) layer grows according to the familiar square-root law,

$$\delta \simeq \sqrt{\pi \alpha t}\,, \tag{1}$$

until its thickness δ attains some value based on a critical local Rayleigh number,

$$\mathrm{Ra}_\delta = \frac{g\beta\Delta T\delta^3}{\nu\alpha}\,, \tag{2}$$

whereupon the fluid in the boundary layer is suddenly removed by a departing thermal. ($\Delta T = T_H - T_0 = T_0 - T_C$ is the temperature difference across each boundary layer.) The average heat flux q through the surface during the stable period between departing thermals is given by

$$q = \frac{2k\Delta T}{\sqrt{\pi\alpha t}} = \frac{2k\Delta T}{\delta}\,. \tag{3}$$

The dimensionless rate of heat transfer through the convection layer is characterized by the Nusselt number

$$\mathrm{Nu} = \frac{qL}{2k\Delta T}\,. \tag{4}$$

Equations (2 – 4) may be combined to obtain

$$\mathrm{Nu} = \frac{L}{\delta} = \left(\frac{\mathrm{Ra}}{\mathrm{Ra}_\delta}\right)^{1/3}\,. \tag{5}$$

Thus, the Nusselt number is equal to the ratio of the depth of the convective layer, L, to the thickness of the boundary layer δ. The relationship between Nu and Ra given by equation (5) is roughly the experimental result obtained by Katsaros, et al. [8]. Moreover, detailed measurements of the periodicity of thermal-plume generation by Sparrow, et al. [9] lend further support to Howard's model.

One is therefore left with the conclusion that the problems of turbulent-free convection in a fluid layer can be solved by means of the transient conduction solutions (1) and (3), valid for a semi-infinite stagnant medium. This has important implications with regard to readily generalizing existing free-convection heat-transfer correlations to include radiating fluid matter. If radiation is considered to be a diffusion process, and the radiative flux is approximated accordingly, then equations (1) and (3) are still valid, provided that the molecular conductivity, k, is replaced by an appropriate (effective) radiative conductivity, k_r. As suggested by Howard's model, the desired radiative conductivity should be obtained once and for all by solving the problem of transient simultaneous conduction and radiation in a semi-infinite, optically thick (stagnant) medium and reducing the result to the same form as equation (3). This is accomplished next. As mentioned previously, if the solution to a free-convection problem in a fluid layer is obtainable by experiment or analysis, then the solution for combined convection and radiation within an optically thick fluid layer can be quickly constructed by simply replacing k with k_r.

4 Radiation and Conduction in an Optically Thick Slab and the Effective Conductivity

Consistent with our purposes outlined above, we consider the temperature profile in a radiating, semi-infinite slab following a step change in temperature at the surface of the slab at time $t = 0$. The slab is initially maintained at a uniform temperature T_0. The energy-conservation equation, incorporating the Rosseland diffusion approximation,

$$\rho c\,\frac{\partial T}{\partial t} = k\,\frac{\partial^2 T}{\partial x^2} + \frac{\partial}{\partial x}\left(\frac{16\sigma n^2}{3\kappa}\,T^3\,\frac{\partial T}{\partial x}\right), \tag{6}$$

together with the boundary and initial conditions

$$x = 0,\ T = T_w;\ x \to \infty,\ T \to T_0;\ t = 0,\ T = T_0, \tag{7}$$

essentially completes the mathematical statement of the problem. The coordinate x is measured from the surface of the slab; n is the

Nomenclature

A = dimensionless constant coefficient, equation (19)
c = specific heat
f = dimensionless similarity temperature variable, equation (8)
g = acceleration due to gravity
k = molecular conductivity
k_r = effective thermal conductivity
κ = absorption coefficient
L = thickness of horizontal fluid layer
M = dimensionless surface-temperature ratio, equation (26)
n = dimensionless exponent, equation (19), or refractive index in equation (6)
N = conduction-radiation parameter defined by equation (11)
Nu = Nusselt number defined by equation (4)
q = average heat flux through boundary
Q = volumetric heat generation rate
Ra = $\dfrac{g\beta\Delta TL^3}{\nu\alpha}$, or defined by equations (2) or (29)
t = time
T = temperature
T_C = temperature at the upper (cold) surface
T_H = temperature at the lower (hot) surface
T_0 = temperature within the turbulent core of the fluid layer
T_w = surface temperature in stagnant slab problem (Section 4)
x = distance measured from surface of radiating slab (Section 4)
α = thermal diffusivity
β = isobaric coefficient of thermal expansion
δ = thermal boundary layer thickness
ΔT = surface-to-fluid core temperature difference
η = dimensionless similarity coordinate, equation (8)
θ = dimensionless turbulent core temperature, equation (25)
ν = kinematic viscosity
ρ = density
σ = Stefan-Boltzmann constant

Downloaded 20 Dec 2010 to 194.27.225.72. Redistribution subject to ASME license or copyright; see http://www.asme.org/terms/Terms_Use.cfm

refractive index, σ, the Stefan-Boltzmann constant, κ, the absorption coefficient, ρ, the density, and c, the heat capacity.

While there are no known closed-form solutions to equation (6) Yang [10] pointed out that equations of this class may be transformed into ordinary differential equations by invoking the usual similarity transformation

$$\eta = \frac{x}{2\sqrt{\alpha t}}, \quad \frac{T}{T_w} = f(\eta). \tag{8}$$

Equation (6) and the above conditions (7) then become

$$\left(1 + \frac{4}{3N} f^3\right) f'' + \frac{4f^2}{N} (f')^2 + 2\eta f' = 0 \tag{9}$$

and

$$f(0) = 1.0, f(\infty) = \frac{T_0}{T_w}. \tag{10}$$

The quantity N in equation (9) is the conduction-radiation parameter

$$N = \frac{k\kappa}{4n^2\sigma T_w{}^3}. \tag{11}$$

The average heat flux at the surface, q, can now be expressed in the form

$$q = \frac{k\left(1 + \frac{4}{3N}\right)T_w}{\sqrt{\alpha t}} f'(0). \tag{12}$$

Moreover, by comparing equation (12) with equation (3), we note that the effective radiative conductivity is given by

$$\frac{k_r}{k} = \left[\frac{\sqrt{\pi}}{2}\left(1 + \frac{4}{3N}\right)\frac{f'(0)}{T_0/T_w - 1}\right]^2. \tag{13}$$

Heinisch and Viskanta [11] have obtained numerical solutions to equations (9) and (10) for the case where the initial temperature of the slab is just twice the surface temperature ($T_0 = 2T_w$). In the present analysis, numerical solutions have been obtained over a broad range of the absolute-temperature ratio parameter T_0/T_w and the conduction-radiation parameter N. Using these solutions, we have constructed the plot shown in Fig. 2, with the ordinate being $(1 + 4/3N)^{1/2} f'(0)$. The application of equation (13) and this plot is sufficient to compute the radiative conductivity ratio k_r/k in terms of T_0/T_w and N. However, for obtaining closed-form approximate results for combined radiation and free-convection problems, it is necessary to have an explicit expression that relates k_r/k to the parameters of the problem. Thus, one is tempted to inquire if a simple formula can be found that correlates all the results displayed in Fig. 2.

It is useful to observe that if equation (6) is forced into the linear form

$$\rho c \frac{\partial T}{\partial t} = k \frac{\partial^2 T}{\partial x^2} + \frac{16\sigma n^2 \overline{T^3}}{3\kappa} \frac{\partial^2 T}{\partial x^2}, \tag{14}$$

by postulating a mean value for T^3, namely $\overline{T^3}$, then we can readily obtain the following rough approximation to $f'(0)$

$$f'(0) = \frac{2}{\sqrt{\pi}} \frac{(T_0/T_w - 1)}{1 + \frac{4}{3N}} \sqrt{1 + \frac{4}{3N}\left(\frac{\overline{T^3}}{T_w{}^3}\right)}. \tag{15}$$

This formula by itself is of limited value since, except for the trivial case $(T_w - T_0)/T_w \ll 1.0$ where $\overline{T^3}$ can be taken approximately equal to $T_w{}^3$, we have no knowledge of $\overline{T^3}$. However, assuming that equation (15) provides the correct relationship between $f'(0)$ and the radiation parameter N, we need only test several plausible choices for the mean temperature in terms of T_0/T_w until we find the function $\overline{T^3}(T_0/T_w)$ that, together with equation (15), adequately correlates the numerical data in Fig. 2. The following choice was reasonably successful in the parameter range of interest here

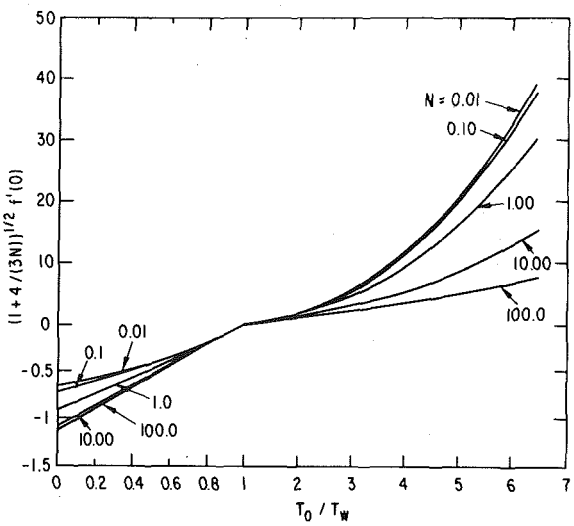

Fig. 2 Values of the dimensionless heat flux at the surface of an optically thick radiating slab. (Note the change in scale for $T_0/T_w > 1$.)

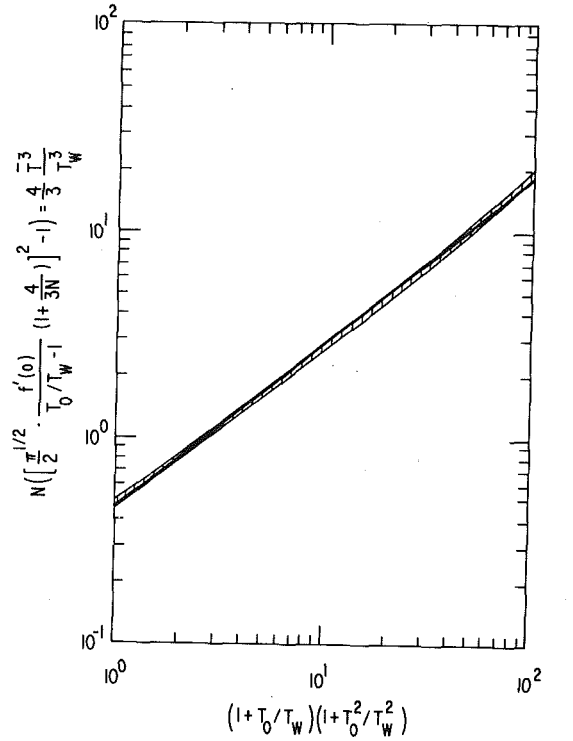

Fig. 3 Correlation for $\overline{T^3}$: —— equation (16); IIII numerical data

$$\frac{\overline{T^3}}{T_w{}^3} = 0.345[(1 + T_0/T_w)(1 + T_0{}^2/T_w{}^2)]^{0.82} \tag{16}$$

It is seen from Fig. 3 that, by using equations (15) and (16), we can predict all the numerical results displayed in Fig. 2 for $f'(0)$ with a root-mean-square relative error of less than 10 percent. Upon inserting equations (15) and (16) into equation (13) we obtain the desired expression for k_r.

$$\frac{k_r}{k} = 1 + \frac{0.46}{N}[(1 + T_0/T_w)(1 + T_0{}^2/T_w{}^2)]^{0.82} \tag{17}$$

The use of this result for combined free convection and internal radiation in a horizontal fluid layer at high temperature is best demonstrated by treating some representative cases of practical interest. What follows compares the results of the present method with available numerical solutions based on an eddy-diffusivity concept

Downloaded 20 Dec 2010 to 194.27.225.72. Redistribution subject to ASME license or copyright; see http://www.asme.org/terms/Terms_Use.cfm

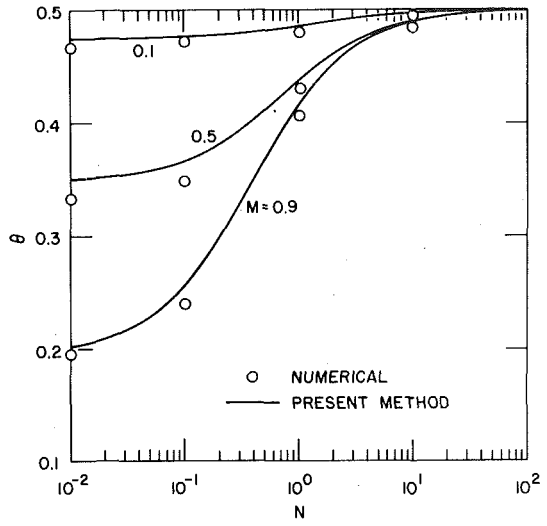

Fig. 4 Effect of internal radiation and wall temperature ratio parameter on the turbulent core temperature within a bottom-heated fluid layer; comparison of present results and numerical solutions

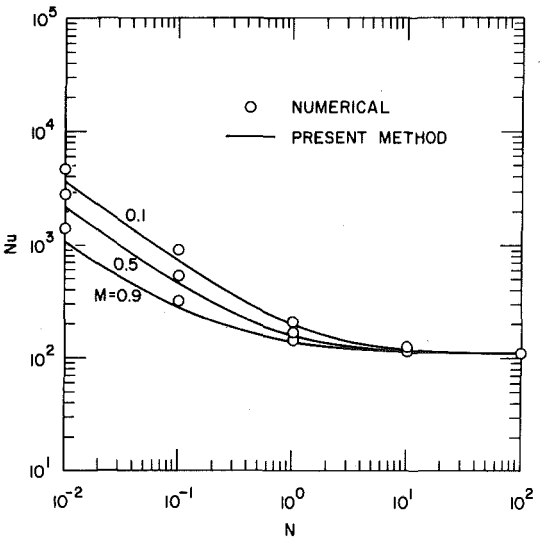

Fig. 5 Effect of internal radiation and wall temperature ratio parameter on the normalized energy transfer through a bottom-heated fluid layer ($Ra = 10^{10}$); comparison of present results and numerical solutions

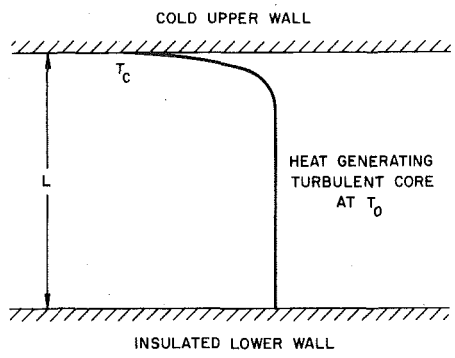

Fig. 6 Schematic of the internally heated fluid layer

to gain some indication of its accuracy.

5 Radiation and Free Convection in a Rayleigh-Bénard Layer

The physical problem treated first was described above in the discussion of Howard's model; namely, we consider a horizontally infinite layer of fluid confined between two isothermal surfaces and heated from below at a steady rate (see Fig. 1). The layer depth and the temperature difference between the hot and cold surfaces, $T_H - T_C$, are assumed to be much larger than those at which convective instability sets in, and the fluid is assumed to radiate heat according to the Rosseland diffusion approximation.

In the absence of internal radiation, assuming constant physical properties, the temperature profile is approximately symmetric with respect to the temperature in the turbulent core, T_0, as shown in Fig. 1. Clearly, without radiation,

$$T_H - T_0 = T_0 - T_C = \tfrac{1}{2}(T_H - T_C). \tag{18}$$

The turbulent convection experiments of Chu and Goldstein [7] in the geometry of interest have led to the relation

$$\mathrm{Nu} = A \cdot \mathrm{Ra}^n; \quad A = 0.183, \quad n = 0.278, \tag{19}$$

where Nu and Ra are based on the total temperature drop $T_H - T_C$. However, for our purposes we will define the characteristic temperature difference in equation (19) to be that across each boundary layer. This is permissible, since the two boundary layers are almost isolated from one another by the turbulent fluid core; that is, there is very little interaction between the lower and upper boundary layers. Thus, solving equation (19) for the heat flux across each boundary layer, we have

$$q = 2A\frac{k}{L}(T_H - T_0)\left[\frac{2\rho c g\beta(T_H - T_0)L^3}{\nu k}\right]^n \tag{20}$$

for the lower boundary and

$$q = 2A\frac{k}{L}(T_0 - T_C)\left[\frac{2\rho c g\beta(T_0 - T_C)L^3}{\nu k}\right]^n \tag{21}$$

for the upper boundary. Of course, under steady-state conditions, the heat fluxes given by (20) and (21) are identical.

According to the foregoing arguments, equations (20) and (21) are readily generalized to include the effect of internal radiation by simply setting $k = k_r$ as given by equation (17). Carrying out this substitution immediately gives

$$q = 2A\frac{k}{L}(T_H - T_0)\left\{1 + \frac{0.46}{N}[(1 + T_0/T_H)(1 + T_0^2/T_H^2)]^{0.82}\right\}^{1-n} \cdot \left[\frac{2g\beta(T_H - T_0)L^3}{\nu\alpha}\right]^n \tag{22}$$

for the heat flux across the lower boundary and

$$q = 2A\frac{k}{L}(T_0 - T_C) \times \left\{1 + \frac{0.46}{N}\frac{T_H^3}{T_C^3}[(1 + T_0/T_C)(1 + T_0^2/T_C^2)]^{0.82}\right\}^{1-n} \cdot \left[\frac{2g\beta(T_0 - T_C)L^3}{\nu\alpha}\right]^n \tag{23}$$

for the upper boundary. In the above expressions, the radiation parameter N is based on the temperature at the lower boundary.

With thermal radiation as well as turbulent convection in the fluid layer, the mean core temperature, T_0, departs from its arithmetic mean value and shifts towards the base temperature as the total temperature drop $T_H - T_C$ is increased. This is due to the fact that the radiation flux is a strong function of the temperature levels within the boundary layers. An implicit relationship between the mean core temperature and the parameters N, T_C/T_H is obtained by setting equation (22) equal to equation (23)

Downloaded 20 Dec 2010 to 194.27.225.72. Redistribution subject to ASME license or copyright; see http://www.asme.org/terms/Terms_Use.cfm

$$N = 0.46 \frac{\{(2 - M\theta)\,[1 + (1 - M\theta)^2]\}^{0.82} - (1 - M)^3 \left(\frac{1-\theta}{\theta}\right)^{(1+n)/(1-n)} \left\{\left[1 + \frac{1 - M\theta}{1 - M}\right]\left[1 + \left(\frac{1 - M\theta}{1 - M}\right)^2\right]\right\}^{0.82}}{\left(\frac{1-\theta}{\theta}\right)^{(1+n)/(1-n)} - 1}, \tag{24}$$

where we have introduced the abbreviations

$$\theta \equiv \frac{T_H - T_0}{T_H - T_C} \text{ (dimensionless core temperature)} \tag{25}$$

and

$$M = \frac{T_H - T_C}{T_H} \text{ (dimensionless surface-temperature ratio).} \tag{26}$$

Equation (22) or (23) immediately gives the overall Nusselt number in terms of θ and N

$$\mathrm{Nu} = \frac{qL}{k(T_H - T_C)} = A(2\theta)^{1+n}\mathrm{Ra}^n \left\{1 + \frac{0.46}{N}\{(2 - M\theta)[1 + (1 - M\theta)^2]\}^{0.82}\right\}^{1-n}. \tag{27}$$

Typical results, showing the effects of radiation on core temperature and free-convective heat transfer, are displayed in Figs. 4 and 5. These analytic and graphical results clearly reveal the conditions under which departures from pure free-convection behavior are to be expected for any combination of radiation parameter and surface-temperature ratio. Also shown in Figs. 4 and 5 is a comparison of our predictions with the results of a numerical model in which the full energy-conservation equation is solved, with turbulent-free convection represented by an eddy-diffusivity relation [5]. The results for θ are especially encouraging, with equation (24) approximating the numerical results to better than 5.0 percent. Also, we conclude from Fig. 5 that equation (27) represents a satisfactory solution for the rate of energy transfer across the fluid layer. The Nusselt number corresponding to equation (27) falls below the numerical-solution values by less than 20 percent over the range of values of N investigated. As anticipated, radiation has the effects of reducing θ below 0.5 while increasing Nu. It is interesting to note that the mean core temperature is not a function of the Rayleigh number (see equation (24)).

6 Radiation and Free Convection in an Internally Heated Layer

Unlike Rayleigh-Bénard convection, turbulent-free convection in an internally heated layer between isothermal, equal-temperature surfaces occurs only in the upper part of the layer. In the lower part of the layer, the temperature profile is such that the fluid is stable to the buoyant force and is therefore relatively stagnant. For this reason, the internally heated layer is usually modeled by dividing the layer into two sublayers. The plane of maximum temperature serves as the dividing line. The lower sublayer is essentially a molecular heat-diffusion layer and is of little interest here. The upper sublayer is bounded below by an adiabatic horizontal surface (at the dividing plane) and is capped by an isothermal surface, as illustrated in Fig. 6. As in the Rayleigh-Bénard layer, experimental observations of the temperature distributions in internally heated layers (with an adiabatic lower boundary) undergoing turbulent-free convection, show that temperature variations are confined to a thin boundary layer adjacent to the upper surface. Of course, there is no boundary layer at the lower surface, since there is no heat flux through this surface. In this case, the temperature of the turbulent core, T_0, is equal to the maximum temperature at the insulated lower boundary.

Once again, to predict the heat flow from such an internally heated layer with internal radiation, we exploit an available empirical correlation for the mean Nusselt number in the absence of radiation. In particular, we adopt the correlation recommended by Kulacki and Emara [12] for free-convection heat transfer alone:

$$\mathrm{Nu} = 0.2015\mathrm{Ra}^{0.226}, \tag{28}$$

where, for internally heated fluids, the Rayleigh number is defined by

$$\mathrm{Ra} \equiv \frac{g\beta Q L^5}{2k\alpha\nu}. \tag{29}$$

In the above expression, Q is the volumetric energy source in W/cm^3. If we make the substitution $k = k_r$ using equation (17), we can readily write an expression for Nu that includes coupled free convection and radiation in a volumetrically heated layer.

$$\mathrm{Nu} = 0.2015\mathrm{Ra}^{0.226}\left[1 + \frac{0.46}{N}([1 + T_0/T_C][1 + T_0^2/T_C^2])^{0.82}\right]^{0.548}. \tag{30}$$

Equation (30) is represented graphically in Fig. 7, where it is compared with the numerical results of Chawla, et al. [4] which are based on the eddy-diffusivity heat flow function derived by Cheung [3]. We see that equation (30) provides a simple yet accurate correlation for the effects of internal radiation in the heat-generating fluid layer.

It is worthwhile to note that thermal effects qualitatively similar to those discussed in this section should also result in exothermically reacting fluid medium having the same parallel-plate geometry illustrated in Fig. 6. Indeed, if the kinetic-chemical heat-release laws governing such reactions are expressible in terms of local fluid temperature only, a theoretical framework identical to that pursued here would predict the effects of internal radiation within a reacting fluid.

7 Thermal Boundary Layer Thickness, Optically Thick Approximation and Howard's Model

Using equation (5) for the (approximate) relation between the thermal-layer thickness and the Nusselt number and replacing the molecular conductivity k by the radiative conductivity k_r, we find for the Rayleigh-Bénard problem that

$$\frac{\delta_H}{L} \simeq \frac{2\theta}{\mathrm{Nu}}\left[1 + \frac{0.46}{N}([2 - M\theta]\,[1 + (1 - M\theta)^2])^{0.82}\right] \tag{31}$$

$$\frac{\delta_C}{L} \simeq \frac{2(1-\theta)}{\mathrm{Nu}}\left[1 + \frac{0.46}{N}(1 - M)^3\left(\left[1 + \frac{1 - M\theta}{1 - M}\right] \times \left[1 + \left(\frac{1 - M\theta}{1 - M}\right)^2\right]\right)^{0.82}\right] \tag{32}$$

are the thicknesses of the lower and upper boundary layers, respectively. Introducing the turbulent core temperature and the Nusselt number through equations (24) and (27), the boundary layer thicknesses are immediately obtained from equations (31) and (32). Plots of δ_c versus N and δ_H versus N with M as a parameter are shown in Fig. 8. The Rayleigh number is fixed at $\mathrm{Ra} = 10^{10}$ in both cases. It is quite clear that the effect of radiation is to increase the boundary layer thickness.

A limitation imposed on the present model is the Rosseland diffusion approximation for internal thermal radiation. For the radiation diffusion approximation to apply, we require that the optical thickness of the thermal boundary layer be larger than unity,[2] namely $\kappa\delta > 1$. Suppose the optical thickness of the fluid layer is $\kappa L \simeq 10^3$. This value, which is typical of those encountered in nuclear safety applications, has been widely employed in previous investigations [1, 2, 4]. Note from Fig. 8 that both the upper and lower boundary layer thickness are equal to or larger than approximately $0.01L$ under all radiation

[2] It can be shown that even $\kappa\delta = 1$ may be considered a fairly large optical thickness.

Downloaded 20 Dec 2010 to 194.27.225.72. Redistribution subject to ASME license or copyright; see http://www.asme.org/terms/Terms_Use.cfm

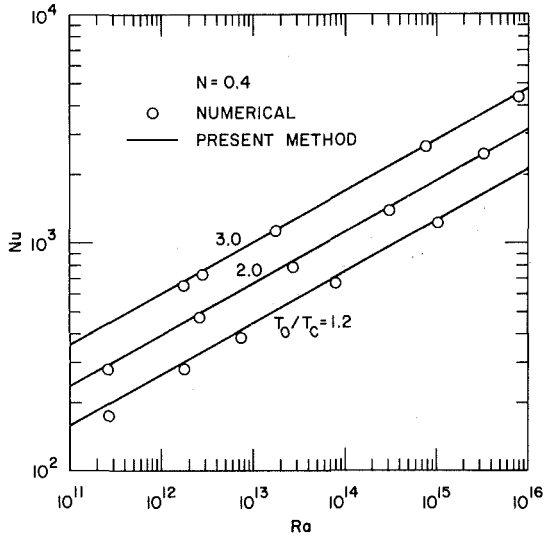

Fig. 7 Effect of Rayleigh number and turbulent core temperature ratio on the normalized energy transfer from an internally heated layer at a fixed value of the radiation parameter *N*

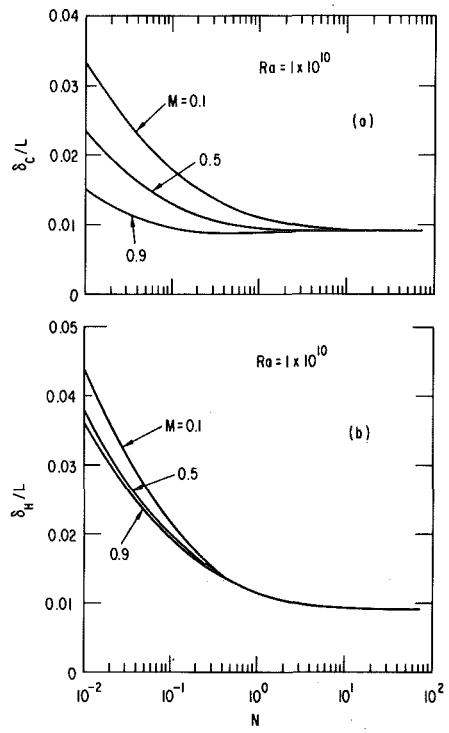

Fig. 8 Predicted upper and lower boundary-layer thicknesses for a bottom heated fluid layer; effects of radiation parameter *N* and wall temperature ratio parameter *M*

conditions; that is, $\delta \geq 0.01L$ or, equivalently,

$$\delta\kappa = \left(\frac{\delta}{L}\right) \cdot (\kappa L) \geq 10.0 \tag{33}$$

Indeed, for the practically important case $\kappa L \simeq 10^3$, the boundary layers are optically thick.

At first glance, the two basic models used in this study, namely Rosseland diffusion and Howard's turbulence (or surface renewal) model, seem to contradict each other. This is because the radiation diffusion approximation is valid in the low Rayleigh number range where the thermal boundary layer is sufficiently thick, whereas the surface renewal concept works only in the high Rayleigh number range where the thermal boundary layer is sufficiently thin. However, there is a common range of validity in which both models apply. It is the existence of such a common region that constitutes the foundation of this study.

It is interesting to estimate the Rayleigh number range over which both Rosseland diffusion and intense turbulence coexist. To accomplish this, we again assume the optical thickness of the fluid layer to be $\kappa L \simeq 10^3$. Thus, from the left-hand equality (33) and the condition $\kappa\delta > 1$, the radiation diffusion model is valid provided $\delta/L > 10^{-3}$. On the other hand, the surface renewal model is valid only if the thermal boundary layer is thin. Measurements of both the free-convective heat transport and the thermal boundary-layer thickness within heated liquid layers [7, 8, 13, 14] indicate that Howard's model is physically sound for, say $\delta/L < 0.05$. The corresponding Rayleigh number range for the Rayleigh-Bénard problem is determined from equations (27, 31) and (32). For radiation parameter $N = 0.4$ and surface-temperature ratio $M = 0.1$, we find that the radiation diffusion model and Howard's surface renewal model simultaneously apply in the Rayleigh number range 0.5×10^7–2.8×10^{13}. At higher values of N and M the range of applicability is even wider. A similar estimate can be made for fluid layers subject to internal volumetric heat generation. For the conditions given in Fig. 7 with $T_0/T_C = 3.0$, the Rayleigh number range over which both models apply is calculated using equation (30) and equation (5) with k replaced by k_r and is found to be 10^{10}–10^{16}. Even at a Rayleigh number as high as $\mathrm{Ra} \simeq 10^{16}$, the optical thickness of the thermal boundary layer is $\kappa\delta \simeq 1.0$, which can still be considered large.

It is recognized that the models exploited here will not apply if thermal radiation strongly affects the turbulence intensity within the thermal boundary layer. The present work along with all the existing (numerical) solutions [1, 2, 4, 5] for the class of fluid layer problems under consideration are based on the assumption that the turbulent motion within the boundary layer is unaffected by radiation. Townsend [15] described the influence of radiation on turbulent fluctuations in free turbulent flow far from solid boundaries. He found that radiative heat transfer decreases or "damps" the turbulence intensity. A similar treatment of the interaction of the temperature field and the turbulent motion in the boundary layer is quite difficult due to the inhomogeneity of the fluid motion, but would constitute a useful next step. However, we expect that as long as the Rayleigh number is sufficiently large or, equivalently, the boundary layer is sufficiently thin, the physical picture of the turbulent heat transport across the boundary layer in the immediate neighborhood of the surface will not change very much in the presence of optically thick radiation; heat transport will still be controlled by diffusion in a marginally stable diffusion layer. Of course, as mentioned above, we cannot make the Rayleigh number arbitrarily large as that would violate the Rosseland approximation.

Finally, we should discuss the assumption of constant (mean) thermo-physical and radiative properties. While necessary to achieve the simple general results presented, there is no question that breakdown of this assumption or the Boussinesq approximation itself will limit the accuracy with which the results can be applied in particular cases. This additional complication is frequently accompanied by a large temperature difference $T_H - T_C$. It would be of interest to determine whether an effective thermal conductivity based on combined conduction and radiation in a stagnant material with variable physical properties, together with an appropriate pure free-convection heat-transfer correlation for the specific fluid material of interest, will correctly model combined radiation and free convection in this situation. However, further calculations of k_r would appear to be premature in the absence of more extensive free-convection data and exact variable property analysis of simultaneous free convection and radiation in a fluid layer.

Conclusions

An effective conductivity for radiative heat transfer within a fluid layer undergoing high Rayleigh number convection has been determined and exploited here to the point of yielding useful qualitative and quantitative heat-transfer information with the recourse to only pure free-convection solutions or empirical correlations. It is recognized that the key underlying assumption of optically thick radiating

Downloaded 20 Dec 2010 to 194.27.225.72. Redistribution subject to ASME license or copyright; see http://www.asme.org/terms/Terms_Use.cfm

matter will not apply in specific free convection situations; however, the present method may still prove valuable in providing reasonable heat transfer bounds, insight as to trends, and guidance to future high-temperature experimental developments in this area.

Acknowledgment

This work was performed under the auspices of the U. S. Department of Energy.

References

1 Anderson, E. E., "Radiative Heat Transfer in Molten UO_2 based on the Rosseland Diffusion Method," *Nuclear Technology,* Vol. 30, 1976, pp. 65–70.

2 Cho, D. H., Chan, S. H., and Hauser, G. M., "Radiative Heat Transfer in a Horizontal Molten Fuel Layer with Volumetric Heating," *Transactions of the American Nuclear Society,* Vol. 30, 1978, pp. 473–474.

3 Cheung, F. B., "Natural Convection in a Volumetrically Heated Fluid Layer at High Rayleigh Numbers," *International Journal of Heat and Mass Transfer,* Vol. 20, 1977, pp. 499–506.

4 Chawla, T. C., Chan, S. H., Cheung, F. B., and Cho, D. H., "Combined Natural Convection and Radiation in a Volumetrically Heated Fluid Layer," ASME JOURNAL OF HEAT TRANSFER, Vol. 102, 1980, pp. 81–85.

5 Cheung, F. B., and Novas, J. B., "Heat Transfer in an Optically Thick Horizontal Fluid Layer Heated from Below," *Letters Heat Mass Transfer,* Vol. 7, 1980, pp. 171–181.

6 Howard, L. N., "Convection at High Rayleigh Number," in *Proceedings of the 11th International Congress on Applied Mechanics,* Springer, Berlin, 1966, pp. 1109–1115.

7 Chu, T. Y., and Goldstein, R. J., "Turbulent Convection in a Horizontal Layer of Water," *Journal of Fluid Mechanics,* Vol. 60, 1973, pp. 141–159.

8 Katsaros, K. B., Liu, W. T., Businger, J. A., and Tillman, J. E., "Heat Transport and Thermal Structure in the Interfacial Boundary Layer Measured in an Open Tank of Water in Turbulent Free Convection," *Journal of Fluid Mechanics,* Vol. 83, 1977, pp. 311–335.

9 Sparrow, E. M., Husar, R. B., and Goldstein, R. J., "Observations and other Characteristics of Thermals," *Journal of Fluid Mechanics,* Vol. 41, 1970, pp. 793–800.

10 Yang, K. T., "Transient Conduction in a Semi-Infinite Solid with Variable Thermal Conductivity," *Journal of Applied Mechanics,* Vol. 25, 1958, pp. 146–147.

11 Heinisch, R. P., and Viskanta, R., "Transient Combined Conduction-Radiation in an Optically Thick Semi-Infinite Medium," *AIAA Journal,* Vol. 6, 1968, pp. 1409–1411.

12 Kulacki, F. A., and Emara, A. A., "Heat Transfer Correlations for Use in PAHR Analysis and Design," *Transactions of the American Nuclear Society,* Vol. 22, 1975, pp. 447–448.

13 Kulacki, F. A., and Nagle, M. Z., "Natural Convection in a Horizontal Fluid Layer with Volumetric Energy Sources," ASME JOURNAL OF HEAT TRANSFER, Vol. 97, 1975, pp. 204–211.

14 Kulacki, F. A., and Emara, A. A., "Steady and Transient Thermal Convection in a Fluid Layer with Uniform Volumetric Energy Sources," *Journal of Fluid Mechanics,* Vol. 83, 1977, pp. 375–395.

15 Townsend, A. A., "The Effects of Radiative Transfer on Turbulent Flow of a Stratified Fluid," *Journal of Fluid Mechanics,* Vol. 4, 1958, pp. 361–375.

Downloaded 20 Dec 2010 to 194.27.225.72. Redistribution subject to ASME license or copyright; see http://www.asme.org/terms/Terms_Use.cfm

Nongray Particulate Radiation in an Isothermal Cylindrical Medium

J. D. Felske
Assistant Professor.

K. M. Lee[1]
Student.

Department of Mechanical Engineering,
State University of New York at Buffalo,
Amherst, NY 14260

The radial radiative heat flux and its divergence are determined both exactly and approximately for homogeneous suspensions of small particles. Scattering is assumed to be small compared to absorption and the absorption coefficient is taken to be inversely proportional to wavelength. The exact solution is reduced to an infinite series of single integrals. The optically thin and the next higher order behavior appear in closed form as the first two terms in the series. Two approximate solutions are also developed. One is in good agreement with the exact solution while the other is not. Finally, a closed form approximate relation is derived for the dimensionless heat flux at the surface. This expression, which also gives the emissivity or absorptivity of the medium, is in excellent agreement with the exact result.

Introduction

The equations describing the radiative heat transfer in an infinitely long cylindrical medium are well known [1, 2]. Using the radial radiative flux formulation of [2], several investigators have studied radiative transfer in nongray gaseous media having discrete absorption bands [3–10]. In [3–5] radiation was taken to be the only mode of energy transfer while in [6–10] combined modes were considered. Nongray continuum radiation due to particulates is also an important contributor to the total radiative transfer in combustion systems [11]. Depending upon the fuel and how it is burned, the importance of this particulate radiation will range from insignificant to dominant. Under all conditions, however, the radiation from the combined gas/particulate mixture may be analyzed in a way such that one term in the solution represents particulate radiation in the absence of any gaseous participation [12]. Hence, the nongray problem concerning a purely particulate medium is of fundamental importance to combined gas/particulate analyses. In [13] the problem of particulate radiation in a parallel plate geometry was considered. Approximate closed form solutions for nonhomogeneous media were developed there. The purpose of the present work is to develop exact and approximate results for isothermal particle suspensions in the more common combustion geometry—cylindrical.

Exact Solution

The particles produced in the combustion of hydrocarbon fuels are often small enough such that the radiative interchange may be predicted using the small particle limit of Mie's equations. In this limit and for these absorbing particles, scattering is negligible and the spectral absorption coefficient is reasonably approximated by [13].

$$k = C/\lambda \tag{1}$$

where $C = c_0 f_v$, in which f_v is the local volume fraction of particles and c_0 is a constant whose value lies between 3 and 7. In the following analysis, the particle concentration will be assumed spatially uniform and hence C will be constant.

The spectral, radial radiative heat flux is given in [2] for the general case wherein the temperature and absorption coefficient are allowed to vary with radius across the cylindrical medium. Using this spectral result, the total radial flux for a homogeneous nongray particulate medium having an absorption coefficient given by equation (1) may be written as

$$q''(r) = 4\int_0^\infty I_{b\lambda}(T_w)\int_0^{\pi/2}\cos\gamma\, D_3(x_1)d\gamma d\lambda - 4\int_0^\infty I_{b\lambda}(T_w)\int_0^{\pi/2}\cos\gamma\, D_3(x_2)d\gamma d\lambda$$

$$+4C\int_0^\infty \lambda^{-1}I_{b\lambda}(T_g)\int_0^{\pi/2}\cos\gamma\int_{r\sin\gamma}^{r_0} D_2(x_3)\times\frac{dr'}{\cos\gamma'}d\gamma d\lambda \tag{2}$$

$$+4C\int_0^\infty \lambda^{-1}I_{b\lambda}(T_g)\int_0^{\pi/2}\cos\gamma\int_{r\sin\gamma}^{r} D_2(x_4)\frac{dr'}{\cos\gamma'}d\gamma d\lambda - 4C\int_0^\infty \lambda^{-1}I_{b\lambda}(T_g)\int_0^{\pi/2}\cos\gamma\int_{r}^{r_0} D_2(x_5)\frac{dr'}{\cos\gamma'}d\gamma d\lambda$$

where $I_{b\lambda}(T)$ is Planck's blackbody intensity function and

$$x_1 = Cr_0\lambda^{-1}\{[1-(r/r_0)^2\sin^2\gamma]^{1/2} + (r/r_0)\cos\gamma\}$$
$$x_2 = Cr_0\lambda^{-1}\{[1-(r/r_0)^2\sin^2\gamma]^{1/2} - (r/r_0)\cos\gamma\}$$
$$x_3 = Cr'\lambda^{-1}\{[1-(r/r')^2\sin^2\gamma]^{1/2} + (r/r')\cos\gamma\} \tag{3}$$
$$x_4 = Cr'\lambda^{-1}\{-[1-(r/r')^2\sin^2\gamma]^{1/2} + (r/r')\cos\gamma\}$$
$$x_5 = -x_4$$

and

$$D_n(x) = \int_0^1 \mu^{n-1}(1-\mu^2)^{-1/2}\exp(-x/\mu)d\mu \tag{4}$$

The terms in equation (2) represent the following heat flows. The first term is the contribution to the radially outward flux at point P (see Fig. 1) from wall emission at points like B. The exponential quantity in this term (which appears through D_3) is the transmittance for the line of sight from B to P. Wall emission from points like A which gets transmitted to point P is accounted for in the second term. Since this flow is radially inward, the term is negative. The third and fourth terms are contributions to the radially outward flux resulting from local particulate emission which is transmitted to point P. The third

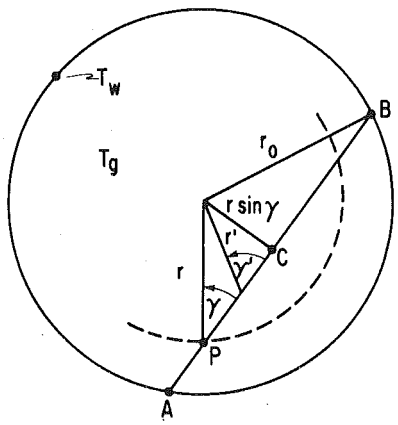

Fig. 1 Fundamental pathlengths for the cylindrical geometry

[1] Presently, graduate student at M.I.T.

Contributed by the Heat Transfer Division for publication in the JOURNAL OF HEAT TRANSFER. Manuscript received by the Heat Transfer Division February 29, 1980.

Copyright © 1981 by ASME

Downloaded 20 Dec 2010 to 194.27.225.72. Redistribution subject to ASME license or copyright; see http://www.asme.org/terms/Terms_Use.cfm

term accounts for such emission along the path from B to C while the fourth term accounts for the section from C to P. The last term in the equation is the local particulate emission along the line of sight AP which is transmitted to point P. It is radially inward and hence it is negative.

The complexity of the integrals does not allow an exact closed form solution to be obtained. Nevertheless, several of the integrals may be performed analytically. This greatly reduces the numerical computation burden and, in addition, allows the optically thin and the next higher order behavior to be achieved in closed form—appearing as the first two terms in the infinite series solution. The transformations leading to the closed form integrations are presented in detail in [14]; a brief outline is given below.

Initially, either the r' or the λ integration may be performed. It was found, however, that performing the λ integration first allows the problem to be pursued further on an analytical basis. (The direction into which the solution proceeds when the r' integration is completed first can be seen from the modified gray result given in the next section.) Letting $x \equiv 1/\lambda$, the spectral integrals in equation (2) may be cast into the form of Riemann's zeta function $\zeta(\nu, \mu/\beta)$. The key in being able to go beyond this first integration and achieve further analytical reduction lies in then expressing the zeta function as an infinite series [15].

$$\zeta(\nu, \mu/\beta) = \frac{\beta^\nu}{\Gamma(\nu)} \int_0^\infty \frac{x^{\nu-1} e^{-\mu x}}{1-e^{-\beta x}} dx = \sum_{n=0}^{\infty} (\mu/\beta + n)^{-\nu} \tag{5}$$

Using this series representation and defining

$$k = \frac{r}{r_0}; \quad p = \frac{Cr_0 T_w}{C_2}; \quad q = \frac{Cr_0 T_g}{C_2} \tag{6}$$

$$\beta_{1\tau} = \frac{(1+n)/\tau}{k\cos\gamma + \sqrt{1-k^2\sin^2\gamma}};$$

$$\beta_{2\tau} = \frac{(1+n)/\tau}{-k\cos\gamma + \sqrt{1-k^2\sin^2\gamma}};$$

$$\beta_3 = \frac{(1+n)/q}{k\cos\gamma + \sqrt{(r'/r_0)^2 - k^2\sin^2\gamma}}; \tag{7}$$

$$\beta_4 = \frac{(1+n)/q}{k\cos\gamma - \sqrt{(r'/r_0)^2 - k^2\sin^2\gamma}} = -\beta_5$$

in which τ will be either p or q, the expression for the radial heat flux may be written as

$$q''(r) = 48C_1C_2^{-4}T_w^4 \sum_{n=0}^{\infty} \int_0^{\pi/2} \cos\gamma \left\{\int_0^1 [f_4(\beta_{1p}) - f_4(\beta_{2p})]d\mu\right\} d\gamma + 192CC_1C_2^{-5}T_g^5 \sum_{n=0}^{\infty} \int_0^{\pi/2} \cos\gamma \int_0^1 \left\{\int_{r\sin\gamma}^{r_0} f_5(\beta_3)dr'/\cos\gamma' + \int_{r\sin\gamma}^{r} f_5(\beta_4)dr'/\cos\gamma' - \int_r^{r_0} f_5(\beta_5)dr'/\cos\gamma'\right\} d\mu d\gamma \tag{8}$$

where

$$f_m(\beta) = \frac{\mu^6}{(1-\mu^2)^{1/2}} \left[\frac{\beta}{(1+n)(1+\beta\mu)}\right]^m \qquad m = 4, 5 \tag{9}$$

In the second term in the above equation the three integrations with respect to r' are the same. Each may be completed in closed form by first expressing $dr'/\cos\gamma'$ in terms of the $\beta_j (j = 3, 4, 5)$. (It should be noted from Fig. 1 that $r\sin\gamma = r'\sin\gamma'$ and hence $\cos\gamma' = [1 - (r/r')^2 \sin^2\gamma]^{1/2}$.) Then the integrations with respect to μ may be completed in closed form by first using trigonometric substitutions followed by partial fraction expansions. The $G_m(\beta)$ functions which appear in the final result below are generated at this point.

The remaining integrations with respect to γ may be completed analytically only when the integrands do not contain the $G_m(\beta)$ functions. Those integrations which can be completed are then able to be summed exactly through the definition of the Riemann zeta function, equation (5). The resulting expression for the radial radiative heat flux then becomes

$$q''(k) = F(q, k)\sigma T_g^4 - F(p, k)\sigma T_w^4 \tag{10}$$

where

$$F(\tau, k) = c_1 k\tau - c_2 k f_1(k^2)\tau^2 + R(\tau, k) \tag{11}$$

in which

$$R(\tau, k) = \frac{3\cdot 5^1}{\pi^5} \sum_{n=0}^{\infty} \frac{1}{(1+n)^4} \int_{\gamma=0}^{\pi/2} \sum_{m=1}^{4} (-1)^{m+1} \binom{6}{m} \times \left\{\frac{G_m(\beta_{1\tau})}{\beta_{1\tau}^2} - \frac{G_m(\beta_{2\tau})}{\beta_{2\tau}^2}\right\} \cos\gamma\, d\gamma \tag{12}$$

and

$$f_1(k^2) = \frac{4}{\pi} \int_{\gamma=0}^{\pi/2} \cos^2\gamma\,(1 - k^2\sin^2\gamma)^{1/2} d\gamma \tag{13}$$

Closed form expressions for the $G_m(\beta)$ functions are given in the Appendix. The function $f_1(k^2)$ may be identified as the hypergeometric function ${}_2F_1(-1/2, 1/2; 2; k^2)$. It decreases monotonically from $f_1(0) = 1.00$ to $f_1(1) = 0.85$ and has very little curvature. The constants c_1 and c_2 have the values $c_1 = 6!\zeta(5)/\pi^4 = 7.664$ and $c_2 = 15\cdot 5!\zeta(6)/\pi^3 = 59.06$.

The solution is therefore seen to be governed by the single function $F(\tau, k)$. That this should be the case is certainly not obvious upon inspection of equation (8). It is, however, clear on physical grounds since for an isothermal medium the radial flux must vanish at all radii when the wall and medium temperatures are equal. The fact that $F \neq F(p, q, k)$ is a consequence of the spectral absorption coefficient being independent of temperature (see equation (1)). As a result, the mean absorption coefficient of the medium for wall emission is independent of the temperature of the medium. Hence the second term in equation (10), which is the part of the emitted wall energy which is absorbed by the medium in the region $0 \le r' \le r$, is a function of the wall temperature but not the medium temperature. Similarly, the radially outward emission of energy by the medium (the first term in equation (10)) is independent of the wall temperature. The fact that $p \propto T_w$ and $q \propto T_g$ results from the mean absorption and emission coefficients being linearly dependent upon the temperature of the sources of radiation [13]. This linearity in temperature stems solely

Nomenclature

a_n, b_n = coefficients in $D_n(x)$ approximation
C = particle concentration parameter
C_1, C_2 = first and second radiation constants
$D_n(x) = \int_0^1 \mu^{n-1}(1-\mu^2)^{-1/2} \exp(-x/\mu) d\mu$
F, F_g, F_d = fundamental functions for the exact, gray, and approximate $D_n(x)$ results, respectively
${}_2F_1$ = Gauss' hypergeometric function
$f_1(k^2) = {}_2F_1(-1/2, 1/2; 2; k^2)$
$f_2(k^2) = {}_2F_1(1/2, 3/2; 3; k^2)$
$I_{b\lambda w}$ = Wien's distribution
k = dimensionless radius
k_m = mean absorption or emission coefficient
k_λ = spectral absorption coefficient
p, q = optical depths for wall and medium emission
q'', q_g'', q_d'' = exact, gray and approximate $D_n(x)$ heat fluxes, respectively
Q = remainder function in div F
R = remainder function in F
r, r_0 local radius and tube radius
T, T_g, T_w = general, medium and wall temperatures, respectively
ζ = Riemann's zeta function
λ = wavelength
σ = Stefan-Boltzmann constant
τ = optical depth

Downloaded 20 Dec 2010 to 194.27.225.72. Redistribution subject to ASME license or copyright; see http://www.asme.org/terms/Terms_Use.cfm

from the λ^{-1} variation of the spectral absorption coefficient since the radiative properties of the particles themselves are assumed independent of temperature.

The Function $F(\tau,k)$. The first two terms in equation (11) appear to be the beginning of a series expansion for $F(\tau, k)$ in terms of the optical depth τ. This observation may be verified by determining the optically thin behavior of the function $R(\tau, k)$. Substituting equations (36) and (39) of the Appendix into equation (12) and taking the limit as $\tau \to 0$, it can be shown that

$$R(\tau, k) \doteq g_1(k)\tau^3 \ln(1/\tau) - g_2(k)\tau^3 \qquad \tau \ll 1 \quad (14)$$

where the functions $g_1(k)$ and $g_2(k)$ are of the order of magnitude 10. Hence for $\tau \ll 1$ it is seen that $R(\tau, k)$ is negligible compared to the first two terms in $F(\tau, k)$, thereby demonstrating that these terms are a valid expansion for $F(\tau, k)$ in the optically thin region. From numerical computations it was found that $F(\tau, k)$ may be determined to within one percent by using simply the first term in equation (11) when $\tau \lesssim 10^{-3}$ and by using only the first two terms when $\tau \lesssim 10^{-2}$. The third term, $R(\tau, k)$, initially achieves importance at small τ as a result of the first two becoming of the same magnitude but of opposite sign. At large τ the first term is much smaller than either of the last two. However, all three terms are important since the second and third terms are of equal magnitude but opposite sign. Therefore, when $\tau \gtrsim 10^{-2}$ all terms must be retained in the computation.

Figure 2 presents the function $F(\tau, k)$. A simple physical interpretation of its behavior is obtained by noting that when $T_w = 0$ K the radial flux is only a consequence of medium emission: $q''(k) = F(q, k)\sigma T_g^4$. Under optically thin conditions, energy emitted within the cylinder $0 \le r' \le r$ escapes from it without being absorbed. Similarly, energy emitted within the surrounding annulus $r \le r' \le r_0$ passes through the cylinder region without being absorbed. The net radially outward flux at r is then simply equal to the total energy emitted within the cylindrical region (proportional to its volume) divided by the surface area of the region: $q''(r) = 4(V/A)k_p\sigma T_g^4$, in which k_p is the Planck mean emission coefficient. For media composed of small particles whose spectral absorption characteristics are given by equation (1), it was shown in [13] that $k_p = 3.83\, CT_g/C_2$. Hence in the optically thin limit, $F(\tau, k) = 7.67\, k$. This result is also predicted by equation (11). The linear proportionality with respect to both τ and k in this limit may be seen in Fig. 2.

Deviation from linearity occurs for $\tau > 10^{-3}$. This is a result of two physical effects. First, of the energy emitted within the cylinder region some is absorbed internally and therefore not all escapes. Hence, the radial flux due to this emission increases at a slower rate with optical depth than in the optically thin region. Secondly, radiation from the surrounding annular region no longer passes completely through the cylinder region but experiences progressively greater absorption in it as the optical depth increases. This, then, contributes an inward radial flux—directly reducing the net outward flux. At the surface of the medium ($r = r_0$) where there is no inward flux for $T_w = 0$, the net flux simply increases with optical depth (at an ever diminishing rate of increase) until blackbody emission is asymptotically achieved. However, at points internal to the medium ($r < r_0$), the ever increasing inward flux (due to increasing absorption in the cylinder region of the increasing emission from the annular region) counterbalances the outward emitted flux. The tradeoff causes a maximum in net radial flux to be achieved. As the optical depth is increased, the annular emission approaches blackbody radiation at temperature T_g and all of it is absorbed within the cylinder region. The energy emitted within the cylinder region also becomes blackbody at T_g and it is absorbed within the annulus. As a result, the net flux, and hence $F(\tau, k)$, go to zero.

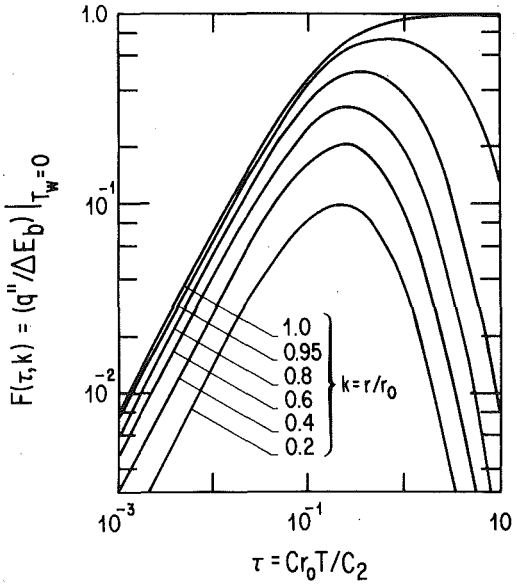

Fig. 2 The single function which determines the radial flux. Also the dimensionless flux when $T_w = 0$

The Function div $F(\tau, k)$. When determining the temperature and concentration distributions in combustion systems, a first law analysis requires a specification of the divergence of the radiative heat flux. Although the present analysis applies strictly to homogeneous systems (where specification of the flux divergence is clearly unnecessary) the results can nevertheless serve as a first approximation to the radiative transfer in nonhomogeneous systems. Such an approximation is particularly useful when the radiative transfer represents only one part of a complex combustion analysis.

The divergence of the radial heat flux is defined by the single function div $F(\tau, k)$. This function may be determined by differentiating equation (11) and using the relationship given in equation (40) of the Appendix. The result is

$$r_0 \operatorname{div} F = 2c_1\tau - c_2[2f_1(k^2) - (k^2/4)f_2(k^2)]\tau^2 + Q(\tau, k) \quad (15)$$

where

$$Q(\tau, k) = \frac{3{\cdot}5!}{\pi^5} \sum_{n=0}^{\infty} \frac{1}{(1+n)^4} \int_{\gamma=0}^{\pi/2} \sum_{m=1}^{4} (-1)^{m+1} \times (4\ \underline{6}\ m) \left\{ \left[\frac{G_m(\beta_{1\tau})}{\beta_{1\tau}^2} - \frac{G_m(\beta_{2\tau})}{\beta_{2\tau}^2} \right] + \frac{\tau^2}{(1+n)^2} \nu(1/\rho)[mG_{m+1}(\beta_{1\tau}) - (m+2)G_m(\beta_{1\tau})] - \frac{\tau^2}{(1+n)^2} \nu(\rho)[mG_{m+1}(\beta_{2\tau}) - (m+2)G_m(\beta_{2\tau})] \right\} \cos\gamma\, d\gamma \quad (16)$$

in which

$$\nu(x) = 2x[(1+x)^{-1} - (1-k^2)/2] \quad (17)$$

$$\rho = \beta_{1\tau}/\beta_{2\tau} \quad (18)$$

The function $f_2(k^2)$ is the hypergeometric function ${}_2F_1$ (1/2, 3/2; 3; k^2). It increases monotonically from $f_2(0) = 1.00$ to $f_2(1) = 1.70$ and has significant upward curvature.

In the optically thin limit the function $Q(\tau, k)$ has the same form as $R(\tau, k)$, with the corresponding $g_i(k)$ functions being of order 100. In this limit, $Q(\tau, k)$ is therefore negligible compared to the first two terms in equation (15). From numerical computation it was found that r_0 div F may be determined to within one percent by using only the first term in equation (15) when $\tau \lesssim 10^{-3}$ and by using only the first two terms when $\tau \lesssim 10^{-2}$. This behavior is similar to that of the function $F(\tau, k)$ itself.

Figure 3 presents the function r_0 div $F(\tau, k)$. As with $F(\tau, k)$ a physical interpretation is facilitated by noting that the function is exactly the flux divergence resulting from medium emission only, i.e., $T_w = 0$ K. In the optically thin limit, there is no self-absorption and all of the energy emitted by a dr element must escape radially. Hence, this emission per unit area (which is directly proportional to optical depth) exactly defines the div q''. Although the energy emitted by each dr element is not the same, the emission per unit area is identical. Hence, in the optically thin limit r_0 div F must be independent of

Downloaded 20 Dec 2010 to 194.27.225.72. Redistribution subject to ASME license or copyright; see http://www.asme.org/terms/Terms_Use.cfm

radius and directly proportional to optical depth. These trends are seen in Fig. 3 and are predicted by the first term in equation (15). As the optical depth increases, the photon mean free path decreases, and the center of the cylinder becomes the first region unable to see the 0 K environment surrounding the medium. It is therefore the first region which sees an essentially isothermal environment at the temperature T_g. Under these circumstances both q'' and div q'' will decrease in the central region of the cylinder as the optical depth increases. The central region itself will expand with increasing optical depth. Hence, with the surface flux increasing monotonically with optical depth while the flux within the medium is approaching zero at ever larger radii, the div q'' will become larger within an ever narrowing annular region. As the optical depth approaches infinity the central region expands to the surface and the div q'' approaches zero everywhere internal to the cylinder. At the surface, however, the div q'' approaches infinity as a result of the step change in flux across the interface.

$q''(r)$: Exact and Approximate Solutions

The Exact Solution. When either the wall or the medium is cold, equation (11) and Fig. 2 give the dimensionless flux exactly. That is, for $T_w = 0$ or $T_g = 0$, $F(\tau, k) = q''(k)/(\sigma T_g{}^4 - \sigma T_w{}^4)$. However, when the wall and medium emissions are both important, equation (10) must be used and the optical depths for both emission and absorption by the medium (q and p respectively) enter the solution. Equivalently, since $p/q = T_w/T_g$ one may consider the parameters q and T_w/T_g as defining the solution at a given radius. It should also be noted that if p and q are interchanged (equivalent to interchanging T_w and T_g) the same value is obtained for the dimensionless flux. Expressions for the heat flux in the optically thin limit may be written by appropriately using the one and two term expressions for $F(\tau, k)$ discussed in the previous section. For example, when both p and q are less than 10^{-3} (equivalently $q \lesssim 10^{-3}$ and $T_w/T_g \lesssim 1.0$) the dimensionless flux is accurately given by

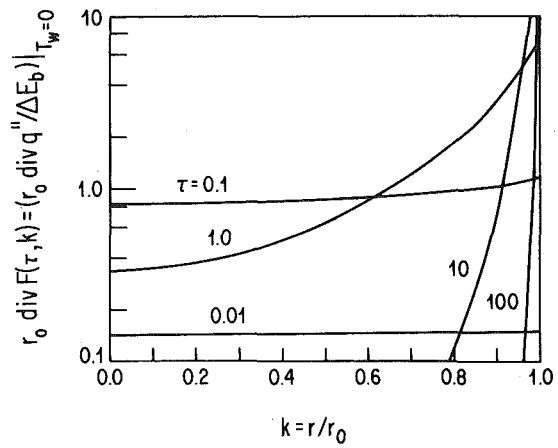

Fig. 3 The single function which determines the flux divergence. Also the dimensionless flux divergence when $T_w = 0$

$$\frac{q''(r)}{\sigma T_g{}^4 - \sigma T_w{}^4} = c_1 \left[\frac{1 - (T_w/T_g)^5}{1 - (T_w/T_g)^4}\right] kq \tag{19}$$

The function of the temperature ratio in brackets above increases monotonically with T_w/T_g. It has the values of 1.0 and 1.25 for $(T_w/T_g) = 0$, 1.0 respectively; and it approximately equals (T_w/T_g) for large arguments.

The dimensionless heat flux has been computed exactly from equation (10) in the following parameter ranges: $10^{-5} \le q \le 10^3$ and $0.0 \le (T_w/T_g) \le 10.0$. When plotted, the results for a fixed temperature ratio always appear similar to Fig. 2 (the dimensionless flux for $T_w/T_g = 0$). The essential difference is that the curve for a given radius shifts toward smaller values of q as T_w/T_g is increased. Plots of the dimensionless flux at various temperature ratios will not been presented. Rather, the results for $q = 0.1$, 1.0, 10.0 are presented in Table 1. The peaks of the curves lie in or near this range of q when $(T_w/T_g) < 10$.

The Gray Approximation. By performing the geometric integrations in equation (2) first, a spectral or gray solution results. The r' integrations may be completed for a medium in which the absorption coefficient is spatially uniform by using the substitution $y = [(r'/r)^2 - \sin^2\gamma]^{1/2}$ along with its implication $dr'/\cos\gamma' = r dy$. Finally, letting $x = \sin\gamma$ and combining the wall emission terms into a single term and the medium emission terms into a single term, the radial heat flux becomes

$$q_\lambda''(k) = F_g(\tau_\lambda, k) E_{b\lambda}(T_g) - F_g(\tau_\lambda, k) E_{b\lambda}(T_w) \tag{20}$$

where

$$F_g(\tau_\lambda, k) = \frac{4}{\pi} \int_{x=0}^{1} \int_{\mu=0}^{1} \frac{\mu^2}{(1-\mu^2)^{1/2}} \left\{\exp\left[-\frac{\tau_\lambda}{\mu}(\sqrt{1-k^2x^2} - k\sqrt{1-x^2})\right] - \exp\left[-\frac{\tau_\lambda}{\mu}(\sqrt{1-k^2x^2} + k\sqrt{1-x^2})\right]\right\} d\mu dx \tag{21}$$

and $\tau_\lambda = k_\lambda r_0$. The above spectral result will also be the solution for the total radiative interchange if the medium is gray and if an appropriate mean absorption coefficient can be defined.

As shown in [13] the Planck and Rosseland mean coefficients corresponding to $k_\lambda = C/\lambda$ have the same form:

$$k_m = BCT/C_2 \tag{22}$$

where B equals 3.83 for the Planck coefficient and 4.00 for the Rosseland. (The value of 3.60 given in [13] for the Rosseland coefficient is in error.) For use over the full range of optical depths it is reasonable to assume a mean value of 3.91. Also, it is noted that since the coefficient k_m is linearly proportional to temperature, the mean emission coefficient (characterized by T_g) will be different from the mean absorption coefficient (characterized by T_w). If this difference is not accounted for, the gray solution will be independent of T_w/T_g. Since this contradicts the nature of the exact solution, the gray result should be modified as follows

$$q_g''(r) = F_g(\tau_g, k)\sigma T_g{}^4 - F_g(\tau_w, k)\sigma T_w{}^4 \tag{23}$$

Table 1 The dimensionless heat flux $q''/\sigma(T_g{}^4 - T_w{}^4)$ as computed exactly and by two approximate methods

	$q = 0.1$			$q = 1.0$			$q = 10.0$		
k	$T_w/T_g = 0.0$	1.0[4]	10.0	0.0	1.0	10.0	0.0	1.0	10.0
	0.0824[1]	0.0918	0.0388	0.0357	2.30E-2	1.79E-4	1.83E-4	5.55E-5	1.85E-7
0.2	0.0915[2]	0.1028	0.0180	0.0144	4.37E-3	−1.80E-6	3.27E-15	−7.65E-14	−3.27E-9
	0.0852[3]	0.0954	0.0320	0.0320	1.88E-2	4.74E-5	5.06E-5	5.39E-6	2.40E-9
	0.258	0.290	0.174	0.166	0.121	1.61E-3	1.63E-3	5.45E-4	1.96E-6
0.6	0.284	0.322	0.123	0.111	0.066	−1.22E-5	2.24E-8	−9.62E-8	−2.24E-12
	0.265	0.300	0.157	0.158	0.109	6.24E-4	6.40E-4	4.97E-4	5.82E-8
	0.474	0.548	0.961	0.963	0.980	1.000	1.000	1.000	1.000
1.0	0.514	0.596	0.989	0.992	0.996	1.000	1.000	1.000	1.000
	0.481	0.558	0.972	0.972	0.985	1.000	1.000	1.000	1.000

[1] Exact solution
[2] Modified gray solution
[3] Solution using $D_n(x) = a_n e^{-b_n x}$ and Wien's distribution (corrected)
[4] Values obtained by interpolation between 0.9 and 1.1 results

Downloaded 20 Dec 2010 to 194.27.225.72. Redistribution subject to ASME license or copyright; see http://www.asme.org/terms/Terms_Use.cfm

where

$$\tau_g = BCr_0T_g/C_2 = 3.91\,q \tag{24}$$

$$\tau_w = BCr_0T_w/C_2 = 3.91\,p \tag{25}$$

In Table 1, values of the heat flux predicted by the above approximate expression are compared with those computed from the exact solution. The modified gray result predicts the general trend with T_w/T_g but it is somewhat inaccurate. It was found to be in good agreement ($\lesssim 5$ percent error) only when $q \lesssim 0.01$ and $(T_w/T_g) \lesssim 10$. Additionally, it predicts negative results (which violate the second law) at large optical depths when $T_w/T_g > 0$. (After careful study of such results we are convinced that the negative values stem from the modified gray approximation and not from computational inaccuracies.) A better approximation is clearly desireable.

Approximate Geometric Integration. The second approximate solution investigated here accounts exactly for the nongray properties of the particles and instead performs the geometric integrations in an approximate way. The functions $D_n(x)$ appearing in equation (2) are approximated as $D_n(x) \simeq a_n e^{-b_n x}$ after the manner of [3, 4]. In addition, Wien's distribution, $I_{b\lambda w} = 2C_1\lambda^{-5}\exp(-C_2/\lambda T)$, is used to approximate the Planck function. Introducing these approximations, the spectral integrals acquire the same form as they had in [13]. This, however, is to be expected since the geometric functions of the cylindrical geometry, $D_n(x)$, are being approximated here in the same way as the geometric functions of the planar geometry, $E_n(x)$, were approximated in [13]. Performing these spectral integrations followed by the r′ integrations, the following approximate result is obtained for the radial heat flux

$$q_d''(k) = \frac{8C_1a_23!}{b_2C_2^4}[F_d(\tau_{gd}, k)T_g^4 - (a_3b_2/a_2)F_d(\tau_{wd}, k)T_w^4] \tag{26}$$

where

$$F_d(\tau, k) = \int_{\gamma=0}^{\pi/2}\{[1 + \tau(\sqrt{1 - k^2\sin^2\gamma} - k\cos\gamma)]^{-4} - [1 + \tau(\sqrt{1 - k^2\sin^2\gamma} + k\cos\gamma)]^{-4}\}\cos\gamma\, d\gamma \tag{27}$$

and

$$\tau_{gd} = b_2Cr_0T_g/C_2 = b_2q \tag{28}$$

$$\tau_{wd} = b_3Cr_0T_w/C_2 = b_3p \tag{29}$$

The coefficients in the $D_n(x)$ approximation are taken to be [4]:

$$a_2 = 3\pi^2/32 \qquad a_3 = \pi/4$$

$$b_2 = 3\pi/8 \qquad b_3 = 3\pi/8 \tag{30}$$

As a consequence, $(a_3b_2/a_2) = 1.0$, $(8C_1a_23!/b_2C_2^4) = 0.924\,\sigma$. Then, normalizing equation (26) by dividing it by the difference between the hemispherical emissive powers computed from Wien's distribution ($E_{bw} = 0.924\,\sigma T^4$), it is seen that the 0.924 coefficient cancels. This automatically corrects for the inherent underprediction of flux embodied in the use of Wien's function. The result is

$$\frac{q''(k)}{\sigma T_g^4 - \sigma T_w^4} \simeq \frac{q_d''(k)}{0.924(\sigma T_g^4 - \sigma T_w^4)} = \frac{F_d(\tau_{gd},k)T_g^4 - F_d(\tau_{wd},k)T_w^4}{T_g^4 - T_w^4} \tag{31}$$

At the surface of the medium ($k = 1$) the dimensionless flux may be determined in closed form. It is straightforward to show using a table of integrals [15] that

$$F_d(\tau, 1) = 1 + \frac{3 + 20\tau^2 - 8\tau^4}{6(1 - 4\tau^2)^3} \pm \frac{4(\tau^3 \pm \tau)}{(1 - 4\tau^2)^3}G_1(2\tau) \tag{32}$$

where the upper signs are to be used for $2\tau > 1$ and the lower signs for $2\tau < 1$. When $2\tau = 1$, $F_d(0.5, 1) = 0.124$. The function $G_1(\beta)$ is given by equation (36) in the Appendix. It should be noted that the emissivity and absorptivity of the nongray cylindrical medium are given, respectively, by

$$\epsilon = F_d(\tau_{gd}, 1) \tag{33}$$

and

$$\alpha = F_d(\tau_{wd}, 1) \tag{34}$$

The numerical computations in Table 1 show that this approximate solution is quite accurate. The largest errors occur when q or p is large (i.e., when q or (T_w/T_g) is large). This, however, is to be expected since the coefficients in the approximations to the $D_n(x)$ were obtained by requiring accurate representations at short pathlengths [4]. The error introduced by using Wien's distribution is nearly the same for all pathlengths and is much less than the error introduced by the $D_n(x)$ approximation at large pathlengths. The simple closed form solution for the heat flux at the surface given by equation (32) is remarkably accurate over the full range of optical depths.

Conclusions

Exact and approximate solutions have been developed for the radial radiative heat flux in a nongray cylindrical medium. In the exact solution, several of the integrals which originally appear in the formulation have been completed in closed form. The final result appears as an infinite series of integrals in which the first two terms (the optically thin and the next higher order term) are known in closed form. Upper limits on the optical depth have been established below which either the first term or the first two terms in the series will accurately represent the radial heat flux. Similar considerations were also given to the determination of the flux divergence.

In addition, two different approximate solutions have been derived. The first approximates the spectral integrations by assuming that the absorption coefficient is independent of wavelength, i.e., that the medium is gray. The gray result is then modified to allow the mean absorption coefficient to be different from the mean emission coefficient. Nevertheless, good agreement with the exact result is only achieved at small optical depths.

The second approximate solution performs the geometric integration in an approximate way and uses Wien's distribution instead of Planck's in the spectral integrations. The values of the radial heat flux predicted by this result are in good agreement with the exact solution over a much wider range than those of the modified gray result. In addition, a simple closed form expression for the heat flux at the surface is obtained. This expression, which is also the emissivity or absorptivity of the medium, accurately predicts the exact result over the full range of optical pathlengths.

Acknowledgments

This work was supported by grants from the SUNY Research Foundation (Faculty Research Fellowship) and the National Science Foundation (ENG-7825053).

References

1 Kuznetsov, Ye. S., "Temperature Distribution in an Infinite Cylinder and in a Sphere in a State of Non-Monochromatic Radiation Equilibrium," English translation in USSR *Computational Mathematics and Mathematical Physics*, Vol. 2, 1963, pp. 230–254.

2 Kesten, A. S., "Radiant Heat Flux Distribution in a Cylindrically Symmetric Nonisothermal Gas With Temperature-Dependent Absorption Coefficient," *Journal of Quantitative Spectroscopy and Radiative Transfer*, Vol. 8, 1968, pp. 419–434.

3 Habib, I. S., and Greif, R., "Nongray Radiative Transport in a Cylindrical Medium," ASME JOURNAL OF HEAT TRANSFER, Vol. 92, 1970, pp. 28–32.

4 Wassel, A. T. and Edwards, D. K., "Molecular Gas Band Radiation in Cylinders," ASME JOURNAL OF HEAT TRANSFER, 1974, pp. 21–26.

5 Nelson, D. A., "Band Radiation within Diffuse-Walled Enclosures; Part I: Exact Solutions for Simple Enclosures," ASME JOURNAL OF HEAT TRANSFER, Vol. 101, 1979, pp. 81–84.

6 Habib, I. S., and Greif, R., "Heat Transfer to a Flowing Nongray Radiating Gas: an Experimental and Theoretical Study," *International Journal of Heat and Mass Transfer*, Vol. 13, 1970, pp. 1571–1582.

7 Tiwari, S. N., and Cess, R. D., "Heat Transfer to Laminar Flow of Nongray Gases Through a Circular Tube," *Applied Scientific Research*, Vol. 25, 1971, pp. 155–170.

8 Wassel, A. T., Edwards, D. K., and Catton, I., "Molecular Gas Radiation and Laminar or Turbulent Heat Diffusion in a Cylinder with Internal Heat Generation," *International Journal of Heat and Mass Transfer*, Vol. 18, 1975, pp. 1267–1276.

9 Wassel, A. T., and Edwards, D. K., "Molecular Gas Radiation in a

Downloaded 20 Dec 2010 to 194.27.225.72. Redistribution subject to ASME license or copyright; see http://www.asme.org/terms/Terms_Use.cfm

Laminar or Turbulent Pipe Flow," ASME JOURNAL OF HEAT TRANSFER, 1976, pp. 101–107.

10 Greif, R., "Laminar Convection with Radiation: Experimental and Theoretical Results," *International Journal of Heat and Mass Transfer*, Vol. 21, 1978, pp. 477–480.

11 Hottel, H. C., and Sarofim, A. F., *Radiative Transfer*, McGraw-Hill, New York, 1967.

12 Felske, J. D., and Tien, C. L., "Calculation of the Emissivity of Luminous Flames," *Combustion Science and Technology*, Vol. 7, 1973, pp. 25–31.

13 Felske, J. D., and Tien, C. L., "The Use of the Milne-Eddington Absorption Coefficient for Radiative Heat Transfer in Combustion Systems," ASME JOURNAL OF HEAT TRANSFER, Vol. 99, 1977, pp. 458–465.

14 Felske, J. D., and Lee, K. M., "Nongray Particulate Radiation in an Isothermal Cylindrical Medium," Fluid and Thermal Sciences Laboratory, Tech. Rept., TR 80-1, SUNY/Buffalo, Feb 1980.

15 Gradshteyn, I. S., and Ryzhik, I. M., *Table of Integrals, Series and Products*, Academic Press, New York, 1965.

APPENDIX

The $G_m(\beta)$ functions are defined by:

$$G_m(\beta) = \int_{\alpha=0}^{\pi/2} (1 + \beta \cos \alpha)^{-m} d\alpha \tag{35}$$

It is clear from the above equation that $G_0(\beta) = \pi/2$. Using a table of integrals [15] it can be shown that

$$G_1(\beta) = \begin{cases} \dfrac{2}{(1-\beta^2)^{1/2}} \tan^{-1}\left[(1-\beta^2)^{1/2}/(1+\beta)\right], & \beta^2 < 1 \\ (\beta^2-1)^{-1/2} \ln\left[\dfrac{1+\beta+(\beta^2-1)^{1/2}}{1+\beta-(\beta^2-1)^{1/2}}\right], & \beta^2 > 1 \end{cases} \tag{36}$$

with $G_1(1) = 1$. For $m > 1$, the $G_m(\beta)$ functions may be expressed in terms of $G_1(\beta)$ through the recurrence relation derived below. From [15] it is seen that the integral defining $G_m(\beta)$ may be written as

$$\int_0^{\pi/2} (1 + \beta \cos \alpha)^{-m} d\alpha = -\frac{1}{(m-1)(1-\beta^2)} \left\{ \beta - (m-1) \int_0^{\pi/2} (1 + \beta \cos \alpha)^{-(m-1)} d\alpha + (m-2)\beta \int_0^{\pi/2} (1 + \beta \cos \alpha)^{-(m-1)} \cos \alpha \, d\alpha \right\} \tag{37}$$

The last term in this equation may be written in terms of $G_m(\beta)$ functions by noting that

$$(1 + \beta \cos \alpha)^{-1} \cos \alpha = [1 - (1 + \beta \cos \alpha)^{-1}]/\beta \tag{38}$$

Substituting the above into equation (37), combining terms and using equation (35), the following relationship is obtained

$$G_m(\beta) = -\frac{1}{(m-1)(1-\beta^2)} [\beta + (m-2)G_{m-2}(\beta) - (2m-3)G_{m-1}(\beta)] \quad m \geq 2 \tag{39}$$

For $m > 0$, the $G_m(\beta)$ functions decrease monotonically to zero as β increases. When $\beta = 0$, $G_m(0) = \pi/2$ for all m; and when $m < n$, $G_m(\beta) > G_n(\beta)$.

In developing the result for div $F(\tau, k)$, derivatives of the $G_m(\beta)$ functions are required. These derivatives may be expressed in terms of the functions themselves. By taking the derivative of equation (35) and then introducing equation (38), it follows that

$$dG_m(\beta)/d\beta = [G_{m+1}(\beta) - G_m(\beta)]m/\beta \tag{40}$$

Hence the appearance of $G_{m+1}(\beta)$ in equation (16).

Downloaded 20 Dec 2010 to 194.27.225.72. Redistribution subject to ASME license or copyright; see http://www.asme.org/terms/Terms_Use.cfm

D. C. Look
Professor.
Mem. ASME

H. F. Nelson
Professor.

A. L. Crosbie
Professor.
Mem. ASME

Thermal Radiative Transfer Group,
Department of
Mechanical and Aerospace Engineering,
University of Missouri-Rolla,
Rolla, MO

Anisotropic Two-Dimensional Scattering: Comparison of Experiment with Theory

Anisotropic scattering from a semi-infinite medium exposed to a laser beam is studied. The situation is two-dimensional and cylindrical because the laser beam is incident normal to the purely scattering media. The back scattered radiation in the normal direction is predicted and measured as a function of the distance from the beam. The latex particles of uniform size with diameters ranging from 0.03 up to 1.011 μ are used as scattering centers in a water solution. The influence of anisotropic scattering shifts the maximum of the radial distribution of the scattered intensity to larger optical radii as the particle size increases. For large optical thicknesses, the asymmetry factor is used as a correlation coefficient to reduce the anisotropic results to those of isotropic scattering.

Introduction

This study is motivated by a desire to obtain a better understanding of two-dimensional, multiple scattering. Results of this study should be of interest to investigators in the fields of astrophysics, biology, chemistry, laser interaction, metallurgy, meteorology, remote sensing, and visibility. Particular applications involve the interaction of a laser beam with a scattering medium, i.e., the decrease in useful penetration range of radiation in underwater surveying, communications and navigation, information loss in atmosphere studies, and determination of the industrial dust composition and removal of the hazardous components. In each of these examples, the laser radiation is dispersed laterally, as well as longitudinally. Consequently, these problems are at least two-dimensional. Furthermore, these situations are complicated because the scattering is anisotropic.

Most of the radiative transfer studies involving multiple scattering assume the radiation transfer to be one-dimensional. A comprehensive review of multi-dimensional scattering radiative transfer literature was presented by Crosbie and Linsenbardt [1]. It shows that very few studies have considered two-dimensional radiative transfer with anisotropic scattering.

Previous Theoretical Studies. Chin and Churchill [2] used a six-flux radiative model to numerically calculate the radiation from a line source located at the center of an anisotropically scattering medium. The top surface was assumed to be partially reflective and the bottom surface was completely absorptive. They presented results for the flux at the upper boundary as a function of distance from the source to show the effects of forward, side, and back scattering phase functions.

Dolin [3] solved for the radiation intensity in an anisotropic scattering medium subjected to a narrow beam of incident intensity. He obtained solutions for the small angle approximation and for the diffusion approximation. Bravo-Zhivotowsky, et al. [4] also used the small angle approximation to solve for the radiative flux in an anisotropically scattering medium.

The Monte Carlo technique was used by Stockham and Love [5] to calculate the radiative emission from isothermal finite cylindrical media with anisotropic scattering.

Crosbie and Dougherty [6] used Ambarzumian's method to obtain exact results for the source function, flux and intensity at the boundary of a two-dimensional, isotropically scattering, semi-infinite cylindrical medium. The incident radiation was collimated and normal to the surface and had a Gaussian spatial distribution. Single and double scattering approximations were also developed [7].

Previous Experimental Studies. The only experimental two-dimensional multiple scattering studies that appear in the literature are those of Look, et al. [8] and the Russian work of Ivanov and Sherbaf [9–11]. The Russian experiments used milk, or rosin, in distilled water to create the scattering medium. Thus, the size distribution of scattering particles and the extinction coefficient were very hard to characterize. Their experiments involved measuring the radial dispersion of a cylindrical light beam as it propagated through a given thickness of the scattering medium. The work of Look, et al. [8] presented the radial distribution of the radiation leaving a semi-infinite medium exposed to a small diameter laser beam. White latex paint was mixed into distilled water to create the scattering medium. The scattering properties of the paint were very hard to characterize.

The only experimental multiple scattering studies in the literature, which use well characterized scattering particles involve one-dimensional radiation transfer in a planar geometry. Several of these studies are listed in Table 1. The listing is intended to indicate the type of studies performed in the past and it is not meant to be exhaustive. The table contains the reference, the composition of the scattering medium (scattering medium), the property that was measured (property measured), the range of properties of the scattering medium (character of medium), and the specific parameters that were investigated (parameters investigated).

All of the experiments involve scattering in a liquid or solid medium contained in a rectangular or cylindrical container with radiation incident on one side, usually the upper surface. Atkins [12] used injection molded solid plastic disks about 4 cm in diameter and 1 mm thick for his scattering medium. When τ_0 was small his experiment became two-dimensional, because radiation was scattered out the edges of the disks. The scattering media used by Hottel, et al. [14–17] was contained between two, 5 cm square glass plates. The separation distance between the inner glass surfaces was varied from 0.5 mm to 5 mm.

The experiments listed in Table 1 were all carried out using visible radiation. A mercury or tungsten source was used in all the cases, except those of references [18] and [19] where an HeNe laser was used. The incident radiation was normal to the surface, except for three cases, where it was 24 deg [19], 35 deg [20], and variable over a range of angles from 0 to 36 deg [23] from the normal. The size parameter was usually changed by changing the size of the scattering particles rather than changing the wavelength of the radiation or the index of refraction of the medium. In most cases uniform latex spheres in distilled water were used to create the scattering medium; however, TiO_2 [21] and teflon [19] particles were also used. The measurements were bidirectional in character. The range of particle size parameters

Contributed by The Heat Transfer Division for publication in the JOURNAL OF HEAT TRANSFER. Manuscript received by The Heat Transfer Division June 16, 1980.

Copyright © 1981 by ASME

Downloaded 20 Dec 2010 to 194.27.225.72. Redistribution subject to ASME license or copyright; see http://www.asme.org/terms/Terms_Use.cfm

Table 1 Experimental studies of one-dimensional, multiple scattering

Year	Reference	Scattering Medium	Property Measured	Character of Medium	Parameters Investigated
1965	Atkins [12]	polydispersed rutile titanium-dioxide spheres and dye in plastic disks	transmission and reflection	$x \cong 1.54$ $n = 1.87$	τ_0, ω
1968	Sarofim, et al. [14]	uniform polyvinyl toluene spheres painted on a glass slide	bidirectional transmission	$9.56 < x < 25.16$ $1.56 < n < 1.61$	θ, p^*, x
1970	Hottel, et al. [13, 16]	uniform polystyrene latex spheres in distilled water	bidirectional transmission and reflection	$0.815 < x < 5.12$ $n = 1.19; 1.20$ $0.25 < \tau_0 < 3000$	θ, p^*, x, τ_0
1971	Sarofim, et al. [17]	uniform polystyrene latex spheres in distilled water	bidirectional transmission and reflection	$x = 1.90; 2.38$ $n = 1.20$ $0.20 < \tau_0 < 2.0$	$\theta, x, \tau_0, \omega$
1971	Hottel, et al. [13, 15]	uniform polystyrene latex spheres in distilled water	bidirectional transmission and reflection	$0.764 < x < 3.05$ $1.14 < n < 1.20$ $0.01 < \tau_0 < 3211$	θ, x, τ_0
1972	Querfield, et al. [23]	uniform polystyrene latex spheres in distilled water	bidirectional transmission	$x = 1.875; 2.348$ $n = 1.194$ $0.05 < \tau_0 < 1.2$	θ, p^*, x, τ_0
1972	Margolis, et al. [24]	uniform polystyrene latex spheres in distilled water	reflection in normal direction	$x = 1.09; 11.03$ $n = 1.194$	x, τ_0, ω
1972	Granatstein, et al. [19]	polydispersed teflon spheres in distilled water	reflection at $\theta = 24$ deg for $\theta_{in} = 24$ deg	$0.264 < x < 2.64$ $n = 1.89 + i\ .0002$	ω
1974	Howard and Novotny [21]	polydispersed, nonspherical titanium-dioxide particles in glycerol	bidirectional reflection	$x \simeq 1.75; 2.33$ $n = 1.90; 2.03$	θ, τ_0
1975	Leader, et al. [18, 20]	uniform polystyrene latex spheres in distilled water	reflection at $\theta = 20$ deg for $\theta_{in} = 35$ deg	$x = 0.54$ $n = 1.194$	ω

was from 0.26 to 25, so that the scattering varied from Rayleigh to Mie. Consequently, the scattering was anisotropic. The experiments cover a wide range of optical depths; however, most of the data were reported for $0.1 < \tau_0 < 10$. It can safely be assumed that multiple scattering occured in these studies because τ_0 was greater than 0.1.

The results of each experimental study compared favorably to theory. In some cases a slight adjustment of an experimental parameter was used to improve the agreement. The results of Atkins [12] compare well with theory [22]; however, the dye absorption coefficient and the magnitude, but not the shape of the scattering phase function, were adjusted to improve the comparison. Other studies adjusted the scattering particle diameter by 3 to 6 percent [13–17, 24] as well as introducing a small absorption for the latex particles [24] to more accurately fit the experimental data.

Objective of the Current Investigation. This paper presents results of a coordinated experimental and theoretical study of two-dimensional multiple scattering radiative transfer. The physical situation involves a collimated radiation source of finite cross sectional area (laser) directed into a scattering medium. The laser beam enters the scattering medium normal to the upper surface. As the laser beam propagates through the medium, photons are scattered out of the beam causing the beam to disperse. Thus, the problem is two-dimensional, because the laser radiation depends on the distance along the beam and the radial coordinate, which is perpendicular to the direction of beam propagation.

In this paper, we examine the radiation scattered out of the top of the medium in the normal direction as a function of radial distance from the incident laser beam. Multiple scattering events occur during the process. A photon, originally in the laser beam, must be scattered out of the beam with a radial component and then scattered in the

Nomenclature

c = scattering cross section divided by the scattering particle volume
C_{sca} = scattering cross section
d = scattering particle diameter
f = fraction of energy that is scattered forward
g = asymmetry factor
G = universal function
$I_N(\tau_r)$ = theoretically predicted intensity leaving the medium normal to the surface, $I^-(\tau_r, 1, \phi)$
I_{exp} = experimentally measured intensity leaving the medium normal to the surface
I_i = see equation (1)
I = intensity
$\bar{I}_0(x)$ = zeroth order modified Bessel function of the first kind
$J_0(x)$ = zeroth order Bessel function of the first kind
n = relative index of refraction (real) of the scattering particle
n_w = index of refraction of the water, 1.33
N = particle number density
p^* = polarization (see Table 1)
$P(\Theta)$ = scattering phase function
P_i = incident power on the medium, $I_i \pi r_0^2$
$R(\beta)$ = reflection function (see equation (8))
r = radial distance from center of incident (laser) beam
r_0 = effective radius of incident (laser) beam
R_0 = inside radius of the barrel
V = voltage reading of the detector
z = distance into the media (normal to surface)
x = size parameter, $n_w\ \pi d/\lambda_0$
β = spatial frequency
$\delta(x)$ = Dirac delta function, i.e., $\int_a^b f(x)\delta(x - x_0)dx = f(x_0)$ where $a < x_0 < b$
η = particle volume concentration
Θ = angle between the incident and scattered ray.
θ = polar angle, used to specify the direction of the intensity, measured between the intensity and the normal to the $r - \phi$ plane
$\bar{\theta}$ = effective acceptance angle of detector system acceptance cone
κ = absorption coefficient of the medium
λ_0 = wavelength of the laser, 0.6328 μm
$\mu = \cos\theta$
σ = scattering coefficient = $\eta\, c = N\, C_{sca}$
τ_0 = optical depth, $(\sigma + \kappa)L$
τ_r = radial optical coordinate, $(\sigma + \kappa)r$
τ_{r_0} = effective optical radius of incident (laser) beam, $(\sigma + \kappa)r_0$
ϕ = azimuthal angle, used to specify the direction of the intensity, measured between the projection of the intensity on the $r - \Psi$ plane and the r-axis
Ψ = azimuthal angle, used to specify the location of a point in the medium, measured around the z-axis
ω = single scattering albedo

Superscripts

$+$ = quantity incident on medium
$-$ = quantity leaving medium
$*$ = effective isotropic scattering quantity

Downloaded 20 Dec 2010 to 194.27.225.72. Redistribution subject to ASME license or copyright; see http://www.asme.org/terms/Terms_Use.cfm

vertical direction so that it returns to the top of the scattering medium. The photons, which exit the medium perpendicular to the surface, are detected.

The direction a photon is deflected after a scattering event has taken place depends on the scattering phase function. This paper presents results for well characterized scattering particles which scatter anisotropically. This is in contrast to the results presented in reference [8], which were for paint. The composition and size of the particles in the paint were difficult to characterize.

Theory

Basic Assumptions. The theoretical development is based on the following assumptions: (1) steady state, (2) coherent scattering, (3) negligible interference and polarization effects, (4) homogeneous medium, (5) no emission, (6) refractive index of unity, and (7) a two-dimensional semi-infinite medium. The assumption of refractive index of unity is questionable; however, it significantly reduces the numerical complexity of the analysis. In addition, this assumption is somewhat justified by the one-dimensional analysis of Giovanelli [25] in which the intensity reflected by a semi-infinite scattering medium exposed to collimated radiation was calculated. For pure scattering, the intensity reflected normal to the surface is only weakly dependent on refractive index. The validity of extending this conclusion to the two-dimensional geometry must await further investigation.

Incident Radiation. In general, the incident intensity is a function of direction (μ,ϕ) and location (r,Ψ), and the problem is three-dimensional in character. However in this investigation, the incident intensity is assumed to be collimated and normal to the surface of the medium $[\delta(\mu-1)\delta(\phi)]$ and is assumed to be independent of Ψ. Specifically, for a laser beam the radial variation is Gaussian [26], and the incident intensity is given by

$$\begin{aligned} I^+(\tau_r,\mu,\phi) &= I_i\delta(\mu-1)\delta(\phi)\exp(-\tau_r{}^2/\tau_{r_0}{}^2) \\ &= I_i\delta(\mu-1)\delta(\phi)\exp(-r^2/r_0{}^2) \end{aligned} \tag{1}$$

where

$$\tau_{r_0} = (NC_{\text{sca}} + \kappa)r_0 \tag{2a}$$

$$\tau_r = (NC_{\text{sca}} + \kappa)r \tag{2b}$$

and N is the number density of scattering particles, C_{sca} is the scattering cross section, κ is the absorption coefficient of the medium, and r_0 is the effective beam radius. The Dirac delta function product, $\delta(\mu-1)\delta(\phi)$, restricts the incident radiation to the normal direction. For this intensity distribution, the incident radiative flux is $\int_0{}^{2\pi}\int_0{}^{1} I^+(\tau_r,\mu,\phi)\mu d\mu d\phi = I_i\exp(-r^2/r_0{}^2)$. Thus, the magnitude of the incident flux at the center of the beam is equal to I_i. The azimuthally symmetric (independent of Ψ) beam allows the source function to be expressed in terms of z and r.

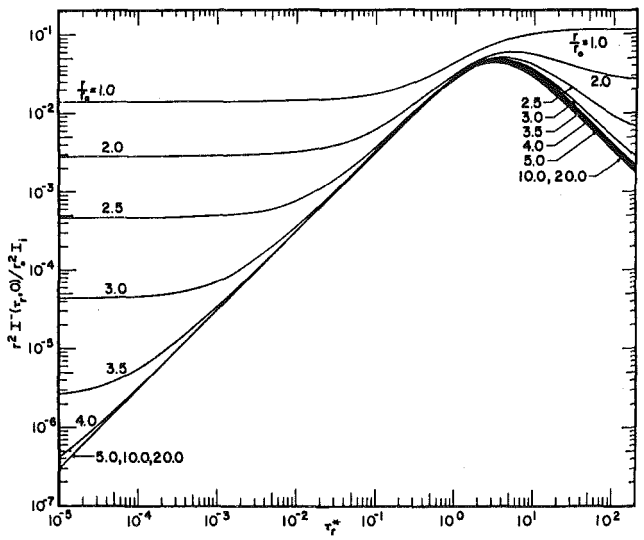

Fig. 1 Theoretical variation in the reflected intensity from a semi-infinite medium

Scattering Phase Function. When the wavelength of the radiation is large compared to the particle diameter, Fraunhofer diffraction around the particles gives rise to a sharp forward peak in the scattering phase function. The narrow diffraction spike can be approximated by a Dirac delta function and remaining angular variation can be approximated with an isotropic component [6].

$$P(\Theta) = 2f\delta(1-\cos\Theta) + (1-f), \tag{3}$$

where f is the fraction which is scattered in the forward direction and Θ is the angle between the incident and scattered ray. Putting this phase function into the equation of transfer, yields the modified transfer equation,

$$\cos\theta\frac{\partial I}{\partial\tau_z{}^*} + \sin\theta\cos\phi\frac{\partial I}{\partial\tau_r{}^*} - \frac{\sin\theta\sin\phi}{\tau_r{}^*}\frac{\partial I}{\partial\phi} + I = S, \tag{4}$$

where

$$S = \frac{\omega^*}{4\pi}\int_{4\pi} \text{I}\, d\Omega, \tag{5}$$

and

$$\left.\begin{aligned} \tau_z{}^* &= (1-\omega f)\tau_z,\ \tau_r{}^* = (1-\omega f)\tau_r, \\ \tau_{r_0}{}^* &= (1-\omega f)\tau_{r_0}, \\ \omega^* &= \omega(1-f)/(1-\omega f). \end{aligned}\right\} \tag{6}$$

For pure scattering ($\omega = 1$), the modified albedo is also unity. Thus, for a strongly "spiked" phase function as in equation (3), the isotropic solutions for the source function, flux, and intensity can be used by adjusting the optical coordinates and the albedo. The effectiveness of this type of approximation has been investigated for the one-dimensional case by Hansen [27], Potter [28], Wang [29], and Sobolev [30].

The choice of f is open to question. The most common approach is to set it equal to the asymmetry factor of the actual phase function.

$$f = g = \frac{1}{2}\int_0{}^{\pi}\cos\Theta\, P(\Theta)\sin\Theta\, d\Theta. \tag{7}$$

This choice is appealing because it yields the correct asymptotic limit in the one-dimensional analysis. Van de Hulst [31] has stressed that g is the fundamental phase function parameter. A value of g near unity indicates strong forward scattering, whereas g near -1 indicates strong backward scattering. The value of g for isotropic scattering is zero.

Solution of Transport Equation. The exact two-dimensional integral equation describing the source function is solved using the method of separation of variables and superposition. No mathematical approximation, such as Eddington's approximation, is employed. The intensity leaving the medium normal to the surface can be expressed as [6]

$$\begin{aligned} I_N(\tau_r{}^*) &= I^-(\tau_r{}^*,\ \mu=1,\phi) \\ &= \frac{\omega^* I_i}{8\pi}\tau_{r_0}{}^{*\,2}\int_0{}^{\infty}\beta J_0(\beta\tau_r{}^*)\exp\left(-\frac{1}{4}\beta^2\tau_{r_0}{}^{*\,2}\right)R(\beta)d\beta. \end{aligned} \tag{8}$$

The quantity, $\omega^* J_0(\beta\tau_r{}^*)R(\beta)/4\pi$ would be the intensity leaving normal to the medium; if it were exposed to collimated radiation with a radial variation in the form of a Bessel function, i.e., $J_0(\beta\tau_r{}^*)\delta(\mu-1)\delta(\phi)$. The Bessel function boundary condition is used to separate variables. The quantity β can be referred to as the spatial frequency of this boundary condition. When $\beta = 0$, the incident radiation is radially uniform, and the problem is one-dimensional. By letting $x = \beta\tau_r{}^*$, equation (8) can be written as

$$I_N(\tau_r{}^*) = \frac{\omega^* I_i}{8\pi}\left(\frac{r_0}{r}\right)^2\int_0{}^{\infty}xJ_0(x)\exp\left[-\frac{1}{4}\left(\frac{r_0}{r}\right)^2x^2\right]R(x/\tau_r{}^*)dx. \tag{9}$$

Equation (9) has been evaluated numerically for a wide range of parameters [6] for $r^2\, I_N(\tau_r{}^*)/r_0{}^2 I_i$. The results for pure scattering are shown in Fig. 1. The expression for the intensity leaving the me-

Downloaded 20 Dec 2010 to 194.27.225.72. Redistribution subject to ASME license or copyright; see http://www.asme.org/terms/Terms_Use.cfm

dium in other directions is much more complex and was not evaluated. However, the flux and power leaving the medium were calculated [6]. As expected, for conservative scattering, the power leaving is $I_i \pi r_0^2$. The interested reader is referred to [6] for the complete details.

Limiting Cases. When r/r_0 is large the exponential term can be approximated by unity and the intensity can be expressed in terms of a universal function of τ_r^*, i.e.,

$$I_N(\tau_r^*) = I_i \left(\frac{r_0}{r}\right)^2 G(\tau_r^*) \tag{10}$$

where

$$G(\tau_r^*) = \frac{\omega^*}{8\pi} \int_0^\infty x J_0(x) R(x/\tau_r^*) dx. \tag{11}$$

Comparison of the results obtained from equations (10) and (11) reveals that the approximation is valid to within one percent when $r/r_0 > 10$, see Fig. 1.

An asymptotic relation for I_N has been developed [29] for small τ_r^* and is repeated here for clarity,

$$I_N(\tau_r^*)/I_i = \frac{\omega^*}{8\pi} \exp(-r^2/r_0^2) + \frac{(\omega^*)^2}{32} \sqrt{\pi}\, (r_0/r) \exp\left[-\frac{1}{2}(r/r_0)^2\right] \bar{I}_0 \left[\frac{1}{2}(r/r_0)^2\right] \tau_r^* \tag{12}$$

where $\bar{I}_0$ is the modified Bessel function of the first kind. The first term represents single scattering, while the second term represents double scattering. When $r/r_0 > 10$, single scattering can be neglected, and G can be approximated by

$$G(\tau_r^*) = \frac{(\omega^*)^2}{32} \tau_r^*. \tag{13}$$

At the other extreme $\tau_r^* \gg 1$ and $r/r_0 > 10$, the behavior is [32]

$$G(\tau_r^*) = 0.33643/\tau_r^* \tag{14}$$

for a purely scattering medium ($\omega^* = 1$). These results are true for other spatial distributions of the incident radiation, i.e., a circle of uniform collimated radiation as long as $r/r_0 > 10$.

Inspection of the numerical results reveals a maximum in G of 0.04331 at

$$\tau_{r_{max}}^* = 3.345 \tag{15}$$

for pure scattering. Thus, the maximum intensity is given by

$$I_{max} = 0.04331\, I_i\, r^2/r_0^2 \tag{16}$$

for $r/r_0 > 10$ and $\omega^* = 1$. The influence of absorption is to reduce the maximum value of G and the optical radius where the maximum occurs.

Experiment

The experimental setup has been discussed in [8]; however, the salient points will be repeated here. The experiment was designed to simulate the theoretical model of semi-infinite optical depth and radius.

Laboratory Setup. The laboratory apparatus used is shown schematically in Fig. 2. The source was a 50 mw He-Ne laser and is incident normal to the surface of the water. A five gallon rectangular smooth surfaced glass tank (21 cm wide, 35 cm long, and 25 cm high) with a cylindrical light trap at the bottom contained the distilled water and the scattering particles. The bottom of the tank and all surfaces of the light trap were sprayed with the highly absorbing, diffusely reflecting flat black paint whose reflectance is less than 2 percent. A detection system probe with an effective acceptance angle of 2.75 deg received the radiation emerging normally from the surface. This power was transmitted to a photomultiplier by a fiber optics bundle and the voltage drop across the load resistor of the photomultiplier was recorded as a function of the detector position, r.

When the particle number density is small, the scattering medium is not semi-infinite in optical depth; however, for this case only single and double scattering are important. When the number density of particles is large, multiple scattering is important and the medium in the tank may be characterized as semi-infinite. The painted bottom and the light trap minimize reflection from the bottom. In addition, the walls of the tank, being smooth glass, reflect specularly. While Fresnel's relation indicates wall reflectances approaching unity at large angles of incidence, tests were run to evalate the importance of this affect. Data were acquired with the laser beam position near a wall of the tank. Wall effects were not detected until the laser beam position was within a 2½ cm in of the tank wall. Since the laser beam was positioned 10 cm from any wall during data acquisition, it was assumed that the reflectance effects of the wall were negligible. Thus, the experimental set-up simulated the theoretical situation.

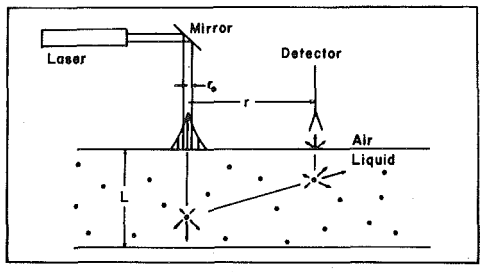

Fig. 2 Schematic of the experimental setup

Table 2 Effective scattering coefficients in water at a wavelength of 0.6328 μm and $n = 1.20$

d(μm)	Std. Dev. (μm)	x	c(cm^{-1})
0.03	—	0.198	110*
0.109	0.0027	0.720	1440
0.312	0.0022	2.060	12500
0.481	0.0018	3.176	23000
0.500	0.0027	3.301	24070
0.527	0.0125	3.480	25600
0.801	0.0035	5.289	36500
1.011	0.0055	6.670	40200

* Experimental value (theoretical value for the 0.03 μm particles was 33.33)

Particle Characterization. The particles used as the scattering centers were selected from those commercially available from Dow Diagnostics, with one exception; that being the 0.03 μm dia particles. These particles were obtained from Monsanto Chemical. The Dow polystyrene latex particles were spherical and uniform in size. The selection of sizes range from 0.109 μm to 1.011 μm in diameter. The uniformity of the spheres is characterized by their standard deviation, which ranges from 0.0027 to 0.0125 μm (see Table 2). Figure 3 illustrates this uniformity. Unfortunately, clear electron microscope pictures of the 0.03 μm particles could not be obtained, because they were too small. Thus, their size distribution could not be determined. All of the particles have essentially a neutral density (~ 1.00 g/cc) and the refractive index is 1.60.

From Mie theory, these particles scatter anisotropically and exhibit a single scattering albedo of unity. The anisotropy character of the particles are illustrated in Fig. 4. This figure illustrates the variation in the scattered radiation from 0.109 and 1.011 μm latex particles in water at $\lambda_0 = 0.6328$ μm. Notice that as the size of the particle increases, the anisotropic nature of the phase function becomes more pronounced. In order to convince ourselves that these particles scatter in fashion described by Mie theory, angular scattering measurements were made with a Brice Phoenix spectrophotometer on the 0.481 μm particles. These data points are included as part of Fig. 5. The agreement between the measured scattered intensity and that predicted by Mie theory is good.

Data Acquisition Procedure. Starting with distilled water in the tank, the amount of radiation scattered normally from the water was recorded as the probe of the detector assembly was moved radially from the center of the laser beam. Once a data set was taken, additional particles were thoroughly mixed into the water and the process was repeated.

Even though some of the particles were large, no settling or other discernable time variations were detected over a period of several hours. For a given concentration of particles (thoroughly mixed) data

Downloaded 20 Dec 2010 to 194.27.225.72. Redistribution subject to ASME license or copyright; see http://www.asme.org/terms/Terms_Use.cfm

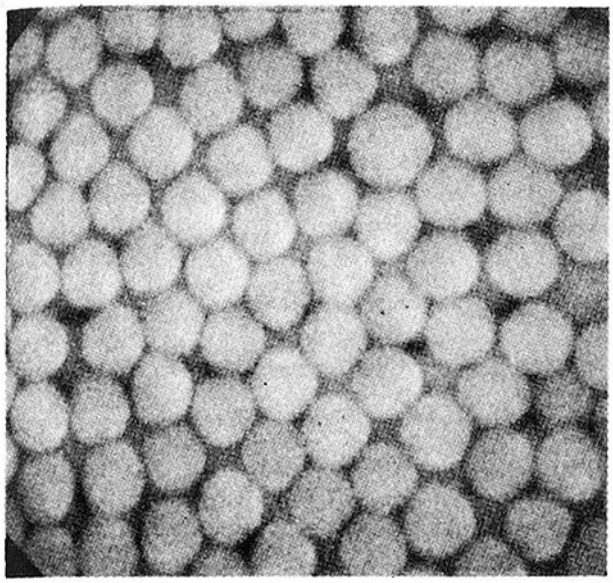

Fig. 3 Electron microscope picture of 1.011 μm dia particles at a magnification of 10,000

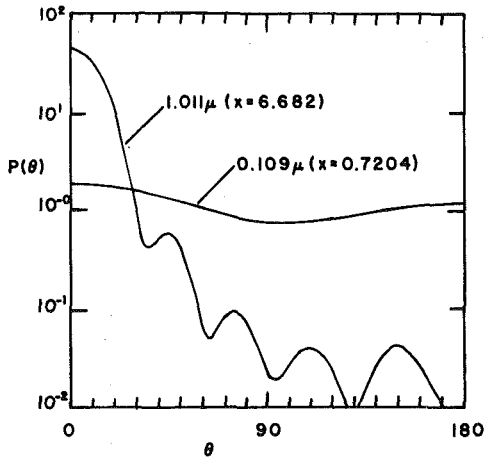

Fig. 4 Scattering phase function for 0.109 and 1.011 μm dia latex particles in water for λ_0

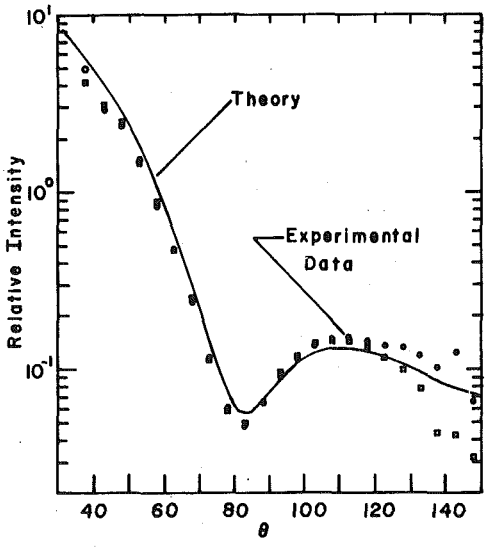

Fig. 5 Comparison of the angular variation of scattered intensity for 0.481 μm diameter latex particles in water for λ_0. Data were acquired by "O" rotating the detector clockwise and "□" reversing the cell and rotating the detector counterclockwise.

was reacquired after time intervals of from 30 to 60 min without remixing. In addition, the concentration was allowed to sit undisturbed for more than 48 hours. It was then remixed and a data set reacquired. The result was that there was essentially no difference in the data for all cases.

The raw data of this study were adjusted slightly before calculations were made and the results plotted. That is, the photomultiplier tube (PMT) dark voltage level was subtracted from the voltage measurements and the location of the center of the laser beam was subtracted from the position reading of the detector.

Relation of Experiment to Theory

In order to relate the raw data (experimental) values to the theoretical results an analysis like that discussed in [8] was made. The resulting expression relating the experimentally measured intensity leaving the medium normal to the surface and that entering the medium is

$$\frac{I_{\text{exp}}}{I_i} = \frac{2}{\pi}\left[\frac{r_0}{\bar{\theta}R_0}\right]^2\left(\frac{V}{P_i}\right)10^{-7} \tag{17}$$

$$= 7.65\left(\frac{V}{P_i}\right)10^{-6},$$

where $\bar{\theta} = 2.75$ deg (0.048 rad), $R_0 = 0.190$ cm, $r_0 = 0.1$ cm and V is in volts and P_i in watts. Inspection of equation (17) reveals that the experimentally determined intensity is very sensitive to the values of r_0, R_0, and $\bar{\theta}$. The sensitivity of the results to r_0 can be eliminated by rearranging

$$\frac{r^2 I_{\text{exp}}}{r_0^2 I_i} = 7.65\left(\frac{V}{P_i}\right)10^{-4}\, r^2. \tag{18}$$

In order to obtain values of the optical thickness, the scattering cross section for the particles had to be determined. It is convenient to write τ_r in terms of the particle volume concentration η (volume of latex particles per unit volume of mixture) and the effective scattering coefficient, c. Thus, one can write

$$\eta = N\pi d^3/6 \tag{19}$$

where d is the diameter of the uniform sized particles. This allows the optical thickness (see equation 2(b)) to be written as

$$\tau_r = \eta[6\, C_{\text{sca}}/\pi d^3]r + \kappa r \tag{20}$$

$$= (\eta c + \kappa)r$$

where c is the scattering cross section divided by the particle volume and κ of distilled water was taken as 0.005 cm^{-1} at λ_0 [33]. The scattering coefficient of the media is of a magnitude such that ω is greater than 0.99 for cases presented. The values of c, which were determined theoretically using Mie theory, are listed in Table 2. The value of c, for the 0.03 μm particles, was determined experimentally and this value was used in data reduction, since the agreement with theory was unacceptable. This disagreement was probably due to the wide size distribution of these particles.

Results and Discussion

The experiments were carried out with a He-Ne laser. The tank was filled with 15,820 cm^3 of distilled water, which yielded a water depth of 21.6 cm. Polystyrene latex particles were used as the scattering centers. The design of the detection system was such that the minimum radial position for which data could be taken was one centimeter away from the center of the incident laser beam. This restricted r/r_0 to be greater than 10. The lower end of the barrel was 0.64 cm above the water surface.

Figure 6 is presented to illustrate the dramatic effect of increasing the concentration of scattering particles (1.011 μm in diameter) on the scattered radiation. Notice from the sequence of pictures A through F, that as the number of particles increased the apparent scattering volume of radiant energy expands ($A \rightarrow F$). Though not presented in the figure, further addition of particles causes this scattering volume to collapse. This effect continues until only radia-

Downloaded 20 Dec 2010 to 194.27.225.72. Redistribution subject to ASME license or copyright; see http://www.asme.org/terms/Terms_Use.cfm

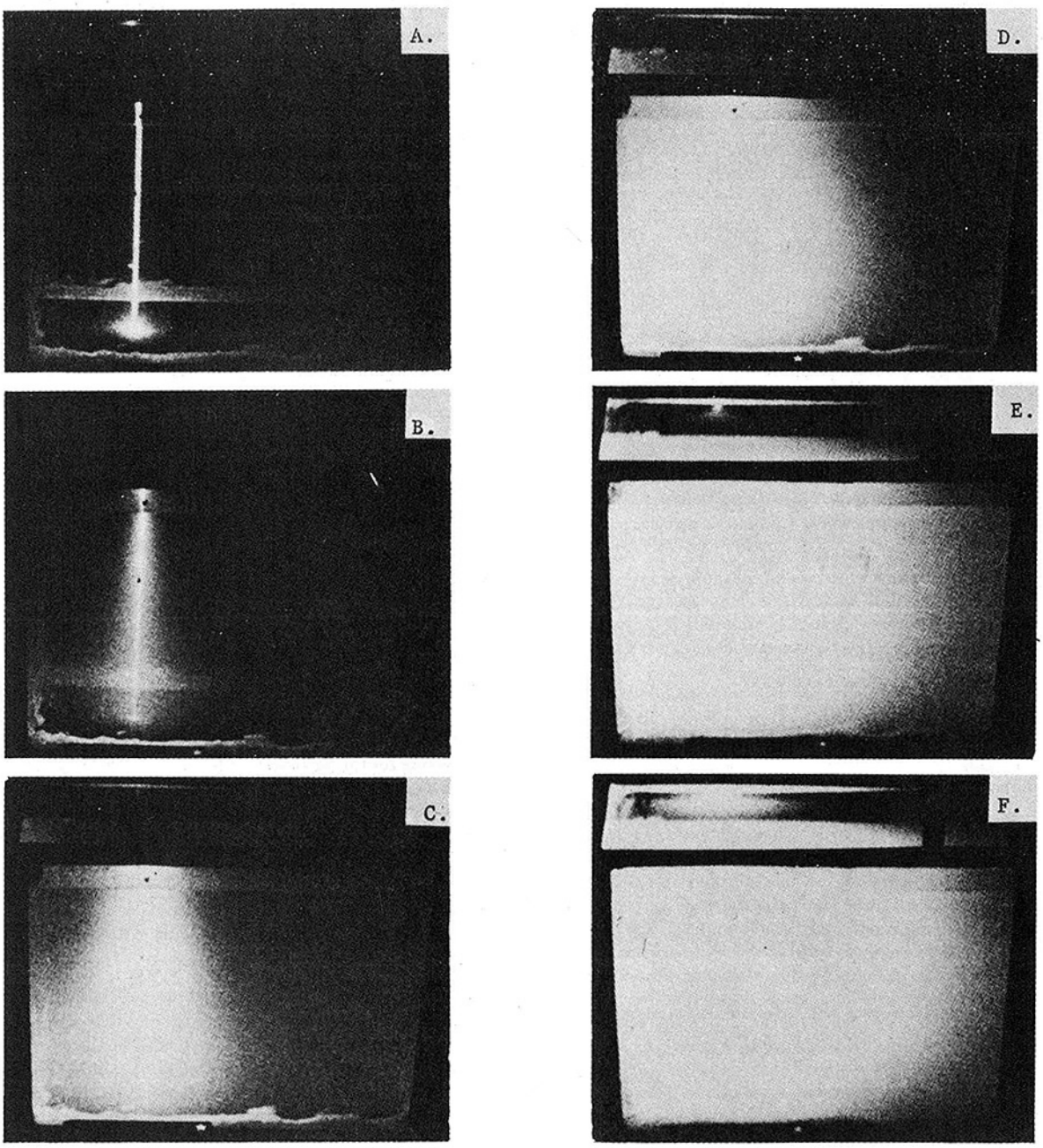

Fig. 6 Composite of pictures of the tank with various concentrations of 1.011 μ diameter polystyrene latex particles in distilled water: (*a*) $\eta = 6.32\ (10^{-6})$ (*b*) $\eta = 3.79\ (10^{-5})$ (*c*) $\eta = 7.59\ (10^{-5})$ (*d*) $\eta = 1.58\ (10^{-4})$ (*e*) $\eta = 3.79\ (10^{-4})$ (*f*) $\eta = 6.95\ (10^{-4})$

tion reflected from the upper surface may be seen. This is the same type of phenomenon discussed in [8].

Theoretically, isotropic results can be reduced to a single curve [6] if one plots $(r/r_0)^2 I_{exp}/I_i$ versus τ_r at r/r_0 greater than 10. Figure 7 is the resulting plot for the anisotropic data obtained in this study. Notice that all of the data did not collapse to a single curve. As was discussed in the theoretical portion of this paper, this condition may be remedied by use of the asymmetry factor, g. That is, the actual optical radius for the anisotropic case, τ_r, and the corresponding effective optical radius for the isotropic case, $\tau_r{}^*$, are related by

$$\tau_r{}^* = (1 - g)\,\tau_r \tag{21}$$

when $\omega = 1$ (see equation (6)). The $(1 - g)$ factor transforms the anisotropic problem to an effective isotropic situation. Correlating the data using $\tau_r{}^*$ collapses the data of Fig. 7 to that shown as Fig. 8. The data appear to correlate better as $\tau_r{}^*$ increases; this is consistent with other one-dimensional investigations [30]. The 0.03 μm data do not correlate as well as the rest because the particles are not as well characterized. The collapsed data may be approximated by the theoretical isotropic results of reference [1].

Table 3 may be used for a detailed comparison of the data being presented. The $(1 - g)$ term was computed using Mie theory for $n = 1.2$ and the size parameter, x, as listed. Notice that the effective locations of the maximum intensity are very near the theoretical value (3.345). In addition, the magnitude of the non-dimensional intensity at the peak varies from approximately 0.032 to 0.047. The differences between theory and experiment are probably due to the simplistic scattering phase function used in the theory. If a more realistic phase function were used, the theory would probably predict a variation in value of $\tau_{r_{max}}{}^*$.

Summary

A comparison of theoretical and experimental results of two-dimensional, multiple anisotropic scattering is presented. The reader is reminded of the physical situation, that is the detector is a large distance from the incident beam ($r \gg r_0$) and $\omega \doteq 1$. A multiple

Downloaded 20 Dec 2010 to 194.27.225.72. Redistribution subject to ASME license or copyright; see http://www.asme.org/terms/Terms_Use.cfm

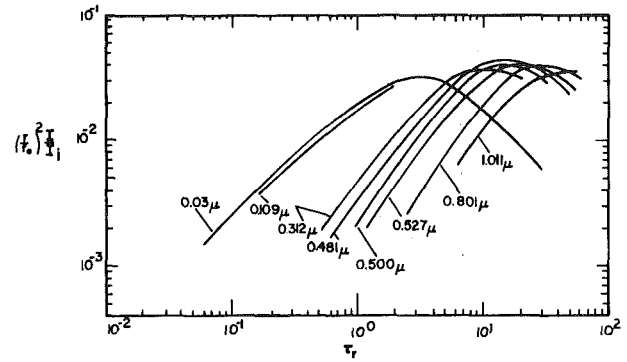

Fig. 7 Nondimensional scattered intensity versus the radial optical thickness, for various particle diameters

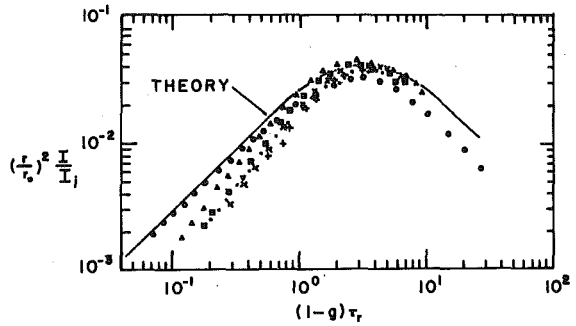

Fig. 8 Nondimensional scattered intensity versus the effective radial optical thickness: ○ ⟹ d = 0.03 μm, • ⟹ d = 0.312 μm, ▲ ⟹ d = 0.481 μm, ■ ⟹ d = 0.500 μm, x ⟹ d = 0.801 μm, + ⟹ d = 1.011 μm.

scattering analysis is required for this study because at least two scattering events are required to redirect the photons back normal to the upper surface.

The theoretical portion of this study indicates

1 that as the asymmetry factor increases the nondimensional scattered intensity curve is shifted in the direction of larger τ_r,

2 the magnitude of the maximum intensity is insensitive to particle size,

3 the anisotropic scattered nondimensional intensity distribution curves are dependent on g, the asymmetry factor, and collapse to a single curve by using $(1-g)$ as a correlation parameter. This yields a universal distribution function, $G(\tau_r{}^*)$, and

4 the maximum intensity of this collapsed curve occurs at $\tau_r{}^* = 3.345$.

The experiment was designed to be consistent with the restrictions of the theory. The results show that:

1 The nondimensional scattered intensity curves are shifted in the direction of larger τ_r as particle size increases for particles between 0.03 μm and 1.011 μm in diameter;

2 the magnitude of the maximum nondimensional intensity is relatively insensitive to particle size;

3 the experimentally determined nondimensional intensity distributions for various particle sizes can be reduced to essentially a single curve by the use of $(1-g)$ as a correlation factor; and

4 the maximum nondimensional intensity of these collapsed curves occurs at $\tau_r{}^*$ values of approximately 3.3.

Based on the results presented here, the adjustment of the scattering coefficient of paint in reference [8] to account for its anisotropic character seems justified. In that investigation, the measured scattering coefficient was reduced by 90 percent, which corresponds to an asymmetry factor of 0.9, to correlate the experimental and theoretical results. Aligning the peaks of the non-dimensional intensity distribution for paint yields a value of 0.85 for g. A simple calculation, assuming the TiO_2, Silica, Calcium Carbonate and Vinyl Acetate particles in the paint as spherical, yields an asymmetry factor of 0.80 to 0.85, depending on the size of TiO_2 particles used. Thus, an asymmetry factor value of about 0.9 seems appropriate for paint. This result adds support for using $(1-g)$ as a correlation factor.

Table 3 Effect of asymmetry factor

$d(\mu)$	x	$\left[\left(\frac{r}{r_0}\right)^2 \frac{I_{exp}}{I_i}\right]_{max}$	$1-g$	$\tau_{r_{max}}$	$\tau^*_{r_{max}}$
0.03	0.198	0.032	0.99	3.3	3.3
0.109	0.720	—	0.91	—	—
0.312	2.060	0.035	0.32	10	3.3
0.481	3.176	0.047	0.19	17	3.2
0.500	3.301	0.040	0.18	17	3.0
0.527	3.400	0.040	0.17	22	3.6
0.801	5.289	0.040	0.10	32	3.3
1.011	6.670	0.032	0.08	39	2.6

Multi-dimensional, radiative transfer with anisotropic scattering, offers many interesting challenges for future work. While the comparisons of theory and experiment of this investigation are quite satisfying, the region of $\tau_r{}^*$ less than one needs further attention. Also, the effects of refractive index of the media, reflection characteristics of the bottom, and absorption ($\omega < 1$) need to be investigated.

Acknowledgment

The authors wish to acknowledge the support of the National Science Foundation Grant No. NSF ENG 78-07935 for the support of this research.

References

1 Crosbie, A. L., and Linsenbardt, T. L., "Two-Dimensional Isotropic Scattering in a Semi-Infinite Medium," *Journal Quantitative Spectroscopy and Radiative Transfer*, Vol. 19, 1978, pp. 257–284.

2 Chin, J. H., and Churchill, S. W., "Anisotropic, Multiply Scattered Radiation from an Arbitrary Cylindrical Source in an Infinite Slab," ASME JOURNAL OF HEAT TRANSFER, Vol. 87, May 1965, pp. 167–172.

3 Dolin, L. S., "Propagation of a Narrow Beam of Light in a Medium with Strongly Anisotropic Scattering," *Soviet Radiophysics*, Vol. 9, 1966, pp. 40–47.

4 Bravo-Zhivotovskiy, D. M., Dolin, L. S., Luchinin, A. G., and Savel'yev, V. A., "Structure of a Narrow-Light Beam in Sea Water," *Atmospheric and Ocean Physics*, Vol. 5, No. 2, 1969, pp. 160–167.

5 Stockham, L. W., and Love, T. J., "Radiative Heat Transfer from a Cylindrical Cloud of Particles," *AIAA Journal*, Vol. 6, No. 10, Oct 1968, pp. 1935–1940.

6 Crosbie, A. L. and Dougherty, R. L., "Two-Dimensional Isotropic Scattering in a Semi-Infinite Cylindrical Medium," *Journal of Quantitative Spectroscopy and Radiative Transfer*, Vol. 20, 1978, pp. 151–173.

7 Crosbie, A. L. "Single and Double Scattering Approximations for a Two-dimensional Cylindrical Medium," *Journal of Quantitative Spectroscopy and Radiative Transfer*, Vol. 21, 1979, pp. 107–114.

8 Look, D. C., Nelson, H. F., Crosbie, A. L., and Dougherty, R. L., "Two-Dimensional Multiple Scattering: Comparison of Theory and Experiment," ASME JOURNAL OF HEAT TRANSFER, Vol. 100, No. 3, Aug 1978, pp. 480–485.

9 Ivanov, A. P., and Sherbaf, I. D., "Optical Conditions in a Turbid Medium Illuminated by a Narrow Light Beam," *Optics and Spectroscopy*, Vol. 18, pp. 391–394, 1965.

10 Ivanov, A. P., and Sherbaf, I. D., "Attenuation of a Narrow Beam in a Turbid Medium," *Journal of Applied Spectroscopy*, Vol. 5, 1966, pp. 147–151.

11 Ivanov, A. P., and Sherbaf, I. D., "Influence of the Angular Dispersion of a Beam of Light on Its Penetration Into a Scattering Medium," *Atmospheric and Oceanic Physics*, Vol. 2, 1966, pp. 188–190.

12 Atkins, J. T., "Absorption and Scattering of Light in Turbid Media," Ph.D. Thesis, University of Delaware (1965): Dissertation Abstracts, 1327, No. 6, 1966, pp. 1844.

13 Hottel, H. C., Sarofim, A. F., Evans, L. B., and Vasalos, I. A., "Radiative Transfer in Anisotropically Scattering Media: Allowance for Fresnel Reflection at the Boundaries," ASME JOURNAL OF HEAT TRANSFER, Vol. 90, Feb 1968, pp. 56–62.

14 Sarofim, A. F., Hottel, H. C., and Fahimian, E. J., "Scattering of Radiation by Particle Layers," *AIAA Journal*, Vol. 6, No. 12, Dec. 1968, pp. 2262–2266.

15 Hottel, H. D., Sarofim, A. F., Dalzell, W. H., and Vasalos, I. A., "Optical Properties of Coatings: Effect of Pigment Concentration," *AIAA Journal*, Vol. 9, No. 10, Oct 1961, pp. 1895–1898.

16 Hottel, H. C., Sarofim, A. F., Vasalos, I. A., and Dalzell, W. H., "Multiple Scatter: Comparison of Theory with Experiment," ASME JOURNAL OF HEAT TRANSFER, Vol. 92, May 1970, pp. 285–291.

17 Sarofim, A. F., Vasalos, I. A., and Jeje, A. A., "Experimental and Theoretical Study of Absorption in an Anisotropically Scattering Medium," ASME Paper No. 71-HT-20, 1971.

18 Leader, J. Carl, "Polarization Dependence in EM Scattering from Rayleigh Scatterers Embedded in a Dielectric Slab. I Theory," *Journal of Applied Physics*, Vol. 46, No. 10, Oct 1975, pp. 4371–4385.

19 Granatstein, V. L., Rhinewine, M., Levine, A. M., Feinstein, D. L., Ma-

Downloaded 20 Dec 2010 to 194.27.225.72. Redistribution subject to ASME license or copyright; see http://www.asme.org/terms/Terms_Use.cfm

zurowski, M. J., and Piech, K. R., "Multiple Scattering of Laser Light from a Turbid Medium," *Applied Optics,* Vol. 11, No. 5, 1972, pp. 1217–1223.

20 Leader, J. Carl, and Dalton, W. A. J., "Polarization Dependence of EM Scattering from Rayleigh Scatterers Embedded in a Dielectric Slab. II Experiment," *Journal of Applied Physics,* Vol. 46, No. 10, Oct 1975, pp. 4386–4391.

21 Howard, F. H., and Novotny, J. L., "Reflectance of a Scattering Medium Containing Polydisperse Nonspherical Particles," 5th International Heat Transfer Conference, Sept 1974, Vol. I. pp. 26–29.

22 Richards, L. W., "The Calculation of the Optical Performance of Paint Films," *Journal of Paint Technology,* Vol. 42, No. 544, 1970, pp. 276–286.

23 Querfield, C. W., Kerker, M., and Kratohvil, J. P., "Multiple Scattering in a Synthetic Foggy Atmosphere—Experimental Results," *Journal of Colloid and Interface Science,* Vol. 39, No. 3, June 1972, pp. 568–582.

24 Margolis, J. S., McCleese, D. J., and Hunt, G. E., "Laboratory Simulation of Diffuse Reflectivity from a Cloudy Planetary Atmosphere," *Applied Optics,* Vol. 11, No. 5, May 1972, pp. 1212–1216.

25 Giovanelli, R. G., "Reflection by Semi-Infinite Diffusers," *Optica Acta,* Vol. 2, No. 4, Dec. 1955, pp. 153–162.

26 Ready, J. T., *Effects of High-Power Laser Radiation,* New York, Academic Press, 1971.

27 Hansen, J. E., "Exact and Approximate Solutions for Multiple Scattering by Cloudy and Hazy Planetary Atmospheres," *Journal of Atmospheric Sciences,* Vol. 26, 1969, pp. 478–487.

28 Potter, J. F., "The Delta Function Approximation in Radiative Transfer Theory," *Journal of Atmospheric Sciences,* Vol. 27, 1970, pp. 943–949.

29 Wang, L., "Anisotropic Nonconservative Scattering in a Semi-Infinite Medium," *The Astrophysical Journal,* Vol. 174, 1972, pp. 671–678.

30 Sobolev, V. V., *Light Scattering in Planetary Atmospheres,* New York, Pergamon Press, 1975, pp. 158–161.

31 Van de Hulst, H. C., and Grossman, K., "Multiple Light Scattering in Planetary Atmospheres," *The Atmospheres of Venus and Mars,* J. C. Brandt and M. B. McElroy, Editors, Gorden & Breach, New York, 1968, pp. 35–55.

32 Crosbie, A. L., "Expansions for Two-Dimensional Radiative Transfer in an Isotropically Scattering Semi-Infinite Medium," *Journal of Quantitative Spectroscopy and Radiative Transfer,* Vol. 19, 1973, pp. 285–301.

33 Zuev, V. E., "*Propagation of Visible and Infrared Radiation in the Atmosphere,*" John Wiley and Sons, New York, 1974, pp. 375.

Downloaded 20 Dec 2010 to 194.27.225.72. Redistribution subject to ASME license or copyright; see http://www.asme.org/terms/Terms_Use.cfm

Dense, Vertical Jets with Two Opposing Buoyancy Components

S. Takao
U. Narusawa

Technical Research Center,
Nippon Kokan K.K.,
Kawasaki, Japan

The height to which dense, vertical jets with two opposing buoyancy components rise was investigated experimentally. In the experiment, the dense, vertical jets were produced by using the temperature difference between the jet at the nozzle and the surroundings as the positive buoyancy component, and by using common salt and $CuSO_4$ alternatingly for the negative buoyancy component. Based on a dimensional argument, it was found that the three nondimensional parameters of (1) the ratio of the jet height to the nozzle diameter, H/r_j, (2) the internal Froude number, Fr, and (3) the density ratio, R, all govern the behavior of the jet. The data were well correlated when H/r_jFr was plotted against against $1/R$ in the range of $0 \leq 1/R \leq 0.9$, showing that H/r_jFr tends to fall with an increase of $1/R$. A least square fitting of the data yielded the explicit form of the jet height to be

$$\frac{H}{2.67\, r_j Fr} = \begin{cases} 1 & \text{for } 0 \leq 1/R \leq 0.27. \\ -\dfrac{0.84}{R} + 1.23 & \text{for } 0.27 \leq 1/R \leq 0.9. \end{cases}$$

1 Introduction

When a jet which is heavier than the surrounding fluid is directed upward, it first rises with rapidly decreasing velocity to a certain height, at which point the entire jet comes to rest and collapses at the top. Then the downflow from the top of the jet completely surrounds the upflow, and the jet settles down to a steady state. At this state, the height of the jet is lower than the height it had originally attained because the upflow is now exchanging the fluid with the heavier downflow rather than the stationary surrounding fluid (see Fig. 1).

Turner [1], as part of a study of cloud behavior, was the first to experimentally determine the height to which a dense, vertical jet with a single buoyancy component will rise. Other research on a jet with negative buoyancy issuing vertically into a homogeneous fluid includes studies of effluent discharge into the ocean [2] and waste gas discharge into the atmosphere [3].

This work deals with the height of a heavy jet into which a positive buoyancy component has been introduced to produce a jet with two opposing buoyancy components. For example, the positive (upward) buoyancy component is provided by the temperature difference between a warm salt solution jet and its surroundings while the salinity of the solution provides the negative (downward) buoyancy component with the overall density of the jet being heavier than the surroundings. This work has arisen out of a study of jet mixing of the contents of a large tank [4], a condition in which the height of the jet is an important factor for mixing efficiency.

2 Dimensional Analysis

Preliminary testing showed that the shape of the dense, vertical jet with two opposing buoyancy components is quite similar to that of the vertical jet with a single buoyancy component, suggesting that a dimensional argument similar to the one used to analyze the vertical jet with a single buoyancy component can be developed as a basis for the experimental investigation.

Turner [1], employing a dimensional argument, has arrived at the conclusion that for a dense, vertical jet with a single buoyancy component, the ratio of the height to the radius of the nozzle, H/r_j, is directly proportional to the internal Froude number at the jet nozzle, i.e.,

$$\frac{H}{r_j \mathrm{Fr}} = C \tag{1}$$

His experimentally obtained value of C is 2.46. For a dense, vertical jet with two buoyancy components, the internal Froude number in addition to the geometrical ratio of H/r_j is also important since both initial buoyancy and momentum are relevant quantities.

The third nondimensional parameter which is important in the analysis of jets is the entrainment coefficient, E, which is the ratio of a mean inflow velocity across the jet boundary to the mean jet upward velocity. In many studies of jets [5–8] E was assumed to be constant along the direction of a jet. On the other hand, Abraham [9], in his theoretical study of a dense, vertical jet with a single buoyancy component, proposed to divide the jet into two regions, one with a positive value of E near the nozzle and another with a negative value of E near the maximum jet height. His analysis yielded the value of 2.74 for C in equation (1) which is in excellent agreement with the experimental results considering the complexity of the actual jet behavior. In the analysis of our experimental results, however, it was implicitly assumed, as Turner [1] had, that the entrainment coefficient does not enter as an important non-dimensional parameter; i.e. E or its change will follow an a priori similarity assumption.

The fourth nondimensional parameter, which is the result of introducing an additional buoyancy component, can be derived from the equation of state. Consider a case in which a warm aqueous solution of common salt is issued upward from a nozzle into fresh water surroundings. Then the linearized equation of state is,

$$\frac{\rho - \rho_\infty}{\rho_\infty} = -\alpha(T - T_\infty) + \beta S. \tag{2}$$

When the above equation is applied to the jet at the nozzle ($\rho = \rho_j$, $T = T_j$, $S = S_j$), the term $\alpha(T_j - T_\infty)$ gives the positive (upward) buoyancy component, while βS_j gives the negative (downward) buoyancy component. Since various combinations of the positive and negative buoyancy components exist for a given net (negative)

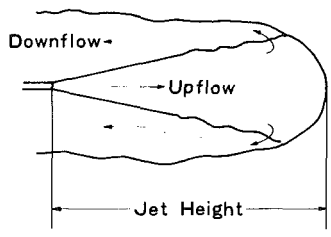

Fig. 1 Sketch of a dense, vertical jet

ibuted by the Heat Transfer Division for publication in the JOURNAL TRANSFER. Manuscript received by the Heat Transfer Division April

Copyright © 1981 by ASME

Downloaded 20 Dec 2010 to 194.27.225.72. Redistribution subject to ASME license or copyright; see http://www.asme.org/terms/Terms_Use.cfm

buoyancy of the jet at the nozzle, the ratio of the two opposing buoyancy components $R = \beta S_j/\alpha(T_j - T_\infty)$, which is usually referred to as the density ratio or the stability parameter in the study of double-diffusive phenomena [10], emerges as an additional nondimensional parameter.

In order to obtain the exact form of the relation among the three parameters of H/r_j, Fr and R, the following experimental investigation was conducted.

3 Experiment

Figure 2 shows a schematic diagram of the experimental apparatus. The experiment was conducted using a 50 cm wide × 100 cm long × 120 cm high acrylic tank with a nozzle located at the center of the tank bottom. A 6000 cc capacity reservoir was suspended from the ceiling and connected to the nozzle in the acrylic tank by a thermally insulated pipe containing an on-off valve. Two scales were attached to the side walls of the tank for determining the jet height. The jet speed issuing from the nozzle could be adjusted by varying the vertical distance between the free surface of the tank and the reservoir in the range of 200 − 1500 mm. During the run the effect of the change in the reservoir fluid level on the jet speed was negligible since the level change was less than 10 mm in 200 mm head runs and less than 50 mm in 1500 mm runs. A distance of 5 − 20 cm between the tip of the nozzle and the bottom of the tank was maintained so that the outer falling stream could be collected in this space. It should be noted that one experimental run had to be completed before the liquid of the outer falling stream filled up this lower space of the tank. Nozzles were made of 2 mm thick glass tubing and a copper-constantan thermocouple was inserted to a depth of 6 cm from the tip of each nozzle to measure the temperature of the jet at the nozzle. The thermocouple was connected to a digital temperature indicator, which enabled us to determine the change of temperature with time. The thermocouple was estimated to be accurate to within ± 0.5°C.

An experimental run started with the filling of both the tank and the nozzle-to-valve pipe with fresh water and leaving it for ~ 4 hr to simulate still surroundings as much as possible. At this point, a set amount (~ 5000 c.c.) of salt solution (colored by methylene blue) with predetermined salinity and temperature was introduced into the reservoir; the temperature of the water in the tank was measured by a thermometer and the valve leading from the reservoir to the nozzle quickly opened with the timer switched on. At the steady state, the height and the temperature of the jet were read. Then the valve from the reservoir to the tank as well as the timer was switched off and the remaining amount of salt solution in the reservoir measured. The jet speed at the nozzle was estimated from the initial and final volume of the salt solution in the reservoir along with the elapsed time for a given run. The error in this method of speed measurement is likely to be caused by the effect of the initial transient state. To estimate the error, jets were issued into the air, and the overall jet speed, obtained from the total elapsed time and from the initial and final volume of the salt solution in the reservoir, was then compared with the steady state jet speed. The latter was obtained by measuring the elapsed time and the amount of jet fluid collected in a measuring cylinder after a steady state was reached. For our experimental range, it was found that the value of the overall jet speed is lower than that of the steady state speed by 2.0 percent or less, confirming that the measurement of the jet speed is sufficiently accurate. The data of any run in which the outer falling stream did not completely surround the core jet were discarded.

The change of density with both concentration and temperature, a quantity required for computing the jet density at the nozzle as well as the density ratio, was obtained from the International Critical Table [11]. To measure the concentration of salt and $CuSO_4$ accurately, a small sample of liquid was extracted before and after each run and its refractive index was read through a refractometer having the capability of analyzing 1/1000 percent difference in concentration. Table 1 indicates the range of our experiment.

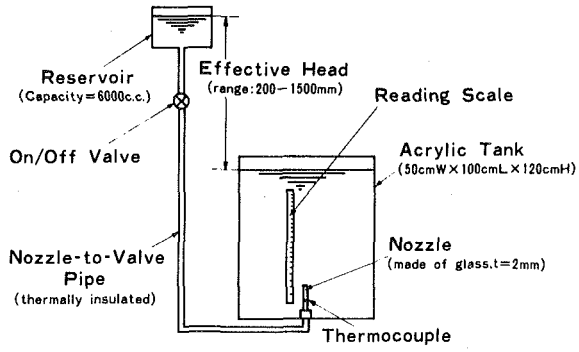

Fig. 2 Schematic diagram of the experimental apparatus

Table 1 Range of experiment

Jet Temperature at the Nozzle	: 25–80°C
Jet Salinity at the Nozzle	: 1–10 weight percent
Nozzle Diameter	: 1.0, 2.0, 3.0, 3.6, 5.6 mm
Temperature of the still surroundings	: 15–25°C
Nozzle Reynolds Number	: >2500

4 Results and Discussion

First, the height of dense, vertical jets with a single negative buoyancy component was measured, using common salt as a tracer. Figure 3 shows the results of the experiment along with the straight line approximations proposed by Turner [1] and by Abraham [9]. As can be seen, most data points fall between Turner's results and Abraham's proposition. The least square fitting of our data yielded the value of C in equation (1) of 2.67. The scattering of data is probably due to the reading error of the jet height, although its fluctuations were small and random.

With the accuracy of our method confirmed through the aforementioned preliminary investigation, the height of the dense, vertical jet with two opposing buoyancy components was measured. The temperature difference between the jet at the nozzle and the surroundings was used as a positive buoyancy component throughout, while common salt was used as a negative buoyancy component initially, followed later by the use of $CuSO_4$ to test the generality of our analysis.

In order to find the relationship among the three nondimensional parameters, the constant, C, in equation (1) was replaced by some function of $1/R$ to assume the following form,

$$\frac{H}{2.67\, r_j \mathrm{Fr}} = f(1/R). \tag{3}$$

Figure 4 is the summary of our experimental results, plotted according to equation (3). The data were found to be closely fitted with a curve, whose functional form obtained from a least square fitting is,

Nomenclature

C = a constant defined in equation (1)
E = entrainment coefficient
Fr = internal Froude number = $[\rho_\infty u_j{}^2/g(\rho_j - \rho_\infty)r_j]^{1/2}$
g = gravitational acceleration
H = jet height
r = nozzle diameter
R = density ratio = $\beta S_j/\alpha(T_j - T_\infty)$
S = salinity
T = temperature
u = jet speed
α = volume expansivity = $-1/\rho(\partial\rho/\partial T)$
β = $1/\rho(\partial\rho/\partial S)$
ρ = density

Subscripts

j = jet nozzle
n = jet with a negative buoyancy component
p = jet with two opposing buoyancy components
∞ = still surroundings

Downloaded 20 Dec 2010 to 194.27.225.72. Redistribution subject to ASME license or copyright; see http://www.asme.org/terms/Terms_Use.cfm

$$\frac{H}{2.67\, r_j \mathrm{Fr}} = \begin{cases} 1 & \text{for } 0 \le 1/R \le 0.27. \\ -\dfrac{0.84}{R} + 1.23 & \text{for } 0.27 \le 1/R \le 0.9. \end{cases} \quad (4)$$

and it is also shown in Fig. 4.

As can be seen, all the data points, including data using $CuSO_4$ instead of common salt as the negative buoyancy component, fall into a consistent curve providing a good overall correlation. Slight scattering of the data is thought to be caused either by the effect of nonlinearity in the equation of state or by the reading error of the jet height, the former becoming nonnegligible as both temperature and salinity differences increase. The data cover the inverse of density ratio, $1/R$, in the range of $0 - 0.9$. At $1/R = 0$ the jets contain only a single negative buoyancy component, and Fig. 4 indicates (1) that for $0 < 1/R < 0.3$ the effect of the positive buoyancy component does not reveal itself (i.e., the jet height can be estimated with reasonable accuracy using equation (1)) and (2) that as $1/R$ moves beyond ~ 0.3 the measured jet height, normalized with respect to $2.67\, r_j$ Fr, decreases roughly linearly with $1/R$.

The physical interpretation of the curve falling with an increase of $1/R$ is as follows: The height to which a one-component, heavy jet rises is expressed by equation (1), and, given a nozzle diameter and a jet speed at the nozzle, the height of the jet depends on $(\rho_j - \rho_\infty)$, which in turn is a function of the concentration of salt in the jet; on the other hand, for the jet with two opposing buoyancy components, $(\rho_j - \rho_\infty)$ is a function of both the salinity and temperature of the jet. If we let a heavy jet with a negative buoyancy component have a salinity of S_n, and a heavy jet with two opposing buoyancy components have a salinity of S_p and a temperature of T_p $(> T_\infty)$ so that the jet density at the nozzle, ρ_j, for both jets is equal, then

$$S_p = \frac{S_n}{1 - 1/R.} \quad (5)$$

Equation (5) shows that, as $1/R$ increases from zero, the salinity of the two-component jet, S_p, has to increase in order to achieve the same initial density, ρ_j, as the one-component jet. As the two-component jet issues from the nozzle, the entrainment decreases the positive buoyancy effect, while the negative buoyancy flux at any vertical distance from the nozzle is higher than the one-component jet, resulting in a jet height lower than that of the one-component jet.

For $1/R > 0.9$, heavy jets with two-components created a "growing cloud" much like a thermal over the nozzle and did not produce an outer falling stream.

4 Conclusions

Based on the dimensional argument followed by the experimental investigation, the following conclusions were derived: (1) The behavior of dense, vertical jets with two opposing buoyancy components are quite similar in nature to that of jets with only a single negative buoyancy component studied previously by many researchers, in that the steady vertical jet only rises to a certain height surrounded by an outer falling stream. (2) The ratio of the jet height to the nozzle diameter, H/r_j, is a function of the internal Froude number, Fr, and the density ratio, R, the latter being a newly introduced nondimensional parameter resulting from the simultaneous presence of two opposing buoyancy components. (3) It was experimentally verified that the form of the relationship among the three nondimensional parameters is

$$\frac{H}{2.67\, r_j \mathrm{Fr}} = f(1/R),$$

and that the value of $H/2.67\, r_j$Fr tends to fall with the increase of $1/R$. (4) The least square fitting of the data gives the following explicit form of $f(1/R)$,

$$f(1/R) = \begin{cases} 1 & \text{for } 0 \le 1/R \le 0.27. \\ -\dfrac{0.84}{R} + 1.23 & \text{for } 0.27 \le 1/R \le 0.9. \end{cases}$$

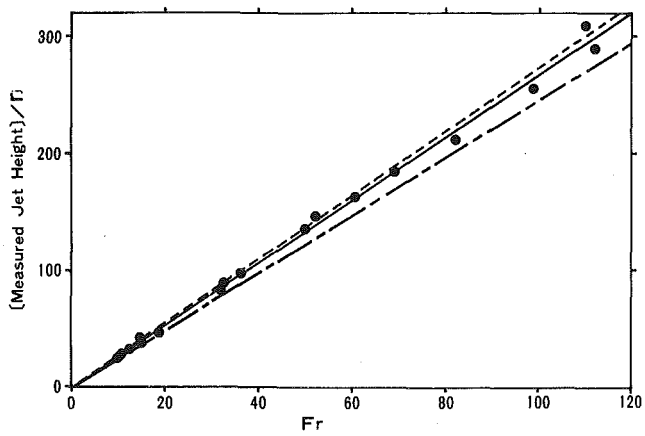

Fig. 3 Experimental results of the height of vertical jets with only a negative buoyancy component. ● = experimental data. —— = least square fitting of the data. --- = Abraham's result [9]. ———— = Turner's result [1]

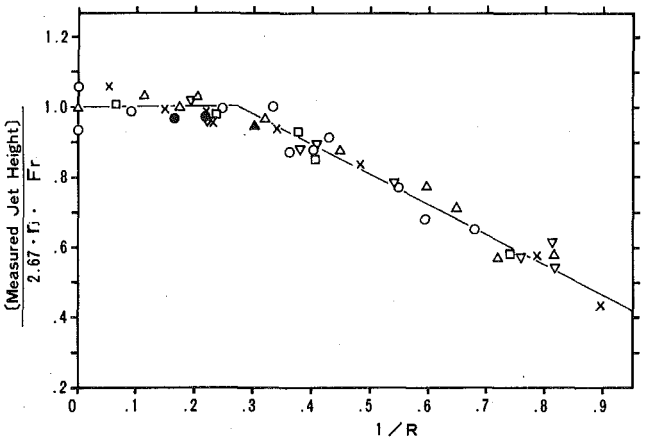

Fig. 4 Experimental results of the height of vertical jets with two opposing buoyancy components. ○ = nozzle diameter 1.0 mm, NaCl jet. □ = nozzle diameter 2.0 mm, NaCl jet. ▽ = nozzle diameter 3.6 mm, NaCl jet. △ = nozzle diameter 5.6 mm, NaCl jet. ● = nozzle diameter 1.0 mm, $CuSO_4$ jet. × = Nozzle diameter 3.0 mm, $CuSO_4$ jet. ▲ = nozzle diameter 5.6 mm, $CuSO_4$ jet. —— = least square fitting of the data (= equation (4)).

References

1 Turner, J. S., "Jets and Plumes with Negative or Reversing Buoyancy," *Journal of Fluid Mechanics,* Vol. 26, 1966, pp. 779–792.

2 Vergara, I., and James, W. P., "Dilution of a Dense, Vertical Jet in Stagnant Homogeneous Fluid," TAMU-SG-79-202, COE Report No. 211, Texas A & M University, Sea Grant College Program, May 1979.

3 Fan, L. N., and Brooks, N. H., "Dilution of Waste Gas Discharge from Campus Buildings," Technical Memorundum 68-1, W. M. Keck Laboratory of Hydraulics and Water Resources, California Institute of Technology, Pasadena, CA, Jan. 1968.

4 Smith, K. A., Lewis, J. P., Randall, G. A. and Meldon, J. H., "Mixing and Roll-Over in LNG Storage Tanks," *Advances in Cryogenic Engineering,* Plenum Press, New York, Vol. 20, 1975, pp. 124–133.

5 Morton, B. R., Taylor, G., and Turner, J. S., "Turbulent Gravitational Convection for Maintained and Instantaneous Sources," *Proceedings of the Royal Society,* A 234, 1956, pp. 1–23.

6 Morton, B. R., "Forced Plumes," *Journal of Fluid Mechanics,* Vol. 5, 1959, pp. 151–163.

7 Ricou, F. P., and Spalding, D. B., "Measurements of Entrainment by Axisymmetric Turbulent Jets," *Journal of Fluid Mechanics,* Vol. 11, 1961, pp. 21–32.

8 Morton, B. R., "Coaxial Turbulent Jets," *International Journal of Heat and Mass Transfer,* Vol. 5, 1962, pp. 955–965.

9 Abraham, G., "Jets with Negative Buoyancy in Homogeneous Fluid," *Journal of Hydraulic Research,* Vol. 5, 1967, pp. 235–248.

10 Turner, J. S., *Buoyancy Effects in Fluids,* Cambridge University Press, 1973.

11 *International Critical Table,* McGraw-Hill, New York, Vol. 3, pp. 52–94.

Downloaded 20 Dec 2010 to 194.27.225.72. Redistribution subject to ASME license or copyright; see http://www.asme.org/terms/Terms_Use.cfm

P. Y. Nizou
Maître-Assistant,
Laboratoire de Thermodynamique,
Institut de Physique,
2, rue de la Houssinière,
44072 Nantes Cedex, France

Heat and Momentum Transfer in a Plane Turbulent Wall Jet

Introduction

The problem of turbulent convection with a jet flowing tangentially to a heated flat surface (wall jet) has been widely studied with different configurations: surface with constant heat flux [1, 2] or with a step wall temperature [3, 4] as well as surface with mass transfer [5]. In all these investigations, the prediction of the heat (or mass) transfer rates follows the same procedure as in a classical boundary layer: St $= R\,C_f/2$, R being the Reynolds analogy factor. However, there remain some discrepancies in the proposed correlations for C_f and there are also some doubts about the value of R. This note attempts to supplement the relation between heat transfer and skin friction for turbulent wall jets and presents some additional results pointing out the differences with a classical boundary layer.

Experimental Conditions

The experiments were made with three slot thicknesses (7,13 and 20.5 mm) leading to slot Reynolds numbers ranging from 9000 to 60,000. The test heating plate (constant heat flux) is 1.50 m long with the beginning of heating located at the nozzle exit. The velocity measurements were made with total-head tubes and also with a hot-wire probe connected to a constant temperature anemometer. Wall shearing stresses were measured by the Preston's method which leads to a relative accuracy of ±2.5 percent on the friction factor C_f. The temperature profiles were obtained by a chromel-constantan thermocouple constructed according to Blackwell and Moffat [6] while the wall temperatures were determined by chromel-constantan thermocouples embedded near the heating surface. The physical characteristics of the fluid are evaluated at ambient temperature and the resulting error in the Stanton number measurement is below ±3 percent. Further details of the experimental apparatus and procedure may be found in [7].

Wall Jet Flow and Friction Factor

Figure 1 describes the regions of the wall-jet flow at a given section and helps to define the nomenclature used.

1 **Representation of the External Inner Layer.** The region extending from the wall to the maximum velocity line (that we will call inner layer) differs notably from a classical boundary layer by virtue of the fact that it is developing under the influence of an external flow: it is a disturbed boundary layer. The extensive experimental study of this inner layer [7] shows that it is possible to represent, for a certain distance from the nozzle exit, the structure of the external inner layer by means of a group of nondimensional iso-velocities $u^* = u/u_m$ where u_m represents the maximum velocity for a given section. This group defined in the region $0{,}7 < u^* < 1$ is made up of straight lines originating from a single point whose x-coordinate ($x = -x_1 = -20e$) is independent of the slot Reynolds number $\mathrm{Re} = u_0 e/\nu$ and whose y-coordinate y_1 is a function of Re.[1] Figure 2 illustrates the validity of such a representation for $e = 7$ mm. Similar findings were obtained for $e = 13$ and 20.5 mm. Hence the velocity profiles associated with the external inner layer can be expressed as

$$u = u_m \cdot f\left[\frac{y - y_1}{x + x_1}, \mathrm{Re}\right] \tag{1}$$

defined for $y_i < y < \delta$, y_i being the lower limit of the wall distance valid for such representation. It has been possible to show that such a representation is consistent with the bibliographical results as well as its superiority over the y/δ defect laws generally used.

2 **Representation of the Friction Factor.** By analogy with classical boundary layer analysis, attempts were made to correlate the friction factor C_f with thickness Reynolds number $u_m\delta/\nu$. The results revealed a systematic influence of the jet nozzle size, as one can see in Fig. 3. In the case of $e = 7$ mm, the experimental results are quite near the Bradshaw-Gee's relation for a wall jet.

$$C_f = 0.0315\left(\frac{u_m\delta}{\nu}\right)^{-0.182}$$

The data for $e = 13$ and 20.5 mm approach the Sigalla relation:

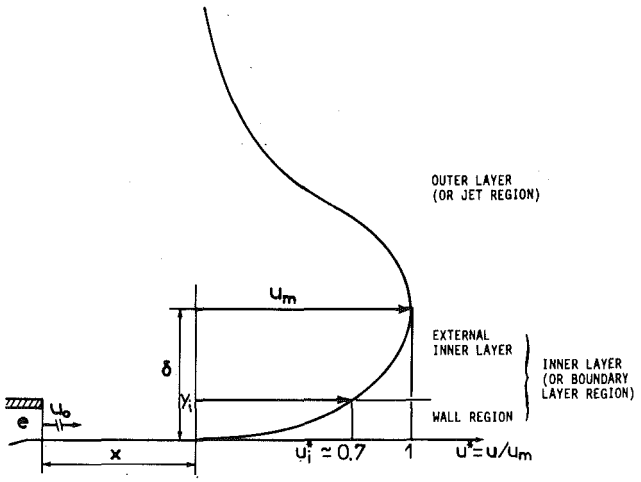

Fig. 1 Wall jet nomenclature

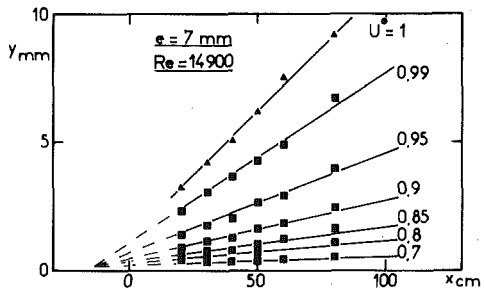

Fig. 2 Nondimensional isovelocities in external inner layer ($e = 7$ mm). Similar straight lines have been found for $e = 13$ mm (Re = 28,000) and $e = 20.5$ mm (Re = 56,000).

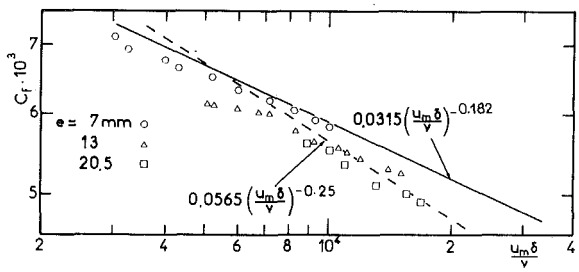

Fig. 3 Experimental values of friction factor: comparison with classical laws

[1] We have proposed [7] to take $x_1 \simeq 20e$, considering an average value obtained from our own results as well as from those obtained from the published literature.

Contributed by the Heat Transfer Division for publication in the JOURNAL OF HEAT TRANSFER. Manuscript received by the Heat Transfer Division November 27, 1979.

Copyright © 1981 by ASME
Downloaded 20 Dec 2010 to 194.27.225.72. Redistribution subject to ASME license or copyright; see http://www.asme.org/terms/Terms_Use.cfm

$$C_f = 0.0565 \left(\frac{u_m \delta}{\nu}\right)^{-0.25} \quad \text{(see [8])}$$

These findings have also been reported by Mabuchi and Kumada [5] who used nozzle thickness of 4 and 10 mm. On the other hand, all data can be brought to lie approximately on a single line by using X_1 ($=x + x_1$) instead of δ as the characteristic length in the Reynolds number. This is demonstrated in Fig. 4 and the experimental results can be well represented by

$$C_f = 0.0810 \left(\frac{u_m X_1}{\nu}\right)^{-0.192} \tag{2}$$

This correlation remains universal because the quantity $X_1 = x + x_1$ (with $x_1 \simeq 20e$) is nearly independent of the experimental conditions [7].

Local Heat Transfer in the Fully Developed Region

Figure 5 shows the dimensionless temperature plotted in logarithmic representation valid near the wall:[2]

$$\frac{T_w - T}{T_\tau} = A_T \log \frac{y u_\tau}{\nu} + B_T \tag{3}$$

with $A_T = 2.8$ and $B_T = 6.7$ based on our experimental results. A comparison is made with a similar law valid for classical thermal boundary layers in air with $A_T = 4.9$ and $B_T = 3.6$ in accordance with the bibliographical compilation of Kader and Yaglom [10]. The temperature profiles are conventional for $y\, u_\tau/\nu < 50$.

Figure 6 presents the evolution of the ratio St/C_f with the nondimensional coordinate X_1/e for $X_1/e > 50$ (fully developed region): Experimental values of the Stanton number are divided by the mean value of the friction factor defined by (2). This representation shows a slight increase of the ratio St/C_f when the quantity X_1/e increases; such a tendancy, in conflict with classical analogies between heat and momentum transfers, has been already experimentally observed by Mathieu [11] in the case of a heated jet flowing tangentially along a wall.

Discussion

The previous results have led us to recognize the difference in heat transfer which exists between a classical boundary layer with low turbulence stream and a wall jet. In the case of classical boundary layers in air (Prandtl number Pr = 0.7), heat transfer is practically governed entirely by the evolution of the phenomenon in the wall region and, hence, the analogy between heat and momentum transfer leads to a simple relation:

$$\mathrm{St}/C_f \simeq \frac{1}{2}\frac{A}{A_T} \simeq \frac{1}{2\mathrm{Pr}_t} \tag{4}$$

where Pr_t is the turbulent Prandtl number within the logarithmic layer [10]. Such an approach is not valid in the case of a wall jet. Indeed we see that

(*a*) If the relation $\mathrm{St}/C_f \simeq 0.5\, A/A_T$ is used indiscriminately, it gives $\mathrm{St}/C_f \simeq 0.75$, instead of the more correct value 0.6, since $A_T/A = 2.8/4.15 \simeq 0.67$.

(*b*) The St/C_f ratio increases slightly with X_1/e.

For most technological applications, it is permissible to consider an average value for the ratio St/C_f. Thus, using the relation (2) we can write for a constant heat flux plate:

$$\mathrm{Nu}_{X/1} = \frac{hX_1}{k} = 0.034 \left(\frac{u_m X_1}{\nu}\right)^{0.808}$$

as shown in Fig. 7. Included are some data obtained from the average

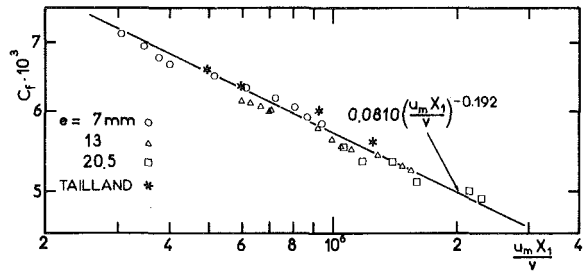

Fig. 4 Experimental values of friction factor: comparison with the proposed correlation with $u_m X_1/\nu$. Comparison with the mean values of Tailland [9]

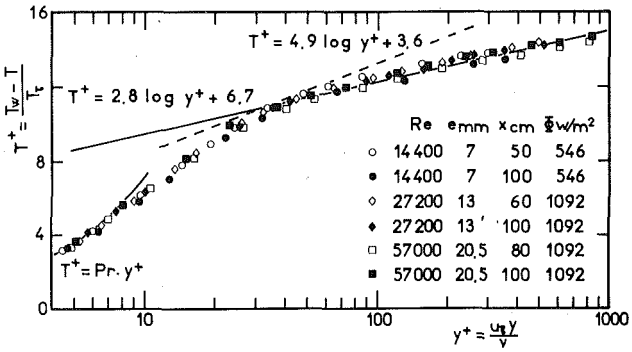

Fig. 5 Logarithmic representation of temperature profiles in inner layer

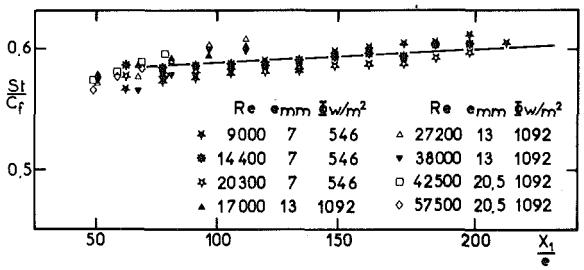

Fig. 6 Relation between Stanton number and friction factor

[2] We can simultaneously write a logarithmic representation of the velocity profiles near the wall with the coefficient initially proposed by Tailland [9], $A = 4.15$ and $B = 8.1$:

$$\frac{u}{u_\tau} = 4.15 \log \frac{y u_\tau}{\nu} + 8.1$$

Nomenclature

A, A_T = respective slopes of velocity and temperature profiles in logarithmic representation

$C_f = 2\tau_w/\rho u_m^2$ = friction factor

e = slot thickness

$h = \Phi/(T_w - T_{ad})$ local heat transfer coefficient

$\mathrm{Nu}_{X/1} = hX_1/k$ = local Nusselt number (k, thermal conductivity)

$\mathrm{Re} = u_0 e/\nu$ slot Reynolds number (ν, kinematic viscosity)

$\mathrm{Re}_{X/1} = u_m X_1/\nu$ local Reynolds number

$\mathrm{St} = h/\rho C_p u_m$ = local Stanton number (ρ, mass density; C_p, specific heat at constant pressure)

T, T_a, T_{ad} = local, ambient and adiabatic (without heating) temperature

$T_\tau = (T_w - T_a)\mathrm{St}\sqrt{C_f/2}$ shear temperature

u = velocity component in the x-direction; $u^* = u/u_m$ nondimensional velocity

$u_\tau = \sqrt{\tau_w/\rho}$ friction velocity

x, y = coordinates along wall and normal to wall

$x = -x_1$, y_1 = coordinates of the virtual origin of the external inner layer according to the proposed schematization ($x_1 \simeq 20e$); $X_1 = x + x_1$

δ = y-coordinate at the maximum velocity point

τ = shearing stress

Φ = local convection heat flux

Subscripts

w = value at the wall

m = value at the maximum velocity point

Downloaded 20 Dec 2010 to 194.27.225.72. Redistribution subject to ASME license or copyright; see http://www.asme.org/terms/Terms_Use.cfm

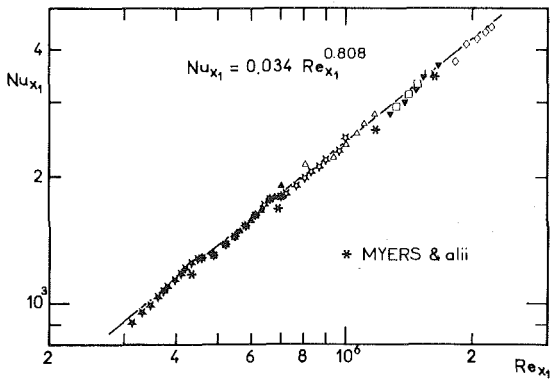

Fig. 7 Mean representation of local Nusselt number versus local Reynolds number. Cross plot as in Fig. 6. Comparison with the mean results of Myers, et al. [3] (constant temperature plate)

correlation proposed by Myers, et al. [3] for a constant temperature plate. We observe that the average value of St/C_f remains expressible by an empirical relation like the Colburn equation which Reynolds, et al. [12] modified (in the range $0.6 < Pr < 1$) to read: $St/C_f = 1/2.Pr^{-0.4}$. For $Pr = 0.7$, this expression gives $St/C_f = 0.577$ for an isothermal plate.

Acknowledgments

The author expresses his gratitude to Dr. B. T. Chao for his valuable assistance in the preparation of the manuscript.

References

1 Seban, R. A., "Heat Transfer and Effectiveness for a Turbulent Boundary Layer with Tangential Fluid Injection," ASME JOURNAL OF HEAT TRANSFER, Nov. 1960, pp. 303–312.

2 Seban, R. A., Back, L. H., "Velocity and Temperature Profiles in a Wall Jet," *International Journal of Heat and Mass Transfer*, Vol. 2, 1961, pp. 255–265.

3 Myers, G. E., Schauer, J. J., Eustis, R. H., "Heat Transfer to Plane Turbulent Wall Jets," ASME JOURNAL OF HEAT TRANSFER, Aug. 1963, pp. 209–214.

4 Myers, G. E., Schauer, J. J., Eustis, R. H., "Plane Turbulent Wall Jet Flow Development and Friction Factor," ASME *Journal of Basic Engineering*, March 1963, p. 47–54.

5 Mabuchi, I., Kumada, M., "Studies on Heat Transfer to Turbulent Jets with Adjacent Boundaries." (1st report) *Bulletin of the JSME*, Vol. 15, No. 88, 1972, pp. 1236–1245.

6 Blackwell, B. F., Moffat, R. J., "Design and Construction of a Low-Velocity Boundary-Layer Temperature Probe," ASME JOURNAL OF HEAT TRANSFER, Vol. 97, May 1975, pp. 313–315.

7 Nizou, P.Y., "Contribution à l'Étude de la Convection Forcée Turbulente dans le Cas d'un Jet Pariétal Plan," Thèse de Doctorat d'Etat, University of Nantes, 1978.

8 Irwin, H. P. A. H., "Measurements in a Self-Preserving Wall Jet in a Positive Pressure Gradient," *Journal of Fluid Mechanics* Vol. 61, 1973, pp. 33–63.

9 Tailland, A., "Contribution à l'Étude d'un Jet Plan Dirigé Tangentiellement à une Paroi Plane," Thèse de Doctorat d'Etat, University of Lyon, 1970.

10 Kader, B. A., Yaglom, A. M., "Heat and Mass Transfer Laws for Fully Turbulent Wall Flows," *International Journal of Heat and Mass Transfer*, Vol. 15, 1972, pp. 2329–2351.

11 Mathieu, J., "Contribution à l'Étude Aérothermique d'un Jet Plan Évoluant en Présence d'une Paroi," *Publications Scientifiques et Techniques du Ministére de l'Air*, No. 374, 1962.

12 Reynolds, W. C., Kays, W. M., Kline, S. J., "Heat Transfer in the Turbulent Boundary Layer," NASA Memorandum 12-1-58 W, 12-2-58 W, 12-3-58 W, 1958.

Downloaded 20 Dec 2010 to 194.27.225.72. Redistribution subject to ASME license or copyright; see http://www.asme.org/terms/Terms_Use.cfm

G. Bergeles
Department of Mechanical Engineering,
National Technical University,
Athens, Greece

A. D. Gosman
Department of Mechanical Engineering,
Imperial College,
London SW7 2BX, England

B. E. Launder
Department of Mechanical Engineering,
University of Manchester,
Manchester M60 1QD, England

The Prediction of Three-Dimensional Discrete-Hole Cooling Processes

Part 2: Turbulent Flow

Computer simulations are described of the injection of a secondary coolant fluid through a row of downstream-facing holes arranged across a surface exposed to a hot parallel gas stream, as occurs in certain discrete-hole cooling systems for turbine blades. The simulation is performed by solving the governing equations numerically, with the effects of turbulence modelled in a way which allows for the anisotropies existing in the real situation. Comparisons with measurements obtained for injection angles of 30 deg and dimensionless blowing rates in the range 0.2 to 0.5 show good agreement in the majority of cases. Discrepancies are however observed at conditions of small upstream boundary layer thickness or large injection rates and the causes of these are identified and discussed.

1 Introduction

In an earlier paper [1] the authors described the development and application of a numerical procedure for calculating the three-dimensional flow and thermal fields arising from coolant injection from a single transverse row of downstream-angled discrete holes into a hot laminar boundary layer, the ultimate aim being to predict discrete-hole cooling of turbine blades as illustrated in Fig. 1. Subsequently, the procedure was extended to encompass turbulent flow through inclusion of a turbulence model which allowed for the anisotropies of transport coefficients exhibited by the real flow; and comparisons were made with experimental data for single-hole [2] and double-row [3] arrangements, with encouraging results. The present paper is concerned with comparisons for the single-row arrangement in turbulent flow and also reports new measurements for this obtained as part of the study.

Previous work in this area has been confined to experiments, a summary of which will be provided later.

2 Description of Calculation Method

Inasmuch as the methodology has already been presented in [1–3] and is extensively described in [4], only an outline will be provided here.

Governing Equations. With reference to Fig. 1, the assumed stationary three-dimensional turbulent flow is governed by the following differential conservation equations for momentum, continuity and energy (or tracer species concentration):

$$\frac{\partial \rho U}{\partial x} + \frac{\partial \rho V}{\partial y} + \frac{\partial \rho W}{\partial z} = 0 \tag{1}$$

$$\rho U \frac{\partial U}{\partial x} + \rho V \frac{\partial U}{\partial y} + \rho W \frac{\partial U}{\partial z} = -\frac{\partial p}{\partial x} + \frac{\partial \tau_{xy}}{\partial y} + \frac{\partial \tau_{zx}}{\partial z} \tag{2}$$

$$\rho U \frac{\partial V}{\partial x} + \rho V \frac{\partial V}{\partial y} + \rho W \frac{\partial V}{\partial z} = -\frac{\partial p}{\partial y} + \frac{\partial \tau_{yy}}{\partial y} + \frac{\partial \tau_{zy}}{\partial z} \tag{3}$$

$$\rho U \frac{\partial W}{\partial x} + \rho V \frac{\partial W}{\partial y} + \rho W \frac{\partial W}{\partial z} = -\frac{\partial p}{\partial z} + \frac{\tau_{yz}}{\partial y} + \frac{\partial \tau_{zz}}{\partial z} \tag{4}$$

$$\rho U \frac{\partial \phi}{\partial x} + \rho V \frac{\partial \phi}{\partial y} + \rho W \frac{\partial \phi}{\partial z} = \frac{\partial J_{\phi,y}}{\partial y} + \frac{\partial J_{\phi,z}}{\partial z} \tag{5}$$

where x, y and z denote the streamwise, vertical and lateral directions, respectively, ϕ stands for either specific enthalpy or the mass fraction of an inert tracer gas (employed in some experimental studies) and $J_{\phi,y}$ and $J_{\phi,z}$ denote the corresponding diffusional fluxes. The remaining, conventional, symbols are defined in the Nomenclature.

Omitted from the above equations are the x-wise gradients in the stresses and diffusion fluxes, and it is also assumed the U is positive everywhere: these form part of the standard boundary layer approximations (the only part involved here) and allow important economies to be made in the numerical solution procedure, as will shortly be outlined. The validity of the assumptions will be discussed later.

The total stress and flux components are obtained from the following anisotropic relations, deduced in [4] from the general turbulence transport models of Launder, et al. [5, 6]:

$$\tau_{xy} = (\mu + \mu_t)\frac{\partial U}{\partial y} \tag{6}$$

$$\tau_{zx} = (\mu + f\mu_t)\frac{\partial U}{\partial z} \tag{7}$$

$$\tau_{yy} = 2(\mu + \mu_t)\frac{\partial V}{\partial y} \tag{8}$$

$$\tau_{zy} = \tau_{yz} = (\mu + \mu_t)\frac{\partial W}{\partial y} + (\mu + f\mu_t)\frac{\partial V}{\partial z} \tag{9}$$

$$\tau_{zz} = 2(\mu + \mu_t)\frac{\partial W}{\partial z} \tag{10}$$

$$J_{\phi,y} = (\Gamma + \Gamma_t)\frac{\partial \phi}{\partial y} \tag{11}$$

$$J_{\phi,z} = (\Gamma + f\Gamma_t)\frac{\partial \phi}{\partial z} \tag{12}$$

where the turbulent viscosity μ_t and diffusivity Γ_t are obtained from

$$\mu_t = 0.09\,\rho k^2/\epsilon \tag{13}$$

$$\Gamma_t = \mu_t/0.9 \tag{14}$$

where k is the turbulence energy and ϵ its dissipation rate, both of which are calculated from their own transport equations:

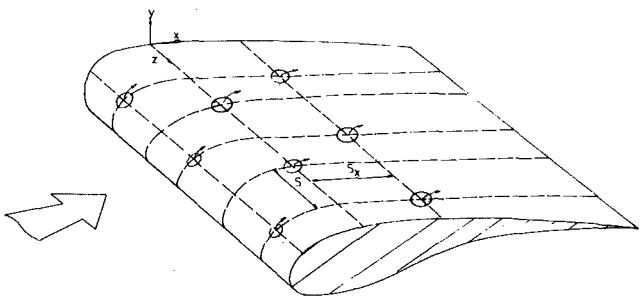

Fig. 1 *Illustration of a discrete-hole cooling arrangement for a turbine blade*

Contributed by the Heat Transfer Division for publication in the JOURNAL OF HEAT TRANSFER. Manuscript received by the Heat Transfer Division, June 2, 1980.

Copyright © 1981 by ASME

Downloaded 20 Dec 2010 to 194.27.225.72. Redistribution subject to ASME license or copyright; see http://www.asme.org/terms/Terms_Use.cfm

$$\rho U\frac{\partial k}{\partial x}+\rho V\frac{\partial k}{\partial y}+\rho W\frac{\partial k}{\partial z}=\frac{\partial}{\partial y}\left[(\mu+\mu_t)\frac{\partial k}{\partial y}\right]+\frac{\partial}{\partial z}\left[(\mu+f\mu_t)\frac{\partial k}{\partial z}\right]+P-\epsilon \quad (15)$$

$$\rho U\frac{\partial \epsilon}{\partial x}+\rho V\frac{\partial \epsilon}{\partial y}+\rho W\frac{\partial \epsilon}{\partial z}=\frac{\partial}{\partial y}\left[\frac{(\mu+\mu_t)}{1.3}\frac{\partial \epsilon}{\partial y}\right]+\frac{\partial}{\partial z}\left[\frac{(\mu+f\mu_t)}{1.3}\frac{\partial \epsilon}{\partial z}\right]+1.44\frac{P\epsilon}{k}-1.9\frac{\epsilon^2}{k} \quad (16)$$

$$P=\mu_t\left[\left(\frac{\partial U}{\partial y}\right)^2+2\left(\frac{\partial V}{\partial y}\right)^2+\left(\frac{\partial W}{\partial y}\right)^2\right]+f\mu_t\left[\left(\frac{\partial U}{\partial z}\right)^2+\left(\frac{\partial V}{\partial z}\right)^2+2\left(\frac{\partial W}{\partial z}\right)^2\right]$$

The quantity f is an anisotropy coefficient for the lateral direction and is intended as an approximation to the variation of w^2/v^2 across the boundary layer, as explained in (2): it is taken as

$$\begin{aligned} f &= 3.5-2.5y/\Delta \qquad y\le\Delta \\ f &= 1 \qquad\qquad\quad y>\Delta \end{aligned} \quad (17)$$

where Δ is the height at which U reaches 0.9 of the free-stream velocity.

Solution Procedure. The foregoing equations are solved by an adaptation of a finite-difference procedure developed by Pratap and Spalding [7] coupled, in some instances, with a similar procedure by Patankar and Spalding [8]. Details of the adaptation are given in [2, 4] and are summarized below.

A computational grid is superimposed on a symmetry element of the flow bounded by the longitudinal planes bisecting a hole and the gap to its neighbor as illustrated in Fig 2. The grid extends upstream some 1.5D where trial and error calculations show the oncoming flow to be undisturbed by injection: the profiles of the dependent variables there are either taken from measurements where available, or are estimated from two-dimensional boundary layer theory.

The vertical extent of the grid is adjusted locally so as to just encompass the region of disturbed flow: the conditions imposed there are therefore those of the free stream. At the adiabatic/impermeable parts of the solid surface, the inner solution is matched to a generalized law of the wall, with corresponding specifications on k and ϵ, while $\partial\phi/\partial y$ is set to zero. Over the injection hole, the inlet velocity components are set on the assumption that the flow enters at a uniform velocity V_j and angle α, and the k and ϵ distributions are set at those of a fully developed pipe flow.

Finite-difference equivalents of equations (2–5, 15) and (16) are derived which connect values of the dependent variables at the neighboring nodes in the lateral and upstream, but not downstream, directions: the latter feature, which is a consequence of the simplifications to the differential equations mentioned earlier, allows the equations to be solved for a given pressure field by a downstream-marching procedure, which moreover requires only two-dimensional storage of the variable fields.

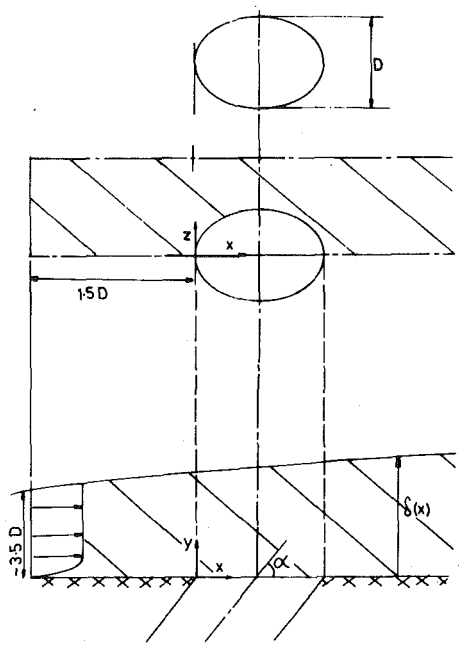

Fig. 2 The domain of solution (shown shaded) for the partially-parabolic calculations

The pressure field is obtained in one of two ways, depending on the region of flow considered. In those parts where strong three-dimensional pressure disturbances are provoked by injection, a set of continuity-based finite-difference equations is solved for the pressure field. In contrast to the equations described above, these contain linkages to neighboring nodes in all directions, require three-dimensional storage and are solved iteratively. After each pressure iteration the velocities and other variables are adjusted via the marching procedure to bring them into balance. During this "semi-elliptic" calculation process due to Pratap and Spalding [7] the pressure at the outlet plane of the grid is estimated by linear extrapolation from the interior; and the negative velocities which are generated immediately downstream of the hole (which are physically realistic but invalidate the key assumptions made at the outset) are suppressed. The latter practice is essential to the working of the method but does introduce some error, as discussed later.

Beyond about 5 hole diameters downstream of injection, the streamwise pressure gradient dp/dx becomes uniform and equal to the free-stream value, thereby allowing application of the noniterative marching "parabolic" procedure of Patanker and Spalding [8] which is similar to the above, but solves only for pressure variations in the cross-stream plane.

Typically the grid employed for each semi-elliptic calculation contains about 400 nodes in each cross-stream plane and some 50 such planes. Around 70 iterations are required for convergence and the

Nomenclature

D = diameter of injection hole
f = anisotropy factor
$J_{\phi,y}, J_{\phi,z}$ = diffusive fluxes of ϕ in y, z directions
k = local mean turbulence energy
M = dimensionless injection rate $\rho_j V_j/\rho_\infty U_\infty$
p = static pressure
P = turbulence energy production rate
Re_D = Reynolds number in coolant passage $\rho V_j D/\mu$
S = spacing between holes
U = local mean velocity in x direction
V = local mean velocity in y direction
V_j = mean injection velocity
$\overline{u^2}$ = mean square velocity fluctuation about V
W = local mean velocity in z direction
$\overline{w^2}$ = mean square velocity fluctuation about W
x = streamwise coordinate measured from leading edge of hole
y = normal coordinate to surface
z = lateral coordinate measured from longitudinal bisector of hole
α = injection angle
Γ,Γ_t = molecular, turbulent diffusion coefficients pertaining to y direction
δ_1 = displacement thickness
ϵ = local mean turbulence energy dissipation rate
η = dimensionless temperature/concentration $(\phi-\phi_\infty)/(\phi_j-\phi_\infty)$, also effectiveness when pertaining to wall
$\bar{\eta}$ = laterally-averaged effectiveness $\int_0^s \eta dx/s$
μ,μ_t = molecular, turbulent viscosity
ρ = density
$\tau_{\ell m}$ = total stress acting in m direction on surface with normal in l direction
ϕ = specific enthalpy or tracer gas concentration

Subscripts

j = jet conditions
w = pertaining to wall
∞ = free-stream conditions

Downloaded 20 Dec 2010 to 194.27.225.72. Redistribution subject to ASME license or copyright; see http://www.asme.org/terms/Terms_Use.cfm

Table 1 Summary of conditions of the single-row test cases

Source	α	M	S/D	δ_1/D	Re_D	ρ_J/ρ_∞
Bergeles [4]	30 deg	0.25	2.667	0.095	3.3×10^4	1.0
Bergeles	30 deg	0.5	2.667	0.095	3.3×10^4	1.0
Eriksen [9]	35 deg	0.2	3.0	0.149	4.4×10^4	0.85
Eriksen	35 deg	0.5	3.0	0.149	4.4×10^4	0.85
Pedersen [10]	35 deg	0.5	3.0	0.156	1.9×10^4	2.0

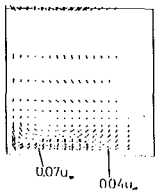

Fig. 3(*a*) Cross-stream velocity

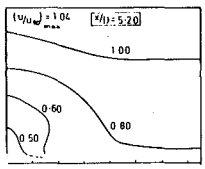

Fig. 3(*b*) Axial velocity

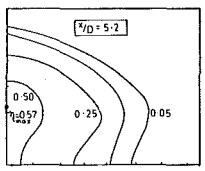

Fig. 3(*c*) Dimensionless temperature

Fig. 3 Predicted distributions in the cross-stream plane at $x/D = 5.2$ for conditions corresponding to Eriksen's [9] $M = 0.5$ experiment

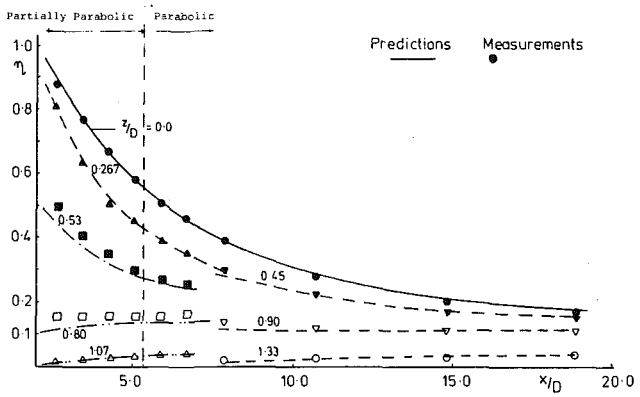

Fig. 4 Comparison of present predictions with local effectiveness data of Bergeles [4] for $M = 0.25$

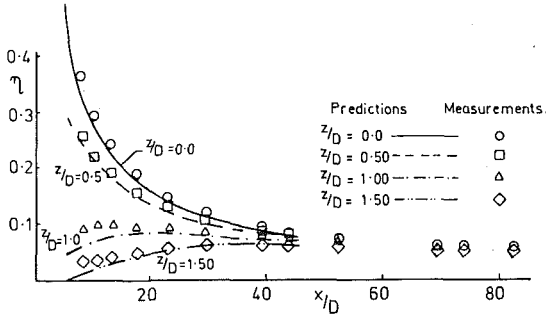

Fig. 5 Comparison with local effectiveness data of Eriksen [9] for $M = 0.2$

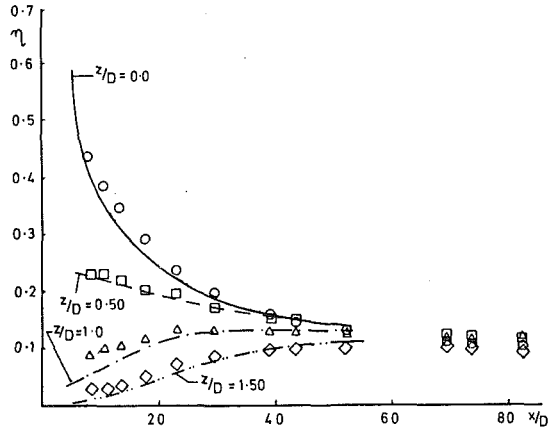

Fig. 6 Comparison with local effectiveness data of Eriksen [9] for $M = 0.5$

associated computing time on an IBM 360/195 machine is about 20 min.

3 Applications

Cases Studied. The cooling effectiveness data selected for assessment of the single-row predictions were obtained by Bergeles [4], Eriksen [9] and Pedersen [10], with those of the former being presented here for the first time. Eriksen measured effectiveness by heating the jet air supply and mapping the surface temperature distribution, while the other two investigators determined the surface concentration of a foreign gas introduced into the jet supply. Table 1 summarizes the experimental conditions in terms of α, M, S/D, δ_1/D, Re_D and ρ_J/ρ_∞, where α and $M(\equiv \rho_J V_J/\rho_\infty U_\infty)$ are the angle and dimensionless rate of injection, respectively.

Predicted Flow Structure. Figures 3(*a*) to (*c*) show a small extract of the detailed three-dimensional field predictions contained in [4], in this case corresponding to the conditions of Eriksen's $M = 0.5$ experiments, although representative of other cases. The plots relate to a cross-stream plane 5.2D downstream of the hole centerline and were specifically chosen to reveal an important feature, namely the vortex structure induced by the injection process and the effects which it has on the distributions of streamwise velocity and (dimensionless) temperature: particularly noteworthy is the transport of "hot" mainstream fluid towards the surface and under the coolant jet, thus limiting its rate of lateral spread and causing the temperature maximum to lift off the surface. This behavior is detrimental to the performance of single-row arrangements, but turns out to have a beneficial effect in multiple-row ones, as is explained in [3].

Comparisons with Effectiveness Data. In the following paragraphs comparisons are described between the predictions and measurements of surface effectiveness, which is equivalent, in the present context, to the level of dimensionless temperature at the surface. The comparisons are grouped according to the injection rate, M.

(a) $M \leq 0.25$. The predicted streamwise variations of the effectiveness η at various lateral locations for Bergeles' [4] experiments at $M = 0.25$ are shown in Fig. 4, along with the data. In the near-field region ($x/D < 5.5$), where the semi-elliptic method was employed, the agreement is good near the center and symmetry planes, but discrepancies of up to about 10 percent are observed at $z/D = 0.53$ and 0.80. Further downstream, where the parabolic method was used, the agreement is good everywhere.

Similar comparisons are made with Eriksen's [9] measurements for $M = 0.2$ in Fig. 5, although in this instance no near-field surveys were made. Reasonable agreement is obtained along $z/D = 0.0$ and 0.5, and at all positions beyond $x/D \sim 25$, the maximum error being about 5 percent. Agreement is less satisfactory for $x/D < 25$ and $z/D \leq 1.0$, where η is underpredicted by up to 20 percent. However, the heat-transfer technique employed for these experiments is known to be subject to significant errors in regions of steep surface temperature gradients such as this, due to conduction within the test plate: al-

Downloaded 20 Dec 2010 to 194.27.225.72. Redistribution subject to ASME license or copyright; see http://www.asme.org/terms/Terms_Use.cfm

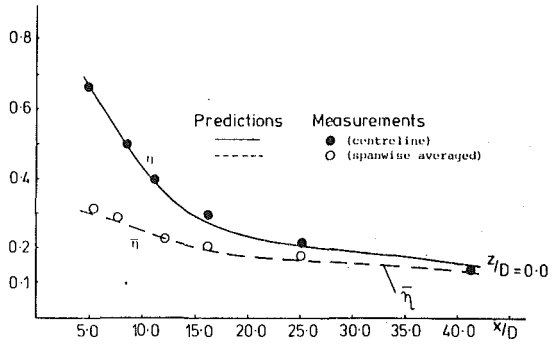

Fig. 7(*a*) Streamwise variation of centerline and spanwise-averaged effectiveness

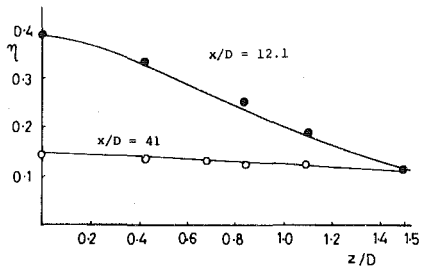

Fig. 7(*b*) Lateral variation of effectiveness at two streamwise locations

Fig. 7 Comparison with data of Pederson [10] for $M = 0.5$

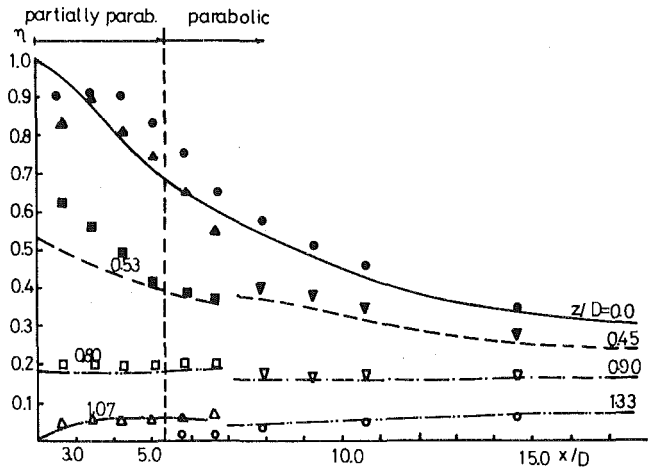

Fig. 8 Comparison of present predictions with local effectiveness data of Bergeles [4] for $M = 0.5$

though corrections may be made, the fact that η is also small in the region compounds the error. It is best therefore in this instance to regard the cause of the discrepancies as being indeterminate.

(b) $M = 0.5$. Eriksen's data for this blowing rate are displayed along with the predictions in Fig. 6. The general picture is much the same as for his $M = 0.20$ data and presumably the same comments apply, although the initial behavior along $z/D = 0.0$ is less well predicted.

The tracer-gas technique employed by Pedersen [10] precludes conduction errors and it is therefore of particular interest to note that, in the comparisons with his $M = 0.5$ data displayed in Fig. 7, the lateral variation shown in graph (b) of η is well predicted, in contrast to the behavior noted above. (The conditions are not, of course identical: in particular there is a more than two-fold difference in density ratio.) The adequacy of the predictions at other locations is evidenced by the good agreement obtained for the spanwise-averaged effectiveness $\bar{\eta}$ in graph (a).

Bergeles [4] also employed the tracer-gas technique, but as Fig. 8 reveals, although the agreement obtained in the far-field region is almost as good as that for the Pedersen case, the discrepancies in the near field (for which only Bergeles provides data) are large, particularly just downstream of the hole. Furthermore, even this level of near-field agreement was procured only by adjusting the injectant velocity distribution in the calculations [4] such that the flow exited from the downstream half of the hole. The explanation for the sensitivity to the jet entry profile, which was not evidenced in the other cases, appears to lie in the fact that the boundary layer in Bergeles' experiments was much thinner than in the other cases (see Table 1) and therefore significantly altered the initial secondary flow profile from the assumed uniform distribution. Certainly there is experimental evidence that this effect does occur [1, 12] and tends to bias the flow distribution in the downstream direction. Although the sensitivity to the initial jet profile is found to diminish with downstream distance from the hole, the accurate prediction of the near field may nonetheless be important due to the possibility of large thermal stresses arising from the steep surface temperature gradients there.

4 Concluding Remarks

From the overall performance of the procedure it can be concluded that it predicts rather satisfactorily the existing far-field data and therefore, if used with due caution, should be helpful in diagnosing shortcomings in existing cooling configurations and in evolving better ones.

The study has shown however that as the boundary-layer thickness is decreased the assumptions of symmetrical jet exit conditions become increasingly untenable and this gives rise to significant errors in the predictions of the effectiveness distribution in the near field. It would appear that if these interaction effects are to be satisfactorily accounted for, it may be necessary to explore alternative approaches, including extending the domain of computation into the holes themselves. This is a conceptually simple matter, but time was not available in the present study to make the necessary changes to the computer code.

A further shortcoming of the prediction method not revealed by the present comparisons, but evident in our single-hole injection studies published elsewhere [2], is a progressive deterioration in accuracy as M is increased beyond about 0.5. The errors are believed to stem in part from the local equilibrium assumptions inherent in the turbulence modelling and also from the inability of the semi-elliptic procedure to properly simulate the zone of recirculation downstream of the hole, even with our patching modification incorporated. It is likely that the turbulence-modelling errors can be reduced by relaxing the quasi-equilibrium assumptions, although care should be taken to do this in a progressive fashion until the right compromise is struck between complexity (and hence cost) and accuracy. The semi-elliptic solution procedure is also capable of improvement, by incorporating modifications to allow a local, fully elliptic calculation of the recirculation bubbles.

Acknowledgments

We gratefully acknowledge the support of this work by the Ministry of Defense Procurement Executive and by Rolls Royce (1971) Ltd.

References

1 Bergeles, G., Gosman, A. D. and Launder, B. E., "The Prediction of Three Dimensional Discrete-Hole Cooling Processes: Part 1: Laminar Flow," ASME JOURNAL OF HEAT TRANSFER, Vol. 98, No. 3, p. 379.

2 Bergeles, G., Gosman, A. D. and Launder, B. E., "The Turbulent Jet in a Cross Stream at Low Injection Rates: a Three-Dimensional Numerical Treatment," *Numerical Heat Transfer*, Vol. 1, 1978, pp. 217–242.

3 Bergeles G., Gosman A. D. and Launder B. E., "Double-Row Discrete-Hole Cooling: An Experimental and Numerical Study" ASME *Journal of Engineering for Power*, 1979, pp. 1–6.

4 Bergeles, G., "Three-Dimensional Discrete-Hole Cooling Processes: An Experimental and Theoretical Study," Ph.D. Thesis, University of London, 1976.

5 Launder, B. E., Reece, G. and Rodi, W., "Progress in the Development of a Reynolds Stress Turbulence Closure," *Journal of Fluid Mechanics*, Vol. 68, 1975, pp. 537–566.

6 Launder, B. E., "On the Effects of a Gravitational Field on the Turbulent Transport of Heat and Momentum," *Journal of Fluid Mechanics*, Vol. 67, 1975, p. 569.

7 Pratap, S. V., and Spalding, D. B., "A Calculation Procedure for Par-

Downloaded 20 Dec 2010 to 194.27.225.72. Redistribution subject to ASME license or copyright; see http://www.asme.org/terms/Terms_Use.cfm

tially-Parabolic Flow Situations," HTS/74/35, Imperial College, Mech. Eng. Dept., Dec. 1974.

8 Patankar, S. V., and Spalding, D. B., "A Calculation Procedure for Heat Mass and Momentum Transfer in Three-Dimensional Parabolic Flows," *International Journal of Heat Mass Transfer*, Vol. 15, (10), 1972, p. 1787.

9 Eriksen, V. L., "Film Cooling Effectiveness and Heat Transfer With Injection Through Holes," NASA CR-72991, 1971.

10 Pedersen, D., "Effect of Density Ratio on Film Cooling Effectiveness for Injection Through a Row of Holes and for a Porous Slot," University of Minnesota, Ph.D. Thesis, 1972.

11 Bergeles, G., Gosman A. D. and Launder, B. E., "The Near-Field Character of a Jet Discharged Normal to a Main Stream," ASME JOURNAL OF HEAT TRANSFER, Vol. 98, Aug. 1976, p. 373.

12 Simitovic, R., "Turbulent Flow in a Rectangular Duct with an Obliquely-Introduced Secondary Jet," Ph.D. Thesis, University of London, 1977.

Downloaded 20 Dec 2010 to 194.27.225.72. Redistribution subject to ASME license or copyright; see http://www.asme.org/terms/Terms_Use.cfm

A Study of Some Turbulence Models for Flow and Heat Transfer in Ducts of Annular Cross-Section

Mujeeb R. Malik
Systems and Applied Sciences Corportion,
17 Research Drive,
Hampton, VA
Assoc. Mem. ASME

R. H. Pletcher
Department of Mechanical Engineering and
Engineering Research Institute,
Iowa State University,
Ames, Iowa
Mem. ASME

A variable property finite-difference calculation procedure is used to predict turbulent flow and heat transfer parameters in annular passages. Predictions from several turbulence models are compared with measurements over a range of flow and thermal conditions. Of the models considered, one utilizing transport equations for turbulence kinetic energy and characteristic mixing length scale gave the best overall performance. The inclusion of turbulence kinetic energy in the turbulence modeling was found not to be crucial for predicting isothermal flows or for predicting all parameters except the temperature distribution for flows with heat transfer at Reynold numbers greater than 110,000.

Introduction

Annular flow geometries continue to be important in many engineering applications. These include propulsion systems, heat exchangers, and fuel assemblies in nuclear reactors. Many of these devices operate under conditions in which property variations are expected to influence greatly the velocity and temperature distributions. Although steady progress has been made in recent years in the prediction of turbulent flows, there are at present few, if any, prediction methods which have been tested extensively by comparison with experimental data for annular flows under variable property conditions. This may be due partly to the difficulties associated with accurately modeling the turbulent transport in flows where thermal boundary conditions can force velocity and temperature distributions to be quite dissimilar.

Previous studies for the annular geometry include the constant property analyses of Kays and Leung [1], Ying [2], Lee [3], Quarmby and Anand [4], and Wilson and Medwill[5]. More recently, Heikel, et al. [6] utilized a Crank-Nicolson finite-difference procedure and the k-ϵ turbulence model to predict flow and heat transfer parameters for the annular geometry under constant property assumptions. Other recent analyses utilizing finite-difference methods for annular flows without heat transfer include those of Hanjalic [7] and Sharma, et al. [8]. A more detailed review of research in this problem area can be found in [9].

The present study was initiated in response to the need which is believed to exist for further development and evaluation of prediction schemes for the annular geometry, particularly for flows in which property variations may be significant. The objectives were to develop a finite-difference procedure which could readily handle the variety of possible hydrodynamic and thermal boundary conditions which occur in annular flows with heat transfer, and to identify the simplest turbulence models which would give satisfactory agreement with measurements over a range of flow and thermal conditions. An earlier paper [10] presented a few preliminary comparisons with experimental data utilizing an L-equation turbulence model which employs a transport equation in ordinary differential form for a length scale. Although velocity profiles and Stanton numbers were in reasonable agreement with measurements, a need for improvement in the predicted temperature profiles was noted. In the present paper, predictions from several turbulence models are compared with experimental data. Particular attention is given to the way in which turbulence modeling details influence the predicted temperature distribution and to the performance of the predictions under variable property conditions. Details of the numerical procedures used are reported separately in [9] and [11].

Contributed by the Heat-Transfer Division for publication in the JOURNAL OF HEAT TRANSFER. Manuscript received by the Heat Transfer Division October 29, 1979.

Analysis

Governing Equations. With boundary layer (thin-shear layer) assumptions, the governing equations for an axisymmetric, steady turbulent flow can be written as

Continuity:

$$\frac{\partial}{\partial x}(\rho u) + \frac{1}{r}\frac{\partial}{\partial y}(r\rho\tilde{v}) = 0 \tag{1}$$

Momentum:

$$\rho u\frac{\partial u}{\partial x} + \rho\tilde{v}\frac{\partial u}{\partial y} = \frac{1}{r}\frac{\partial}{\partial y}\left[r\left(\mu\frac{\partial u}{\partial y} - \rho\overline{u'v'}\right)\right] - \frac{dp}{dx} \tag{2}$$

Energy:

$$\rho C_p u\frac{\partial T}{\partial x} + \rho C_p\tilde{v}\frac{\partial T}{\partial y} = \frac{1}{r}\frac{\partial}{\partial y}\left[r\left(\lambda\frac{\partial T}{\partial y} - \rho C_p\overline{v'T'}\right)\right] + \left(\mu\frac{\partial u}{\partial y} - \rho\overline{u'v'}\right)\frac{\partial u}{\partial y} - \beta Tu\frac{dp}{dx} \tag{3}$$

Conventional no-slip boundary conditions apply for the velocities, while either the temperatures or heat flux may be specified at the walls. In the above, $\tilde{v} = (\rho v + \overline{\rho' v'})/\rho$. The terms $-\rho\overline{u'v'}$ and $-\rho C_p\overline{v'T'}$ appearing in equations (2) and (3) represent the apparent turbulent shear stress and turbulent heat flux, respectively, and must be modeled using empirical information.

Turbulence Modeling. The simplest and currently most common modeling approach follows a concept originally advanced by Boussinesq in 1877—that the turbulent shearing stress can be related to the rate of mean strain as

$$-\rho\overline{u'v'} = \mu_T\frac{\partial u}{\partial y} \tag{4}$$

where μ_T is an apparent turbulent (or, eddy) viscosity yet to be defined. The implied assumption in equation (4) is that the stress-strain law for time-averaged turbulent flows is of the same form as that for a Newtonian fluid in laminar motion. The term $-\rho C_p\overline{v'T'}$ represents an additional transport of heat which is caused by the turbulent motion and can be modeled by assuming that this transport is of diffusive type, so that the form of Fourier's law applies, i.e.,

$$-\rho C_p\overline{v'T'} = \lambda_T\frac{\partial T}{\partial y} \tag{5}$$

where λ_T is an apparent turbulent (or, eddy) conductivity which can be related to turbulent viscosity μ_T by defining a turbulent Prandtl number such as

$$\mathrm{Pr}_T = \frac{\mu_T C_p}{\lambda_T} \tag{6}$$

In general, the turbulent Prandtl number may vary throughout the flow, although quite accurate results usually can be obtained by using

Copyright © 1981 by ASME
Downloaded 20 Dec 2010 to 194.27.225.72. Redistribution subject to ASME license or copyright; see http://www.asme.org/terms/Terms_Use.cfm

a constant value of Pr_T. A constant value of $Pr_T = 0.9$ was used for all predictions of this paper. All turbulence models to be evaluated in the present paper follow the general forms indicated by equations (4–6).

Length-Scale Transport Equation (Model A). A turbulence model utilizing a one-dimensional transport equation for the characteristic mixing length scale in the central part of the flow was proposed in [10]. The model is based on the mixing length hypothesis whereby

$$\mu_T = \rho \ell^2 \left|\frac{\partial u}{\partial y}\right| \tag{7}$$

For the regions closest to the walls, ℓ is taken as

$$\ell_i = \kappa y_w [1 - \exp(-y_w^+/A^+)] \tag{8}$$

Here κ is the von Kármán constant taken as 0.41 and A^+ is a damping constant evaluated as 26 in the present study unless otherwise indicated. Away from the walls (in the outer region), the mixing length was evaluated as

$$\ell_o = C_1 L \tag{9}$$

where L was determined from the solution to the transport equation,

$$u_m \frac{dL}{dx} = C_2 |u| \left[\left(\frac{L}{\delta}\right) - \left(\frac{L}{\delta}\right)^2\right] \tag{10}$$

The switch from ℓ_i to ℓ_o in equation (7) is made at the distance from the walls where ℓ_i first becomes equal to ℓ_o.

In some thin shear flows near equilibrium, L is proportional to δ ($d\delta/dx \simeq dL/dx$) and equation (9) can be evaluated as $\ell_o = 0.089\delta$. Equation (10) then becomes unnecessary. This is not true in general, however, since L can be expected to depend more on the large eddy structure and its characteristic relaxation time than merely on the width of the shear layer. Equation (10) can be developed as a one-dimensional specialization of a more general transport equation for length scale (see [9]), such as the one proposed by Bradshaw [12]. The constants C_1 and C_2 were evaluated as 0.12 and 1.09, respectively, by referring to experimental measurements.

The mixing length given by equation (9) will eventually become discontinuous at the radius of maximum velocity after the boundary layers growing on the walls have merged as they tend towards the fully developed state. To overcome this, an average of the outer length scale predicted for the flow along each wall was used for the central core region after the shear layers had merged. As the flow becomes fully developed ($dL/dx = 0$) equation (10) gives $L = \delta$. Then from equation (9) and the fact that the values of L are averaged for the two walls, we have,

$$\bar{\ell}_o = C_1 \frac{(L_1 + L_2)}{2} = C_1 \frac{\delta_1 + \delta_2}{2} \tag{11a}$$

After the boundary layers have met, $\delta_1 + \delta_2 = r_2 - r_1$, that is, the two shear layers fill the annulus; so the mixing length in the outer region for fully developed flow will be given as

$$\bar{\ell}_o = C_1 (r_2 - r_1)/2 \tag{11b}$$

This same turbulence model (with adjustment for the use of different definitions of shear layer width) has been found to give better predictions of separating external flows than obtained from purely algebraic models [13]. Further details on Model A can be found in [10].

Bridging (Model B). It should be noted that after the boundary layers have merged, equation (7) will give zero turbulent viscosity at the radius of maximum velocity ($\partial u/\partial y = 0$). Equations (5) and (6) imply zero turbulent conductivity at that point, which is unrealistic when asymmetric thermal boundary conditions exist. Use of this model will likely lead to an inaccurate prediction of the temperature profile. This shortcoming, however, is not associated only with Model A; Bradshaw's shear layer interaction model (see [14]), for example, and many others will also predict zero turbulent heat transport at the radius of zero shear.

An improvement in the predicted temperature distribution has been noted for fully developed flow when the turbulent viscosity (thus, the turbulent conductivity) profile predicted by equation (7) is "bridged." (see Fig. 12) just by assuming a linear distribution between the peaks in μ_T which occur near each wall. Similar schemes for treating the eddy viscosity near the point of zero velocity gradient in the wall mixing zone of a wall jet have been suggested by Pai and Whitelaw [15] and by Dvorak [16]. In the latter study, a cosine fairing was used for the eddy viscosity. No studies of this type have been noted to date for annular flows.

***k-L* Model (Model C).** A more general remedy for the problem of predicting unrealistically small values of μ_T (thus, λ_T) in the central core can be provided by utilizing the Prandtl-Kolmogorov formulation,

$$\mu_T = C_\mu \rho k^{1/2} \ell \tag{12}$$

where k is the turbulence kinetic energy per unit mass. A modeled form of the transport equation for k is [17]:

Nomenclature

A = Nusselt number correlation constant
A^+ = van Driest damping constant
C = Nusselt number correlation constant
C_1, C_2, C_D, C_μ = empirical constants or functions
C_f = overall, skin-friction coefficient for annulus, $2[\tau_2 + r^*\tau_1]/[\rho u_b^2 (1 + r^*)]$
C_p = specific heat
D_h = hydraulic diameter, $2(r_2 - r_1)$
k = turbulence kinetic energy per unit mass
ℓ = mixing length
ℓ_i = mixing length in the wall regions
ℓ_o = mixing length in the outer regions of the shear layers
$\bar{\ell}_o$ = average of the outer region mixing lengths
L = turbulent length scale
Nu = Nusselt number, $\dot{q}_w D_h/(T_w - T_b)\lambda_b$
p = static pressure
Pr_k = Prandtl number for diffusion of k
Pr_T = Prandtl number for turbulent diffusion of heat
$\dot{q}$ = Heat flux
r = radial coordinate
r^* = radius ratio, r_1/r_2
Re = Reynolds number, $\rho U_b D_h/\mu$
St = Stanton number, $\dot{q}_w/\rho_b U_b C_p (T_2 - T_b)$
T = absolute temperature
u = axial velocity
u_τ = friction velocity, $\sqrt{\tau_w/\rho}$
v = radial velocity
x = coordinate along the annulus
y = coordinate normal to the inner wall, $r - r_1$
y_w = distance from the wall, $|r - r_w|$
y_w^+ = dimensionless distance from the wall, $y_w u_\tau/\nu$
β = coefficient of thermal expansion, $-\frac{1}{\rho}\frac{\partial \rho}{\partial T}\Big|_p$
δ = boundary layer thickness
ϵ = dissipation rate of turbulence kinetic energy
λ = thermal conductivity
λ_T = turbulent conductivity
μ = dynamic viscosity
μ_T = turbulent viscosity
ν = kinematic viscosity
ρ = density
τ = shear stress

Subscripts

b = bulk conditions
m = radius of maximum velocity
o = bulk value at the inlet

Superscripts

$\bar{(\ )}$ = time mean quantity
$(\ )'$ = fluctuation component of a quantity

Downloaded 20 Dec 2010 to 194.27.225.72. Redistribution subject to ASME license or copyright; see http://www.asme.org/terms/Terms_Use.cfm

$$\rho u \frac{\partial k}{\partial x} + \rho \tilde{v} \frac{\partial k}{\partial y} = \frac{1}{r} \frac{\partial}{\partial y} \left[r \left(\mu + \frac{\mu_T}{\mathrm{Pr}_k} \right) \frac{\partial k}{\partial y} \right] + \mu_T \left(\frac{\partial u}{\partial y} \right)^2 - C_D \rho k^{3/2} / \ell \quad (13)$$

Equation (13) is valid only where flow is fully turbulent. For that reason, the boundary condition for equation (13) is not specified at the walls where flow is largely influenced by laminar viscosity, but instead, is specified at some distance from the walls. The boundary conditions employed were

$$k(x, y_w^+) = -\rho \overline{u'v'}(x, y_w^+) / C_D^{2/3} \quad (14)$$

A value of $y_w^+ \approx 60$ has been used successfully. This inner boundary condition for k follows from a specialization of equation (13) under the usual assumptions that in the fully turbulent region near the wall, the generation and dissipation terms balance one another and Prandtl's mixing length formula (equation (7)) holds in that region. The length scale needed in equation (13) is provided as indicated for Model A. The present results were obtained using $C\mu = 0.548$, $C_D = 0.164$, and $\mathrm{Pr}_k = 1.47$.

Method of Solution. The governing equations were solved numerically by a finite-difference procedure using the turbulence modeling assumptions indicated above. The system of equations is parabolic, permitting the solution to be marched in the main flow direction. An explicit three-level scheme of the DuFort-Frankel type was employed. Between 70 and 100 cross-stream grid increments were used. No case reported here required more than three minutes of CPU time on an IBM 360/65 computer. Further details of the calculation method are described in [9] and [11].

Results

Hydrodynamic Results. It is reasonable to require that turbulence models appropriate for annular flows will give good predictions for a parallel wall (high-aspect ratio channel) duct. The parallel wall condition was simulated in the present computational scheme by utilizing $r^* = 0.99$. Figure 1 compares the predictions of Models A and B with the measurements of Dean [14] and Byrne, et al. [18] for the centerline velocity development in a high-aspect ratio rectangular duct. The proposed length scale model predicts the velocity overshoot in fair agreement with Dean's data. The overshoot in the velocity is a consequence of the interaction between the shear layers; this was also observed in the data of Barbin and Jones [19] for pipe flow. A sudden drop in the centerline velocity is observed when bridging (Model B) is used immediately upon merger of the two wall-boundary layers. It can be concluded, therefore, that linear bridging is not appropriate to predict details of hydrodynamically developing flow. It will be shown later that for fully developed flow, it is a good approximation. Predictions based on two simple mixing length models are also shown in Fig. 1. These simpler models do not provide satisfactory agreement with the data after the wall-boundary layers merge. The model of Pletcher and Nelson [20], in which a switch is made from $\ell_o = 0.089$ to the empirically based distribution proposed by Nikuradse (see [21]) for developed flow, gives a satisfactory fully developed value for u_m/u_b but does not predict correctly the details of the overshoot region.

Figure 2 shows predictions of velocity development at four different cross stream locations (including the centerline) in a parallel wall duct. The experimental data of Byrne, et al. [18] and predictions of the k-ϵ model as reported by Stephenson [22] are also given. The present predictions generally provide the best agreement with the experimental data. It can be concluded that nonmonotonic development of centerline velocity in a plane duct is well predicted by the proposed length scale transport model. Other parameters such as the momentum and displacement thicknesses also develop nonmonotonically in turbulent channel flow. These also have been found to be well predicted by Model A [9].

Good results have also been observed in predicting hydrodynamic flow development in a high-aspect ratio rectangular channel using a turbulence kinetic energy model (Model C). Figure 3 compares predictions from Model C with the velocity distribution measured

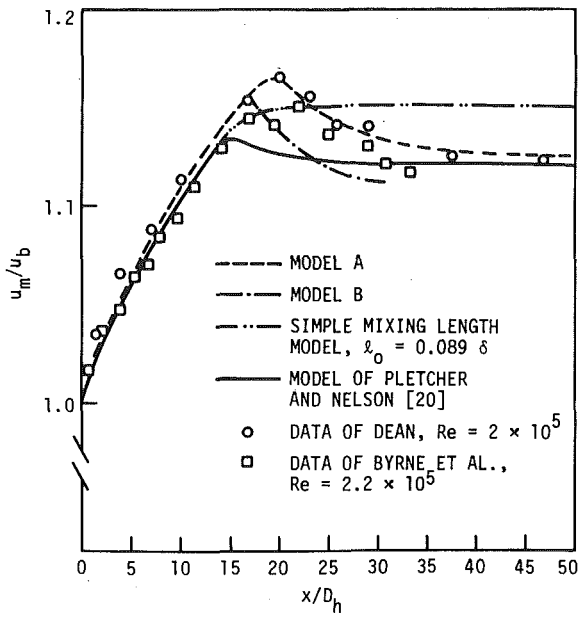

Fig. 1 Predicted development of maximum velocity in an annulus ($r^* = 0.99$, $\mathrm{Re} = 2 \times 10^5$) compared with measurements for a parallel wall duct

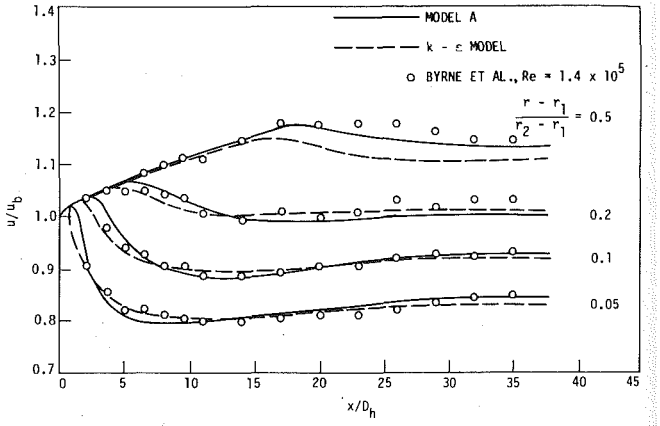

Fig. 2 Predicted velocity development compared with measurements in the entrance region of an annulus ($r^* = 0.99$)

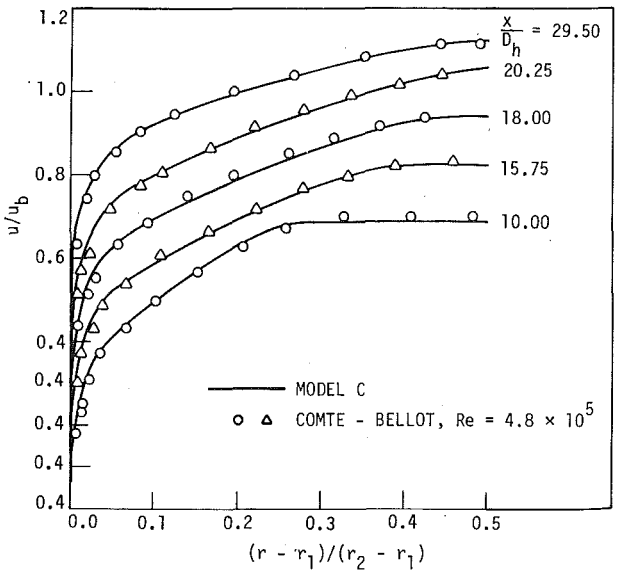

Fig. 3 Predicted velocity profiles in an annulus ($r^* = 0.99$) compared with the measurements of Comte-Bellot [23] obtained in a plane duct

Downloaded 20 Dec 2010 to 194.27.225.72. Redistribution subject to ASME license or copyright; see http://www.asme.org/terms/Terms_Use.cfm

by Comte-Bellot [23]. A free stream turbulence level of 0.02 percent was specified at the inlet in the predictions. The present predictions compare very well with the data. Calculations were also made using Model A, but these predictions (which are not shown) were too close to those of Model C to include on the figure. It can be concluded that for hydrodynamic development, at least, employing a turbulence kinetic energy equation has no real advantage, and that the length scale transport model predicts the flow development with sufficient accuracy. The turbulence kinetic energy profiles predicted by Model C were shown in [9] to be in good agreement also with the measurements in [23].

Figure 4 compares the velocity development predicted by Model A (again, Model C gave nearly identical results) with the measurements and k-ϵ model predictions reported by Heikal, et al. [6] for an annular passage with $r^* = 0.25$. Predictions of both models agree fairly well with the measurements, except very near the inlet. In Fig. 5, velocity profile predictions are compared with the experimental data of Ball and Azer [24] for fully developed flow in an annulus ($r^* = 0.25$). The predictions of model B seem to compare slightly better with the experimental data than those of model A.

Another comparison between the predictions of Models A, B, and C is given in Table 1 where the predicted fully developed shear stresses at the inner and outer wall are compared with the experimental data of Kuzay [25] taken in an annulus of radius ratio 0.556. The force balance measurements were obtained from a force balance calculation using the measured pressure drop and radius of zero stress. The present predictions are closest to the values measured by the Preston tube.

The momentum transfer in turbulent shear layers is strongly affected by occurrences very near the wall and if these are modeled appropriately, the engineering parameters can be predicted with reasonable accuracy even though the outer layer is modeled more approximately. The present models should predict annular flow reasonably well as long as the velocity distribution near the inner and outer wall can be described by a logarithmic law, such as $u^+ = 1/\kappa \log y^+ + B$. Figure 6 shows the predicted inner and outer wall velocity profiles drawn on "law of the wall" coordinates, as compared with the results of Lawn and Elliot [26] for $r^* = 0.396$. At this radius ratio, the predictions agree quite well with the data and seem to suggest that a universal logarithmic region exists near each wall. However, there is considerable controversy as to whether this law holds for very small radius ratios. Rehme [27] shows that the law holds for both walls with universal constants. On the other hand, the results of Lawn and Elliot [26] indicate that for radius ratios as small as 0.088, the velocity distribution near the inner wall does not match the law of the wall with the usual constants. Even then, only B seems to be affected appreciably. As indicated in Fig. 7, it was possible to reproduce the Lawn and Elliot results for $r^* = 0.088$ using Model A by taking $A^+ = 26r^{*0.1}$ in the van Driest damping function. This is consistent with the suggestion of Huffman and Bradshaw [28] that for axisymmetric boundary layers, only the viscous sublayer is influenced significantly by large transverse curvature. The change in A^+ causes a shift in the

Table 1 Predicted inner and outer wall shear stresses in an annulus ($r^* = 0.556$) as compared to the data of Kuzay [25]

Method	τ_1 Newtons/m^2	τ_2 Newtons/m^2	Effective stress $= \frac{\tau_2 + r^*\tau_1}{1 + r^*}$ Newtons/m^2
Measurements Re = 33156			
Force balance	0.1968	0.1798	0.1860
Clauser plot	0.2077	0.1626	0.1790
Preston tube	0.2222	0.1926	0.2033
Predictions Re = 32285			
Model A	0.2204	0.1863	0.1987
Model B	0.2226	0.1913	0.2027
Model C	0.2189	0.1857	0.1977

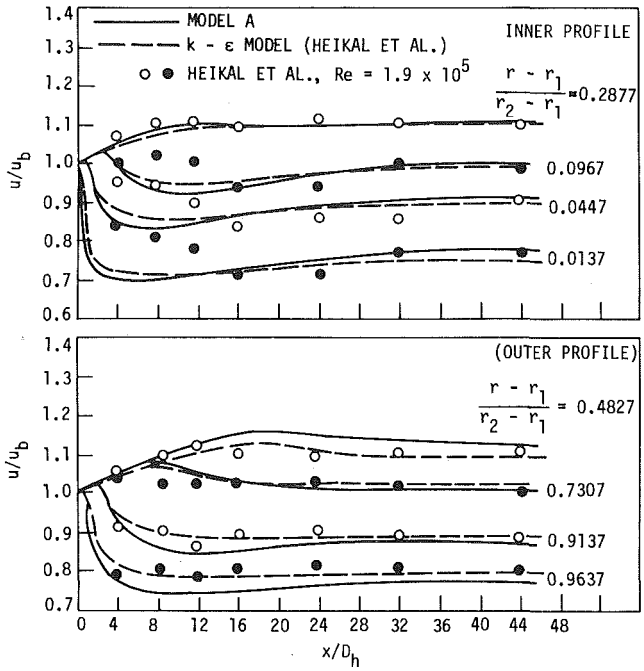

Fig. 4 Predicted velocity development in an annulus ($r^* = 0.25$) compared with the measurements of Heikal, et al. [6]

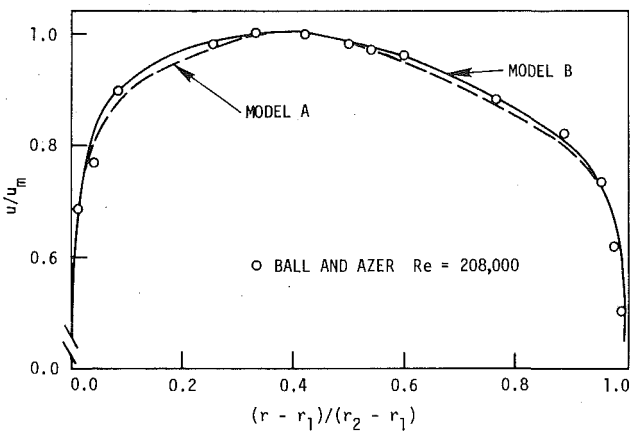

Fig. 5 Fully developed velocity profile in an annulus ($r^* = 0.25$)

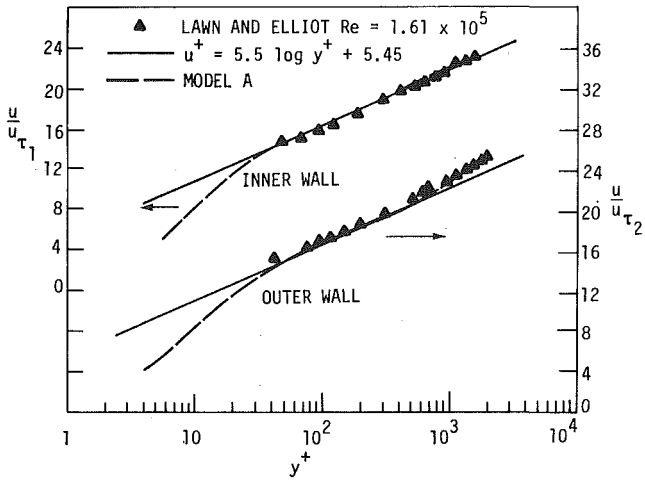

Fig. 6 Velocity distribution on law of the wall coordinates ($r^* = 0.396$)

Downloaded 20 Dec 2010 to 194.27.225.72. Redistribution subject to ASME license or copyright; see http://www.asme.org/terms/Terms_Use.cfm

predicted velocity profiles corresponding roughly to a change in the value of B in any logarithmic law fit to the predicted results. It is interesting to note that Hanjalic [7] also modified B for the inner wall when using a three-equation model for predicting the Lawn and Elliot results.

Table 2 gives the values predicted for the radius of zero shear and the ratio of shear stesses for the same annulus using the transverse curvature correction. The present predictions are for $\mathrm{Re} = 2.37 \times 10^5$. The results of Lawn and Elliot [26] are also given in the table. It should be noted that the radius of zero shear (r_o) and that of maximum velocity (r_m) may not be the same. The experimental results of [26] show that for $r^* = 0.088$, $r_m/r_o = 1.05$ and that $r_m/r_o \to 1$ as $r^* \to 1$. The present turbulence models and for that matter any model based on the Boussinesq assumption relating the stress to the rate of mean strain cannot differentiate between these two radii whether or not μ_T is determined by an algebraic expression or by employing one or more transport equations for turbulence quantities.

Thermal Results. Experience to date with Models A, B, and C indicates that all three models give predictions for Stanton numbers which are within 3 percent for Reynolds numbers greater than about 110,000. The differences between the three predictions are more evident at lower Reynolds numbers being as much as 8 percent for Re = 20,000. This is illustrated in Fig. 8 where Stanton number predictions of Models A and B are compared with the measurements of Furber, et al. [29] for Re = 20,000 and $r^* = 0.68$.

In Table 3, fully developed Stanton numbers obtained for an annulus ($r^* = 0.556$) with the outer wall heated are given. It can be seen that the difference between the predictions of Models A and B reduce with Reynolds number and that the prediction of Model C lies between that of Model A and B. The differences in the predictions of the three models are more evident in the temperature profiles near the middle of the annulus. This will be illustrated later.

In Fig. 9, the predicted Stanton numbers obtained from Model A for the entrance region of a parallel plate duct ($r^* = 0.99$) heated with constant heat flux on one side are compared with the data of Byrne, et al. [18]. Heating started a short distance downstream of the inlet in the experiments (taken to be $x/D_h = 0.3$ in the predictions). The agreement appears to be quite good.

The predicted effect of property variations on Nusselt number is indicated in Fig. 10 for Model A, in which the flow of air is through an annulus of $r^* = 0.5$ with the inner wall heated, giving rise to ratios of T_w to T_o up to 4.0. The flow was assumed to be hydrodynamically fully developed at the inlet to the heated section. The results shown were obtained 56.5 hydraulic diameters from this inlet and are compared with the measurements of Dalle Donne and Meerwald [30] for $8 \times 10^4 \le \mathrm{Re}_b \le 2 \times 10^5$. Dalle Donne and Meerwald proposed to correlate their measurements of local heat transfer coefficient for $r^* = 0.5$ using a form,

$$\mathrm{Nu}_b = A\mathrm{Re}_b^{0.8}\mathrm{Pr}^{0.4}(T_w/T_o)^C \qquad (15)$$

Table 2 Predicted (Model A with curvature correction) and measured [26] values of some parameters for an annulus with $r^* = 0.088$

Method	$\frac{r_o}{r_2}$	$\frac{\tau_1}{\tau_2}$	$\frac{2\tau_1}{\rho u_b^2 C_f}$	$\frac{2\tau_2}{\rho u_b^2 C_f}$
Measurements	0.362 ± 0.0031	1.61	1.532 ± 0.028	0.952 ± 0.01
Predictions	0.3623	1.603	1.529	0.953

Table 3 Predicted fully developed Stanton numbers for an annulus ($r^* = 0.556$) with the outer wall heated

Model	St	
	Re = 32285	Re = 64131
A	0.002907	0.002514
B	0.003103	0.002661
C	0.002938	0.002657

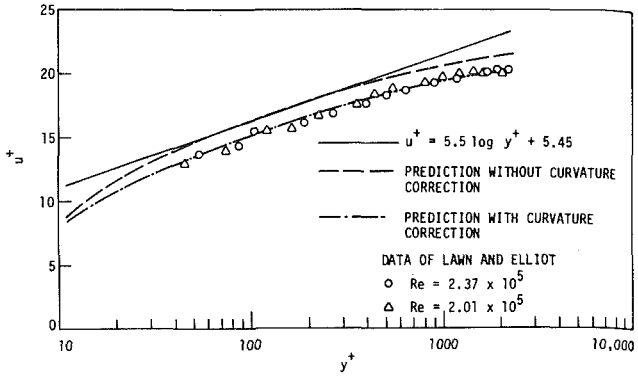

Fig. 7 Velocity distribution near the inner wall of an annulus ($r^* = 0.088$); prediction for $\mathrm{Re} = 2.37 \times 10^5$

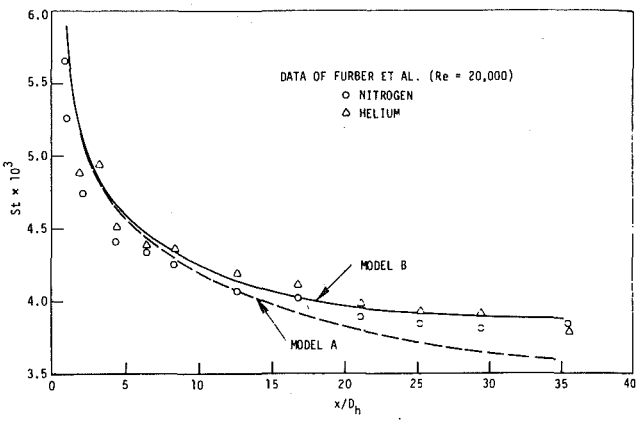

Fig. 8 Local Stanton number variation for hydrodynamically developed flow in an annulus ($r^* = 0.68$); inner wall heated

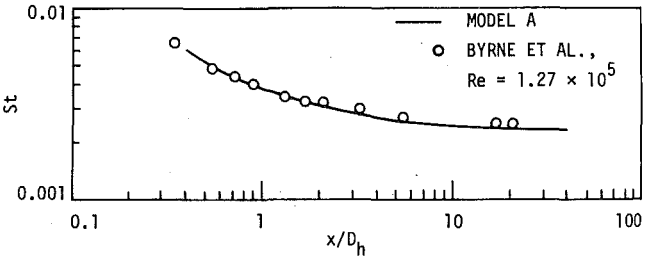

Fig. 9 Predicted Stanton number distribution compared with the measurements of Byrne et al. [18] for hydrodynamically developing flow in an annulus ($r^* = 0.99$)

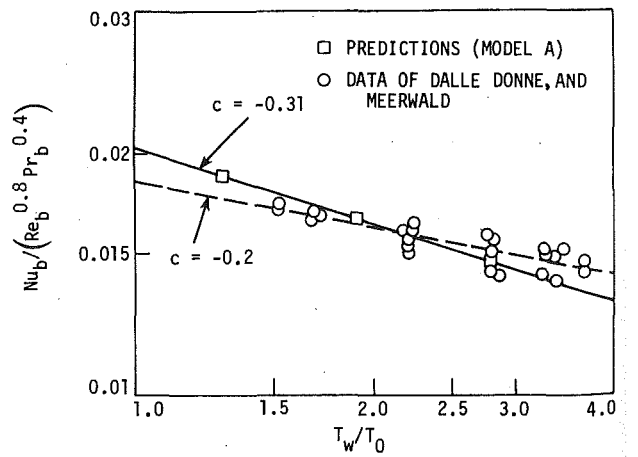

Fig. 10 Correlation of Nusselt number with wall-to-inlet temperature ratio for flow of air through an annulus ($r^* = 0.5$), $x/D_h = 56.3$

Downloaded 20 Dec 2010 to 194.27.225.72. Redistribution subject to ASME license or copyright; see http://www.asme.org/terms/Terms_Use.cfm

Values of $A = 0.0186$ and $C = -0.2$ were suggested. The present predictions of Model A suggest $A \approx 0.0204$ and $C = -0.31$ as indicated in Fig. 10. This slight discrepancy between predictions and measurements was not expected in light of the excellent agreement observed earlier [10] between the predictions of Model A and the data of Furber, et al. [29] for nitrogen heated over a similar range of temperature ratios. From [30] it can be noted that the preponderance of experimental data available for annular passages would suggest that A in equation (14) should be closer to 0.02 (rather than 0.0186), for which the exponential parameter of -0.2 would be inappropriate. This suggests that the data of Dalle Donne and Meerwald, while perhaps correct, are slightly inconsistent with other available data for annular passages.

As indicated previously, all three turbulence models evaluated gave Stanton numbers which agreed very closely at moderate to high Reynolds numbers, but which differed noticeably in the predicted temperature distribution in the central portion of the annulus. Figure 11 shows the predicted temperature profiles at 14.4 hydraulic diameters downstream of heating compared to the measurements of Ball and Azer [24] taken in an annulus ($r^* = 0.25$) with uniform heat flux at the inner wall and with an insulated outer wall. The temperature profile predicted by Model A does not compare well with the measurements, but is seen to be improved by the use of bridging (Model B). There should be no doubt that bridging is only an approximation used to improve the thermal predictions. The idea of bridging is demonstrated in Fig. 12 which also contains experimental data for turbulent viscosity reported by Ball and Azer [24] and Jonsson and Sparrow [31]. The experimental data show that the turbulent viscosity does decrease, but remains non-zero near the radius of maximum velocity. The reason that the bridging model provides improved thermal results is as follows.

Linear bridging is used in order to obtain a non-zero turbulent conductivity (near the radius of maximum velocity) which is calculated by $\lambda_T = \mu_T C_p / \mathrm{Pr}_T$. A constant value of $\mathrm{Pr}_T = 0.9$ was used in the present predictions. Experimental results of Kuzay [25] and Ball and Azer [24] show that Pr_T varies throughout the flow and that it reaches a small value at the radius of maximum velocity ($0.4 \sim 0.6$ instead of 0.9). So the use of a rather elevated value of μ_T with a "large" value of Pr_T at and near the radius of maximum velocity perhaps results in the same λ_T which would be obtained if the actual (experimental) value of μ_T with the observed value of Pr_T had been used.

Resources have not permitted the computation of every case with all three models. Whenever all three models have been used, predictions of temperature profiles by Model C have fallen between those of Models A and B.

Figure 13 shows a comparison between the temperature profiles predicted by all three models and the measurements of Kuzay [25], in which the outer wall was heated. In this experiment, an unheated length of 15 hydraulic diameters was followed by a heated length of 36 diameters. It can be seen from the figure that Model A predicts an unrealistically large temperature gradient in the region of maximum velocity because of the very small eddy conductivity predicted there. Both models B and C offer improvements to the predictions, but neither prediction is in really good agreement with the measurements.

Conclusions

1 The accurate prediction of confined turbulent flow development provides an interesting test to turbulence modeling. Flow parameters, including the maximum velocity, do not approach their fully developed value monotonically, but rather overshoot the asymptotic values. This behavior is not predicted by the simplest algebraic turbulence models, although algebraic models have been modified to accommodate this effect [32,33]. Use of a simplified transport equation for a length scale in the turbulence modeling resulted in predictions of these phenomena which are at least as accurate as those provided by the k-ϵ two-equation model.

2 Hydrodynamic features of annular flows are predicted quite accurately by both Models A and C. Model B does not predict the

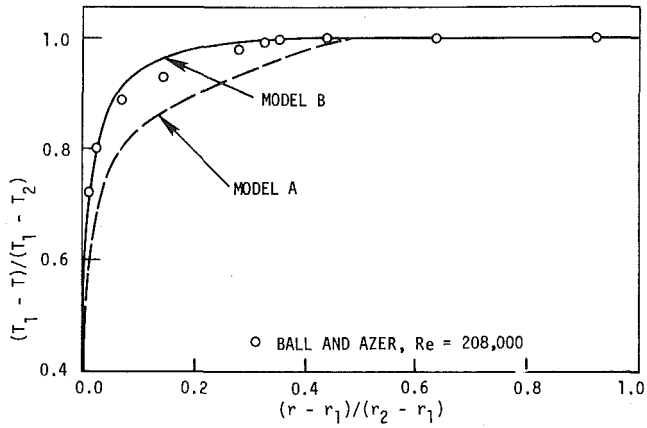

Fig. 11 Predicted temperature profiles (Re = 215,000) for the flow of air through an annulus ($r^* = 0.25$) compared with the data of Ball and Azer [24] at 14.4 diameters downstream of the start of heating

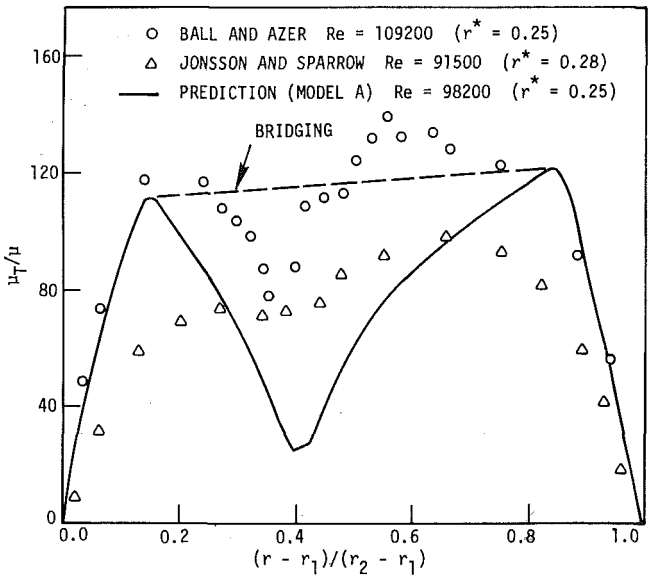

Fig. 12 Predicted and measured distribution of turbulent viscosity in fully developed flow through an annulus

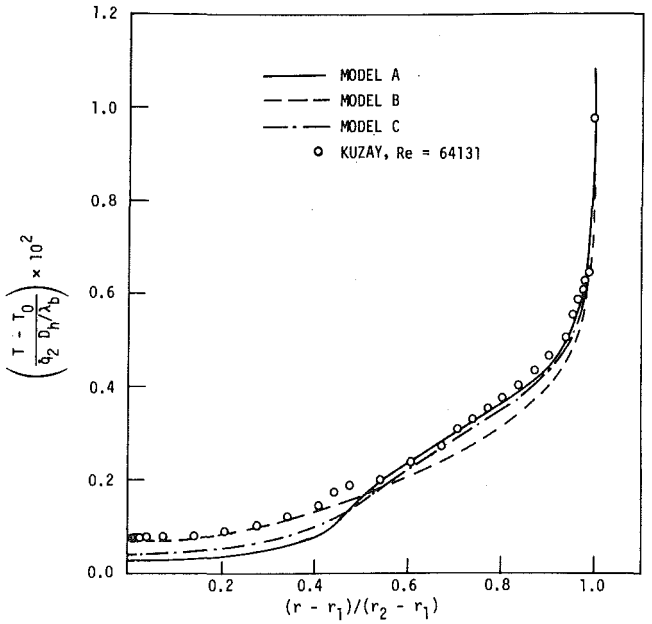

Fig. 13 Predicted temperature profiles for the flow of air through an annulus ($r^* = 0.556$) compared with the data of Kuzay [25] at 33 diameters downstream of the start of heating

Downloaded 20 Dec 2010 to 194.27.225.72. Redistribution subject to ASME license or copyright; see http://www.asme.org/terms/Terms_Use.cfm

overshoot phenomena adequately, but provides accurate predictions after the flow has become hydrodynamically fully developed.

3 All three models were found to predict within 8 percent of the same value for Stanton number in all cases and within 3 percent for Reynolds numbers greater than 1.1×10^5. These predictions were generally in good agreement with measured values of Stanton numbers. Differences were apparent, however, in the predicted temperature profiles, where Models B and C were found to provide predictions somewhat more in line with measurements than those of Model A. Overall, Model C appeared to predict most reliably all aspects of the flow (hydrodynamic and thermal), although Model A was found to be sufficiently accurate for isothermal cases.

4 Property variations were shown to have a significant effect on the heat transfer coefficient. The present calculation method was found to predict these effects in reasonable agreement with experimental measurements, especially when the additional comparisons shown in [10] are taken into account. The predictions suggest that the Nussult number can be correlated using a wall-to-inlet temperature ratio raised to the exponent of -0.31.

Acknowledgment

This work was supported by the Engineering Research Institute of Iowa State University through funds provided by the National Science Foundation under Grants ENG 74-22193 and ENG 78-12901. Part of this work was done while the authors were visiting in the Department of Aeronautics, Imperial College, London. The authors wish to express their appreciation to Professor Peter Bradshaw of Imperial College for his cooperation and interest.

References

1 Kays, W. M., and Leung, E. Y., "Heat Transfer in Annular Passages—Hydrodynamically Developed Turbulent Flow with Arbitrarily Prescribed Heat Flux," *International Journal of Heat and Mass Transfer*, Vol. 6, 1963, pp. 537–557.

2 Ying, W. M., "A Theoretical Method of Predicting Heat Transfer and Friction Factor in Annuli with Roughened Core Tubes," M.S. Thesis, Imperial College, London, 1967.

3 Lee, Y., and Park, S. D., "Developing Turbulent Flow and Heat Transfer in Concentric Annuli," *Transactions of the Canadian Society for Mechanical Engineers*, Vol. 1, 1972, pp. 13–24.

4 Quarmby, A., and Anand, R. K., "Turbulent Heat Transfer in the Thermal Entrance Region of Concentric Annuli with Uniform Wall Heat Flux," *International Journal of Heat and Mass Transfer*, Vol. 13, 1970, pp. 395–511.

5 Wilson, N. W., and Medwell, J. O., "An Analysis of Heat Transfer for Fully Developed Turbulent Flow in Concentric Annuli," ASME JOURNAL OF HEAT TRANSFER, Vol. 90, 1968, pp. 43–50.

6 Heikal, M. R. F., Walklate, P. J., and Hatton, A. P., "The Effect of Free Stream Turbulence Level on the Flow and Heat Transfer in the Entrance Region of an Annulus," *International Journal of Heat and Mass Transfer*, Vol. 20, 1977, pp. 763–771.

7 Hanjalic, K., "Prediction of Turbulent Flow in Annular Ducts with Differential Transport Model of Turbulence," *Wärmeund Stoffübertragung*, Vol. 7, 1974, pp. 71–78.

8 Sharma, B. I., Launder, B. E. and Scott, C. J., "Computation of Annular, Turbulent Flow with Rotating Core Tube," ASME *Journal of Fluids Engineering*, Vol. 98, 1976, pp. 753–758.

9 Malik, M. R., "Prediction of Laminar and Turbulent Flow Heat Transfer in Annular Passages," Ph.D. Thesis, Department of Mechanical Engineering, Iowa State University, Ames, 1978.

10 Malik, M. R. and Pletcher, R. H., "Computation of Annular Turbulent Flows with Heat Transfer and Property Variations," *Heat Transfer 1978, Proceedings of the Sixth International Heat Transfer Conference*, Vol. 2, Hemisphere Publishing, 1978, pp. 537–542.

11 Malik, M. R. and Pletcher, R. H., "Calculation of Variable Property Heat Transfer in Ducts of Annular Cross-Section," *Numerical Heat Transfer*, Vol. 3, 1980, pp. 241–257.

12 Bradshaw, P., "Turbulence Research—Progress and Problems," *Proceedings of the 1976 Heat Transfer and Fluid Mechanics Institute*, Stanford University Press, 1976, pp. 128–139.

13 Pletcher, R. H., "Prediction of Incompressible Turbulent Separating Flow," ASME *Journal of Fluids Engineering*, Vol. 100, 1979, pp. 427–433.

14 Dean, R. B., "Interaction of Turbulent Shear Layers in Duct Flow," Ph.D Thesis, London University, 1972.

15 Pai, B. R., and Whitelaw, J. H., "The Prediction of Wall Temperature in the Presence of Film Cooling," Heat Transfer Section Report EHT/TN/A/22, Imperial College, 1970.

16 Dvorak, F. A., "Calculation of Turbulent Boundary Layers and Wall Jets Over Curved Surfaces," *AIAA Journal*, Vol. 11, 1973, pp. 517–524.

17 Launder, B. E., and Spalding, D. B., *Mathematical Models of Turbulence*, Academic Press, New York, 1972.

18 Byrne, J., Hatton, A. P. and Mariott, P. G., "Turbulent Flow and Heat Transfer in the Entrance Region of a Parallel Wall Passage," *Proceedings of the Institute of Mechanical Engineers*, Vol. 184, 1969–70, pp. 697–712.

19 Barbin, A. R., and Jones, J. B., "Turbulent Flow in the Inlet Region of a Smooth Pipe," ASME *Journal of Basic Engineering*, Vol. 85, 1963, pp. 29–34.

20 Pletcher, R. H., and Nelson, R. M., "Heat Transfer to Laminar and Turbulent Flow in Tubes with Variable Fluid Properties," *Heat Transfer 1974, Proceedings of the Fifth International Heat Transfer Conference*, Vol. 2, 1974, pp. 146–150.

21 Schlichting, H., *Boundary Layer Theory*, 6th ed., McGraw Hill, New York, 1968, p. 568.

22 Stephenson, P. L., "A Theoretical Study of Heat Transfer in Two-Dimensional Turbulent Flow in a Circular Pipe and Between Parallel and Diverging Plates," *International Journal of Heat and Mass Transfer*, Vol. 19, 1976, pp. 413–423.

23 Comte-Bellot, G., "Turbulent Flow Between Parallel Walls," Ph.D. Thesis, University of Grenoble, France, 1963 (also available as ARC 31 609).

24 Ball, H. D., and Azer, N. Z., "Experimental Investigation of Eddy Diffusivities of Air in Turbulent Annular Flow," *Proceedings of the 1972 Heat Transfer and Fluid Mechanics Institute*, Stanford University Press, 1972, pp. 19–38.

25 Kuzay, T. M., "Turbulent Heat and Momentum Transfer Studies in an Annulus with Rotating Inner Cylinder," Ph.D. Thesis, University of Minnesota, 1973.

26 Lawn, C. J., and Elliot, C. J., "Fully Developed Turbulent Flow Through Concentric Annuli," C.E.G.B. Report RD/B/N1878, Berkeley Nuclear Lab., England, 1971.

27 Rehme, K., "Turbulence Measurements in Smooth Concentric Annuli with Small Radius Ratios," ASME *Journal of Fluid Mechanics*, Vol. 72, 1975, pp. 189–206.

28 Huffman, G. D., and Bradshaw, P., "A Note on von Karman Constant in Low Reynolds Number Turbulent Flows," ASME *Journal of Fluid Mechanics*, Vol. 53, 1972, pp. 45–60.

29 Furber, B. N., Appleby, G. G., and Facer, R. I., "Forced Convection Heat Transfer in an Annulus," *Heat Transfer 1974, Proceedings of the Fifth International Heat Transfer Conference*, Vol. 2, 1974, pp. 155–159.

30 Dalle Donne, M., and Meerwald, E., "Heat Transfer and Friction Coefficients for Turbulent Flow of Air in Smooth Annuli at High Temperatures," *International Journal of Heat and Mass Transfer*, Vol. 16, 1973, pp. 787–809.

31 Jonsson, V. K., and Sparrow, E. M., "Turbulent Diffusivity for Momentum in Concentric Annuli," ASME *Journal of Basic Engineering*, Vol. 88, 1966, pp. 550–552.

32 Emery, A. F., and Gessner, F. B., "The Numerical Prediction of the Turbulent Flow and Heat Transfer in the Entrance Region of a Parallel Plate Duct," ASME JOURNAL OF HEAT TRANSFER, Vol. 98, 1976, pp. 594–600.

33 Cebeci, T., and Chang, K. C., "A General Method for Calculating Momentum and Heat Transfer in Laminar and Turbulent Duct Flows," *Numerical Heat Transfer*, Vol. 1, 1978, pp. 39–68.

Downloaded 20 Dec 2010 to 194.27.225.72. Redistribution subject to ASME license or copyright; see http://www.asme.org/terms/Terms_Use.cfm

H. W. Coleman
Mechanical Engineering Department,
Mississippi State University,
Mississippi State, MS 39762,
Mem. ASME

R. J. Moffat
Mechanical Engineering Department,
Stanford University,
Stanford, CA 94305,
Mem. ASME

W. M. Kays
Dean, School of Engineering,
Stanford University,
Stanford, CA 94305,
Fellow ASME

Heat Transfer in the Accelerated Fully Rough Turbulent Boundary Layer

Heat transfer behavior of a fully rough turbulent boundary layer subjected to favorable pressure gradients was investigated experimentally using a porous test surface composed of densely packed spheres of uniform size. Stanton numbers and profiles of mean temperature, turbulent Prandtl number, and turbulent heat flux are reported. Three equilibrium acceleration cases (one with blowing) and one non-equilibrium acceleration case were studied. For each acceleration case of this study, Stanton number increased over zero pressure gradient values at the same position or enthalpy thickness. Turbulent Prandtl number was found to be approximately constant at 0.7–0.8 across the layer, and profiles of the non-dimensional turbulent heat flux showed close agreement with those previously reported for both smooth and rough wall zero pressure gradient layers.

Introduction

Surface roughness can have profound effects on the structure and behavior of a turbulent boundary layer. In general, Stanton numbers and skin friction coefficients are greater in a turbulent boundary layer influenced by roughness than in a smooth wall layer at the same flow conditions. This enhancement of heat transfer (and wall shear) because of roughness effects must be understood and accounted for in the analysis and design of systems naturally influenced by roughness. In addition, an understanding of roughness effects can be used to advantage in the design of systems where enhanced heat transfer is desirable.

An experimental study of the effects of roughness on the fluid dynamics and heat transfer in the turbulent boundary layer has been in progress at Stanford for the past several years. Results of this investigation for zero pressure gradient flows have been reported previously [1–4]. The present study considered the effects of acceleration on a turbulent boundary layer in the fully rough state. This subject was investigated not only because of its importance in the flow in nozzles and over turbine blades and reentry vehicles, but also to provide basic information by observing the response of the flat plate turbulent boundary layer to the imposed perturbations of roughness and acceleration.

The influence of surface roughness on turbulent flows is usually divided into three regimes, which are characterized by the magnitude of the roughness Reynolds number, Re_k, where

$$\mathrm{Re}_k = \frac{k_s U_\tau}{\nu} \tag{1}$$

The equivalent sand grain roughness parameter, k_s, is a commonly used, single-length-scale descriptor of rough surfaces determined by comparison with Nikuradse's [5] classic rough pipe flow experiments. For $\mathrm{Re}_k \leq 5$, the roughness elements are contained entirely within the viscous sublayer and the flow is termed smooth. For $5 < \mathrm{Re}_k <$ 55–70 the elements protrude progressively further into the sublayer, and the flow is called transitionally rough. For $\mathrm{Re}_k >$ 55–70 the viscous sublayer is effectively destroyed, and the flow is termed fully rough.

Experimental results for zero pressure gradient turbulent boundary layers on the present rough surface were reported by Healzer [1, 2] and Pimenta [3, 4]. Healzer constructed the basic experimental apparatus and reported $C_f/2$ and St data both with and without blowing for several velocities which included the transitionally rough and fully rough flow regimes. He confirmed that, for fully rough flow over the present surface, both $C_f/2$ and St were independent of Reynolds number, i.e.,

$$C_f/2 = f\left(\frac{\delta_2}{r}, F\right) \tag{2}$$

$$\mathrm{St} = g\left(\frac{\Delta_2}{r}, F\right) \tag{3}$$

Pimenta reported results of an extensive investigation of the fluid dynamics and heat transfer in both transitionally rough and fully rough zero pressure gradient layers both with and without blowing. His observations on the fully rough state included:

1 The effect of roughness on the turbulent field structure extended over most of the layer.

2 Blowing made the layer behave as if the surface had physically larger roughness elements.

3 For very large enthalpy thicknesses, the Stanton number appeared to converge to an asymptotic value.

4 Reynolds shear stress correlation coefficients were unchanged from the values reported for smooth wall flows.

Previously published studies of the combined effects of acceleration and roughness on the turbulent boundary layer have reported only values of wall heat flux. Reshotko, et al. [6], and Banerian and McKillop [7] investigated nozzle wall flows, while Chen [8] cited experimental results for flow over hemispheres and Hodge [9] cited experimental results for flow over a hemisphere-cylinder. No boundary layer measurements were obtained in any of these studies.

The fluid dynamic results of the present study have been previously reported [10]. Those results showed that the proper acceleration parameter for use with rough wall flows is

$$K_r = \frac{r}{U_\infty}\frac{dU_\infty}{dx} \tag{4}$$

where r is a characteristic roughness length. It was shown analytically and experimentally that in a constant K_r acceleration for $F \geq 0$ and constant, the fully rough layer develops toward an equilibrium state where $C_f/2$, δ_2, H, β, and G are all constant and the profiles of mean velocity and components of the Reynolds stress tensor exhibit similarity in the flow direction. This equilibrium state satisfies the criteria formulated by Rotta [11] for exact equilibrium behavior:

$$\begin{aligned} C_f/2 &= \text{constant} \\ d\delta_1/dx &= \text{constant} \\ \beta &= \text{constant} \end{aligned} \tag{5}$$

Experimental Apparatus and Measurement Techniques

A brief description of the experimental apparatus and measurement techniques will be presented below. Details of the apparatus, mea-

Contributed by the Heat Transfer Division for publication in the JOURNAL OF HEAT TRANSFER. Manuscript received by the Heat Transfer Division December 3, 1979.

Copyright © 1981 by ASME

Downloaded 20 Dec 2010 to 194.27.225.72. Redistribution subject to ASME license or copyright; see http://www.asme.org/terms/Terms_Use.cfm

surement techniques and calibrations, qualification tests, and tabular data listings were reported by Coleman [12].

The experimental apparatus is a closed-loop wind tunnel using air as both the primary and transpiration fluids. Air temperature is controlled using water-cooled heat exchangers in both the primary and transpiration loops. The test section is 2.44 m long, 0.51 m wide and 0.10 m high at its entrance. A flexible plexiglass upper wall (constructed in five sections connected by thin plexiglass joints) can be adjusted to produce the desired variation in U_∞.

The test surface consists of 24 plates each 0.10 m in the axial direction. The plates (Fig. 1) are 12.7 mm thick and uniformly porous. They are constructed of 11 layers of 1.27 mm dia copper spheres packed in the most dense array and brazed together. This configuration produces a rough test surface which is uniform and deterministic.

Each plate is thermally isolated from neighboring plates and has individual electrical power and transpiration air controls and thermocouples for determining plate temperature. Stanton numbers were determined by subtracting the plate losses (known from energy balance qualification tests) from the measured power input. Uncertainty of the resulting St data is within ±0.0001 Stanton number units (i.e., *if St = 0.00200, the uncertainty is within ±5 percent).*

The Stanton number data reported were taken with a constant wall temperature and with a wall-to-freestream temperature difference of approximately 17°C to maintain a constant property boundary layer. The freestream velocity at the test section inlet was nominally 26.8 m/s. All data were taken with a 1.27 mm wide, 0.80 mm high phenolic trip installed 77 mm upstream of the test surface. The turbulent boundary layer was in a fully rough state for all cases reported. Roughness Reynolds number (based on k_s = 0.79 mm) varied from 66 to 113 for the $F = 0$ runs and 55 to 78 for the $F = 0.0039$ run.

Mean temperature profiles were measured with a 0.076 mm dia, butt-welded, Chromel-constantan thermocouple mounted in a traversing probe holder. The probe was designed with a length of approximately 16 mm to minimize conduction errors and was calibrated in an oil bath against a quartz thermometer.

Measurements of mean velocity and components of the Reynolds stress tensor were made using hot wire anemometry. Skin friction coefficients were determined [10] using these measurements and the momentum and continuity equations integrated from $y = 0$ to a point in the boundary layer where $\overline{u'v'}$ data had been obtained.

Discussion of Experimental Results

The experimental program covered five different cases:

(1) $K_r = 0$	$F = 0$	(baseline)
(2) $K_r = 0.15 \times 10^{-3}$	$F = 0$	(equilibrium)
(3) $K_r = 0.29 \times 10^{-3}$	$F = 0$	(equilibrium)
(4) $K_r = 0.29 \times 10^{-3}$	$F = 0.0039$	(equilibrium)
(5) $K = 0.28 \times 10^{-6}$	$F = 0$	(nonequilibrium)

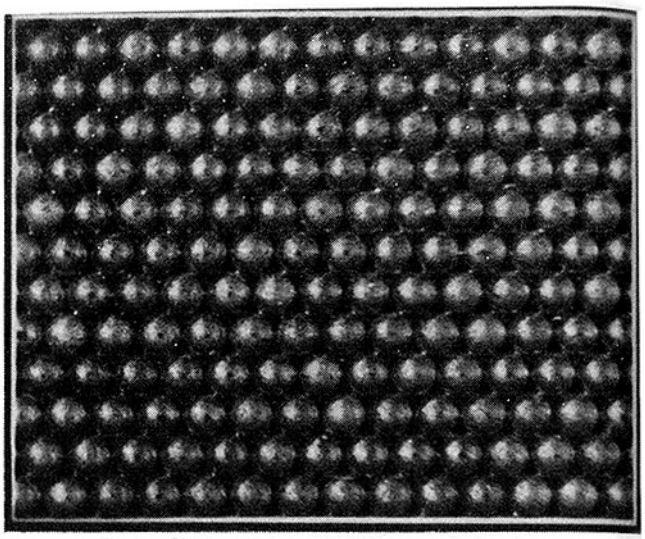

Fig. 1 Closeup photograph of the rough test surface

Case (1) was run as a baseline set, to compare the present data with those of Pimenta [3] for identical conditions. Cases (2, 3) and (4) are equilibrium acceleration runs for a fully rough turbulent boundary layer. In Case (5) the smooth wall acceleration parameter $K = (\nu/U_\infty^2)(dU_\infty/dx)$ was maintained constant.

An accelerating turbulent flow on a smooth wall with K = constant yields a boundary layer with constant momentum thickness Reynolds number [13]. This flow is an equilibrium flow for smooth wall layers in the sense that mean velocity profiles become similar and G and β are constant, but is not truly an equilibrium flow in the sense of equation (5) since $d\delta_1/dx \sim 1/U_\infty^2 \neq$ constant. Case (5) represents a nonequilibrium run for the fully rough layer. Thus, one would not expect similarity in profiles or constant values of $C_f/2$, δ_2, H, β and G for K = constant.

Stanton Number. The behavior observed for the four cases of accelerated flow investigated is summarized in Figs. 2–5. Shown in these figures are the variation of K_r, the integral fluid dynamic quantities $C_f/2$, δ_2, and H [10], and Stanton number (which illustrates the integral behavior of the thermal field). In each of these figures, the data are plotted versus nondimensional distance along the test section, x/r. In the discussion which follows, $F = 0$ unless specifically *stated otherwise.*

In Case (2) (Fig. 2), K_r was maintained at a constant value of 0.15×10^{-3} from x = 1.12 m to 2.24 m, with the freestream velocity in-

Nomenclature

$C_f/2$ = skin friction coefficient, $\tau_w/(\rho U_\infty^2)$
C_p = specific heat of fluid
F = blowing fraction, $\rho_w V_w/\rho_\infty U_\infty$
G = Clauser shape factor, $(H - 1)/(H\sqrt{C_f/2})$
H = shape factor, δ_1/δ_2
I = total enthalpy referenced to freestream, $(i + U^2/2) - (i_\infty + U^2_\infty/2)$
i = static enthalpy
k = thermal conductivity
k_s = equivalent sand grain roughness
K = smooth wall acceleration parameter, $(\nu/U^2_\infty)(dU_\infty/dx)$
K_r = rough wall acceleration parameter, $(r/U_\infty)(dU_\infty/dx)$
P = mean pressure
Pr_T = turbulent Prandtl number, ϵ_M/ϵ_H
$\dot{q}''$ = heat flux
r = radius of spheres comprising test surface
Re_k = roughness Reynolds number, $k_s U_\tau/\nu$
St = Stanton number, $\dot{q}''_w/[\rho_\infty U_\infty C_p(T_w - T_{\infty,0})]$
T = mean temperature
$\Delta T = (T_w - T_{\infty,0})$
$T_\tau = (\Delta T)\,\mathrm{St}/\sqrt{C_f/2}$
u' = longitudinal velocity fluctuation
U = mean longitudinal velocity
U_τ = friction velocity, $U_\infty\sqrt{C_f/2}$
v' = velocity fluctuation normal to surface
V = mean velocity normal to surface
x = longitudinal coordinate, measured from wind tunnel nozzle exit plane
y = coordinate normal to surface, measured from plane of the crests of spherical elements
α = thermal diffusivity
β = pressure gradient parameter, $(\delta_1/\tau_w)(dP/dx)$
Δ = thermal boundary layer thickness, $(T_w - T)/T_w - T_\infty) = 0.99$
Δ_2 = enthalpy thickness, $\int_0^\infty [\rho U/\rho_\infty U_\infty][(T - T_\infty)/(T_w - T_\infty)]dy$
δ = momentum boundary layer thickness, $U/U_\infty = 0.99$
δ_1 = displacement thickness, $\int_0^\infty [1 - (\rho U/\rho_\infty U_\infty)]dy$
δ_2 = momentum thickness, $\int_0^\infty [\rho U/\rho_\infty U_\infty][1 - (U/U_\infty)]dy$
ϵ_H = eddy diffusivity for heat
ϵ_M = eddy diffusivity for momentum
ν = kinematic viscosity
ρ = density
τ = shear stress

Subscripts

a = position where K or K_r becomes constant
0 = total value
w = wall value
∞ = freestream value

Downloaded 20 Dec 2010 to 194.27.225.72. Redistribution subject to ASME license or copyright; see http://www.asme.org/terms/Terms_Use.cfm

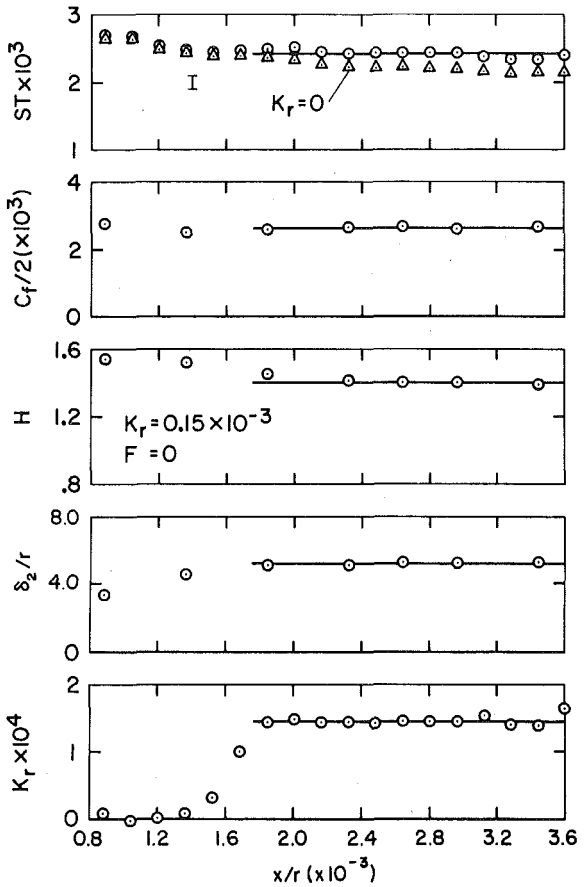

Fig. 2 Data for $K_r = 0.15 \times 10^{-3}$, $F = 0$ equilibrium acceleration case

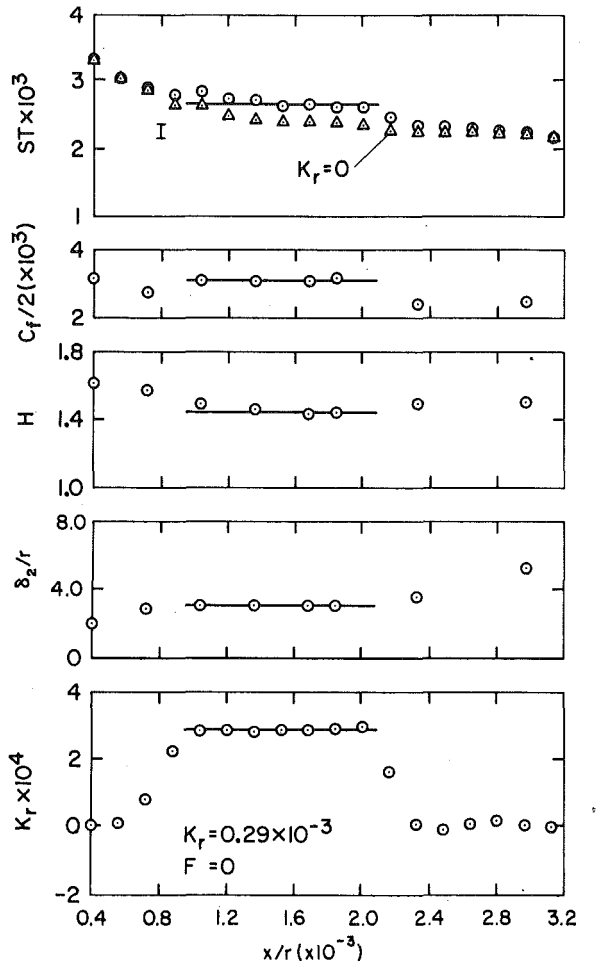

Fig. 3 Data for $K_r = 0.29 \times 10^{-3}$, $F = 0$ equilibrium acceleration case

creasing from 26.8 m/s to 35.1 m/s. The momentum thickness, boundary layer shape factor and skin friction coefficient all appear to reach constant values in the constant-K_r region, indicating that equilibrium flow was established. Stanton numbers in the acceleration region are about 10 percent larger than for the $K_r = 0$ case and appear to be approximately constant within the data uncertainty. The behavior is different from that observed for accelerated smooth wall layers. Smooth wall Stanton number is unaffected for small K, then decreases as K increases [13] compared to an unaccelerated case at the same Reynolds number or same x-position.

Data for Cases (3) and (4), for which a region where $K_r = 0.29 \times 10^{-3}$ was established, are shown in Figs. 3 and 4. In Case (3), $F = 0$, while in Case (4) the blowing fraction had a uniform value ($F = 0.0039$) along the entire test section. In both these cases, K_r was constant from $x = 0.61$ m to $x = 1.32$ m. The freestream velocity increased from 26.8 m/s to 39.3 m/s, and equilibrium flow was achieved in the acceleration region, with δ_2, H, and $C_f/2$ all approaching constant values. Stanton number again increased in the region of acceleration, then decreased rapidly to the $K_r = 0$ baseline data when the favorable pressure gradient was removed.

The summary data for the nonequilibrium case, $K = 0.28 \times 10^{-6}$, are presented in Fig. 5. The smooth wall acceleration parameter K was held constant from $x = 0.61$ m to $x = 1.32$ m. The freestream velocity, U_∞, increased from 26.8 m/s to 45.7 m/s, and K_r varied from 0.25–0.50 $\times 10^{-3}$ in this region. The shape parameter H decreased along the entire test section, while δ_2 increased as the layer entered the region of acceleration, then leveled off and finally decreased. This δ_2 behavior is similar to that observed previously in an asymptotic accelerated smooth wall layer [14, 15]. The skin friction coefficient showed very little variation, and appeared to remain about constant. This is not surprising considering the small variation of momentum thickness in the acceleration region. Stanton number showed the same increase over $K_r = 0$ values observed in the equilibrium cases and recovered immediately to unaccelerated baseline values when the acceleration was removed.

While St and $C_f/2$ for the nonequilibrium case exhibit the same behavior as observed for the equilibrium cases, the profiles of mean velocity and Reynolds stress tensor quantities did not exhibit similarity [12] as they did in Cases (2–4). In the K = constant region δ, δ_2, Δ and Δ_2 were all at an apparent maximum with δ, δ_2 and Δ showing a decrease by the end of the acceleration region [12]. In the authors' opinion, the apparently constant values of St and $C_f/2$ in Case (5) would probably not be maintained if the region of K = constant were extended. Unfortunately, the physical limitations of the test apparatus did not allow a longer region of K = constant acceleration.

As noted above, Stanton number appeared to be approximately constant, within the data uncertainty, in regions where K_r was constant. It is impossible to reach a firm conclusion in this regard due to the uncertainty in the data and the relatively short regions of acceleration. The same data could also support the contention that Stanton number for $K_r > 0$ varies as some weak function of Δ_2. The Stanton number data in the accelerated region for all three equilibrium runs are shown versus Δ_2/r in Fig. 6 and compared with zero pressure gradient data for both $F = 0$ and $F = 0.0039$. The accelerated data show an increase over the $K_r = 0$ data by ~10 percent for $F = 0$ and ~20 percent for $F = 0.0039$.

As previously reported [10], the roughness Reynolds number increased above its zero pressure gradient values as the layer passed through the region of acceleration in each of the cases studied in this investigation. The fully rough turbulent boundary layer thus progressed to a "rougher" state when accelerated. The increase in Stanton number noted in the acceleration regions is not surprising, therefore, since one would expect *a priori* that a rougher layer should exhibit larger Stanton numbers than a less rough layer.

Coleman and Hodge [16] presented results of an analysis describing the response of a rough wall turbulent boundary layer to pressure

Downloaded 20 Dec 2010 to 194.27.225.72. Redistribution subject to ASME license or copyright; see http://www.asme.org/terms/Terms_Use.cfm

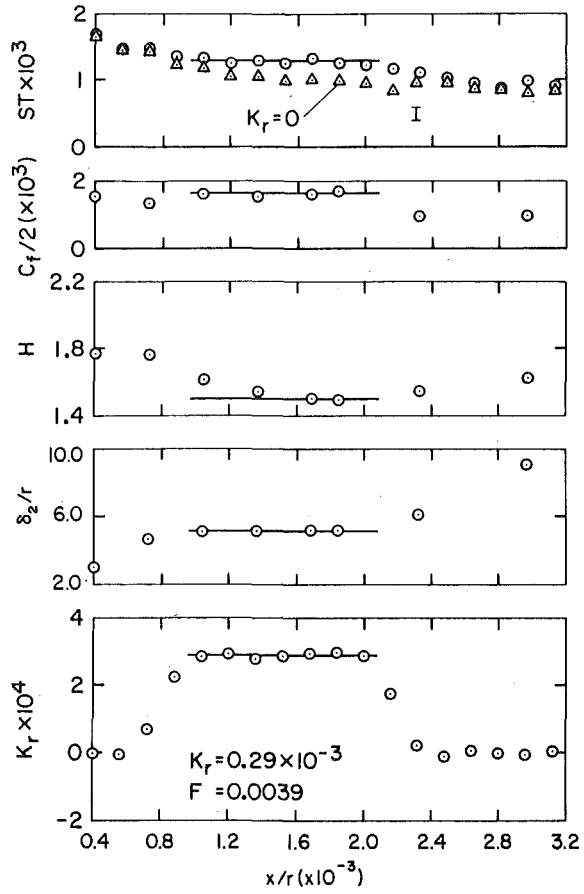

Fig. 4 Data for $K_r = 0.29 \times 10^{-3}$, $F = 0.0039$ equilibrium acceleration case

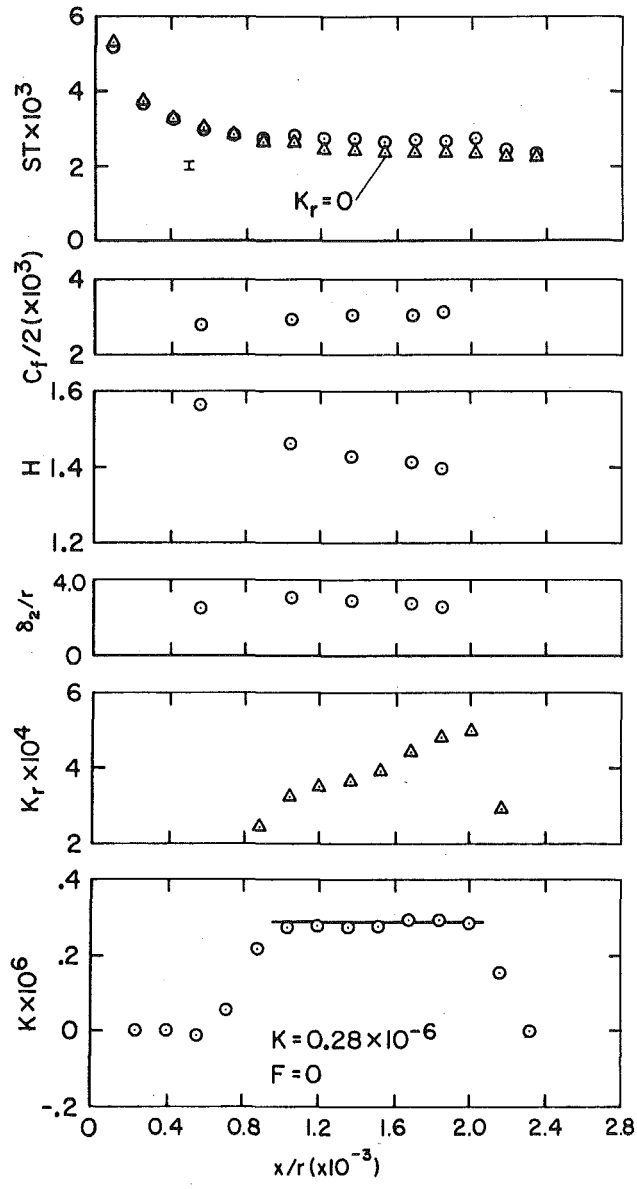

Fig. 5 Data for $K = 0.28 \times 10^{-6}$, $F = 0$ nonequilibrium acceleration case

gradients and showed that it was possible for the layer to either progress toward a rougher state, a less rough state, or remain in the same roughness state when accelerated. The specific response depends on the history of the layer, the local state of the layer, and the strength of the acceleration. In this investigation, the $K_r = 0$ layer moved toward a less rough state, while for all cases of $K_r > 0$ it moved toward a rougher state.

Mean Temperature Profiles. Profiles of mean temperature in the equilibrium acceleration regions exhibited similarity when plotted in $(T_w - T)(T_w - T_\infty)$ versus y/Δ_2 coordinates. This is illustrated using the data from the $K_r = 0.15 \times 10^{-3}$ case in Fig. 7, where x_a denotes the x position at which K_r becomes constant. Similarity is observed to extend down to the closest data point from the surface ($y = 0.33$ mm).

Mean temperature profiles for the same case are plotted in Fig. 8 in $(T_w - T)/(T_w - T_\infty)$ versus U/U_∞ coordinates. Pimenta [3] found these coordinates useful since fully rough $K_r = 0$ data are linear when plotted in this manner. The present profile at $x = 0.86$ m (prior to the acceleration region) exhibits this linearity. The two profiles in the acceleration region however, are not linear and do not exhibit similarity in these coordinates. It should be noted that the accelerated profiles, if extrapolated to $U/U_\infty = 0$, still show the temperature "jump" condition discussed by Pimenta, indicating that the apparent (extrapolated) wall position is different for the mean temperature and mean velocity fields.

Turbulent Prandtl Number and Heat Flux. The results discussed below were obtained from calculations using St, $C_f/2$, U, and T data and the energy, momentum, and continuity equations integrated to a position y_1 in the boundary layer. These integrations yield

$$\tau = \tau_w + \rho_\infty U_\infty U F + \left(U_\infty{}^2 \frac{d\rho_\infty}{dx} + \frac{2\rho_\infty U^2{}_\infty}{r} K_r\right)$$

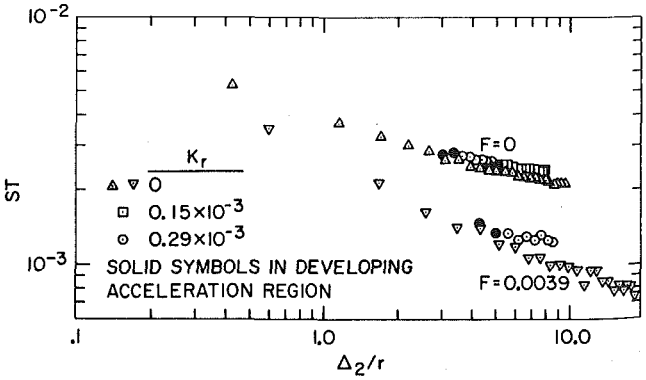

Fig. 6 Equilibrium acceleration Stanton number data versus (enthalpy thickness/sphere radius)

$$\times \left[\left(\int_0^{y_1} \left(\frac{U}{U_\infty}\right)^2 dy\right) - \frac{y_1}{2}\right] - \left(U_\infty \frac{d\rho_\infty}{dx} + \frac{\rho_\infty U_\infty}{r} K_r\right)\left(U \int_0^{y_1} \frac{U}{U_\infty} dy\right)$$
$$+ \rho_\infty U^2{}_\infty \frac{d}{dx}\left[\int_0^{y_1} \left(\frac{U}{U_\infty}\right)^2 dy\right] - \rho_\infty U_\infty U \frac{d}{dx}\left(\int_0^{y_1} \frac{U}{U_\infty} dy\right) \quad (6)$$

Downloaded 20 Dec 2010 to 194.27.225.72. Redistribution subject to ASME license or copyright; see http://www.asme.org/terms/Terms_Use.cfm

for the shear stress distribution and

$$\dot{q}''/\dot{q}''_w = 1 + \frac{U}{\dot{q}''_w} + \frac{F}{\mathrm{St}}\left(1 - \frac{I}{I_w}\right) + \left(\frac{I}{\dot{q}''_w}\int_0^{y_1}\frac{\rho U}{\rho_\infty U_\infty}dy\right)\frac{d}{dx}(\rho_\infty U_\infty) + \left(\frac{I}{\dot{q}''_w}\rho_\infty U_\infty\right)\frac{d}{dx}\left(\int_0^{y_1}\frac{\rho U}{\rho_\infty U_\infty}dy\right) - \left(\frac{1}{\dot{q}''_w}\int_0^{y_1}\frac{\rho UI}{\rho_\infty U_\infty I_w}dy\right)\frac{d}{dx}(\rho_\infty U_\infty I_w) - \left(\frac{\rho_\infty U_\infty I_w}{\dot{q}''_w}\right)\frac{d}{dx}\left(\int_0^{y_1}\frac{\rho UI}{\rho_\infty U_\infty I_w}dy\right) \quad (7)$$

for the heat flux distribution. Since the fluid dynamics data were taken under isothermal conditions, Equation (6) assumes $\rho = \rho_\infty(x)$, while equation (7) retains $\rho = \rho(x, y)$. (Although these variations were included in the analysis, numerically they were insignificant in all cases.)

The shear stress and heat flux contain both turbulent and laminar contributions and may be written as

$$\tau = -\rho_\infty\overline{u'v'} + \rho_\infty\nu\frac{\partial U}{\partial y} \quad (8)$$

and

$$\dot{q}'' = \rho C_p\overline{v't'} - k\frac{\partial T}{\partial y} \quad (9)$$

If the turbulent contributions are modeled using eddy diffusivities for momentum and heat, equations (8) and (9) become

$$\tau = \rho_\infty(\epsilon_m + \nu)\frac{\partial U}{\partial y} \quad (10)$$

and

$$\dot{q}'' = \rho C_p(\epsilon_H + \alpha)\frac{\partial T}{\partial y} \quad (11)$$

where

$$-\overline{u'v'} = \epsilon_m\frac{\partial U}{\partial y} \quad (12)$$

and

$$-\overline{v't'} = \epsilon_H\frac{\partial T}{\partial y} \quad (13)$$

The turbulent Prandtl number is defined as the ratio of the eddy diffusivities for momentum and heat

$$\mathrm{Pr}_T = \epsilon_m/\epsilon_H \quad (14)$$

In order to demonstrate the consistency of the Pr_T results calculated using the method outlined above with the Pr_T data obtained by Pimenta [3] from measurements of $\overline{u'v'}$, $\overline{v't'}$, and dT/dU, values of Pr_T were calculated using the present method for the unaccelerated, unblown $U_\infty = 27$ m/s case reported by Pimenta. Results of this calculation are compared in Fig. 9 with the measured values of Pr_T reported by Pimenta. The two methods give results which agree well in the inner region. The calculated data were very uncertain in the outer region where $\partial U/\partial y$ and $\partial T/\partial y$ aproach zero since the uncertainty in the numerical calculations of the derivatives increases dramatically as $y \to \delta$. Pimenta avoided this increase in uncertainty by measuring T and U sequentially with the same probe, without moving it, and by calculating dT/dU from the linear $(T_w - T)/(T_w - T_\infty)$ versus U/U_∞ plots discussed previously.

Calculated values of Pr_T for the four acceleration cases of this study are presented in Fig. 10. Also shown are the bounds on the smooth wall acceleration data reported by Kearney [17] for $K \leq 2.5 \times 10^{-6}$ and the calculated data for Pimenta's $K_r = 0$ case. The rough wall data lie at the lower edge of the smooth wall data range. It appears from the present data that the use of a constant $\mathrm{Pr}_T = 0.7$–0.8 would be a reasonable assumption in a prediction method modeling accelerated

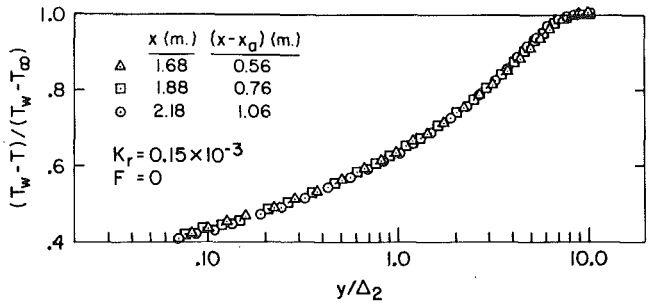

Fig. 7 Nondimensional mean temperature profiles illustrating similarity in flow direction

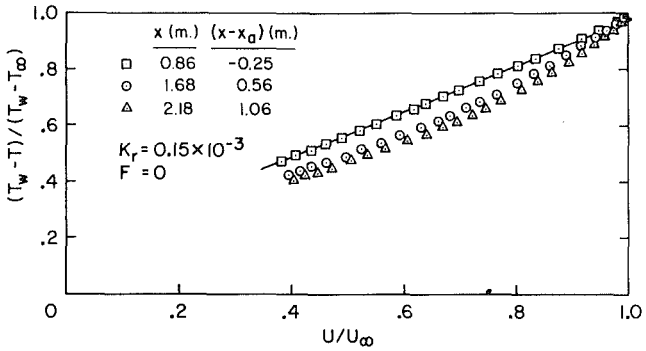

Fig. 8 Nondimensional mean temperature versus nondimensional mean velocity

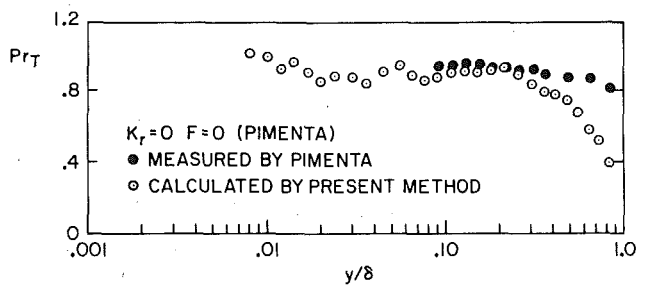

Fig. 9 Comparison of turbulent Prandtl numbers measured by Pimenta [3] and calculated by present method for $K_r = 0$

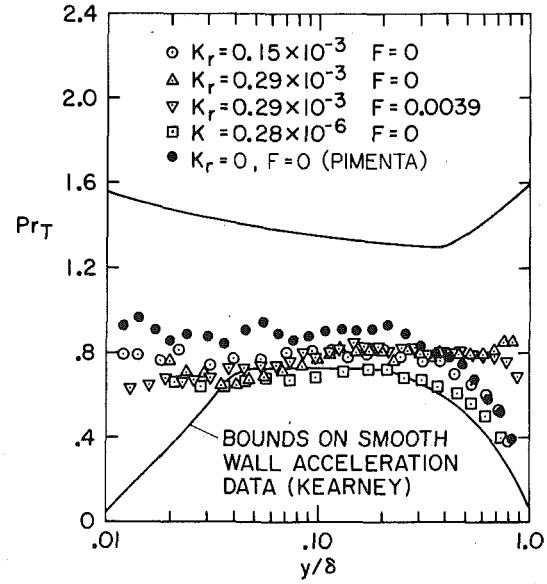

Fig. 10 Turbulent Prandtl number distributions for acceleration cases of the present study

Downloaded 20 Dec 2010 to 194.27.225.72. Redistribution subject to ASME license or copyright; see http://www.asme.org/terms/Terms_Use.cfm

flow over the present rough surface. Comparison of the present data with those of Pimenta indicates that for fully rough flow the turbulent Prandtl number may be decreased slightly by acceleration.

Calculated values of the turbulent heat flux $\overline{v't'}$ for the two unblown equilibrium runs are shown in Fig. 11 as $\overline{v't'}/U_\tau T_\tau$ versus y/δ. Comparison of these values with the unaccelerated data measured by Pimenta [3] and Orlando [18] on rough and smooth walls, respectively, indicates that the distribution of $\overline{v't'}/U_\tau T_\tau$ appears to be relatively insensitive to acceleration and surface condition, at least within the ranges of the data available and the estimated uncertainty of the data (±15 to 20 percent).

Summary and Conclusions

The statements and conclusions made below should be understood to apply to the incompressible turbulent flow of a fluid over a surface similar to the one used in this study and within the ranges of parameters and variables investigated.

- A fully rough turbulent boundary layer in a constant-K_r acceleration with $F \geq 0$ and constant develops toward an equilibrium state where $C_f/2$, δ_2, H, β, and G are all constant [10]. In that state, the profiles of mean velocity and mean temperature are similar in the flow direction, and roughness Reynolds number increases in the flow direction. Stanton numbers are greater at a given x-position or enthalpy thickness than for a zero pressure gradient. Stanton number may approach a constant value, though this cannot be verified satisfactorily due to the uncertainty in the data.
- Turbulent Prandtl numbers calculated using the data of the present experiment indicate an approximately constant value of 0.7–0.8 across the layer. These values are in the lower range of the data previously reported for smooth wall accelerated layers and are slightly below the values reported for the fully rough zero pressure gradient case.
- The profiles of $\overline{v't'}/U_\tau T_\tau$ calculated from the present accelerated data are in good agreement with those reported for smooth and rough wall zero pressure gradient layers. It thus appears that the turbulent heat flux profile, nondimensionalized in this manner, is relatively insensitive to surface condition and favorable pressure gradient.

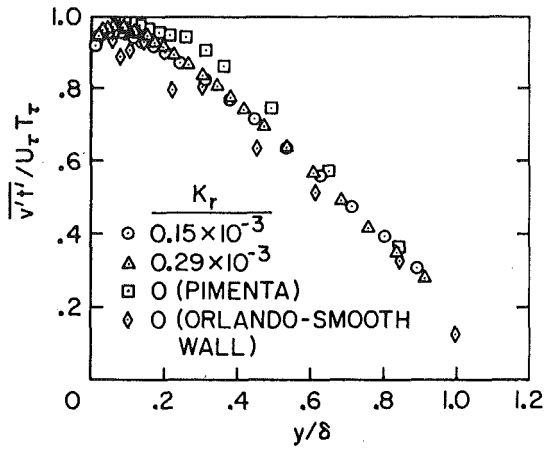

Fig. 11 Comparison of the unblown $\overline{v't'}/U_\tau T_\tau$ profiles for the equilibrium accelerations of the present study with unaccelerated profiles for smooth and rough wall layers

Acknowledgments

This research was made possible by support from the Office of Naval Research, Contract N00014-67-A-0112-0072. The experimental apparatus was constructed during an earlier contract from the Department of the Navy, Contract N00123-71-0-0372. The authors wish to thank Dr. W. H. Thielbahr, Mr. James Patton, and Dr. Ralph Roberts for their support.

The first author also gratefully acknowledges financial support from Sandia Laboratories during the research program.

References

1 Healzer, J. M., "The Turbulent Boundary Layer on a Rough, Porous Plate: Experimental Heat Transfer with Uniform Blowing," Ph.D. Dissertation, Stanford University, 1974. (Also Report HMT-18, Thermosciences Division, Dept. of Mech. Eng., Stanford University, 1974.)

2 Moffat, R. J., Healzer, J. M., and Kays, W. M., "Experimental Heat Transfer Behavior of a Turbulent Boundary Layer on a Rough Surface with Blowing," ASME JOURNAL OF HEAT TRANSFER, Vol. 100, No. 1, 1978, pp. 134–142.

3 Pimenta, M. M., "The Turbulent Boundary Layer: An Experimental Study of the Transport of Momentum and Heat with the Effect of Roughness," Ph.D. Dissertation, Stanford University, 1975. (Also Report HMT-21, Thermosciences Division, Dept. of Mech. Eng., Stanford University, 1975.)

4 Pimenta, M. M., Moffat, R. J., and Kays, W. M., "The Structure of a Boundary Layer on a Rough Wall with Blowing and Heat Transfer," ASME JOURNAL OF HEAT TRANSFER, Vol. 101, No. 2, 1979, pp. 193–198.

5 Nikuradse, J., "Stromungsgestze in rauhen Rohren," *VDI Forschungsheft,* No. 361, English Translation, NACA TM 1292, 1933.

6 Reshotko, M., Boldman, D. R., and Ehlers, R. C., "Heat Transfer in a 60° Half-Angle of Convergence Nozzle with Various Degrees of Roughness," NASA TN D-5887, 1970.

7 Banerian, G., and McKillop, A. A., "The Effects of Surface Roughness in Nozzles on Heat Transfer," *Proceedings of the Fifth International Heat Transfer Conference,* Vol. II, pp. 234–238, 1974.

8 Chen, K. K., "Compressible Turbulent Boundary-Layer Heat Transfer to Rough Surfaces in Pressure Gradient," *AIAA Journal,* Vol. 10, 1972, pp. 623–629.

9 Hodge, B. K., "Extended Mixing Length Hypothesis Applications to Transpired or Roughwall Compressible Boundary Layers," ASME Paper No. 78-HT-22, 1978.

10 Coleman, H. W., Moffat, R. J., and Kays, W. M., "The Accelerated Fully Rough Turbulent Boundary Layer," *Journal of Fluid Mechanics,* Vol. 82, Part 3, 1977, pp. 507–528.

11 Rotta, J. C., "Turbulent Boundary Layers in Incompressible Flow," *Progress in Aeronautical Sciences,* Vol. 2, pp. 1–219, Pergamon Press, 1962.

12 Coleman, H. W., "Momentum and Energy Transport in the Accelerated Fully Rough Turbulent Boundary Layer," Ph.D. Dissertation, Stanford University, 1976. (Also Report HMT-24, Thermosciences Division, Dept. of Mech. Eng., Stanford University, 1976.)

13 Kays, W. M. and Moffat, R. J., "The Behavior of Transpired Turbulent Boundary Layers," *Studies in Convection: Theory, Measurement and Applications,* Vol. 1, edited by B. E. Launder, Academic Press, New York, 1975, pp. 223–319.

14 Julien, H. L., Kays, W. M., and Moffat, R. J., "The Turbulent Layer on a Porous Plate: Experimental Study of the Effects of a Favorable Pressure Gradient," Report No. HMT-4, Thermosciences Division, Dept. of Mech. Eng., Stanford University, 1969.

15 Loyd, R. J., Moffat, R. J., and Kays, W. M., "The Turbulent Boundary Layer on a Porous Plate: An Experimental Study of the Fluid Dynamics with Strong Favorable Pressure Gradients and Blowing," Report No. HMT-13, Thermosciences Division, Dept. of Mech. Eng., Stanford University, 1970.

16 Coleman, H. W., and Hodge, B. K., "Conditions Which Prescribe the Evolution of Turbulent Flow Influenced by Roughness," AIAA Paper No. 79-1564, 1979.

17 Kearney, D. W., Moffat, R. J., and Kays, W. M., "The Turbulent Boundary Layer: Experimental Heat Transfer with Strong Favorable Pressure Gradients and Blowing," Report No. HMT-12, Thermosciences Division, Dept. of Mech. Eng., Stanford University, 1970.

18 Orlando, A. F., Moffat, R. J., and Kays, W. M., "Turbulent Transport of Heat and Momentum in a Boundary Layer Subject to Deceleration, Suction and Variable Wall Temperature," Report No. HMT-17, Thermosciences Division, Dept. of Mech. Eng., Stanford University, 1974.

Downloaded 20 Dec 2010 to 194.27.225.72. Redistribution subject to ASME license or copyright; see http://www.asme.org/terms/Terms_Use.cfm

Perturbation Solutions of Transient Heat Transfer to a Porous Medium from a Fluid Stream[1]

P.-C. Lu
Professor,
Department of Mechanical Engineering,
University of Nebraska,
Lincoln, Neb
Mem. ASME

Asymptotic behavior of the two-phase, thermal response of a porous medium, with a fluid throughflow, to a sudden change of the oncoming stream temperature is examined via four cases of perturbation solutions: (1) massive blowing, fast interphase (thermal) link, small conductivity, and small (thermal) interaction at the entrance, (2) moderate blowing, and fast interphase link, (3) massive blowing, moderate interphase link, and small interaction at the entrance, and (4) small conductivity, as well as weak interphase link. Schumann's classical, two-phase, and non-diffusive model is shown to be just the outer limit of Case (1). The "single-phase model" is derived. Associated boundary layers are displayed. Certain numerical trend reported in the literature is also explained.

Introduction

To complement the numerical studies reported by various authors [1–7] on the transient temperature response of a porous medium to a sudden change in temperature of the oncoming fluid, the present paper concentrates on the asymptotic behavior of the following system (which is explained in more detail in the next section).

$$\begin{cases} \mathrm{F}\dfrac{\partial^2\theta}{\partial\zeta^2} + \mathrm{FB}(\nu-\theta) = \dfrac{\partial\theta}{\partial\tau} & (1) \\ -g\dfrac{\partial\nu}{\partial\zeta} = \mathrm{B}(\nu-\theta) & (2) \\ \tau = 0 : \theta = 0 & (3) \\ \zeta = 0 : \nu - 1 = S(\theta-1) & (4) \\ gS(\theta-1) = \dfrac{\partial\theta}{\partial\zeta} & (5) \\ \zeta = 1 : \dfrac{\partial\theta}{\partial\zeta} + b\theta = 0 & (6) \end{cases}$$

where (in dimensionless terms) θ and ν are respectively the medium and fluid temperatures (above a certain reference value); ζ is the distance from the entrance; τ, the time; F, the Fourier number, B, the interphase Biot number; g, the mass flow rate; and where S and b, represent the thermal interaction at the bounding faces of the medium.

The asymptotic behavior of the governing system is exhibited through a number of perturbation solutions, singular and regular as the case may be ([8–10]).

Case 1 $\mathbf{B \gg 1, B/g \sim 0(1), BF \sim 0(1), Sg \sim 0(1)}$. Roughly speaking, in practical terms, this case represents the situation with massive blowing, strong interphase (thermal) link, small conductivity, and small (thermal) interaction at the entrance. The technique of singluar perturbation yields an outer limit which is exactly the classical Schumann model [1]. For the inner limit, it is found that isothermal boundary layers exist near the entrance and the exit, with thicknesses $\sim 0(1/\sqrt{\mathrm{B}})$.

Case 2 $\mathbf{B \gg 1, g \sim 0(1)}$. Here the interphase link is strong, but the blowing is moderate. The outer limit in the singular perturbation yields identical temperatures for the two phases, and thus renders support to the single-phase model treated in the literature [4–7]. In an attempt to improve the accuracy of the result based on the outer limit, it becomes possible to explain the numerical trend displayed in [2], which indicates that the fluid temperature deviates more from the single-phase solution at small time, while the bed temperature deviates more at large time. Finally, an investigation into the inner limit shows that a boundary layer of thickness $\sim 0(1/\mathrm{B})$, with an exponential fluid-temperature distribution, exists near the entrance. Thus, the composite limit [8–10] effectively displays a two-phase response.

Case 3 $\mathbf{g \gg 1, Sg \sim 0(1)}$. This regular case, which corresponds to the situation with massive blowing and weak interaction at the entrance, yields a series of terms representing conductive temperature distributions in the presence of heat generation (proportional to the temperature).

Case 4 $\mathbf{F \ll 1, B \ll 1}$. This regular case yields zeroth-order terms (with error $\sim 0(\mathrm{FB})$) showing a purely conductive temperature distribution in the bed, and a fluid temperature with an exponential character. For higher-order terms, equivalent heat generation shows up in the bed. In practice, the present case is typified by small conductivity and weak interphase link.

The Problem

Referring to Burch, et al. [2], it can be shown that the equations governing the evolution of the temperatures of the two mutually embedded phases in the form of a porous medium with a fluid through-flow are (see Nomenclature).

$$\begin{cases} \dfrac{\partial^2 T_m}{\partial x^2} + \dfrac{h_v}{K_m}(T_f - T_m) = \dfrac{1}{\alpha_m}\dfrac{\partial T_m}{\partial t} & (7) \\ -GC_f\dfrac{\partial T_f}{\partial x} = h_v(T_f - T_m) & (8) \end{cases}$$

The effective, volumetric, interphase, heat-transfer coefficient h_v, as defined in Bird, et al. [11], is in general related to the Reynolds number of the flow through the porous medium. Many other works in the literature ([12–13], for instance) also employ h_v in this fashion. However, the reader must be alerted to the possibility of building a volumetric heat-transfer coefficient upon heat-exchange per unit area of the interphase surface, with void fraction of the medium explicitly displayed in the formulation (see [1], or [14–16]).

The mass flux G, which sets up the convective mechanism in equation (8) is raised to a constant for $t \geq 0$ from zero (for $t < 0$). The initial condition to be investigated specifically is

$$t = 0 : T_m = T_i, \text{ a constant} \quad (9)$$

The boundary condition[2] for the porous medium at the exit face,

---

[1] Work performed under NSF Grant ENG78-04060.
Contributed by the Heat Transfer Division of THE AMERICAN SOCIETY OF MECHANICAL ENGINEERS for presentation at the Winter Annual Meeting, New York, NY, December 2–7, 1979. Revised manuscript received by the Heat Transfer Division February 14, 1980. Paper No. 79-WA/HT-44.

[2] Equations (9) and (10) reflect the fact that there is no flow for $t < 0$, and the bed is initially in thermal equilibrium with the stationary fluid filling it; for $t \geq 0$, fluid from a reservoir at T_{f_0} flows through the bed and exits (across a thermal boundary layer) into another reservoir still maintained at the initial temperature [2]. This situation can, of course, be modified to suit actual cases.

Copyright © 1981 by ASME
Downloaded 20 Dec 2010 to 194.27.225.72. Redistribution subject to ASME license or copyright; see http://www.asme.org/terms/Terms_Use.cfm

beyond which the fluid temperature T_i prevails, is

$$x = L: -K_m \frac{\partial T_m}{\partial x} = h(T_m - T_i) \tag{10}$$

At the entrance of the porous medium, there are two boundary conditions to be enforced:

$$x = 0: GC_f(T_{f_0} - T_f) = h_f(T_{f_0} - T_m) \tag{11}$$

$$-K_m \frac{\partial T_m}{\partial x} = h_f(T_{f_0} - T_m) \tag{12}$$

where condition (11) expresses the energy transfer (by convection) from the oncoming stream to the inlet face of the porous medium, and condition (12) represents that (by conduction) from the inlet face to the interior of the solid phase [2]. Clearly the thermal link[3] between the fluid and the solid at the entrance is represented by the heat transfer coefficient h_f; that at the exit, h; and that (interphase) in the range $0 < x < L, h_v$.

Obviously, the fluid in equation (8) is assumed to be incapable of storing energy or conducting heat. Thus, it is impossible to enforce an initial condition for the fluid temperature in the present investigation. The reader may notice later certain singularities in T_f (i.e., ν), which can always be traced back to the absence of a time-derivative term in equation (8), and a remedy of which is beyond the scope of the present investigation. (Essentially, a thermal front would move through the bed. Before the arrival of this front, the true initial ν prevails; after the arrival, the theoretically predicted ν-value takes over. The discontinuity, if any, at the front is the singularity being alluded to.)

Introducing dimensionless quantities, as explained in the Nomenclature, into equations (7–12), we have equations (1–6) quoted in the previous section.

Case 1 $\mathrm{B} \gg 1, \mathrm{B}/g \sim 0(1), \mathrm{BF} \sim 0(1), Sg \sim 0(1)$. In seeking solutions in the form of power series of 1/B for the first case examined in the present study, we set $\gamma = g/\mathrm{B} \sim 0(1), f = \mathrm{BF} \sim 0(1)$, and $\sigma = \mathrm{B}S \sim 0(1)$. Then, substituting the expansions

$$\theta = \theta^{(0)} + \theta^{(1)}/\mathrm{B} + \theta^{(2)}/\mathrm{B}^2 + \dots \tag{13}$$

$$\nu = \nu^{(0)} + \nu^{(1)}/\mathrm{B} + \nu^{(2)}/\mathrm{B}^2 + \dots \tag{14}$$

into equations (1–3), we have:[4]

$$\begin{cases} \dfrac{\partial \theta^{(0)}}{\partial \tau} = f(\nu^{(0)} - \theta^{(0)}) & (15) \\ -\gamma \dfrac{\partial \nu^{(0)}}{\partial \zeta} = \nu^{(0)} - \theta^{(0)} & (16) \\ \tau = 0: \theta^{(0)} = 0 & (17) \\ \zeta = 0: \nu^{(0)} = 1 & (18) \end{cases}$$

$$\begin{cases} \dfrac{\partial \theta^{(i)}}{\partial \tau} = f \dfrac{\partial^2 \theta^{(i-1)}}{\partial \zeta^2} + f(\nu^{(i)} - \theta^{(i)}), \; i = 1, 2, \dots & (19) \\ -\gamma \dfrac{\partial \nu^{(i)}}{\partial \zeta} = \nu^{(i)} - \theta^{(i)} & (20) \\ \tau = 0: \theta^{(i)} = 0 & (21) \\ \zeta = 0: \gamma \nu^{(i)} = \dfrac{\partial \theta^{(i-1)}}{\partial \zeta} & (22) \end{cases}$$

The solutions of the system, equations (15–18), are found [4, 17] to be

$$\theta^{(0)} = f \exp\left(-\frac{\zeta}{\gamma}\right) \int_0^\tau \exp(-fs) \cdot I_0\left(2\sqrt{\frac{f}{\gamma}\zeta s}\right) ds \tag{23}$$

$$\nu^{(0)} = \exp\left(-\frac{\zeta}{\gamma}\right)\left\{\exp(-f\tau) \cdot I_0\left(2\sqrt{\frac{f}{\gamma}\zeta\tau}\right) + f\int_0^\tau \exp(-fs) \cdot I_0\left(2\sqrt{\frac{f}{\gamma}\zeta s}\right) ds\right\} \tag{24}$$

where I_0 is the modified Bessel function of the first kind, of order zero. Equations (23) and (24) do not satisfy any boundary condition for θ since the ζ-derivative term of θ is lost on the way to equation (15). They cannot be of use near $\zeta = 0$ and 1, being outer limits of the singular perturbation and supposed to match with the corresponding inner limits according to the matching principle [8–10].

To investigate the behavior of θ near $\zeta = 0$, for large B, we magnify the neighborhood of $\zeta = 0$ by introducing $\zeta' = \sqrt{\mathrm{B}}\zeta$. Equations (1) and (2) become, on letting $\mathrm{B} \to \infty$ with ζ' fixed

$$\begin{cases} f \dfrac{\partial^2 \theta_{(0)}}{\partial \zeta'^2} + f(\nu_{(0)} - \theta_{(0)}) = \dfrac{\partial \theta_{(0)}}{\partial \tau} & (25) \\ -\gamma \dfrac{\partial \nu_{(0)}}{\partial \zeta'} = 0 & (26) \end{cases}$$

[3] Although h_v, h and h_f are under the influence of the common mass-flow rate as well as the thermal diffusivity of the bed, they can be made large or small independently of one another. For instance, h_v can be varied through the tortuosity of the bed; or, h_f (h) can be increased by augmenting heat transfer at the inlet (exit) face.

[4] The boundary condition for ν used here is a combination of equations (4) and (5) with $(\theta - 1)$ eliminated between them. Our preference for this is prompted by experience gained in Case 2.

Nomenclature

$a_2 = g/2$
$a_4 = b + g/2$
B = interphase Biot number, $h_v L^2/K_m$
$B' = \mathrm{B}/g$
$b = hL/K_m$
C = specific heat capacity, J/K · kg
F = Fourier number, $\alpha_m t^*/L^2$
$f = \mathrm{BF}$
G = mass flow rate per unit of flow passage area (mass flux), kg/s · m²
$g = LGC_f/K_m$
h = exit heat-transfer coefficient, W/m² · K
h_f = heat transfer coefficient at the entrance, W/m² · K
h_v = effective volumetric heat transfer coefficient between the two phases in the bed W/m³ · K
K = thermal conductivity, W/m · K
L = length of bed in the flow direction, m
$S = h_f/(GC_f)$
s = dummy variable of integration
T = temperature, K
T_{f_0} = temperature of the *entering* fluid stream, far ahead of the entrance, K
t = time, s
t^* = time of observation *around* which the phenomenon is being examined, s
x = coordinate in the flow direction originating from the entrance, m
α = thermal diffusivity, m²/s
$\gamma = g/\mathrm{B}$
$\nu = (T_f - T_i)/(T_{f_0} - T_i)$
ν_0' = zeroth-order term in an expansion of ν in Case 4
ν_1' = first order term in an expansion of ν in Case 4
$\sigma = \mathrm{B}S$
$\tilde{\sigma} = Sg$
$\tau = t/t^*$
$\tau' = \mathrm{F}\tau$
$\theta = (T_m - T_i)/(T_{f_0} - T_i)$
θ_0' = zeroth-order term in an expansion of θ in Case 4
θ_1' = first-order term in an expansion of θ in Case 4
$\zeta = x/L$
$\zeta' = \sqrt{\mathrm{B}}\zeta$
$\zeta'' = \mathrm{B}\zeta$

Superscripts

c = composite expansion, zeroth-order
(0) = zeroth-order term of an outer expansion
(1) = first-order term of an outer expansion

Subscripts

f = fluid stream
i = initial value
m = porous medium (solid bed)
0 = zeroth-order term in an expansion
1 = first-order term in an expansion
(0) = zeroth-order term in an inner expansion
(1) = first-order term in an inner expansion

Downloaded 20 Dec 2010 to 194.27.225.72. Redistribution subject to ASME license or copyright; see http://www.asme.org/terms/Terms_Use.cfm

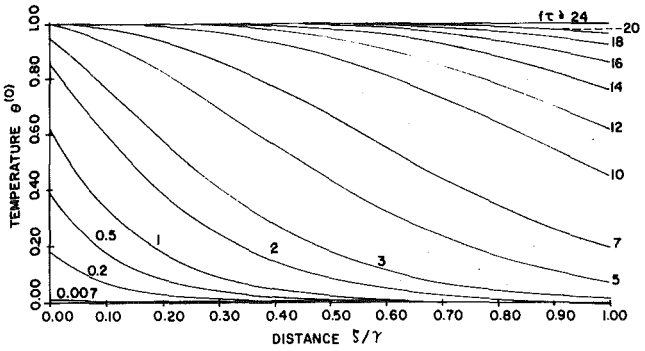

Fig. 1 Outer limit of the bed temperature, Case 1

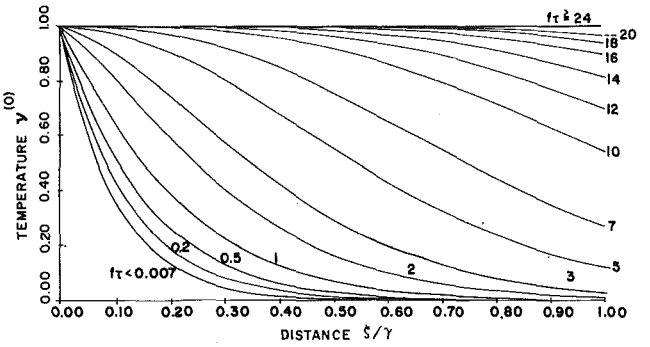

Fig. 2 Outer limit of the fluid temperature, Case 1

where $\theta_{(0)}$ and $\nu_{(0)}$ are the inner limits of θ and ν, respectively. The solutions of equations (25) and (26)

$$\nu_{(0)} = 1 \tag{27}$$

$$\theta_{(0)} = 1 - \exp(-f\tau) \tag{28}$$

satisfy the boundary conditions (4) and (5), the initial condition for $\theta_{(0)}$, and the matching principle [8–10] that $\theta_{(0)}$ approach as $\zeta' \to \infty$ the value of $\theta^{(0)}$ at $\zeta = 0$. Physically, they represent the temperature variations of the two phases in a thin boundary layer with a thickness of order $1/\sqrt{B}$. The layer is seen to be isothermal (but with different temperatures for the two phases); the bed temperature varies exponentially with time. Omitting details, we may also report that a similar boundary layer exists near $\zeta = 1$ across which $\nu^{(0)}(1, \tau)$ and $\theta^{(0)}(1, \tau)$ prevail.

In the above, we have clearly regained the classical Schumann model[5] [1] as a rational approximation for large B. The existence of the boundary layers actually enhances the already firm position of the Schumann model in applications.

Figures 1 and 2 show plots of $\theta^{(0)}$ and $\nu^{(0)}$, respectively.

Case 2 $\mathbf{B \gg 1, g \sim 0(1)}$. Substituting the expansions (13) and (14) into equations (1–6), we have for this case

$$\begin{cases} \mathrm{F}\dfrac{\partial^2\theta^{(0)}}{\partial\zeta^2} - \mathrm{F}g\dfrac{\partial\theta^{(0)}}{\partial\zeta} = \dfrac{\partial\theta^{(0)}}{\partial\tau} & (29) \\ \nu^{(0)} = \theta^{(0)} & (30) \\ \tau = 0: \theta^{(0)} = 0 & (31) \\ \zeta = 0: \dfrac{\partial\theta^{(0)}}{\partial\zeta} [= g(\nu^{(0)} - 1)] = g(\theta^{(0)} - 1) & (32) \\ \zeta = 1: \dfrac{\partial\theta^{(0)}}{\partial\zeta} + b\theta^{(0)} = 0 & (33) \end{cases}$$

$$\begin{cases} \mathrm{F}\dfrac{\partial^2\theta^{(i)}}{\partial\zeta^2} - \mathrm{F}g\dfrac{\partial\theta^{(i)}}{\partial\zeta} + \mathrm{F}g^2\dfrac{\partial^2\nu^{(i-1)}}{\partial\zeta^2} = \dfrac{\partial\theta^{(i)}}{\partial\tau} \quad i = 1, 2, \ldots \\ \nu^{(i)} = -g\dfrac{\partial\nu^{(i-1)}}{\partial\zeta} + \theta^{(i)} & (35) \\ \tau = 0: \theta^{(i)} = 0 & (36) \\ \zeta = 0: \dfrac{\partial\theta^{(i)}}{\partial\zeta} = g\left(\theta^{(i)} - g\dfrac{\partial\nu^{(i-1)}}{\partial\zeta}\right) & (37) \\ \zeta = 1: \dfrac{\partial\theta^{(i)}}{\partial\zeta} + b\theta^{(i)} = 0 & (38) \end{cases}$$

Here, the order of the governing system is reduced by 1 (see equations (30) and (35)). Thus, only one boundary condition can be enforced at $\zeta = 0$ for $\theta^{(i)}, i = 0, 1, 2, \ldots$. One is tempted here to enforce equation (5); but a more careful look into the matter suggests the linear combination of equations (4) and (5), with $(\theta - 1)$ eliminated:

$$\zeta = 0: \frac{\partial\theta}{\partial\zeta} = g(\nu - 1) \tag{39}$$

A brief explanation is given as follows: In the system, equations (1–6), equation (4) can, of course, by replaced by equation (39). Then, eliminating ν between equations (1) and (2), integrating the result from $\zeta = 0$ to 1, and employing our new boundary condition, equation (39), we have[6]

$$\frac{g}{\mathrm{B}}\left(\frac{\partial\theta}{\partial\tau} - \mathrm{F}\frac{\partial^2\theta}{\partial\zeta^2}\right) + \mathrm{F}g\theta + \int_0^\zeta \frac{\partial\theta(s,\tau)}{\partial\tau}\,ds - \mathrm{F}\frac{\partial\theta}{\partial\zeta} = \mathrm{F}g \tag{40}$$

This governing equation is to be solved subject to the remaining conditions, i.e., equations (3, 5) and (6).

Now, substituting equation (13) into equation (40) will lose the second-order derivative, and the accompanying ability to satisfy the boundary condition at $\zeta = 0$, i.e., equation (5). Differentiating this intermediate result with respect to ζ, we again have equations (29) and (34). But this differentiation calls for an extra boundary condition; and equation (39) is *naturally* the choice since it has already been used in deriving equation (40). Substituting equation (13) into equation (39), we have equations (32) and (37). To summarize, we see that, when one out of two boundary conditions at $\zeta = 0$ is to to selected, the natural choice is a certain linear combination of the two. Intuitively, this choice is also seen to be proper since the resulting outer expansion (valid far away from the entrance) is independent of the thermal-link parameter at the entrance, S. Furthermore, the steady solutions (exact) for θ and ν of equations (1, 2) and (4–6) have been rendered, by the author, into inner and outer expansions which fully substantiate the above choice of the boundary condition.

Concentrating on the zeroth-order terms only, we see that $\theta^{(0)}$ and $\nu^{(0)}$ are the outer limits in the singular perturbation; and there exists a boundary layer near $\zeta = 0$. Introducing $\zeta'' = \mathrm{B}\zeta$, we obtain, on letting $\mathrm{B} \to \infty$ with ζ'' fixed, the corresponding inner limits

$$\begin{cases} \dfrac{\partial^2\theta_{(0)}}{\partial\zeta''^2} = 0 & (41) \\ -g\dfrac{\partial\nu_{(0)}}{\partial\zeta''} = \nu_{(0)} - \theta_{(0)} & (42) \\ \zeta'' = 0: \dfrac{\partial\theta_{(0)}}{\partial\zeta''} = 0 & (43) \\ \nu_{(0)} = S(\theta_{(0)} - 1) + 1 & (44) \\ \zeta'' = \infty: \theta_{(0)} = \theta^{(0)}(0, \tau) & (45) \end{cases}$$

where the matching principle is again incurred.

The inner limits are easily obtained in detail as follows:[7]

[5] Actually, Schumann's formulation contains the time-derivative of ν. Modern authors chose to ignore this in interpreting his work, probably because of difficulty in justifying the retention of energy storage while omitting heat conduction in the fluid.

[6] This integro-differential formulation of the problem, which may serve as a basis for general numerical simulation, is not available in the literature as far as the author can determine.

[7] Note that no initial condition can be enforced on $\theta_{(0)}$; yet, the solution fits equation (3) automatically.

Downloaded 20 Dec 2010 to 194.27.225.72. Redistribution subject to ASME license or copyright; see http://www.asme.org/terms/Terms_Use.cfm

$$\theta_{(0)} = \theta^{(0)}(0,\tau) \tag{46}$$

$$\nu_{(0)} = (S-1)[\theta^{(0)}(0,\tau) - 1]\exp(-\zeta''/g) + \theta^{(0)}(0,\tau) \tag{47}$$

It is interesting to see that S plays a role only in the boundary layer.[8] The boundary layer is thus seen to be isothermal in bed temperature (which is time-dependent), but has the typical exponential (with respect to distance from the entrance) character as far as fluid temperature is concerned. The thickness of the boundary layer is, naturally, of order 1/B.

In the rest of the present section, we will study the structure of $\theta^{(0)}$ (and $\nu^{(0)}$) in more detail. First of all, equation (29) (together with equation (30)) substantiates the single-phase model, found so frequently in the literature [4–7], which *assumes* that the fluid and bed have identical temperatures. Secondly, numerical solutions for θ and ν available in [2] (for B = 5, b = 1, S = 0.4, and g = 1) show that ν is very close to $\nu^{(0)}$ (= $\theta^{(0)}$) for large time, and θ is rather close to $\theta^{(0)}$ for small time, but that θ is very much smaller than $\theta^{(0)}$ at large time, and ν is very much larger than $\nu^{(0)}$ (= $\theta^{(0)}$) at small time. (See Fig. 4 of [2]). This numerical trend can be explained by examining $\theta^{(1)}$ and $\nu^{(1)}$ in equations (34) and (35). At large time, equation (34) becomes

$$\frac{\partial^2\theta^{(1)}}{\partial\zeta^2} - g\frac{\partial\theta^{(1)}}{\partial\zeta} = -g^2\frac{\partial^2\nu^{(0)}}{\partial\zeta^2} = -g^2\frac{\partial^2\theta^{(0)}}{\partial\zeta^2}$$

For an estimation, we may neglect the first term on the lefthand side and obtain

$$\theta^{(1)} \sim g\frac{\partial\theta^{(0)}}{\partial\zeta} + \text{constant}$$

But, from equation (37), we have at $\zeta = 0$:

$$\frac{\partial\theta^{(1)}}{\partial\zeta} = g\theta^{(1)} - g^2\frac{\partial\theta^{(0)}}{\partial\zeta}$$

$$\sim g^2\frac{\partial\theta^{(0)}}{\partial\zeta} + g\times\text{constant} - g^2\frac{\partial\theta^{(0)}}{\partial\zeta}$$

$$\therefore \text{constant} \sim \frac{1}{g}\frac{\partial\theta^{(1)}}{\partial\zeta}\bigg|_{\zeta=0} \sim \frac{\partial^2\theta^{(0)}}{\partial\zeta^2}\bigg|_{\zeta=0}$$

$$\ll 0\left(\left|\frac{\partial\theta^{(0)}}{\partial\zeta}\right|'\right)$$

We can therefore ignore the constant of integration in our estimate of $\theta^{(1)}$ which is a measure of the deviation of $\theta^{(0)}$ from the true solution θ. Then, equation (35) yields

$$\nu^{(1)} = -g\frac{\partial\theta^{(0)}}{\partial\zeta} + \theta^{(1)} \sim 0$$

which indicates very small deviation of $\nu^{(0)}$ from ν. On the other hand, for small time, equation (34) yields with equation (36):

$$\theta^{(1)} \sim 0$$

which demonstrates that the deviation of $\theta^{(0)}$ from θ should be small. Then, equation (35) yields the small-time estimate

$$\nu^{(1)} \sim -g\frac{\partial\theta^{(0)}}{\partial\zeta}$$

The estimates for $\theta^{(1)}$ and $\nu^{(1)}$, (for large and small time, respectively) are also seen to be opposite in sign—another feature found in Fig. 4 of [2].

Equation (29) can be solved with the initial-boundary conditions by applying a finite Fourier transform [18]; the result is the same as quoted in [2] where the classical separation of variables is employed.

$$\theta^{(0)} = \tilde{\theta}^{(0)} - \exp\left[\frac{g}{2}\left(\zeta - \frac{g\tau'}{2}\right)\right]\sum_m \frac{\mathcal{F}(\eta_m)}{N_m} \times exp\,(-\eta_m{}^2\tau')\cdot[\eta_m\cos(\eta_m\zeta) + a_2\sin(\eta_m\zeta)] \tag{48}$$

where

$$\tilde{\theta}^{(0)} = 1 + D\exp(g\zeta)$$

with

$$D = -b/[(g+b)\exp(g)]$$

is the steady part of the solution; where η_m are the positive roots of (see Nomenclature for a_2 and a_4)

$$Q_1(\eta_m,a_2,a_4) = (\eta_m{}^2 - a_2a_4)\sin\eta_m - (a_4+a_2)\eta_m\cos\eta_m \tag{49}$$

$$= 0 \tag{50}$$

where

$$N_m = Q_2(\eta_m,a_2,a_4)$$

with

$$Q_2(\eta_m, a_2, a_4) = \frac{1}{2}\cdot\frac{(\eta_m{}^2 + a_2{}^2)[(\eta_m{}^2 + a_4{}^2) + a_4] + a_2(\eta_m{}^2 + a_4{}^2)}{(\eta_m{}^2 + a_4{}^2)} \tag{51}$$

and where

$$\mathcal{F}(\eta_m) = \int_0^1 [\exp(-g\zeta/2) + \mathrm{D}\exp(g\zeta/2)][\eta_m\cos(\eta_m\zeta) + a_2\sin(\eta_m\zeta)]d\zeta \tag{52}$$

The composite limits [8–10] ${\theta_0}^c$ ${\nu_0}^c$ can also be formed:

$${\theta_0}^c = \theta^{(0)} \tag{53}$$

$${\nu_0}^c = \nu^{(0)} - (S-1)[1-\theta^{(0)}(0,\tau)]\exp(-\mathrm{B}\zeta/g) \tag{54}$$

These limits are uniformly valid, to 0(1/B), and represent in effect a *two-phase* response, with dependence on B and S clearly exhibited. They are plotted in Fig. 3 for B = 5, S = 0.4, g = 1, and b = 0.2 to show the general trend.

Higher-order terms ($i \geq 1$), if needed, can be solved from equation (34) and conditions (36–38) by applying the same transform. Equation (35) then yields $\nu^{(i)}$ for $i \geq 1$.

Case 3 $g \gg 1$, $Sg \sim 0(1)$. The regular expansions

$$\theta = \theta_0 + \theta_1/g + \theta_2/g^2 + \ldots$$

$$\nu = \nu_0 + \nu_1/g + \nu_2/g^2 + \ldots$$

yield, on substituting into equations (1–6):

$$\left\{\begin{array}{l} \dfrac{\partial\nu_0}{\partial\zeta} = 0 \\ -\dfrac{\partial\nu_i}{\partial\zeta} = \mathrm{B}(\nu_{i-1} - \theta_{i-1}),\ i = 1, 2, \ldots \end{array}\right\} \tag{55}$$

$$\frac{\partial^2\theta_i}{\partial\zeta^2} + \mathrm{B}(\nu_i - \theta_i) = \frac{\partial\theta_i}{\partial\tau'},\ i = 0, 1, 2, \ldots \tag{56}$$

$$\tau = 0: \theta_i = 0,\ i = 0, 1, 2, \ldots \tag{57}$$

$$\zeta = 0: \nu_0 = 1$$

$$\nu_1 = \tilde{\sigma}(\theta_0 - 1) \tag{58}$$

$$\nu_i = \tilde{\sigma}\theta_{i-1}, i = 2, 3, \ldots$$

$$\left\{\begin{array}{l} \dfrac{\partial\theta_0}{\partial\zeta} - \tilde{\sigma}\theta_0 = -\tilde{\sigma} \\ \dfrac{\partial\theta_i}{\partial\zeta} - \tilde{\sigma}\theta_i = 0,\ i = 1, 2, \ldots \end{array}\right\} \tag{59}$$

$$\zeta = 1: \frac{\partial\theta_i}{\partial\zeta} + b\theta_i = 0,\ i = 0, 1, 2, \ldots \tag{60}$$

Thus, we have for the zeroth-order terms

$$\nu_0 = 1 \tag{61}$$

[8] This fact, the general form of the expansions, and the matching have also been checked against the (exact) steady solutions.

Downloaded 20 Dec 2010 to 194.27.225.72. Redistribution subject to ASME license or copyright; see http://www.asme.org/terms/Terms_Use.cfm

$$\theta_0 = \tilde{\theta}_0 - \sum_m \frac{\mathcal{G}(\tilde{\eta}_m)}{\mathcal{N}_m} \times \exp\left[-(\tilde{\eta}_m{}^2 + \mathrm{B})\,\tau'\right][\eta_m \cos(\tilde{\eta}_m\zeta) + \tilde{\sigma}\sin(\tilde{\eta}_m\zeta)] \quad (62)$$

where

$$\tilde{\theta}_0 = 1 - c[(\sqrt{\mathrm{B}} + \tilde{\sigma})\exp(\sqrt{\mathrm{B}}\zeta) - (\sqrt{\mathrm{B}} - \tilde{\sigma})\exp(-\sqrt{\mathrm{B}}\zeta)]$$

with

$$c = b/[(\sqrt{\mathrm{B}} + \tilde{\sigma})(\sqrt{\mathrm{B}} + b)\exp(\sqrt{\mathrm{B}}) - (\sqrt{\mathrm{B}} - \tilde{\sigma})(\sqrt{\mathrm{B}} - b)\exp(-\sqrt{\mathrm{B}})]$$

where $\tilde{\eta}_m$ are the positive roots of

$$Q_1(\tilde{\eta}_m, \tilde{\sigma}, b) = 0$$

with Q_1 defined by equation (49); where

$$\mathcal{G}(\tilde{\eta}_m) = \int_0^1 \tilde{\theta}_0[\tilde{\eta}_m \cos(\tilde{\eta}_m\zeta) + \tilde{\sigma}\sin(\tilde{\eta}_m\zeta)]d\zeta$$

and where

$$\mathcal{N}_m = \mathrm{Q}_2(\tilde{\eta}_m, \tilde{\sigma}, b)$$

with Q_2 defined by equation (51). In physical terms, θ_0 is seen to be a conductive temperature distribution in a solid with heat generation ($\propto 1 - \theta_0$).

In terms of θ_0, we also obtain

$$\nu_1 = \mathrm{B}\int_0^\zeta \theta_0(s,\tau')ds - \mathrm{B}\zeta + \tilde{\sigma}[1 - \theta_0(0,\tau')] \quad (63)$$

The higher-order terms can be obtained in the same fashion, applying the same transform.

Case 4 $\mathbf{F \ll 1, B \ll 1}$. For this case, regular perturbations

$$\theta = \theta'_0 + \theta'_1(\mathrm{BF}) + \theta'_2(\mathrm{BF})^2 + \ldots$$
$$\nu = \nu'_0 + \nu'_1(\mathrm{BF}) + \nu'_2(\mathrm{BF})^2 + \ldots$$

give rise to the following systems:

$$\mathrm{F}\frac{\partial^2\theta'_0}{\partial\zeta^2} = \frac{\partial\theta'_0}{\partial\tau} \quad (64)$$

$$-g\frac{\partial\nu'_0}{\partial\zeta} = \mathrm{B}(\nu'_0 - \theta'_0) \quad (65)$$

$$\tau = 0: \theta'_0 = 0 \quad (66)$$

$$\zeta = 0: 1 - \nu'_0 = S(1 - \theta'_0) \quad (67)$$

$$\frac{\partial\theta'_0}{\partial\zeta} - gS\theta'_0 = -gS \quad (68)$$

$$\zeta = 1: \frac{\partial\theta'_0}{\partial\zeta} + b\theta'_0 = 0 \quad (69)$$

$$F\frac{\partial^2\theta'_i}{\partial\zeta^2} + (\nu'_{i-1} - \theta'_{i-1}) = \frac{\partial\theta'_i}{\partial\tau}, \; i = 1, 2, \ldots \quad (70)$$

$$-g\frac{\partial\nu'_i}{\partial\zeta} = \mathrm{B}(\nu'_i - \theta'_1) \quad (71)$$

$$\tau = 0: \theta'_i = 0 \quad (72)$$

$$\zeta = 0: \nu'_i = S\theta'_i \quad (73)$$

$$\frac{\partial\theta'_i}{\partial\zeta} - gS\theta'_i = 0 \quad (74)$$

$$\zeta = 1: \frac{\partial\theta'_i}{\partial\zeta} + b\theta'_i = 0 \quad (75)$$

Note that the error for each perturbation is 0(BF), not 0(B) or 0(F). More precisely, this is the case in which $\mathrm{BF} \ll 1$.

Physically, the zeroth-order solutions indicate a purely conductive temperature distribution in the bed, and an exponential temperature distribution for the fluid. For higher order terms, equivalent heat generation shows up in the bed.

To be specific, we have

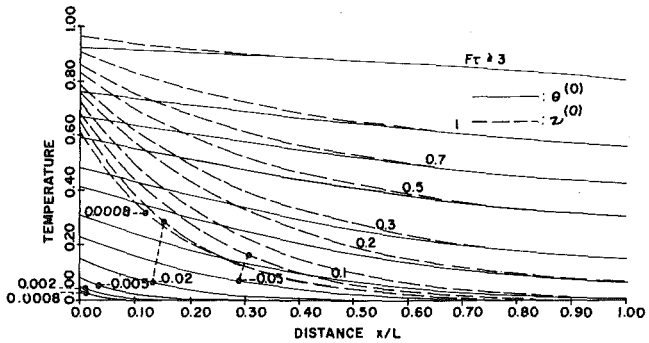

Fig. 3 *Composite limits, Case 2, with* $B = 5$, $S = 0.4$, $g = 1$ *and* $b = 0.2$ *(The solid curves are valid for all values of* B *and* S*.)*

$$\theta'_0 = c'\left(1 - \frac{b\zeta}{b+1}\right) - \sum_m \frac{\mathcal{H}(\eta'_m)}{\mathcal{N}'_m} \times \exp(-\eta'_m{}^2\tau')[\eta'_m \cos(\eta'_m\zeta) + \tilde{\sigma}\sin(\eta'_m\zeta)] \quad (76)$$

where

$$c' = \tilde{\sigma}(b+1)/[b(\tilde{\sigma}+1) + \tilde{\sigma}]$$

where η'_m are the positive roots of

$$Q_1(\eta'_m, \tilde{\sigma}, b) = 0$$

with Q_1 defined by equation (49); where

$$\mathcal{N}'_m = Q_2(\eta'_m, \tilde{\sigma}, b)$$

with Q_2 defined by equation (51); and where

$$\mathcal{H}(\eta'_m) = \int_0^1 c'\left(1 - \frac{b\zeta}{b+1}\right)[\eta'_m \cos(\eta'_m\zeta) + \tilde{\sigma}\sin(\eta'_m\zeta)]d\zeta$$

We also have

$$\nu'_0 = \mathrm{B}'\exp(-\mathrm{B}'\zeta)\int_0^\zeta \exp(\mathrm{B}s)\theta'_0(s,\tau)ds + \{1 - S[1 - \theta'_0(0,\tau')]\}\exp(-\mathrm{B}'\zeta) \quad (77)$$

Concluding Remarks

Perturbation approaches to four practical cases are outlined in some detail, with representative numerical results included for two of the cases.

To investigate the possible singularity near the start of temperature change for the fluid, it is seen that the energy storage (and heat conduction) in the fluid stream must be considered.

Although we chose to use such vivid expressions as "massive blowing" and the like in the discussion, we always mean that the corresponding dimensionless parameter is large (e.g., "massive blowing" $\rightarrow g \gg 1 \rightarrow G \gg K_m/LC_f$) or small.

References

1 Schumann, T. E. W., "Heat Transfer: Liquid Flowing through a Porous Prism" *Journal of Franklin Institute*, Vol. 208, 1929, pp. 405–416.

2 Burch, D. M., Allen, R. W., and Peavy, B. A., "Transient Temperature Distributions within Porous Slabs Subjected to Sudden Transpiration Heating," ASME JOURNAL OF HEAT TRANSFER, Vol. 98, 1976, pp. 221–225.

3 Furnas, , C. C., "Heat Transfer from a Bed of Broken Solids," *Transactions of the American Institute of Chemical Engineers*, Vol. 24, 1929, pp. 142–169.

4 Riaz, M., "Analytical Solutions for Single- and Two-phase Models of Packed-Bed Thermal Storage Systems," ASME JOURNAL OF HEAT TRANSFER, Vol. 99, 1977, pp. 489–492.

5 Jefferson, C. P., "Prediction of Breakthrough Curves in Packed Beds," *AIChE Journal*, Vol. 18, 1972, pp. 409–416.

6 Vortmeyer, D., and Schaeffer, R. J., "Equivalence of One- and Two-phase Models for Heat Transfer Processes in Packed Beds: One Dimensional Theory," *Chemical Engineering Sciences*, Vol. 29, 1974, pp. 483–491.

7 Riaz, M., "Transient Analysis of Pakced-Bed Thermal Storage Systems," *Solar Energy*, Vol. 21, 1978, pp. 123–128.

8 Van Dyke, M., *Perturbation Methods in Fluid Mechanics*, Academic Press, New York, 1964.

Downloaded 20 Dec 2010 to 194.27.225.72. Redistribution subject to ASME license or copyright; see http://www.asme.org/terms/Terms_Use.cfm

9 Cole, J. D. *Perturbation Methods in Applied Mathematics,* Blaisdell, Waltham, Mass., 1968.
10 Nayfeh, A. H., *Perturbation Methods,* John Wiley, New York, 1973.
11 Bird, R. B., Stewart, W. E. , and Lightfoot, E. N., *Transport Phenomena,* §13.4. John Wiley, New York, 1960.
12 Koh, J. C. Y., and Colony, R., "Analysis of Cooling Effectiveness for Porous Material in a Cooling Passage," ASME JOURNAL OF HEAT TRANSFER, Vol. 96, pp. 324–330.
13 Koh, J. C. Y., and Benson, B. A., "A Summary of Research on Fluid Flow and Heat Transfer in Porous Media at Boeing," *Workshop on Heat and Mass Transfer in Porous Media,* Case Western Reserve University, Cleveland, 1975, pp. 103–152.
14 Margolis, S. B., "Anharmonic Analysis of Time-dependent Packed Bed Thermocline," *Quarterly of Applied Mathematics,* Vol. 36, 1978, pp. 97–114.
15 Margolis, S. B., "An Analytical Solution for the Multidimensional Degradation of a Packed Bed Therymocline," *Journal of Franklin Institute,* Vol. 307, 1979, pp. 39–58.
16 Margolis, S. B., "Thermocline Degradation in a Packed Bed Thermal Storage Tank," ASME JOURNAL HEAT TRANSFER, Vol. 100, 1978, pp. 371–374.
17 Hansen, H., *Warmeubertragung in Gegenstrom, Gleichstrom und Kreuzstrom,* Springer-Verlag, Berlin, 1950.
18 Roettinger, I., "A Generalization of the Finite Fourier Transformation and Applications," *Quarterly of Applied Mathematics,* Vol. 5, 1947, pp. 298–319.

Downloaded 20 Dec 2010 to 194.27.225.72. Redistribution subject to ASME license or copyright; see http://www.asme.org/terms/Terms_Use.cfm

An Exact Solution of the Sublimation Problem in a Porous Medium

Sui Lin

Department of Mechanical Engineering,
Concordia University,
Montreal, Quebec, Canada H3G 1M8

Sublimation problem with coupled heat and mass transfer taking place in a porous half-space is defined and exact solutions for temperature and moisture distributions as well as the position of the moving sublimation front are obtained. The condition for the limitation of the sublimation process is also determined.

1 Introduction

Sublimation of frozen moisture in a porous medium has wide applications in separation processes, food technology, heat and moisture migration in soils and grounds, etc. The processes of heat and mass transfer in a porous medium are affected by both the temperature and moisture concentration gradients. An increase in the temperature above the sublimation point of moisture builds a moving sublimation front in the porous medium. The location of the moving front is unknown and has to be determined as a part of the solution. The coupled heat and mass transfer problems with moving phase front are nonlinear and solutions involve considerable mathematical difficulties. Exact solutions of such problems are limited to only a few idealized situations.

Mathematical formulation of the heat and mass transfer in capillary porous bodies has been established by Luikov [1]. For solving the problem of evaporation of liquid moisture from a porous medium, Gupta [2] made an assumption that the effect of the temperature gradient on the mass transfer is small and may be neglected. His approximate solution of the problem includes the effect of the moisture variation on the heat transfer. An exact solution of the same problem described by Gupta [2] was later given by Cho [3]. Another exact solution of the problem without Gupta's assumption and with two more complicated models was presented by Mikhailov [4]. For the problem of freezing (desublimation) of humid porous half-space, Mikhailov also presented an exact solution [5].

In the following, sublimation of frozen moisture in a porous medium will be studied. An analytical model of the sublimation process taking place in a porous half-space is defined and exact solutions for temperature and moisture distributions as well as the position of the moving sublimation front are obtained.

2 Statement of the Problem

We consider a rigid solid porous half-space containing uniformly frozen moisture. The porous body exists in an environment having a very low pressure, so that there is practically only the vapour pressure of the moisture acting on the frozen phase. It is therefore assumed that, during the sublimation process, the vapor pressure acting on the frozen phase is equal to the environmental pressure which remains unchanged. Under this assumption, the sublimation process will take place at a fixed sublimation temperature corresponding to the vapor pressure acting on the frozen phase.

For the purpose of formulation of the sublimation problem, the following assumptions are made:

1 The vapor pressure of the moisture in the sublimation process is very low so that the vapor can be considered as an ideal gas.

2 The frozen moisture is uniformly distributed in the porous half-space which is initially at a uniform molar concentration of the moisture, $C_{m,0}$. For the purpose of simplicity, the value of $C_{m,0}$ is assumed to be greater than the value of the molar concentration of the vapor at the sublimation state, p_v/R_0T_v, where p_v and T_v are the vapor pressure acting on the frozen phase and the corresponding sublimation temperature respectively, and R_0 is the universal gas constant.

3 The frozen humid body is initially at a uniform temperature T_0, which is lower than the sublimation temperature T_v. The sublimation process takes place when the temperature of the frozen body reaches the sublimation temperature.

4 The porous body is sublimated by maintaining the surface at $x = 0$ at a constant molar concentration of the moisture, $C_{m,s}$, which is lower than the initial concentration $C_{m,0}$, and at a constant temperature T_s, which is higher than the sublimation temperature T_v.

5 In the frozen region, $s(\tau) < x < \infty$, there is no moisture movement, where $x = s(\tau)$ locates the sublimation front. In the vapor region, $0 < x < s(\tau)$, there are heat and moisture flows.

6 The convective terms in the vapor region are small and may be neglected.

7 The thermophysical properties of each phase remain constant, but may differ for different phases.

8 The Soret effect, or the thermal diffusion, gives rise to a mass flux which is normally very small relative to the normal Fickian flux, and may be neglected.

The sublimation process can be presented by the following differential equations.

$$\frac{\partial T_1(x,\tau)}{\partial \tau} = a_1 \frac{\partial^2 T_1(x,\tau)}{\partial x^2}, \quad s(\tau) < x < \infty \tag{1}$$

$$\frac{\partial T_2(x,\tau)}{\partial \tau} = a_2 \frac{\partial^2 T_2(x,\tau)}{\partial x^2}, \quad 0 < x < s(\tau) \tag{2}$$

$$\frac{\partial C_m(x,\tau)}{\partial \tau} = a_m \frac{\partial^2 C_m(x,\tau)}{\partial x^2}, \quad 0 < x < s(\tau) \tag{3}$$

where a_1 and a_2 are the volume averaged thermal diffusivities in the frozen and vapor regions, respectively, and a_m is the volume averaged mass diffusivity of the vapor moisture in the porous body. For evaluation of the values of a_1, a_2 and a_m, the method described by Slattery [6] may be used.

The initial and boundary conditions can be described as

$$T_1(x,0) = T_1(\infty,\tau) = T_0 \tag{4}$$

$$T_2(0,\tau) = T_s \tag{5}$$

$$C_m(0,\tau) = C_{m,s} \tag{6}$$

On the sublimation front, there exists an equality between the temperatures,

$$T_1(s,\tau) = T_2(s,\tau) = T_v \tag{7}$$

The heat and moisture mass balance at the sublimation front can be expressed as

$$-k_2 \frac{\partial T_2(s,\tau)}{\partial x} + k_1 \frac{\partial T_2(s,\tau)}{\partial x} = C_{m,0} M_m L \frac{ds(\tau)}{d\tau} \tag{8}$$

$$a_m \frac{\partial C_m(s,\tau)}{\partial x} = [C_{m,0} - C_m(s,\tau)] \frac{ds(\tau)}{d\tau} \tag{9}$$

Contributed by the Heat Transfer Division for publication in the JOURNAL OF HEAT TRANSFER Manuscript received by the Heat Transfer Division April 28, 1980.

Copyright © 1981 by ASME

Downloaded 20 Dec 2010 to 194.27.225.72. Redistribution subject to ASME license or copyright; see http://www.asme.org/terms/Terms_Use.cfm

3 Solution of the Problem

The system of equations (1, 2, 4, 5, 7) and (8), describing the temperature distributions in the frozen and vapor regions in the sublimation process in a porous medium is the same as that describing the temperature distributions in the solid and liquid regions in a melting process for a pure substance. Therefore, Neumann's solution [7] can be used to obtain the temperature distributions. The solution of equation (1) which satisfies the initial and boundary conditions (4) and (7) can be obtained as

$$T_1(x,\tau) = T_0 + \frac{T_v - T_0}{\text{erfc}\,(\sqrt{a_2/a_1}\lambda)}\,\text{erfc}\left(\frac{x}{2\sqrt{a_1\tau}}\right) \tag{10}$$

where λ is a dimensionless constant having the following relation

$$\lambda = \frac{s(\tau)}{2\sqrt{a_2\tau}} \tag{11}$$

The solution of equation (2) which satisfies the boundary conditons (5) and (7) is expressed as

$$T_2(x,\tau) = T_s - \frac{T_s - T_v}{\text{erf}\,(\lambda)}\,\text{erf}\left(\frac{x}{2\sqrt{a_2\tau}}\right) \tag{12}$$

Substituting equations (10–12) into equation (8), the constant λ is determined by

$$\frac{k_2}{k_1}\sqrt{\frac{a_1}{a_2}}\left(\frac{T_s - T_v}{T_v - T_0}\right)\frac{\exp(-\lambda^2)}{\text{erf}\,(\lambda)}\,\frac{-\exp[(-a_2/a_1)\lambda^2]}{\text{erfc}\,(\sqrt{a_2/a_1}\lambda)} = \frac{\sqrt{\pi}\,a_1 C_{m,0} M_m L}{k_1(T_v - T_0)}\sqrt{\frac{a_2}{a_1}}\lambda \tag{13}$$

The solution of equation (3) is chosen in the form

$$C_m(x,\tau) = A + B\,\text{erf}\left(\frac{x}{2\sqrt{a_m\tau}}\right) \tag{14}$$

where A and B are the constants of integration, which can be determined by making use of the boundary conditons (6) and (9) as follows.

$$A = C_{m,s} \tag{15}$$

and

$$B = \frac{\sqrt{\pi}\lambda\,(C_{m,0} - C_{m,s})}{\sqrt{a_m/a_2}\exp[(-a_2/a_m)\lambda^2] + \sqrt{\pi}\lambda\,\text{erf}\,(\sqrt{a_2/a_m}\lambda)} \tag{16}$$

Substituting equations (15) and (16) into equation (14), the distribution of the molar concentration of the moisture is given by

$$C_m(x,\tau) = C_{m,s} + \frac{\sqrt{\pi}\lambda\,(C_{m,0} - C_{m,s})}{\sqrt{a_m/a_2}\exp[(-a_2/a_m)\lambda^2] + \sqrt{\pi}\lambda\,\text{erf}\,(\sqrt{a_2/a_m}\lambda)} \times \text{erf}\left(\frac{x}{2\sqrt{a_m\tau}}\right) \tag{17}$$

The solution of the molar concentration in the vapor region for the sublimation process, equation (17), has its limitation that the molar concentration of the vapor at $x = s$ must not exceed the value of p_v/R_0T_v.

Let

$$C_{m,max} = \frac{P_v}{R_0 T_v} \tag{18}$$

and

$$C = \frac{C_{m,0} - C_{m,\max}}{C_{m,\max} - C_{m,s}} \tag{19}$$

The condition for the limitation of the sublimation process can then be obtained from equation (17) by putting $x = s$ and $C_m(s,\tau) \leqq C_{m,max}$:

$$C \leqq \frac{1}{\sqrt{\pi}\alpha\exp(\alpha^2)\,\text{erf}\,(\alpha)} \tag{20}$$

where

$$\alpha = \lambda\sqrt{\frac{a_2}{a_m}} \tag{21}$$

For the purpose of discussion of the analytical results, the following dimensionless parameters are introduced.

$$U_1 = \frac{T_1 - T_0}{T_v - T_0} \tag{22}$$

$$U_2 = \frac{T_2 - T_v}{T_s - T_v} \tag{23}$$

$$\theta = \frac{C_m - C_{m,s}}{C_{m,0} - C_{m,s}} \tag{24}$$

$$\eta = \frac{x}{2\sqrt{a_2\tau}} \tag{25}$$

$$a_{21} = \frac{a_2}{a_1} \tag{26}$$

$$\text{Lu} = \frac{a_m}{a_2} \tag{27}$$

$$\nu = \frac{a_2 C_{m,0} M_m L}{k_2(T_s - T_v)} \tag{28}$$

$$KT = \frac{k_1(T_v - T_0)}{k_2(T_s - T_v)} \tag{29}$$

Then equations (10, 12, 13) and (17) can be written in the dimensionless forms as follows:

$$U_1 = \frac{\text{erfc}\,(\sqrt{a_{21}}\eta)}{\text{erfc}\,(\sqrt{a_{21}}\lambda)} \tag{30}$$

Nomenclature

A,B = constants of integration
a = thermal diffusivity
a_m = mass diffusivity
a_{21} = dimensionless thermal diffusivity defined by equation (26)
C = dimensionless molar concentration defined by equation (19)
C_m = molar concentration of vapor moisture
erf( ) = error function
erfc( ) = complimentary error function
exp( ) = exponential function
k = thermal conductivity
KT = dimensionless heat flux defined by equation (29)
L = latent heat of sublimation
Lu = Luikov number defined by equation (27)
M = molecular mass
p = vapor pressure
p_v = total pressure, or vapor pressure of moisture acting on the frozen phase
R_0 = universal gas constant
$s(\tau)$ = position of sublimation front
T = temperature
T_v = sublimation temperature
U_1 = dimensionless temperature defined by equation (22)
U_2 = dimensionless temperature defined by equation (23)
x = space coordinate
η = dimensionless variable defined by equation (25)
θ = dimensionless molar concentration defined by equation (24)
λ = dimensionless constant expressed by equation (11)
ν = dimensionless latent heat of sublimation defined by equation (28)
τ = time

Subscripts

0 = initial condition in frozen region
1 = frozen region, $s(\tau) < x < \infty$
2 = vapor region, $0 < x < s(\tau)$
m = moisture
s = at surface $x = 0$

Downloaded 20 Dec 2010 to 194.27.225.72. Redistribution subject to ASME license or copyright; see http://www.asme.org/terms/Terms_Use.cfm

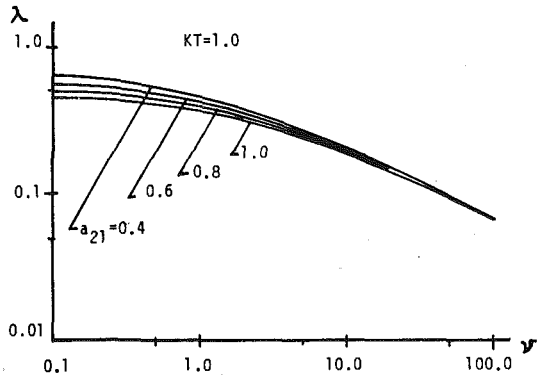

Fig. 1 Dimensionless constant λ as a function of dimensionless latent heat of sublimation ν with dimensionless thermal diffusivity a_{21} as a parameter and $KT = 1.0$

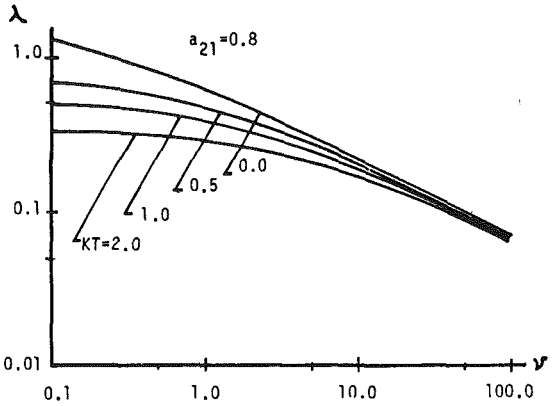

Fig. 2 Dimensionless constant λ as a function of dimensionless latent heat of sublimation ν with dimensionless heat flux KT as a parameter and a_{21} = 0.8

$$U_2 = 1 - \frac{\text{erf}(\eta)}{\text{erf}(\lambda)} \tag{31}$$

$$\frac{\exp(-\lambda^2)}{\text{erf}(\lambda)} - \frac{\sqrt{a_{21}}\,KT\exp(-a_{21}\lambda^2)}{\text{erfc}(\sqrt{a_{21}}\lambda)} = \sqrt{\pi}\,\nu\,\lambda \tag{32}$$

$$\theta = \frac{\sqrt{\pi}\,\lambda\,\text{erf}(\eta/\sqrt{\text{Lu}})}{\sqrt{\text{Lu}}\exp(-\lambda^2/\text{Lu}) + \sqrt{\pi}\,\lambda\,\text{erf}(\lambda/\sqrt{\text{Lu}})} \tag{33}$$

4 Discussion and Conclusions

From equation (11), it can be seen that the motion of the sublimation front is proportional to the constant λ which can be determined by equation (13). The higher the value of λ, the faster is the movement of the sublimation front. Figures 1 and 2 show that λ is a function of the dimensionless latent heat of sublimation, ν, with a_{21} and KT as parameters, respectively. A larger latent heat of sublimation, ν, yields smaller λ and thus slower sublimation. Figure 1 shows the effect of the ratio of the thermal diffusivity in the vapor region to that in the frozen region, a_{21}, on the sublimation speed; smaller a_{21} results in faster sublimation. Figure 2 indicates the effect of KT on the sublimation speed. KT represents the ratio of the steady heat flux in the frozen region to that in the vapor region with the same heat conduct distance. It is shown that the lower the value of KT, the faster is the sublimation. The top curve in Fig. 2 with $KT = 0$ represents the case of that where the initial temperature in the frozen region is equal to the sublimation temperature.

By making use of dimensionless representation, the temperature distributions in the vapor and frozen region, U_2 and U_1, and the molar concentration of the moisture in the vapor region, θ, are only functions of the combined coordinate η. The dimensionless representation results also significantly in a reduction of the number of parameters. When the value of the constant λ is determined by equation (13), or from Fig. 1 or 2, U_2 is only a function of η, U_1 is a function of η with one parameter a_{21}, and θ is a function of η with Lu as a parameter.

As an illustration, the distribution of the dimensionless temperatures and the dimensionless molar concentration of the moisture vapor are plotted in Fig. 3 with λ = 0.4. For the fixed value of λ, the temperature distribution in the vapor region, U_2, can be presented by only one curve as shown in Fig. 3. The effect of the ratio of the thermal diffusivity in the vapor region to that in the frozen region, a_{21}, on the temperature distribution in the frozen region, U_1, is also shown in Fig. 3. We consider a high value of a_{21} resulting from a small value of a_1. It is expected that the smaller the value of the thermal diffusivity, a_1, the slower will heat diffuse into the frozen region, or the more will heat be absorbed by the material in the frozen region. Therefore, the smaller the value of a_1, or the higher the value of a_{21} the steeper is the temperature profile in the frozen region, as shown in Fig. 3. We consider now a constant heat flux being supplied at the phase interface from the vapor region. A steeper temperature profile in the frozen region at the phase interface transmits more heat away from the interface into the frozen region. Therefore, less heat is available for sublimation of the frozen moisture. Hence, it can be concluded that an increase of the value of a_{21} results in a decrease of the sublimation speed, as shown in Fig. 1.

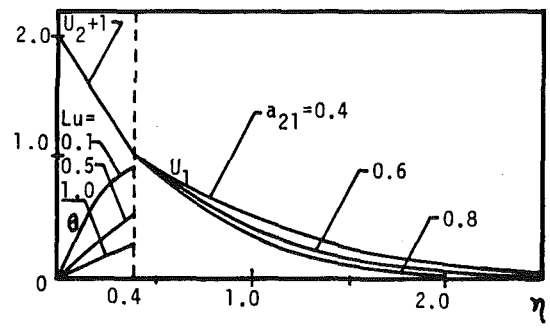

Fig. 3 Dimensionless temperatures, U_1 and U_2, and dimensionless molar concentration θ as functions of dimensionless variable η with λ = 0.4

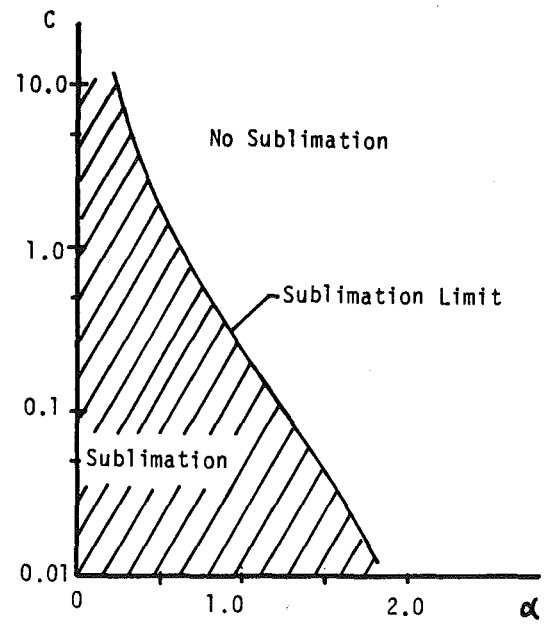

Fig. 4 Condition for the limitation of the sublimation process.

The dimensionless molar concentration of the moisture in the vapor region, θ, described by equation (33), has one parameter Lu for a fixed value of λ. The Luikov number, Lu, represents the ratio of the moisture diffusivity to the thermal diffusivity in the vapor region. The higher the value of Lu, the higher is the capability of the moisture diffusing away from the phase interface, and therefore the flatter is the molar concentration gradient needed for the moisture diffusion. The effect of Lu on the molar concentration distribution is also shown in Fig. 3.

Downloaded 20 Dec 2010 to 194.27.225.72. Redistribution subject to ASME license or copyright; see http://www.asme.org/terms/Terms_Use.cfm

The condition for the limitation of the sublimation process, described by equation (20), is presented in Fig. 4. Sublimation can only take place in the region under the sublimation limit curve. The dimensionless parameter C is defined by equation (19),

$$C = \frac{C_{m,0} - C_{m,\max}}{C_{m,\max} - C_{m,s}}$$

For a fixed value of the sublimation pressure, either a high value of $C_{m,0}$ or a high value of $C_{m,s}$ gives a high value of C. In the sublimation process, a high value of C requires a slow motion of the sublimation front (that is a small value of λ) or a high capability of the moisture diffusing through the vapor region (that is a high value of Lu) in order to maintain the process under the sublimation limit. The dimensionless parameter α defined by equation (21), can be written as

$$\alpha = \lambda\sqrt{a_2/a_m} = \lambda/\sqrt{\mathrm{Lu}}$$

Therefore it is expected that the higher the value of C in the sublimation process, the lower is the value of α required as shown in Fig. 4.

Acknowledgment

The present work is being supported by the Natural Sciences and Engineering Research Council of Canada, under Grant No. A7929.

References

1 Luikov, A. V., "Systems of Differential Equations of Heat and Mass Transfer in Capillary-Porous Bodies," *International Journal of Heat Mass Transfer*, Vol. 18, 1975, pp. 1–14.

2 Gupta, L. N., "An Approximate Solution of the Generalized Stefan's Problem in a Porous Medium," *International Journal of Heat Mass Transfer*, Vol. 17, 1974, pp. 313–321.

3 Cho, S. H., "An Exact Solution of the Coupled Phase Change Problem in a Porous Medium," *International Journal of Heat Transfer*, Vol. 18, 1975, pp. 1139–1142.

4 Mikhailov, M. D., "Exact Solution of Temperature and Moisture Distributions in a Porous Half-Space with Moving Evaporation Front," *International Journal of Heat Mass Transfer*, Vol. 18, 1975, pp. 797–804.

5 Mikhailov, M. D., "Exact Solution for Freezing of Humid Porous Half-Space," *International Journal of Heat Mass Transfer*, Vol. 19, 1976, pp. 651–655.

6 Slattery, J. C., *Momentum, Energy, and Mass Transfer in Continua*, McGraw-Hill, New York, 1972, Sections 7.3 and 10.3

7 Carslaw, H. S., and Jaeger, J. C., *Conduction of Heat in Solids*, Oxford University Press, London, 1959, Chapter XI.

Downloaded 20 Dec 2010 to 194.27.225.72. Redistribution subject to ASME license or copyright; see http://www.asme.org/terms/Terms_Use.cfm

Krishna P. Singh
Vice President—Engineering.
Mem. ASME

Michael J. Holtz
Chief Engineer.

Joseph Oat Corporation,
Camden, N.J. 08104

A Comparison of Thermal Performance of Two and Four Tube Pass Designs for Split Flow Shells

Governing equations for heat transfer in a split flow heat exchanger with two tube passes are developed and solved. The expressions for the "temperature efficiency" P and "LMTD temperature correction factor", F are derived. F and P values for two tube pass and four tube pass are compared over the practical range of values of thermal flow rate ratio R and reduced thermal flux, η (NTU).

Introduction

Split flow heat exchangers, designated as the "G-type" in TEMA standards [1] find extensive application in the process and power industries due to their relatively superior heat transfer and pressure drop characteristics. Schindler and Bates [2] present an excellent discussion on the merits of the split flow design over the conventional "E-type shell" construction.

They have also derived the relationships between the temperature efficiency P, reduced thermal flux η and thermal flow rate ratio R for split flow, two tube pass heat exchanger. Singh and Holtz [3] presented similar relationships for split flow, four tube pass exchanger. Although the relationships for four tube pass and two tube pass cases are mathematically completely different, one would suspect from physical reasoning that their actual performances may not be so dissimilar. One of the objectives of this paper is to compare the heat transfer performance of two and four tube pass arrangements in the meaningful range of the governing dimensionless parameters. Another goal in this paper is to derive heat transfer expressions for a split flow, two tube pass heat exchanger. This entails determining tube and shell side fluid temperatures as functions of the surface area coordinate; and of course, the relationships between P, η and R. Schindler and Bates [2] obtain these relationships by dividing the heat transfer region into two concurrent and one countercurrent subregion. They utilize integrated heat transfer relations for each subregion in terms of (as yet undetermined) terminal temperatures; and appeal to temperature continuity across inter-subregion boundaries to determine the unknown terminal temperatures. Further manipulation of the mathematical expressions yields the desired relationships among P, η and R. The approach presented in this paper, on the other hand, is based on the first principles. Fundamental heat transfer relations for a differential element in a subregion are written. The resulting differential equations are integrated. The constants of integration are found using temperature continuity across subregion interfaces. In this manner, the overall characteristics as well as details of the temperature field are determined. The knowledge of the temperature profiles of the tubeside and shellside streams is essential in many design calculations. For example, the computation of tube/shell longitudinal stress in fixed tubesheet heat exchangers and U-bend stress in U-tube exchangers [4] require evaluation of the total longitudinal expansion of the tubes. Temperature profiles also reveal regions of inadequate or reverse heat transfer [3], locations of possible high thermal stress in the tubesheet, etc. In view of these considerations, the formulation in this paper seeks to synthesize the overall apparatus response from the elemental relationships. The difference from the Schindler, et al. solution is not so much in the conceptual approach as it is in the methodology. The thermal-hydraulic assumptions implied in the analysis are the traditional ones listed in reference [3] from (*a*) to (*g*) (excluding (*h*)). A brief description of the analysis now follows.

Contributed by the Heat Transfer Division for publication in the JOURNAL OF HEAT TRANSFER. Manuscript received by the Heat Transfer Division, March 21, 1980.

Analysis

As shown in Fig. 1, the shell side stream enters the shell at the shell nozzle located midway along the shell. The shell stream subdivides into two equal substreams flowing in opposite directions in the upper half of the shell. Having traversed the two extremities of the shell, these two substreams cross over the longitudinal baffle and flow towards the outlet nozzle located midway along the shell length in the bottom half of the shell. The heat transfer region is subdivided into three subregions as indicated in Fig. 1. If A_i is used to denote the surface area on tubes in subregion i, then we note that $A_1 = A_3 = 0.25A^*$; and $A_2 = 0.5A^*$, where A^* is the overall heat transfer surface. To fix ideas, we set up a coordinate system in each subregion such that the origin of the coordinate A (tube surface area) is located in the plane where the shell side fluid enters the subregion, and the magnitude of A increases in the direction of the shell side flow. Thus the origin of surface area parameter A in subregion 3 is at the left-hand tube sheet in Fig. 1. Noting that the shell side and tube side flows are cocurrent in subregions 1 and 3, and countercurrent in subregion 2, the following heat transfer relations can be readily written:

$$0.5M_s\delta_i dT = M_t dt;\ i = 1, 2, 3 \tag{1}$$

$$0.5M_s dT = -U(T - t)dA \tag{2}$$

Where M_s and M_t are shell side and tube side thermal flow rates, U is the overall heat transfer coefficient, T and t denote shellside and tubeside fluid temperatures at a typical elemental surface dA defined by surface coordinate location A. δ_i characterizes the flow pattern

$$\delta_i = (-1)^i \tag{2a}$$

From equation (2), we have

$$\frac{dT}{dA} = \frac{-2U}{M_s}(T - t) \tag{3}$$

or

$$\frac{d^2T}{dA^2} = \frac{-2U}{M_s}\left(\frac{dT}{dA} - \frac{dt}{dA}\right) \tag{4}$$

Substituting for dt/dA from equation (1), we obtain a second order differential equation in T

$$\frac{d^2T}{dA^2} + \alpha_i \frac{dT}{dA} = 0;\ i = 1, 2, 3 \tag{5}$$

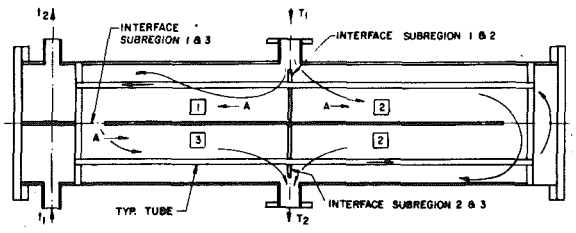

Fig. 1 Schematic of split flow, two pass heat exchanger

Copyright © 1981 by ASME
Downloaded 20 Dec 2010 to 194.27.225.72. Redistribution subject to ASME license or copyright; see http://www.asme.org/terms/Terms_Use.cfm

where

$$\alpha_i = \frac{2U}{M_s}\left(1 - \frac{\delta_i}{2R}\right) \tag{6}$$

and R is the ratio of thermal flow rate on the tube side to that on the shell side; i.e.,

$$R = \frac{M_t}{M_s} \tag{6a}$$

Solution of equation (5) yields

$$T = a_i + b_i e^{-\alpha_i A};\ i = 1, 2, 3 \tag{7}$$

This yields, together with equation (3)

$$t = a_i + b_i\left(1 - \frac{M_s\alpha_i}{2U}\right)e^{-\alpha_i A};\ i = 1, 2, 3 \tag{8}$$

The special case where $\alpha_i = 0$ is treated separately later in this section. Six constants of integration, a_i, b_i are evaluated by using interface conditions between the subregions and the boundary conditions, as follows.

(i) Between subregions 1 and 2, ($A = 0$) continuity in T requires

$$a_1 + b_1 = a_2 + b_2 \tag{9}$$

(ii) Similarly, continuity in t requires (at $A = 0$)

$$a_1 + b_1\left(1 - \frac{M_s\alpha_1}{2U}\right) = a_2 + b_2\left(1 - \frac{M_s\alpha_2}{2U}\right) \tag{10}$$

From equations (9) and (10) we have

$$b_2 = \frac{\alpha_1}{\alpha_2}b_1 \tag{11}$$

$$a_2 = a_1 + b_1\left(1 - \frac{\alpha_1}{\alpha_2}\right) \tag{11a}$$

(iii) At the interface between subregions 1($A = A_1$) and 3($A = 0$), continuity of T yields

$$a_1 + b_1\theta_1 = a_3 + b_3 \tag{12}$$

where

$$\theta_i = e^{-\alpha_i A_i} \tag{12a}$$

(iv) Continuity of tube side fluid temperature at the interface between subregion 2($A = A_2$) and subregion 3($A = A_3$) yields

$$a_3 + b_3\theta_3\left(1 - \frac{M_s\alpha_3}{2U}\right) = a_2 + b_2\theta_2\left(1 - \frac{M_s\alpha_2}{2U}\right) \tag{13}$$

Substituting for a_2 and b_2 from equations (11), (11a) and (13), we have

$$a_3 + b_3\theta_3\left(1 - \frac{M_s\alpha_3}{2U}\right) = a_1 + b_1\left[1 - \frac{\alpha_1}{\alpha_2} + \frac{\theta_2\alpha_1}{\alpha_2}\left(1 - \frac{M_s\alpha_2}{2U}\right)\right] \tag{13a}$$

From equations (12) and (13a), we have

$$b_3 = \chi b_1 \tag{14}$$

where

$$\chi = \frac{1 - \theta_1 - \frac{\alpha_1}{\alpha_2} + \frac{\theta_2\alpha_1}{\alpha_2}\left(1 - \frac{M_s\alpha_2}{2U}\right)}{\theta_3\left(1 - \frac{M_s\alpha_3}{2U}\right) - 1} \tag{15}$$

Furthermore, equation (12) gives

$$a_3 = a_1 + b_1(\theta_1 - \chi) \tag{16}$$

Finally, two boundary conditions may be specified as

(v) $T = T_1$ at $A = 0$ in subregion 1.

(vi) $t = t_1$ at $A = 0$ in subregion 3.

From equations (7) and (8), we obtain using the above condition:

$$T_1 = a_1 + b_1 \tag{17}$$

$$t_1 = a_1 + b_1\left(\theta_1 - \frac{\chi\alpha_3 M_s}{2U}\right) \tag{18}$$

Hence

$$T_1 - t_1 = b_1\left(1 - \theta_1 + \frac{\chi\alpha_3 M_s}{2U}\right)$$

or

$$b_1 = \frac{(T_1 - t_1)}{1 - \theta_1 + \frac{\chi\alpha_3 M_s}{2U}} \tag{19}$$

Finally

$$a_1 = \frac{T_1\left(\frac{\chi\alpha_3 M_s}{2U} - \theta_1\right) + t_1}{1 - \theta_1 + \frac{\chi\alpha_3 M_s}{2U}} \tag{20}$$

Thus all the constants of integration are expressed in terms of input data, and the temperature profiles of both shellside and tubeside fluids become completely known.

It is of some interest to derive the relationship between temperature efficiency P, reduced thermal flux η and thermal flow rate ratio R where these nondimensional quantities are defined in terms of previously introduced terms as follows.

$$P = \frac{t_2 - t_1}{T_1 - t_1} \quad (a)$$

$$\eta = \frac{UA^*}{M_t} \quad (b) \tag{21}$$

R is defined by equation (6a).

Noting that the tube outlet temperature t_2 is given by the subregion 1 solution for t at $A = A_1$, we have

$$t_2 = a_1 + b_1\theta_1\left(1 - \frac{M_s\alpha_1}{2U}\right) \tag{22}$$

Equations (18) and (22) yield

Nomenclature

A^* = overall heat transfer surface
A_i = heat transfer surface in subregion i
a_i, b_i = constants of integration in subregion i
A = surface area coordinate in a subregion with reference to its local coordinate system (Fig. 1)
F_4, F_2 = LMTD correction factor for split flow four-tube pass and two-tube pass exchangers, respectively
M_s = thermal flow rate of shellside fluid
M_t = thermal flow rate of tubeside fluid
P = temperature efficiency (equation (21a))
P_4, P_2 = temperature efficiency of four-tube pass and two-tube pass (split flow) exchanger, respectively
R = thermal flow rate (flow rate times specific heat) ratio (equation (6a))
U = overall heat transfer coefficient
T = shellside fluid temperature at a generic surface coordinate A
t = tubeside fluid temperature of a generic surface coordinate A
t_1 = tube inlet temperature
t_2 = tube outlet temperature
T_1 = shell inlet temperature
T_2 = shell outlet temperature
η = number of transfer units (also referred to as reduced thermal flux in this paper) equation (21b)

Downloaded 20 Dec 2010 to 194.27.225.72. Redistribution subject to ASME license or copyright; see http://www.asme.org/terms/Terms_Use.cfm

$$t_2 - t_1 = b_1\left(\frac{\chi\alpha_3 M_s}{2U} - \frac{M_s\alpha_1\theta_1}{2U}\right) \tag{23}$$

The expression for P now follows from equations (19) and (23)

$$P = \frac{t_2 - t_1}{T_1 - t_1} = \frac{\frac{M_s}{2U}(\chi\alpha_3 - \alpha_1\theta_1)}{1 - \theta_1 + \frac{\chi\alpha_3 M_s}{2U}} \tag{24}$$

or

$$P = \frac{\frac{2}{\eta R}(\theta_1 \ln\theta_1 - \chi \ln\theta_3)}{1 - \theta_1 - \frac{2\chi \ln\theta_3}{\eta R}} \tag{25}$$

θ_1 and χ can be readily expressed in terms of dimensionless quantities, as follows.

$$\theta_1 = \theta_3 = \frac{-\eta R}{e^2}\left(1 + \frac{1}{2R}\right) \qquad (a)$$

$$\theta_2 = e^{-\eta R}\left(1 - \frac{1}{2R}\right) \qquad (b) \tag{26}$$

$$\chi = \frac{1 - \theta_1 - \frac{2\ln\theta_1}{\ln\theta_2} + \frac{2\theta_2 \ln\theta_1}{\ln\theta_2}\left(1 + \frac{\ln\theta_2}{\eta R}\right)}{\theta_3\left(1 + \frac{2\ln\theta_3}{\eta R}\right) - 1} \qquad (c)$$

All necessary heat transfer relations are now available in terms of the conventional dimensionless parameters.

Special case: Referring to equation (6), $R = 0.5$ makes α_2 zero. For this case the governing equation (equation (5)) becomes for $i = 2$

$$\frac{d^2T}{dA^2} = 0 \tag{27}$$

which is integrated to yield

$$T = a_2 + b_2 A \tag{28}$$

The corresponding expression for the tubeside fluid temperature follows from equation (8)

$$t = a_2 + b_2\left(A + \frac{M_s}{2U}\right) \tag{29}$$

Using the boundary conditions as before, the following relationships between the constants of integration follow:

$$\begin{aligned} a_2 &= a_1 + b_1 \\ b_2 &= -\alpha_1 b_1 \\ b_3 &= \chi b_1 \end{aligned} \tag{30}$$

where

$$\chi = \frac{1 - \theta_1 + 2\ln\theta_1\left(1 + \frac{1}{\eta R}\right)}{\theta_3\left(1 + \frac{2\ln\theta_3}{\eta R}\right) - 1} \tag{31}$$

The expressions for P (equation (25)), b_1 (equation (19)), a_1 (equation (20)) remain unchanged.

Temperature Correction Factor

Equations (25) and (26) completely characterize the heat transfer behavior of two tube pass split flow heat exchanger. For a given value of η and R the temperature efficiency P is readily evaluated. Thus the well-known ten Broeck Charts can be conveniently constructed for this geometry. Furthermore, the log mean temperature difference correction factor, (LMTD) F, can be computed using the basic relationship

$$F = \frac{\ln\frac{1-P}{1-PR}}{\eta(R-1)} \tag{32}$$

It should be noted that the above equation shows F to be an explicit function of three variables, namely η, P and R. P can be expressed in terms of η and R using equation (25); thus F becomes a function of η and R only. In principle it is possible to express η in terms of P and R by rearranging and manipulating equation (25) and thus render F to be a function of P and R, which is the most common form of representation in the so-called "temperature correction factor" charts. However, η is a highly complex function of P and R, requiring an iterative solution to compute η for given values of P and R. It is most convenient to generate P for selected values of η and R (using equation (25)) and then proceed to compute F using equation (32). The design charts are thus generated for practical use. Schindler and Bates [2] published such charts for the two pass split flow heat exchanger; hence, these are not presented here. It is, however, of some interest to examine how the LMTD correction factor, F, and temperature efficiency P compare for two and four tube pass split flow geometries. The values of P and F are calculated for four tube pass using the Singh and Holtz [3] solution. The differences ΔP and ΔF are plotted as functions of η (with R as the parameter) in Figs. 2 and 3 where

$$\Delta P = P_2 - P_4; \text{ and } \Delta F = F_2 - F_4$$

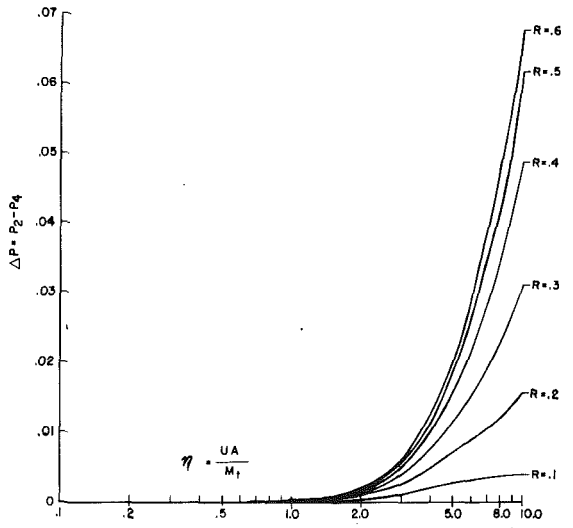

Fig. 2 Differential temperature efficiency versus reduced thermal flux (NTU)

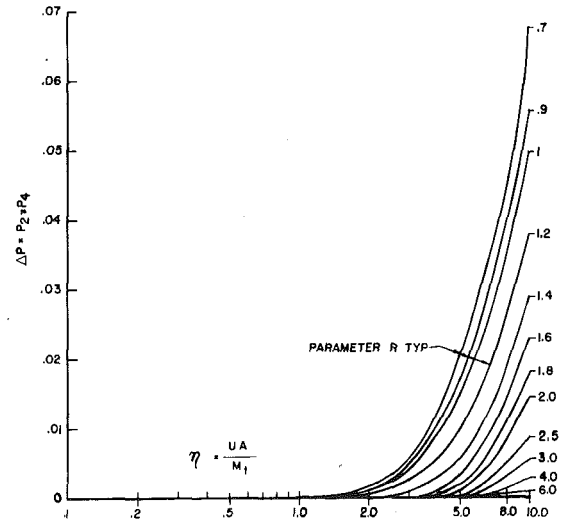

Fig. 3 Differential temperature efficiency versus reduced thermal flux (NTU)

Downloaded 20 Dec 2010 to 194.27.225.72. Redistribution subject to ASME license or copyright; see http://www.asme.org/terms/Terms_Use.cfm

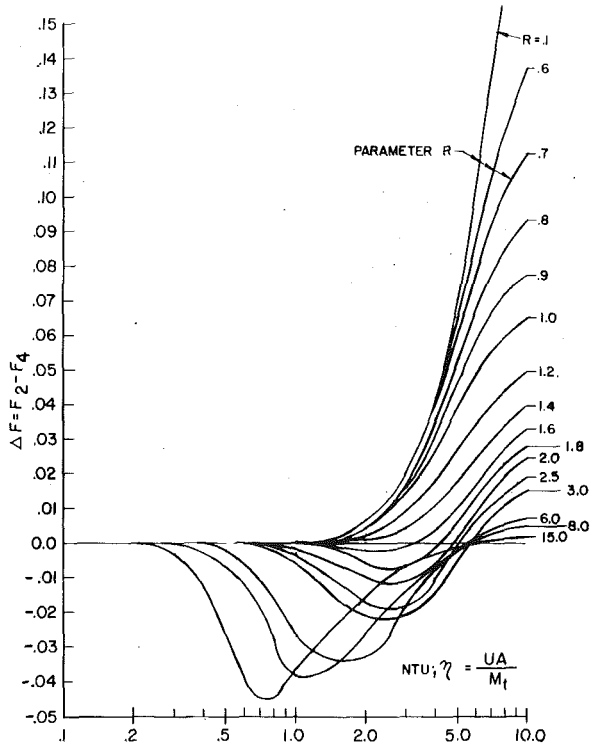

Fig. 4 Differential temperature correction factor ΔF versus NTU

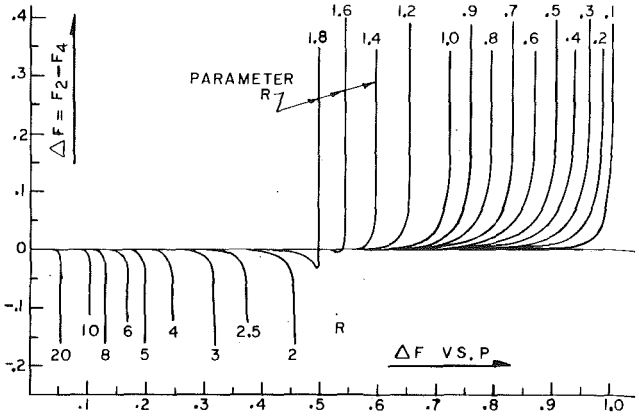

Fig. 5 Temperature efficiency, P

The plots for ΔP (Figs. 2 and 3) show that the difference in temperature efficiency is highest around $R = 0.7$, and decreases rather rapidly for greater or smaller values of R. ΔP is also seen to be a monotonically increasing function of η. ΔF is plotted versus η in Fig. 4 with R as parameter. Greater values of ΔF appear to correspond with large η and small R. In the most meaningful design range, however ($\eta < 3$), we notice that ΔF is less than 0.05. Thus the thermal performance of the two geometries is nearly equal in this range. Figure 5 shows ΔF as a function of P. Thus, Fig. 5 may be used to determine the relative efficacies of two and four pass geometries directly from the input data usually available (P and R). The following conclusions may be drawn from the foregoing discussion:

1 Two and four pass split flow designs have nearly identical operating performance characteristics in the meaningful design range.

2 Two pass design has a performance edge over four pass for relatively small R (<1.6). Four pass design becomes increasingly more efficient for greater R (Fig. 4). This fact is further borne out by Fig. 5. However, four tube pass design may not be suitable for high R values due to tubeside pressure drop limitations.

3 The figures presented here should enable a practicing engineer to make rapid comparison between two and four (or more) pass configurations for his particular problem.

4 It can be deduced from the foregoing that in the meaningful range of design data, six and more pass geometries will behave likewise. Thus the temperature performance curves for two pass and four pass currently available can be used to predict the performance of multipass designs with satisfactory accuracy.

Acknowledgment

The authors are thankful to Dr. Jerry Taborek of HTRI for his thoughtful comments on this paper during its preparation.

References

1 *Standards of Tubular Manufacturer's Association,* Sixth edition, New York, 1978, p. 3.

2 Schindler, D. L., and Bates, H. T., "True Temperature Difference in a 1–2 Divided-Flow Heat Exchanger," *Chemical Engineering Progress Symposium,* Series No. 30, Vol. 56, 1960, pp. 203–206.

3 Singh, K. P., and Holtz, M. J., "Generalization of the Split Flow Heat Exchanger Geometry for Enhanced Heat Transfer," *AIChE Symposium Series,* No. 189, Vol. 72, 1979, pp. 219–226.

4 Singh, K. P., and Holtz, M., "On Thermal Expansion Induced Stresses in U-Bends of Shell-and-Tube Heat Exchangers," ASME *Journal of Engineering for Power,* Vol. 101, No. 4, 1979, pp. 634–639.

Downloaded 20 Dec 2010 to 194.27.225.72. Redistribution subject to ASME license or copyright; see http://www.asme.org/terms/Terms_Use.cfm

Journal of Heat Transfer

Technical Notes

This section contains shorter technical papers. These shorter papers will be subjected to the same review process as that for full papers.

Similarity Rule for Solidification Heat Transfer with Change in Volume

N. Shamsundar[1]

Nomenclature

Bi = Biot number, hL/k
c = specific heat of solid PCM
F = frozen fraction, volume of solid/volume of enclosure
h = convective heat transfer coefficient
k = thermal conductivity of solid PCM
L = characteristic dimension; see Fig. 2
Q = instantaneous heat flux on cooled surface
Q_0 = value of Q when solidification commences
Ste = Stefan number, $c(T_{sat} - T_b)/\lambda$
t = time, counted from start of solidification
T_{sat} = melting temperature
T_b = temperature of coolant fluid
λ = latent heat
ρ_s, ρ_l = density of solid PCM, liquid PCM
τ = dimensionless time, $\int_0^t k(T_{sat} - T_b)dt/\rho_s \lambda L^2$
ϕ = similarity function, $(Q_0/Q - 1)/\text{Bi}$

Introduction

Solidification governed by heat conduction in the solid and convective heat removal at the boundary of the solid is a problem encountered in many applications. In almost all applications, control of the microstructure or some such important aspect is achieved by varying the coolant flow rate and/or the temperature. The analysis of the heat transfer process for irregularly shaped multidimensional objects under such conditions is generally performed by (usually) expensive finite-difference [1] or finite-element [2] numerical methods. A similarity rule discovered recently [3] enables a substantial reduction in computational effort. For a given geometry, the application of the similarity rule makes only two numerical calculations of phase change necessary. In these calculations, the coolant flow rate and temperature remain constant in time. The response to any specified timewise variation of coolant flow rate and temperature is then obtained by the analytical or numerical integration of a first-order ordinary differential equation in time. It is apparent that the similarity rule plays in solidification problems the role of a poor cousin to Duhamel's theorem.

As presented in [3], the similarity rule applies only if the volume change attending solidification is ignored. The aim of this note is to revalidate the similarity rule when the effects of the volume change are too large to be ignored.

Analysis

Consider a lump of matter that is initially molten, and is caused to cool by transferring heat convectively to a cooling fluid which flows past the walls of the container surrounding the lump. The convective coefficient and the temperature of the coolant are assumed spatially uniform, but may vary with time. Initially, the superheat in the molten liquid is removed by the coolant until solidification is initiated at the cooled surface. Let the total heat flux on the cooled surface at this instant be Q_0. Subsequently, the molten liquid is separated from the cooled surface by the growing solid layer. Let the heat flux on the cooled surface at time t be Q. Then, the similarity rule states that

- The quantity $(Q_0/Q - 1)/\text{Bi}$ is a function of the solid fraction only.
- The shape and location of the solid-liquid interface depend on the solid fraction only.

For strict validity, it is necessary that (1) sensible heat and superheat are negligible compared to latent heat, (2) the temperature on the cooled surface is spatially uniform. Under these conditions, the rule can be proved mathematically. In practice, these conditions are not met, although many important classes of problems are such that these conditions are approximately satisfied. Numerical calculations show that even when these conditions are violated considerably the validity of the similarity rule is singularly unimpaired [3].

The main consequence of the reduction in volume accompanying solidification is the development of a shrinkage cavity. The cavity may be well-dispersed as porosities, or it may be in one piece. Obviously, well distributed porosities serve only to reduce the effective conductivity and volumetric latent heat of the substance, and the similarity rule remains valid. Consider, then, a massive, single cavity such as that frequently observed during solidification of salts and waxes with moderate rates of cooling (freezing time $\sim$ 1 hr).

In our model, the cavity is treated as a single void across which there is no heat transfer, growing at the top of the container. At some instant during the solidification process, a vertical cross-section will be as shown in Fig. 1 using full lines. During a small interval of time after this instant, the interface between solid and liquid will move from the position Σ to the position Σ' (shown by dashes). The calculation of the position Σ' is performed as if there were no density change *during* the time interval using, say, a finite-difference method. Next, the free surface AB is moved to a position $A'B'$ such that (1) $A'B'$ is horizontal; (2) A' and B' lie on Σ'; and (3) mass is conserved, i.e., volume $AA'B'B$ = cross-hatched volume $\times$ $(\rho_s/\rho_l - 1)$.

Following the adoption of this model, the invocation of the similarity rule presents no difficulties, because the only effects of the cavity upon the temperature field in the solid are: (1) the addition of one more adiabatic boundary, namely, the boundary of the cavity, and (2) nonuniformities in wall flux adjacent to the cavity. A perusal of the conditions for the validity of the similarity rule shows that the additional adiabatic boundary has no effect on these condtions pro-

[1] Assistant Professor, Department of Mechanical Engineering, University of Houston, Houston, Tex. 77004, Assoc. Mem. ASME.

Contributed by the Heat Transfer Division for publication in the JOURNAL OF HEAT TRANSFER. Manuscript received by the Heat Transfer Division May 16, 1980.

Copyright © 1981 by ASME

Downloaded 20 Dec 2010 to 194.27.225.72. Redistribution subject to ASME license or copyright; see http://www.asme.org/terms/Terms_Use.cfm

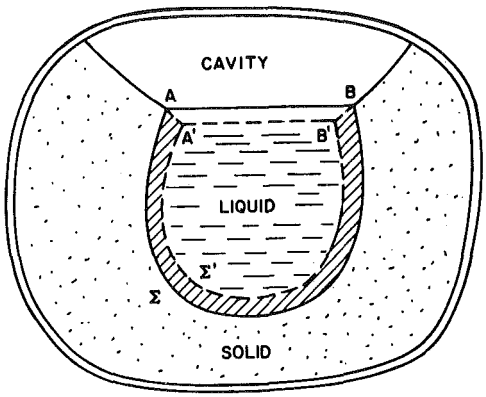

Fig. 1 Sketch of cross-section during solidification, showing solid, liquid and cavity at time t and time $t + \Delta t$

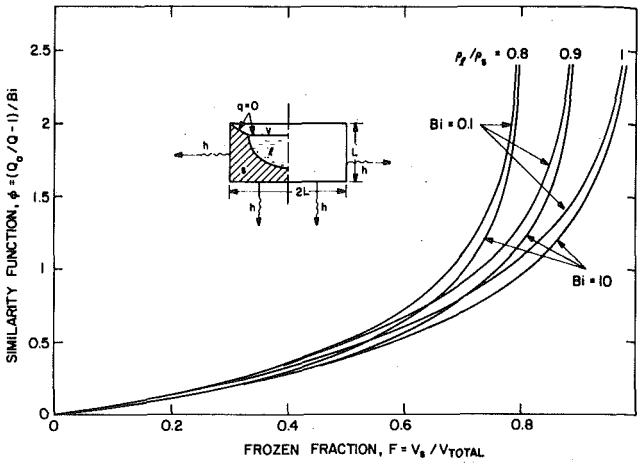

Fig. 2 Similarity function plotted against frozen fraction, showing effect of density change

vided that, in comparing cases with different Biot numbers, the density ratio ρ_l/ρ_s is the same. Nonuniformities in wall-flux violate requirement (2) of the similarity rule. Nevertheless, the rule may be expected to be approximately valid because, as shown in [3], moderate variations of wall-flux do not seem to affect the rule. As far as requirement (2) is concerned, it is immaterial whether the nonuniformity is caused by geometry or by a cavity. Hence, before applying the similarity rule to problems involving a cavity, one should ascertain if the cavity introduces nonuniformities more severe than those arising from the geometry of the container. An important consequence of this state of affairs is that the final shape of the cavity is independent of the cooling rates existing during the solidification process. This is in agreement with the conclusions drawn in [4] from numerical calculations based on the present model.

Results and Discussion

The shrinkage model just described was implemented via an enthalpy-based finite-difference method in order to solve a model problem. This calculation, presented in [4], pertains to two-dimensional solidification of a PCM in the 2 × 1 rectangular container shown as an inset in Fig. 2. Results for parameters values ρ_l/ρ_s = 0.8, 0.9, and 1,[2] Biot number = 0.1, 1, and 10, and Stefan number = 0.01, 0.1 were presented in the form of Q/Q_0 and solid fraction plotted against a dimensionless time-variable. The results to be presented in this paper were obtained by replotting the earlier results in terms of the similarity variables.

Figure 2 shows the outcome. That the similarity rule is valid can be concluded by observing the closeness of the curves for Bi = 0.1 and Bi = 10 for each of the three density ratios. The small separation that does exist is caused by violation of condition (2) of the similarity rule. As explained in [3], the vicinity of the square corner has large nonuniformity in surface temperature. The local surface heat flux distributions presented in [4] show that nonuniformities caused by the cavity are minor compared to those caused by the corner away from the cavity. This explains why shrinkage does not seem to affect the validity of the similarity rule in this case.

An interesting observation is that during the early stages of solidification there is little influence of density change to be seen. This finding can be explained when it is observed that, in these stages, the cavity is small and cannot possibly have much influence. During later stages, the similarity curves separate and order themselves according to the density ratio. These findings are in agreement with comments made in [4] concerning the curves of frozen fraction against time and heat flux against time.

In order to understand the results better and to present them in a more convenient form for possible applications, we shall replot the results shown in Fig. 2 on a different basis. In this, we shall look for guidance to the similar problem of freezing with negligible density change in a cylindrical container. The quasi-stationary formula given by London and Seban [5] for this case is equivalent to $\phi = -\frac{1}{2}\ln(1 - F)$. Therefore, it seems logical to try plotting the similarity function against $\log [1/(1 - F)]$ for our problem. However, a little reasoning will show the need for slightly modifying this quantity to reflect the presence of density change.

It helps at this point to bring up the interpretation of the similarity function in terms of the conduction shape factor S between the solid-liquid interface and the convectively cooled surface. In fact, $\phi = P/LS$, where P is the perimeter of the container, as shown in [3]. At the termination of solidification, the solid-liquid interface vanishes, S becomes zero and ϕ becomes infinite. These considerations show that the new abscissa variable should be such that it is zero at $F = 0$, infinite at the end of solidification (when $F = \rho_l/\rho_s$), and it should become $\log [1/(1 - F)]$ for $\rho_s = \rho_l$. Such a variable is $\log [1/(1 - F\,\rho_s/\rho_l)] = \log (m_{\text{total}}/m_{\text{liquid}})$.[3]

The plot of ϕ against $\log [1/(1 - F\rho_s/\rho_l)]$ is shown in Fig. 3. To preserve clarity, the results for the case $\rho_l/\rho_s = 0.9$ are omitted. For purposes of comparison, the result for the cylinder is also shown. The curves have separated with respect to ρ_l/ρ_s at all times, the crossovers of Fig. 2 have been eliminated, and the ordering with respect to ρ_l/ρ_s is in a direction opposite to that in Fig. 2. It is pleasing to observe how similar all the curves are to the one for the cylinder, and that they are almost straight lines. This finding enables curves for values of ρ_l/ρ_s and Bi intermediate to those used in Fig. 3 to be obtained by drawing interpolatory straight lines.

For applications, one may wish to obtain the dependence of F and Q on time. This can be performed in a straightforward way by applying the energy conservation principle. As explained in [3], the dimensionless time τ is given by

$$2\,d\tau/dF = 1/\text{Bi} + \phi(F),\ \tau = 0 \text{ at } F = 0,$$

which is an ordinary differential equation for τ. If Bi is constant or a known function of F, this equation can be solved by evaluating $\int_0^F \phi dF$. Since ϕ may be approximated as a linear function of $\log [1/(1 - F\ \rho_s/\rho_l)]$, analytical expressions for τ in terms of F can be obtained.

Example. Sodium nitrate inside long containers with 40 mm × 20 mm cross-sections is cooled by air flowing across the walls. If the air flow varies so as to result in a Biot number variation given by Bi = 10 + 15F, and the air temperature varies according to $T_b = 275 - 40t$, t being in hours and T_b in °C, find

1 the solidification time
2 the heat flux when half the mass has solidified, and
3 the heat flux and amount of solid at t = 20 min.

[2] For $\rho_l/\rho_s = 1$, the cross-section considered corresponds to the bottom half of a square container that is cooled on all four sides uniformly.

[3] This variable is suitable for problems involving two- or three-dimensional cavities, provided the temperature distribution is two-dimensional. For cavities associated with three-dimensional temperature distributions, other variables suggest themselves; for example, for freezing in a sphere, $1/\sqrt{(1 - F\rho_s/\rho_l)} - 1$.

Downloaded 20 Dec 2010 to 194.27.225.72. Redistribution subject to ASME license or copyright; see http://www.asme.org/terms/Terms_Use.cfm

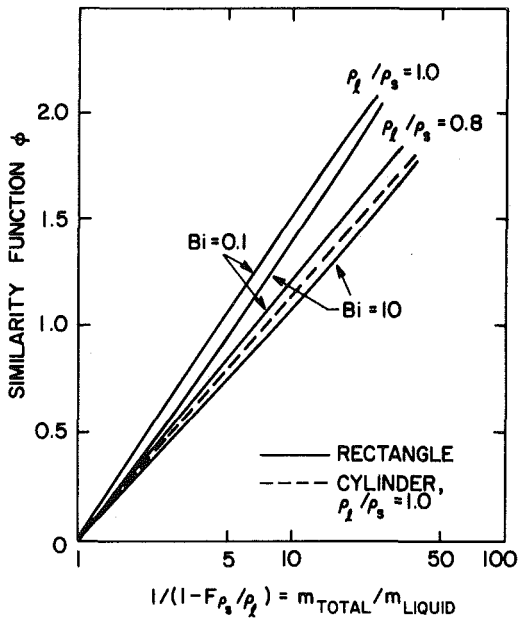

Fig. 3 Similarity function plotted against total mass of PCM/mass of liquid PCM

Solution. The necessary properties of sodium nitrate are: $T_{sat} = 305°C$, $k = 0.57$ W/m·°C, $\rho_s = 2260$ kg/m^3, $\rho_l = 1900$ kg/m^3, $\lambda = 182$ kJ/kg.

For $\rho_l/\rho_s = 1900/2260 = 0.84$, and Bi ranging from 10 to 25, we see from Fig. 3 that $\phi \approx 0.5 \ln [1/(1 - F\,\rho_s/\rho_l)]$. From the equation for $d\tau/dF$, we obtain the following results after integration:

$$2\tau = \int_0^F dF/\mathrm{Bi} + \int_0^F \phi dF$$

$$= \int_0^F dF/(10 + 15F) + \int_0^F 0.5 \ln [1/(1 - 1.19F)]\, dF$$

$$= (1/15) \ln (1 + 1.5F)$$

$$+ [1.19\,F - (1 - 1.19\,F) \ln \{1/(1 - 1.19\,F)\}]/2.38 \qquad (1)$$

1 The solidification time is obtained by using $F = \rho_l/\rho_s = 0.84$ in the above equation. The result is $\tau = 0.237$. To obtain the physical time, we have to solve the equation

$$\tau = (k/\rho_s \lambda L^2) \int_0^t (T_{sat} - T_b)\, dt$$

$$= (k/\rho_s \lambda L^2)\,(30t + 20t^2) = 0.237 \qquad (2)$$

for t. This equation has only one positive root, $t = 0.48$ hr.

2 The heat flux per unit length perpendicular to the cross-section is

$$Q = \hat{Q}\, 4hL\,(T_{sat} - T_b) = 4\,hL\,(T_{sat} - T_b)/(1 + \mathrm{Bi}\phi) \qquad (3)$$

for $F = 0.42$, Bi = 16.3 and $\phi = 0.347$. In order to obtain T_b it is necessary to find t. Performing a calculation similar to that of part (1), we get $\tau = 0.049$ and $t = 0.12$ hr. Using these results in equation (3), we get $T_{sat} - T_b = 34.8°C$ and $Q = 194$W/m.

3 For $t = 20$ min, $\tau = 0.152$ from the left part of equation (2). With this value of τ, equation (1) is solved by trial and error to get $F = 0.73$ or *87 percent by mass of solid.* Next calculations are made as in part (2) to obtain Bi = 21, $\phi = 1.02$, $T_{sat} - T_b = 43°C$, and $Q = 93$ W/m.

It is of interest to compare the results obtained above with estimates based upon Bi = constant = 15 and $T_{sat} - T_b$ = constant = 40°C. The estimates are (1) $t = 0.48\ h$, (2) $Q = 22$ W/m, (3) $Q = 74$ W/m, 92 percent solid. If, for purposes of estimation, shrinkage is also ignored and the mean of ρ_s and ρ_l is used, the estimates are (1) $t = 0.69\ h$, (2) $Q = 184$ W/m, (3) $Q = 91$ W/m, 78 percent solid. Comparing these estimates to the results given earlier shows the necessity of considering the effects of variable Bi and T_b and of density change, the more so for smaller values of Bi.

Conclusions

The similarity rule remains valid with no modification when the shrinkage cavity is either concentrated at the top of the container, or when finely dispersed pores are formed. By plotting the similarity function ϕ against log $[1/(1 - F\,\rho_s/\rho_l)]$, plots that are almost straight lines are obtained if the container is rectangular. Such a representation facilitates interpolation for results pertaining to intermediate parameter values and enables obtaining analytical formulae for the freezing time and heat flux in terms of the frozen fraction F.

Acknowledgments

This research was supported by the U.S. Department of Energy and the Solar Energy Research Institute through the Energy Foundation of Texas.

References

1 Shamsundar, N., and Sparrow, E. M., "Analysis of Multidimensional Conduction Phase Change via the Enthalpy Model," ASME JOURNAL OF HEAT TRANSFER, Vol. 97, 1975, pp. 333–340.

2 Comini, G., del Giudice, S., Lewis, R. W., and Zienkiewicz, O. C., "Finite Element Solution of Nonlinear Heat Conduction Problems with Special Reference to Phase Change," *International Journal for Numerical Methods in Engineering*, Vol. 8, 1976, pp. 901–910.

3 Shamsundar, N., and Srinivasan, R., "A New Similarity Method for Analysis of Multidimensional Solidification," ASME JOURNAL OF HEAT TRANSFER, Vol. 101, 1979, pp. 585–591.

4 Shamsundar, N., and Sparrow, E. M., "Effect of Density Change on Multidimensional Conduction Phase Change," ASME JOURNAL OF HEAT TRANSFER, Vol. 98, 1976, pp. 550–557.

5 London, A. L., and Seban, R. A. "Rate of Ice Formation," *Trans. ASME*, Vol. 65, 1943, pp. 771–778.

Applicability of the Bubble Flux Density Concept

R. L. Judd[1]

Introduction

Several years ago, Shoukri and Judd [1] advanced a theory for incorporating the effect of surface conditions in the prediction of nucleate boiling heat transfer. It was shown that if the surface characterization parameters m and C were known for a particular boiling surface as the result of fitting the relationship

$$(N/A)_{r_c} = C\,(1/r_c)^m \qquad (1)$$

to a set of experimental measurements obtained with water boiling on the surface where $(N/A)_{r_c}$ is the cumulative active site density for those cavities having radii equal to or greater than r_c, then the number of bubbles emitted per unit area per unit time (bubble flux density Φ) could be predicted. A simple relationship was found to correlate heat flux Q/A with bubble flux density Φ irrespective of the surface finish involved when the theory was tested with two sets of experimental data for water boiling on copper surfaces having various finishes taken from Shoukri [2] and Singh [3], respectively. The inference drawn from these successful correlations was that the bubble flux density determined by the theory encompassed all the surface effects although the need to determine the surface characteristics as described by the empirical constants m and C restricted the usefulness of the theory. Although water data were used exclusively to confirm the theory, Shoukri and Judd also indicated how the theory might be modified to incorporate boiling organic fluids. The purpose of this short technical note is to perform an analysis as suggested by the

[1] Professor, McMaster University, Hamilton, Ontario, Canada L8S 4L7

Contributed by the Heat Transfer Division for publication in the JOURNAL OF HEAT TRANSFER. Manuscript received by the Heat Transfer Division July 21, 1980.

Downloaded 20 Dec 2010 to 194.27.225.72. Redistribution subject to ASME license or copyright; see http://www.asme.org/terms/Terms_Use.cfm

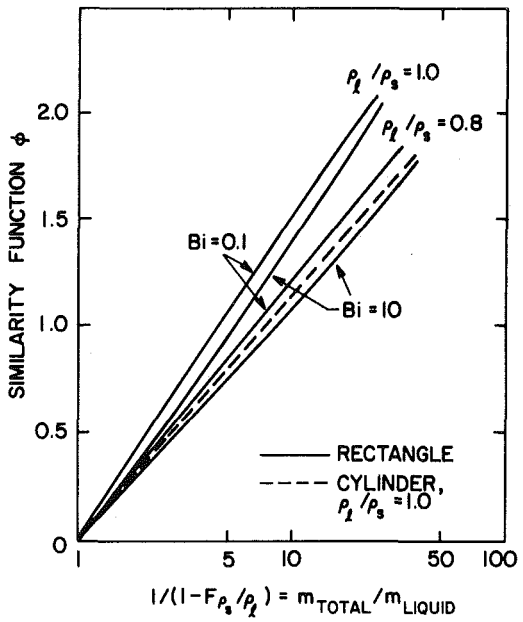

Fig. 3 Similarity function plotted against total mass of PCM/mass of liquid PCM

Solution. The necessary properties of sodium nitrate are: T_{sat} = 305°C, k = 0.57 W/m·°C, ρ_s = 2260 kg/m^3, ρ_l = 1900 kg/m^3, λ = 182 kJ/kg.

For ρ_l/ρ_s = 1900/2260 = 0.84, and Bi ranging from 10 to 25, we see from Fig. 3 that $\phi \approx 0.5 \ln [1/(1 - F\,\rho_s/\rho_l)]$. From the equation for $d\tau/dF$, we obtain the following results after integration:

$$2\tau = \int_0^F dF/\mathrm{Bi} + \int_0^F \phi dF$$

$$= \int_0^F dF/(10 + 15F) + \int_0^F 0.5 \ln [1/(1 - 1.19F)]\, dF$$

$$= (1/15) \ln (1 + 1.5F)$$

$$+ [1.19\,F - (1 - 1.19\,F) \ln \{1/(1 - 1.19\,F)\}]/2.38 \qquad (1)$$

1 The solidification time is obtained by using $F = \rho_l/\rho_s = 0.84$ in the above equation. The result is $\tau = 0.237$. To obtain the physical time, we have to solve the equation

$$\tau = (k/\rho_s \lambda L^2) \int_0^t (T_{sat} - T_b)\, dt$$

$$= (k/\rho_s \lambda L^2)\,(30t + 20t^2) = 0.237 \qquad (2)$$

for t. This equation has only one positive root, t = 0.48 hr.

2 The heat flux per unit length perpendicular to the cross-section is

$$Q = \hat{Q}\, 4hL\,(T_{sat} - T_b) = 4\,hL\,(T_{sat} - T_b)/(1 + \mathrm{Bi}\phi) \qquad (3)$$

for F = 0.42, Bi = 16.3 and ϕ = 0.347. In order to obtain T_b it is necessary to find t. Performing a calculation similar to that of part (1), we get τ = 0.049 and t = 0.12 hr. Using these results in equation (3), we get $T_{sat} - T_b$ = 34.8°C and Q = 194W/m.

3 For t = 20 min, τ = 0.152 from the left part of equation (2). With this value of τ, equation (1) is solved by trial and error to get F = 0.73 or *87 percent by mass of solid.* Next calculations are made as in part (2) to obtain Bi = 21, ϕ = 1.02, $T_{sat} - T_b$ = 43°C, and Q = 93 W/m.

It is of interest to compare the results obtained above with estimates based upon Bi = constant = 15 and $T_{sat} - T_b$ = constant = 40°C. The estimates are (1) t = 0.48 h, (2) Q = 22 W/m, (3) Q = 74 W/m, 92 percent solid. If, for purposes of estimation, shrinkage is also ignored and the mean of ρ_s and ρ_l is used, the estimates are (1) t = 0.69 h, (2) Q = 184 W/m, (3) Q = 91 W/m, 78 percent solid. Comparing these estimates to the results given earlier shows the necessity of considering the effects of variable Bi and T_b and of density change, the more so for smaller values of Bi.

Conclusions

The similarity rule remains valid with no modification when the shrinkage cavity is either concentrated at the top of the container, or when finely dispersed pores are formed. By plotting the similarity function ϕ against log $[1/(1 - F\,\rho_s/\rho_l)]$, plots that are almost straight lines are obtained if the container is rectangular. Such a representation facilitates interpolation for results pertaining to intermediate parameter values and enables obtaining analytical formulae for the freezing time and heat flux in terms of the frozen fraction F.

Acknowledgments

This research was supported by the U.S. Department of Energy and the Solar Energy Research Institute through the Energy Foundation of Texas.

References

1 Shamsundar, N., and Sparrow, E. M., "Analysis of Multidimensional Conduction Phase Change via the Enthalpy Model," ASME JOURNAL OF HEAT TRANSFER, Vol. 97, 1975, pp. 333–340.

2 Comini, G., del Giudice, S., Lewis, R. W., and Zienkiewicz, O. C., "Finite Element Solution of Nonlinear Heat Conduction Problems with Special Reference to Phase Change," *International Journal for Numerical Methods in Engineering,* Vol. 8, 1976, pp. 901–910.

3 Shamsundar, N., and Srinivasan, R., "A New Similarity Method for Analysis of Multidimensional Solidification," ASME JOURNAL OF HEAT TRANSFER, Vol. 101, 1979, pp. 585–591.

4 Shamsundar, N., and Sparrow, E. M., "Effect of Density Change on Multidimensional Conduction Phase Change," ASME JOURNAL OF HEAT TRANSFER, Vol. 98, 1976, pp. 550–557.

5 London, A. L., and Seban, R. A. "Rate of Ice Formation," *Trans. ASME,* Vol. 65, 1943, pp. 771–778.

Applicability of the Bubble Flux Density Concept

R. L. Judd[1]

Introduction

Several years ago, Shoukri and Judd [1] advanced a theory for incorporating the effect of surface conditions in the prediction of nucleate boiling heat transfer. It was shown that if the surface characterization parameters m and C were known for a particular boiling surface as the result of fitting the relationship

$$(N/A)_{r_c} = C\,(1/r_c)^m \qquad (1)$$

to a set of experimental measurements obtained with water boiling on the surface where $(N/A)_{r_c}$ is the cumulative active site density for those cavities having radii equal to or greater than r_c, then the number of bubbles emitted per unit area per unit time (bubble flux density Φ) could be predicted. A simple relationship was found to correlate heat flux Q/A with bubble flux density Φ irrespective of the surface finish involved when the theory was tested with two sets of experimental data for water boiling on copper surfaces having various finishes taken from Shoukri [2] and Singh [3], respectively. The inference drawn from these successful correlations was that the bubble flux density determined by the theory encompassed all the surface effects although the need to determine the surface characteristics as described by the empirical constants m and C restricted the usefulness of the theory. Although water data were used exclusively to confirm the theory, Shoukri and Judd also indicated how the theory might be modified to incorporate boiling organic fluids. The purpose of this short technical note is to perform an analysis as suggested by the

[1] Professor, McMaster University, Hamilton, Ontario, Canada L8S 4L7

Contributed by the Heat Transfer Division for publication in the JOURNAL OF HEAT TRANSFER. Manuscript received by the Heat Transfer Division July 21, 1980.

Copyright © 1981 by ASME

Downloaded 20 Dec 2010 to 194.27.225.72. Redistribution subject to ASME license or copyright; see http://www.asme.org/terms/Terms_Use.cfm

theory in order to show that the bubble flux density concept is applicable to methanol as well.

Analysis

Singh, et al. [4] presented experimental results for both water and methanol boiling on the same copper surfaces having varying degrees of roughness obtained by different preparation techniques. A plot of cumulative active site density $(N/A)_{r_c}$ versus effective cavity radius ρ (for water $\rho = r_c$) taken from this reference is depicted in Fig. 1. The slope and intercept of the straight lines correlating the water data in this graph were used to obtain the values of m and C required for the present analysis, yielding the values presented in Table 1.

The values tabulated are admittedly somewhat imprecise because of the obvious difficulty involved with determining the slopes and intercepts of the lines plotted in Fig. 1; unfortunately the values used to plot the data points were not tabulated in reference [3] so that it was not possible to obtain the surface characterization parameters m and C by linear regression. However, complete experimental data for water and organics boiling on the same surface under varying conditions of surface finish are very rare indeed so that there was no reasonable alternative to proceeding in this manner.

Plotting $(N/A)_{r_c}$ versus ρ for water and methanol on a single graph simplifies the determination of $\eta = \rho/r_c$ according to the procedure described in reference [1]. This parameter is essentially the ratio of the effective cavity radius for methanol at a particular level of heat flux to the cavity radius for water at the same level of heat flux which can be readily obtained from Fig. 1 by means of a scale and dividers. The values corresponding to each of the methanol data points plotted in the graph are listed in Table 2.

In accordance with the theory developed in reference [1], computer programs were written to solve for the bubble growth time t_g in the relationship

$$\sqrt{t_g} = \frac{1}{2}\left[\left(\frac{X}{Y}\right) \pm \sqrt{\left(\frac{X}{Y}\right)^2 + 35.4\,X}\right] \tag{2}$$

where

$$Y = \frac{2}{\sqrt{\pi}}\,\mathrm{Ja}\,\sqrt{\alpha_\ell} \text{ and } X = 0.4215\,\beta\sqrt{\frac{2\sigma g_c}{g(\rho_l - \rho_v)}}$$

and the bubble waiting time t_w in the relationship

$$r_c = \frac{\sqrt{\pi\alpha_\ell}}{2K}\left(\frac{\sin\beta}{1+\cos\beta}\right) \times\left[\gamma_w \pm \sqrt{{\gamma_w}^2 - 4\left(\frac{A/(\theta_w - \theta_{\mathrm{sat}})}{\sqrt{\pi\alpha_\ell}}\right)(1+\cos\beta)K}\right] \tag{3}$$

where

$$K = \left[\sqrt{\frac{1}{t_w + t_g}} + \frac{\theta_{\mathrm{sat}}}{\theta_w - \theta_{\mathrm{sat}}}\sqrt{\frac{1}{t_w}}\right]$$

$$\gamma_w = 1 - \frac{2}{\pi}\sum_{m=0}^{\infty}\frac{C_m}{m!(2m+1)2}\,2m\left(\sqrt{\frac{t_g}{t_w + t_g}}\right)^{2m+1}$$

$$C_m = 2(2m-1)C_{m-1} \text{ and } C_0 = 1$$

The results of these two computer programs were combined according to

$$f(r_c) = \frac{1}{t_w + t_g} \tag{4}$$

in order to be able to predict the frequency of bubble formation for methanol boiling on a copper surface $f(r_c)$ as a function of cavity radius r_c and superheat $\Delta T = \theta_w - \theta_{\mathrm{sat}}$ for the special case of subcooling $\theta_{\mathrm{sat}} = 0$. Subsequently, another computer program was written to predict the bubble flux density Φ in accordance with

$$\Phi = mC\int_{r_{c\min}}^{r_{c\max}}\frac{f(r_c)}{{r_c}^{m+1}}\,dr_c \tag{5}$$

in which m and C were the values obtained by fitting the data points obtained by plotting $(N/A)_{r_c}$ versus r_c for water. The integration limits refer to the size of the largest and smallest cavities which are able to remain active at a particular level of superheat according to classical nucleation theory. The computation is relatively insensitive to the value of $r_{c_{\max}}$ which was arbitrarily set at $2.5 * 10^{-2}$ mm for the

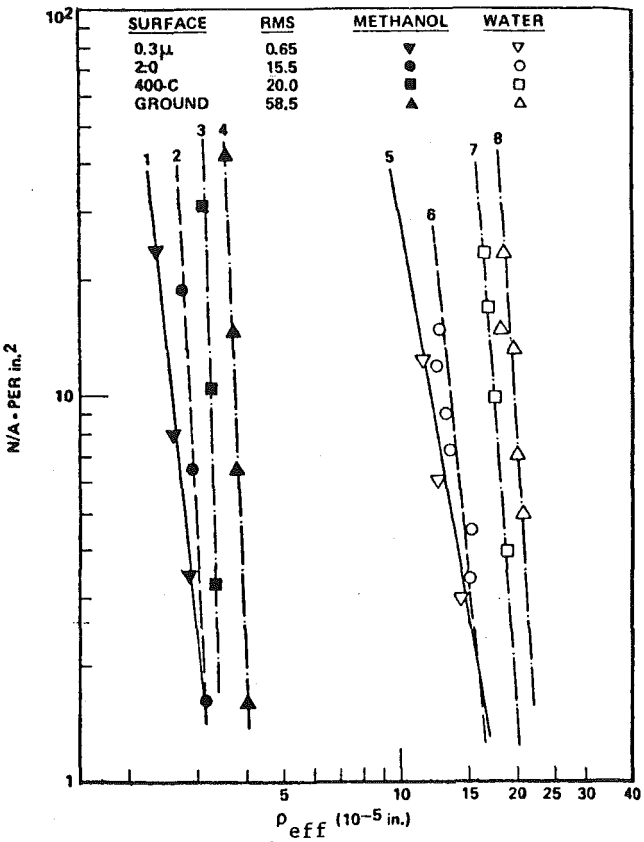

Fig. 1 Observed cumulative site density distribution for water and methanol abstracted from reference [4]

Table 1 Surface characterization parameters

Finish	m	C (Sites/m²)
0.3 μ	−5.6	$1.90 * 10^{-27}$
2 − 0	−9.7	$1.41 * 10^{-49}$
400 − C	−12.7	$1.28 * 10^{-64}$
Ground	−15.5	$1.71 * 10^{-78}$

Table 2 Ratio ρ/r_c for methanol

Finish	$(N/A)_{r_c}$ (Sites/m²)	η (−)
0.3 μ	5400	0.187
	12400	0.189
	36900	0.191
2 − 0	2500	0.191
	10000	0.210
	29100	0.225
400 − C	5100	0.174
	16400	0.186
	48000	0.195
Ground	6200	0.188
	31300	0.195
	54400	0.201
	66300	0.202

Downloaded 20 Dec 2010 to 194.27.225.72. Redistribution subject to ASME license or copyright; see http://www.asme.org/terms/Terms_Use.cfm

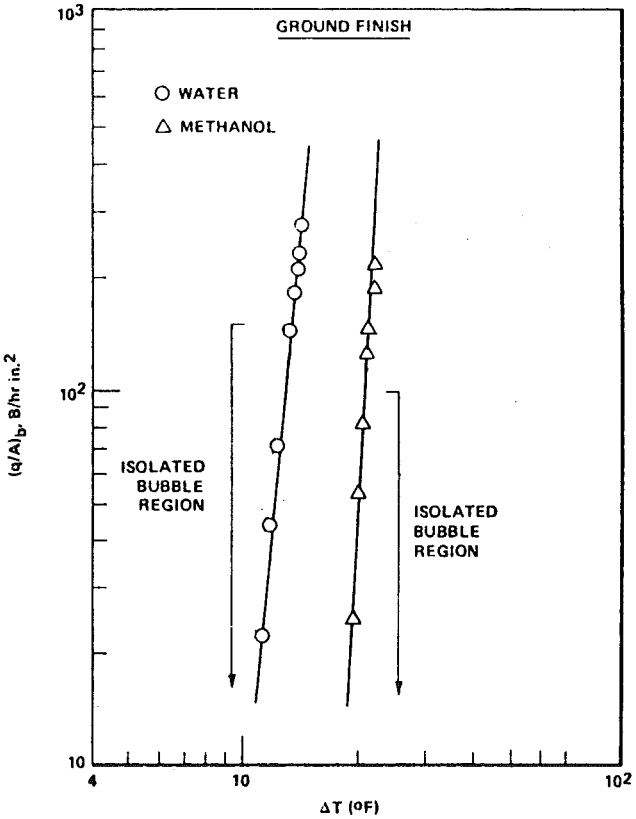

Fig. 2 Boiling heat flux/superheat correlation for water and methanol abstracted from reference [4]

same reasons given in reference [1] but $r_{c_{min}}$ was now determined by the relationship

$$r_{c_{min}} = \frac{1}{\eta} * \frac{2\sigma T_{sat}}{\rho_v h_{fg} \Delta T} \tag{6}$$

Physical properties appropriate to methanol boiling at atmospheric pressure were used throughout this analysis and the values of ΔT used were obtained from Fig. 2 and similar diagrams found in reference [3] corresponding to the other surface finishes investigated.

Discussion

When the values of nucleate boiling heat flux (Q_{NB}/A_T) were plotted against bubble flux density Φ, the data points were observed to cluster together as illustrated in Fig. 3. The implication of this observation is that a single relationship exists between heat flux and bubble flux density for the particular surface-liquid combination irrespective of surface finish. Furthermore, it would appear that boiling heat flux is directly proportional to bubble flux density which is entirely consistent with the assumption that each bubble is responsible for the transfer of a fixed amount of energy from the surface to the liquid in the isolated bubble regime. *However, it is important to be aware that the bubble flux density used in plotting Fig. 3 was predicted from theoretical considerations; further confirmation of the relationship between boiling heat flux and bubble flux density will have to await experimental determination of these parameters.*

While it was expected that the bubble flux density concept would draw the results for water and methanol together, it is somewhat surprising that the data points for the two different fluids would tend

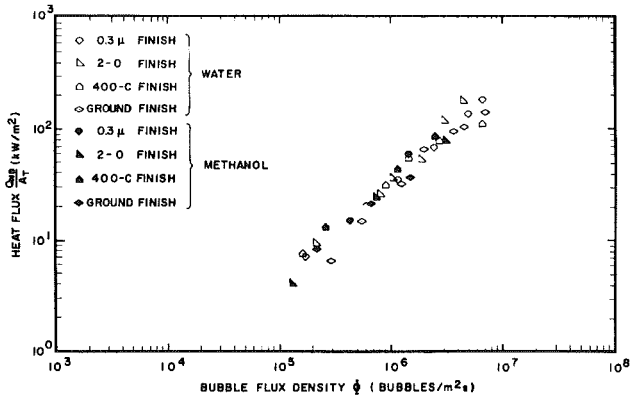

Fig. 3 Boiling heat flux/bubble flux density for water and methanol

to cluster about the same line. The mechanism by which the energy transfer associated with each bubble is accomplished cannot be deduced from this sort of analysis, and since there is no reason to believe that a water bubble would be responsible for the transfer of the same amount of energy as a methanol bubble under the same boiling conditions, the apparent agreement may simply be fortuitous. Nevertheless, it is significant that this treatment of the data is capable of unifying the results arising from nucleate boiling experiments performed with different surface finishes, indicating that nucleate boiling heat flux can be predicted by a relationship of the form

$$\frac{Q_{NB}}{A_T} = \text{Constant} * \Phi = \text{Constant} * mC \int_{r_{c_{min}}}^{r_{c_{max}}} \frac{f(r_c)}{r_c^{m+1}} dr_c \tag{7}$$

where

$$r_{c_{min}} = \frac{1}{\eta} * \frac{2\sigma T_{sat}}{\rho_v h_{fg} \Delta T}$$

and

$$r_{c_{max}} \rightarrow \text{large value}$$

In this relationship, the surface condition is completely incorporated in the surface characterization parameters m and C. The difficulty with this approach to predicting nucleate boiling heat flux remains that its use is restricted to those situations where m, C and η are known in advance which in the present circumstance requires experiments to have been performed already. Consequently, no further progress with this approach is possible until some way is devised to predict these parameters a priori.

Acknowledgment

The author is especially grateful to M. Sheehy and R. Janzen who developed the computer programs and generated the heat flux/bubble flux density correlation data for methanol.

References

1 Shoukri, M., and Judd, R. L., "On the Influence of Surface Conditions in Nucleate Boiling—the Concept of Bubble Flux Density," ASME JOURNAL OF HEAT TRANSFER, Nov. 1978, p. 618.

2 Shoukri, M., "Nucleation Site Activation in Saturated Boiling," Mech. Eng. Thesis, McMaster University, 1974.

3 Singh, A., "Effect of Surface Conditions on Nucleation and Boiling Characteristics," Ph.D. Thesis, Department of Mechanical Engineering, M.I.T., 1974.

4 Singh, A., Mikic, B. B., and Rohsenow, W. M., "Relative Behaviour of Water and Organics in Boiling," *Proceedings of the Sixth International Heat Transfer Conference,* Toronto, Aug. 1978.

Downloaded 20 Dec 2010 to 194.27.225.72. Redistribution subject to ASME license or copyright; see http://www.asme.org/terms/Terms_Use.cfm

The Effect of Crossflow at the Entrance on Heat Transfer Enhancement in Tubes

D. E. Metzger[1] and J. V. Cordaro[1]

Nomenclature

d = tube inside diameter
h = heat transfer coefficient, based on $(t - t_b)$
k = fluid thermal conductivity
L = tube length
Nu = average Nusselt number, hd/k
Re = Reynolds number, Vd/ν
t = tube temperature
t_b = average fluid bulk temperature in tube
V = bulk average axial fluid velocity in tube
V_c = upstream cross-flow channel velocity
V^* = velocity ratio, V_c/V
ν = fluid kinematic viscosity

Introduction

Flow distribution from a supply duct or manifold into multiple branch tubes is a situation which very frequently occurs in a wide variety of applications. In this situation, the flow entering the branch line will generally have a component of velocity that is perpendicular to the axis of the branch tube. Depending on the number of branches, the size of the supply duct, etc., the perpendicular velocity component at the entrance to a particular tube can have a very wide range of values compared to the mean axial velocity in the tube. Under these circumstances it is expected that this crossflow velocity will induce a secondary flow in the branch tube. In turn, the secondary flow will produce heat transfer coefficients in the branch tube higher than those normally associated with an axial flow entrance condition.

Despite the prevalence of this type of flow situation in various heat exchange devices, there are few prior results available that can be used to predict the heat transfer rates. Measured heat transfer coefficients have been presented for flow in the vicinity of a tee-shaped junction between one inlet and two outlet tubes [1] and for flow in the vicinity of right-angle mitred bends in a single tube [2]. More recently [3], measurements have been made in the main line or supply tube just downstream of fluid withdrawal to a branch tube; but no measurements were made in the branch tube itself. Although not directly applicable to the present situation, these prior studies demonstrate significant enhancement of heat transfer associated with the induced secondary flow. It is reasonable to expect similar behavior in tubes supplied from a crossflow.

In the present study, an apparatus was designed and constructed to allow determination of the circumferentially and axially averaged heat transfer coefficient in short branch tubes for a wide range of crossflow velocities and tube Reynolds numbers. The branch tubes were aligned perpendicular to the supply duct, and air was used as the test fluid. Three different circular cross-section branch tube diameters were used in the study, with overlapping length-to-diameter ratios spanning a range of 5 to 20. The flow velocity in the supply duct upstream of the branch tube was systematically varied from zero up to nearly 30 times the mean axial branch tube velocity. Branch tube Reynolds numbers based on mean axial velocity were varied from 10,000 to 100,000. Measured results with entrance crossflow are compared with measured zero-crossflow results obtained in the same test sections.

[1] Department of Mechanical and Energy Systems Engineering, Arizona State University, Tempe, AZ 85281.

Contributed by the Heat Transfer Division for publication in the JOURNAL OF HEAT TRANSFER. Manuscript received at ASME Headquarters February 8, 1980.

Experiments

The experiments were conducted in an apparatus with interchangeable instrumented branch line tubes leading from a primary flow channel, as shown in Fig. 1. Dry, filtered air passed through a primary flow metering section consisting of both orifice and laminar flow elements with the laminar flow element used for low flowrates. A similar metering section is used to measure the branch line flow downstream of the instrumented tubes. Plenums were located at both upstream and downstream ends of the primary channel and downstream on the branch line. Downstream valves on both exit plenums were used to control the flow split and branch tube Reynolds number.

The primary channel is constructed of 0.32 cm wall thickness rectangular aluminum tubing with inside dimensions 2.54 cm by 1.27 cm. The flanged ends of the channel are faired to the channel dimensions as shown in Fig. 1. The branch line flow is withdrawn from the center of one long side of the channel through interchangeable plugs with circular hole diameters matching the three branch tube diameters used in the study: 0.32, 0.48, and 0.64 cm.

The branch line tubes were fabricated from high conductivity copper cylinders with an outer diameter of 1.65 cm. For each of the three tube inner diameters four different length tubes were made with length-to-diameter ratios of 5, 10, 15, and 20.

Each of the interchangeable copper tubes is instrumented with thermocouples and the tubes are wrapped with electrical resistance heating wire. The assembly is then surrounded with an insulating cylindrical jacket. The heaters are used to preheat the copper tubes prior to each test run. The primary and branch flows are adjusted to desired values during the heating phase. When steady flow velocities and temperatures and a tube temperature of approximately 70°C are achieved, the heater power is reduced to zero and the copper tube is allowed to cool in the presence of the flow through the branch line.

The heat transfer coefficients associated with the branch flow, averaged over the tube length, were determined from the cooling transients. The high thermal conductivity and thick walls of the copper tubes serve to even the spatial temperature distribution in the tube and allow use of a single lumped capacitance model of the transient response for data reduction purposes. The adequacy of this approach was examined carefully at the outset of the test program. Additional details on the experimental apparatus and test and data reduction procedures are available in [4].

Results and Discussion

Initially tests were conducted without an entrance crossflow velocity component to provide baseline results for comparison with the results from tests with crossflow. These baseline tests were conducted with the instrumented tubes supplied directly from the upstream plenum through an adapter disk machined to accept the interchangeable plugs used in the primary channel. The axial alignment of plenum and tubes established a zero crossflow approach velocity to an abrupt, square-edged tube entrance condition.

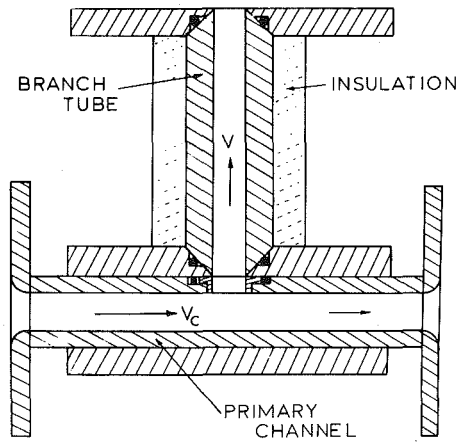

Fig. 1 Test section detail

Copyright © 1981 by ASME

Downloaded 20 Dec 2010 to 194.27.225.72. Redistribution subject to ASME license or copyright; see http://www.asme.org/terms/Terms_Use.cfm

The baseline results can be compared with published values for average heat transfer in short tubes [5, 6]. The results summarized in [5] are described by an L/d enhancement of the Colburn equation:

$$\mathrm{Nu} = 0.023\mathrm{Pr}^{0.67}\mathrm{Re}^{0.8}[1 + (d/L)^{0.7}] \quad (1)$$

Those of [6] are from 15 to 35 percent higher than (1), with the larger differences at the smaller L/d values. The present baseline test results are bracketed by the [5, 6] results, agreeing best with those of [6] at the low end of the Re range (10^4) and best with [5] at the high end (10^5). This is true for all three tube diameters used in the present tests; and differences in the Nu values obtained with the different diameter tubes are within the estimated experimental uncertainty. Estimated uncertainties [7] in Re range from ±1.5 to ±2.0 percent, with the higher values associated with the smallest tube diameter. For Nu, uncertainties range from ±5 to ±7 percent, with the higher values associated with lower Re.

The crossflow testing was conducted with the branch tube Reynolds number held nominally constant (±3 percent) at values of 10^4, 2×10^4, 5×10^4, and 10^5. At each of these values the crossflow was systematically increased from its lowest values (with all the channel flow directed through the branch tube) through a range of values to an upper limit set by the flow supply capacity. This upper limit is dependent on tube diameter and Reynolds number. For the 0.64 cm tubes, the maximum value of crossflow is approximately 29 and 3 times the mean axial tube flow at $\mathrm{Re} = 10^4$ and $\mathrm{Re} = 10^5$, respectively. For the smaller tubes these maximum attainable crossflow ratios (V^*) are smaller for the same values of Reynolds numbers because of the higher required tube velocities. For the 0.32 cm tubes, the maximum values of the ratios are approximately 7 and 1 at the lowest and highest Reynolds numbers respectively. Experimental uncertainties for V^* are estimated to be from ±4 to ±5 percent, with the higher values associated with the smallest tube diameter.

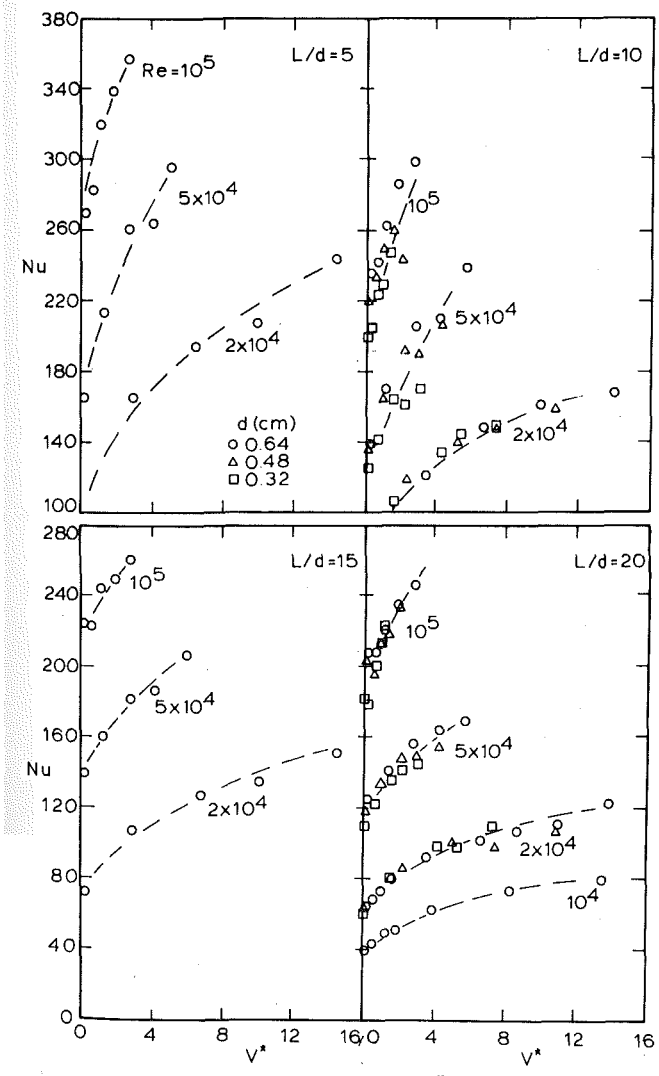

Fig. 2 Results with crossflow

Figure 2 presents Nusselt number results for each of the four values of L/d at each of the nominal Reynolds numbers as a function of V^*. Again, where all three tube sizes were used ($L/D = 10$ and 20) there is reasonably good agreement between the results from one size and those of another. This should provide some degree of confidence in scaling the present results for use with different branch tube sizes. The lowest V^* value results shown in Fig. 2 correspond to cases where all primary channel flow is routed through the branch tube. Nusselt numbers for these cases ($0.06 < V^* < 0.26$) agree within experimental uncertainties with the corresponding zero crossflow values from the baseline tests.

The experimental results show that there can be a significant effect of a crossflow or transverse entrance velocity component on the average heat transfer in short tubes; a situation common in heat exchange devices where multiple branch cooling passages are supplied from a manifold. The heat transfer enhancement increases with increasing crossflow-to-tube velocity ratio; the amount depending on both Reynolds number and tube length-to-diameter ratio.

References

1 Wesley, D. A., and Sparrow, E. M., "Circumferentially Local and Average Turbulent Heat-Transfer Coefficients in a Tube Downstream of a Tee," *International Journal of Heat and Mass Transfer*, Vol. 19, 1976, pp. 1205–1214.

2 Ede, A. J., and LeFevre, E. J., "The Effect of a Right-Angled Bend on Heat Transfer in a Pipe," *International Developments in Heat Transfer*, ASME, New York, 1961, pp. 634–645.

3 Sparrow, E. M., and Kemink, R. G., "Heat Transfer Downstream of a Fluid Withdrawal Branch in a Tube," ASME JOURNAL OF HEAT TRANSFER, Vol. 101, 1979, pp. 23–28.

4 Metzger, D. E., and Cordaro, J. V., "Heat Transfer in Short Tubes Supplied from a Cross-Flowing Stream," ASME Paper 79WA/HT-16, 1979.

5 McAdams, W. H., *Heat Transmission*, McGraw-Hill, New York, 1954.

6 Mills, A. F., "Experimental Investigation of Turbulent Heat Transfer in the Entrance Region of a Tube," *Journal of Mechanical Engineering Science*, Vol. 4, No. 1, 1962, pp. 63–77.

7 Kline, S. J. and McClintock, F. A., "Describing Uncertainties in Single-Sample Experiments," *Mechanical Engineering*, Vol. 75, Jan., 1953, p. 3.

Double Diffusive Instability in a Vertical Layer of a Porous Medium

A. A. Khan[1] and A. Zebib[1]

Nomenclature

L = layer thickness
T = temperature
ΔT = temperature difference across the layer
S = solute concentration
K = permeability
ϵ = porosity
κ_T = thermal diffusivity
κ_S = solute diffusivity
ρ, ρ_r = density and reference density
c = specific heat
α = coefficient of expansion $= -\frac{1}{\rho_r}\frac{\partial \rho}{\partial T}\Big|_r$

[1] Department of Mechanical, Industrial and Aerospace Engineering, College of Engineering, Rutgers University, Piscataway, N.J. 08854.

Contributed by the Heat Transfer Division for publication in the JOURNAL OF HEAT TRANSFER. Manuscript received by the Heat Transfer Division March 10, 1980.

Downloaded 20 Dec 2010 to 194.27.225.72. Redistribution subject to ASME license or copyright; see http://www.asme.org/terms/Terms_Use.cfm

The baseline results can be compared with published values for average heat transfer in short tubes [5, 6]. The results summarized in [5] are described by an L/d enhancement of the Colburn equation:

$$\mathrm{Nu} = 0.023\mathrm{Pr}^{0.67}\mathrm{Re}^{0.8}[1 + (d/L)^{0.7}] \quad (1)$$

Those of [6] are from 15 to 35 percent higher than (1), with the larger differences at the smaller L/d values. The present baseline test results are bracketed by the [5, 6] results, agreeing best with those of [6] at the low end of the Re range (10^4) and best with [5] at the high end (10^5). This is true for all three tube diameters used in the present tests; and differences in the Nu values obtained with the different diameter tubes are within the estimated experimental uncertainty. Estimated uncertainties [7] in Re range from ±1.5 to ±2.0 percent, with the higher values associated with the smallest tube diameter. For Nu, uncertainties range from ±5 to ±7 percent, with the higher values associated with lower Re.

The crossflow testing was conducted with the branch tube Reynolds number held nominally constant (±3 percent) at values of 10^4, 2×10^4, 5×10^4, and 10^5. At each of these values the crossflow was systematically increased from its lowest values (with all the channel flow directed through the branch tube) through a range of values to an upper limit set by the flow supply capacity. This upper limit is dependent on tube diameter and Reynolds number. For the 0.64 cm tubes, the maximum value of crossflow is approximately 29 and 3 times the mean axial tube flow at $\mathrm{Re} = 10^4$ and $\mathrm{Re} = 10^5$, respectively. For the smaller tubes these maximum attainable crossflow ratios (V^*) are smaller for the same values of Reynolds numbers because of the higher required tube velocities. For the 0.32 cm tubes, the maximum values of the ratios are approximately 7 and 1 at the lowest and highest Reynolds numbers respectively. Experimental uncertainties for V^* are estimated to be from ±4 to ±5 percent, with the higher values associated with the smallest tube diameter.

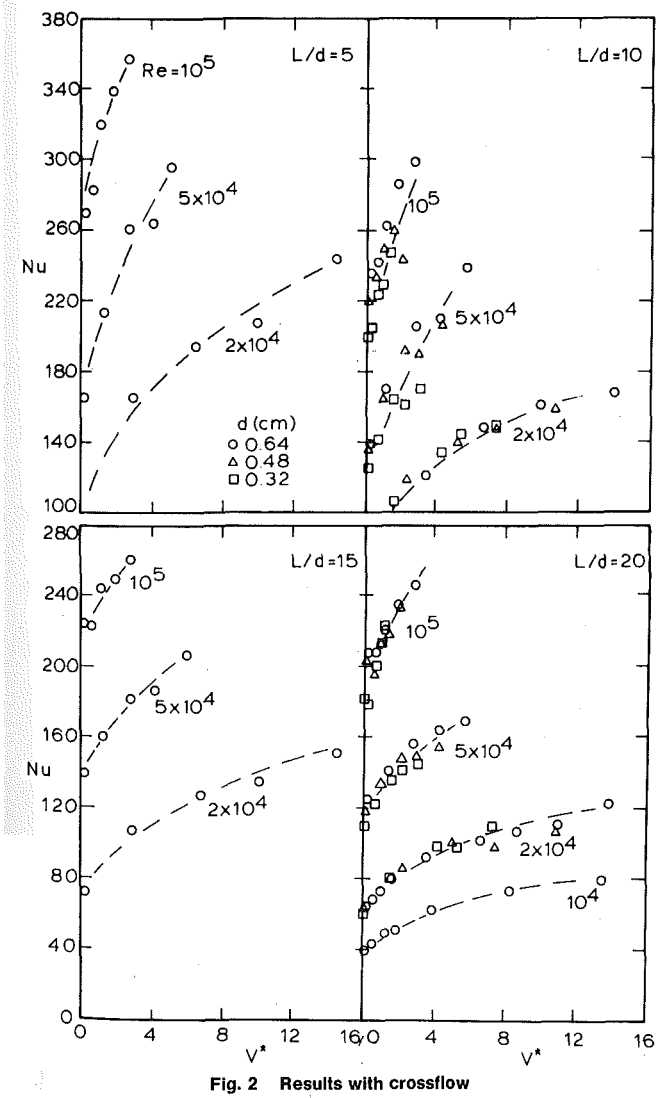

Fig. 2 Results with crossflow

Figure 2 presents Nusselt number results for each of the four values of L/d at each of the nominal Reynolds numbers as a function of V^*. Again, where all three tube sizes were used (L/D = 10 and 20) there is reasonably good agreement between the results from one size and those of another. This should provide some degree of confidence in scaling the present results for use with different branch tube sizes. The lowest V^* value results shown in Fig. 2 correspond to cases where all primary channel flow is routed through the branch tube. Nusselt numbers for these cases ($0.06 < V^* < 0.26$) agree within experimental uncertainties with the corresponding zero crossflow values from the baseline tests.

The experimental results show that there can be a significant effect of a crossflow or transverse entrance velocity component on the average heat transfer in short tubes; a situation common in heat exchange devices where multiple branch cooling passages are supplied from a manifold. The heat transfer enhancement increases with increasing crossflow-to-tube velocity ratio; the amount depending on both Reynolds number and tube length-to-diameter ratio.

References

1 Wesley, D. A., and Sparrow, E. M., "Circumferentially Local and Average Turbulent Heat-Transfer Coefficients in a Tube Downstream of a Tee," *International Journal of Heat and Mass Transfer*, Vol. 19, 1976, pp. 1205–1214.

2 Ede, A. J., and LeFevre, E. J., "The Effect of a Right-Angled Bend on Heat Transfer in a Pipe," *International Developments in Heat Transfer*, ASME, New York, 1961, pp. 634–645.

3 Sparrow, E. M., and Kemink, R. G., "Heat Transfer Downstream of a Fluid Withdrawal Branch in a Tube," ASME JOURNAL OF HEAT TRANSFER, Vol. 101, 1979, pp. 23–28.

4 Metzger, D. E., and Cordaro, J. V., "Heat Transfer in Short Tubes Supplied from a Cross-Flowing Stream," ASME Paper 79WA/HT-16, 1979.

5 McAdams, W. H., *Heat Transmission*, McGraw-Hill, New York, 1954.

6 Mills, A. F., "Experimental Investigation of Turbulent Heat Transfer in the Entrance Region of a Tube," *Journal of Mechanical Engineering Science*, Vol. 4, No. 1, 1962, pp. 63–77.

7 Kline, S. J. and McClintock, F. A., "Describing Uncertainties in Single-Sample Experiments," *Mechanical Engineering*, Vol. 75, Jan., 1953, p. 3.

Double Diffusive Instability in a Vertical Layer of a Porous Medium

A. A. Khan[1] and A. Zebib[1]

Nomenclature

L = layer thickness
T = temperature
ΔT = temperature difference across the layer
S = solute concentration
K = permeability
ϵ = porosity
κ_T = thermal diffusivity
κ_S = solute diffusivity
ρ, ρ_r = density and reference density
c = specific heat
α = coefficient of expansion $= -\frac{1}{\rho_r}\frac{\partial \rho}{\partial T}\Big|_r$

[1] Department of Mechanical, Industrial and Aerospace Engineering, College of Engineering, Rutgers University, Piscataway, N.J. 08854.

Contributed by the Heat Transfer Division for publication in the JOURNAL OF HEAT TRANSFER. Manuscript received by the Heat Transfer Division March 10, 1980.

Copyright © 1981 by ASME

Downloaded 20 Dec 2010 to 194.27.225.72. Redistribution subject to ASME license or copyright; see http://www.asme.org/terms/Terms_Use.cfm

β = coefficient of expansion $= \frac{1}{\rho_r}\frac{\partial \rho}{\partial S}\Big|_r$

R_s = salinity Rayleigh number

R_a = thermal Rayleigh number $= \frac{gK\alpha\Delta TL}{\nu\kappa_T}$

ψ = streamfunction
t = time
$r = (\rho c)_m/(\rho c)_f$
$H = \kappa_T/\kappa_S$
k = wave number
$P = H/r$
$N = H/\epsilon$
σ_1 = growth rate
$\sigma = rR_a\sigma_1$

Subscripts

x = partial derivative with respect to x
z = partial derivative with respect to z
m = medium
f = fluid
o = steady-state
r = reference state

Superscript

$'$ = derivative with respect to x

Introduction

The stability of the steady motion driven by side heating of a stably stratified fluid which saturates an infinite vertical slab of a porous medium is considered. The steady mean motion is a function of the salinity Rayleigh number R_s. When $R_s = 0$, Gill [1] showed that the corresponding equilibrium situation is always stable. For values of $R_s > 0$, double-diffusive instabilities may be excited depending on the values of the salinity and thermal Rayleigh numbers. This thermal concentration instability was investigated by Gershuni, et al. [2] in the limit $R_s \to \infty$. The spontaneous formation of thermohaline convecting layers within a porous medium is of geophysical interest and has been postulated to occur in geothermal areas [3–5].

In this paper, we present a linear stability analysis of two-dimensional perturbations for values of $R_s \geqslant 0$. A Galerkin method is used to solve the resulting eigenvalue problem for the growth rates. The parameter values $r = 0.62$, $\epsilon = 0.38$ and $H = 260$ are assumed. These values correspond to a brine solution saturating a layer filled with glass beads. Our results for $R_s = 0$ and $R_s \to \infty$ are in complete agreement with those of Gill [1] and Gershuni, et al. [2]. We also find that for $R_s < 7.901$ there are no two-dimensional instabilities. The instabilities for $R_s \geqslant 7.901$ are found to be all stationary.

Formulation

Consider the physical and coordinate systems shown in Fig. 1. The vertical boundaries are isothermal and rigid, and the fluid is initially linearly stratified. The nondimensional, Darcy-Boussinesq equations are

$$\psi_{xx} + \psi_{zz} = -T_x + S_x,$$

$$rT_t + \psi_z T_x - \psi_x T_z = \frac{1}{R_a}(T_{xx} + T_{zz}),$$

$$\epsilon S_t + \psi_z S_x - \psi_x S_z = \frac{\epsilon}{HR_a}(S_{xx} + S_{zz}), \tag{1}$$

where length, time, velocity, temperature and salinity concentration have been assumed dimensionless with respect to L, $L\nu/(gK\alpha\Delta T)$, $gK\alpha\Delta T/\nu$, ΔT, and $\alpha\Delta T/\beta$, respectively. The boundary conditions associated with (1) are

$$\psi = S_x = 0, \quad x = \pm\,1/2,$$

$$T = 0, \quad x = -1/2,$$

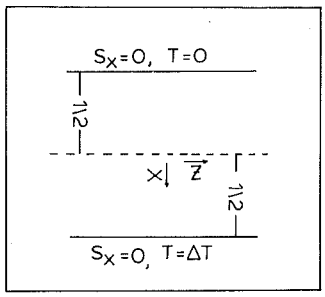

Fig. 1 Physical and coordinate systems

$$T = 1, \quad x = 1/2. \tag{2}$$

For an infinitely long layer, the steady solution to (1) and (2) is given by

$$T_0 = x + 1/2,$$

$$So_x = R_s\psi_0,$$

$$\psi_0 = \frac{1}{R_s}[1 - \cos hR_s^{1/2}x/\cos hR_s^{1/2}/2]. \tag{3}$$

where the salinity Rayleigh number R_s is defined by

$$R_s = -\frac{HR_a}{\epsilon}So_z, \tag{4}$$

and So_z is the nondimensional imposed concentration gradient.

The stability of the steady motion given by (3) to two-dimensional perturbations is now considered; let

$$\psi = \psi_0(x) + \phi(x)\exp(\sigma_1 t + ikz),$$

$$T = T_0(x) + \theta(x)\exp(\sigma_1 t + ikz),$$

$$S = S_0(x_1 z) + \sigma(x)\exp(\sigma_1 t + ikz), \tag{5}$$

in (1) and neglect higher order terms in ϕ, θ, and Σ. The resulting eigenvalue problem is

$$\phi'' - k^2\phi = -\theta' + \sigma'$$

$$\phi'' - k^2\theta = \sigma\theta + ikR_a\phi - ikR_a\psi'_0\theta,$$

$$\sigma'' - k^2\sigma = P\sigma\sigma + ikR_aN(So_x\phi - \psi'_0\Sigma) + R_s\phi', \tag{6}$$

with the boundary conditions

$$\theta = \phi = \sigma' = 0 \text{ at } x = \pm 1/2, \tag{7}$$

The parameters $P = H/r$ and $N = H/\epsilon$ were introduced by Gershuni, et al. [2] and thus the physical problem is influenced by ϵ, r, and H only through the ratios H/r and H/ϵ.

Numerical Calculations

Equations (6) and (7) with ψ'_0 and So_x given by (3) are solved numerically by a Galerkin method. The perturbations ϕ, θ, and σ are expanded in complete sets of functions which satisfy the homogeneous conditions in (7). Thus, we assume the representations (cf. Hart [6] and Paliwal and Chen [7]).

$$\theta = \sum_{n=1}^{N} a_n Y_n,$$

$$\phi = \sum_{n=1}^{N} B_n Y_n,$$

$$\sigma = c_0 + \sum_{n=1}^{N} c_n Y'_n, \tag{8}$$

where the basis functions $Y_n(x)$ are the eigensolutions of

$$Y''_n + \lambda_n^2 Y_n = 0, \qquad Y_n(\pm 1/2) = 0 \tag{9}$$

Downloaded 20 Dec 2010 to 194.27.225.72. Redistribution subject to ASME license or copyright; see http://www.asme.org/terms/Terms_Use.cfm

The expansions in (8) are substituted in $(6)_1 - (6)_3$ and operated on by

$$\int_{-1/2}^{1/2} Y_m dx, \int_{-1/2}^{1/2} Y_m dx, \quad \text{and} \quad \int_{-1/2}^{1/2} dx, \quad \int_{-1/2}^{1/2} Y'_n dx$$

respectively. The first of these operations leads to

$$b_m = \frac{1}{(\lambda_m^2 + k^2)} \left[\sum_{n=1}^{N} a_n Z_{nm} + \lambda_m^2 c_m \right], \quad m = 1, 2, \ldots N, \quad (10)$$

where $Z_{nm} = \int_{-1/2}^{1/2} Y'_n Y_m dx / \int_{-1/2}^{1/2} Y_n^2 dx$. Thus with b_n given in terms of a_n and c_n in (10), together with the last three operations, the original system (6) is converted to a $(2N + 1) \times (2N + 1)$ matrix eigenvalue problem with eigenvalues σ. The solution is accomplished by a standard library subroutine for complex matrices. The stability boundary is determined by computing parameter values for which $\text{Max}(\text{Re}(\sigma)) = 0$. Overstability is indicated if the associated $Im(\sigma) \neq 0$. The value of N needed for convergence in the cases considered was found to be 10.

Figures 2–4 show the numerical results. The stability boundary for the parameter values considered is composed of stationary states. When $R_s = 0$, the basic flow is stable, and remains stable for values of $R_s < 7.901$. There is a minimum value for the imposed concentration gradient which renders the flow unstable, in this case it corresponds to $R_s = 7.901$. This is in qualitative agreement with the behavior of continuous fluids when transition takes place from shear to double-diffusive instabilities at some finite value of $R_s > 0$ [6, 7].

Figures 2 and 3 show the neutral curves for $R_s = 8, 9, 10, 100$ and 251. These curves have minima for R_a when R_s equals 8, 9 and 10. However, for $10 \leq R_s < 251$, the neutral curves become flat as $k \to 0$, and no minimum is well defined, although the value R_{a_c} is clearly indicated.

In the limit $R_s \to \infty$, appropriate for strong stratification, it is seen from (3) that $\psi_0 \to 0$ and $So_x \to 1$. Thus, the basic state is characterized by zero horizontal density gradient and is in a mechanical equilibrium (except in boundary layers near the vertical boundaries of thickness $0(R_s^{-1/2})$ where $So_x \to 0$). This is the situation considered by Gershumi, et al. [2]. Their results for critical states with $\sigma = 0$ are

$$K_c = R_s^{1/4} \sqrt{\pi} \quad \text{and} \quad \text{Ra}_c = R_s^{3/4} \frac{\sqrt{8\pi}}{|N - 1|}. \quad (11)$$

These asymptotic values are shown by the dashed lines in Fig. 4, and they are in excellent agreement with the exact solution for $R_s > 1000$.

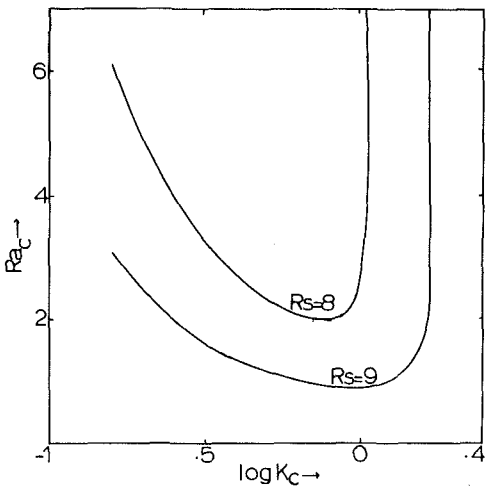

Fig. 2 Neutral curves for $R_s = 8$ and 9

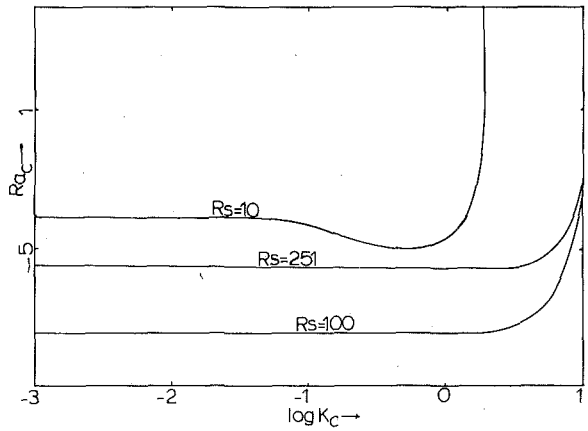

Fig. 3 Neutral curves for $R_s = 10$, 100 and 251

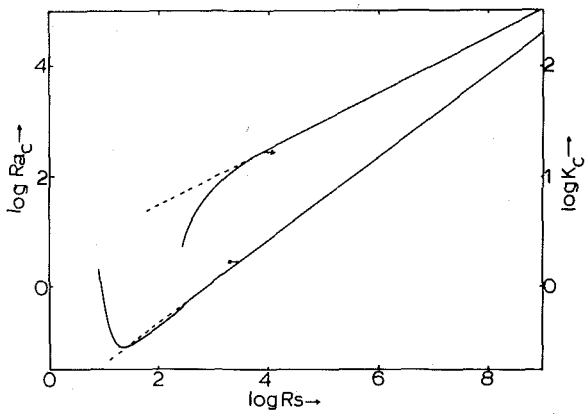

Fig. 4 Variation of Ra_c and K_c with R_s. The dashed lines represent the asymptotic results for $R_s \to \infty$.

Acknowledgment

The authors wish to thank C. F. Chen for suggesting the problem and for helpful discussions. This research was supported by an N.S.F. Grant Eng. 78-16962.

References

1 Gill, A. E., "A Proof that Convection in a Porous Vertical Slab is Stable," *Journal of Fluid Mechanics*, Vol. 35, 1969, pp. 545–547.

2 Gershuni, G. Z., Zhukhovitskii, E. M., and Lyubimov, D. V., "Thermal Concentration Instability of a Mixture in a Porous Medium," *Soviet Physics—Doklady*. Vol. 21, No. 7, 1976.

3 Nield, D. A., "Onset of Thermohaline Convection in a Porous Medium, Water Resources Research," Vol. 4, 1968, pp. 553–560.

4 Turner, J. S., and Gustafson, L. B., "The Flow of Hot Saline Solutions from Vents in the Sea Floor—Some Implications for Exhalative Massive Sulfide and Other Ore Deposits, *Economic Geology*, Vol. 73, 1978, pp. 1082–1100.

5 Griffiths, R. W., "Layered Double-Diffusive Convection in a Porous Medium," *Journal of Fluid Mechanics*, in press, 1980.

6 Hart, J. E., "On Sideways Diffusive Instability," *Journal of Fluid Mechanics*, Vol. 49, 1971, pp. 279–288.

7 Paliwal, R. C., and Chen, C. F., "Double Diffusive Instability in an Inclined Fluid Layer," Part II, *Journal of Fluid Mechanics*, Vol. 98, 1980 pp. 769–785.

Downloaded 20 Dec 2010 to 194.27.225.72. Redistribution subject to ASME license or copyright; see http://www.asme.org/terms/Terms_Use.cfm

Application of the P-1 Approximation to Radiative Heat Transfer in a Nongray Medium

W. W. Yuen[1] and D. J. Rasky[2]

Nomenclature

a_w = absorption coefficient at wavenumber w
A_p = Planck's mean absorption coefficient
$A_{iw} (i = 0, 1, 2, 3)$ = expansion coefficients defined by equation (5)
d = spectral line spacing
e_{bw} = blackbody emissive power
e_{bw1} = blackbody emissive power evaluated at T_1
e_{bw2} = blackbody emissive power evaluated at T_2
e_{bw0} = blackbody emissive power evaluated at $z = 0$
$e^{(1)}_{bw0} = \partial e_{bw}/\partial z \ (z = 0)$
e_{b1i} = blackbody emissive power evaluated at w_i and T_1
e_{b2i} = blackbody emissive power evaluated at w_i and T_2
e_{b0i} = blackbody emissive power evaluated at w_i and $z = 0$
$e^{(1)}_{b0i} = \partial e_{bw}/\partial z \ (z = 0, w = w_i)$
$F_i^{(k)}$ = integral of F_{kw} over the ith band
F_{kw} = function defined by equation (8)
$G_i^{(k)}$ = integral of G_{kw} over the ith band
G_{kw} = function defined by equation (9)
i_w = radiative intensity
$i_{bw} = e_{bw}/\pi$
$i_{bw1} = e_{bw1}/\pi$
$i_{bw2} = e_{bw2}/\pi$
L = separation between two plates for the one-dimensional system
$L_w = a_w L$
q = radiative heat flux
Q = heat generation rate
S = mean line intensity
T_1 = temperature of the lower boundary
T_2 = temperature of the upper boundary
z = coordinate
γ = line half-width
$\eta = z/L$
$\mu = \cos\theta$
w = wavenumber
ρ = density of gas
$\psi_{n,w}$ = spherical harmonic n-moment

1 Introduction

Interest in predicting the heat transfer rate through an absorbing emitting medium has been increasing as more problems with high temperature have arisen. But realistic solutions to these problems, even in a very simple geometric system, are difficult to obtain because of the frequency and temperature-dependent radiation properties of the medium.

In the present work the P-1 approximation method, which has been demonstrated [1] to be effective in generating accurate approximate solutions to the gray problem, will be generalized for nongray problems. In contrast to most of the existing approaches [2–4], the present method has the advantage that all solutions will be formulated in terms of the spectral absorption coefficient. The method is thus applicable for all media including those for which correlations of total band absorptance are not available. For gases, the present technique will be demonstrated to be superior. Even for situations in which the simultaneous effects of all absorption bands are considered, only simple iterations are required for its solution.

2 Mathematical Formulation

The mathematical development for the P-1 approximation is well known. In essence, the transfer equation and the energy equation are combined to yield

$$\frac{\partial \psi_{1,w}}{\partial z} + a_w \psi_{0,w} = 4 a_w e_{bw} \tag{1}$$

$$\frac{\partial \psi_{0,w}}{\partial z} + 3 a_w \psi_{1,w} = 0 \tag{2}$$

where $\psi_{0,w}$ and $\psi_{1,w}$ are the zeroth and first moment of the spectral intensity function at wavenumber w, a_w the absorption coefficient, e_{bw} the blackbody emission power, and z the coordinate. The energy equation becomes

$$\frac{d}{dz} \int_0^\infty \psi_{1,w} dw = Q \tag{3}$$

with Q being the internal heat generation rate. As in the gray analysis, the intensity boundary conditions are replaced by Marshak's boundary condition. Only two of such conditions are required for the P-1 approximation. They are

$$\int_0^1 i_w \mu d\mu = \frac{1}{2} i_{bw1} \qquad at\ z = -\frac{L}{2}$$

$$\int_{-1}^0 i_w \mu d\mu = \frac{-1}{2} i_{bw2} \qquad at\ z = \frac{L}{2} \tag{4}$$

where $\mu = \cos\theta$, $i_{bw1} = i_{bw}(T_1)$, $i_{bw2} = i_{bw}(T_2)$. In the above equations, the two plates are assumed to be at temperature T_1 and T_2 and located at $z = -L/2$ and $z = L/2$, respectively.

Despite their apparent simplicity, equations (1–4) are still difficult to solve exactly. A simple approximate solution, however, can be generated by assuming that the average intensity function, $\psi_{0,w}$ is given by

$$\psi_{0,w} = A_{0w} + A_{1w} z + A_{2w} z^2 + A_{3w} z^3 \tag{5}$$

Substituting equation (5) into equation (2), a similar polynomial expression for ψ_{1w} can be generated. Utilizing equation (4) and requiring that coefficients for the zeroth and first power of z on both sides of equation (1) to be equal, solutions for the four expansion coefficients can be obtained. Utilizing the above expressions, equations (2) and (3) and assuming that Q = constant, the following equations result:

$$\int_0^\infty F_{1w} (e_{bw1} + e_{bw2} - 2 e_{bw0}) dw = -3QL \tag{6}$$

$$\int_0^\infty \left[G_{2w} (e_{bw1} - e_{bw2}) + \left(G_{2w} + \frac{4}{3} G_{1w} \right) e_{bw0}{}^{(1)} L \right] dw = 0 \tag{7}$$

where $e_{bw0} = e_{bw}\ (z = 0)$ and $e_{bw0}{}^{(1)} = \partial e_{bw}/\partial z\ (z = 0)$. In the above equations, F_{kw} and G_{kw} are functions defined as

$$F_{kw} = \frac{6 L_w{}^k}{1 + L_w + 3 L_w{}^2/8} \tag{8}$$

$$G_{kw} = \frac{32 L_w{}^k}{L_w{}^3 + 4 L_w{}^2 + 8 L_w + 32/3} \tag{9}$$

with $L_w = a_w L$. For a given nongray medium with a known absorption coefficient a_w, equation (6) can be readily solved iteratively to yield the unknown centerpoint temperature $T(z = 0)$. Equation (7) can be similarly solved to generate $dT/dz\ (z = 0)$. These results can be used to determine the unknown expansion coefficients and subsequently the temperature profile and heat transfer. It is interesting to note that in the limit of a gray medium (a_w = const.), solutions to equations (6) and (7) correspond exactly to the traditional diffusion approximation.

[1] Assistant Professor, Department of Mechanical and Environmental Engineering, University of California, Santa Barbara, Calif. 93106.
[2] Graduate Student, Department of Mechanical and Environmental Engineering, University of California, Santa Barbara, Calif. 93106.

Contributed by The Heat Transfer Division and presented at the 19th AIChE/ASME National Heat Transfer Conference, Orlando, Fla., July 27–30, 1980. Revised manuscript received by The Heat Transfer Division April 21, 1980. Paper No. 80-HT-28.

Copyright © 1981 by ASME
Downloaded 20 Dec 2010 to 194.27.225.72. Redistribution subject to ASME license or copyright; see http://www.asme.org/terms/Terms_Use.cfm

3 Analytical Solution

Surprisingly, direct information on a_w for the different common absorbing gases (CO_2, H_2O, etc.) is scarce. Because of its highly irregular and complex behavior, most of the existing spectroscopic data on gaseous absorption are presented in terms of the correlation parameters for the wide-band total-absorptance model [5]. To generate an expression for a_w which is needed for the P-1 approximation, the present work proposes to utilize these data indirectly. Based on the Elsassar "narrow band" expression for a_w and evaluating at the center of the narrow band, the present work assumes that the absorption coefficient is given by

$$a_w = \left(\frac{\rho S}{d}\right) \frac{\sinh [2\pi\gamma/d]}{\cosh [2\pi\gamma/d] - 1} \tag{10}$$

where ρ is the gas density, S/d the mean-line-intensity-to-spacing ratio and γ/d is the line-width-to-spacing ratio for the considered narrow band. Over a wide band, it can be shown that S/d is a function of wave number and γ/d a function of temperature and pressure. They are tabulated for the various gases in reference [5].

Equations (6) and (7) can be further simplified by assuming that the blackbody emissive power e_{bw} varies only slowly over the range of w at which F_{kw} and G_{kw} are significantly different from zero. Treating e_{bw} as a constant in the integration, equations (6) and (7) become

$$\sum_{i=1}^{n} F_i^{(1)} (e_{b1i} + e_{b2i} - 2e_{b0i}) = -3QL \tag{6a}$$

$$\sum_{i=1}^{n} \left[G_i^{(2)} (e_{b1i} - e_{b2i}) + e_{b0i}{}^{(1)} L \left(G_i^{(2)} + \frac{4}{3} G_i^{(1)} \right) \right] = 0 \tag{7a}$$

where the subscript i stands for evaluation at the center (or the head) of the ith band w_i and $F_i^{(k)}$, $G_i^{(k)}$ are integrals of the function F_{kw} and G_{kw} over the ith band. It is interesting to note that utilizing equation (10), $F_i^{(k)}$ and $G_i^{(k)}$ can be evaluated in closed-form for all values of k.

Even without explicit numerical computations, a number of interesting analytical expressions can be readily generated. For the case with equal wall temperature ($T_1 = T_2$) and nonzero heat generation ($Q \neq 0$), assuming that the blackbody emissive power can be approximated by the following linearization

$$e_{b0i} = e_{b1i} + \left(\frac{de_{bi}}{dT}\right)_{T_1} (T_0 - T_1) \tag{14}$$

equation (10a) yields

$$T_0 = T_1 + \frac{\frac{3}{2} QL}{\sum_{i=1}^{n} F_i^{(1)} \left(\frac{de_{bi}}{dT}\right)_{T_1}} \tag{15}$$

In the optically thin limit, equation (21) is reduced to

$$T_0 = T_1 + \frac{QL}{4 \sum_{i=1}^{n} \left[\tau C_3 \left(\frac{de_b}{dT}\right)_{T_1} \right]_i} \tag{16}$$

where $\tau = \rho L (C_1/C_3) \sinh (2\pi\gamma/d)/(\cosh (2\pi\gamma/d) - 1)$, and C_1, C_3 the wide-band correlation constants tabulated in reference [5]. Equation (16) is the correct optically thin limiting expression for T_0 as discussed in reference [3]. In the large path-length limit ($\rho L \rightarrow$ large), equation (15) is reduced to

$$T_0 = T_1 + \frac{QL}{6.96 \sum_{i=1}^{n} \left[C_3 \left(\frac{de_b}{dT}\right)_{T_1} \right]_i} \tag{17}$$

Except for a simple numerical factor, equation (23) is again identical to the corresponding expression developed in reference [3]. (The numerical value 6.96 is replaced by 2π in that reference.)

For the case with unequal wall temperatures ($T_1 \neq T_2$) and zero heat generation ($Q = 0$), the overall heat transfer is the more interesting physical quantity. Utilizing equations (6–9) and the definition of heat flux, it can be shown that in the large pathlength limit

$$q \rightarrow \sigma T_1^4 - \sigma T_2^4 - \sum_{i=1}^{n} (e_{b1i} - e_{b2i})(1n\tau)_i \tag{18}$$

Since $1n\tau$ is the large pathlength limit of the wide-band total gas absorptance, equation (18) suggests that in that limit the different bands absorb independently and their effects add linearly to yield the total attenuation. Since the contribution due to the different bands can be quite substantial, the above expression also illustrates that calculations in which only one absorption band is considered can lead to significant error in the heat flux prediction at the large pathlength limit.

4 Numerical Results and Discussion

To demonstrate quantitatively the effectiveness and the accuracy of the present method, solutions with CO_2 as the absorbing medium are now generated. Assuming that $Q = 0$ and the only relevant absorption band is the 4.3 μ band, solution to equations (10a) and (10b) yield the following expressions for the heat flux and the temperature distribution

$$q = \sigma T_1^4 - \sigma T_2^4 - (e_{b1c} - e_{b2c}) \left[\frac{1}{32} G_c^{(3)} + \frac{1}{8} G_c^{(2)} + \frac{1}{4} G_c^{(1)} \right] + [e_{b1c} - e_{b2c}) G_c^{(2)} \left[\frac{G_c^{(2)} + 4G_c^{(1)}}{24G_c^{(2)} + 32G_c^{(1)}} \right] \tag{19}$$

$$\frac{e_{bc}(z) - e_{b2c}}{e_{b1c} - e_{b2c}} = \frac{1}{2} - \frac{1}{4A_pL} \left[G_c^{(2)} \eta + \frac{1}{2} G_c^{(4)} \eta^3 \right] - \frac{G_c^{(2)} \left[G_c^{(4)} (\eta - 4\eta^3) + 4G_c^{(3)} \eta - \frac{16}{3} G_c^{(2)} \eta^3 \right]}{4A_pL \left[8G_c^{(2)} + 32/3 G_c^{(1)} \right]} \tag{20}$$

Table 1 Comparison of the dimensionless heat flux ($q/\sigma T_2^4$) for two typical cases obtained from the present P_1 approximation and those obtained from other techniques

	Case 1	Case 2
Wide-band Curtis-Godson method	195.029	189.481
Hottel's method	195.038	189.491
Method based on isothermal band absorption	194.887	189.727
P_1 approximation	194.1	189.2

Case 1: T_1 1500 K, T_2 = 400 K, P_{CO_2} = 0.2 atm, P_{N_2} = 10 atm, L = 1 cm.
Case 2: T_1 = 1500 K, T_2 = 400 K, P_{CO_2} = 1.0 atm, P_{N_2} = 0, L = 10 cm.

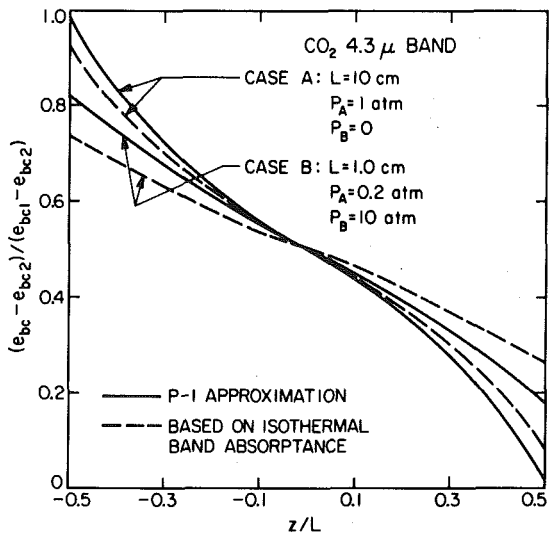

Fig. 1

Downloaded 20 Dec 2010 to 194.27.225.72. Redistribution subject to ASME license or copyright; see http://www.asme.org/terms/Terms_Use.cfm

In the above expression, $\eta = z/L$; the subscript c implies properties evaluated at the head of the 4.3 μ band and $A_p = 1/L \int_{\Delta_i} a_w L \, dw$ is the Planck mean absorption coefficient.

Assuming that $T_1 = 1500$ K and $T_2 = 400$ K, and evaluating $a_w q^+$ the average temperature, the heat flux calculated from equation (19) for two specific cases and those obtained from other techniques [2] are compared in Table 1. The agreement is excellent. The accuracy of the temperature profile result is illustrated in Fig. 1. It is important to note that the present mathematical development represents at least a ten-fold reduction in complexity comparing to all of the specific existing techniques.

Acknowledgment

This work is based upon work supported by the National Science Foundation Grant No. ENG78-05587.

References

1 Ozisik, M. N., *Radiative Transfer*, John Wiley & Sons, New York, 1973.

2 Chan, S. H., and Tien, C. L., "Infrared Radiative Heat Transfer in Non-Gray Non-Isothermal Gases," *International Journal of Heat and Mass Transfer*, Vol. 14, 1971, pp. 19–26.

3 Tiwari, S. N., "Applications of Infrared Band Model Correlation to Non-Gray Radiation," *International Journal of Heat and Mass Transfer*, Vol. 20, 1977, pp. 741–751.

4 Crosbie, A. L., and Viskanta, R., "Nongray Radiative Transfer in a Planar Medium Exposed to a Collimated Flux," *Journal Quantitative Spectroscopy Radiation Transfer*, Vol. 10, 1970, pp. 465–485.

5 Edwards, D. K., "Molecular Gas Band Radiation," *Advances in Heat Transfer*, Vol. 12, Academic Press, New York, 1976, pp. 116–195.

The Effects of Nonuniform Heat Transfer from an Annular Fin of Triangular Profile

P. J. Heggs,[1] D. B. Ingham,[2] and M. Manzoor[3]

Nomenclature

$h = (h_b + h_t)/2$, average heat transfer coefficient
h_b = heat transfer coefficient at fin-base
h_t = heat transfer coefficient at fin-tip
k = thermal conductivity
r = radial distance from tube axis
r_b = radius of fin-base
r_t = radius of fin-tip
t = half thickness of fin-base
$x = (r_t - r)/L$, dimensionless distance from fin-tip
Bi $= ht/k$, Biot number
H = nonuniform heat transfer coefficient
L = fin length
$M = (L/t)^2$ Bi/cos α, dimensionless
$N = 2(1 + \xi)$, dimensionless
$R = r_t/L$, dimensionless
T_b = temperature of fin-base
T_∞ = temperature of fluid
$\alpha = \tan^{-1}(t/L)$
$\epsilon = h_b/h_t$, dimensionless
$\theta = (T - T_\infty)/(T_b - T_\infty)$, dimensionless temperature
$\xi = (1 - \epsilon)$, dimensionless

Introduction

Finned surfaces are presently designed on the basis that the heat transfer coefficient is uniform over the fin surface as this permits the use of well established analytic solutions [1–3]. However, experimental investigations indicate that the heat transfer coefficient is not invariant [4–6]. In particular, for the annular geometry the heat transfer coefficient varies both radially and angularly over the fin surface (Wong [4]).

Analytic investigation of the effects of nonuniform heat transfer involve the use of assumed variation of the heat transfer coefficient, e.g., Han and Lefkowitz [7] employ heat transfer coefficients which vary as given powers of the displacement from the fin-base.

In this note the analytic solution for the temperature distribution within an annular triangular fin (Fig. 1) with linearly varying heat transfer coefficient is derived, and the corresponding fin efficiency is compared with experimental results.

[1] Senior Lecturer, Department of Chemical Engineering, University of Leeds, Leeds, England.

[2] Senior Lecturer, Department of Applied Mathematical Studies, University of Leeds, Leeds, England.

[3] Graduate Student, Department of Applied Mathematical Studies, University of Leeds, Leeds, England.

Contributed by the Heat Transfer Division for publication in the JOURNAL OF HEAT TRANSFER. Manuscript received by the Heat Transfer Division July 14, 1980.

Analysis

In the following analysis it is assumed that the thermal conductivity of the fin material, k, is constant and the heat transfer coefficient, H, varies linearly from h_b at the fin-base to h_t at the fin-tip, i.e.,

$$H(r) = \frac{2h}{(1+\epsilon)}\left(1 - (1-\epsilon)\frac{r_t - r}{r_t - r_b}\right) \tag{1}$$

where h is the average value of H and ϵ is the ratio of the heat transfer coefficient at the fin-base to that at the fin-tip.

For steady-state, one-dimensional conductive heat flow, an energy balance over an element of the fin, gives

$$\frac{d}{dr}\left(ry\frac{d}{dr}\theta\right) - \frac{H}{k\cos\alpha}r\theta = 0 \tag{2}$$

where the fin profile is described by

$$y(r) = \frac{t}{L}(r_t - r)$$

The inclusion of the exact representation for the incremental surface area, $(2\pi r\, dr/\cos\alpha)$, does not complicate the solution procedure, and has the advantage that the solution will be valid, even for small fin length to fin-base thickness ratios. This has particular significance as Lau and Tan [8] have recently shown, for a variety of fins, that the applicability of the one-dimensional approximation does not require the fin length to be large in comparison to the relevant transverse dimension.

The temperature distribution, and hence the heat transfer rate of the fin, are determined by solving equation (2) subject to the conditions

$$\text{i} \quad \text{at } r = r_b,\ \theta = 1 \tag{3}$$

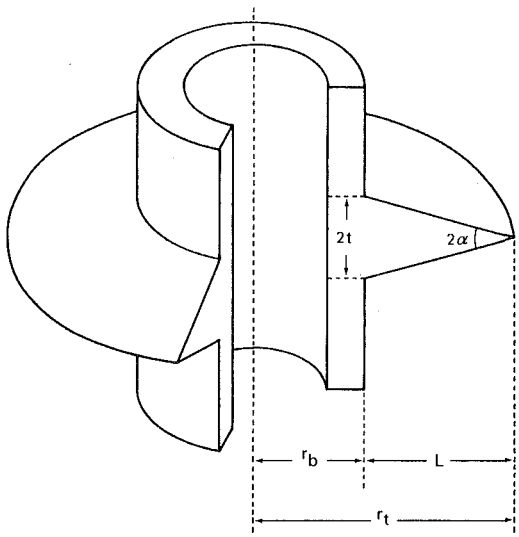

Fig. 1 The annular fin of triangular profile

Downloaded 20 Dec 2010 to 194.27.225.72. Redistribution subject to ASME license or copyright; see http://www.asme.org/terms/Terms_Use.cfm

In the above expression, $\eta = z/L$; the subscript c implies properties evaluated at the head of the 4.3 μ band and $A_p = 1/L \int_{\Delta_i} a_w L \, dw$ is the Planck mean absorption coefficient.

Assuming that $T_1 = 1500$ K and $T_2 = 400$ K, and evaluating $a_w q^+$ the average temperature, the heat flux calculated from equation (19) for two specific cases and those obtained from other techniques [2] are compared in Table 1. The agreement is excellent. The accuracy of the temperature profile result is illustrated in Fig. 1. It is important to note that the present mathematical development represents at least a ten-fold reduction in complexity comparing to all of the specific existing techniques.

Acknowledgment

This work is based upon work supported by the National Science Foundation Grant No. ENG78-05587.

References

1 Ozisik, M. N., *Radiative Transfer*, John Wiley & Sons, New York, 1973.

2 Chan, S. H., and Tien, C. L., "Infrared Radiative Heat Transfer in Non-Gray Non-Isothermal Gases," *International Journal of Heat and Mass Transfer*, Vol. 14, 1971, pp. 19–26.

3 Tiwari, S. N., "Applications of Infrared Band Model Correlation to Non-Gray Radiation," *International Journal of Heat and Mass Transfer*, Vol. 20, 1977, pp. 741–751.

4 Crosbie, A. L., and Viskanta, R., "Nongray Radiative Transfer in a Planar Medium Exposed to a Collimated Flux," *Journal Quantitative Spectroscopy Radiation Transfer*, Vol. 10, 1970, pp. 465–485.

5 Edwards, D. K., "Molecular Gas Band Radiation," *Advances in Heat Transfer*, Vol. 12, Academic Press, New York, 1976, pp. 116–195.

The Effects of Nonuniform Heat Transfer from an Annular Fin of Triangular Profile

P. J. Heggs,[1] D. B. Ingham,[2] and M. Manzoor[3]

Nomenclature

$h = (h_b + h_t)/2$, average heat transfer coefficient
h_b = heat transfer coefficient at fin-base
h_t = heat transfer coefficient at fin-tip
k = thermal conductivity
r = radial distance from tube axis
r_b = radius of fin-base
r_t = radius of fin-tip
t = half thickness of fin-base
$x = (r_t - r)/L$, dimensionless distance from fin-tip
Bi $= ht/k$, Biot number
H = nonuniform heat transfer coefficient
L = fin length
$M = (L/t)^2$ Bi/cos α, dimensionless
$N = 2(1 + \xi)$, dimensionless
$R = r_t/L$, dimensionless
T_b = temperature of fin-base
T_∞ = temperature of fluid
$\alpha = \tan^{-1}(t/L)$
$\epsilon = h_b/h_t$, dimensionless
$\theta = (T - T_\infty)/(T_b - T_\infty)$, dimensionless temperature
$\xi = (1 - \epsilon)$, dimensionless

Introduction

Finned surfaces are presently designed on the basis that the heat transfer coefficient is uniform over the fin surface as this permits the use of well established analytic solutions [1–3]. However, experimental investigations indicate that the heat transfer coefficient is not invariant [4–6]. In particular, for the annular geometry the heat transfer coefficient varies both radially and angularly over the fin surface (Wong [4]).

Analytic investigation of the effects of nonuniform heat transfer involve the use of assumed variation of the heat transfer coefficient, e.g., Han and Lefkowitz [7] employ heat transfer coefficients which vary as given powers of the displacement from the fin-base.

In this note the analytic solution for the temperature distribution within an annular triangular fin (Fig. 1) with linearly varying heat transfer coefficient is derived, and the corresponding fin efficiency is compared with experimental results.

[1] Senior Lecturer, Department of Chemical Engineering, University of Leeds, Leeds, England.

[2] Senior Lecturer, Department of Applied Mathematical Studies, University of Leeds, Leeds, England.

[3] Graduate Student, Department of Applied Mathematical Studies, University of Leeds, Leeds, England.

Contributed by the Heat Transfer Division for publication in the JOURNAL OF HEAT TRANSFER. Manuscript received by the Heat Transfer Division July 14, 1980.

Analysis

In the following analysis it is assumed that the thermal conductivity of the fin material, k, is constant and the heat transfer coefficient, H, varies linearly from h_b at the fin-base to h_t at the fin-tip, i.e.,

$$H(r) = \frac{2h}{(1+\epsilon)}\left(1 - (1-\epsilon)\frac{r_t - r}{r_t - r_b}\right) \tag{1}$$

where h is the average value of H and ϵ is the ratio of the heat transfer coefficient at the fin-base to that at the fin-tip.

For steady-state, one-dimensional conductive heat flow, an energy balance over an element of the fin, gives

$$\frac{d}{dr}\left(ry\frac{d}{dr}\theta\right) - \frac{H}{k\cos\alpha}r\theta = 0 \tag{2}$$

where the fin profile is described by

$$y(r) = \frac{t}{L}(r_t - r)$$

The inclusion of the exact representation for the incremental surface area, $(2\pi r\, dr/\cos\alpha)$, does not complicate the solution procedure, and has the advantage that the solution will be valid, even for small fin length to fin-base thickness ratios. This has particular significance as Lau and Tan [8] have recently shown, for a variety of fins, that the applicability of the one-dimensional approximation does not require the fin length to be large in comparison to the relevant transverse dimension.

The temperature distribution, and hence the heat transfer rate of the fin, are determined by solving equation (2) subject to the conditions

$$\text{i} \quad \text{at } r = r_b,\ \theta = 1 \tag{3}$$

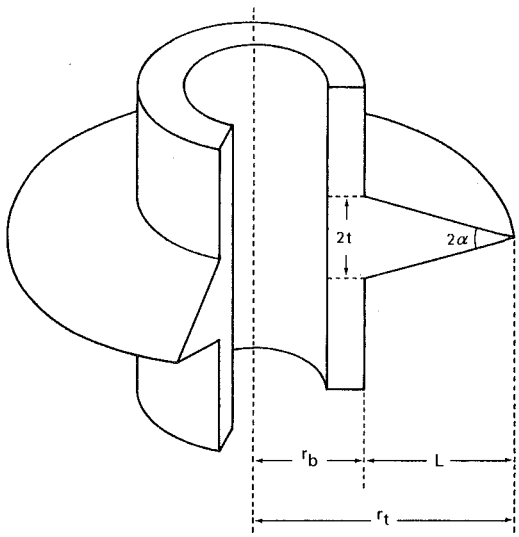

Fig. 1 The annular fin of triangular profile

Copyright © 1981 by ASME

Downloaded 20 Dec 2010 to 194.27.225.72. Redistribution subject to ASME license or copyright; see http://www.asme.org/terms/Terms_Use.cfm

ii at $r = r_t$, θ is finite. (4)

Using the dimensionless distance from the fin-tip as the new independent variable, and introducing the dimensionless quantities M, N, R and ξ, equation (2) becomes

$$\chi(R-x)\frac{d^2\theta}{dx^2} + (R-2x)\frac{d\theta}{dx} - MN(1-\xi x)(R-x)\theta = 0 \quad (5)$$

Applying the method of Frobenius, and following the solution procedure described by Smith and Sucec [2], the temperature distribution is found to be given by

$$\theta(r) = \frac{\sum_{n=0}^{\infty} a_n \left[\frac{r_t - r}{r_t - r_b}\right]^n}{\sum_{n=0}^{\infty} a_n} \quad (6)$$

where

$$a_0 = 1$$

$$a_1 = MN$$

$$a_2 = \frac{(2+NMR)a_1 - MN(1+\xi R)a_0}{4R} \quad (7)$$

$$a_n = \frac{(n(n-1)+MNR)a_{n-1} - MN(1+\xi R)a_{n-2} + MN\xi a_{n-3}}{n^2 R}, \quad n \geq 3$$

The solution for constant heat transfer coefficient, as derived by Smith and Sucec [2], is recovered by substituting $\epsilon = 1$ (i.e., $h_b = h_t$) into the above solution.

The rate at which one fin dissipates heat is given by

$$q = 4\pi r_b \frac{kt}{L} \frac{\sum_{n=1}^{\infty} n a_n}{\sum_{n=0}^{\infty} a_n} (T_b - T_\infty). \quad (8)$$

and the fin efficiency, which is defined as the ratio of the heat dissipated by fin to that which would be dissipated if the entire fin surface were at base temperature, is given by

$$\eta = \frac{\left(\sum_{n=1}^{\infty} n a_n \Big/ \sum_{n=0}^{\infty} a_n\right)}{MN\left(R - \frac{1}{2}(1+\xi R) + \frac{1}{3}\xi\right)\Big/(R-1)} \quad (9)$$

It can readily be shown that η is a function of the three independent parameters h_b/h_t, r_t/r_b and $L/t(\mathrm{Bi}/\cos\alpha)^{1/2}$.

Results and Conclusions

Although experimental investigations of fin arrays fail to agree on the form of the variation of the heat transfer coefficient, they agree that the minimum value of the heat transfer coefficient occurs at the fin-base. Therefore, the possible values that the parameters ϵ (= h_b/h_t) can realistically take lie between zero and unity. The fin efficiencies for the two extreme cases $\epsilon = 0$ and $\epsilon = 1$ are graphically presented in Fig. 2. The fin efficiencies for values of ϵ between zero and unity lie between the respective curves, e.g. as illustrated by the $\epsilon = 0.4$ curves in Fig. 2.

It is apparent from these results that for a given value of the average heat transfer coefficient, the maximum fin efficiency is given by $\epsilon = 1$ and the minimum by $\epsilon = 0$. Since $\epsilon = 1$ corresponds to the case of constant heat transfer coefficient it may be deduced that linear variation of the heat transfer coefficient reduces the fin efficiency;

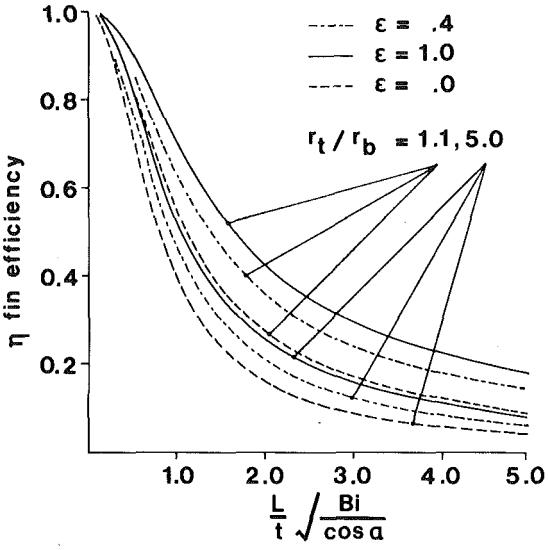

Fig. 2 Efficiency of the annular fin of triangular profile

within the practical range of values of the parameter M, the maximum reduction in the fin efficiency is of the order of 30 per cent. However, in practice, reductions in the fin efficiency are unlikely to be so pronounced, as experimental results indicate that the heat transfer coefficient at the fin-base is nonzero, i.e., $\epsilon \neq 0$.

Yudin and Tokhtarova [6] investigated the effects of heat transfer nonuniformity from an annular rectangular fin, and on the basis of a combined analytic and experimental study derived the relation

$$\eta_{H\ \text{Nonuniform}} = \left(1.0 - 0.058\frac{L}{t}\mathrm{Bi}^{1/2}\right)\eta_{H\ \text{Constant}} \quad (10)$$

The fin efficiency of the triangular annular fin, equation (9), agrees to within 3 per cent of Yudin and Tokhtarova's solution when $\epsilon = 0.4$. The slight discrepancy may be attributed to the difference in fin profiles. It is therefore suggested that the $\epsilon = 0.4$ curves in Fig. 2 be employed for the design of annular triangular fins.

Thus, it is unnecessary to implement higher order variations of the heat transfer coefficient, as results consistent with experimental investigations can be obtained using the linear variation.

Acknowledgment

The financial support given to M. Manzoor by the Science Research Council is gratefully acknowledged.

References

1 Gardner, K. A., "Efficiency of Extended Surface," Trans. ASME, Vol. 67, 1945, pp. 621–631.

2 Smith, P. J. and Sucec, J., "Efficiency of Circular Fin of Triangular Profile," ASME JOURNAL OF HEAT TRANSFER, Vol. 91, 1969, pp. 181–182.

3 Kern, D. Q., and Kraus, A. D., *Extended Surface Heat Transfer*, McGraw-Hill, New York, 1972.

4 Wong, P. W., "Mass and Heat Transfer from Circular Finned Cylinders," *Journal Institution of Heating and Ventilating Engineers*, 1966, pp. 1–23.

5 Stachiewicz, J. W., "Effect of Variation of Local Film Coefficient on Fin Performance," ASME JOURNAL OF HEAT TRANSFER, Vol. 91, 1969, pp. 21–26.

6 Yudin, V. F., and Tokhtorova, L. C., "Investigation of the Correction Factor ψ for the Theoretical Effectiveness of a Round Fin," *Thermal Engineering*, 1973, pp. 66–68.

7 Han, L. S., and Lefkowitz, S. G., ASME Paper No. 60-WA-41, 1960.

8 Lau, W. and Tan, C. W., "Errors in One-Dimensional Heat Transfer Analysis," ASME JOURNAL OF HEAT TRANSFER, Vol. 95, 1973, pp. 549–551.

Downloaded 20 Dec 2010 to 194.27.225.72. Redistribution subject to ASME license or copyright; see http://www.asme.org/terms/Terms_Use.cfm

Tube Wall Temperatures of an Eccentrically Located Horizontal Tube within a Narrow Annulus with Tube Contact

R. W. Alperi[1]

Introduction

A previous article [1] indicated the analytical solution for an eccentrically located, horizontal tube within another cylinder which formed a narrow annulus. The tube could be heated using either an electrical power source or a hot water source. It was postulated that it could be possible that the upper portion of the eccentric annulus (postulated to have the smallest clearance) could become vapor blanketed (dryout) while saturated boiling occurred over the remainder of the annular region. The analytical tube wall temperature distribution was the subject of that paper. However, as an extreme case of eccentricity, the tube could be located against the wall of the cylinder which encloses the tube (metal-to-metal contact). In that case, the boundary conditions and resulting solution vary and are the subject of this Technical Note.

Analysis

Under the conditions proposed above, the upper region would have metal-to-metal contact and dependent on the contact resistance (due to applied force and foreign material deposits) could have a high or low overall resistance to heat transfer. The narrow annular region on either side of the metal-to-metal contact region could have a small heat transfer coefficient (h_2) due to being steam blanketed while the remainder of the annular region has local boiling and a high heat transfer coefficient (h_1). Two modes of heating the central tube are considered, electrical heating and hot water heating. For the case where the tube is heated by an electrical heater, the inside tube wall is assumed to have a constant heat flux as the boundary condition while the inside wall temperature is assumed to be constant when the tube is heated by a hot water energy source. Axial conduction effects are neglected in this analysis.

The governing equation for the steady-state temperature distribution in a tube which has a variable circumferential heat transfer coefficient along the outer radius is

$$\frac{\partial^2 t}{\partial r^2} + \frac{1}{r}\frac{\partial t}{\partial r} + \frac{1}{r^2}\frac{\partial^2 t}{\partial \Psi^2} = 0 \tag{1}$$

The boundary conditions for the two cases considered here are:

Electrically Heated

$$@\ r = R_i,\ -K\frac{\partial t}{\partial r} = q'' = \text{Constant}$$

$$@\ r = R_0,\ -\phi_3 \le \Psi \le \phi_3,\ -K\frac{\partial t}{\partial r} = q_3 \tag{2}$$

$$\left.\begin{matrix}\phi_3 \le \Psi \le \phi_2 \\ -\phi_2 \le \Psi \le -\phi_3\end{matrix}\right\} -K\frac{\partial t}{\partial r} = h_2(t - t_\infty)$$

$$\left.\begin{matrix}\phi_2 \le \Psi \le \pi \\ -\pi \le \Psi \le -\phi_2\end{matrix}\right\} -K\frac{\partial t}{\partial r} = h_1(t - t_\infty)$$

where q_3 is the heat transfer in the contact material.

Hot Water Heated

$$@\ r = R_i,\ t = t_w = \text{Constant}$$

$$\left.\begin{matrix}@\ r = R_0\end{matrix}\right\} \text{Same as for electrically heated case} \tag{3}$$

The general solution for each case can be written as

$$t = H_0 + H_1 \ell nr + (H_2 \ell nr + H_3)\Psi + \sum_{m=1}^{\infty}(A_m r^m + B_m r^{-m})\cos m\Psi + \sum_{m=1}^{\infty}(C_m r^m + D_m r^{-m})\sin m\Psi \tag{4}$$

Method of Solution

Initially, the inner boundary condition is used in the assumed temperature solution. Then the heat flux around the periphery of the tube is expanded as a Fourier series and the Fourier coefficients are evaluated. In the heat flux expressions, the assumed temperature is used in the evaluations. In particular, the conductive heat transfer in the contact region is replaced by an equivalent heat transfer term which uses the concept that the heat transfer at the tube surface ($r = R_0$) is equal to the local heat transfer by conduction in the contact material ($q_3 = -K_3/\partial t/\partial r$). In general, the heat transfer in the contact material would need to be solved to obtain the temperature distribution in the contact material. However, an analytical solution can be obtained by assuming the contact material has the same thermal conductivity as the tube material ($K_3 = K$) and the temperature profile at the tube surface is the same as is in the contact material at their point of contact. This assumption has been verified by inspection of temperature profiles obtained from some limited experimental data and numerical solutions of similar configurations. Once the heat flux distribution from the wall is obtained as a Fourier series, this can be set equal to the actual heat flux in the tube wall at $r = R_0$ and by comparing the coefficients of the terms, the table of coefficients is formed. It should be noted that in this way, only the thermal conductivity (K_3) of the contact material appears in the table of coefficients and represents the influence of the contact material since the assumed temperature distribution was utilized in the contact material heat transfer term.

Constant Heat Flux

Evaluating the above expression with the constant heat flux boundary condition for the electrically heated tube case at the inner boundary results in expressions for H_1 and A_m in terms of B_m. Hence, the expression for temperature becomes:

$$t = H_0 - \frac{q''R_i}{K}\ell nr + \sum_{m=1}^{\infty} B_m(r^m R_i^{-2m} + r^{-m})\cos m\Psi \tag{5}$$

The above expression was evaluated at the outer boundary condition where the product of $h(t - t_\infty)$ was expanded in terms of a Fourier series for the three different regions assumed in this analysis and the coefficients of the like terms are equated to each other. The resulting coefficients are summarized in Table 1. As can be seen, there are $m = n$ equations that can be solved uniquely for the individual coefficients utilizing the constant term also shown in Table 1.

In Table 1, the following definitions are utilized:

$$\alpha_0 = H_0 - t_\infty,\ \alpha_0' = \frac{-q''R_i}{KR_0}$$

$$\alpha_m = R_0^m R_i^{-2m} + R_0^{-m} \tag{6}$$

$$\alpha_m' = m(R_0^{m-1}R_i^{-2m} - R_0^{-m-1})$$

The final solution for temperature can then be written as

$$t = \alpha_0 - \frac{q''R_i}{K}\ln\frac{r}{R_0} + \sum_{m=1}^{\infty} B_m(r^m R_i^{-2m} + r^{-m})\cos m\Psi + t_\infty \tag{7}$$

[1] Fellow Engineer, Bettis Atomic Power Laboratory, Box 79, West Mifflin, Pa. 15122

Contributed by the Heat Transfer Division for publication in the JOURNAL OF HEAT TRANSFER. Manuscript received by the Heat Transfer Division February 8, 1980.

Copyright © 1981 by ASME

Downloaded 20 Dec 2010 to 194.27.225.72. Redistribution subject to ASME license or copyright; see http://www.asme.org/terms/Terms_Use.cfm

Table 1 Summary of solution coefficients, constant heat flux

α_0	B_1	B_2	B_3	$B_4, \ldots$	B_n	CONSTANT TERM
$-\frac{1}{\pi}\{(h_1-h_2)\phi_2-h_1\pi + h_2\phi_3\}$	$-\frac{1}{\pi}\{(h_1-h_2)a_1 \sin\phi_2 + (K_3a_1'+h_2a_1)\sin\phi_3\}$	$-\frac{1}{\pi}\{(h_1-h_2)a_2\frac{\sin 2\phi_2}{2} + (K_3a_2'+h_2a_2)\frac{\sin 2\phi_3}{2}\}$	$-\frac{1}{\pi}\{(h_1-h_2)a_3\frac{\sin 3\phi_2}{3} + (K_3a_3'+h_2a_3)\frac{\sin 3\phi_3}{3}\}$	$-\frac{1}{\pi}\{(h_1-h_2)a_4\frac{\sin 4\phi_2}{4} + (K_3a_4'+h_2a_4)\frac{\sin 4\phi_3}{4}\}$	$-\frac{1}{\pi}\{(h_1-h_2)a_n\frac{\sin n\phi_2}{n} + (K_3a_n'+h_2a_n)\frac{\sin n\phi_3}{n}\}$	$q''\frac{R_i}{R_0} + K_3a_0'\phi_3$
$\frac{2(h_1-h_2)\sin\phi_2}{\pi} + \frac{2h_2}{\pi}\sin\phi_3$	$\frac{1}{\pi}\{(h_1-h_2)a_1(\frac{\sin 2\phi_2}{2}+\phi_2) + (h_2a_1+K_3a_1')(\frac{\sin 2\phi_3}{2}+\phi_3) - (h_1a_1+Ka_1')\pi\}$	$\frac{1}{\pi}\{(h_1-h_2)a_2(\frac{\sin 3\phi_2}{3}+\sin\phi_2) + (h_2a_2+K_3a_2')(\frac{\sin 3\phi_3}{3}+\sin\phi_3)\}$	$\frac{1}{\pi}\{(h_1-h_2)a_3(\frac{\sin 4\phi_2}{4}+\frac{\sin 2\phi_2}{2}) + (h_2a_3+K_3a_3')(\frac{\sin 4\phi_3}{4}+\frac{\sin 2\phi_3}{2})\}$	$\frac{1}{\pi}\{(h_1-h_2)a_4(\frac{\sin 5\phi_2}{5}+\frac{\sin 3\phi_2}{3}) + (h_2a_4+K_3a_4')(\frac{\sin 5\phi_3}{5}+\frac{\sin 3\phi_3}{3})\}$	$\frac{1}{\pi}\{(h_1-h_2)a_n(\frac{\sin(n+1)\phi_2}{n+1}+\frac{\sin(n-1)\phi_2}{n-1}) + (h_2a_n+K_3a_n')(\frac{\sin(n+1)\phi_3}{n+1}+\frac{\sin(n-1)\phi_2}{n-1})\}$	$-\frac{2K_3}{\pi}a_0'\sin\phi_3$
$\frac{2(h_1-h_2)}{\pi}\frac{\sin 2\phi_2}{2} + \frac{2h_2}{\pi}\frac{\sin 2\phi_3}{3}$	$\frac{1}{\pi}\{(h_1-h_2)a_1(\frac{\sin 3\phi_2}{3}+\sin\phi_2) + (h_2a_1+K_3a_1')(\sin\phi_3+\frac{\sin 3\phi_3}{3})\}$	$\frac{1}{\pi}\{(h_1-h_2)a_2(\frac{\sin 4\phi_2}{4}+\phi_2) + (h_2a_2+K_3a_2')(\frac{\sin 4\phi_3}{4}+\phi_3) - \pi(h_1a_2+Ka_2')\}$	$\frac{1}{\pi}\{(h_1-h_2)a_3(\frac{\sin 5\phi_2}{5}+\sin\phi_2) + (h_2a_3+K_3a_3')(\frac{\sin 5\phi_3}{5}+\sin\phi_3)\}$	$\frac{1}{\pi}\{(h_1-h_2)a_4(\frac{\sin 6\phi_2}{6}+\frac{\sin 2\phi_2}{2}) + (h_2a_4+K_3a_4')(\frac{\sin 6\phi_3}{6}+\frac{\sin 2\phi_3}{2})\}$	$\frac{1}{\pi}\{(h_1-h_2)a_n(\frac{\sin(n+2)\phi_2}{n+2}+\frac{\sin(n-2)\phi_2}{n-2}) + (h_2a_n+K_3a_n')(\frac{\sin(n+2)\phi_3}{n+2}+\frac{\sin(n-2)\phi_3}{n-2})\}$	$-2K_3\frac{a_0'}{\pi}\frac{\sin 2\phi_3}{2}$
⋮	⋮	⋮	⋮	⋮	⋮	⋮
$\frac{2h_2}{\pi}\frac{\sin m\phi_3}{m} + 2(h_1-h_2)\frac{\sin m\phi_2}{m\pi}$	$\frac{1}{\pi}\{(h_1-h_2)a_1(\frac{\sin(m+1)\phi_2}{m+1} + \frac{\sin(m-1)\phi_2}{m-1}) + (h_2a_1+K_3a_1')(\frac{\sin(m+1)\phi_3}{m+1} + \frac{\sin(m-1)\phi_3}{m-1})\}$	$\frac{1}{\pi}\{(h_1-h_2)a_2(\frac{\sin(m+2)\phi_2}{m+2} + \frac{\sin(m-2)\phi_2}{m-2}) + (h_2a_2+K_3a_2')(\frac{\sin(m+2)\phi_3}{m+2} + \frac{\sin(m-2)\phi_3}{m-2})\}$	. . .	. . .	$\frac{1}{\pi}\{(h_1-h_2)a_n(\frac{\sin(n+m)\phi_2}{n+m}+\frac{\sin(n-m)\phi_2}{n-m}) + (h_2a_n+K_3a_n')(\frac{\sin(n+m)\phi_3}{n+m}+\frac{\sin(n-m)\phi_3}{n-m})\}$ IF $n=m$, $\frac{\sin(n-m)\phi}{n-m}=\phi$ PLUS ADDED TERM $\{-(h_1a_n+Ka_n')\pi\}$	$-2K_3\frac{a_0'}{\pi}\frac{\sin m\phi_3}{m}$

Table 2 Summary of solution coefficients, constant wall temperature

γ_0	B_1	B_2	B_3	$B_4, \ldots$	B_n	CONSTANT TERM
$\frac{1}{\pi}\{(h_1-h_2)\phi_2-h_1\pi+\phi_3h_2 - \frac{(\pi K-K_3\phi_3)}{R_0\ln\frac{R_0}{R_i}}\}$	$-\frac{1}{\pi}\{(h_1-h_2)\gamma_1\sin\phi_2 + (K_3\gamma_1'+h_2\gamma_1)\sin\phi_3\}$	$-\frac{1}{\pi}\{(h_1-h_2)\gamma_2\frac{\sin 2\phi_2}{2} + (K_3\gamma_2'+h_2\gamma_2)\frac{\sin 2\phi_3}{2}\}$	$-\frac{1}{\pi}\{(h_1-h_2)\gamma_3\frac{\sin 3\phi_2}{3} + (K_3\gamma_3'+h_2\gamma_3)\frac{\sin 3\phi_3}{3}\}$	$-\frac{1}{\pi}\{(h_1-h_2)\gamma_4\frac{\sin 4\phi_2}{4} + (K_3\gamma_4'+h_2\gamma_4)\frac{\sin 4\phi_3}{4}\}$	$-\frac{1}{\pi}\{(h_1-h_2)\gamma_n\frac{\sin n\phi_2}{n} + (h_2\gamma_n+K_3\gamma_n')\frac{\sin n\phi_3}{n}\}$	$\frac{(t_w-t_\infty)}{R_0\ln\frac{R_0}{R_i}}(K-\frac{K_3\phi_3}{\pi})$
$\frac{2(h_1-h_2)}{\pi}\sin\phi_2 + \frac{2}{\pi}(h_2+\frac{K_3}{R_0})\sin\phi_3$	$\frac{1}{\pi}\{(h_1-h_2)\gamma_1(\frac{\sin 2\phi_2}{2}+\phi_2) + (h_2\gamma_1+K_3\gamma_1')(\frac{\sin 2\phi_3}{2}+\phi_3) - \pi(h_1\gamma_1+K\gamma_1')\}$	$\frac{1}{\pi}\{(h_1-h_2)\gamma_2(\frac{\sin 3\phi_2}{3}+\sin\phi_2) + (h_2\gamma_2+K_3\gamma_2')(\frac{\sin 3\phi_3}{3}+\sin\phi_3)\}$	$\frac{1}{\pi}\{(h_1-h_2)\gamma_3(\frac{\sin 4\phi_2}{4}+\frac{\sin 2\phi_2}{2}) + (h_2\gamma_3+K_3\gamma_3')(\frac{\sin 4\phi_3}{4}+\frac{\sin 2\phi_3}{2})\}$	$\frac{1}{\pi}\{(h_1-h_2)\gamma_4(\frac{\sin 5\phi_2}{5}+\frac{\sin 3\phi_2}{3}) + (h_2\gamma_4+K_3\gamma_4')(\frac{\sin 5\phi_3}{5}+\frac{\sin 3\phi_3}{3})\}$	$\frac{1}{\pi}\{(h_1-h_2)\gamma_n(\frac{\sin(n+1)\phi_2}{n+1}+\frac{\sin(n-1)\phi_2}{n-1}) + (h_2\gamma_n+K_3\gamma_n')(\frac{\sin(n-1)\phi_3}{n-1}+\frac{\sin(n+1)\phi_3}{n+1})\}$	$\frac{2K_3}{\pi}\frac{\sin\phi_3}{R_0}(\frac{t_w-t_\infty}{\ln\frac{R_0}{R_i}})$
$\frac{2(h_1-h_2)}{\pi}\frac{\sin 2\phi_2}{2} + \frac{2}{\pi}(h_2+\frac{K_3}{R_0})\frac{\sin 2\phi_3}{2}$	$\frac{1}{\pi}\{(h_1-h_2)\gamma_1(\frac{\sin 3\phi_2}{3}+\sin\phi_2) + (h_2\gamma_1+K_3\gamma_1')(\frac{\sin 3\phi_3}{3}+\sin\phi_3)\}$	$\frac{1}{\pi}\{(h_1-h_2)\gamma_2(\frac{\sin 4\phi_2}{4}+\phi_2) + (h_2\gamma_2+K_3\gamma_2')(\frac{\sin 4\phi_3}{4}+\phi_3) - \pi(h_1\gamma_2+K\gamma_2')\}$	$\frac{1}{\pi}\{(h_1-h_2)\gamma_3(\frac{\sin 5\phi_2}{5}+\sin\phi_2) + (h_2\gamma_3+K_3\gamma_3')(\frac{\sin 5\phi_3}{5}+\sin\phi_3)\}$	$\frac{1}{\pi}\{(h_1-h_2)\gamma_4(\frac{\sin 6\phi_2}{6}+\frac{\sin 2\phi_2}{2}) + (h_2\gamma_4+K_3\gamma_4')(\frac{\sin 6\phi_3}{6}+\frac{\sin 2\phi_3}{2})\}$	$\frac{1}{\pi}\{(h_1-h_2)\gamma_n(\frac{\sin(n+2)\phi_2}{n+2}+\frac{\sin(n-2)\phi_2}{n-2}) + (h_2\gamma_n+K_3\gamma_n')(\frac{\sin(n+2)\phi_3}{n+2}+\frac{\sin(n+2)\phi_3}{n-2})\}$	$\frac{2K_3}{\pi}\frac{\sin 2\phi_3}{R_0\ 2}(\frac{t_w-t_\infty}{\ln\frac{R_0}{R_i}})$
⋮	⋮	⋮	⋮	⋮	⋮	⋮
$\frac{2}{\pi}(h_2+\frac{K_3}{R_0})\frac{\sin m\phi_3}{m} + 2\frac{(h_1-h_2)}{\pi}\frac{\sin m\phi_2}{2}$	$\frac{1}{\pi}\{(h_1-h_2)\gamma_1(\frac{\sin(m+1)\phi_2}{m+1}+\frac{\sin(m-1)\phi_2}{m-1}) + (h_2\gamma_1+K_3\gamma_1')(\frac{\sin(m+1)\phi_3}{m+1}+\frac{\sin(m-1)\phi_3}{m-1})\}$	$\frac{1}{\pi}\{(h_1-h_2)\gamma_2(\frac{\sin(m+2)\phi_2}{m+2}+\frac{\sin(m-2)\phi_2}{m-2}) + (h_3\gamma_2+K_3\gamma_2')(\frac{\sin(m+2)\phi_3}{m+2}+\frac{\sin(m-2)\phi_3}{m-2})\}$	. . .	. . .	$\frac{1}{\pi}\{(h_1-h_2)\gamma_n(\frac{\sin(n+m)\phi_2}{n+m}+\frac{\sin(n-m)\phi_2}{n-m}) + (h_2\gamma_n+K_3\gamma_n')(\frac{\sin(n+m)\phi_3}{n+m}+\frac{\sin(n-m)\phi_3}{n-m})\}$ IF $n=m$, $\frac{\sin(n-m)\phi}{n-m}=\phi$ PLUS ADDED TERM $\{-(h_1\gamma_n+K\gamma_n')\pi\}$	$\frac{2K_3}{\pi}\frac{\sin m\phi_3}{R_0}\frac{m}{m}(\frac{t_w-t_\infty}{\ln\frac{R_0}{R_i}})$

Constant Wall Temperature

Evaluating the general solution for temperature (3) similarly for a constant wall temperature results in the following expression for temperature

$$t = t_\infty + \gamma_0 + \sum_{m=1}^{\infty} B_m(r^m R_i^{-2m} + r^{-m})\cos m\Psi \qquad (8)$$

where the coefficients of B_m and γ_0 are summarized in Table 2. The following definitions are utilized in Table 2:

$$\gamma_m = R_0^{-m} - R_i^{-2m}R_0^m$$
$$\gamma_0 = t_w - t_\infty + H_1 \ln\frac{R_0}{R_i} \qquad (9)$$
$$\gamma_0' = \frac{-H_1}{R_0}$$
$$\gamma_m' = -m(R_0^{-m-1} + R_i^{-2m}R_0^{m-1})$$

It should be noted that H_0 and H_1 are arbitrary Fourier coefficients and can be obtained from the terms used in their definitions; however, they are not required in the final temperature solution since the α_0, γ_0, and γ_0' terms are found directly from the table.

Results

The above temperature solutions were used to evaluate the tube wall temperatures for an arbitrary-sized region of metal-to-metal contact ($\phi_3 = 9$ deg for the constant heat flux case and $\phi_3 = 5$ deg for the constant wall temperature case) and varying degrees of vapor blanketing that might occur within the narrow annulus crevice region. This was done by varying the vapor blanketed angle (ϕ_2) from the metal-to-metal contact region to π radians (no vapor blanketing to being all vapor blanketed). Values of $h_1 = 17{,}038.2$ W/M^2°C and $h_2 = 567.9$ W/M^2°C were used for these calculations. The thermal conductivity utilized in these calculations for both the tube and the metal-to-metal contact region was 17.3 W/M °C. This implies good tube to cylinder support metal contact; hence, good thermal heat transfer occurs in that region. A low value of the thermal conductivity in the metal-to-metal contact region (ϕ_3) would indicate high contact resistance and poor thermal heat transfer. The tube has an outside radius of 6.35 mm and an inside radius of 5 mm which corresponds to the Shippingport PWR 1*A* and 1*D* steam generator tube size. Typical cases of an electrically heated tube are shown in Fig. 1 and for water heated tubes in Fig. 2. As can be seen, the temperature variations are significant between the areas of vapor blanketing and the region of local boiling. In the electrically heated tube case, the tube wall temperatures in the region of the metal-to-metal contact shows only a slight decrease in temperature while the water-heated tube, since it does not have the power input potential available as does the electrically heated case (constant heat flux), shows a significant temperature decrease due to the assumed good heat conduction path. If the metal-to-metal contact region is assumed to have a high contact resistance (low thermal conductivity), then the tube wall temperatures

Downloaded 20 Dec 2010 to 194.27.225.72. Redistribution subject to ASME license or copyright; see http://www.asme.org/terms/Terms_Use.cfm

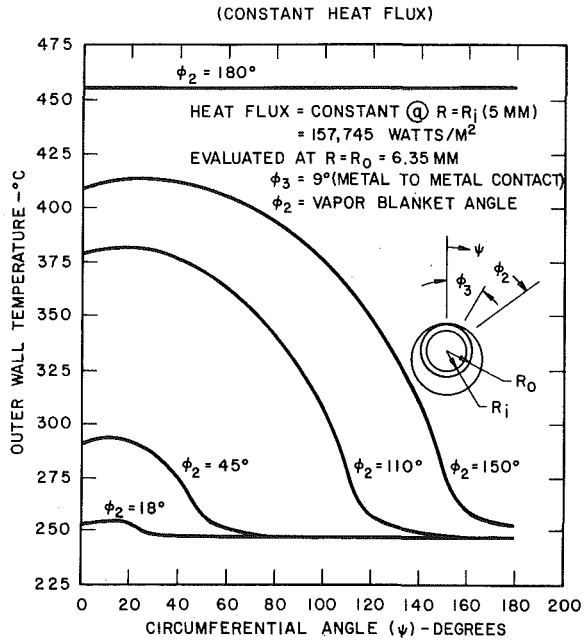

Fig. 1 Circumferential variation of wall temperature (constant heat flux)

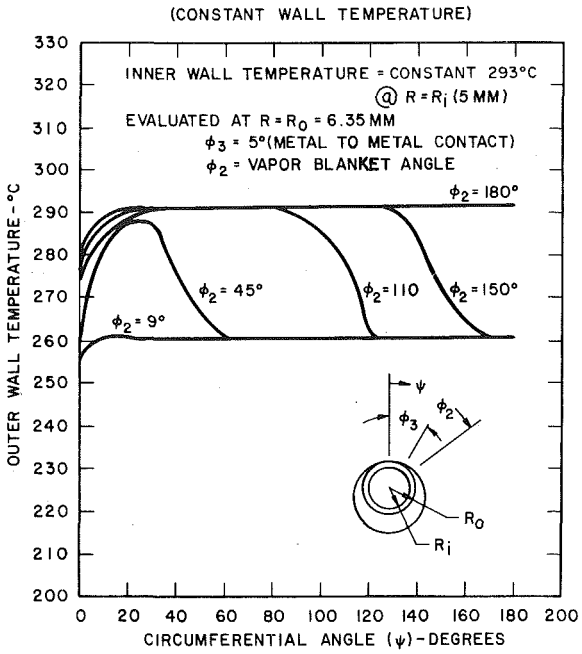

Fig. 2 Circumferential variation of wall temperature (constant wall temperature)

become very high in that region for the electrically heated tube case due to the constant heat flux assumption. However, for the water heated case, the temperature rise is limited to that available to it, i.e., the inner fluid temperature. It is significant to note that the results indicate that the wall temperatures vary significantly around the periphery and interpretation of their meaning does depend on understanding the position of the tube and the physical nature of any contact before one can make a judgement on the external heat transfer conditions.

Reference

1 Alperi, R. W., "Tube Wall Temperatures of an Eccentrically Located Horizontal Tube Within a Narrow Annulus," ASME JOURNAL OF HEAT TRANSFER, Vol. 100, 1978, pp. 548–550.

Downloaded 20 Dec 2010 to 194.27.225.72. Redistribution subject to ASME license or copyright; see http://www.asme.org/terms/Terms_Use.cfm